



# Conference Proceedings of the 5<sup>th</sup> European sCO2 Conference 2023



## **Location:**

**Vienna House Diplomat Prague  
Evropská 15  
160 41 Prague  
Czech Republic**

**Date: March 14th to 16th, 2023**

## Conference Committee

Dieter Brillert, Universität Duisburg-Essen, Chair of Turbomachinery (conference chair)  
Rene Pecnik, Technical University of Delft, Department of Process and Energy  
Albannie Cagnac, EDF R&D, Fluid Dynamics, Power Generation and Environment Department  
Václav Dostál, Czech Technical University in Prague  
Otakar Frýbort, Research Centre Řež, Energy Technology Department  
Uwe Gampe, Technische Universität Dresden, Chair of Thermal Power Machinery and Plants  
Markus Haider, Technical University of Vienna, Institute for Energy Systems and Thermodynamics  
Andreas Jäger, Technische Universität Dresden, Chair of Thermal Power Machinery and Plants  
Jörg Starflinger, University of Stuttgart, Institute of Nuclear Technology and Energy Systems (IKE)  
Teemu Turunen-Saaresti, LUT University, School of Energy Systems  
Andreas Werner, Technical University of Vienna, Institute for Energy Systems and Thermodynamics  
Marco Astolfi, Energy Department of Politecnico di Milano

## Imprint

Conference Proceedings of the 5th European sCO<sub>2</sub> Conference

2023

ISSN 2510-7852

DOI: 10.17185/duublico/77259

URN: urn:nbn:de:hbz:465-20230427-152859-2

Publishing Institution:

Universität Duisburg-Essen

Universitätsbibliothek, DuEPublico

Universitätsstraße 9-11

45141 Essen

<https://duublico2.uni-due.de>



This work may be used under a [Creative Commons Attribution 4.0 International license](https://creativecommons.org/licenses/by/4.0/).





## Agenda - March 15<sup>th</sup>

09:00 – 09:15

### Welcome and Introduction

Dieter Brillert (1) and Václav Dostál (2)

1: University of Duisburg-Essen / UDE

2: Czech Technical University in Prague / CTU

09:15 – 09:45

### Keynote Speech

Otakar Frýbort, Research Centre Řež

09:45 – 10:15

### Coffee break

10:15 – 11:45

### Heat Exchanger and Transfer (Session 01)

Chairman: Jörg Starflinger, University Stuttgart

#### Subsessions

- **128 - Optimization of the air channels on the Diverse Ultimate Heat Sink for sCO<sub>2</sub> power cycle**  
Filip, Radomír (1); Tioual-Demange, Sarah; Taiclet, Guillaume (2)  
1: Research Centre Řež, Czech Republic  
2: Fives group, France
- **132 - Thermodynamic Analysis of a Reactive Particle-to-sCO<sub>2</sub> Heat Exchanger for Recovering Stored Thermochemical Energy**  
Siefering, Bryan J.; Umer, Muhammad (1); Stechel, Ellen B. (2); Fronk, Brian M. (1)  
1: The Pennsylvania State University  
2: Arizona State University
- **147 - A methodology to design air-cooled condensers for supercritical power cycles using carbon dioxide and carbon dioxide mixtures**  
Rodríguez-de Arriba, Pablo; Crespi, Francesco; Sánchez, David; Muñoz, Antonio  
Department of Energy Engineering, University of Seville, Spain



10:15 – 11:45

## sCO2 Applications and Energy Systems (Session 02)

Chairman: Václav Dostál, *TU Prague*

### Subsessions

- **125 - Part load analysis of a constant inventory supercritical CO2 power plant for waste heat recovery in cement industry**  
Astolfi, Marco; Alfani, Dario; Binotti, Marco; Silva, Paolo; Persico, Giacomo  
*Politecnico di Milano, Italy*
- **116 - Performance and Cost Potential for Direct-Fired Supercritical CO2 Natural Gas Power Plants**  
Pidaparti, Sandeep R.; White, Charles W. (1); Liese, Eric; Weiland, Nathan T. (2)  
*1: National Energy Technology Laboratory/NETL Support Contractor*  
*2: National Energy Technology LaboratorysCO2 power cycle design without heat source*
- **139 - Influence of variations of flue gas and ambient temperature on the dynamics and performance of a MW scale supercritical CO2 waste heat to power unit**  
Olumayegun, Olumide; Marchionni, Matteo; Usman, Muhammad; Tassou, Savvas A.  
*Brunel University London, United Kingdom*

11:45 – 12:00

Group photo

12:00 – 13:15

Lunch

13:15 – 14:45

### Panel Session

Chairman: Rene Pecnik, *TU Delft*

Albannie Cagnac, *Électricité de France / EDF*

#### **Future outlook and challenges for implementing sCO2 energy conversion systems**

David Sánchez (1); Stefan Glos (2); Leonhard Wolscht (3)

*1: Universidad de Sevilla*

*2: Siemens Energy AG*

*3: MAN Energy Solution*

14:45 – 15:15

Coffee Break



15:15 – 16:45      Heat Exchanger and Transfer / sCO<sub>2</sub> Experiments and  
Loops (Session 03)

Chairman: Andreas Werner, *TU Vienna*

Subsessions

- **120 - Parametric analysis of heat exchanger design in a techno-economic optimization of a sCO<sub>2</sub> system**  
Geotelip, Thiago C. V.; Gampe, Uwe; Rath, Sebastian; Jäger, Andreas (1); Glos, Stefan (2)  
*1: Technische Universität Dresden, Germany*  
*2: Siemens Energy AG Mülheim, Germany*
- **127 - Modeling of Autonomous Brayton Cycle (ABC) Loop with GAMMA+ code for Micro Modular Reactor Simulation Application**  
Choi, Sungwook; Lee, Jeong Ik  
*KAIST, Republic of South Korea*
- **151 - CO<sub>2</sub> purification for sCO<sub>2</sub> loop in Rez - summary of the test results**  
Berka, Jan (1); Hlinčík, Tomáš; Purkarová, Eliška; Vagenknechtová, Alice; Ballek, Jakub-Vojtěch  
*1: Centrum vyzkumu Rez s.r.o., Czech Republic*  
*2: University of Chemistry and Technology Prague - Department of Gaseous and Solid Fuels and Air Protectio*

15:15 – 16:45      Fluid and Material Aspects (Session 04)

Chairman: Andreas Jäger, *TU Dresden*

Subsessions

- **118 - Review of HAYNES(R) 282(R) alloy for supercritical CO<sub>2</sub> structural applications**  
Tossey, Brett; Deodeshmukh, Vinay (1); Pint, Bruce (2)  
*1: Haynes International Inc., United States of America*  
*2: Oak Ridge National Laboratory, United States of America*
- **109 - Exergetic and Entropy Analysis of the PCRC and RCMCI Brayton Cycles Using s-CO<sub>2</sub> Mixtures. Case Study: Marine Applications**  
Tafur-Escanta, Paul Michael (1); Valencia-Chapi, Robert (2); Muñoz-Antón, Javier (1)  
*1: Universidad Politécnica de Madrid, Spain*  
*2: Universidad Técnica del Norte, Ecuador*
- **112 - Influence of the equation of state on the design of sCO<sub>2</sub>-power cycles**  
Rath, Sebastian; Gampe, Uwe; Jäger, Andreas  
*TU Dresden, Germany*

## Agenda - March 16<sup>th</sup>

09:00 – 10:30

### sCO2 Applications and Energy Systems / Heat Exchanger (Session 05)

Chairman: Paolo Silva, *Politecnico di Milano*

#### Subsessions

- **119 - Techno-economic analysis and optimization of sCO2 power cycle**  
Son, In Woo; Lee, Jeong Ik; Jeong, Yongju  
*The Korea Advanced Institute of Science and Technology (KAIST), Republic of South Korea*
- **130 - Performance analysis of PTES layouts evolving sCO2 for industrial WHR integration**  
Maccarini, Simone; Barberis, Stefano; Shamsi, Syed Safeer Mehdi; Gini, Lorenzo; Traverso, Alberto  
*Thermochemical Power Group, Department of Mechanical Engineering, University of Genova, Italy*
- **134 - Experimental and Numerical Study on Thermal Hydraulic Performance of Trapezoidal Printed Circuit Heat Exchanger for Supercritical CO2 Brayton Cycle**  
Ji, Yuxuan; Wang, Zheng; Wang, Mingxuan; Liu, Yafei; Xu, Haoran; Zhu, Peiwang; Xiao, Gang  
*Zhejiang University, People's Republic of China*

09:00 – 10:30

### Turbomachines and Cycles (Session 06)

Chairman: Teemu Turunen-Saaresti, *LUT University*

#### Subsessions

- **111 - Further development of a through-flow program by considering real gas equations of state**  
Ren, Haikun; Schuster, Sebastian; Brillert, Dieter  
*University of Duisburg-Essen, Chair of Turbomachinery, Germany*
- **155 - Design and Computational Assessment of a Supercritical CO2 Compressor for Waste Heat Recovery Applications**  
Romei, Allesandro; Persico, Giacomo; Gaetani, Paolo (1); Bellobuono, Ernani Fulvio; Toni, Lorenzo; Valente, Roberto (2)  
*1: Laboratory of Fluid Machines, Energy Dept., Politecnico di Milano, Italy*  
*2: Centrifugal Compressor and Expanders, NPD Baker Hughes, Nuovo Pignone, Italy*
- **145 - Design and Evaluation of Low Specific Speed Expander for Geothermal Energy Application**  
Patil, Abhay; Nielson, Jordan; Smith, Natalie (1); Weiss, Nathan (2)  
*1: Southwest Research Institute, United States of America*  
*2: Sage Geosystems Inc, United States of America*

10:30 – 11:00

### Coffee Break



11:00 – 12:30

## sCO2 Experiments and Loops (Session 07)

Chairman: Otakar Frýbort, *Research Centre Řež*

### Subsessions

- **114 - System analysis of experimental sCO2 cycle Sofia**  
Kriz, Daniel; Vlcek, Petr; Frybort, Otakar  
*Research Centre Rez, Czech Republic*
- **113 - Design and setup of the suCOO-Lab sCO2 test facility at TU Dresden**  
Rath, Sebastian; Gampe, Uwe; Breikopf, Cornelia; Jäger, Andreas  
*TU Dresden, Germany*
- **110 - Study of PID-based S-CO2 System Control Method**  
Kim, Gi Hyeon; Lee, Jeong Ik  
*Korea Advanced Institute of Science and Technology, Republic of South Korea*

11:00 – 12:30

## Turbomachines and Cycles (Session 08)

Chairman: Uwe Gampe, *TU Dresden*

### Subsessions

- **106 - Transient simulation and analysis of a supercritical CO2 heat removal system under different abnormal operation conditions**  
Hofer, Markus (1); Hecker, Frieder (2); Buck, Michael; Starflinger, Jörg (1)  
*1: University Stuttgart, Germany*  
*2: Simulator Centre of KSG/GfS*
- **115 - Dynamic Simulation and Experimental Validation of a 35 MW Heat Pump Based on a Transcritical CO2 Cycle**  
Wolscht, Leonhard (1); Knobloch, Kai (2); Jacquemoud, Emmanuel; Jenny, Philipp (1)  
*1: MAN Energy Solutions, Switzerland*  
*2: Department of Energy Conversion and Storage, Technical University of Denmark*
- **124 - Analysis of the potential of CO2 based mixtures to improve the efficiency of cogenerative waste heat recovery power plants**  
Morosini, Ettore (1); Donielli, Michele (2); Alfani, Dario; Astolfi, Marco (1); Di Marcoberardino, Gioele (2); Manzolini, Giampaolo (1)  
*1: Politecnico di Milano, Italy*  
*2: Università degli studi di Brescia, Italy*

12:30 – 13:30

Lunch



13:30 – 15:00

## sCO2 Experiments and Loops (Session 09)

Chairman: Marco Astolfi, *Politecnico di Milano*

### Subsessions

- **131 - The steady behavior of the supercritical carbon dioxide natural convection loop**  
Draskic, Marko; Bugeat, Benjamin; Pecnik, Rene  
*TU Delft, The Netherlands*
- **121 - Performance comparison of temperature sensors for closed cycles operating with supercritical CO2**  
Belleoud, Pierre; Palma, Eduardo Anselmi (1); Chetwynd-Chatwin, Jason (2); Roumeliotis, Ioannis (1)  
*1: Cranfield University, Bedfordshire, United Kingdom*  
*2: Rolls-Royce plc, Bristol, United Kingdom*
- **108 - sCO2 Test Facility at TU Wien: Design, Operation and Results**  
Illyés, Viktoria; Thanheiser, Stefan; Schwarzmayer, Paul (1); David, Pierre-Luc; Guerif, Xavier (2); Werner, Andreas; Haider, Markus (1)  
*1: TU Wien, Austria*  
*2: Kelvion Thermal Solutions*

13:30 – 15:00

## Turbomachines and Cycles (Session 10)

Chairman: Rene Pecnik, *TU Delft*

### Subsessions

- **146 - Design of Compact Radial Turboexpanders for sCO2 Power Systems**  
Romei, Alessandro; Persico, Giacomo (1); Biliotti, Davide, Milani, Alberto (2); Lottini, Fabrizio; Marconcini, Michele (3)  
*1: Politecnico di Milano*  
*2: Baker Hughes, Nuovo Pignone*  
*3: Università degli Studi di Firenze*
- **122 - Design of an axial sCO2 turbine for a demo plant in an industrial environment**  
Glos, Stefan; Musch, Christian; Stueer, Carmen; Schlehuber, Dominic; Wechsung, Michael  
*Siemens-Energy, Germany*
- **136 - Design and testing of a supercritical CO2 compander for 2 MW**  
Sauerborn, Markus; Schmitz, Ulrich; Bohn, Jürgen; Enneking, Martin; Brenner, Jens  
*Atlas Copco Energas GmbH/Atlas Copco Gas and Process*

15:00 – 15:15

## Closing Session

- Best paper award
- Announcement of the conference location and date for 2025



## Papers

- Hofer, Markus; Hecker, Frieder; Buck, Michael; Starflinger, Jörg ..... Page 11  
 Transient simulation and analysis of a supercritical CO<sub>2</sub> heat removal system  
 under different abnormal operation conditions  
<https://doi.org/10.17185/dupublico/77260>
- Illyés, Viktoria; Thanheiser, Stefan; Schwarzmayr, Paul; David, Pierre-Luc;  
 Guerif, Xavier; Werner, Andreas; Haider, Markus..... Page 22  
 sCO<sub>2</sub> test facility at TU Wien: design, operation and results  
<https://doi.org/10.17185/dupublico/77261>
- Tafur-Escanta, Paul Michael; Valencia-Chapi, Robert; Muñoz-Antón, Javier..... Page 38  
 Exergetic and Entropy Analysis of the PCRC and RCMCI Brayton Cycles  
 Using s-CO<sub>2</sub> Mixtures. Case Study: Marine Applications  
<https://doi.org/10.17185/dupublico/77263>
- Kim, Gi Hyeon; Lee, Jeong Ik..... Page 48  
 Study of PID-based S-CO<sub>2</sub> Precooler System Control Method  
<https://doi.org/10.17185/dupublico/77265>
- Ren, Haikun; Schuster, Sebastian; Brillert, Dieter ..... Page 58  
 Further development of a through-flow program by considering real gas equation of state  
<https://doi.org/10.17185/dupublico/77266>
- Rath, Sebastian; Gampe, Uwe; Jäger, Andreas ..... Page 66  
 Influence of the equation of state on the design of sCO<sub>2</sub>-power cycles  
<https://doi.org/10.17185/dupublico/77268>
- Rath, Sebastian; Gampe, Uwe; Breitkopf, Cornelia; Jäger, Andreas..... Page 78  
 Design and setup of the suCOO-Lab sCO<sub>2</sub> test facility at TU Dresden  
<https://doi.org/10.17185/dupublico/77269>
- Kriz, Daniel; Vlcek, Petr; Frybort, Otakar ..... Page 84  
 System analysis of experimental sCO<sub>2</sub> cycle Sofia  
<https://doi.org/10.17185/dupublico/77271>
- Wolscht, Leonhard; Knobloch, Kai; Jacquemoud, Emmanuel; Jenny, Philipp..... Page 93  
 Dynamic Simulation and Experimental Validation of a 35 MW Heat Pump Based  
 on a Transcritical CO<sub>2</sub> Cycle  
<https://doi.org/10.17185/dupublico/77273>
- Pidaparti, Sandeep R.; White, Charles W.; Liese, Eric; Weiland, Nathan T. .... Page 106  
 Performance and Cost Potential for Direct-Fired Supercritical CO<sub>2</sub> Natural Gas Power Plants  
<https://doi.org/10.17185/dupublico/77275>

- Tossey, Brett; Deodeshmukh, Vinay; Pint, Bruce ..... Page 121  
 Review of HAYNES® 282® alloy for supercritical CO<sub>2</sub> structural applications  
<https://doi.org/10.17185/dupublico/77277>
- Son, In Woo; Lee, Jeong Ik; Jeong, Yongju..... Page 130  
 Techno-economic analysis of sCO<sub>2</sub> power cycle for coal-fired power system  
<https://doi.org/10.17185/dupublico/77279>
- Gotelip, Thiago; Gampe, Uwe; Rath, Sebastian; Jäger, Andreas; Glos, Stefan..... Page 140  
 Parametric analysis of heat exchanger design in a techno-economic optimization of a  
 sCO<sub>2</sub> system  
<https://doi.org/10.17185/dupublico/77280>
- Belleoud, Pierre; Anselmi Palma, Eduardo; Chetwynd-Chatwin, Jason; Roumeliotis, Ioannis .. Page 153  
 Performance comparison of temperature sensors for closed cycles operating with  
 supercritical CO<sub>2</sub>  
<https://doi.org/10.17185/dupublico/77283>
- Glos, Stefan; Musch, Christian; Stueer, Carmen; Schlehuber, Dominic; Wechsung, Michael ... Page 162  
 Design of an axial sCO<sub>2</sub> turbine for a demo plant in an industrial environment  
<https://doi.org/10.17185/dupublico/77286>
- Morosini, Ettore; Doninelli, Michele; Alfani, Dario; Astolfi, Marco; Di Marcoberardino, Gioele;  
 Manzolini, Giampaolo..... Page 169  
 Analysis of the potential of CO<sub>2</sub> based mixtures to improve the efficiency of cogenerative  
 waste heat recovery power plants  
<https://doi.org/10.17185/dupublico/77287>
- Alfani, Dario; Astolfi, Marco; Binotti, Marco; Silva, Paolo; Persico, Giacomo ..... Page 179  
 Part load analysis of a constant inventory supercritical CO<sub>2</sub> power plant for waste heat  
 recovery in cement industry  
<https://doi.org/10.17185/dupublico/77288>
- Choi, Sungwook; Lee, Jeong Ik..... Page 186  
 Modeling of Autonomous Brayton Cycle Loop with GAMMA+ code for Micro Modular  
 Reactor Simulation Application  
<https://doi.org/10.17185/dupublico/77289>
- Filip, Radomír; Tioual-Demange, Sarah; Taiclet, Guillaume ..... Page 194  
 Optimisation of the air channels on the Diverse Ultimate Heat Sink for sCO<sub>2</sub> power cycles  
<https://doi.org/10.17185/dupublico/77298>
- Maccarini, Simone; Barberis, Stefano; Mehdi, Shamsi Syed Safeer; Gini, Lorenzo;  
 Traverso, Alberto ..... Page 206  
 Performance analysis of PTES layouts evolving sCO<sub>2</sub> for industrial WHR integration  
<https://doi.org/10.17185/dupublico/77306>

- Draskic, Marko; Bugeat, Benjamin; Pecnik, Rene..... Page 217  
 The steady behavior of the supercritical carbon dioxide natural circulation loop  
<https://doi.org/10.17185/dupublico/77307>
- Siefering, Bryan J.; Umer, Muhammad; Stechel, Ellen B.; Fronk, Brian ..... Page 226  
 Thermodynamic Analysis of a Reactive Particle-to-sCO<sub>2</sub> Heat Exchanger for Recovering  
 Stored Thermochemical Energy  
<https://doi.org/10.17185/dupublico/77309>
- Ji, Yuxuan; Wang, Zheng; Wang, Mingxuan; Liu, Yafei; Xu, Haoran; Zhu, Peiwan;  
 Xiao, Gang..... Page 236  
 Experimental and Numerical Study on Thermal Hydraulic Performance of Trapezoidal  
 Printed Circuit Heat Exchanger for Supercritical CO<sub>2</sub> Brayton Cycle  
<https://doi.org/10.17185/dupublico/77317>
- Sauerborn, Markus; Schmitz, Ulrich; Bohn, Jürgen; Enneking, Martin; Brenner, Jens ..... Page 244  
 Design and testing of a supercritical CO<sub>2</sub> compander for 2 MW output power  
<https://doi.org/10.17185/dupublico/77319>
- Olumayegun, Olumide; Marchionni, Matteo; Usman, Muhammad; Tassou, Savvas A. .... Page 252  
 Influence of variations of flue gas and ambient temperature on the dynamics and  
 performance of a MW scale supercritical CO<sub>2</sub> waste heat to power unit  
<https://doi.org/10.17185/dupublico/77321>
- Patil, Abhay; Nielson, Jordan; Smith, Natalie; Weiss, Nathan..... Page 264  
 Design and Evaluation of Low Specific Speed Expander for Geothermal Energy Application  
<https://doi.org/10.17185/dupublico/77324>
- Romei, Alessandro; Persico, Giacomo; Biliotti, Davide; Milani, Alberto; Lottini, Fabrizio;  
 Marconcini, Michele..... Page 272  
 Design of Compact Radial Turboexpanders for sCO<sub>2</sub> Power Systems  
<https://doi.org/10.17185/dupublico/77327>
- Rodríguez-de Arriba, Pablo; Crespi, Francesco; Sánchez, David; Muñoz, Antonio ..... Page 283  
 A methodology to design air-cooled condensers for supercritical power cycles using  
 carbon dioxide and carbon dioxide mixtures  
<https://doi.org/10.17185/dupublico/77329>
- Berka, Jan; Hlinčík, Tomáš; Purkarová, Eliška; Vagenknechtová, Alice; Ballek, Jakub-Vojtěch . Page 294  
 CO<sub>2</sub> purification and purity control for the sCO<sub>2</sub> experimental loop at Rez – a summary  
 of the test results  
<https://doi.org/10.17185/dupublico/77330>
- Romei, Alessandro; Persico, Giacomo; Gaetani, Paolo; Bellobuono, Ernani Fulvio;  
 Toni, Lorenzo; Valente, Roberto; Milani, Alberto ..... Page 301  
 Design and Computational Assessment of a Supercritical CO<sub>2</sub> Compressor for Waste Heat  
 Recovery Applications  
<https://doi.org/10.17185/dupublico/77332>

## TRANSIENT SIMULATION AND ANALYSIS OF A SUPERCRITICAL CO<sub>2</sub> HEAT REMOVAL SYSTEM UNDER DIFFERENT ABNORMAL OPERATION CONDITIONS

**Markus Hofer\***

University of Stuttgart  
Stuttgart, Germany

Email: hofer@ike.uni-stuttgart.de

**Frieder Hecker**

Simulator Centre of KSG | GfS  
Essen, Germany

**Michael Buck**

University of Stuttgart  
Stuttgart, Germany

**Jörg Starflinger**

University of Stuttgart  
Stuttgart, Germany

### ABSTRACT

The supercritical carbon dioxide (sCO<sub>2</sub><sup>1</sup>) heat removal system, which is based on multiple closed Brayton cycles with sCO<sub>2</sub> as the working fluid, is an innovative, self-propelling and modular heat removal system for existing and future nuclear power plants. Previous studies analysed its design, layout, control and operation. In addition, this novel study considers different sudden failures during the accident progress, e.g. failure of single sCO<sub>2</sub> cycles, control systems and valves. These abnormal conditions were investigated with the thermal-hydraulic system code ATHLET for a generic Konvoi pressurized water reactor. In most cases, the failure of a single sCO<sub>2</sub> cycle can be compensated. On the one hand, failure of the fans of the gas cooler leads to a pressure increase which may be mitigated by an inventory control system or cycle shutdown. On the other hand, unintended fan speed-up may cause compressor surge without adequate countermeasures. Furthermore, the system can operate under the cyclic blow-off from the steam generator safety valves when the relief valves are not available. Finally, the unintended closure of the valve which controls the steam flow through the compact heat exchanger triggers a fast cycle shutdown but a subsequent restart might be possible.

### INTRODUCTION

In case of a station blackout and loss of ultimate heat sink accident in a nuclear power plant, the plant accident management strongly depends on the recovery of electricity. If not available, core integrity will be violated, like in the Fukushima Daiichi accident. Such scenarios inspire the development of advanced decay heat removal systems. Since space is a limitation in

existing power plants, the supercritical carbon dioxide decay heat removal system (sCO<sub>2</sub>-DHRS) was proposed because of its compactness and self-propelling features [1,2]. Such a system could be incorporated into newly-built nuclear power plants as well as retrofitted to existing nuclear power plants. The system is not only self-propelling but its excess electricity can even be used to support other accident measures, e.g. recharging batteries. Moreover, no cooling water is required because the decay heat is transferred to the ambient air. To assess the benefits for nuclear safety, the sCO<sub>2</sub>-DHRS needs to be analysed in detail.

Figure 1 shows the scheme of the sCO<sub>2</sub>-DHRS attached to the steam generator (SG) of a pressurized water reactor (PWR). For better visualization, only one primary loop, which is connected to the pressurizer (PRZ), the corresponding steam generator (SG) and one attached sCO<sub>2</sub> cycle of the sCO<sub>2</sub>-DHRS are displayed. In the case of a station blackout and loss of ultimate heat sink accident, the main coolant pumps stop and the containment is isolated. In the following, natural circulation develops on the primary side via the hot legs (HL), the u-tubes and cold legs (CL) and the heat is transferred to the secondary side of the steam generators (SG). Natural circulation also builds up on the secondary side of the steam generators via the compact heat exchangers (CHX) of the sCO<sub>2</sub>-DHRS. After the start of the accident, all sCO<sub>2</sub> cycles are ramped up to their design heat removal capacity simultaneously. Later, when the decay power is lower than the total heat removal capacity, the operation of the cycles is adapted to the declining decay heat by control and successive shutdown of single cycles as shown later in Figure 2. In the CHX, the steam condenses and heats the sCO<sub>2</sub>. The pressurized and heated sCO<sub>2</sub> is expanded in the turbine, which

---

<sup>1</sup> sCO<sub>2</sub> is defined as carbon dioxide at supercritical conditions with  $p > 73.8$  bar and  $T > 31$  °C

\* corresponding author(s)

drives the compressor and generates power for the fans of the gas cooler (UHS). The compressor and the turbine are mounted on a common shaft together with the alternator and are referred to as turbo-alternator-compressor (TAC) or turbomachinery. After the turbine, the remaining heat of the  $s\text{CO}_2$  is removed in the gas cooler to the ambient air, which serves as the diverse ultimate

heat sink. For simplicity, the heat exchanger to the diverse ultimate heat sink will be called “UHS” in the following. Finally, the  $s\text{CO}_2$  is compressed and flows to the CHX. Similarly, the  $s\text{CO}_2$ -DHRS can be directly attached to the reactor pressure vessel (RPV) of a boiling water reactor [1].

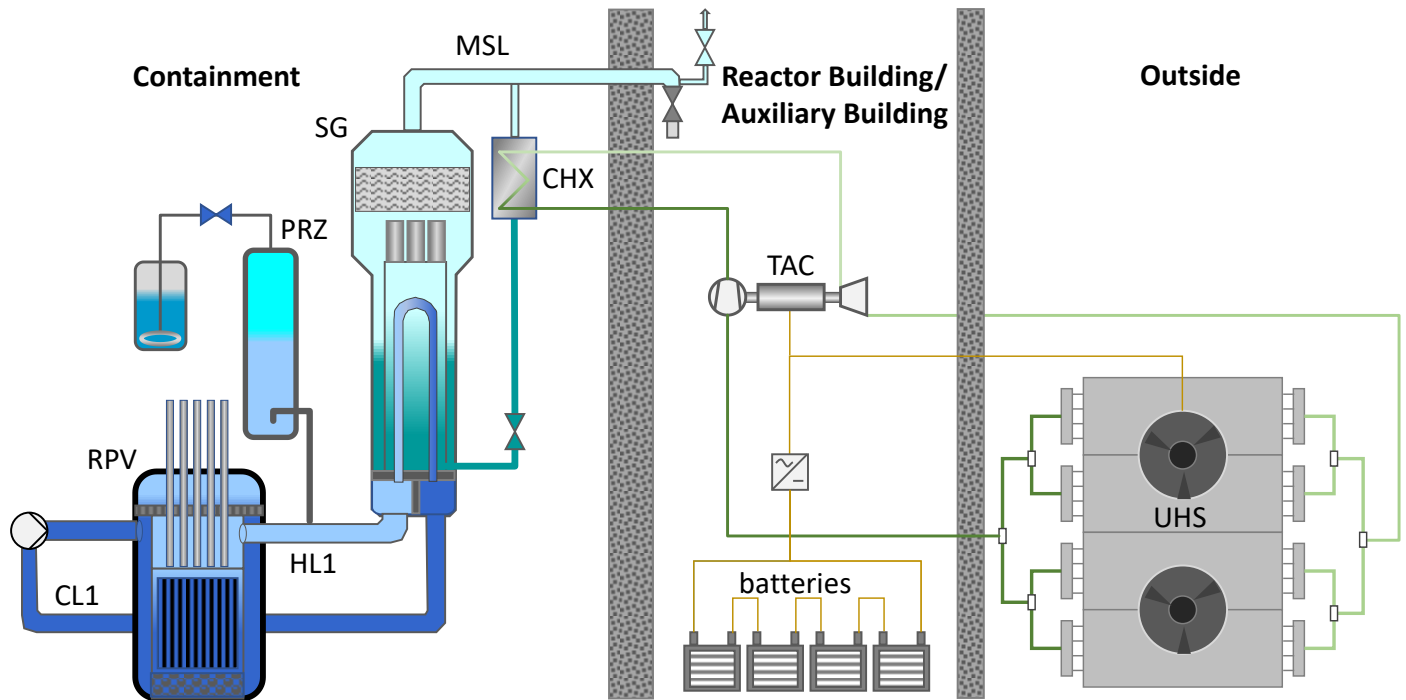


**Figure 1:** The  $s\text{CO}_2$  heat removal system attached to the steam generator (SG) of a pressurized water reactor (PWR)

A comprehensive review of all kinds of  $s\text{CO}_2$  power generation applications as well as cycle, component and control aspects was given by White et al. [1]. Wu et al. [2] provided an extensive review of the  $s\text{CO}_2$  Brayton cycle for nuclear applications, considering experimental and numerical work, the application as a power conversion system as well as a heat removal system. Among other things, they highlight the need for further safety analysis and dynamic simulations. The safety and thermal-hydraulics of water-cooled nuclear power plants are discussed in detail by D’Auria et al. [3]. For the simulation of the thermo-hydraulic behaviour, different system codes are used, e.g. CATHARE, RELAP, TRACE, ATHLET, SCTRAN and SAS4A/SASSYS-1 [3–6]. Because  $s\text{CO}_2$  is considered a working fluid for 4th generation reactor concepts as well as for the proposed heat removal system, work is in progress to extend or couple these system codes for the simulation of  $s\text{CO}_2$  power cycles [5–13].

The thermal-hydraulic system code ATHLET [4,14,15], which is used for this study, is applied to analyse the whole spectrum of leaks and transients in nuclear power plants of Generation II-IV as well as Small Modular Reactors. The highly modular code structure of ATHLET includes advanced thermal-

hydraulics as well as physical and numerical models. The main modules are thermo-fluid dynamics, heat transfer and heat conduction, neutron kinetics, control and balance-of-plant and the numerical time integration method. For a detailed study of the code features, the ATHLET “Models and Methods” manual [14] can be used. Bestion [4] compares different thermal-hydraulic system codes, regarding their models, capabilities and limitations. A short introduction to ATHLET is provided in [7,16].

Venker [7] investigated the  $s\text{CO}_2$ -DHRS for a boiling water reactor in detail by implementing first extensions for the simulation of the heat removal system in ATHLET. The successive shutdown of single cycles enabled the decay heat removal for more than 72 h. However, the component models, design and control of this system should be improved and different ambient temperatures and decay heat curves need to be considered in the future. Within the project  $s\text{CO}_2$ -HeRo, Hajek et al. [17] and Vojacek et al. [18] described the basic principles for the integration of the  $s\text{CO}_2$ -DHRS into the European PWR fleet including safety, reliability and thermodynamic design considerations and first simulations with Modelica. As part of the project  $s\text{CO}_2$ -4-NPP, the validation status for modelling  $s\text{CO}_2$

cycles was provided for the codes CATHARE, Modelica and ATHLET including a blind benchmark [12]. Successful simulations were performed but it was also found that component models need further improvement and some numerical issues need to be solved in the future. Hofer et al. [11] presented improved models for ATHLET, including heat exchanger and turbomachinery models. The turbomachinery models are performance map based and use a real gas similarity approach [19] to account for changes in the inlet conditions. They also provided a design approach for the sCO<sub>2</sub>-DHRS and analysed the sCO<sub>2</sub> cycle with varying decay heat [20] and at different ambient temperatures [16,21]. The cycle was successfully operated in part-load by adapting the rotational speed of the turbomachinery, keeping the compressor inlet temperature constant and without the need for inventory control. In [16,21], the modelling and design were improved, including new sCO<sub>2</sub> turbomachinery performance maps [22] with a higher surge margin, and the start-up from an operational readiness state was considered. Using Modelica coupled with ATHLET, Frýbort et al. [23] presented a first analysis of the challenging push-start from shutdown conditions and an alternative control strategy for low ambient temperatures, which is a combination of inventory control and UHS bypassing. Future analysis is required to analyse the feasibility of the push start, e.g. start at low ambient temperatures or determination of an appropriate heating procedure. The sCO<sub>2</sub>-DHRS was integrated and simulated coupled to an EPR, VVER 1000 and Konvoi PWR with CATHARE, ATHLET/Modelica and ATHLET, respectively [16,24,25]. In all power plants, the same modular sCO<sub>2</sub>-DHRS with a heat removal capacity of 10 MW per sCO<sub>2</sub> cycle was installed and successful coupled simulations with different numbers of systems were performed.

In the field of sCO<sub>2</sub> cycles for power generation, various dynamic analyses were conducted considering normal operation as well as failure conditions. Despite the focus on power generation, many findings are also relevant for the considered heat removal system. Hexemer et al. [10,26] presented a detailed TRACE model of a recuperated sCO<sub>2</sub> cycle with two turbines. They highlighted the importance of performing a detailed transient analysis before the system design is finalized. Moreover, attention is drawn to the problem of compressor surge and turbine flow reversal. Nathan [27] investigated control strategies for an indirect sCO<sub>2</sub> recompression cycle. The major control strategies are high and low-temperature control, turbine bypass, and inventory control. These strategies enable successful cycle operation for different transients, like start-up and shutdown, part-load operation, loss-of-load, loss of heat sink and over-power. Moisseytsev and Sienicki [28] performed extensive steady-state and transient studies with the Plant Dynamics Code, including validation with data from Sandia National Laboratories and the sCO<sub>2</sub> Integrated System Test facility. Moreover, the Plant Dynamics Code was coupled to SAS4A/SASSYS-1, e.g. to analyse a wide range of thermal transients in the sodium-CO<sub>2</sub> reactor heat exchanger. For normal operation, design-basis accidents and severe accidents, the maximum gradient of the wall temperature was 0.2 K/s, 1 K/s,

2 K/s, respectively [29]. Wang et al. [30] highlighted the importance of failure analysis and analysed the loss of heat source, loss of cooling water and pipeline leakage for a recompression sCO<sub>2</sub> cycle and presented emergency measures to mitigate these failure conditions. Fast intervention was required in the last two scenarios to prevent system damage, e.g. discharging CO<sub>2</sub> after the loss of cooling water to avoid over-pressure.

This study presents the first analysis of various failures during the operation of the sCO<sub>2</sub>-DHRS coupled with a generic Konvoi PWR. The design, layout and control of the applied sCO<sub>2</sub> cycle and the integration into the Konvoi PWR have already been discussed shortly in this chapter and can be found in detail in [21,24]. Furthermore, the applied models and their validation with data from small-scale experimental facilities were provided in [11,12,22].

In this paper, firstly, the normal operation and the operation strategy of the sCO<sub>2</sub>-DHRS are revisited also considering the failure of a sCO<sub>2</sub> cycle. Secondly, the failure of the fans (loss of cooling) of one cycle is analysed. Thirdly, the consequences of an unintended speed-up of the fans are presented including the effect of a fast intervention. Fourthly, the behaviour of the sCO<sub>2</sub>-DHRS during the cyclic blow-off from the steam generator safety valves is analysed. Finally, failures in the control of the steam flow through the CHX are investigated including a fast cycle shutdown and a subsequent restart.

Overall, the ATHLET simulations show that the sCO<sub>2</sub>-DHRS can cope with some of these events but other cases either require fast intervention or further design or control improvements.

## **NORMAL OPERATION AND FAILURE OF A SINGLE SCO<sub>2</sub> CYCLE**

In this chapter, the normal operation of the sCO<sub>2</sub>-DHRS is discussed in comparison to the operation after the failure of one sCO<sub>2</sub> cycle. All simulations in this and the following chapters were performed with a sCO<sub>2</sub>-DHRS consisting of four sCO<sub>2</sub> cycles coupled to a generic Konvoi PWR with a thermal power of 3840 MW considering a long-term station blackout and loss of ultimate heat sink scenario. With respect to the sCO<sub>2</sub> cycles, three process parameters were controlled: the compressor inlet temperature via the fan speed of UHS, the balance of decay heat and heat removal by controlling the turbine inlet temperature via the shaft speed of the turbomachinery and the CHX outlet temperature on the H<sub>2</sub>O side via the corresponding valve (Figure 1). If not stated otherwise, all simulations were conducted at the highest ambient temperature, which is 45 °C. Additionally, a conservatively low decay heat curve was applied in this chapter because this requires the highest operational flexibility from the sCO<sub>2</sub>-DHRS [24].

Firstly, the normal operation and the operation strategy of the sCO<sub>2</sub>-DHRS are revisited. On the left side of Figure 2, the decay power and the total thermal power removed by the sCO<sub>2</sub> cycles are shown. On the right side, the shaft speed of all four sCO<sub>2</sub> cycles is displayed. Solid lines mark the normal operation and dotted lines the operation after the failure of cycle 3, which



is discussed later. After the start of the accident, the sCO<sub>2</sub>-DHRS is ramped up to its design shaft speed and design thermal power to reduce the steam blown down via the relief valves of the steam generators. Then, the shaft speed is kept constant until the turbine inlet temperature of the sCO<sub>2</sub> cycle has decreased to 260 °C. This temperature decrease on the NPP and sCO<sub>2</sub> side starts after the decay power has dropped below the removed thermal power. In the following, the shaft speed is controlled to keep the turbine inlet temperature constant. The limit of 260 °C was selected to ensure a sufficiently high turbine inlet temperature and to keep the primary circuit in a hot state to avoid reactivity increase and hence the need for early boron injection on the NPP side. To further ensure a sufficient thermal power input to the sCO<sub>2</sub> cycles, single cycles are shut down successively after 3.8 h, 9.3 h and 25.9 h, respectively. After each shutdown, the control increases the shaft speed of the remaining cycles automatically to match the decay power again. Altogether, this allows a smooth operation along the decay heat curve.

Secondly, the failure of a single cycle after the equilibrium of decay power and the removed power is discussed to justify the shutdown strategy of the sCO<sub>2</sub> cycles. In the simulation, relative switch-off speeds in relation to the cycle design point speed of

50 %, 35 % and 30 % were specified for the first, second and third cycles, respectively. The switch-off speeds were selected relatively low to be able to buffer the sudden failure of another operating cycle. The sudden failure of cycle 3 is exemplarily shown in Figure 2 concurrently with the second shutdown at around 9.3 h, indicated by the dotted lines. As a result, the removed thermal power drops to a lower value but the shaft speed control easily adapts the operation of the remaining cycle 4 to match the decay heat curve again. Thus, a cycle failure can normally be buffered by the remaining cycles. However, additional backup cycles should be installed to cover the unavailability of one or multiple cycles due to failures or maintenance, especially in the early phase of the accident. The next chapter provides an example of reduced heat removal after only 5 h and the last chapter before the conclusion considers a cycle failure after only 2 h. Additionally, the progress of the accident with only two or three available sCO<sub>2</sub> cycles can be found in [24]. Two cycles are not sufficient to handle the accident from the start and with three cycles the danger of recriticality may occur and the core is almost uncovered.

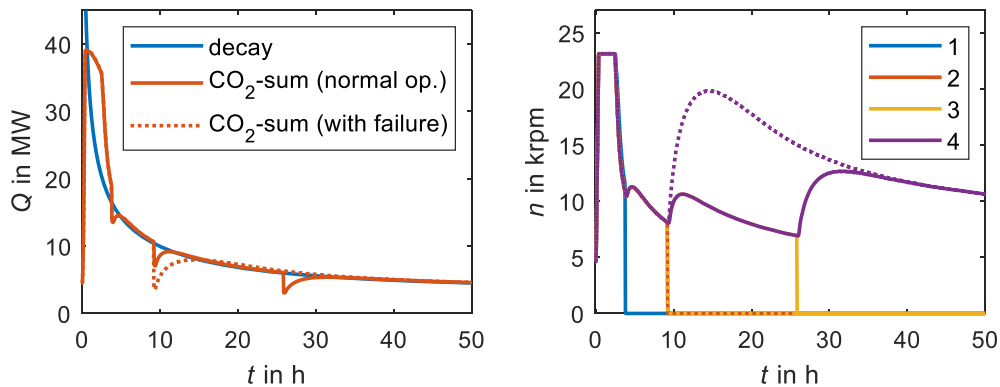


**Figure 2:** Normal operation (solid lines) vs. failure of cycle 3 concurrent with the shutdown of cycle 2 (dotted lines): decay power and total power removed by the sCO<sub>2</sub> cycles (left); shaft speed of turbomachinery for each of the four cycles (right)

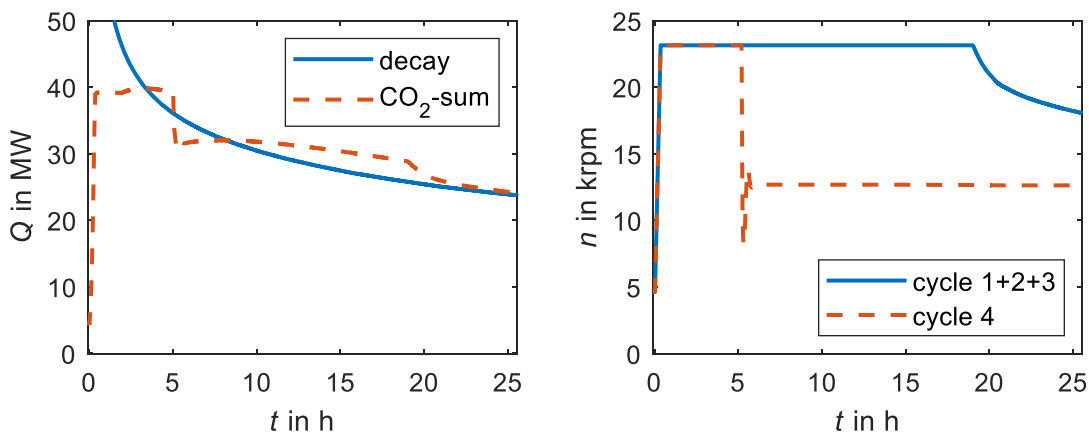


**Figure 3:** Fan failure of cycle 4: decay power and total power removed by the sCO<sub>2</sub> cycles (left); shaft speed of turbomachinery for each cycle (right)

## FAN FAILURE

In this chapter, the complete failure of the fans of the UHS of one sCO<sub>2</sub> cycle is analysed. It was assumed arbitrarily that the failure occurs 5 h after the start of the accident. In this case, a conservatively high decay heat curve was applied to highlight the effect of reduced heat removal [24]. Four sCO<sub>2</sub> cycles were under operation and the fan failure was considered in cycle 4. After the fan failure, a natural convection-driven air flow rate provided a small cooling power to the sCO<sub>2</sub> cycle. Under these conditions the assumed air mass flow rate was 3 % of its design flow rate [38].

On the left of Figure 3, the decay power compared to the total thermal power removed by all sCO<sub>2</sub> cycles is shown. The first 5 h are identical to the analysis in [24] and qualitatively similar to the previous chapter. Then, as a result of the fan failure, the removed thermal power drops from 39.3 MW to 30.8 MW, initially, and increases to 32 MW again. The reason for this behaviour is mainly related to the fact that cycle 4 is not switched off but continues to operate at reduced shaft speed, as can be observed in Figure 3 on the right. Since the total thermal power consumption of the sCO<sub>2</sub> cycles drops below the decay heat curve, the primary and secondary sides of the NPP start to heat up again but no additional mass is lost because the pressures stay below the set point of the valves. After 8.2 h, the equilibrium of the decay power and the removed thermal power is reached again and the temperatures and pressures start to decrease again until the shaft speed control adapts the removed thermal power to the decay power. Cycles 1 to 3 operate identically, therefore, these cycles are represented by a single line in this and the next figure.

In the following, some consequences of the fan failure are analysed in more detail. Figure 4 displays the compressor inlet temperature  $T_{comp,in}$  and the turbine inlet temperature  $T_{turb,in}$ .  $T_{comp,in}$  increases steeply after the fan failure because the cooling capacity of the UHS is reduced significantly. First, this also leads to an increase of  $T_{turb,in}$  but then  $T_{turb,in}$  decreases steeply to almost 250 °C. This is related to the control of the H<sub>2</sub>O outlet temperature of the CHX attempting to keep the condensate temperature at 150 °C by closing the control valve, hence blocking the water-steam flow through the CHX. When  $T_{turb,in}$  drops below its target value of 260 °C, the shaft speed control is activated and decreases the shaft speed to increase  $T_{turb,in}$  to its target value again. After approximately 45 min, the control succeeds at about half the nominal speed, and  $T_{turb,in}$  stays constant at 260 °C and also  $T_{comp,in}$  stabilizes at a value of 142.5 °C. In the other sCO<sub>2</sub> cycles,  $T_{comp,in}$  is controlled to its target value of 55 °C and  $T_{turb,in}$  follows the behaviour of the corresponding secondary steam temperature.

After the transient, the thermal power of the CHX of cycle 4 stabilizes at 2 MW together with an electrical power consumption of the turbomachinery of only 0.03 MW, which can be provided easily from the excess power of the other cycles.

It should be noted, that due to the constant mass inventory of the sCO<sub>2</sub> cycle, the considerably increased temperatures on the low-pressure side of cycle 4, lead to significantly higher

cycle pressures. After the operation of cycle 4 stabilized again, the compressor inlet pressure is at 25.2 MPa and the outlet pressure at 27.2 MPa. Compared to the design values of the cycle, these values are 12.6 MPa and 5.8 MPa higher, respectively. If a constant mass inventory is also considered in future analysis, the pipe and component design have to take the higher pressures into account. An alternative may be an additional inventory control system. However, this would increase the complexity of the system and the required sCO<sub>2</sub> storage tank has to be quite large due to the large volume of the low-pressure side. Generally, it should be noted that the operation of the sCO<sub>2</sub> cycle might be quite unstable due to changes in the natural convection-driven airflow, which was assumed constant in the simulation. Therefore, another option is the intentional shutdown of the cycle affected by the fan failure and a later restart.

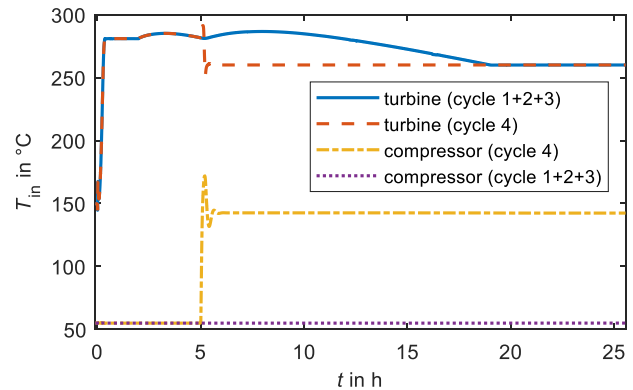


**Figure 4:** Fan failure of cycle 4: Compressor inlet temperature and turbine inlet temperature for each cycle

## UNINTENDED FAN SPEED UP

This chapter discusses the unintended speed-up of the fans, e.g. due to a failure of their control. Normally, the fan speed of the UHS is controlled to keep the compressor inlet temperature constant at its design value of 55 °C. However, in this case, it was assumed that the fan speed increased within 5 s to its design speed, due to a defect in the control system, 5 h after the start of the accident. In contrast to the other analyses, which considered an ambient temperature of +45 °C, this analysis was conducted at the lowest considered ambient temperature of -45 °C because the sensitivity of the cycle to changes in the fan speed is increasing with decreasing ambient temperature. To lessen this increase in sensitivity to a certain extent, the heat transfer area of the UHS is reduced by disconnecting UHS modules from the cycle. At the assumed ambient temperature, only one quarter of the UHS was in operation.

As a result of the fan speed up, the air flow rate and cooling power are increasing and the cycle temperatures are decreasing steeply together with the cycle pressures due to the constant mass inventory. Since the active turbomachinery shaft speed control tries to keep the turbine inlet temperature constant, the shaft speed also decreases rapidly. After 20 s, the compressor inlet

temperature, pressure and mass flow rate already decreased by 15 K, 3 MPa and 2.5 kg/s, and the compressor operating point considerably approached the surge line. Around 30 s later, the compressor inlet drops below the critical pressure into the two-phase region and the simulation stops, since no subcritical CO<sub>2</sub> properties were implemented. At this point, the implemented turbomachinery control already decreased the shaft speed and the cycle mass flow rate to less than 30 % of the design shaft speed and 8.5 kg/s, respectively. At the end of the simulation, the theoretical surge line is almost crossed.

A further simulation analysed the effects of a fast intervention. The fan speed was increased within 5 s to its design value, as in the previous simulation. Then, the speed was decreased to its initial value within the same time and, finally, the speed control took over again. All other boundary conditions are identical to the previous simulation. On the left of Figure 5, the air mass flow rate visualizes the shaft speed increase and the following decrease and the resulting compressor inlet

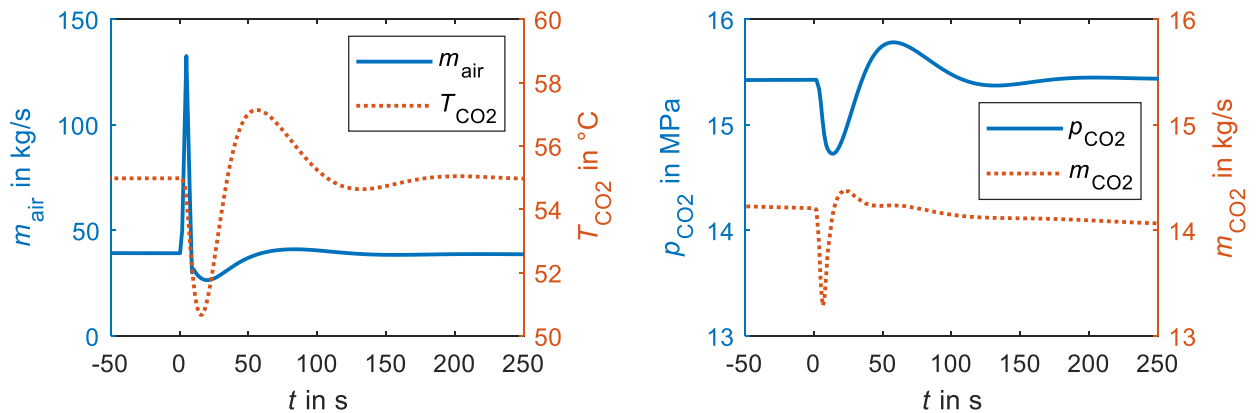


**Figure 5:** Fan control failure of cycle 4 (with intervention);  $t = 0$  marks the start of the fan speed-up: Air mass flow rate and compressor inlet temperature (left); pressure and mass flow rate at the compressor inlet (right)

### CYCLIC BLOW-OFF FROM THE STEAM GENERATOR SAFETY VALVES

In this chapter, the steam generators are blown down via the safety valves instead of considering the partial depressurization to 7.5 MPa via the diverse blow-off valves. This might occur if the batteries of the diverse blow-off valves are not available or if the control of these valves does not work as intended. The simulation was conducted with the conservatively high decay heat curve since this results in an increased blowdown via the safety valves.

In terms of the long-term behaviour, after the blow-off has stopped, this simulation is very similar to the simulation with active diverse blow-off valves and partial depressurization to 7.5 MPa. After 3.1 h, the equilibrium of the decay power and the total thermal power of all sCO<sub>2</sub> cycles is reached and the shaft speed control adapts the thermal power of the CO<sub>2</sub> cycles to the decay power.

In the following, the transient behaviour of the sCO<sub>2</sub> cycles during the blow-off via the safety valves is analysed. Therefore, only the first 3 h of the accident are shown. All sCO<sub>2</sub> cycles and steam generators behave equally. Thus, some parameters of the

temperature is displayed with the start of the fan speed-up shifted to  $t = 0$ . This temperature shows an oscillation between 50.5 °C and 57 °C and after approximately 200 s the specified target value of 55 °C is reached again. Since the different conditions in the cycle are related, almost all parameters show similar oscillations, e.g. the magnitude of the compressor inlet pressure variation is 1 MPa and the cycle mass flow rate varies by 1.1 kg/s, which is also shown in Figure 5 on the right. Therefore, if the fan speed increase is stopped and decreased again to its initial value in time, this will only shortly affect the operation of the sCO<sub>2</sub> cycle.

It can be concluded that such an event requires a fast intervention or rather additional safety procedures, e.g. an upper limit for the fan speed relative to its current operation point. At least compressor surge can also be avoided by the opening of the turbine bypass or the compressor recirculation.

CHX attached to steam generator 1 and of sCO<sub>2</sub> cycle 1 are shown. Figure 6 presents the temperatures on the H<sub>2</sub>O side and the sCO<sub>2</sub> side. During the first 20 min, the sCO<sub>2</sub>-DHRS is ramped up from its operational readiness state to full power. This can be observed from the increase of the H<sub>2</sub>O outlet and the sCO<sub>2</sub> inlet temperature of the CHX.

All parameters on the H<sub>2</sub>O side are influenced by the cyclic blow-off behaviour of the safety valves. The safety valves open at 8.83 MPa and close when the pressure drops below 8.33 MPa. Subsequently, the pressure starts to increase, rapidly at first and then slower. In Figure 6, this can be observed from the H<sub>2</sub>O inlet temperature of the CHX, which follows the behaviour of the pressure. At the start of the accident, the frequency of the blow-off is high and then decreases together with the declining decay heat. During the phase of pressure build-up, the steam enters the H<sub>2</sub>O inlet superheated from hot structures on top of the steam generator, by approximately 4 K on average. When the safety valve opens, this results in an inlet pressure and temperature drop of around 1 MPa and 10 K. In the beginning, the temperature drop is twice as high. The outlet temperature of the CHX experiences higher drops of up to 30 K but comes back to its

initial level considerably faster within 10 s. This behaviour is mainly related to the mass flow rate which also exhibits very short peaks related to the distribution of the natural circulation-driven flow on the H<sub>2</sub>O side. The control of the H<sub>2</sub>O outlet temperature reacts hardly, varying the relative opening area of the valve by just 3 %. This is a result of the chosen small proportional and integral gain and the omission of the derivative gain to avoid a negative interaction of the controllers.

On the sCO<sub>2</sub> side, the sCO<sub>2</sub> outlet temperature of the CHX closely follows the behaviour of the H<sub>2</sub>O inlet temperature, just shifted by approximately 15 K with exception of the ramp-up phase. The changes are within the same magnitude of 10 K, also at the following turbine outlet and UHS inlet. At the compressor inlet, the changes are reduced to less than 0.5 K by the thermal inertia of the UHS and the control of the compressor inlet temperature. The related variations of the pressures on the sCO<sub>2</sub> side are approximately 1 bar or less. The related cycle mass flow rate exhibits small peaks of approximately 0.8 kg/s magnitude or less. In the future, it should be analysed in more detail, if the cyclic thermal load poses a problem for the integrity of the components.

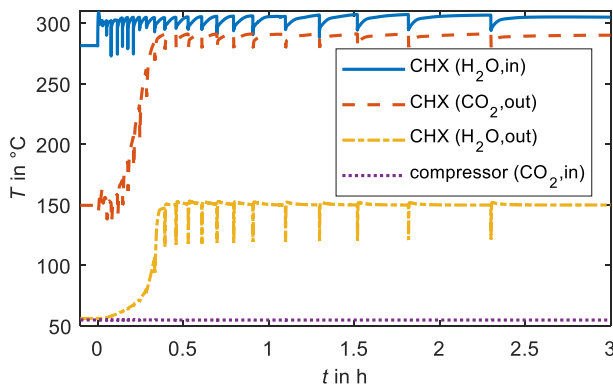


**Figure 6:** Steam generator blowdown via the safety valves: Temperatures of steam generator 1 (H<sub>2</sub>O side) and cycle 1 (sCO<sub>2</sub> side)

### VALVE FAILURE IN THE CONDENSATE LINE

In this chapter, the failure of the H<sub>2</sub>O CHX outlet temperature control is discussed. Normally, this control adapts the valve opening in the pipe after the CHX (Figure 1) to adjust the H<sub>2</sub>O mass flow rate and thereby the H<sub>2</sub>O outlet temperature with the intention to reduce the maximum temperature difference between the fluids in the CHX. The extreme cases of a control failure are a completely opened or closed valve. Opening the valve completely leads to an increase in the CHX H<sub>2</sub>O outlet temperature. The increase depends on the pressure drop in the pipes on the H<sub>2</sub>O side and the opened valve and the current water level in the steam generator. The outlet temperature may even increase to the level of the inlet temperature with condensation occurring over the whole length of the CHX. This would enable a higher heat removal from the NPP due to the increased heat transfer coefficient on the H<sub>2</sub>O side. However, also the thermal stress in the CHX increases due to a higher temperature

difference between the fluids. If the applied CHX can bear high thermal stresses, the outlet temperature control may not be required except for the operational readiness state and the start-up. Moreover, a smaller CHX could be designed due to better heat transfer. If the CHX is not designed to bear high temperature differences, the valve opening can still be adjusted manually in case of a defect in the control system because this control generally acts very slowly.

If a failure of the control leads to a closed valve at the CHX outlet, this almost immediately stops the heat input to the corresponding sCO<sub>2</sub> cycle. Simulations with a considerably high decay heat curve were conducted to illustrate this fact.

In the first simulation, it was arbitrarily assumed that the valve after the CHX on the H<sub>2</sub>O side closes suddenly, 2 h after the start of the accident. Closing this valve stops the steam flow completely. As a result, the turbine inlet temperature on the sCO<sub>2</sub> side decreases steeply, which activates the shaft speed control. Since the target of the control is to keep the turbine inlet temperature constant at 260 °C, the shaft speed also decreases rapidly. Within 25 s, the shaft speed and the thermal power transfer in the CHX have already decreased to zero. The fast temperature changes might lead to high thermal stresses, which should be analysed further. If no restart of the shutdown sCO<sub>2</sub> cycle is considered, the primary and secondary loops of the NPP heat up since the decay heat is higher than the heat removal capacity of the sCO<sub>2</sub> cycles. In the primary loop, about 8 % of the total mass inventory is blown off before the primary side starts to cool down again as the equilibrium of the decay power and the total thermal power of the cycles is reached. Since no issues related to the boron concentration are observed, this simulation can be seen as an additional example of a successfully handled accident sequence even after the failure of one sCO<sub>2</sub> cycle.

A further simulation analysed the restart of the sCO<sub>2</sub> cycle assuming that the issue with the closed valve could be solved quickly. Figure 7 shows different parameters during the shutdown and following start-up procedure with the closing of the valve shifted to 0 s. On the top left, the shaft speed relative to its design speed and the relative valve opening area are displayed to illustrate the described procedure. The closing of the valve and the resulting shutdown have already been described together with the previous case. Thereafter, the valve was kept closed for 5 min and then opened to its opening area during the operational readiness state. From this point, the valve opening and the turbomachinery speed were increased linearly within 20 min until the design speed was reached again. After the ramp-up procedure, the valve opening area is controlled again to keep the CHX outlet temperature at the H<sub>2</sub>O side at its target value of 150 °C. On the top right of Figure 7, the mass flow rates of sCO<sub>2</sub> and H<sub>2</sub>O are provided at the compressor inlet and the CHX inlet, respectively. The H<sub>2</sub>O mass flow rate stays at zero while the valve is closed. After the reopening of the valve, it increases to about 0.5 kg/s and then gradually increases together with the sCO<sub>2</sub> mass flow rate. While the valve is closed, a reverse flow through the sCO<sub>2</sub> compressor can be observed which peaks shortly after the shutdown and then decreases towards zero. On

the bottom left, the compressor and turbine inlet temperatures are shown. The turbine inlet temperature drops steeply to 137 °C within 25 s. After the shutdown, the turbine inlet temperature decreases further down to a minimum value of 61 °C and then increases to 85 °C again because the flow in the cycle has almost reduced to zero. The compressor inlet temperature always remains close to its target value of 55 °C. After the restart, the turbine inlet temperature increased to a higher value due to the heat-up of the corresponding steam generator. In the bottom right of Figure 7, the thermal power of the CHX is displayed. The

slightly higher value after the restart compared to before the shutdown is also related to the higher temperatures on the H<sub>2</sub>O side. Even without opening the compressor recirculation and the turbine bypass, the compressor operation keeps a sufficient margin to the surge line during the whole procedure. This is related to the already increased turbine inlet temperature at the start of the restart procedure. In the future, it should be investigated further under which conditions a restart can be conducted.

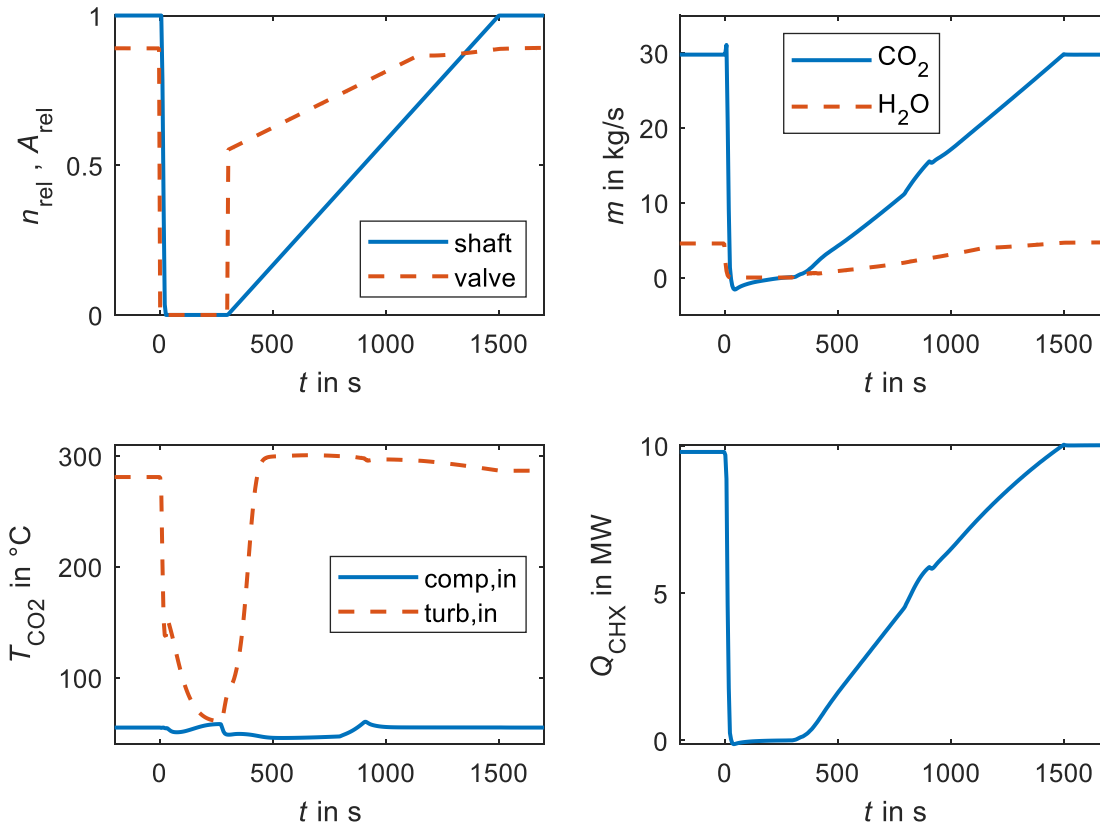


**Figure 7:** Unintended closing of the valve at CHX H<sub>2</sub>O outlet and reopening 5 min later: various parameters during the shutdown and restart of the related CO<sub>2</sub> cycle

## CONCLUSION

In this study, different sudden failures during the operation of the sCO<sub>2</sub>-DHRS were analysed with the thermal-hydraulic system code ATHLET. The system was coupled to a generic Konvoi PWR with a thermal power of 3840 MW and conservative boundary conditions were applied with regard to ambient temperature and decay heat during a combined long-term station blackout and loss of the ultimate heat sink scenario.

The results, which are summarized in Table 1, show that the applied design of the sCO<sub>2</sub>-DHRS, which was presented in previous studies, can cope with some of the assumed events but other cases either require fast intervention or further design or control improvements. In most cases, the failure of a single sCO<sub>2</sub>

cycle can be compensated, either by the control of the cycles and the thermal inertia of the PWR or by losing some inventory in case of an early failure. However, additional backup cycles should be installed to cover the unavailability of one or multiple cycles in case of a very early failure or maintenance. On the one hand, failure of the fans of the gas cooler leads to a pressure increase which may be mitigated by an inventory control system or the shutdown of the respective cycle. On the other hand, unintended fan speed-up can cause compressor surge or a drop of the cycle pressure into the two-phase region. This requires a fast intervention, e.g. preventing or stopping and reverting the speed-up within a couple of seconds. Moreover, the sCO<sub>2</sub>-DHRS can operate under the cyclic blow-off from the steam generator

safety valves when the relief valves are not available. Finally, the unintended closure of the valve which controls the steam flow through the CHX triggers a fast cycle shutdown but a subsequent restart might be possible.

In the future, it may be investigated further under which conditions and how a restart can be conducted. Furthermore, it should be analysed in detail if thermal stresses caused by high thermal gradients or high temperature differences can cause damage to the components. This is also related to the analysis of the necessity of the control of the CHX outlet temperature on the H<sub>2</sub>O side. For highly transient cases, not only the thermal inertia of the heat exchangers but also of the pipe walls and the material of the turbomachinery should be modelled. Moreover, the mechanical inertia of the turbomachinery should be considered. Finally, advanced control strategies may help to reduce thermal stresses and enable adequate countermeasures in various failure scenarios.

**Table 1:** Summary of analysed failures: Impact and possible measures

Failure name	Impact	Measures
Failure of (single) sCO <sub>2</sub> cycle	All except early failures can be compensated	Back-up cycles for early or multiple cycle failures
Fan failure (loss of cooling)	Decreased heat removal capacity; high cycle pressures	See previous; inventory control system, intentional shutdown
Unintended fan speed-up	Fast decrease of cycle temperatures and pressures; compressor surge	Stop/limit fan speed increase; opening of bypass/recirculation
Cyclic blow-off from the steam generator safety valves	Cyclic thermal load, partially cyclic behaviour of cycle parameters	Integrity check of components (thermo-mechanical analysis)
Valve failure in the condensate line (completely open valve)	Increased heat removal, temperatures and temperature differences	Integrity check of CHX; if positive: option for higher heat removal/smaller CHX design
Valve failure in the condensate line (completely closed valve)	Stop of heat removal of corresponding cycle, cycle shutdown	Cycle restart after the issue is solved, backup cycles

## NOMENCLATURE

<i>A</i>	opening area of the valve (m <sup>2</sup> )
<i>m</i>	mass flow rate (kg/s)
<i>n</i>	rotational speed (krpm)
<i>p</i>	pressure (MPa)
<i>t</i>	time (h)

<i>T</i>	temperature (°C)
<i>Q</i>	thermal power (MW)

## Subscripts

comp	compressor
in	inlet
out	outlet
rel	relative
turb	turbine

## Acronyms

CHX	compact heat exchanger
CL	cold leg
DHRS	decay heat removal system
FWL	feed water line
H <sub>2</sub> O	water
HL	hot leg
LCQ	steam generator blowdown system
MSL	main steam line
NPP	nuclear power plant
PRZ	pressurizer
RPV	reactor pressure vessel
PWR	pressurized water reactor
sCO <sub>2</sub>	supercritical carbon dioxide
SG	steam generator
TAC	turbomachinery (turbo-alternator-compressor)
UHS	gas cooler/ heat exchanger to the diverse ultimate heat sink (ambient air)

## ACKNOWLEDGEMENTS

The research presented in this paper has received funding from the Euratom research and training programme 2014-2018 under grant agreement No. 847606 “Innovative sCO<sub>2</sub>-based Heat removal Technology for an Increased Level of Safety of Nuclear Power plants” (sCO<sub>2</sub>-4-NPP).

The work of University of Stuttgart was also funded by the German Ministry for Economic Affairs and Energy (BMWi. Project No. 1501557) on basis of a decision by the German Bundestag

## REFERENCES

- [1] White, M.T., Bianchi, G., Chai, L., Tassou, S.A. and Sayma, A.I. (2021) Review of supercritical CO<sub>2</sub> technologies and systems for power generation. *Applied Thermal Engineering*, 185. <https://doi.org/10.1016/j.applthermaleng.2020.116447>
- [2] Wu, P., Ma, Y., Gao, C., Liu, W., Shan, J., Huang, Y. et al. (2020) A review of research and development of supercritical carbon dioxide Brayton cycle technology in nuclear engineering applications. *Nuclear Engineering and Design*, Elsevier. 368, 110767. <https://doi.org/10.1016/j.nucengdes.2020.110767>
- [3] D’Auria, F. (2017) *Thermal-Hydraulics of Water Cooled Nuclear Reactors*. Elsevier.



- <https://doi.org/10.1016/C2015-0-00235-0>
- [4] Bestion, D. (2008) System code models and capabilities. *THICKET*, Grenoble. p. 81–106.
- [5] Wu, P., Gao, C. and Shan, J. (2018) Development and Verification of a Transient Analysis Tool for Reactor System Using Supercritical CO<sub>2</sub> Brayton Cycle as Power Conversion System. *Science and Technology of Nuclear Installations*, Hindawi. 2018, 1–14. <https://doi.org/10.1155/2018/6801736>
- [6] Wang, H., Sun, L., Wang, H., Shi, L. and Zhang, Z. (2013) Dynamic Analysis of S-CO<sub>2</sub> Cycle Control With Coupled PDC-SAS4A/SASSYS-1 Codes. *International Conference on Nuclear Engineering, Proceedings, ICONE*, American Society of Mechanical Engineers Digital Collection. 2, 633–40. <https://doi.org/10.1115/ICONE20-POWER2012-54547>
- [7] Venker, J. (2015) Development and Validation of Models for Simulation of Supercritical Carbon Dioxide Brayton Cycles and Application to Self-Propelling Heat Removal Systems in Boiling Water Reactors. Stuttgart. <https://doi.org/10.18419/opus-2364>
- [8] Mauger, G., Tauveron, N., Bentivoglio, F. and Ruby, A. (2019) On the dynamic modeling of Brayton cycle power conversion systems with the CATHARE-3 code. *Energy*, Elsevier Ltd. 168, 1002–16. <https://doi.org/10.1016/j.energy.2018.11.063>
- [9] Batet, L., Alvarez-Fernandez, J.M., Mas de les Valls, E., Martinez-Quiroga, V., Perez, M., Reventos, F. et al. (2014) Modelling of a supercritical CO<sub>2</sub> power cycle for nuclear fusion reactors using RELAP5–3D. *Fusion Engineering and Design*, North-Holland. 89, 354–9. <https://doi.org/10.1016/J.FUSENGDES.2014.03.018>
- [10] Hexemer, M. and Rahmer, K. (2011) Supercritical CO<sub>2</sub> Brayton Cycle Integrated System Test (IST) TRACE Model and Control System Design. *Supercritical CO<sub>2</sub> Power Cycle Symposium*, Boulder, Colorado. p. 1–58.
- [11] Hofer, M., Buck, M. and Starflinger, J. (2019) ATHLET extensions for the simulation of supercritical carbon dioxide driven power cycles. *Kerntechnik*, 84, 390–6. <https://doi.org/10.3139/124.190075>
- [12] Hofer, M., Buck, M., Cagnac, A., Prusek, T., Sobecki, N., Vlcek, P. et al. (2020) Deliverable 1.2: Report on the validation status of codes and models for simulation of sCO<sub>2</sub>-HeRo loop. sCO<sub>2</sub>-4-NPP.
- [13] Hofer, M., Theologou, K. and Starflinger, J. (2021) Qualifizierung von Analysewerkzeugen zur Bewertung nachwärmegetriebener, autarker Systeme zur Nachwärmeabfuhr – sCO<sub>2</sub>-QA -. Stuttgart.
- [14] Austregesilo, H., Bals, C., Hora, A., Lerchl, G., Romstedt, P., Schöffel, P. et al. (2016) ATHLET Models and Methods. Garching.
- [15] Gesellschaft für Anlagen- und Reaktorsicherheit gGmbH. (2019) ATHLET. <https://user-codes.grs.de/athlet>
- [16] Hofer, M., Ren, H., Hecker, F., Buck, M., Brillert, D. and Starflinger, J. (2022) Simulation, analysis and control of a self-propelling heat removal system using supercritical CO<sub>2</sub> under varying boundary conditions. *Energy*, Pergamon. 123500. <https://doi.org/10.1016/J.ENERGY.2022.123500>
- [17] Hajek, P., Vojacek, A. and Hakl, V. (2018) Supercritical CO<sub>2</sub> Heat Removal System - Integration into the European PWR fleet. *2nd European SCO<sub>2</sub> Conference*, Essen. p. 0–7. <https://doi.org/10.17185/duublico/460>
- [18] Vojacek, A., Hakl, V., Hajek, P., Havlin, J. and Zdenek, H. (2016) Deliverable 1.3: Documentation system integration into European PWR fleet. sCO<sub>2</sub>-HeRo.
- [19] Pham, H.S., Alpy, N., Ferrasse, J.H., Boutin, O., Tothill, M., Quenaut, J. et al. (2016) An approach for establishing the performance maps of the sc-CO<sub>2</sub> compressor: Development and qualification by means of CFD simulations. *International Journal of Heat and Fluid Flow*, 61, 379–94. <https://doi.org/10.1016/j.ijheatfluidflow.2016.05.017>
- [20] Hofer, M., Buck, M. and Starflinger, J. (2021) OPERATIONAL ANALYSIS OF A SELF-PROPELLING HEAT REMOVAL SYSTEM USING SUPERCRITICAL CO<sub>2</sub> WITH ATHLET. *4th European SCO<sub>2</sub> Conference*, online. p. 1–11. <https://doi.org/10.17185/DUEPUBLICO/73983>
- [21] Hofer, M., Ren, H., Hecker, F., Buck, M., Brillert, D. and Starflinger, J. (2021) Simulation and analysis of a self-propelling heat removal system using supercritical CO<sub>2</sub> at different ambient temperatures. *4th European Supercritical CO<sub>2</sub> Conference*, online. p. 1–14. <https://doi.org/10.17185/DUEPUBLICO/73943>
- [22] Ren, H., Hacks, A., Schuster, S. and Brillert, D. (2021) Mean-line analysis for supercritical CO<sub>2</sub> centrifugal compressors by using enthalpy loss coefficients. *4th European Supercritical CO<sub>2</sub> Conference*, online. <https://doi.org/10.17185/duublico/73948>
- [23] Frýbort, O., Kriz, D., Melichar, T., Vlcek, P., Hakl, V., Vyskocil, L. et al. (2021) Deliverable 5.4: Thermodynamic performance of the heat recovery system integrated into the plant. sCO<sub>2</sub>-4-NPP.
- [24] Hofer, M., Buck, M., Prusek, T., Sobecki, N., Vlcek, P., Kriz, D. et al. (2021) Deliverable 2.2: Analysis of the performance of the sCO<sub>2</sub>-4-NPP system under accident scenarios based on scaled-up components data. sCO<sub>2</sub>-4-NPP.
- [25] Sobecki, N., Delmaere, T., Hofer, M. and Vlcek, P. (2022) Deliverable 5.5: Integration of data from real design parameters into the thermal-hydraulic code and simulations based on accident scenarios. sCO<sub>2</sub>-4-NPP.
- [26] Hexemer, M.J., Hoang, H.T., Rahner, K.D., Siebert, B.W. and Wahl, G.D. (2009) Integrated Systems Test (IST) Brayton Loop Transient Model Description and Initial Results. *S-CO<sub>2</sub> Power Cycle Symposium*, Troy. p. 1–172.
- [27] Carstens and Nathan. (2007) Control strategies for supercritical carbon dioxide power conversion systems. *Massachusetts Institute of Technology*.

- [28] Moiseyev, A. and Siemicki, J.J. (2016) SIMULATION OF S-CO<sub>2</sub> INTEGRATED SYSTEM TEST WITH ANL PLANT DYNAMICS CODE. *The 5 Th International Symposium-Supercritical CO<sub>2</sub> Power Cycles*, San Antonio.
- [29] Moiseyev, A. and Siemicki, J.J. (2019) Analysis of thermal transients for SCO<sub>2</sub> Brayton cycle heat exchangers. *Proceedings of the ASME Turbo Expo*, 9, 1–12. <https://doi.org/10.1115/GT2019-90374>
- [30] Wang, R., Li, X., Qin, Z., Wang, L., Lin, Z., Wang, X. et al. (2022) Dynamic response and emergency measures under failure conditions of sCO<sub>2</sub> Brayton cycle. <https://doi.org/10.1002/ese3.1300>

## SCO<sub>2</sub> TEST FACILITY AT TU WIEN: DESIGN, OPERATION AND RESULTS

**Viktoria Illyés\***

TU Wien  
Vienna, Austria

Email: viktoria.illyes@tuwien.ac.at

**Stefan Thanheiser**

TU Wien  
Vienna, Austria

**Paul Schwarzmayr**

TU Wien  
Vienna, Austria

**Pierre-Luc David**

Kelvion Thermal Solutions  
Nantes, France

**Xavier Guerif**

Kelvion Thermal Solutions  
Nantes, France

**Andreas Werner**

TU Wien  
Vienna, Austria

**Markus Haider**

TU Wien  
Vienna, Austria

### ABSTRACT

At TU Wien, a test facility working with supercritical carbon dioxide (sCO<sub>2</sub>) was commissioned in 2018. Since then, it has been used for various research tasks. This paper gives an overview about the three configurations of the facility with a focus on design, operation, and results.

The authors present the design of components in the three configurations of the test facility: proof of concept of the simple cycle in supercritical and transcritical operation mode, heat transfer measurements, and future work. Special emphasis is given to challenges during engineering and operation. Our most relevant lessons learned are: that a commercial CO<sub>2</sub> pump is not sufficient for cycle experiments, how to design a measurement section for heat transfer measurements, and that during experimental research, measurement-concepts and data reduction must be prioritized at all times.

### INTRODUCTION

SCO<sub>2</sub> research progressed since Brun, Friedman and Dennis' book on sCO<sub>2</sub> power cycle activities in 2017, [1]. The chapter "Test facilities", [2], describes four American test facilities in detail and mentions activities in Japan and South Korea. Considering the amount of experimental work in the last years, recent review papers focus on specific topics: Wu et al. [3] focused on Brayton cycles in nuclear engineering applications and White et al. [4] presents sCO<sub>2</sub> turbomachinery designs, most of which are planned to be tested or already were. A list of experimental facilities is given in Table 1. Yu et al.'s bibliometric analysis [5] presents the main players in sCO<sub>2</sub> Brayton cycles: United States, China, South Korea, Australia, and India. This fact more or less also shows in experimental cycles. Europe's research is clearly not as advanced, having only small scale test facilities and does not execute extensive research in turbomachinery as only two test facilities have a turbine [4].

The TU Wien test facility stands out as it is a transcritical cycle. The review papers show that most of the theoretical and experimental research is done on Brayton cycles with the exception of Net Powers Allam cycle and one of KIER's cycles being transcritical.

Experimental work with conditions suitable for sCO<sub>2</sub> research is expensive, labor-intensive and full of risks of not having considered every practical aspect. Some of the scientific community acknowledges the need to publish "practical aspects", "guidelines" or "lessons learned". SNL published their lessons learned on the process of constructing and operating the loop for turbocompressor testing [6]. They also provide a guideline of design and operation of sCO<sub>2</sub> R&D systems, [7]. BMPC have published practical aspects of sCO<sub>2</sub> Brayton system testing [8]. In the project report of the Australian solar-driven sCO<sub>2</sub> Brayton cycle, a section is dedicated to lessons learned regarding materials, [9]. Within the sCO<sub>2</sub>-HeRo project an extensive description of operational experiences is given for the sCO<sub>2</sub>-HeRo, SCARLETT and SUSEN test loops, [10]. Cranfield University presented broad lessons learned on cost assessment, the test facility and modelling, [11], and on commissioning, [12], and experiments, [13].

In this context, we show never before published results from our facility during its phase of proof-of-concept and early heat transfer measurements. We also include a lessons learned section to give practical advice.

### Test facility at TU Wien and its configurations

Three major sets of experiments were conducted or are scheduled in various configurations of the test facility, see Figure 1: testing during the national project, heat transfer measurements and future experiments in the EU-funded project SCARABEUS. In the test facility's first configuration during our national project, the aim was the proof of concept and gaining experience in operation of the simple transcritical and supercritical cycle.

\* corresponding author(s)

**Table 1:** sCO<sub>2</sub> test facilities, names in italics are brand or project related names.

Organization	Name test facility	Location	Timeframe/status	Ref.	Reviewed
SNL	more than one test rig	Albuquerque, NM, USA	research ongoing with several test rigs	[6], [7]	[2], [3], [4]
SwRI	SwRI SunShot facility, 1 MWe sCO <sub>2</sub> test loop	San Antonio, TX, USA	SunShot finished (2011-2018), last paper published in 2018	[14], [15]	[2], [3], [4]
Echogen Power Systems	<i>EPS100</i>	Akron, OH, USA (Olean, NY)	test program in Olean, NY, USA completed in 2014; research ongoing at Akron test facility	[2]	[2], [3], [4]
Naval Nuclear Laboratory op. by BMPC	<i>Integrated System Test (IST)</i>	West Mifflin, PA, USA	finished	[8]	[2], [4]
GTI Energy, SwRI, GE Global Research, DOE many others through Joint Industry Program	<i>STEP Demo</i> , 10 MWe sCO <sub>2</sub> Pilot Plant Test Facility	San Antonio, TX, USA	commissioning and start-up expected late 22 or early 23, testing in 23	[16]–[18]	[3]
Net Power, Baker Hughes	<i>50-MWth test facility, Serial #1 Utility Scale Plant</i>	La Porte, TX, USA	La Porte demonstration site connected the grid in fall 21 (2012-2021), first utility-scale power plant in Permian West, TX expected to go online in 26	[19], [20]	[4]
KAERI, KAIST, POSTECH	<i>SCIEL</i>	Daejeon, KR	finished	[21]	[2], [3], [4]
KAIST, KAERI	<i>SCO2PE</i>	Daejeon, KR	finished	[22], [23]	[2]
KIER	5 cycles so far	Daejeon, KR	full 5 <sup>th</sup> cycle commissioning expected in 2020, not yet published	[24], [25]	[2], [3], [4]
TIT, IAE	bench scale test facility	Tokyo, JP	finished	[26]	[4]
Shouhang, EDF	10MWe supercritical cycle + CSP demonstration	Shouhang, CN	2018-2023, commissioning of retrofit cycle to industrial CSP plant planned end of 2021, no news since end of 2019	[27]	[4]
CHNG, TPRI	5 MW fossil-fired supercritical CO <sub>2</sub> power cycle pilot loop	Xi'an, CN	experiments were planned in 2020, no news since 19	[28]	[3]
Indian Institute of Science, SNL	test facility for supercritical CO <sub>2</sub> Brayton cycle	Bangalore, IN	research seems ongoing	[29]	/
CSIRO	Solar-Driven Supercritical Brayton Cycle	Newcastle, AUS	project completed (2012-2017), now collaboration with US DOE => joined the STEP Demo project	[9]	[3]
The University of Queensland	Refrigerant and Supercritical CO <sub>2</sub> Test Loop, <i>PHPL</i>	Queensland, AUS	no news on test loop since 2016; ASTRI project ongoing, demonstration planned end of 22	[30]–[32]	/
Baker Hughes	Prototype compressor test rig	Florence, IT	2018-2021, results paper published in 2022	[33]	/
CVR	<i>SUSEN</i> test loop	Prague, CZ	since ~2007, research on several experimental projects (e.g., COMPASsCO <sub>2</sub> ) is ongoing	[34], [35]	/
IKE	<i>SCARLETT</i>	Stuttgart, DE	finished, team involved in other sCO <sub>2</sub> projects	[36], [37]	/

<b>Organization</b>	<b>Name test facility</b>	<b>Location</b>	<b>Timeframe/status</b>	<b>Ref.</b>	<b>Reviewed</b>
Project Consortium (University Duisburg-Essen, CVR, University of Stuttgart)	<i>sCO<sub>2</sub>-HeRo</i> loop	Duisburg, DE	projects sCO <sub>2</sub> -HeRo (2015-2018), sCO <sub>2</sub> -Flex (2018-2021) and sCO <sub>2</sub> -4-NPP (2019-2022) finished	[10], [38]	[4]
Cranfield University	<i>Rolls-Royce sCO<sub>2</sub> Test Rig</i>	Bedfordshire, UK	research ongoing, in operation	[11]–[13]	/
Brunel University, Engoia	<i>HT2C</i> facility	London, UK	project I-ThERM finished (2015-2021)	[39]	[4]
LUT University	<i>LUTsCO<sub>2</sub></i> facility	Lappeenranta, FIN	only design published so far, research ongoing	[40]	/
TU Wien	sCO <sub>2</sub> test facility	Vienna, AUT	project SCARABEUS (2019-2023) ongoing, experiments expected in 23	This paper.	/

The experimental set-up consisted of the pump, a heater, an expansion valve as a substitute for the turbine, a water-cooler and a tank, see Figure 2. The CO<sub>2</sub> was heated up to 320 °C with thermal oil and reached a pressure of 240 bar at a mass flow rate up to 0.33 kg/s.

In the second configuration, heat transfer measurements were conducted for heating up supercritical CO<sub>2</sub> at pressures up to 220 bar and temperatures up to 150 °C. For cooling and condensing experiments, the test facility was modified with a new test section including a pre-cooler and test tubes with microfins and several improvements were undertaken. The experiments took place at sub- and supercritical pressures up to 100 bar, temperatures up to 180 °C and for a working fluid consisting of pure CO<sub>2</sub> and a CO<sub>2</sub>+refrigerant mixture.

In the third configuration (SCARABEUS), the test facility operates as a recuperated Rankine cycle. The commissioning will take place in April 2023. The facility will operate at high temperatures up to 650 °C. One part of the planned research focuses on Printed Circuit Heat Exchangers (PCHE): two different designs will be tested. The main focus, however, lies on testing novel zeotropic CO<sub>2</sub>-based working fluids that allow condensation at high temperatures. The goal is to condense the working fluid at air temperatures as high as 35 °C, which we will prove by experiments.

<b>NATIONAL PROJECT</b>	<b>HEAT TRANSFER</b>	<b>SCARABEUS</b>
<ul style="list-style-type: none"> <li>• Simple cycle layout with expansion valve</li> <li>• T<sub>max</sub>=320 °C</li> <li>• P<sub>max</sub>=240 bar</li> </ul>	<ul style="list-style-type: none"> <li>• Test section for heat transfer when heating up supercritical CO<sub>2</sub></li> <li>• New test section for cooling &amp; condensing</li> <li>• Several improvements in cycle</li> </ul>	<ul style="list-style-type: none"> <li>• Recuperated cycle</li> <li>• T<sub>max</sub>=650°C</li> <li>• P<sub>max</sub>=235 bar</li> <li>• Air cooled condenser</li> <li>• Printed circuit heat exchangers as recuperator</li> </ul>
<ul style="list-style-type: none"> <li>• Proof of concept and practical knowledge of transcritical and supercritical cycle</li> </ul>	<ul style="list-style-type: none"> <li>• Heat transfer measurements</li> <li>• Pure CO<sub>2</sub></li> <li>• CO<sub>2</sub> + refrigerant mixture</li> </ul>	<ul style="list-style-type: none"> <li>• Proof of concept of CO<sub>2</sub> mixtures (at high temperatures and condensing with ambient air)</li> </ul>

**Figure 1:** visualization of projects and tasks.

The paper is structured in four parts: 1) a design section covering the national project, heat transfer, and SCARABEUS, 2) a section about operation and results of the national project, 3) methods and results of the heat transfer measurements, and 4) a selection of our lessons learned.

#### **DESIGN – NATIONAL**

The test facility in its first configuration consists of five major parts, as can be seen in Figure 2 and Table 2. The high- and low-pressure sides are designed for pressures up to 240 bar and the 100 bar, respectively. The piston pump is able to provide a mass flow rate of up to 0.33 kg/s and can move liquid and supercritical CO<sub>2</sub> under some constraints. The CO<sub>2</sub> is heated up to 320 °C in a 200 kW shell-and-tube heat exchanger with the thermal oil Therminol VP-1. An expansion valve substitutes the turbine's pressure loss. The cooler is a shell-and-tube heat exchanger with water as a coolant. During start-up and in transcritical mode, the CO<sub>2</sub> is present in liquid form and stored in the tank. In supercritical mode, the tank is by-passed.

In this configuration, operation of the transcritical and supercritical cycle was tested. The conditions during experiments are shown in Figure 3. The pump receives the CO<sub>2</sub> from the tank, where it is liquid in the case of the transcritical operation. With a cooling water temperature of around 8 °C, working fluid temperatures as low as 15 °C corresponding to a pressure of ~43 bar can be achieved at state 1. The upper limit for transcritical operation is 26 °C to have a sufficient margin to the critical point. In Figure 3, a temperature of 19.5 °C and a corresponding pressure of 56.6 bar on the low-pressure side is shown. At the outlet of the piston pump, state 2, while cooling the pump with water, the outlet temperature is at around 40 °C. The CO<sub>2</sub> then enters the heater and reaches a temperature of up to 320 °C for which the inlet thermal oil temperature is at 360 °C. The expansion valve mimics the pressure loss of the turbine and is controlled to set the high pressure of the system to 220 bar. After expansion, the still hot CO<sub>2</sub> at the system's low-pressure side enters the water cooler, which controls the temperature (and thereby the pressure) at state 1. For supercritical operation, the facility is started up in transcritical operation. Then, the tank is

bypassed by cutting it off with automatic valves. The cooler slowly increases the temperature until the pressure on the low-pressure side reaches supercritical values at 4\* and 1\*. States as shown in Figure 3, yellow colored isobaric line, could not be reached with this approach because the facility does not have a mass management system for the working fluid.

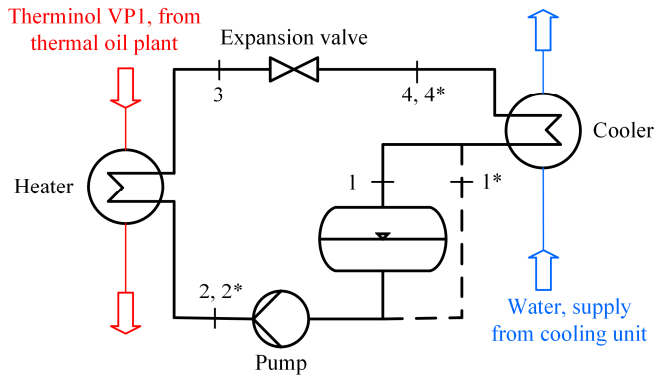


Figure 2: scheme of major components of the test facility.

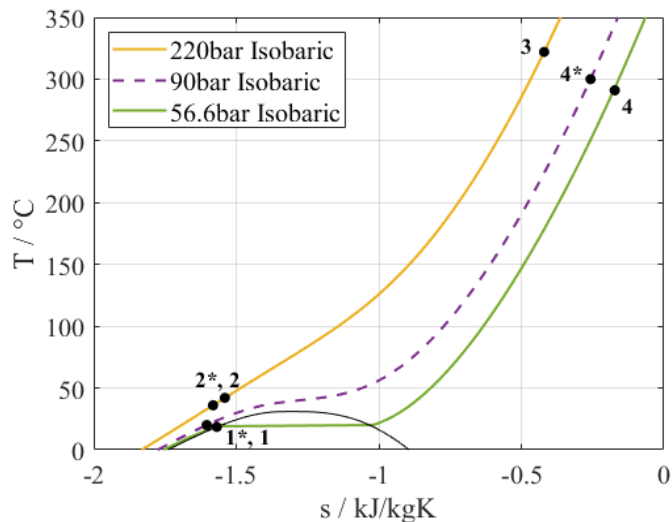


Figure 3: Ts-diagram of supercritical and transcritical cycle conditions as tested in the facility.

Table 2: List of major components of the test facility.

Component	
Heater	200 kW, Shell-and-Tube, CO <sub>2</sub> tube-side, thermal oil VP-1 shell-side
Cooler/condenser	355 kW, Shell-and-Tube, CO <sub>2</sub> tube-side, water shell-side
Pump	Piston-pump (SPECK-TRIPLEX-PLUNGERPUMPE P52/51-300CZ), max. 50 L/min, P <sub>max</sub> =280 bar
Expansion valve	Pneumatic control valve, type 3252
Tank	55 L

For heat input, an electrically heated thermal oil is used. It is provided by an external utility. Although Therminol VP-1 can be used for temperatures up to 400 °C, the maximum inlet temperature in the primary heat exchanger of the CO<sub>2</sub> facility is limited to 360 °C as the thermal oil has to be pressurized to prevent evaporation at these high temperatures. The systems pressure needs to be at around 10 bar.

For the working fluid we use CO<sub>2</sub> of food grade, by Linde under the name Biogon C E 290. It has a quality of more than 99.7% CO<sub>2</sub>. We buy gas cylinders with riser pipe to be able to fill the test facility with liquid CO<sub>2</sub>. It has to be assumed that the CO<sub>2</sub> gets contaminated with lubricant from the pump as this was observed during plant modification.

For safety, a Hazard and Operability Study (HAZOP) under professional lead was performed after the functional design of the plant. A hard-wired shut-down of safety and integrity level 2 (SIL2) of the thermal oil pump and heater in the case of excessive temperature was necessary. The number and position of safety valves was determined. For heat exchangers, it is necessary to consider a rupture of a heat exchanger pipe. In this case, the CO<sub>2</sub> from the high-pressure side of the heat exchanger would expand towards the low-pressure-shell-side, which is designed for 16 bar. The water line's design pressure is only 8 bar. The expanding CO<sub>2</sub> from the test facility's high-pressure levels into the low-pressure heating and cooling systems would lead to overpressure there. As the CO<sub>2</sub> would mix with water (cooler) or thermal oil (heater), the amount of gas-liquid-mixture to be discharged would have been too high to deal with for a safety valve. The solution was to include burst discs directly on the heat exchangers' low-pressure side. A system of flash lines and flash tanks were designed to collect the blown out mixture. All the parts of the test rig were pressure tested individually with water. A leak test under supervision from the notified body was performed with nitrogen in the finished version of the facility as a last step before approval. After that, major modifications have to be checked and approved by the notified body.

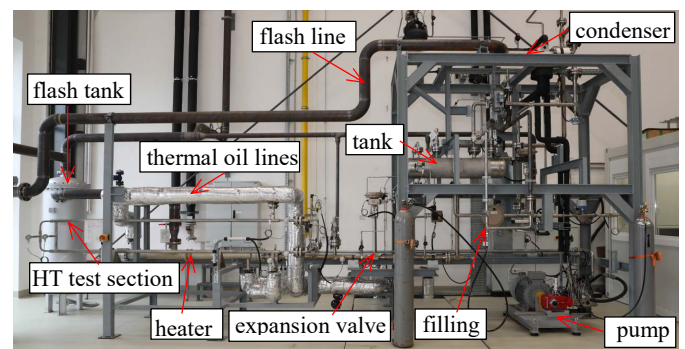


Figure 4: components of the test facility.

## DESIGN – HEAT TRANSFER

### First test section

The first test section for measuring the heat transfer coefficient of CO<sub>2</sub> to the inside of a tube wall is depicted in Figure 5. The



test section, a counter flow heat exchanger, consisted of a single tube with the CO<sub>2</sub> flowing inside, surrounded by an outside shell where thermal oil (VP-1) provided the heat source. The tube was U-shaped, where each U-part was about 3 m long. Regrettably, the design suffered from a lack of time and money. The results were not as expected and practically unusable due to the following issues:

- The Coriolis sensor that measured the mass flow of CO<sub>2</sub> into the test section was positioned upstream on the low-pressure side of the pump. This meant that the (by-design) leakage across the high-pressure gaskets inside the pump could not be accounted for during the heat transfer measurements upstream.
- Since the flow of CO<sub>2</sub> from the tank to the pump was in a saturated state, any heat from the environment transferred to the working fluid caused evaporation, leading to a two-phase flow in the Coriolis sensor and further degrading its accuracy. Density measurements that were also available from the Coriolis sensor could have at least indicated a two-phase flow, but they were not recorded during that early tests (yet).
- The test section had practically no straight inlet section that could have normalized the CO<sub>2</sub>'s flow profile, causing heavy turbulences in the first section.
- The bend in the middle of the test section is simply impractical and should have been avoided. A straight tube would have been easier to handle concerning all aspects of heat transfer measurements and result analysis.
- If a bend was necessary, it should have been in a horizontal rather than a vertical plane. The hydrostatic pressure difference between the U-parts already complicates the measurements.
- The entire measurement concept was not thought out well. Instead of measuring surface temperatures, only bulk inlet and outlet temperatures were measured. This meant that further assumptions on the heat transfer mechanism, in particular on the thermal-oil side, had to be made, decreasing the accuracy of the final results. Additionally, some of the boundary conditions for typical heat transfer correlations were not met.
- The special behavior of CO<sub>2</sub> near the critical point was not considered at all. Non-equilibrium effects greatly influence the heat transfer under such conditions. Non-equilibrium is due to thermo-physical properties barely reaching a stationary state. For example, the density experiences a hysteresis effect depending on the direction of the isobaric process it is undergoing [41].
- The sensors used were of poor quality, resulting in high inaccuracies. The PT100 resistance temperature detectors (RTDs) were 3-wire and only class B.
- Even though the greatest impacts on heat transfer are expected to occur at pressures slightly above the critical pressure (going through the pseudo-critical point), and only coolers would be operating at such pressures in a supercritical CO<sub>2</sub> power cycle, the test section could only

be used to measure the heat transfer coefficient when heating the CO<sub>2</sub>.

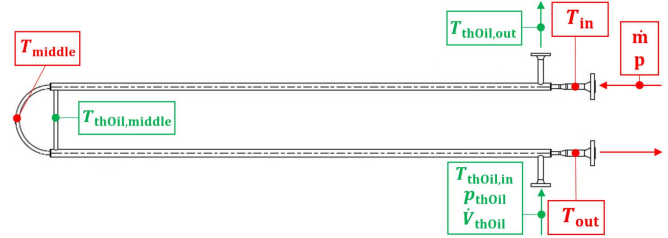


**Figure 5:** First test section for heat transfer measurements of supercritical CO<sub>2</sub>.

### Second heat transfer test section: precooling, test tubes

During our current project SCARABEUS, the facility was extended by a new test section to measure the heat transfer during in-tube cooling and condensation under enhanced heat transfer conditions by using microfins on the inner surface. This new test section is a horizontal tube-in-tube heat exchanger cooled by water. The positions of measurement devices are shown in Figure 6 and Figure 7. To control the inlet vapor content of CO<sub>2</sub>, a precooling was installed.

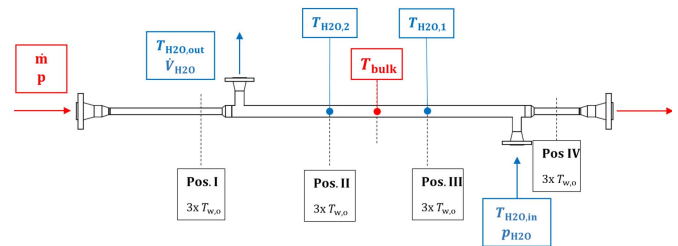


**Figure 6:** schematic of current test tube for heat transfer measurements when cooling and condensing; red...working fluid, blue...water, black...wall temperature.

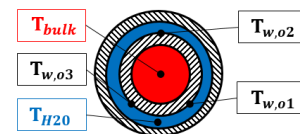


**Figure 7:** position of the temperature sensors at the cross section of the current test tube.

Many of the first test section's flaws were eliminated. The most important being (many) high level temperature sensors (PT100, 4-wire, class AA). These were located directly in the CO<sub>2</sub>, in the water channel and at the outer wall of the inner tube.

A much lower uncertainty of reduced data can be observed in this new heat transfer measurement section. A part of those experiments is shown in [42].

### DESIGN – SCARABEUS

The SCARABEUS concept (Supercritical CARbon dioxide /Alternative Blends for Efficiency Upgrade of Solar power plants) envisions a power block to be coupled with concentrated solar power (CSP) plants. Using a CO<sub>2</sub>-based, binary mixture as a working fluid instead of water/steam, this cycle shows an improved efficiency, smaller turbomachinery, fewer equipment

and an air-cooled condenser that enables dry cooling. Even at high ambient temperatures, condensation of the working fluid becomes feasible with ambient air, thus, making a recuperated Rankine cycle possible. The change in properties necessary to enable condensation with air at high ambient temperature is achieved by blending the CO<sub>2</sub> with an additive with a higher critical point. Condensation of a mixture undergoes a temperature glide as the isobaric lines in the two phase region are sloped in the T<sub>s</sub>-diagram, see Figure 9. Therefore, condensation of binary mixtures shows less irreversibilities compared to condensing a pure fluid.

The test facility is used for the experimental validation of the SCARABEUS concept in a slightly changed layout as can be seen in Figure 8 and will test one mixture as a working fluid. As of today, a carbon dioxide and hexafluorobenzene (C<sub>6</sub>F<sub>6</sub>) mixture of 8 % molar fraction of C<sub>6</sub>F<sub>6</sub> will be used. The mixture did not perfectly meet all target properties but presents the best compromise. It is thermally stable up to 600 °C [43], slightly toxic (same hazard class as CO<sub>2</sub>) and moderately flammable. To reduce the operational risks, a lower percentage of C<sub>6</sub>F<sub>6</sub> will be used than we would suggest for an actual plant. The target maximum temperature of 650 °C had to be reduced to 550 °C.

For the chosen mixture, the T<sub>s</sub>-diagram looks as shown in Figure 9. The Peng-Robinson EoS with a binary interaction parameter of  $k_{ij}=0.033$  was used to calculate the properties. This approach shows good agreement with experimental data of compositions close to design (around 85% molar fraction of C<sub>6</sub>F<sub>6</sub>). The critical point is estimated at around 70 °C and 107 bar. Thermo-physical properties at and near the critical point cannot reliably be calculated by EoS as these usually have convergence issues and give no solutions at these conditions.

Compared to pure CO<sub>2</sub>, the two-phase region reaches higher temperatures and isobaric lines are sloped in the two-phase region of the T<sub>s</sub>-diagram. This means that condensation of the mixture happens in a temperature glide. For example, at a low pressure of 95 bar, the working fluid would start condensing at 106 °C and be fully liquid at around 52 °C.

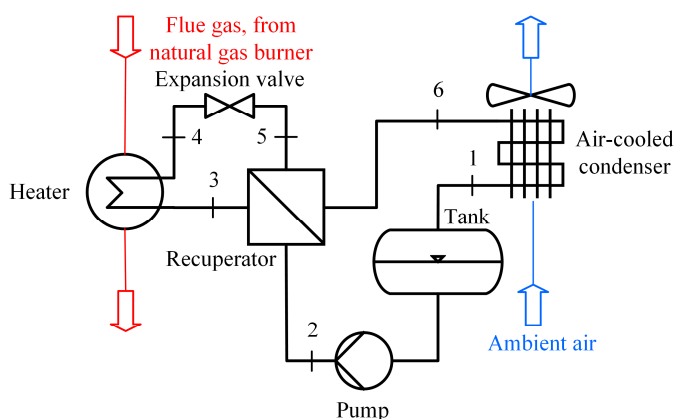


**Figure 8:** scheme of major components of the test facility as for the SCARABEUS project.

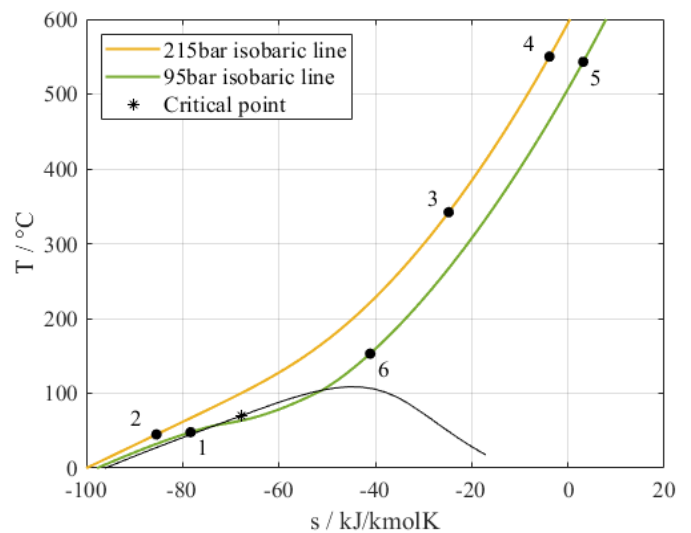


**Figure 9:** T<sub>s</sub>-diagram with recuperated cycle states as to be tested in the facility operated with CO<sub>2</sub>+C<sub>6</sub>F<sub>6</sub>.

Three new heat exchangers make up the modified cycle, each of them specifically designed for the CO<sub>2</sub>+C<sub>6</sub>F<sub>6</sub> mixture, but for 650 °C since at this time we did not know about temperature limitations due to thermal degradation:

**Table 3:** list of components for SCARABEUS.

Component	
Heater	220 kW, supplies the cycle with a design temperature of 650 °C by using 850 °C flue gas from a natural gas burner, material: Inconel 617
Air-cooled condenser (ACC)	120 kW, fins at the air-side and microfins at the inner surface, for heat transfer enhancement see [42] and [44]
Recuperator	350 kW, Printed circuit heat exchanger (PCHE), stainless steel
Expansion valve	Custom-built valve to withstand 650 °C

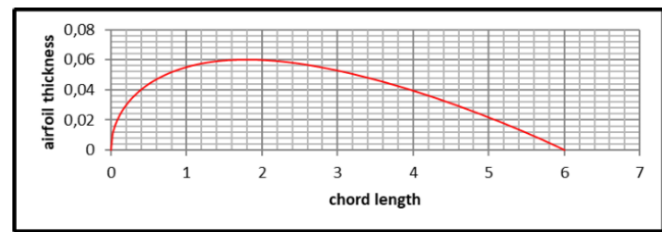
### The recuperator – a printed circuit heat exchanger

The recuperator will be a printed circuit heat exchanger (PCHE), a technology of compact heat exchangers withstanding high pressures and temperatures while ensuring high safety levels. Two PCHE's with different geometries will be tested: airfoil and S-shaped.

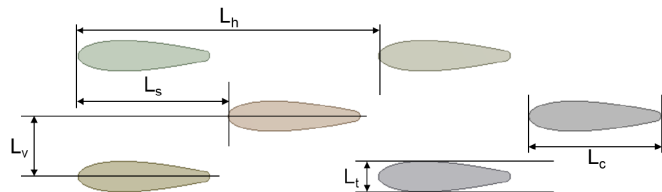
To determine optimized geometries, a CFD analysis was carried out with ANSYS CFX 2019 R3. Besides proper boundary conditions representing the thermal-hydraulic problem at hand, the mesh and the chosen turbulence model have the biggest impact on the results of the simulation. Therefore, a mesh independency study was conducted to be able to get reliable results as well as the best possible ratio of good results to simulation time. The selection of a fitting turbulence model can't be handled separately because the quality of the mesh directly influences the results with the chosen turbulence model. Vice versa, there are different requirements on the mesh for different turbulence models. In the used software package, many different

models are available. The refinement of the boundary layer, the overall refinement of the mesh as well as the number of elements around the fins with particular attention to the fillets at the beginning and the end of the fins were modified. Based on experimental results from a zig-zag configuration heat exchanger for H<sub>2</sub>, from two turbulence models k-ε and SST, SST was chosen as it better predicts the pressure losses.

Temperature prediction was equally good for both models. Figure 10 shows the geometrical model of the airfoils, the characteristic dimensionless numbers and the channel modelled in CFD. Figure 11 shows the S-shape. As mechanical stress peaks would occur at the sharp edge of the airfoil, it is slightly rounded which is in line with the manufacturing requirements. The trivial result of maximizing the heat transfer rate to pressure drop ratio leads to large numbers for the horizontal and vertical pitch and therefore to bigger overall dimensions of the PCHE. Bigger dimensions generally mean higher material and manufacturing costs. Instead, the optimization is fed with a zigzag channel PCHE as a reference case and the surface area is reduced by the optimizing function at a given heat transfer and pressure drop.



$$v(x) = \frac{L_T}{0.2} \left( 0.2969 \sqrt{\frac{x}{L_c}} - 0.126 \left(\frac{x}{L_c}\right) - 0.3537 \left(\frac{x}{L_c}\right)^2 + 0.2843 \left(\frac{x}{L_c}\right)^3 - 0.1015 \left(\frac{x}{L_c}\right)^4 \right)$$



Dimensionless number	Definition
Staggered	$\zeta_S = 2L_s/L_h$
Horizontal	$\zeta_H = L_h/L_c$
Vertical	$\zeta_V = L_v/L_t$



**Figure 10:** Geometrical characterization and modelling in CFD of airfoil shape.

The CFD results show that S-shape configuration with lower vertical pitches and airfoils in almost every parameter set show a reduction in surface area when compared to zigzag channels.

The following design conclusions can be made about the S-shape:

- Transverse pitch ↑ means size reduction ↓
- Vertical pitches ↓ means performance ↑
- Further decreasing the pitch is not possible due to manufacturing.
- A maximum of 7.6% of surface reduction is possible with S-shapes compared to zigzag.

For airfoil, the following is true:

- No clear dependencies on parameters
- Staggered number ↑ means size reduction ↑ (So, staggered arrangement performs best while inline arrangement performs worst.)
- Effects of vertical and horizontal number are correlated, see Figure 12
- With a Multi-Objective Genetic Algorithm, the optimized airfoil shape leads to a surface reduction of 17.7% compared to the zigzag shape.

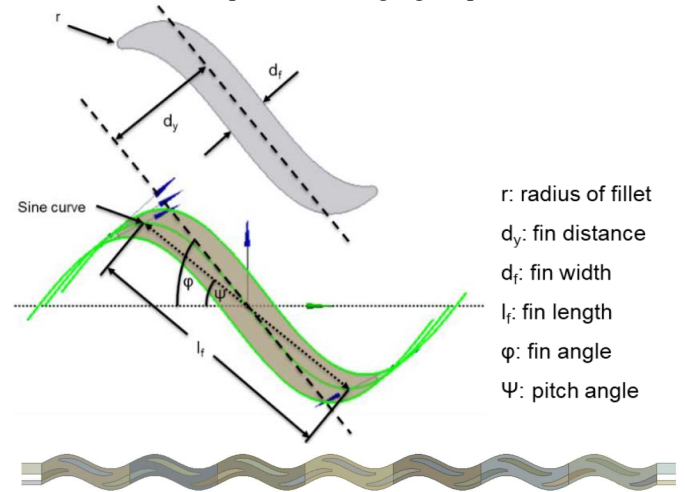


**Figure 11:** Geometrical characterization and modelling in CFD of S-shape.

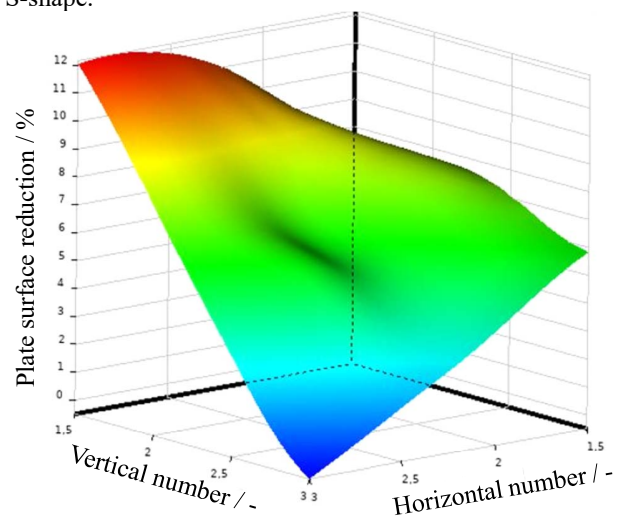


**Figure 12:** Correlation between vertical, horizontal number and surface reduction at a staggered number of 0.5.



## Safety

Additional safety measures are necessary when working with hazardous substances in relevant amounts in an indoor test facility. A fire-resistant enclosure surrounds the entire test facility, see Figure 13 and Figure 14. It serves two purposes: 1) closing off the air supply in the case of fire and preventing the spread of fire for thirty minutes and 2) providing a space for continuous air ventilation during normal operation to dilute potential leakage and venting it outside over the chimney.

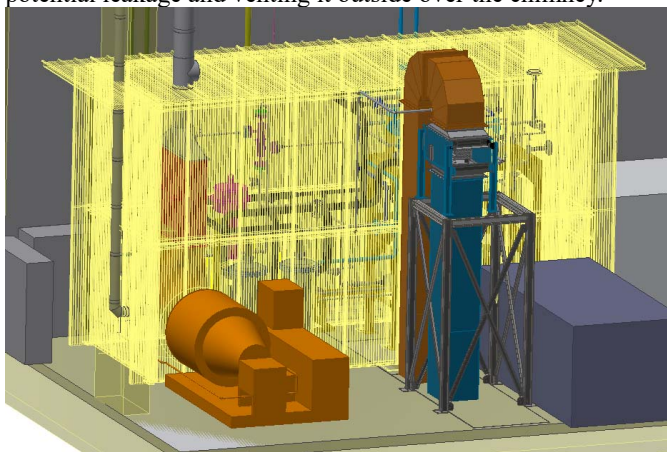


Figure 13: fire-resistant enclosure as planned.



Figure 14: fire-resistant enclosure steelframe as built.

Breaking new ground in research, e.g., adding a hazardous substance to your working fluid and heating it up to 650 °C, can be challenging when it comes to questions of safety.

The first issue is thermal degradation of substances at this elevated temperatures. Small scale testing was accounted for in the project plan of SCARABEUS and showed the limits for operation in the test facility. No laboratory would give a quote on identifying the degradation products which made it impossible to test the 650 °C and potentially create lighter harmful substances with the fluoride from C<sub>6</sub>F<sub>6</sub>.

The second issue is flammability, which is the case for hexafluorobenzene. Since the substance is rarely used, no data on flammability in the mixture with carbon dioxide diluted in air

at extreme conditions (leaking from 220 bar and 650 °C to ambient conditions) is available.

The third issue is toxicity and reactivity. Carbon dioxide itself is hazardous to humans as it is an asphyxiant gas. Three CO<sub>2</sub> detectors at the vicinity of the test facility are used to detect potential leakages in the range of allowed workplace concentrations. Small leakages of the CO<sub>2</sub>+C<sub>6</sub>F<sub>6</sub> mixture do not bring an additional risk with them since the enclosure contains those possible leakages and C<sub>6</sub>F<sub>6</sub> will condensate at ambient conditions. From theoretical analysis, sulfur dioxide (SO<sub>2</sub>) and titanium tetrachloride (TiCl<sub>4</sub>) might seem a good additive choice for SCARABEUS, but SO<sub>2</sub> is highly toxic and TiCl<sub>4</sub> is reactive with air humidity and releases hydrochloric acid.

For a test facility of our size and relevant mixtures defined by the project, one filling with SO<sub>2</sub>+CO<sub>2</sub> would involve 40 kg of SO<sub>2</sub>. When a burst disc breaks, this amount would be released to the surroundings. During the proposal, the idea was to pass the released amount over an active carbon filter to strip the additive. SO<sub>2</sub> can only be stripped if active carbon is impregnated with potassium carbonate and its efficiency is decreased at elevated temperatures, even at 50 °C. There is no filtering effect at temperatures higher than 100 °C. Massive amounts of the pricy impregnated active carbon is needed to ensure the necessary contact times. Measures like this were not budgeted for and seem unrealistic for a research or industrial project.

The only way to pursue is to reduce the amount of used additive or not use them at all. A dispersion calculation allows to estimate acceptable amounts. The ALOHA (Area Locations of Hazardous Atmospheres) software from the EPA's (Environmental Protection Agency) CAMEO software package is used to evaluate the dispersion calculation. The results are danger zones for the IDHL value (Immediately Dangerous to Life and Health) and the AEGL (Acute Exposure Guideline Levels) and time estimations on how long these zones prolong.

The results showed very high concentrations for short periods of a few minutes. Using a smaller amount of C<sub>6</sub>F<sub>6</sub>, thus, leading to a reduced additive concentration in the working fluid, will be possible. Neither SO<sub>2</sub> nor TiCl<sub>4</sub> are safe enough to use at our test facility. The danger zone (IDHL=100 ppm, AEGL-3=30 ppm) for SO<sub>2</sub> is shown in Figure 15.

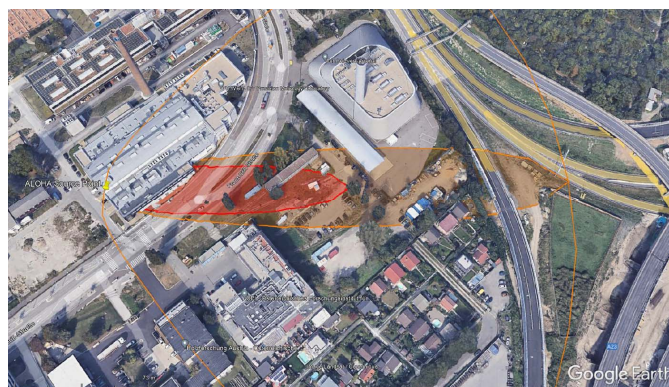


Figure 15: results of the dispersion calculation with heavy gas model for a release of 37 kg SO<sub>2</sub> in 3 min with wind direction west, IDHL zone in red, AEGL-3 zone in orange.

## OPERATION AND RESULTS – NATIONAL

Our process control system is set up in the software APROL of B&R. Most of our hardware, except the SIL relevant logic components, come from B&R.

### Filling CO<sub>2</sub> using a natural circulation cooling system

There are several possible ways to fill a plant or test rig with its working fluid, in this case CO<sub>2</sub>. The most obvious one is to use a pump that feeds the working fluid from a storage vessel directly into the system. A process without a pump, only utilizing the pressure difference between the tank and the plant, is possible, but faces the challenge of diminishing pressure differences when both the tank and the system are in a saturated (two-phase) state at the same ambient temperature. Then, both the tank and the plant are at the same saturation pressure and no flow between them can occur. There are two ways to create a (negative) pressure gradient from the tank to the system again:

- Heat the tank, which increases the saturation pressure there
- Cool (at least a part of) the plant, decreasing its pressure

The test rig presented in this paper utilized a natural circulation cooling system that managed to effectively transfer the CO<sub>2</sub> from gas cylinders into the plant without the need of a pump or any other additional equipment. The basic setup is shown in Figure 16:

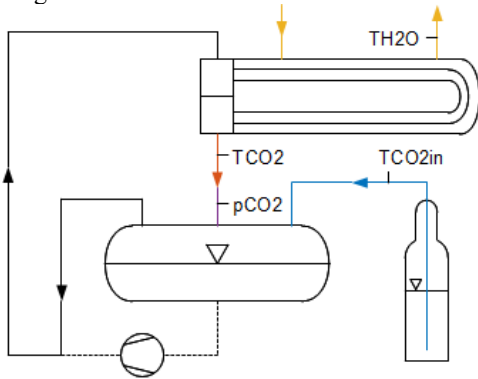


**Figure 16:** Sketch of the natural circulation cooling system used to fill the test rig with CO<sub>2</sub>.

A gas cylinder containing CO<sub>2</sub> in a saturated state is attached to the plant's drum. The gas cylinder has a dip tube to make sure that only the liquid phase is being transferred into the system. CO<sub>2</sub> vapor flows from the drum past the pump (which is shut down) into the plant's cooler (see Figure 2, the heater and expansion valve are omitted in Figure 16). Since the cooling water temperature is about 8 °C and therefore lower than the plant's ambient temperature of about 22 °C in the lab, the CO<sub>2</sub> condenses. Gravity then pulls the liquid CO<sub>2</sub> down into the drum, which creates a void in the cooler that pulls additional gaseous CO<sub>2</sub> into it, resulting in a continuous circulation. Figure 17 demonstrates an actual filling process:

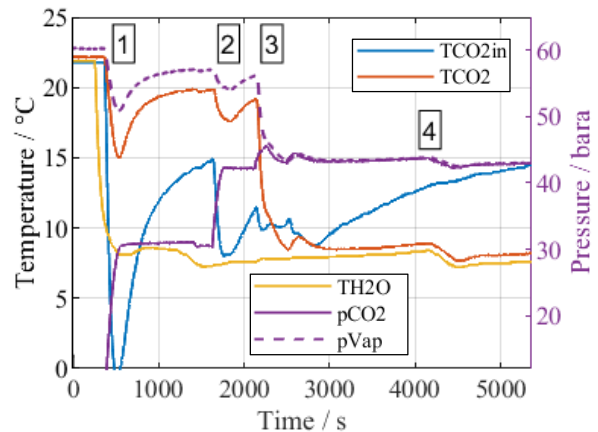


**Figure 17:** Filling CO<sub>2</sub> using natural circulation cooling.

See Figure 16 for the position of the individual sensors listed in the legend of Figure 17. Before the start of the process, all temperatures (CO<sub>2</sub> inlet temperature *TCO2in*, CO<sub>2</sub> temperature at the outlet of the cooler *TCO2*, cooling water return temperature *TH2O*) are at the ambient temperature of 22 °C and the CO<sub>2</sub> pressure *pCO2* is at 0 barg (the plant is empty). At the time marked with 1, the cooling water valve is opened and cold water at about 8 °C started flowing through the cooler, resulting in a steep decline in the water return temperature. Shortly after, the valve to the first gas cylinder is opened. The expansion of the CO<sub>2</sub> in the gas cylinder into the still empty plant causes a sharp decrease in the CO<sub>2</sub> inlet temperature, which also cools down the test rig as a whole. The CO<sub>2</sub> pressure increases, but it does not reach the saturation pressure *pVap* yet, which is calculated at the CO<sub>2</sub> temperature *TCO2*. At step 2, another gas cylinder is hooked to the plant, the CO<sub>2</sub> pressure increases further, but the vapor pressure is still not reached. Only after step 3, when two additional (half full) cylinders are attached in short sequence, the CO<sub>2</sub> pressure reaches the vapor pressure, after which both pressures remain practically identical. The fact that the CO<sub>2</sub> vapor is continuously flowing through the cooler and condensing there can be seen at the time marked with 4: the cooling water's two-step temperature controller activates and cools down the water by a few degrees. The CO<sub>2</sub> temperature follows the water temperature very closely, causing the CO<sub>2</sub> pressure in the plant to decrease. The quick reaction time strongly suggests that CO<sub>2</sub> is flowing through the cooler and natural circulation is established.

### Full operation

The process of successful start-up, transcritical operation and shut-down is shown in Figure 18 and Figure 19 with the help of a few parameters. The steps are as follows:

- 0-1:
- The sCO<sub>2</sub> pump is controlled to provide 0.3 kg/s CO<sub>2</sub>.
  - The electrical heater to heat the thermal oil that will serve as a heat source for the CO<sub>2</sub> is set to manual power. It heats the thermal oil in a primary circuit to 360 °C. With a controlled valve, thermal oil from the secondary circuit is mixed with the primary circuit thermal oil to reach a set temperature of currently 60 °C at  $T_{ThOil,ElHeater,Out}$ . By controlling the thermal oil mass flow rate the thermal oil temperature at the inlet of the CO<sub>2</sub> heater is adjusted.
  - The water valve controlling the duty at the condenser is opened manually.
- 1-2:
- The temperature in the tank is controlled by the water flow rate in the condenser. The pressure in the tank/ at the low-pressure side of the test facility remains constant, too.
  - This effects back on the thermal oil plant and results in lower temperatures there.
- 2-8:
- The temperature controller for the thermal oil temperature of the heater's outlet  $T_{ThOil,ElHeater,Out}$  is set to 340 °C and starts ramping up.
- 3-12:
- The expansion valve controls the pressure on the high-pressure side to 110 bar.
- Pressure oscillations in the pressure on the high-pressure side of the test facility caused by evaporating CO<sub>2</sub> are clearly visible.
- 4-5:
- The temperature at the outlet of the heater sinks. The controller tries to increase the thermal oil mass flow to reach the temperature  $T_{ThOil,CO_2Heater,In}$ . We will later find out that the thermal oil plant was not properly vented and air was in the system.
- 6-7:
- The thermal oil mass flow rate breaks down.
- 8-9:
- The set value for the pressure on the high-pressure side is set to 220 bar. The expansion valve begins to close.
- 9-10:
- 10 minutes of successful transcritical operation with controlled values.
- 10-11:
- The expansion valve controller is set to 110 bar.
- 11-12:
- The coolers in the thermal oil plant cool down the thermal oil temperatures.
- 12-end:
- The expansion valve is opened and the pressure on the high-pressure side quickly decreases to the low-pressure side level.
  - The CO<sub>2</sub> pump and thermal oil pump are turned off.

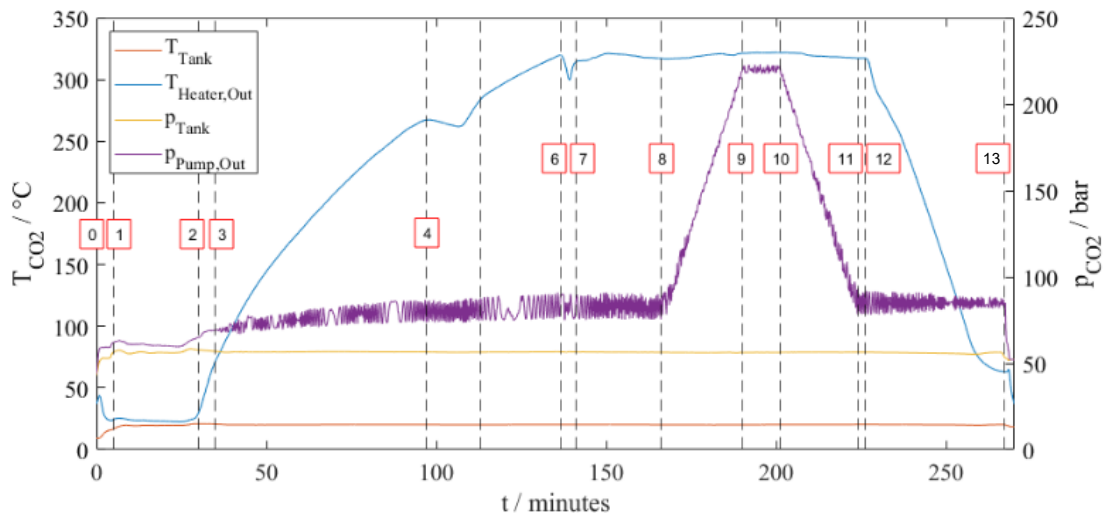


Figure 18: a few selected parameters of the successful transcritical operation.



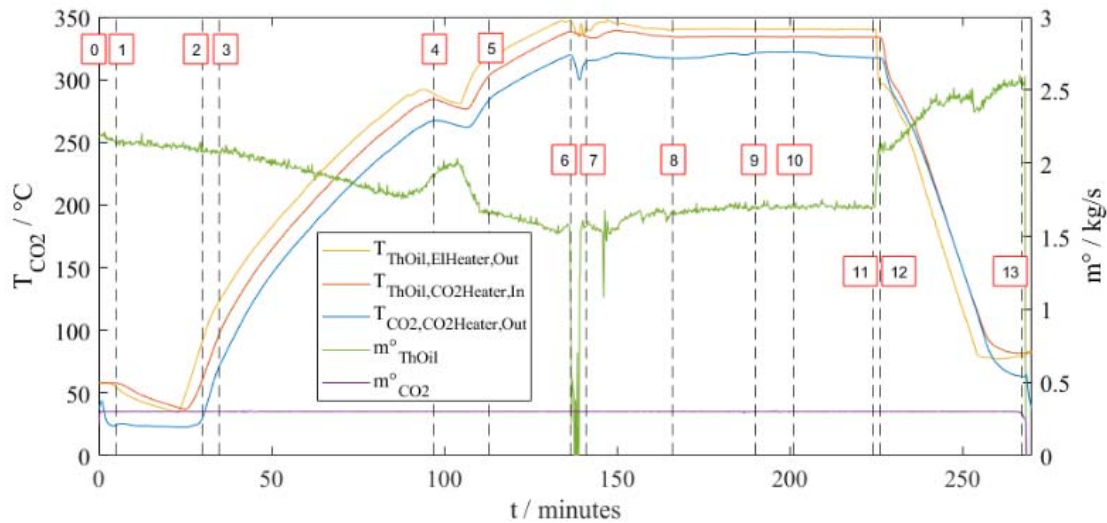


Figure 19: a few selected parameters of the successful transcritical operation.

## METHODS AND RESULTS – HEAT TRANSFER

As already mentioned in the design section, some grave mistakes were made during the design phase of the test section. Non-normalized flow into the test section (caused by a lack of an inlet section) caused turbulences so strong that the results in the first half of the test section were completely unusable. In the second half, results were better, but the use of inaccurate measurement equipment led to confidence intervals in the range of several orders of magnitude. This was exacerbated by the fact that small temperature differences had to be measured to accurately determine the heat fluxes, especially when going through the pseudo-critical point, where a spike in the CO<sub>2</sub>'s specific heat capacity resulted in only minor temperature increases from the inlet to the outlet. CO<sub>2</sub> properties are calculated according to Span and Wagner [45]. A comparison of the results to the predictions when using Gnielinski's correlation [46] is shown in Figure 20:

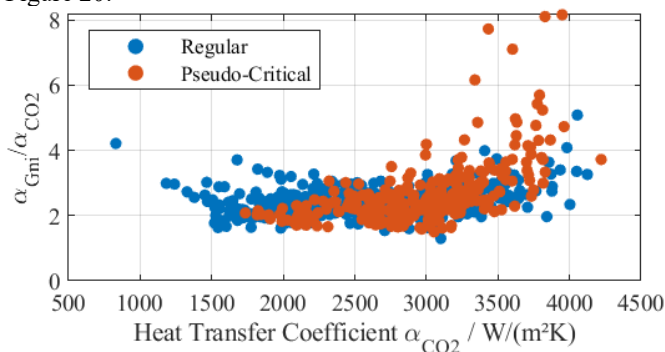


Figure 20: Results of the first test section compared to the predictions when using Gnielinski's correlation.

Figure 20 shows the relative predictions of Gnielinski's correlation to the test section results, categorized in measurements where the CO<sub>2</sub> did not go through the pseudo-critical point (blue points) and those where it did (red points).

Results at lower pressures tended to be higher, which is qualitatively correct. One can see that the results were consistently lower than what could be expected from Gnielinski's correlation, most of them by a factor greater than two, and some of the pseudo-critical measurements even going as far as 8 times lower than what could be expected.

## LESSONS LEARNED

**Measurement equipment and data reduction has to be the first thing to consider.**

- Do not compromise here.
- Check with data reduction and error calculation where you could save money. Overly complicated post-processing is avoided and time is saved.
- Plan for over-determined systems to do correction calculations.
- High class temperature sensors are necessary for heat transfer measurements.
- Wall temperature measurement are necessary for heat transfer measurement.
- There is no ideal placement of the Coriolis sensor.
- Use the full potential of Coriolis sensor.
- Use a differential pressure sensor for level measurement, not one using time domain reflectometry.

Collecting data of a certain quality is the heart of experimental research. Besides maybe the side quest of gaining operational experience, creating data is the sole purpose to build an expensive, time-consuming test facility. This is why the measurement system must have priority during the entire project. Saving an insignificant amount of money on a low-quality temperature sensor may not be worth it in the long run.

Performing the data reduction and an error calculation early on might save money at the correct measurement devices. In



other fields, this issue is more prevalent, see for example how experimental physicists deal with it [47].

When there are possibilities to place measurement devices to achieve mathematically over-determined systems, this additional information can be used. A correction calculation according to VDI-guidelines can show inconsistencies in the data, streamline your results and provide smaller error ranges [48].

In the current test facility with a leaking pump, there is no perfect placement for the Coriolis sensor. For future experiments, the position will be changed from the low pressure side before the pump to the high-pressure side after the pump. The sensor will withstand the pressures from a material standpoint but is not recommended to be used by the suppliers. The Coriolis sensor comes with the possibility to simultaneously measure density and temperature. This information can be used to detect gas in the piping where there should be liquid.

**Safety measures are necessary and cost intensive.**

- Do not only check technical feasibility but speak to suppliers and get a quote.
- Plan for “in-house” preliminary tests tailored to answer project-specific answers.
- Be aware of possible limitations.

See *Safety* in chapter *DESIGN – SCARABEUS* for more information.

**A commercial pump with leakage is not suitable for loops.**

Per design, the used piston pump does have leakages over the low-to-high pressure sealing and the low-to-ambient pressure sealing which provide cooling exactly where heat from friction is produced. An estimated loss of less than 1% might not seem much when the pump is only passed once as it is in its commercial application for filling CO<sub>2</sub> gas cylinders. For the test facility it means losing the inventory over the course of two days.

For future experiments, the leakage from the low-to-high pressure sealing will be collected in a secondary circuit equipped with a cooler to control the pressure. When filled up, it will be pumped back to the main circuit by a second pump.

Unfortunately, the second leakage from the low-to-ambient pressure sealing is not collectable.

**The pump is not efficient without subcooling.**

Maximizing mass flow rate and reducing the amount of leakage are contrary goals. As we use a pump with three pistons, the reached mass flow rate should be linearly correlated to the number of revolutions. Figure 21 shows that the correlation is not linear in comparison to exemplarily shown linear fits of data points at lower numbers of revolutions. The explanation for such behavior is cavitation issues. In the original configuration, the required NPSH value was not reached by far. The state of the CO<sub>2</sub> was too close to the saturated state we have in the tank. The tank is located approx. 1.6 m above the pump. The hydrostatic pressure increase is smaller than for water at a similar temperature range and was not considered accordingly. The by the 1.6 m gained enthalpy difference is probably eaten up by the Coriolis sensor located before the pump.

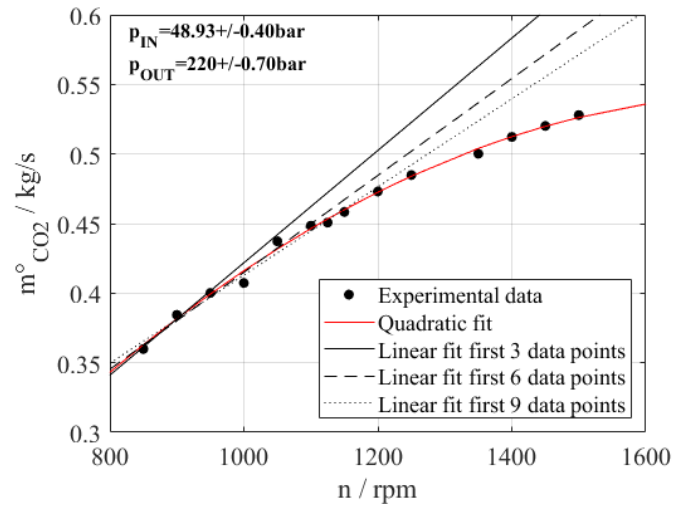


**Figure 21:** correlation of mass flow rate and number of revolutions.

The following measures were taken to reduce the cavitation issues for the coming SCARABEUS experiments:

- Water cooling of the pump inlet block and pistons.
- Reduced amount of sealing material to reduce the heat brought in by friction.
- Increased allowed number of revolutions from 900 rpm to 1500 rpm in discussion with supplier.
- Subcooling the working fluid by 10 K from saturation conditions before entering the pump in an additional heat exchanger.

**CONCLUSION**

The sheer size of the original (national) project made it difficult for the small team of scientists to execute it properly within the given time and budget constraints, and lots of mistakes were made because of it. However, the operational experience and lessons learned – in particular the insufficiencies of commercial CO<sub>2</sub> pumps, design of heat transfer measurement equipment and prioritizing measurements and data reduction – have already proved invaluable to the follow-up project SCARABEUS and will continue to serve as the knowledge base for every future project. We failed fast – at least we failed forward.

**NOMENCLATURE**

**Abbreviations**

AEGL	Acute Exposure Guideline Levels
BMPC	Bechtel Marine Propulsion Corporation
CFD	Computational Fluid Dynamics
CHNG	China HuaNeng Group
CSIRO	Commonwealth Scientific and Industrial Research Organisation
CSP	Concentrated Solar Power
CVR	Research Center Rez
DOE	U.S. Department of Energy
EDF	Électricité de France

EoS	Equation of State
EPA	Environmental Protection Agency
GE	General Electric
HAZOP	Hazard and Operability Study
HT2C	High Temperature Heat to Power Conversion facility
IAE	Institute of Applied Energy
IDHL	Immediately Dangerous to Health and Life
IKE	Institut für Kernenergie und Energiesysteme
IST	Integrated System Test
iThERM	Industrial Thermal Energy Recovery Conversion and Management
KAERI	Korean Atomic Energy Research Institute
KAIST	Korea Advanced Institute of Science and Technology
KIER	Korean Institute of Energy Research
LUT University	Lappeenranta-Lahti University of Technology
NPSH	Net Positive Suction Head
SCARABEUS	Supercritical CARBON dioxide/Alternative Blends for Efficiency Upgrade of Solar power plants
SCARLETT	Supercritical CARBON dioxide Loop at IKE Universität Stuttgart
SCIEL	Supercritical CO <sub>2</sub> Compressor Performance Test Facility
sCO <sub>2</sub> -HeRO	Supercritical CO <sub>2</sub> Heat Removal system
SCO2PE	Supercritical CO <sub>2</sub> Pressurising Experiment
SIL	Safety and Integrity Level
SNL	Sandia National Laboratories
STEP	Supercritical Transformational Electric Power Project
SwRI	Southwest Research Institute
PCHE	Printed Circuit Heat Exchanger
PHPL	Pinjarra Hills High Pressure Test Loop
POSTECH	Pohang University of Science and Technology
RTD	Resistance Temperature Detector
TIT	Tokyo Institute of Technology
TPRI	Xi'an Thermal Power Research Institute

### Variables

$\alpha_{CO_2}$	heat transfer coefficient as calculated from experimental results (W/m <sup>2</sup> /K)
$\alpha_{Gni}$	heat transfer coefficient as calculated by Gnielinski's correlation (W/m <sup>2</sup> /K)
$\dot{m}_{ThOil}$	mass flow rate of thermal oil (kg/s)
$\dot{m}, \dot{m}_{CO_2}$	mass flow rate of CO <sub>2</sub> (kg/s)
$n$	revolutions (rpm, revolutions per minute)
$p$	CO <sub>2</sub> pressure (bar)
$p_{CO_2}$	CO <sub>2</sub> pressure in the test facility during filling, measured at the tank (bar), see Figure 14
$p_{H_2O}$	water pressure at inlet of test tube (bar), see Figure 6
$p_{Tank}$	CO <sub>2</sub> pressure in the tank (representative for the low-pressure side of the cycle) (bar)

$p_{Pump,Out}$	
$p_{Vap}$	calculated saturation pressure of CO <sub>2</sub> with TCO <sub>2</sub> as input (bar)
$P_{IN}$	CO <sub>2</sub> pressure pump at inlet (bar)
$P_{OUT}$	CO <sub>2</sub> pressure pump at outlet (bar)
$p_{thOil}$	thermal oil pressure (bar)
$T_{bulk}$	CO <sub>2</sub> temperature at the middle of the heat exchanger of the test tube ("bulk temperature") (°C), see Figure 6
$TCO_2$	CO <sub>2</sub> temperature at the outlet of the water cooler during filling (°C), see Figure 14
$T_{CO_2,CO_2Heater,Out}$	CO <sub>2</sub> temperature at the outlet of the heater (°C)
$TCO_{2in}$	temperature of CO <sub>2</sub> entering the test facility during filling (°C), see Figure 14
$TH_2O$	water temperature at the outlet of the water cooler during filling (°C), see Figure 14
$T_{H_2O,in}$	water temperature at the inlet of the test tube (°C), see Figure 6
$T_{H_2O,1}$	water temperature at position III of the test tube (°C), see Figure 6
$T_{H_2O,2}$	water temperature at position II of the test tube (°C), see Figure 6
$T_{H_2O,out}$	water temperature at the outlet of the test tube (°C), see Figure 6
$T_{in}$	CO <sub>2</sub> temperature (°C) at inlet of test section, Figure 5
$T_{middle}$	CO <sub>2</sub> temperature (°C) at the middle of test section, see Figure 5
$T_{out}$	CO <sub>2</sub> temperature (°C) at outlet of test section, Figure 5
$T_{Tank}$	CO <sub>2</sub> temperature in the tank (representative for the low-pressure side of the cycle) (bar)
$T_{Heater,Out}$	CO <sub>2</sub> temperature at the outlet of the heater (°C)
$T_{ThOil,ElHeater,Out}$	thermal oil temperature at the outlet of the electrical heater of the thermal oil plant (°C)
$T_{ThOil,CO_2Heater,In}$	thermal oil temperature at the inlet of the CO <sub>2</sub> heater (°C)
$T_{thOil,in}$	thermal oil temperature (°C) at inlet of test section, see Figure 5
$T_{thOil,middle}$	thermal oil temperature (°C) at inlet of test section, see Figure 5
$T_{thOil,out}$	thermal oil temperature (°C) at outlet of test section, see Figure 57
$T_{w,o}$	wall temperature (°C) at outer wall of inner tube of the test tube, see Figure 6, for positions of sensors $T_{w,o1}$ , $T_{w,o2}$ , and $T_{w,o3}$ see Figure 7
$V^{\circ}_{H_2O}$	volume flow rate of water (l/min)
$V^{\circ}_{thOil}$	volume flow rate of thermal oil (l/min)

### ACKNOWLEDGEMENTS

The authors gratefully thank FFG (Austrian Research Promotion Agency) for funding the current project "CO<sub>2</sub> as a working medium for heat recovery", Proj. No.: 853568.

The SCARABEUS project has received funding from European Union's Horizon 2020 research program under grant agreement N°814985.

## REFERENCES

- [1] K. Brun, P. Friedman, and R. Dennis, Eds., *Test facilities*, vol. Fundamentals and Applications of Supercritical Carbon Dioxide (sCO<sub>2</sub>) Based Power Cycles. Elsevier, 2017. Accessed: Dec. 22, 2022. [Online]. Available: <https://linkinghub.elsevier.com/retrieve/pii/B9780081008041000141>.
- [2] E. M. Clementoni, T. Held, J. Pasch, and J. Moore, "Test facilities," in *Fundamentals and Applications of Supercritical Carbon Dioxide (SCO<sub>2</sub>) Based Power Cycles*, Elsevier, 2017, pp. 393–414. doi: 10.1016/B978-0-08-100804-1.00014-1.
- [3] P. Wu *et al.*, "A review of research and development of supercritical carbon dioxide Brayton cycle technology in nuclear engineering applications," *Nucl. Eng. Des.*, vol. 368, p. 110767, Nov. 2020, doi: 10.1016/j.nucengdes.2020.110767.
- [4] M. T. White, G. Bianchi, L. Chai, S. A. Tassou, and A. I. Sayma, "Review of supercritical CO<sub>2</sub> technologies and systems for power generation," *Appl. Therm. Eng.*, vol. 185, p. 116447, Feb. 2021, doi: 10.1016/j.applthermaleng.2020.116447.
- [5] A. Yu, W. Su, X. Lin, and N. Zhou, "Recent trends of supercritical CO<sub>2</sub> Brayton cycle: Bibliometric analysis and research review," *Nucl. Eng. Technol.*, vol. 53, no. 3, pp. 699–714, Mar. 2021, doi: 10.1016/j.net.2020.08.005.
- [6] L. Rapp, "Experimental Testing of a 1MW sCO<sub>2</sub> Turbocompressor," presented at the The 7th International Supercritical CO<sub>2</sub> Power Cycles Symposium, San Antonio, Texas, Apr. 2019.
- [7] M. D. Carlson, "Guidelines for the design and operation of supercritical carbon dioxide R&D systems," presented at the SOLARPACES 2019: International Conference on Concentrating Solar Power and Chemical Energy Systems, Daegu, South Korea, 2020, p. 130003. doi: 10.1063/5.0033262.
- [8] E. M. Clementoni and T. L. Cox, "Practical Aspects of supercritical carbon dioxide Brayton system testing," presented at the The 4th International Symposium - Supercritical CO<sub>2</sub> Power Cycles, Pittsburgh, Pennsylvania, Sep. 2014.
- [9] CSIRO, "Solar-driven Supercritical CO<sub>2</sub> Brayton Cycle (1-UFA004) Project results and lessons learnt." May 30, 2017. [Online]. Available: <http://www.csiro.au/energy>.
- [10] A. J. Hacks *et al.*, "Operational experiences and design of the sCO<sub>2</sub>-HeRo loop," *Conf. Proc. Eur. SCO<sub>2</sub> Conf. Eur. Conf. Supercrit. CO<sub>2</sub> SCO<sub>2</sub> Power Syst. 2019 19th-20th Sept. 2019*, p. 125, Oct. 2019, doi: 10.17185/DUEPUBLICO/48906.
- [11] E. Anselmi, V. Pachidis, M. Johnston, I. Bunce, and P. Zachos, "An Overview of the Rolls-Royce sCO<sub>2</sub>-Test Rig Project at Cranfield University," presented at the The 6th International Supercritical CO<sub>2</sub> Power Cycles Symposium, Pittsburgh, Pennsylvania, Mar. 2018.
- [12] E. Anselmi, I. Bunce, and V. Pachidis, "An Overview of Initial Operational Experience With the Closed-Loop sCO<sub>2</sub> Test Facility at Cranfield University," in *Volume 9: Oil and Gas Applications; Supercritical CO<sub>2</sub> Power Cycles; Wind Energy*, Phoenix, Arizona, USA, Jun. 2019, p. V009T38A022. doi: 10.1115/GT2019-91391.
- [13] E. Anselmi, P. Belleoud, I. Roumeliotis, and V. Pachidis, "Update of the sCO<sub>2</sub>-Test Rig at Cranfield University," in *Volume 9: Supercritical CO<sub>2</sub>*, Rotterdam, Netherlands, Jun. 2022, p. V009T28A024. doi: 10.1115/GT2022-83273.
- [14] J. Moore *et al.*, "Commissioning of a 1 MWe Supercritical CO<sub>2</sub> Test Loop".
- [15] J. J. Moore, M. Day-Towler, J. Mortzheim, S. Cich, and D. Hofer, "TESTING OF A 10 MWe SUPERCRITICAL CO<sub>2</sub> TURBINE," 2018.
- [16] J. Marion, M. Kutin, A. McClung, J. Mortzheim, and R. Ames, "The STEP 10 MWe sCO<sub>2</sub> Pilot Plant Demonstration," in *Volume 9: Oil and Gas Applications; Supercritical CO<sub>2</sub> Power Cycles; Wind Energy*, Phoenix, Arizona, USA, Jun. 2019, p. V009T38A031. doi: 10.1115/GT2019-91917.
- [17] J. Marion, S. Macadam, A. McClung, and J. Mortzheim, "The STEP 10 MWe sCO<sub>2</sub> Pilot Demonstration Status Update," 2022.
- [18] J. Marion, "Supercritical CO<sub>2</sub>, 10 MW Demonstration Project Under Construction," *Glob. J. Energy Equip.*, vol. Turbomachinery International, no. Vol 63, 5, Oct. 2022.
- [19] S. Martin *et al.*, "Progress Update on the Allam Cycle: Commercialization of Net Power and the Net Power Demonstration Facility," *SSRN Electron. J.*, 2019, doi: 10.2139/ssrn.3366370.
- [20] NET Power, "First Utility-Scale Project," Dec. 2022. <https://netpower.com/first-utility-scale-project/>.
- [21] J. E. Cha, S. W. Bae, J. Lee, S. K. Cho, J. I. Lee, and J. H. Park, "Operation Results of a Closed Supercritical CO<sub>2</sub> Simple Brayton Cycle," 2016.
- [22] S. J. Bae, Y. Ahn, J. Lee, S. G. Kim, S. Baik, and J. I. Lee, "Experimental and numerical investigation of supercritical CO<sub>2</sub> test loop transient behavior near the critical point operation," *Appl. Therm. Eng.*, vol. 99, pp. 572–582, Apr. 2016, doi: 10.1016/j.applthermaleng.2016.01.075.
- [23] J. Lee, S. Baik, S. K. Cho, J. E. Cha, and J. I. Lee, "Issues in performance measurement of CO<sub>2</sub> compressor near the critical point," *Appl. Therm. Eng.*, vol. 94, pp. 111–121, Feb. 2016, doi: 10.1016/j.applthermaleng.2015.10.063.
- [24] J. Cho *et al.*, "Development of the Supercritical Carbon Dioxide Power Cycle Experimental Loop in KIER," in *Volume 9: Oil and Gas Applications; Supercritical CO<sub>2</sub> Power Cycles; Wind Energy*, Seoul, South Korea, Jun. 2016, p. V009T36A013. doi: 10.1115/GT2016-57460.
- [25] B. Choi *et al.*, "Development of a 500 °C semi-pilot scale supercritical CO<sub>2</sub> power cycle test loop," presented at the

- SOLARPACES 2020: 26th International Conference on Concentrating Solar Power and Chemical Energy Systems, Freiburg, Germany, 2022, p. 090003. doi: 10.1063/5.0085681.
- [26] M. Aritomi, T. Ishizuka, Y. Muto, and N. Tsuzuki, "Performance Test Results of a Supercritical CO<sub>2</sub> Compressor Used in a New Gas Turbine Generating System," *J. Power Energy Syst.*, vol. 5, no. 1, pp. 45–59, 2011, doi: 10.1299/jpes.5.45.
- [27] Y. Le Moullec *et al.*, "Shouhang-EDF 10MWe supercritical CO<sub>2</sub> cycle + CSP demonstration project," *Conf. Proc. Eur. SCO<sub>2</sub> Conf. Eur. Conf. Supercrit. CO<sub>2</sub> SCO<sub>2</sub> Power Syst. 2019 19th-20th Sept. 2019*, p. 138, Oct. 2019, doi: 10.17185/DUEPUBBLICO/48884.
- [28] H. Li, Y. Zhang, M. Yao, Y. Yang, W. Han, and W. Bai, "Design assessment of a 5 MW fossil-fired supercritical CO<sub>2</sub> power cycle pilot loop," *Energy*, vol. 174, pp. 792–804, May 2019, doi: 10.1016/j.energy.2019.02.178.
- [29] L. Seshadri *et al.*, "Design of 20 kW Turbomachinery for Closed Loop Supercritical Carbon Dioxide Brayton Test Loop Facility," in *Volume 9: Oil and Gas Applications; Supercritical CO<sub>2</sub> Power Cycles; Wind Energy*, Phoenix, Arizona, USA, Jun. 2019, p. V009T38A016. doi: 10.1115/GT2019-90876.
- [30] B. Twomey *et al.*, "The University of Queensland Refrigerant and Supercritical CO<sub>2</sub> Test Loop," in *Volume 3: Coal, Biomass and Alternative Fuels; Cycle Innovations; Electric Power; Industrial and Cogeneration; Organic Rankine Cycle Power Systems*, Seoul, South Korea, Jun. 2016, p. V003T25A013. doi: 10.1115/GT2016-58110.
- [31] "ASTRI Australian Solar Thermal Research Institute," ASTRI, Public Dissemination Report, Jun. 2019. Accessed: Dec. 22, 2022. [Online]. Available: <https://www.astri.org.au/publications/reports/>.
- [32] "AUSTRALIAN SOLAR THERMAL RESEARCH INSTITUTE (ASTRI)," ASTRI, Public Dissemination Report, 2021. Accessed: Dec. 22, 2022. [Online]. Available: <https://www.astri.org.au/publications/reports/>.
- [33] L. Toni, G. Persico, P. di Milano, E. F. Bellobuono, R. Valente, and P. Gaetani, "Experimental and Numerical Performance Survey of a MW-Scale Supercritical CO<sub>2</sub> Compressor Operating in Near-Critical Conditions".
- [34] P. Hajek and O. Frybort, "EXPERIMENTAL LOOP S-CO<sub>2</sub> SUSEN".
- [35] A. Vojacek, V. Dostal, F. Goettelt, M. Rohde, and T. Melichar, "Performance Test of the Air-Cooled Finned-Tube Supercritical CO<sub>2</sub> Sink Heat Exchanger," *J. Therm. Sci. Eng. Appl.*, vol. 11, no. 3, p. 031014, Jun. 2019, doi: 10.1115/1.4041686.
- [36] W. Flaig, R. Mertz, and J. Starflinger, "Setup of the Supercritical CO<sub>2</sub> Test Facility 'SCARLETT' for Basic Experimental Investigations of a Compact Heat Exchanger for an Innovative Decay Heat Removal System," *J. Nucl. Eng. Radiat. Sci.*, vol. 4, no. 3, p. 031004, Jul. 2018, doi: 10.1115/1.4039595.
- [37] "Data of simple CO<sub>2</sub> experiment for code validation," DELIVERABLE NO. 2.1, 2017.
- [38] S. Schuster, A. Hacks, and D. Brillert, "Lessons from testing the sCO<sub>2</sub>-HeRo turbo-compressor-system".
- [39] G. Bianchi *et al.*, "Design of a high-temperature heat to power conversion facility for testing supercritical CO<sub>2</sub> equipment and packaged power units," *Energy Procedia*, vol. 161, pp. 421–428, Mar. 2019, doi: 10.1016/j.egypro.2019.02.109.
- [40] G. Petruccelli, A. Uusitalo, A. Grönman, T. Turunen-Saaresti, and M. Zocca, "CLOSED-LOOP SUPERCRITICAL CARBON DIOXIDE WIND TUNNEL: DESIGN AND COMPONENTS," presented at the The 4th European sCO<sub>2</sub> Conference for Energy Systems, Online, Mar. 2021.
- [41] R. C. Hendricks, R. J. Simoneau, and R. V. Smith, "Survey of Heat Transfer to Near-Critical Fluids," National Aeronautics and Space Administration Washington, D. C., NASA TN D-5886, Technical Note, 1970.
- [42] V. Illyés *et al.*, "Design of an Air-Cooled Condenser for CO<sub>2</sub>-Based Mixtures: Model Development, Validation and Heat Exchange Gain with Internal Microfins," in *Volume 9: Supercritical CO<sub>2</sub>*, Rotterdam, Netherlands, Jun. 2022, p. V009T28A016. doi: 10.1115/GT2022-82438.
- [43] G. Di Marcoberardino *et al.*, "Experimental characterisation of CO<sub>2</sub> + C<sub>6</sub>F<sub>6</sub> mixture: Thermal stability and vapour liquid equilibrium test for its application in transcritical power cycle," *Appl. Therm. Eng.*, vol. 212, p. 118520, Jul. 2022, doi: 10.1016/j.applthermaleng.2022.118520.
- [44] P.-L. David, "Public report on the heat transfer characteristics using CO<sub>2</sub> blends," D4.3 Public report, 2021. [Online]. Available: <https://www.scarabeusproject.eu/2021/07/10/d4-3-public-report-on-the-heat-transfer-characteristics-using-co2-blends/>
- [45] R. Span and W. Wagner, "A New Equation of State for Carbon Dioxide Covering the Fluid Region from the Triple-Point Temperature to 1100 K at Pressures up to 800 MPa," *J. Phys. Chem. Ref. Data*, 1996, doi: <https://doi.org/10.1063/1.555991>.
- [46] V. Gnielinski, "G1 Heat Transfer in Pipe Flow. In: VDI Heat Atlas," Berlin, Heidelberg: Springer, 2010. [Online]. Available: [https://doi.org/10.1007/978-3-540-77877-6\\_34](https://doi.org/10.1007/978-3-540-77877-6_34)
- [47] M. Drosig, *Dealing with Uncertainties: a Guide to Error Analysis*, 2., Enlarged edition. Berlin: Springer, 2009.
- [48] Verein Deutscher Ingenieure e.V., Ed., "Kontrolle und Verbesserung der Qualität von Prozessdaten und deren Unsicherheiten mittels Ausgleichsrechnung bei Betriebs- und Abnahmemessungen (Control and quality improvement of process data and their unvertainties by means of correction calculation for operation and acceptance tests)." Beuth Verlag GmbH, Berlin.

## ANNEX A

### DETAILS ON EQUIPMENT

Component	Manufacturer	Detail
Heater	Funke	200 kW, Shell-and-Tube, CO <sub>2</sub> tube-side, thermal oil VP-1 shell-side
Cooler/ condenser	Funke	355 kW, Shell-and-Tube, CO <sub>2</sub> tube-side, water shell-side
Pump	Speck Triplex Pumpen	Piston-pump (SPECK-TRIPLEX-PLUNGERPUMPE P52/51-300CZ), max. 50 L/min, Pmax=180 bar
Expansion valve	Samson	Pneumatic control valve, type 3252
Tank	Reisenauer	55 L

Measurement equipment	Type	Manufacturer
Temperature	PT100 class AA, A, B	Wika, Endress+Hauser,
Pressure		ICCP Messtechnik GmbH
Mass flow, density	Coriolis	Endress+Hauser
Level (1 <sup>st</sup> try)	Time Domain Reflectometry	Endress+Hauser
Level (2 <sup>nd</sup> try)	Differential pressure	Endress+Hauser

## EXERGETIC AND ENTROPY ANALYSIS OF THE PCRC AND RCMCI BRAYTON CYCLES USING S-CO<sub>2</sub> MIXTURES. CASE STUDY: MARINE APPLICATIONS

**Paul Tafur-Escanta\***

Universidad Politécnica de Madrid  
Madrid, Spain  
Universidad de las Fuerzas Armadas – ESPE  
Sangolquí, Ecuador  
Email: pm.tafur@alumnos.upm.es

**Robert Valencia-Chapi**

Universidad Técnica del Norte  
Ibarra, Ecuador

**Javier Muñoz-Antón**

Universidad Politécnica de Madrid  
Madrid, Spain

### ABSTRACT

Brayton cycle using supercritical carbon dioxide (s-CO<sub>2</sub>) as a working fluid is a high-efficiency trend technology that has been an understudy for improvement. The performance of the cycles explains with a thermodynamic analysis that accounts for two aspects: on one side a general trend in their behavior and on the other the effect of the irreversibilities, especially the irreversibilities taking place in the regenerator.

This study focuses on the impact of binary mixtures based on pure CO<sub>2</sub> on the thermal efficiency of the configurations: Recompression with Main Compressor Intercooling (RCMCI) and Partial Cooling with Recompression (PCRC) cycles at the design point, considering the irreversibilities caused by each component of the cycle. In the PCRC cycle, small-size heat recuperators and low-temperature high-heat recuperators are achieved. The efficiency in the RCMCI cycle is better due to the low recompressor work. The methodology used in the calculation of the plant performance is to establish heat recuperator total conductance values of between 5 and 20 MW/K. Based on the exergetic and entropy analysis of the cycles studied, a comparison between pure supercritical carbon dioxide and s-CO<sub>2</sub> mixtures (CO<sub>2</sub>/CH<sub>4</sub>, C<sub>3</sub>H<sub>8</sub>, and CO<sub>2</sub>/H<sub>2</sub>S) is carried out. Acquired results have revealed that the blends increase thermal efficiency compared to the standard fluid in the cycles studied. In PCRC configurations, the mixture that obtains the highest efficiency is the one that contains Methane, while in RCMCI configurations it is the one that contains Hydrogen Sulfide. Meanwhile, in the RCC cycle, the mixture with Propane is the one with the highest efficiency.

### INTRODUCTION

The interest of the scientific community in recent years has focused on the study of s-CO<sub>2</sub> Brayton cycles because it achieves high efficiencies and the components are small. Several authors agree that CO<sub>2</sub> Brayton cycles are promising for applications in concentrated solar power plants (CSP) [1-3], however, they have also been evaluated in nuclear [4-5], geothermal [6-7], waste heat recovery [8], heat pump [9-10], marine applications [11,12 and 27], among others.

In the study by [11], they model a waste heat recovery system coupled to a regenerative recompression s-CO<sub>2</sub> Brayton cycle in shipboard applications. In the analysis of some parameters, it is concluded that the increase in the minimum temperature of the cycle (32-50°C) produces a decrease in the efficiency of the cycle of almost 11%. On the contrary, if the maximum temperature of the cycle is increased by 100 °C, the efficiency increases by around 10%. In his recent research [12] he developed a thermodynamic model of the recompression cycle for marine applications, the optimized cycle reaches a maximum efficiency of 43.98% and if the efficiency of the recuperators increases up to a value of 0.95, then the size total Decreases turbomachinery. The studies analyzed for this research have shown that s-CO<sub>2</sub> technology has great potential if combined with marine applications that have waste heat recuperator systems, helping to improve the energy efficiency of ships, and leading to a significant reduction in CO<sub>2</sub> emissions into the environment [27].

All these applications have different ambient temperature conditions, so it is necessary to optimize the compressor inlet temperature (in addition to other parameters such as compressor

\* corresponding author(s)

inlet pressure, mass fraction going to the recompressor, etc.) to achieve better performance [13]. One way of unleashing the great thermodynamic potential of the  $s\text{-CO}_2$  Brayton cycles is by performing the compression around the critical point of  $\text{CO}_2$ , a little above it, to avoid the sudden change in the thermophysical properties of the fluid. However, applications such as cryogenics and nuclear that are at low ambient temperatures or in CSP with high ambient temperatures imply that the compressor inlet temperature decreases or increases as the case may be, causing the thermal efficiency of the cycle to drop.

To correct this drawback, numerous authors have investigated the addition of certain dopants, generally chemical compounds to carbon dioxide, producing a mixture that has a lower or higher critical temperature than the pure base fluid (pure  $\text{CO}_2$ ). Valencia et al. [14] evaluated different dopants and classified them into compounds that help lower the critical temperature ( $\text{C}_2\text{H}_6$ ,  $\text{CH}_4$ , Kr, He) and compounds that help raise the critical temperature ( $\text{C}_3\text{H}_8$ ,  $\text{C}_5\text{H}_{10}$ ,  $\text{C}_5\text{H}_{12}$ ,  $\text{H}_2\text{S}$ ,  $\text{SO}_2$ ) compared to the pure  $\text{CO}_2$ . Manzoloni et al. [15] evaluate two additives ( $\text{Ni}_2\text{O}_4$  and  $\text{TiCl}_4$ ), their study considers typical ambient temperatures of solar thermal plants and turbine inlet temperatures of  $550^\circ\text{C}$  and  $700^\circ\text{C}$ , obtaining efficiencies between 43% and 50%, respectively. The efficiencies obtained are 2% higher than those obtained with pure  $\text{CO}_2$ . Siddiqui, M [15], in his research, analyzes the binary mixture  $\text{CO}_2/\text{C}_7\text{H}_8$  to improve performance in a recompression cycle. Assuming a minimum temperature of  $50^\circ\text{C}$  and turbine inlet temperatures of  $350^\circ\text{C}$  and  $400^\circ\text{C}$ , the results show an increase in efficiency of 14.5% and 8%, respectively. Along the same lines, Tafur et al. [17] present four chemical compounds as dopants for  $\text{CO}_2$  in recompression  $\text{CO}_2$  Brayton cycles coupled to CSP. The authors perform an economic and performance evaluation. Concluding that the  $\text{CO}_2/\text{COS}$  mixture with a molar fraction of 0.70/0.30 obtains an efficiency of around 45%, surpassing that of pure  $\text{CO}_2$ , which obtained around 41.25%. In a recent investigation [18], two additives ( $\text{C}_6\text{F}_6$  and  $\text{TiCl}_4$ ) are proposed as working fluids in Rankine and Pre-compression cycles with maximum cycle temperatures and pressures of  $550^\circ\text{C}$  and  $700^\circ\text{C}$ , 200 bar, and 300 bar. The results obtained show efficiencies above 50%.

Finally, Niu et al. [19] studied six dopants divided into three groups. In the first group: mixtures increase the temperature of the critical point of  $\text{CO}_2$  but reduce the specific work of the system. In the second group: the same previous condition but with results of increased specific work. Finally, the third group: are the mixtures with a lower critical pressure and a higher critical temperature than pure  $\text{CO}_2$ . The results showed that the  $\text{CO}_2/\text{C}_3\text{H}_8$  mixture (third group) has potential for application in solar power tower systems due to the increase in thermal efficiency of 2.34% and exergetic efficiency of 1.51% compared to pure  $\text{CO}_2$ .

The cited bibliography indicates that the addition of dopants is applied to working fluids in cycles that are coupled to solar energy concentration systems. However, the literature also shows that there are dopants that relocate the critical point, thus

obtaining critical temperatures around  $20$  and  $30^\circ\text{C}$  even lower, therefore, they can be of relevant analysis and study as working fluids in  $s\text{-CO}_2$  Brayton cycles for marine applications.

The main objective of this work is to carry out a thermodynamic analysis of three additives ( $\text{CH}_4$ ,  $\text{C}_3\text{H}_8$ , and  $\text{H}_2\text{S}$ ) that improve the thermal efficiency of  $s\text{-CO}_2$  Brayton cycles under typical temperature conditions of marine applications.

## MATERIALS AND METHODS

In this work, three configurations [28] are considered to analyze the three mixtures under study: Recompression with Main Compressor Intercooling (RCMCI, Figure 1b) and Partial Cooling with Recompression (PCRC, Figure 1c), which are derived from the main cycle that is the Recompression cycle (RCC, Figure 1a).

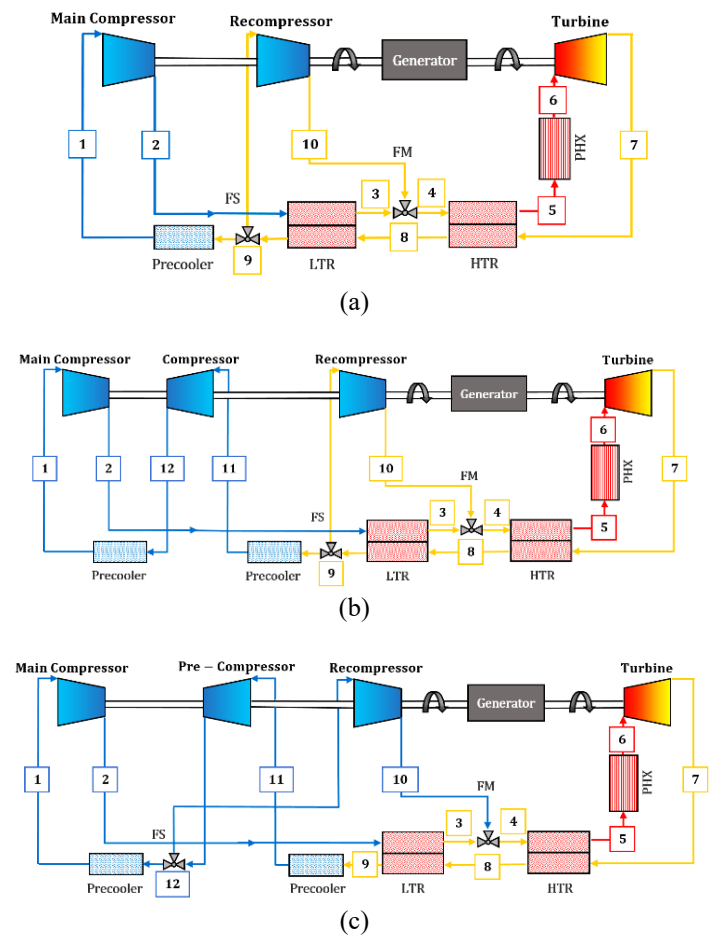


**Figure 1.** Relevant  $s\text{-CO}_2$  Brayton cycles layout, (a) Recompression, (b) Recompression with Main Compressor Intercooling, and (c) Partial Cooling with Recompression.

Table 1 lists the main assumptions for the present investigation. On the one hand, the compressor inlet temperature is evaluated in a range between  $32^\circ\text{C}$  and  $40^\circ\text{C}$ , the turbine inlet temperature is  $550^\circ\text{C}$  and the maximum pressure of the cycle is

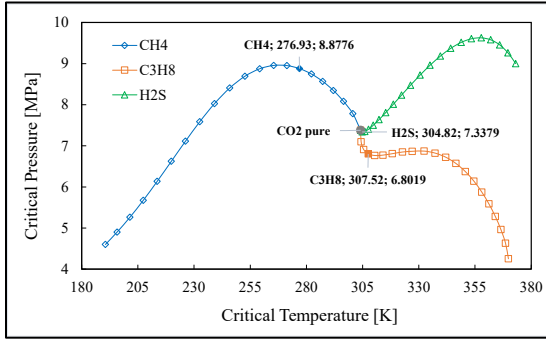


20 MPa, to contrast the results with other investigations with the same parameters [11]. The efficiencies of the compressors and turbine are 0.89 and 0.93, respectively. On the other hand, this takes into account the pressure drops in the components of the cycle, the values considered, as well as the methodology applied to calculate the maximum efficiency that has been obtained from previous research [14, 17, 20-22].

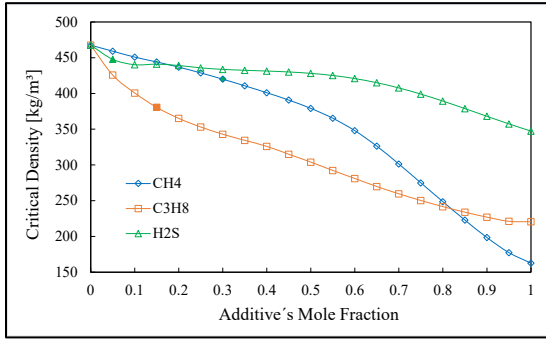
TABLE I. MAIN INPUT PARAMETERS

	<i>Nomenclature</i>	<i>Value</i>	<i>Units</i>
Compressor inlet temperature	$T_1$	32 – 40	°C
Maximum cycle pressure [11 – 12]	$P$	20	MPa
Maximum cycle temperature [11 – 12]	$T_6$	550	°C
Compressor and turbine efficiency [14, 17, 20-22]	$\eta_{mc}, \eta_t$	0.89/0.93	-
UA (Heat Total Recuperator Conductance) for the LTR and HTR [14, 17, 20-22]	$UA_{LT}, UA_{HT}$	2500 to 10000	kW/K

The software SCSP (Supercritical Concentrated Solar Power Plant) [23] is used for the evaluation of the s-CO<sub>2</sub> Brayton cycle. This software has been developed for the Grupo de Investigaciones Termoenergéticas of Universidad Politécnica de Madrid. The fluid's properties, shown in Figure 2, were obtained from the REFPROP v10.0 database developed by NIST [24].



(a)



(b)

**Figure 2.** Fluid's Properties. (a) Critical pressure vs. Critical temperature, (b) Critical density vs Additive's mole fraction.

Figure 2a shows the evolution of the critical pressure and critical temperature as a function of the molar fraction of the added compound. In the case of the CO<sub>2</sub>/CH<sub>4</sub> mixture, the critical temperature decreases, while the critical pressure increases to a maximum point and then drastically decreases, compared to the values of pure CO<sub>2</sub>. In the mixtures CO<sub>2</sub>/C<sub>3</sub>H<sub>8</sub> and CO<sub>2</sub>/H<sub>2</sub>S the critical temperature increases, in the one containing C<sub>3</sub>H<sub>8</sub> the critical pressure also decreases; in the one containing H<sub>2</sub>S, the critical pressure increases to a maximum point and then decreases, always maintaining its values above pure CO<sub>2</sub>.

Figure 2b shows the evolution of the critical density against the molar fraction of the additive. In this case, all the mixtures decrease their critical density as the molar fraction of the added compound increases.

### Energetic Analysis

Based on the first law of thermodynamics, the energy balance equations in the heat recuperators (LTR and HTR) of the RCMCI configuration are presented:

$$(1 - \gamma)(h_3 - h_2) = h_9 - h_8 \quad (1)$$

$$h_5 - h_4 = h_8 - h_7 \quad (2)$$

The heat transfer rates ( $\dot{Q}_{PHX}, \dot{Q}_{Pre}$ ) to and from the cycle:

$$\dot{Q}_{PHX} = \dot{m}_{mix}(h_5 - h_6) \quad (3)$$

$$\dot{Q}_{Pre_1} = (1 - \gamma)\dot{m}_{mix}(h_{11} - h_9) \quad (4)$$

$$\dot{Q}_{Pre_2} = (1 - \gamma)\dot{m}_{mix}(h_1 - h_{12}) \quad (5)$$

The expressions for the work in the turbine ( $\dot{W}_T$ ), compressors ( $\dot{W}_C, \dot{W}_{RC}, \dot{W}_{MC}, \dot{W}_{Pre-c}$ ), net output ( $\dot{W}_{net}$ ), and thermal efficiency ( $\eta_{th}$ ) are as follows:

$$\dot{W}_T = \dot{m}_{mix}(h_6 - h_7) \quad (6)$$

$$\dot{W}_{MC} = (1 - \gamma)\dot{m}_{mix}(h_2 - h_1) \quad (7)$$

$$\dot{W}_C = (1 - \gamma)\dot{m}_{mix}(h_{12} - h_{11}) \quad (8)$$

$$\dot{W}_{Pre-c} = \dot{m}_{mix}(h_{12} - h_{11}) \quad (9)$$

$$\dot{W}_{RC} = \gamma * \dot{m}_{mix}(h_{10} - h_9) \quad (10)$$

$$\dot{W}_{net,RCC} = \dot{W}_T - (\dot{W}_{MC} + \dot{W}_{RC}) \quad (11)$$

$$\dot{W}_{net,RCMCI} = \dot{W}_T - (\dot{W}_{MC} + \dot{W}_C + \dot{W}_{RC}) \quad (12)$$

$$\dot{W}_{net,PCRC} = \dot{W}_T - (\dot{W}_{MC} + \dot{W}_{Pre-C} + \dot{W}_{RC}) \quad (13)$$

$$\eta_{th} = \frac{\dot{W}_{net}}{\dot{Q}_{PHX}} \quad (14)$$

### Exergetic Analysis

Based on the second law of thermodynamics, the expressions for entropic generation and exergy flow are proposed:

$$\sigma_T = \dot{m}_{mix}(s_7 - s_6) \quad (15)$$

$$\sigma_{MC} = (1 - \gamma)\dot{m}_{mix}(s_2 - s_1) \quad (16)$$

$$\sigma_C = (1 - \gamma)\dot{m}_{mix}(s_{12} - s_{11}) \quad (17)$$

$$\sigma_{RC} = \gamma * \dot{m}_{mix}(s_{10} - s_9) \quad (18)$$

$$\sigma_{LTR} = \dot{m}_{mix}(s_9 - s_8) + (1 - \gamma)\dot{m}_{mix}(s_3 - s_2) \quad (19)$$

$$\sigma_{HTR} = \dot{m}_{mix}(s_8 - s_7) + \dot{m}_{mix}(s_5 - s_4) \quad (20)$$

The total heat input exergy and the exergetic efficiency are expressed as [25]:

$$\dot{E}_{in} = \dot{Q}_{PHX} \left(1 - \frac{T_o}{T_{hs}}\right) \quad (21)$$

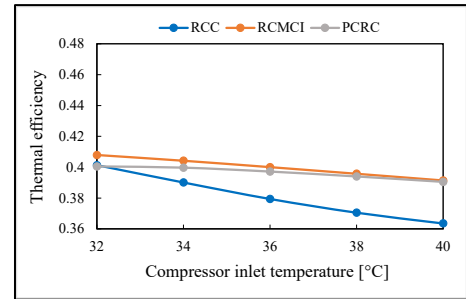
$$\eta_{ex} = \frac{\dot{W}_{net}}{\dot{E}_{in}} \quad (22)$$

$$\eta_{ex} = \frac{\eta_{th}}{\eta_{carnot}} \quad (23)$$

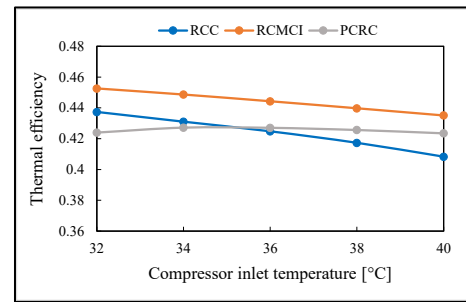
Where  $T_o$  is the ambient temperature and  $T_{hs}$  is the temperature of the heat source [11].

### RESULTS AND DISCUSSION

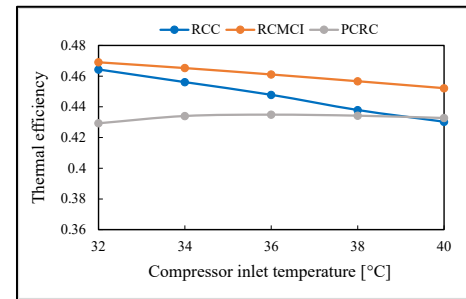
Figure 3 shows the efficiencies obtained when using pure CO<sub>2</sub> as the working fluid. In addition, it is observed that the thermal size (UA) in heat recuperators has an important influence on the increase in thermal efficiency. In addition, the results of thermal efficiencies of this study consider a very important design parameter in heat exchangers ("pinch point"), it has been considered as eligible values of efficiency those that are above a pinch point of 5°C.



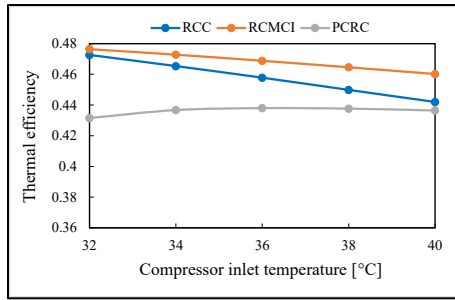
(a)



(b)



(c)



(d)

**Figure 3.** Thermal Efficiency vs Compressor inlet temperature. Using CO<sub>2</sub> pure. (a) 5000 kW/K, (b) 10000 kW/K, (c) 15000 kW/K and (d) 20000 kW/K.

In the RCC and RCMCI cycles, the efficiencies decrease as the compressor inlet temperature increases. While in the PCRC cycle, the efficiency drops a little when the UA is 5000 kW/K (Figure 3a), however, when the UA values increase (Figure 3b, c, d) the thermal efficiency in this cycle starts to increase as the compressor inlet temperature increases.

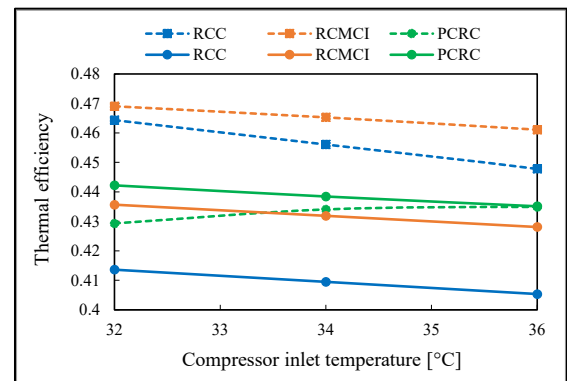
Table 2 summarizes the results obtained and compares them with previous investigations. The efficiencies values show a slight deviation, this is due to the pressure drops in the components considered by the authors, [26] in the heat exchangers with 130 kPa with a conservative design and another with the best design, [11] without taking pressure drops into account and with the best design. And finally, the results of the presented model for an RCC cycle with a UA value of 15000 kW/K that consider pressure drop values of 2% in the heat recuperators (LTR and HTR), a primary heat exchanger (PHX) and precoolers (PC). The efficiency values obtained are in agreement with the literature studied. Their values differ due to the pressure drop values used by each author.

TABLE II. COMPARISON OF RESULTS WITH THE PUBLISHED LITERATURE. CONSERVATIVE DESIGN (C.D.) AND BEST DESIGN (B.D.)

Design parameters	Literature [26]		Literature [11] B.D.	Present model results
	C.D.	B.D.		
Maximum cycle temperature	550 °C	550 °C	550 °C	550 °C
Minimum cycle temperature	32 °C	32 °C	32 °C	32 °C
Maximum cycle pressure	20 MPa	20 MPa	20 MPa	20 MPa
Cycle pressure ratio	2.6	2.6	2.6	2.7
Compressor efficiency	89 %	95.5 %	95.5 %	89 %
Turbine efficiency	90 %	92.9 %	92.9 %	93 %
Pressure drop	130 kPa in HX	130 kPa in HX	-	2 % in HX's and Precooler
Thermal efficiency	45.27 %	47.36 %	48.45 %	46.43 %

## CO<sub>2</sub>/CH<sub>4</sub> mixture

Figure 4 compares the efficiencies obtained with pure CO<sub>2</sub> (segmented line) versus those obtained by the mixture containing methane (solid line). The study shows that in the RCC and RCMCI cycle, better efficiencies are achieved with pure CO<sub>2</sub>, however, in the PCRC cycle the mixture obtains better efficiencies between 32 °C and 35 °C of compressor inlet temperature.



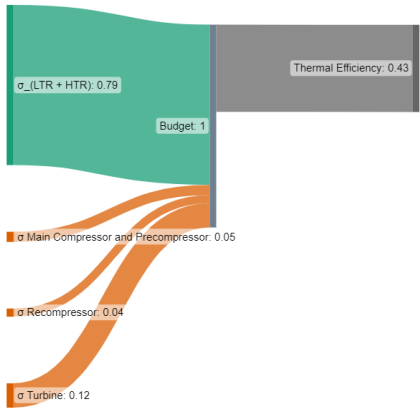
**Figure 4.** Thermal Efficiency vs Compressor inlet temperature. Using CO<sub>2</sub>/CH<sub>4</sub> mixture (solid line), with mole fraction 0.70/0.30 and 15000 kW/K.

Figure 5 shows the values of the irreversibilities (entropic generation) in percentages produced in the different components of the cycle and the thermal efficiency of the cycle. The values obtained with pure CO<sub>2</sub> are compared to the mixture for a compressor inlet temperature of 32 °C. It is shown that the irreversibilities in LTR and HTR are relevant since the sum of them represents around 79% and 57% when pure CO<sub>2</sub> and the mixture are used as working fluid, respectively.

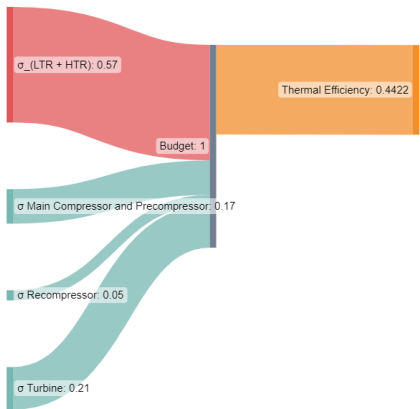
From the analysis, it is obtained that this mixture increases the heat transfer rates in the HTR, LTR, and precooler between streams 12 and 1. And it is only less in the precooler between streams 9 and 11. Furthermore, the mass fraction flowing to the recompressor also decreases when using the mix with a value of 0.38. Whereas, when pure CO<sub>2</sub> is used it is 0.52.

Finally, the mass flow rate of each working fluid are 502.77 kg/s for standard fluid and 488.85 kg/s for the mixture with methane.

In the exergetic analysis, the efficiency of the second law is obtained, and the results show values of 76.51% and 79% for pure CO<sub>2</sub> and the mixture, respectively.



(a)



(b)

**Figure 5.** Entropic generation in the components of the PCRC cycle. (a) CO<sub>2</sub> pure and (b) CO<sub>2</sub>/CH<sub>4</sub> mixture.

**CO<sub>2</sub>/H<sub>2</sub>S mixture**

Figure 6 compares the efficiencies obtained with pure CO<sub>2</sub> (segmented line) versus those obtained by the mixture containing hydrogen sulfide (solid line). The study shows that in the RCC and RCMCI cycle, better efficiencies are achieved with the mixture, however, in the PCRC cycle the mixture obtains slightly lower efficiencies between 32 °C and 34 °C of compressor inlet temperature, while similar values are obtained at 34 °C and 40 °C.

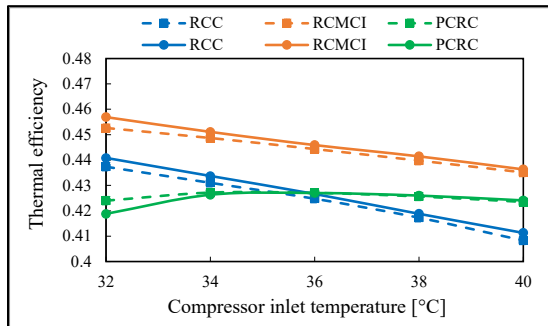
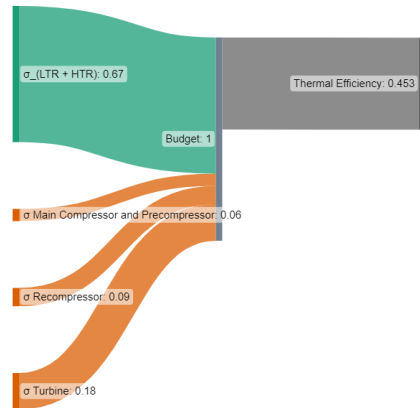


**Figure 6.** Thermal Efficiency vs Compressor inlet temperature. Using CO<sub>2</sub>/H<sub>2</sub>S mixture (solid line), with mole fraction 0.95/0.05 and UA 10000 kW/K.

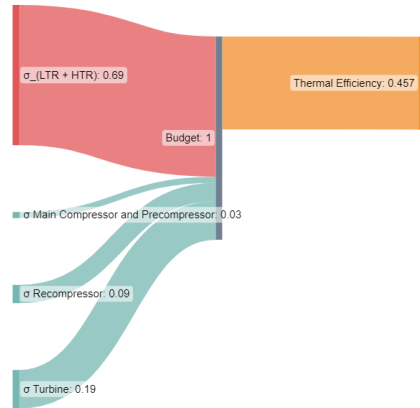
Figure 7 shows the values of the irreversibilities (entropic generation) in percentages produced in the different components of the cycle and the thermal efficiency of the cycle. The sum of the irreversibility values of the HTR and LTR are around 67% and 69% when using pure CO<sub>2</sub> and the mixture, respectively.

When the analysis of the cycle parameters is carried out, it is obtained that with the mixture the work of the main compressor and the other compressor is reduced. The values of the work of the recompressor and turbine are similar. The heat transfer rate in the precooler between lines 9 and 11 increases, between streams 12 and 1, and the LTR decreases. The mass fractions and the mass flow in the mixture and the pure fluid are similar with values of 0.41; 563.1 kg/s and 552.8 kg/s respectively.

In the exergetic analysis, the efficiency of the second law is obtained, and the results show values of 79.45% and 80.29% for pure CO<sub>2</sub> and the mixture, respectively.



(a)



(b)

**Figure 7.** Entropic generation in the components of the RCMCI cycle. (a) CO<sub>2</sub> pure and (b) CO<sub>2</sub>/ H<sub>2</sub>S mixture.

## CO<sub>2</sub>/C<sub>3</sub>H<sub>8</sub> mixture

Figure 8 compares the efficiencies obtained with pure CO<sub>2</sub> (segmented line) versus those obtained by the mixture containing propane (solid line). The study shows that in the PCRC and RCMCI cycles, slightly lower efficiencies are achieved with the mixture, however, in the RCC cycle the mixture obtains a better efficiency for values of 36 °C and 40 °C of compressor inlet temperature.

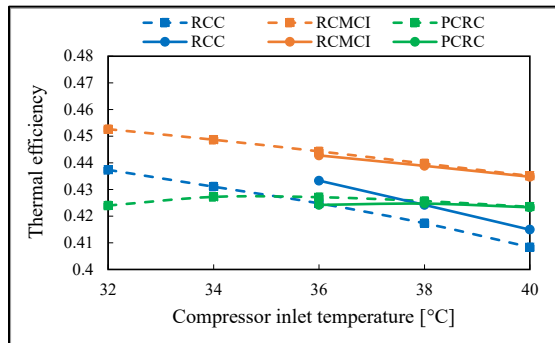
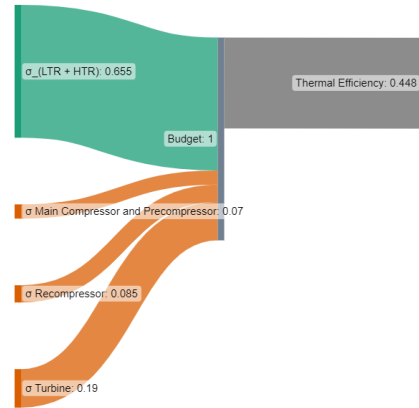


**Figure 8.** Thermal Efficiency vs Compressor inlet temperature. Using CO<sub>2</sub>/C<sub>3</sub>H<sub>8</sub> mixture (solid line), with mole fraction 0.85/0.15 and UA 10000 kW/K.

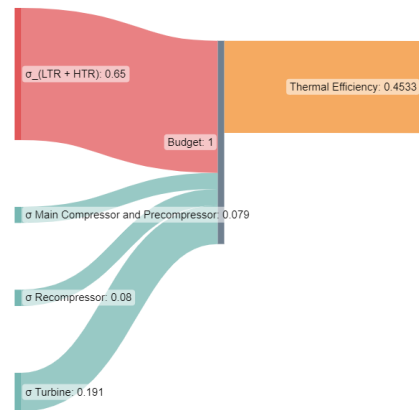
Figure 9 shows the values of the irreversibilities (entropic generation) in percentages produced in the different components of the cycle and the thermal efficiency of the cycle. The values obtained with pure CO<sub>2</sub> are compared with the mixture for a compressor inlet temperature of 36 °C (Critical temperature of the mixture). It is shown that the sum of the irreversibilities in LTR and HTR represent similar values of the order of 65.5% and 65% when using pure CO<sub>2</sub> and the mixture, respectively.

When this mixture is used, the main compressor work increases, but the recompressor and turbine work decreases. Heat transfer rates in the HTR and Precooler increase, however in the LTR they decrease. The mass fraction flowing to the recompressor is 0.36 for the mixture and 0.38 for pure CO<sub>2</sub>. In addition, the mass flow also decreases when using the mixture with a value of 538.84 kg/s; while, in the standard fluid it is 645 kg/s.

In the exergetic analysis, the efficiency of the second law is obtained, and the results show values of 79.5% and 80.05% for pure CO<sub>2</sub> and the mixture, respectively.



(a)



(b)

**Figure 9.** Entropic generation in the components of the RCC cycle. (a) CO<sub>2</sub> pure and (b) CO<sub>2</sub>/ C<sub>3</sub>H<sub>8</sub> mixture.

## CONCLUSIONS

An energy and exergy analysis of s-CO<sub>2</sub> Brayton cycle configurations using binary mixtures as working fluid for shipboard power applications has been presented. This work takes into account the influence of the main operating parameters such as the temperature at the compressor and turbine inlet, the pressure ratio, the irreversibilities generated, and the pressure drop in the system components, etc. Within the thermal efficiency analysis, it is obtained that the CO<sub>2</sub>-based mixtures produce a better efficiency than the pure fluid. The entropic generation in the heat recuperators (LTR and HTR) is significantly higher compared to the other components. The sum of their values represents more than 55% of the irreversibilities of the entire system. Temperature variation at the compressor inlet will result in drastic changes in thermal and exergetic efficiency. In addition, the value of the exergetic efficiency given by the mixtures is always higher than with pure CO<sub>2</sub>.

The study of the three Brayton s-CO<sub>2</sub> cycle configurations has determined that the configuration that obtains the best thermal efficiency values is the RCMCI followed by the RCC and finally the PCRC when the compressor inlet temperature is 32°C. Each configuration has a particular mixture that gives better efficiency than the standard fluid.

- For the RCMCI configuration, the CO<sub>2</sub>/H<sub>2</sub>S mixture in mole fraction (0.95/0.05):
  - A slight increase in the irreversibilities of the components is shown, however, the works of the main compressor and the other compressor are reduced as well as the rates of heat transfer in the LTR and precooler between streams 12 and 1.
- For the PCRC configuration the CO<sub>2</sub>/CH<sub>4</sub> mixture with a molar fraction of 0.70/0.30:
  - This mixture provides a higher rate of heat transfer in the HTR, LTR, and precooler between streams 12 and 1. In addition, the work of the main compressor, precompressor, and turbine is also greater. In this case, the irreversibilities generated in the heat recuperators (HTR and LTR) decrease by 20%.
- For the RCC configuration the CO<sub>2</sub>/C<sub>3</sub>H<sub>8</sub> mixture with a molar fraction of 0.85/0.15:
  - When using this mixture, the irreversibility values in the components are similar. However, it shows an increase in the heat transfer rate in the HTR and precooler and the work of the recompressor and turbine decreases in comparison with the values obtained when pure CO<sub>2</sub> is used.

Finally, the thermal efficiency values obtained by the mixtures are higher than the values obtained by pure CO<sub>2</sub> in each studied architecture. This improvement in efficiency will be of great help to reduce the levels of CO<sub>2</sub> emissions on shipboard systems, contributing to a great extent to the objectives of sustainable development, specifically with Climate Action.

## NOMENCLATURE

COS	Carbonyl sulfide
CSP	Concentrated solar power
CH <sub>4</sub>	Methane
C <sub>3</sub> H <sub>8</sub>	Propane
C <sub>6</sub> F <sub>6</sub>	Hexafluorobenzene
C <sub>7</sub> H <sub>8</sub>	Toluene
CO <sub>2</sub>	Carbon dioxide
<i>h</i>	Enthalpy [kJ/kg]
H <sub>2</sub> S	Hydrogen sulfide
HTR	High temperature recuperator
$\dot{m}_{mix}$	Mass flow of the mixture [kg/s]
NIST	National Institute of Standards and Technology
Ni <sub>2</sub> O <sub>4</sub>	Dinitrogen tetroxide
RCC	Recompression cycle

LTR	Low temperature recuperator
PCRC	Partial Cooling with recompression
$\dot{Q}_{Pre_1}$	The heat transfer rates in the precooler 1 [kW]
$\dot{Q}_{Pre_2}$	The heat transfer rates in the precooler 2 [kW]
$\dot{Q}_{PHX}$	The heat transfer rates in the primary heat exchanger [kW]
REFPROP	Reference Fluid Thermodynamic and Transport Properties
RCMCI	Recompression with main compressor intercooling cycle
<i>s</i>	Entropy [kJ/kg-K]
s-CO <sub>2</sub>	Supercritical carbon dioxide
SCSP	Supercritical Concentrated Solar Power Plant
TiCl <sub>4</sub>	Titanium chloride
<i>T<sub>hs</sub></i>	Temperature of the heat source [K]
<i>T<sub>o</sub></i>	Ambient temperature [K]
UA	Heat total recuperator conductance [kW/K]
$\dot{W}_{net}$	Net work output [kW]

## Greek Symbols

$\dot{E}_{in}$	Total heat input exergy [kW]
$\eta_{carnot}$	Carnot Efficiency
$\eta_{th}$	Thermal Efficiency
$\eta_{ex}$	Exergetic Efficiency
$\sigma_C$	Entropy generated in the compressor [kW/K]
$\sigma_{HTR}$	Entropy generated in the high-temperature recuperator [kW/K]
$\sigma_{LTR}$	Entropy generated in the low-temperature recuperator [kW/K]
$\sigma_{MC}$	Entropy generated in the main compressor [kW/K]
$\sigma_{RC}$	Entropy generated in the recompressor [kW/K]
$\sigma_T$	Entropy generated in the turbine [kW/K]
$\gamma$	Split Fraction

## REFERENCES

- [1] Yang, J., Yang, Z., & Duan, Y. (2021). Novel design optimization of concentrated solar power plant with S-CO<sub>2</sub> Brayton cycle based on annual off-design performance. *Applied Thermal Engineering*, 192, 116924. <https://doi.org/10.1016/j.applthermaleng.2021.116924>
- [2] Khatoun, S., & Kim, M. H. (2022). Preliminary design and assessment of concentrated solar power plant using supercritical carbon dioxide Brayton cycles. *Energy Conversion and Management*, 252,



115066. <https://doi.org/10.1016/j.enconman.2021.115066>
- [3] Yang, J., Yang, Z., & Duan, Y. (2022). A review on integrated design and off-design operation of solar power tower system with S-CO<sub>2</sub> Brayton cycle. *Energy*, 246, 123348. <https://doi.org/10.1016/j.energy.2022.123348>
- [4] Yu, A., Su, W., Lin, X., & Zhou, N. (2021). Recent trends of supercritical CO<sub>2</sub> Brayton cycle: Bibliometric analysis and research review. *Nuclear Engineering and Technology*, 53(3), 699-714. <https://doi.org/10.1016/j.net.2020.08.005>
- [5] Miao, X., Zhang, H., Sun, W., Wang, Q., & Zhang, C. (2022). Optimization of a recompression supercritical nitrous oxide and helium Brayton cycle for space nuclear system. *Energy*, 242, 123023. <https://doi.org/10.1016/j.energy.2021.123023>
- [6] Geng, C., Lu, X., Yu, H., Zhang, W., Zhang, J., & Wang, J. (2022). Theoretical Study of a Novel Power Cycle for Enhanced Geothermal Systems. *Processes*, 10(3), 516. <https://doi.org/10.3390/pr10030516>
- [7] Cao, Y., Li, P., Qiao, Z., Ren, S., & Si, F. (2022). A concept of a supercritical CO<sub>2</sub> Brayton and organic Rankine combined cycle for solar energy utilization with typical geothermal as auxiliary heat source: Thermodynamic analysis and optimization. *Energy Reports*, 8, 322-333. <https://doi.org/10.1016/j.egy.2021.11.258>
- [8] Alshahrani, S., Vesely, L., Kapat, J., Saleel, C. A., & Engeda, A. (2022). Performance Investigation of Supercritical CO<sub>2</sub> Brayton Cycles in Combination With Solar Power and Waste Heat Recovery Systems. *Journal of Solar Energy Engineering*, 144(6), 061004. <https://doi.org/10.1115/1.4054663>
- [9] Tafur-Escanta, P., Valencia-Chapi, R., López-Guillem, M., Fierros-Peraza, O., & Muñoz-Antón, J. (2022). Electrical energy storage using a supercritical CO<sub>2</sub> heat pump. *Energy Reports*, 8, 502-507. <https://doi.org/10.1016/j.egy.2022.01.073>
- [10] Albert, M., Ma, Z., Bao, H., & Roskilly, A. P. (2022). Operation and performance of Brayton Pumped Thermal Energy Storage with additional latent storage. *Applied Energy*, 312, 118700. <https://doi.org/10.1016/j.apenergy.2022.118700>
- [11] Sharma, O. P., Kaushik, S. C., & Manjunath, K. (2017). Thermodynamic analysis and optimization of a supercritical CO<sub>2</sub> regenerative recompression Brayton cycle coupled with a marine gas turbine for shipboard waste heat recovery. *Thermal Science and Engineering Progress*, 3, 62-74. <https://doi.org/10.1016/j.tsep.2017.06.004>
- [12] Du, Y., Hu, C., Yang, C., Wang, H., & Dong, W. (2022). Size optimization of heat exchanger and thermoeconomic assessment for supercritical CO<sub>2</sub> recompression Brayton cycle applied in marine. *Energy*, 239, 122306. <https://doi.org/10.1016/j.energy.2021.122306>
- [13] Wan, X., Wang, K., Zhang, C. M., Zhang, T. C., & Min, C. H. (2022). Off-design optimization for solar power plant coupling with a recompression supercritical CO<sub>2</sub> Brayton cycle and a turbine-driven main compressor. *Applied Thermal Engineering*, 209, 118281. <https://doi.org/10.1016/j.applthermaleng.2022.118281>
- [14] Valencia-Chapi, R., Coco-Enríquez, L., & Muñoz-Antón, J. (2019). Supercritical CO<sub>2</sub> mixtures for advanced brayton power cycles in line-focusing solar power plants. *Applied Sciences*, 10(1), 55. <https://doi.org/10.3390/app10010055>
- [15] Manzolini, G., Binotti, M., Bonalumi, D., Invernizzi, C., & Iora, P. (2019). CO<sub>2</sub> mixtures as innovative working fluid in power cycles applied to solar plants. Techno-economic assessment. *Solar Energy*, 181, 530-544. <https://doi.org/10.1016/j.solener.2019.01.015>
- [16] Siddiqui, M. E. (2021). Thermodynamic performance improvement of recompression brayton cycle utilizing CO<sub>2</sub>-C<sub>7</sub>H<sub>8</sub> binary mixture. *Mechanics*, 27(3), 259-264. <https://doi.org/10.5755/j02.mech.28126>
- [17] Tafur-Escanta, P., Valencia-Chapi, R., López-Paniagua, I., Coco-Enríquez, L., & Muñoz-Antón, J. (2021). Supercritical CO<sub>2</sub> Binary Mixtures for Recompression Brayton s-CO<sub>2</sub> Power Cycles Coupled to Solar Thermal Energy Plants. *Energies*, 14(13), 4050. <https://doi.org/10.3390/en14134050>
- [18] Crespi, F., de Arriba, P. R., Sánchez, D., Ayub, A., Di Marcoberardino, G., Invernizzi, C. M., ... & Manzolini, G. (2022). Thermal efficiency gains enabled by using CO<sub>2</sub> mixtures in supercritical power cycles. *Energy*, 238, 121899. <https://doi.org/10.1016/j.energy.2021.121899>
- [19] Niu, X., Ma, N., Bu, Z., Hong, W., & Li, H. (2022). Thermodynamic analysis of supercritical Brayton cycles using CO<sub>2</sub>-based binary mixtures for solar power tower system application. *Energy*, 124286. <https://doi.org/10.1016/j.energy.2022.124286>



- [20] Tafur-Escanta, P., Gutiérrez-Gualotuña, E., Villavicencio-Poveda, A., Valencia-Chapi, R., & Muñoz-Antón, J. (2022). Effect of Heat exchanger's Pressure Drops on the Thermal Efficiency of Brayton Cycles Complex Configurations with s-CO Mixtures as Working Fluid. In *XV Multidisciplinary International Congress on Science and Technology* (pp. 245-258). Springer, Cham. [https://doi.org/10.1007/978-3-031-08280-1\\_17](https://doi.org/10.1007/978-3-031-08280-1_17)
- [21] P. Tafur-Escanta, R. Valencia-Chapi, J. Muñoz-Antón, Complex Configurations of Partial Cooling with Recompression Brayton Cycles Using s-CO<sub>2</sub> Mixtures, in: 27th SolarPACES International Conference, Solar Power and Chemical Energy Systems, 2021. <https://www.solarpaces-conference.org/home>
- [22] Valencia-Chapi, R., Tafur-Escanta, P., Coco-Enriquez, L., & Muñoz-Antón, J. (2022, May). Supercritical CO<sub>2</sub> mixtures for Brayton power cycles complex configurations with concentrating solar power. In *AIP Conference Proceedings* (Vol. 2445, No. 1, p. 090009). AIP Publishing LLC. <https://doi.org/10.1063/5.0086032>
- [23] Coco-Enriquez, L. (2017). NUEVA GENERACION DE CENTRALES TERMOSOLARES CON COLECTORES SOLARES LINEALES ACOPLADOS A CICLOS SUPERCRITICOS DE POTENCIA. Tesis (Doctoral), Universidad Politécnica de Madrid. <https://doi.org/10.20868/UPM.thesis.44002>
- [24] Lemmon, E.W.; Bell, I.H.; Huber, M.L.; McLinden, M.O. NIST Standard Reference Database 23: Reference Fluid Thermodynamic and Transport Properties-REFPROP; Version 10.0; National Institute of Standards and Technology: Gaithersbg, MD, USA, 2018. Available online: <https://www.nist.gov/sites/default/files/documents/2018/05/23/refprop10a.pdf> (accessed on 20 July 2022).
- [25] Cengel, Y. A., Boles, M. A., & Kanoğlu, M. (2011). *Thermodynamics: an engineering approach* (Vol. 5, p. 445). New York: McGraw-hill.
- [26] Dostal, V., Driscoll, M. J., & Hejzlar, P. (2004). A supercritical carbon dioxide cycle for next generation nuclear reactors.
- [27] Wang, Z., Jiang, Y., Han, F., Yu, S., Li, W., Ji, Y., & Cai, W. (2022). A thermodynamic configuration method of combined supercritical CO<sub>2</sub> power system for marine engine waste heat recovery based on recuperative effects. *Applied Thermal Engineering*, 200, 117645. <https://doi.org/10.1016/j.applthermaleng.2021.117645>
- [28] Tafur-Escanta, P., Barrera-Cifuentes, L., Gutiérrez-Gualotuña, E., Muñoz-Antón, J., & Villavicencio-Poveda, Á. (2022, October). Study of the Integration of Additives in CO<sub>2</sub> in s-CO<sub>2</sub> Brayton Cycles Configurations as a Working Fluid. In *2022 IEEE Sixth Ecuador Technical Chapters Meeting (ETCM)* (pp. 1-6). IEEE. <https://doi.org/10.1109/ETCM56276.2022.9935720>

## STUDY OF PID-BASED S-CO<sub>2</sub> PRECOOLER SYSTEM CONTROL METHOD

Gi Hyeon Kim

<sup>a</sup> Department of Nuclear and Quantum Engineering,  
Korea Advanced Institute of Science and Technology  
373-1 Guseong-dong Yuseong-gu, Daejeon, 305-701,  
Korea

Email: orca2005@kaist.ac.kr

Jeong Ik Lee

<sup>\*</sup> Department of Nuclear and Quantum Engineering,  
Korea Advanced Institute of Science and Technology  
373-1 Guseong-dong Yuseong-gu, Daejeon, 305-701,  
Korea

Email: jeongiklee@kaist.ac.kr

### ABSTRACT

The distributed power supply must change its output according to the surrounding demand. Therefore, in order to use the supercritical CO<sub>2</sub> Brayton cycle for a distributed power source, the output of the power generation cycle must be controlled according to the needs of the surroundings. This study focuses on the pre-cooler among the various components of the Brayton cycle of supercritical carbon dioxide and conducts control studies. The design of the controller that fixes the temperature at the outlet of the pre-cooler through the control of the pre-cooler was carried out through the Autonomous Brayton Cycle loop in KAIST. In this study, a control methodology is first developed from a computer simulation code. The experimental data from the Autonomous Brayton Cycle loop, computational simulation is performed and the response to the input of the pre-cooler system is calculated. PID controller is designed by modeling the pre-cooler system and using classic control theory. The suggested controller development process in this study can reduce trial and error in future control development for the supercritical CO<sub>2</sub> power cycle.

### INTRODUCTION

The S-CO<sub>2</sub> Brayton cycle is attracting attention as a power generation cycle that can be used for the next-generation nuclear power plants instead of the steam cycle currently used. The S-CO<sub>2</sub> Brayton cycle is an original technology applicable to nuclear power generation and various fields such as waste heat recovery and solar power generation [1]. There are several reasons why the S-CO<sub>2</sub> Brayton cycle is receiving attention. First, when the turbine inlet temperature condition exceeds 500 °C, the efficiency of the S-CO<sub>2</sub> Brayton cycle becomes higher than that of the steam Rankine cycle or the helium Brayton cycle [2]. In addition, the compression work of the S-CO<sub>2</sub> Brayton cycle can be significantly reduced due to the compression process taking place near the critical point of CO<sub>2</sub>

[3]. Therefore, the size of components such as turbines and compressors can be significantly reduced.

Due to its small size and high efficiency, the S-CO<sub>2</sub> Brayton cycle is suitable for small modular reactor (SMR) applications. The small size and high efficiency of the SMR are positive factors for using the SMR as a distributed power source. Distributed power generation is a power generation method in which the power source is placed near the power demand, unlike the existing centralized power source. This generation method is receiving attention because it can reduce the number of transmission facilities, improve system stability, and reduce the initial investment burden. To use any power generation system as a distributed power source, the output of the power generation system should be able to adjust according to the needs. Due to this requirement, various attempts have been made to control the output of the S-CO<sub>2</sub> Brayton cycle under different circumstances.

Currently, many S-CO<sub>2</sub> Brayton cycles proposed for output control are turbine bypass control and inventory control. If these two control methods are applied to a simple recuperated cycle, it is shown in Figure 1 [4 & 5].

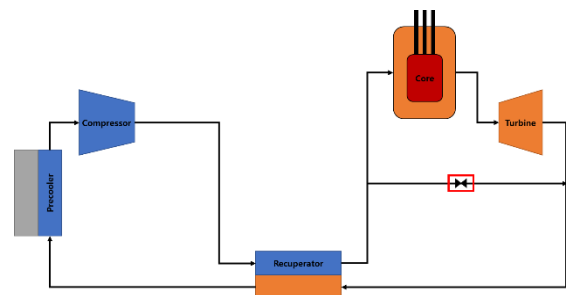


Fig. 1(a) Simple recuperated with turbine bypass control

\* corresponding author(s)

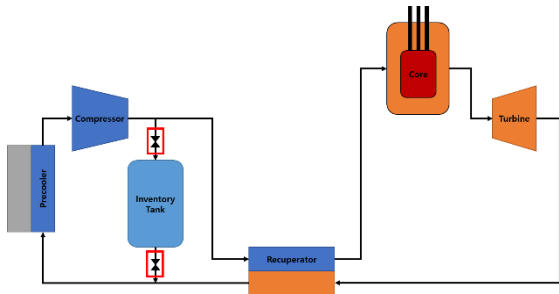


Fig. 1(b) Simple recuperated with inventory control

The turbine bypass control in Figure 1(a) and the inventory control in Figure 1(b) are aimed at global control of the system output. However, experiments on the system suggest that a controller for each component as well as a global controller is needed for a stable S-CO<sub>2</sub> system. For example, in the Sandia report published in 2019, it was mentioned that perturbation occurred in the heating and cooling of the close loop due to manual control, which caused instability of the turbomachinery and imposed faster thermal transients than required for equipment [7]. Therefore, this study discusses the PID controller design methodology to keep the CO<sub>2</sub> temperature at the outlet of the precooler constant. This solves the problem raised in the Sandia report by maintaining the compressor inlet temperature constant, thereby securing the stability of the turbomachinery.

If PID control is used, it is necessary to appropriately determine the PID control parameters to properly control the system. However, due to the limitations of the experimental system that can test the S-CO<sub>2</sub> Brayton cycle, these control methods and control parameters are calculated and verified through the system simulation code in the open literatures [7,8,9,10]. In this paper, the authors aim to obtain actual experimental data from a supercritical Brayton cycle experimental facility, Autonomous Brayton Cycle (ABC) test loop, and to establish PID control logic using the obtained data so that it can be used for the power cycle control in the future.

### ABC TEST LOOP

ABC test loop is an abbreviation for the Autonomous Brayton Cycle test loop. This experimental facility was constructed for an integrated experiment on the simple recuperated S-CO<sub>2</sub> cycle. ABC loop is made of a turbo alternator compressor (TAC), printed circuit heat exchanger (PCHE) type recuperator, electric cartridge type heater, and precooler. In addition, for the control experiment, control valves are attached to the inlet and outlet of the compressor, and other control valves are attached to the water flow path of the precooler. The turbine bypass flow path and turbine bypass valve are attached for the experiment on turbine bypass control.

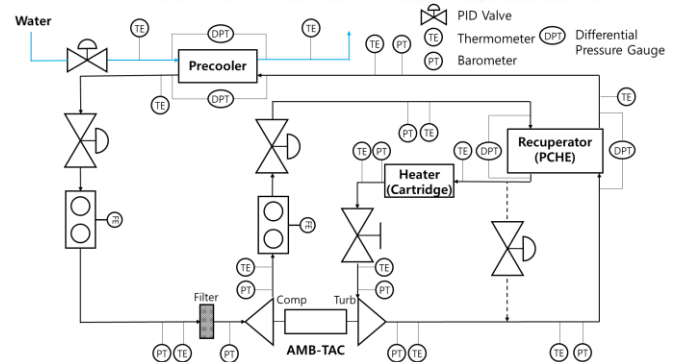
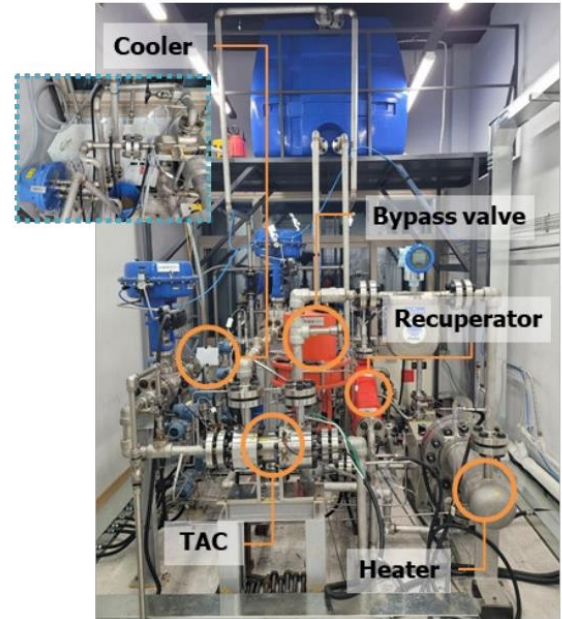


Fig. 2 ABC test loop and schematic diagram [11]

As the name suggests, the ABC test loop is designed to enable the I/O of data using the computer to automatically test the S-CO<sub>2</sub> Brayton cycle. The pressure, temperature, and mass flow rate of each flow path are converted into digital signals and input to the computer in real-time through the Programmable Logic Controller (PLC). The computer controls the opening/closing degree of the control valve and the heater output through the PLC by performing calculations based on the received data and the user's input. In addition, it is possible to calculate values such as enthalpy or the effectiveness of a heat exchanger that cannot simply be measured with a measuring instrument in real-time. Calculation of thermodynamic data is performed in real-time based on NIST's REFPROP and the measured physical quantity, and it is programmed so that the user can easily change the physical quantity to be calculated.

Since the ABC test loop is designed to perform an integrated experiment on the Brayton cycle, there are various experiments performed with the test loop so far. One of them is the compressor surge protection control experiment. A surge is a phenomenon that occurs when the mass flow rate in the compressor decreases below a certain value, the surge limit.

When a surge occurs, the compressor generates strong vibration and noise, which may damage or even destroy the compressor. Therefore, it is important to secure the surge margin above a certain level, which is a number that indicates how far the compressor is from the current surge limit.

The compressor surge protection control experiment is an experiment to check whether the surge margin can be restored by automatically recognizing a dangerous situation when the surge margin of the compressor falls below a certain value. For the experiment, the control valves of the inlet and outlet were reduced while maintaining the rotational speed of the compressor. This reduces the compressor inlet mass flow and therefore the surge margin. Baek showed that when the surge margin falls below 15%, the experimental device automatically recognizes it and opens the valve to restore the surge margin, thereby avoiding a surge [11].

As such, various experiments are possible with the current ABC test loop, and further improvements and upgrades are planned for expanding the capabilities of the test loop. Recent improvements include increasing the power output of the electric cartridge heater and replacing the bearings of the TAC from ball bearings with magnetic bearings. The target of recent experiments using the ABC test loop is to demonstrate stable operation over a wide range of magnetic bearing TAC.

## MARS

The Multi-dimensional Analysis of Reactor Safety (MARS) code is a nuclear thermal-hydraulic safety code developed by Korea Atomic Energy Research Institute (KAERI). MARS was developed based on USNRC's RELAP5/MOD3.2.1.2 and COBRA-TF to calculate the transient multi-dimensional behavior of thermal-hydraulic systems in light water reactors [12]. The basic field equation of the MARS code consists of two phasic continuity equations, two phasic momentum equations, and two phasic energy equations. This code is being used by the Korea Institute of Nuclear Safety (KINS) to evaluate the safety of actual nuclear power plants [13].

In this study, data obtained from actual experiments with the ABC test loop will be simulated using the MARS code, and the open loop characteristics of the heat exchanger used for the precooler will be analyzed from the MARS simulation. There are two main reasons for not using the actual ABC test loop experimental data immediately and simulating the system with MARS code. First of all, in the actual system, there are many other components such as compressors, turbines, and heaters in addition to the heat exchanger, so it is difficult to see the response of only the heat exchanger. In addition, to design the controller, the response of the open loop system should be analyzed. However, in the ABC test loop, the fluid in the precooler passes through the other components and back to the heat exchanger. This causes feedback that is physically difficult to interpret, making the open loop system uninterpretable.

Therefore, the MARS code should be able to properly simulate the experimental equipment and predict the experimental results. That is, the MARS code must accurately calculate the heat exchange between CO<sub>2</sub> and water in the

precooler under transient conditions. However, since the MARS code is designed to evaluate the safety of a water-cooled reactor, the physical properties of S-CO<sub>2</sub> are not applied. In addition, since the heat exchange model was created centered on the reactor core, the transient behavior of PCHE was not well simulated. The KAIST research team solved these problems as follows. First, the precise physical properties of CO<sub>2</sub> were implemented to the MARS code based on NIST's REFPROP database. Second, the heat transfer correlation of PCHE was added to the heat structure set of the MARS code [14].

The results of the compressor surge avoidance control experiment were used to simulate with the MARS code. The result of comparing the MARS code with the actual experimental data is shown in Figures 3 to 5. It can be confirmed that the MARS code simulates the actual experiment well.

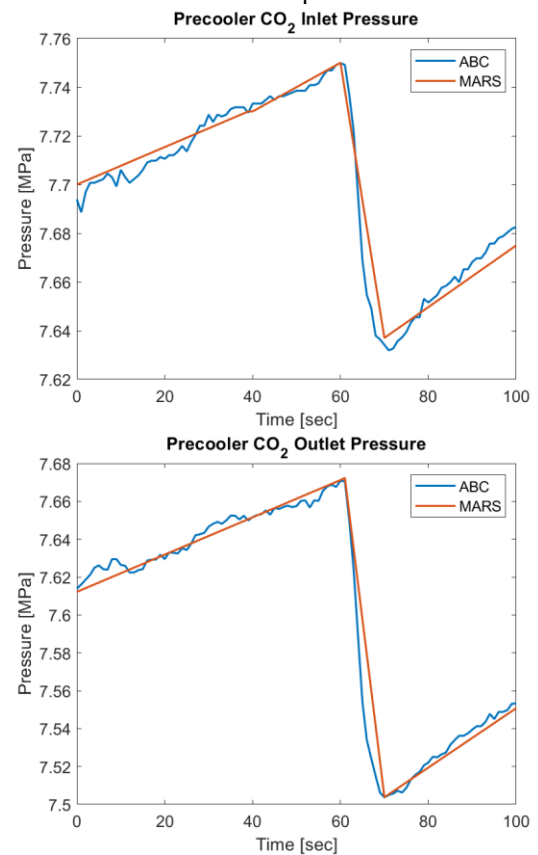


Fig. 3 CO<sub>2</sub> pressure comparison of ABC compressor surge avoidance control experiment and MARS simulation



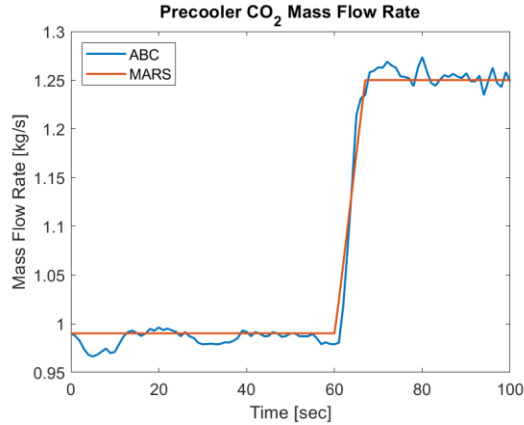


Fig. 4 CO<sub>2</sub> mass flow rate comparison of ABC compressor surge avoidance control experiment and MARS simulation

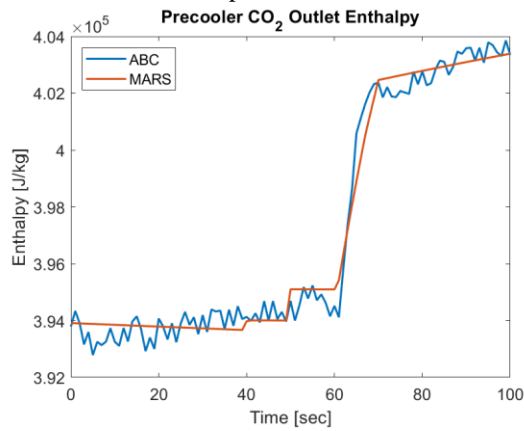


Fig. 5 CO<sub>2</sub> outlet enthalpy comparison of ABC compressor surge avoidance control experiment and MARS simulation

## DIGITAL CONTROL

The ABC test loop in the real world is, of course, a system in which a physical quantity continuously changes with time. However, the computer controls the ABC test loop, which is digital. The process of the computer controlling the ABC test loop is as follows. The physical quantity of the ABC test loop is converted into an electrical signal through a measuring instrument. The electrical signal output from the instrument goes through the PLC and is measured once per iteration for each time the computer passes through the iteration. For a single iteration, the computer performs calculations based on the measured data. The computer controls by sending a signal to the ABC test loop based on the calculated result and the user's input. That is, the computer replaces the controller of the classical control system, which receives the output value of the system, and controls the system by giving feedback. Therefore, to control the ABC test loop, the system must be analyzed in the discrete-time domain rather than the continuous-time domain.

The signal in the discrete-time domain uses Z-transform to figure out the characteristic of the signal in the frequency domain. This is one of the differences between the discrete-time domain signal to the continuous-time domain, and the

characteristic of the continuous-time domain signal is analyzed using Laplace transform. Z-transform is a transformation that transforms a discrete-time domain signal into a complex frequency-domain form and is defined as the following equation for signal  $x(k)$ , whereas  $k$  is a positive integer.

$$X(z) = Z\{x(k)\} = \sum_{k=0}^{\infty} x(k)z^{-k} \quad (1)$$

Using Z-transform, it is possible to obtain a transfer function that is a linear transformation between the discrete-time input signal  $u(k)$  and the output signal  $y(k)$  for any system. The transfer function is important in designing the appropriate controller and system characteristics. If the Z-transforms of  $u(k)$  and  $y(k)$  are  $U(z)$  and  $Y(z)$ , the transfer function  $G(z)$  is given as follows.

$$G(z) = \frac{Y(z)}{U(z)} = \frac{Z\{y(k)\}}{Z\{u(k)\}} \quad (2)$$

## OPEN LOOP SYSTEM ANALYSIS

In general, to design a controller for an arbitrary system, the process variable (PV) must first be determined. Next, check which variable to manipulate in the system to control the PV as a setpoint (SP). Then, devise the model for the given system. Finally, the controller can be designed based on the model and the appropriateness of the controller can be checked by applying the designed controller to the system. The PV of the controller targeted in this study is the compressor inlet temperature, that is, the pre-cooler CO<sub>2</sub> outlet temperature. The variable of the system to control this is the control valve attached to the waterside pipe. Therefore, the system that uses the opening/closing rate of the control valve as the system input and the CO<sub>2</sub> outlet temperature as the system output is a pre-cooler system that must be controlled. Figure 6 shows this as a block diagram.

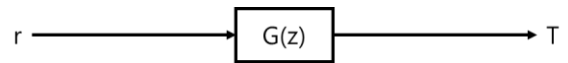


Fig. 6 Block diagram of pre-cooler open loop system

According to the results of previous studies, in the case of a steam-water heat exchanger, a transfer function exists between the flow rate of water and the outlet temperature of the water, and it can be calculated physically [15]. Assuming that S-CO<sub>2</sub> pre-cooler will respond similarly, it will be possible to design a controller that controls the outlet temperature by adjusting the flow rate using the previously proposed function for steam-water heat exchanger. Similarly, to design the controller of the pre-cooler system, the characteristics of the open loop system should be identified and the open loop transfer function should be calculated. However, the pre-cooler system in this study, there is no linear relationship between system input and output because the physical properties of CO<sub>2</sub> are non-linear near the critical point. Therefore, it is necessary to separate the non-linear elements from the system and approximate the system as a linear system, and the method to calculate these non-linear elements is required.

To approximate the pre-cooler system linearly, this study focused on the amount of heat exchanged in the pre-cooler. The

heat gained by water and the heat lost by CO<sub>2</sub> has to be the same if heat loss is neglected, and this amount of heat is calculated as in Equation (3).

$$\dot{m}_{water}c_{p,water}\Delta T_{water} = \dot{m}_{CO_2}\Delta h_{CO_2} \quad (3)$$

From the equation, the amount of heat gained by water increases linearly with the mass flow rate of water. In addition, CO<sub>2</sub> loses heat as much as the amount of heat gained by water, and the enthalpy of CO<sub>2</sub> changes. Therefore, in this study, it is assumed that the relationship between the mass flow rate of water and the outlet enthalpy of CO<sub>2</sub> can be approximated as a linear system. With this assumption, the block diagram in Figure 6 can be redrawn as in Figure 7.

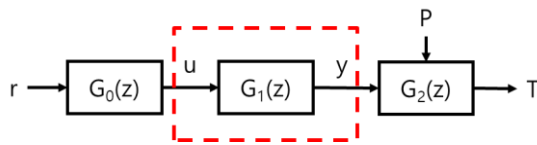


Fig. 7 Modified block diagram of pre-cooler open loop system

In Figure 7, the nonlinear elements are separated from the system, and the remaining part is approximated as a linear system. To avoid confusion in the future, the system inside the red dotted line will be referred to as a linearized pre-cooler system, and the entire system will be referred to as a pre-cooler system.  $G_0(z)$  is a relational expression between the valve open fraction and the water mass flow. This relationship has a different formula depending on the type of valve and can be calculated using the flow coefficient and formula provided by the valve manufacturer. In the case of  $G_2(z)$ , the formula is to convert the CO<sub>2</sub> outlet enthalpy to the CO<sub>2</sub> outlet temperature. If the CO<sub>2</sub> outlet pressure and CO<sub>2</sub> outlet enthalpy are known, so it can be calculated in various ways, such as using the REFPROP library directly. Therefore, it is possible to calculate  $G_2(z)$  with one additional pressure measurement at the pre-cooler outlet. That is, if only the linearized pre-cooler system  $G_1(z)$  is obtained, the characteristics of the entire open loop system can be identified, and an appropriate controller can be designed according to the classical control theory.

### ON-DESIGN TRANSFER FUNCTION

For the on-design conditions of the ABC test loop, CO<sub>2</sub> from the recuperator enters the pre-cooler at 321.74K, 8.6MPa, and exits at 308.15K, 7.6MPa. In addition, the inlet temperature and pressure of water were kept constant at 298.15 K and 1 bar, respectively during the experiment. To calculate the transfer function of the open loop linearized pre-cooler system under the on-design conditions, the response of the system was simulated using the MARS code when the water flow rate was doubled while the CO<sub>2</sub> inlet condition was fixed to the on-design conditions.

The input signal of the system is the water flow rate, and the output signal of the system is the CO<sub>2</sub> outlet enthalpy. In order to adjust the input signal  $u(k)$  of the transfer function to the unit

step input and set the initial value of output signal  $y(k)$  as 0, the original input signal  $u_0(k)$  and the output signal  $y_0(k)$  were normalized using Equation (4).

$$u(k) = \frac{u_0(k)}{u_{0,min}} - 1$$

$$y(k) = 1 - \frac{y_0(k)}{y_{0,max}} \quad (4)$$

The output signal  $y(k)$ , which is the response of the system to the input signal  $u(k)$  to which normalization of Equation (4) is applied, is shown in Figure 8.

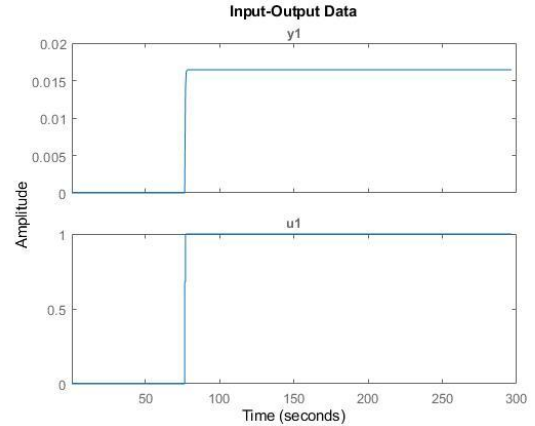


Fig. 8 System response for a unit step input

When the transfer function  $G_1(z)$  is obtained from the step response using the least square method, it can be approximated by Equation (5) having 1 zero and 2 poles.

$$G_1(z) = \frac{0.02004 z + 0.001064}{z^2 + 0.3433 z - 0.05896} \quad (5)$$

Figure 11 compares system responses between the transfer function and the actual system for a unit step input. The blue line is the response of the transfer function whereas the grey line is the response of the MARS simulation. The transfer function perfectly simulates the real system, so it is possible to approximate the linearized pre-cooler system with the transfer function  $G_1(z)$ .

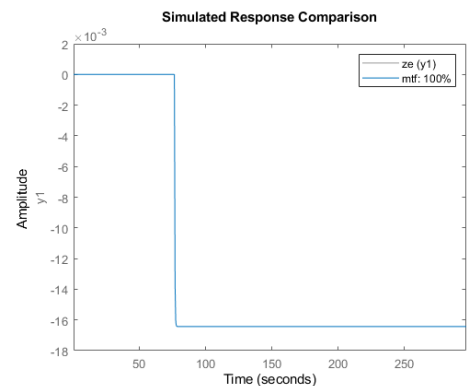


Fig. 9 System response comparison for a unit step input

In addition, poles, which are values that make the denominator of this transfer function as zero, are  $-0.4690$  and  $0.1257$ . The poles of transfer function  $G1(z)$  are located inside the unit circle on the complex plane. Since the poles of the linearized precooler system in the discrete-time domain exist inside the unit circle, the linearized precooler system is asymptotically stable. If the system is asymptotically stable, every mode converges to zero as time approaches infinity, which results in output convergence. In other words, the heat exchanger performance does not diverge and become unstable during operation.

To examine whether the approximate transfer function simulates the actual heat exchanger well, the test case of Figure 10 consisting of unit step input and ramp function was used.

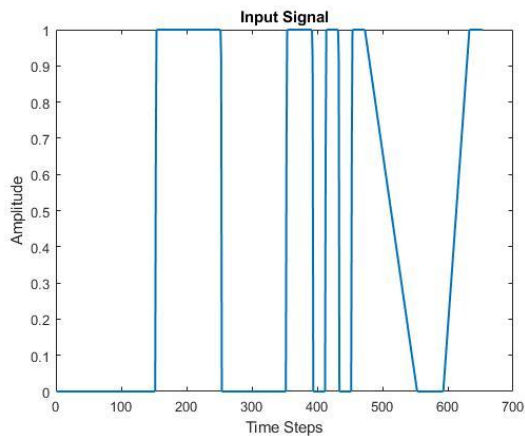


Fig. 10 Complex input signal for system test

Figure 11 shows the comparison between the simulation result using the MARS code and the result calculated through the transfer function. In this case, the y-axis is the actual enthalpy value, not the normalized value from Equation (4). The error between these two enthalpy values is 1.06%. Therefore, as shown in Figure 11, it can be confirmed that the response of the system calculated from the transfer function closely simulates the response of the real system even for more complex inputs.

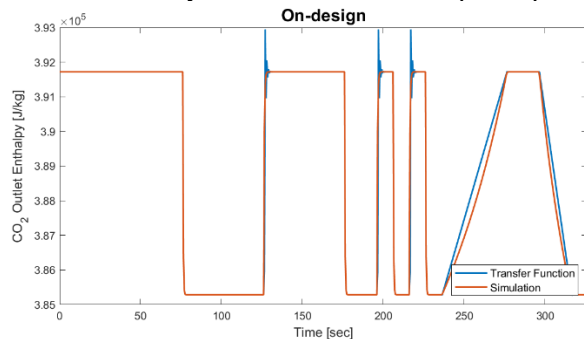


Fig. 11 On-design system response comparison for complex signal

## OFF-DESIGN TRANSFER FUNCTION

Kwon et al. work presented a method for approximating the amount of heat transferred from the recuperator and precoolers under the off-design condition in the S-CO<sub>2</sub> Brayton cycle [16]. In this study, it was shown that the amount of heat transferred from the precoolers in the off-design condition can be obtained by multiplying the constant calculated using the on-design condition in the original logarithmic mean temperature difference (LMTD) method and the linear correction value obtained in the off-design condition. Inspired by this, this study hypothesized that the response of the linearized precooler system under the off-design conditions could be obtained by multiplying the transfer function to the on-design conditions by the correction value.

To verify the hypothesis, the test case of Figure 10 used input as an input signal for 8 different off-design conditions, and the system response was investigated with the transfer function and MARS code. The inlet condition of the water remained the same at the on-design condition. Each off-design condition is indicated by an arrow drawn from the CO<sub>2</sub> inlet condition to the outlet condition in Figure 12. The middle red arrow indicates the on-design condition.

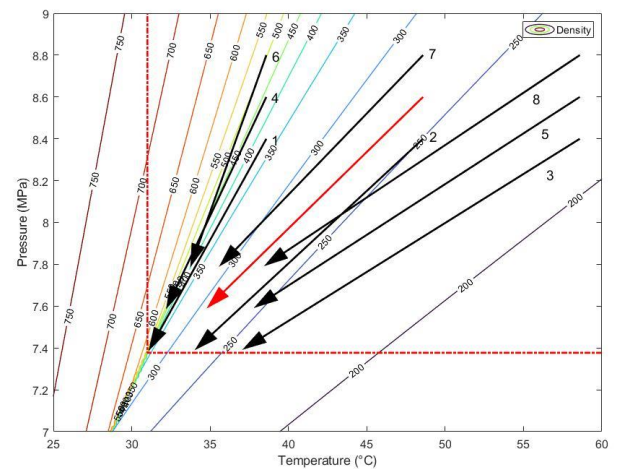


Fig. 12 Off-design CO<sub>2</sub> conditions

Figure 13 shows the comparison of the response of the system under off-design condition 1 and the response calculated with the transfer function shown in Equation (4). As shown in the figure, the transfer function predicts the response of the system similarly, but incorrectly predicts the amplitude of the response.



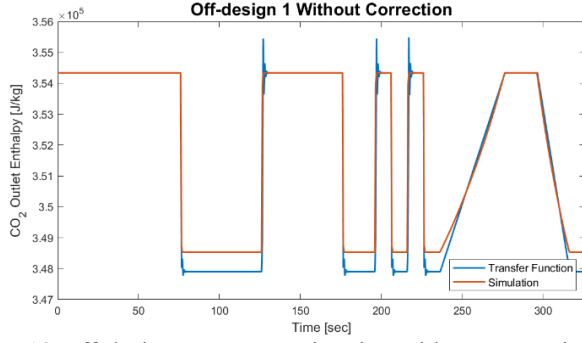


Fig. 13 Off-design response estimation without correction

Therefore, the amplitude should be corrected by multiplying the appropriate scalar  $C_f$  containing the information of the off-design condition. This correction factor was calculated as in Equation (6).

$$C_f = \frac{A_{min,on}}{A_{min,off}} \quad (6)$$

It can be confirmed that the transfer function multiplied by the correction value approximates the system response better for all 8 off-design conditions as shown in Figures 14 to 21.

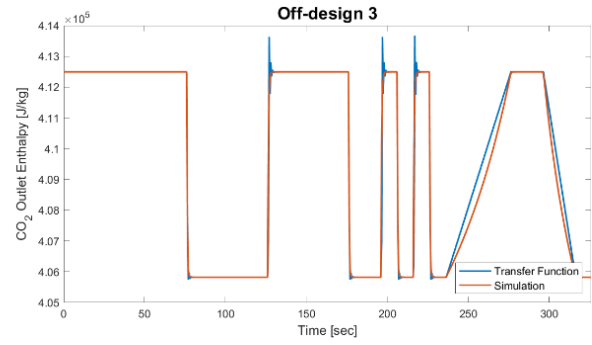


Fig. 16 Response estimation of off-design 3 (maximum error: 0.8349%)

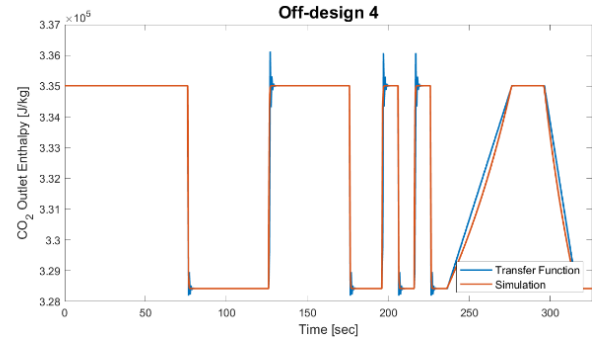


Fig. 17 Response estimation of off-design 4 (maximum error: 1.415%)

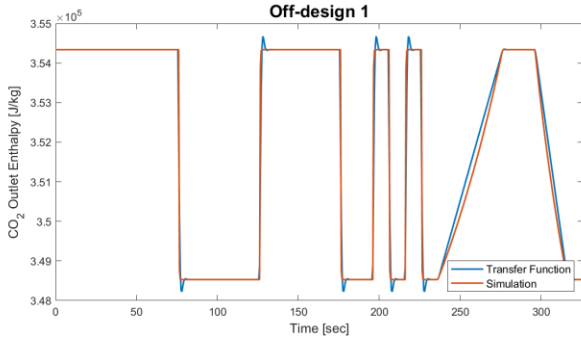


Fig. 14 Response estimation of off-design 1 (maximum error: 1.283%)

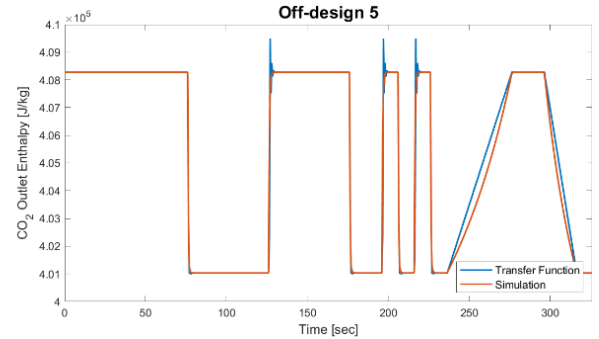


Fig. 18 Response estimation of off-design 5 (maximum error: 0.8885%)

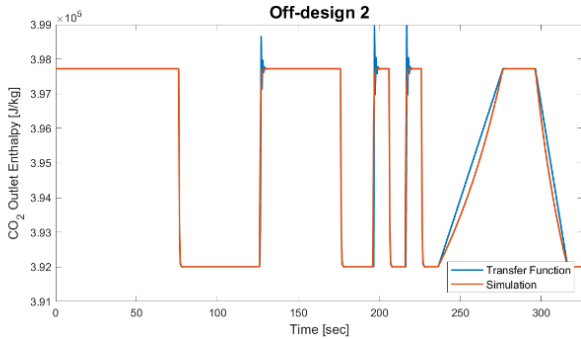


Fig. 15 Response estimation of off-design 2 (maximum error: 1.035%)

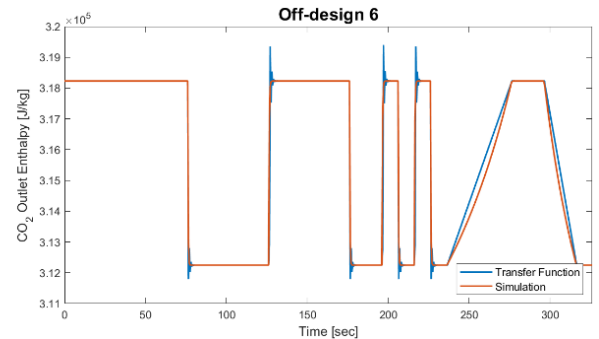


Fig. 19 Response estimation of off-design 6 (maximum error: 1.352%)

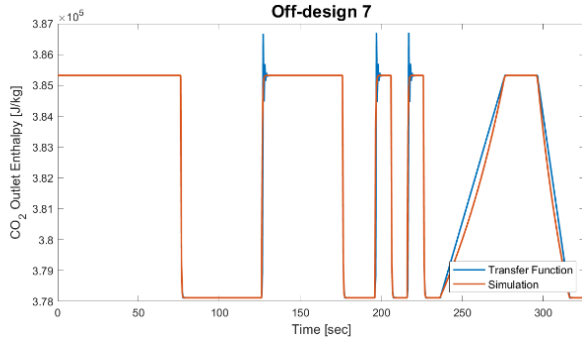


Fig. 20 Response estimation of off-design 7 (maximum error: 1.252%)

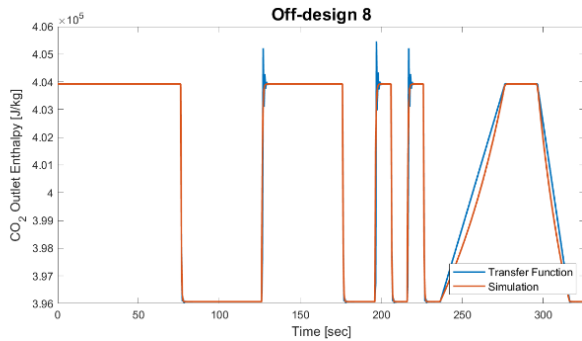


Fig. 21 Response estimation of off-design 8 (maximum error: 1.195%)

Figure 22 shows the results plotted against temperature by calculating the correction factor for each off-design condition and on-design condition. The value next to each data point is a correction factor that is exact with the design condition number, respectively. Points of the same color have the same pressure. For the same pressure, as the temperature increases, the correction factor  $C_f$  increases. Since  $C_f$  is the correction factor that is multiplied by the transfer function, the larger the  $C_f$ , the greater the change in the amount of enthalpy  $\text{CO}_2$  loses in response to the change in water flow rate. Therefore, as the  $\text{CO}_2$  inlet temperature increases, the  $\text{CO}_2$  outlet temperature for the entire precooler system becomes more sensitive to changes in the water valve fraction.

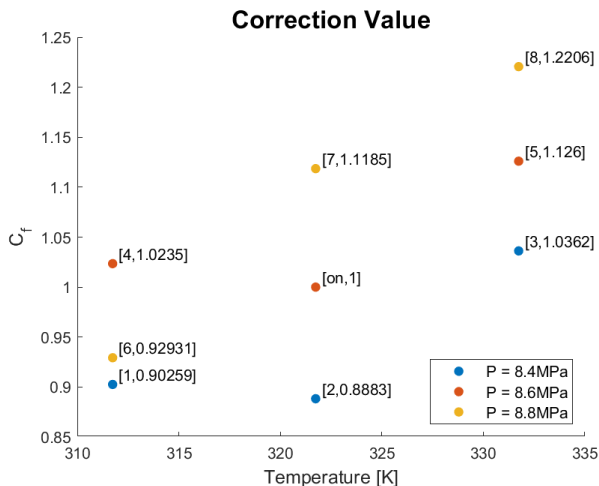


Fig. 22 Correction factor  $C_f$  of tested conditions

## CONTROLLER DESIGN USING TRANSFER FUNCTION

Ziegler-Nichols method is popular to determine the PID control parameters of various system, including the S- $\text{CO}_2$  system. The Ziegler-Nichols method is a method for heuristically determining the parameters of the PID controller [17]. The advantage of this method is that the parameters of the controller can be obtained from iterative tuning work even without system analysis. However, the controller determined with the Ziegler-Nichols method requires additional tuning due to having an aggressive gain, and having a large overshoot and vibration response [18]. In addition, to calculate the settling time and overshoot to evaluate the system, it is necessary to attach a controller and obtain data from simulation or experiment. By finding a closed loop transfer function using the open loop transfer function of the system to be controlled, it is possible to design controller that does not suffer from the limitations of the Ziegler-Nichols method.

$$C(z) = K_p + \frac{Tz + 1}{2z - 1} K_i + \frac{z - 1}{Tz} K_d \quad (7)$$

The transfer function of the PID controller in the discrete-time domain is given as Equation (7). Applying this to the open loop linearized precooler system and receiving unit feedback to apply PID control, a block diagram can be drawn as shown in Figure 23.

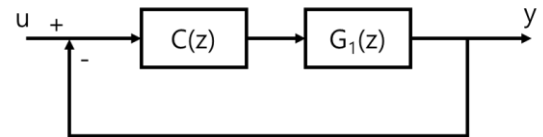


Fig. 23 Feedback loop with PID controller

The transfer function of the closed-loop system in Figure 24 is calculated as Equation (8). To determine the appropriate PID control parameters, the Equation (8) transfer function is tuned for  $K_p$ ,  $K_i$ , and  $K_d$  values.

$$\frac{Y(z)}{U(z)} = \frac{G_1(z)}{1 + G_1(z)C(z)} \quad (8)$$

Using the calculation results to determine whether the settling time and overshoot of the system are appropriate, a PID controller to control the system can be designed.

Figure 24 shows the system's response for input signal at Figure 10 calculated based on the transfer function of the closed-loop system calculated using Equation (8). Where,  $K_p = 1.0171$ ,  $K_i = 0$ ,  $K_d = -0.1722$ . When the PD controller is applied, the system perfectly removes overshoots.

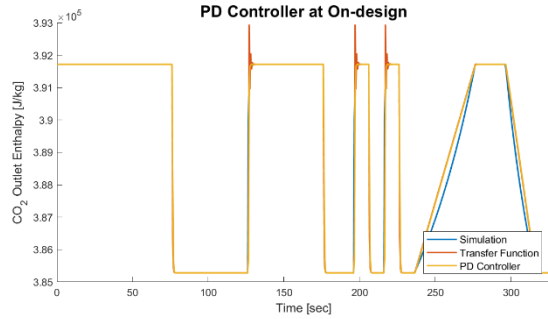


Fig. 24 Response of the system with PD controller

The PID controller in Figure 23 controls  $G_1(z)$ . Therefore, to control the whole precooler system in Figure 8, a little modification of the system is still required.

Figure 25 is a block diagram drawn reflecting this modification.  $G_3(z)$  is a function that calculates the enthalpy of CO<sub>2</sub> using temperature and pressure, and  $G_4(z)$  is a function that converts the flow rate of the valve into the opening/closing rate of the valve. These are the inverse functions of  $G_2(z)$  and  $G_0(z)$  that can be calculated using REFPROP and valve data, respectively. Therefore, the PID controller calculated using Figure 23 can be used for the whole system control.

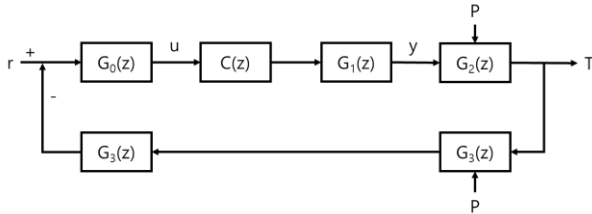


Fig. 25 Precooler system with PID controller

## SUMMARY AND FUTURE WORKS

In this study, the data obtained from the ABC test loop, a simple recuperated S-CO<sub>2</sub> Brayton cycle experimental facility, was used for designing a controller for the S-CO<sub>2</sub> Brayton cycle. To obtained data was first simulated with the MARS code so that an appropriate transfer function can be found using the verified simulation. The transfer function of the open loop linearized precooler system was obtained from the response to the unit step input of the system. It was shown that this transfer function well simulates the open loop response of the linearized precooler system under the on-design condition. In addition, even when the precooler system is under the off-design conditions, it was shown that the transfer function obtained for the on-design conditions can be used by simply multiplying an appropriate scalar value. This means that if the controller is designed under any one condition, the same controller can be used in a wide range in the case of the S-CO<sub>2</sub> precooler controller system. Finally, it was shown that it is possible to design a PID controller to control the S-CO<sub>2</sub> linearized precooler system using the transfer function calculated under the on-design conditions, and a method for applying it to the entire S-CO<sub>2</sub> precooler system is presented.

The conclusions of this study suggest several further studies. First, the PID controller designed with the transfer function has

to be applied to the actual experimental system and verified. Next, knowing the characteristics of the open-loop system in the discrete-time domain, various control techniques such as perfect tracking control, full-state feedback control, model predictive control, and disturbance observer control can be used in addition to PID control. It is necessary to study the design and application of the controller using these techniques in the S-CO<sub>2</sub> system. Finally, in this study, the system's response was calculated after simulating the system with the system code. To improve the method, a study to design a controller by analyzing the dynamics of the system with the system response obtained by applying an appropriate filter to the response of the actual experimental device can be also proposed.

## NOMENCLATURE

$A_{min,on}$	Minimum amplitude at on-design condition
$A_{min,off}$	Minimum amplitude at off-design condition
$C(z)$	Controller transfer function
$c_{p,water}$	Water specific heat
$G_0(z)$	Valve open fraction to mass flow rate function
$G_1(z)$	Precooler system linear transfer function
$G_2(z)$	CO <sub>2</sub> enthalpy to temperature function
$G_3(z)$	CO <sub>2</sub> temperature to enthalpy function
$G_4(z)$	Valve mass flow rate to open fraction function
$\Delta h_{CO_2}$	Precooler CO <sub>2</sub> enthalpy difference
$k$	Positive integer
$K_p$	Coefficient of PID proportional term
$K_i$	Coefficient of PID integral term
$K_d$	Coefficient of PID derivation term
$\dot{m}_{CO_2}$	Mass flow rate of CO <sub>2</sub> at precooler
$\dot{m}_{water}$	Mass flow rate of water at precooler
$P$	Pressure
$r$	Valve input signal
$T$	Time step size at discrete-time domain
$\Delta T_{water}$	Temperature difference of water
$u$	Input signal
$U(z)$	Z-transform of input signal
$y$	Output signal
$Y(z)$	Z-transform of output signal

## ACKNOWLEDGEMENTS

This research was supported by Civil-Military Technology Cooperation Program (iCMTC) funded by the Agency for Defense Development – South Korea (17-CM-EN-04).

## REFERENCES

- [1] Ahn, Yoonhan, et al. "Review of supercritical CO<sub>2</sub> power cycle technology and current status of research and development." Nuclear Engineering and Technology 47.6 (2015): 647-661.
- [2] Dostal, V., Hejzlar, P., & Driscoll, M. J. (2006). High-performance supercritical carbon dioxide cycle for next-generation nuclear reactors. Nuclear Technology, 154(3), 265-282.

- [3] Dostal, V., Driscoll, M. J., & Hejzlar, P. (2004). A supercritical carbon dioxide cycle for next generation nuclear reactors (Doctoral dissertation, Massachusetts Institute of Technology, Department of Nuclear Engineering).
- [4] Oh, B. S., & Lee, J. I. (2019, September). Study of autonomous control system for S-CO<sub>2</sub> power cycle. In 3rd European supercritical CO<sub>2</sub> Conference (pp. 19-20).
- [5] Lariviere, B., Marion, J., Macadam, S., McDowell, M., Lesemann, M., McClung, A., & Mortzheim, J. (2021, March). sCO<sub>2</sub> power cycle development and STEP Demo pilot project. In 4th Eur. SCO<sub>2</sub> Conf. Energy Syst., Online Conference.
- [6] Lance, B. W. (2019). Applied Controls for sCO<sub>2</sub> Brayton Cycles (No. SAND-2019-8739). Sandia National Lab.(SNL-NM), Albuquerque, NM (United States).
- [7] Gao, C., Wu, P., Liu, W., Ma, Y., & Shan, J. (2021). Development of a bypass control strategy for supercritical CO<sub>2</sub> Brayton cycle cooled reactor system under load-following operation. *Annals of Nuclear Energy*, 151, 107917.
- [8] Heifetz, A., & Vilim, R. (2015). Turbine bypass, mass inventory, and mixed-mode generator power control of S-CO<sub>2</sub> recompression cycle. *Nuclear Technology*, 189(3), 268-277.
- [9] Alfani, D., Binotti, M., Macchi, E., Silva, P., & Astolfi, M. (2021). sCO<sub>2</sub> power plants for waste heat recovery: design optimization and part-load operation strategies. *Applied Thermal Engineering*, 195, 117013.
- [10] Oh, B. S., & Lee, J. I. (2019, September). Study of autonomous control system for S-CO<sub>2</sub> power cycle. In 3rd European supercritical CO<sub>2</sub> Conference (pp. 19-20).
- [11] Baek, J. Y., Lee, J. J., & Lee, J. I. System Modeling of KAIST S-CO<sub>2</sub> ABC Test Loop.
- [12] Chung, B. D., Kim, K. D., Bae, S. W., Jeong, J. J., Lee, S. W., Hwang, M. K., & Yoon, C. (2010). MARS code manual volume I: code structure, system models, and solution methods (No. KAERI/TR--2812/2004). Korea Atomic Energy Research Institute.
- [13] Park, J. H., Bae, S. W., Park, H. S., Cha, J. E., & Kim, M. H. (2018). Transient analysis and validation with experimental data of supercritical CO<sub>2</sub> integral experiment loop by using MARS. *Energy*, 147, 1030-1043.
- [14] Baek, J. Y., Lee, J. J., Kim, S. J., & Lee, J. I. (2019). Improvements of MARS Code for Analyzing S-CO<sub>2</sub> Cycle Coupled to PWR type SMR. In Transactions of the Korean Nuclear Society Autumn Meeting.
- [15] Hempel, A. (1961). On the dynamics of steam liquid heat exchangers.
- [16] Kwon, J. S., Bae, S. J., Heo, J. Y., & Lee, J. I. (2019). Development of accelerated PCHE off-design performance model for optimizing power system operation strategies in S-CO<sub>2</sub> Brayton cycle. *Applied Thermal Engineering*, 159, 113845.
- [17] Ziegler, J. G., & Nichols, N. B. (1942). Optimum settings for automatic controllers. *trans. ASME*, 64(11).
- [18] Van der Zalm, G. M. (2004). Tuning of PID-type controllers: A literature overview. Technische Universiteit Eindhoven: Eindhoven, The Netherlands.

## FURTHER DEVELOPMENT OF A THROUGH-FLOW PROGRAM BY CONSIDERING REAL GAS EQUATION OF STATE

**Haikun Ren\***

University of Duisburg-Essen  
Duisburg, Germany  
haikun.ren@uni-due.de

**Sebastian Schuster**

University of Duisburg-Essen  
Duisburg, Germany

**Dieter Brillert**

University of Duisburg-Essen  
Duisburg, Germany

### ABSTRACT

Numerical methods are significant in the turbomachine design process and off-design analysis. One of these methods is the through-flow method in the meridional plane, which is utilised in an early design phase. It provides robust and quick numerical analysis of turbomachinery by only giving a few characteristic geometric parameters.

This work further develops the through-flow program *tFlow* by incorporating real gas equation of state (EOS), in order to verify the application of real gas EOS with the through-flow method. This allows the program to support a more reliable calculation regarding, for instance, carbon dioxide (CO<sub>2</sub>) in a high-pressure region, where the gas does not behave like an ideal gas. The program is verified against one-dimensional (1D) solutions for the flow through a converging-diverging nozzle at different flow conditions. Furthermore, the calculation results verify the application of the Jameson-Schmidt-Turkel (JST) scheme in terms of real gas EOS. Consequently, this development brings the possibility to employ *tFlow* in a broader range, for example, for supercritical CO<sub>2</sub> (sCO<sub>2</sub>) compressors or turbines.

### INTRODUCTION

The modern design process of turbomachinery requires numerical analysis in an early design phase, where only few information is specified. To obtain a relatively robust analysis, the through-flow method [1] is widely applied, since it only solves the flow conditions at the meridional plane and, therefore, does not need numerous parameters especially regarding the geometry in contrast to fully three-dimensional (3D) computational fluid dynamics (CFD) methods. This feature also allows a faster computation. In recent years, researchers such as Baralon et al. [2], Sutrmayr and Hirsch [3], and Pacciani [4] focused on the through-flow method based on the Euler equations with finite-volume method due to its benefit from radial mass transport and capability of using the Euler equations in conjunction with a time-marching approach. Under this background, an Euler-based through-flow computer program

named *tFlow* has been developed by Föllner et al. [5] and extended by Jenzen et al. [6] to solve the flow conditions in axial turbomachines and radial compressors. Caused by the increased interest in real gas properties in recent years, especially in the field sCO<sub>2</sub> applications, it seems sensible to extend through-flow methods to gases like CO<sub>2</sub>, which do not behave like an ideal or perfect gas in the considered pressure and temperature range. This development will provide a quick and robust preliminary design phase for e.g. sCO<sub>2</sub> turbomachines.

Thus, aiming this gap, the present work contributes to the through-flow calculation with real gas EOS. Since several assumptions such as some constant parameters are invalid within real gas EOS as mentioned before, special attention has been taken during the calculation of the fluid properties in this work.

In this work, the EOS of Span and Wagner [7] incorporated in Refprop is employed to solve the fluid properties. Furthermore, lookup tables (LUTs) are established to reduce the computation consumption. As a test case, the flow conditions in a converging-diverging verification (CDV) nozzle is calculated and compared with the results of a 1D quasi-analytical analysis as well as results of literature.

### GOVERNING EQUATIONS

The through-flow method applied in the presented program is based on Wu's work [1], where the flow field is only solved at the meridional plane  $S_{2,m}$ , as shown in Figure 1. Therefore, the requirement on geometry and meshing mainly focuses on  $S_{2,m}$ . Then, the program solves the channel flow by considering a 3D axisymmetric system. The program neglects the calculation of wall boundary layer, namely at the shroud and hub, so that the inviscid Euler equations can be employed as the governing equations. This allows both simpler construction of the equation system (without wall functions and turbulence models) and lower cost of the calculation (lower requirement of cell number) in contrast to the viscous Navier-Stokes equations. This selection keeps the benefit of the through-flow method in computing speed while the robustness of the calculation remains. Finally, the applied Euler equations can be written as [5]

\* corresponding author(s)

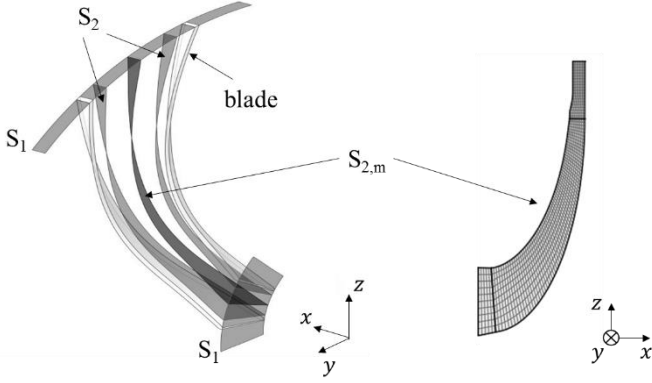


**Figure 1:** Stream surfaces in a blade row [1, 6]

$$\frac{\partial \mathbb{U}}{\partial t} + \frac{\partial \mathbb{F}}{\partial x} + \frac{\partial \mathbb{G}}{\partial y} + \frac{\partial \mathbb{H}}{\partial z} = \mathbb{S}, \quad (1)$$

where

$$\mathbb{U} = \begin{pmatrix} \rho \\ \rho w_x \\ \rho w_y \\ \rho w_z \\ \rho e_t \end{pmatrix}, \quad \mathbb{F} = \begin{pmatrix} \rho w_x \\ \rho w_x^2 + p \\ \rho w_x w_y \\ \rho w_x w_z \\ \rho w_x h_t \end{pmatrix},$$

$$\mathbb{G} = \begin{pmatrix} \rho w_y \\ \rho w_y w_x \\ \rho w_y^2 + p \\ \rho w_y w_z \\ \rho w_y h_t \end{pmatrix}, \quad \mathbb{H} = \begin{pmatrix} \rho w_z \\ \rho w_z w_x \\ \rho w_z w_y \\ \rho w_z^2 + p \\ \rho w_z h_t \end{pmatrix}.$$

The parameters  $t, x, y, z, \rho, w, p, e_t$  and  $h_t$  represent time,  $x$ -,  $y$ -,  $z$ -coordinate, density, relative velocity, pressure, specific total internal energy and specific total enthalpy respectively.  $\mathbb{U}$  denotes the vector of conservative variables, while  $\mathbb{F}$ ,  $\mathbb{G}$  and  $\mathbb{H}$  are the inviscid flux vectors. The Euler equations are combined with an additional source term  $\mathbb{S}$  expressed by

$$\mathbb{S} = \rho \mathbf{f}_{blockage} + \rho \mathbf{f}_b + \rho \mathbf{f}_f + \rho \mathbf{f}_{cor} + \rho \mathbf{f}_c. \quad (2)$$

The first term  $\rho \mathbf{f}_{blockage}$  represents volume forces caused by tangential blockage due to blade number and thickness.  $\rho \mathbf{f}_b$  and  $\rho \mathbf{f}_f$  introduce the blade force and losses respectively. The last two terms denote Coriolis and centrifugal forces in a moving frame such as rotor block and, therefore, can be neglected for computation of a non-moving frame like stator.

The blockage model considers the tangential blockage factor given by Hirsch and Warzee [8], which is introduced to the Euler-equations as an integration factor according to Yao and Hirsch [9]. To enable this model, blockage in conjunction with the coordinates in meridional plane must be specified as input data for the through-flow program. The blade force model introduces the blade force  $\mathbf{f}_b$ , which describes the flow deviation due to blade profile without generating losses. The time-marching approach of Sturmayer [10] is employed here to describe the blade

force, where a target flow angle at the trailing edge must be specified to define the flow deviation.

In eq.(1), seven variables to be solved are identified from five equations:  $\rho, w_x, w_y, w_z, p, e_t$  and  $h_t$ , where

$$e_t = e + \frac{1}{2}(w_x^2 + w_y^2 + w_z^2), \quad (3)$$

$$h_t = h + \frac{1}{2}(w_x^2 + w_y^2 + w_z^2). \quad (4)$$

Since the specific enthalpy  $h$  relates to the specific internal energy  $e$ , the pressure  $p$  and the specific volume  $v = 1/\rho$ , namely  $h \equiv e + p/\rho$ , one of the variables can be solved with this correlation. Therefore, an equation is still required to solve the entire equation system. To fill this gap, the equation of state is applied which can be expressed by

$$p = p(\rho, e). \quad (5)$$

It describes that the pressure is calculated from the density and the internal energy, which are the reference states in the presented program. Since this work focuses on  $\text{CO}_2$  flow, the EOS of Span and Wagner [7] is applied to solve eq.(5). However, the direct incorporation of the EOS of Span and Wagner does not exhibit benefit in computing speed, because

- 1) the EOS is in form of the Helmholtz energy based on density and temperature and requires additional iterations once the reference states differ to them (e.g. density and internal energy used in the presented program) and
- 2) the EOS is a polynomial consists of the ideal-gas part and the residual part of the Helmholtz energy that include 8 and 42 terms respectively [7] and, thus, contains much more calculation process in contrast to an ideal gas EOS.

Therefore, lookup tables (LUTs) are applied to overcome this issue. It is achieved by extracting fluid states from Refprop based on reference states ( $\rho$  and  $e$ ) and sorting out them in different tables. Gradient of states regarding reference states is also calculated to enable the linear Taylor series interpolation of the states, for example

$$p = p_{i,j} + \Delta \rho \left( \frac{\partial p}{\partial \rho} \right)_{e,(i,j)} + \Delta e \left( \frac{\partial p}{\partial e} \right)_{\rho,(i,j)}, \quad (6)$$

where  $i$  and  $j$  are the index of the density and internal energy vector. Since the differences  $\Delta \rho$  and  $\Delta e$  between adjoining elements in the vectors are constant, it is simple to interpolate index  $i$  and  $j$  by following for instance  $i = \text{ceil}((\rho - \rho_{i=1}) / \Delta \rho)$ . This avoids the dependence of computation speed on the size of LUT. Finally, LUTs with a size of 1300 x 1300 are established covering pressure from 1 to 1300 bar and temperature from 0 to 1000 °C. In the current work, the application of LUTs reduces the computation time by a factor of about 20, in contrast to calculation with the EOS of Span and Wagner.



## NUMERICAL SCHEME

Since a real gas EOS is applied in the present work, special care shall be taken when a numerical scheme for the flux discretization is being selected. Numerical schemes using central differencing and applying artificial viscosity like the Jameson-Schmidt-Turkel (JST) scheme [11] are well suited since assumptions regarding the EOS are not a necessary condition during the derivation. Therefore, this work applies the JST scheme. In contrast, other schemes like the flux difference scheme of Roe [12] are derived assuming a perfect gas when eq.(1) is linearized by finding the Jacobian matrix of the flux vectors. These schemes required modification before applied to real gas EOS [13].

## VALIDATION AND DISCUSSION

The extension of the through-flow program with real gas EOS has been validated by comparing the calculation results to those obtained by a 1D quasi-analytical analysis<sup>1</sup> and Tegethoff et al. [13], where calculations of CO<sub>2</sub> flow in the NASA CDV nozzle are conducted. The correlation between the cross-sectional area  $A$  and the axis coordinate  $x$  is written as

$$A(x) = \begin{cases} 1.75 - 0.75 \cos((0.2x - 1) \cdot \pi), & x < 5 \\ 1.25 - 0.25 \cos((0.2x - 1) \cdot \pi), & x \geq 5 \end{cases} \quad (7)$$

Note that the unit of length is given in inch. To reduce the influence of mesh on the results, a mesh independence analysis is implemented. The reference mesh resolution has 20 cells in  $x$ -direction and 2 in  $z$ -direction (20 x 2), whose outlet Mach number  $Ma_{out}$  is regarded as the reference one  $Ma_{out,ref}$ . The definition of refinement factor is introduced to normalise the refinement of the mesh resolution in both directions. Finally, a mesh refinement factor of 10 (resolution of 200 x 20) is applied according to Figure 2, not only considering a balance between computation speed and accuracy but also keeping the resolution at the shock location as same as that in the reference.

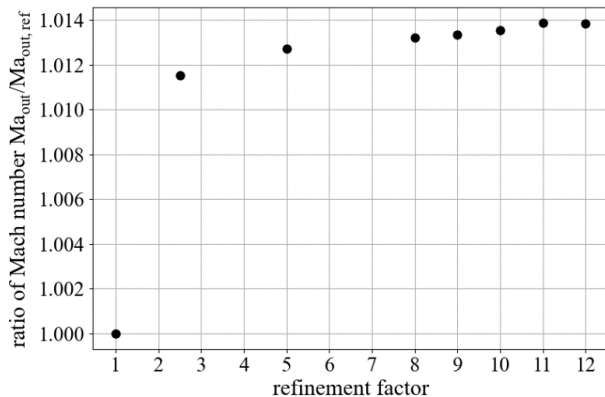


**Figure 2:** Mesh independence analysis based on reference condition ( $p_{out}/p_{t,in} = 0.08$ ) regarding outlet Mach number

<sup>1</sup> The 1D quasi-analytical analysis program calculates the fluid properties at each selected section by considering real gas EOS. Concrete description is given in Appendix A.

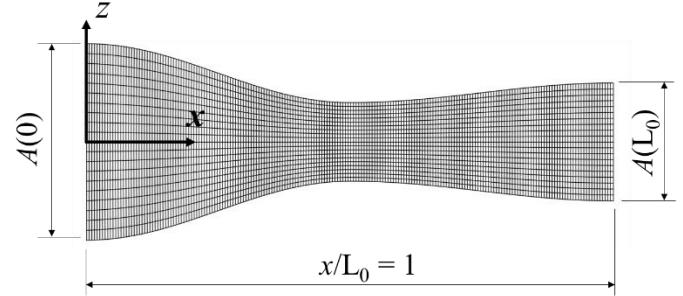


**Figure 3:** Mesh of the NASA CDV nozzle [5]

Considered  $L_0$  as the maximum of  $x$  (where  $x = 10$ ), the mesh is shown in Figure 3. Since the nozzle is considered as a 2D geometry, the value of the area is applied one to one for  $z$ -coordinate. In 2D calculation, the gradient of flow properties is sensitive to the gradient of the cross-sectional area  $A$ . This could cause 2D effects in the diverging part of the nozzle and, therefore, influence the result at the outlet. Indeed, this anxiety is observed from the simulation result.

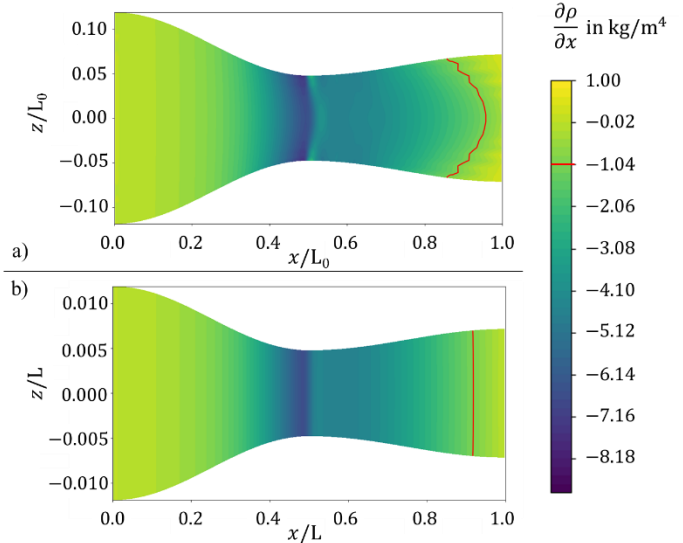


**Figure 4:** a) 2D effect within original NASA CDV nozzle; b) elimination of 2D effect through extended NASA CDV nozzle with factor 10

As shown in Figure 4 a), the density gradient in  $x$ -direction is quasi constant in the converging part, but it becomes higher at the mean line in the diverging part and builds peaks. An example is denoted by the red curve at the gradient of density  $\frac{\partial \rho}{\partial x} = -1.04 \text{ kg/m}^4$ . Such effect can be explained by phenomena “expansion plane” normally observed in converging-diverging nozzle with a sharp gradient at the throat. Finally, this effect causes a higher calculated Mach number at the outlet. Since both the 1D quasi-analytical analysis and Tegethoff’s calculation do not include

such 2D effect, measure needs to be taken to avoid this. Thus, the original geometry of the NASA CDV nozzle is extended considering a factor of 10 in  $x$ -direction, namely  $L = 10L_0$ , as shown in Figure 5. This extension reduces the gradient of the nozzle's cross-sectional area significantly and, therefore, almost eliminates this effect, as shown in Figure 4 b). Based on this measure, the calculation results from  $tFlow$  are comparable with the references.

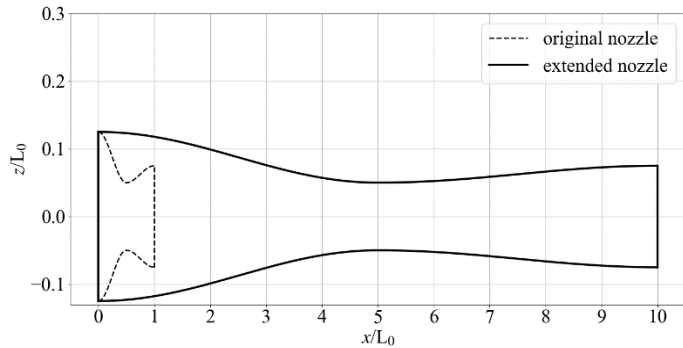


**Figure 5:** Extension of the original NASA CDV nozzle considering a factor of 10

Since Tegethoff et al. have developed a numerical scheme based on Roe scheme called Generalised Ideal Roe (GIRoe) scheme [13], which is available for solving real gas properties, and employed it in her calculation, it is a good chance to compare the calculation results of  $tFlow$  with her work. In her case, the inlet total pressure is set to 1200 bar and the total inlet temperature is 500 K. A ratio of pressures  $p_{out}/p_{t,in} = 0.75$  is considered for the shocked flow case, while another one equal to 0.08 is set for the supersonic flow case. The pressure is relatively high because a large deviation of the compressibility factor between ideal and real gas is intended to exhibit the robustness of the calculation with “strong” real gas effect.

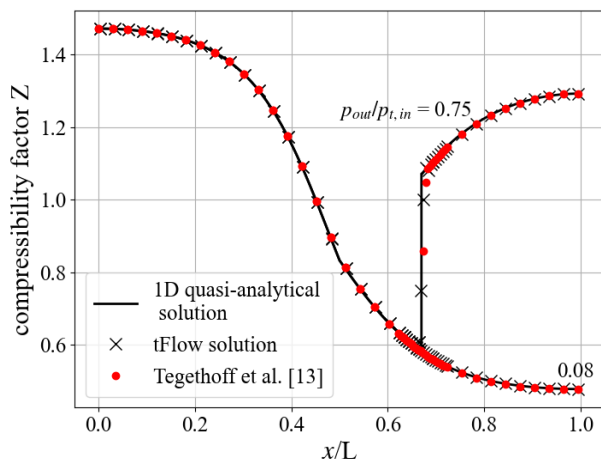


**Figure 6:** Comparison of compressibility factor

Figure 6 shows the comparison of both pressure ratios with respect to the compressibility factor. In the case of supersonic flow, the compressibility factor varies from about 1.5 to 0.5,

where a relatively large difference to ideal gas ( $Z = 1$ ) is involved in this validation as desired, indicating good robustness and accuracy of this through-flow program for calculating flow properties of real gas. The case of shocked flow validates the shock location as well as the fluid states after the shock. Denser grid points are displayed around this location to show more details of the shock. The skip of the compressibility factor from 0.60 to 1.06 further verifies the robustness of the calculation for a dramatic change of the compressibility factor. Figure 7 shows the comparison by means of Mach number, indicating an excellent agreement between  $tFlow$ , the 1D quasi-analytical analysis and Tegethoff's calculation as well.

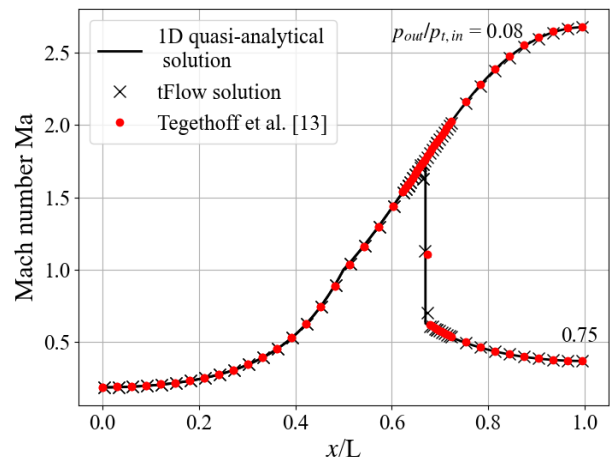


**Figure 7:** Comparison of Mach number

Besides, the good agreement also means that there is no obvious difference between Roe-based and JST scheme. Therefore, this study verifies the application of JST scheme in the through-flow method by considering real gas EOS.

## CONCLUSION

This work develops the through-flow program,  $tFlow$ , further by considering real gas EOS. The JST scheme is firstly applied since other schemes incorporated in the program are not available for real gas EOS. In addition, a set of LUTs is established to speed up the calculation and, hence, keeps the benefit of the through-flow method.

The validation of this development is conducted by comparing the results of  $tFlow$  with those of the 1D quasi-analytical analysis and Tegethoff's calculation with respect to  $sCO_2$  flow in the NASA CDV nozzle, where the fluid states vary within a wide range of compressibility factor involving “strong” real gas effect. Since 2D effect is found by the original nozzle geometry and not included in both 1D quasi-analytical and Tegethoff's calculation, the nozzle is extended by a factor of 10 to eliminate this impact. The comparison shows an excellent agreement between  $tFlow$ , the 1D quasi-analytical analysis and Tegethoff's calculation, validating the application of real gas EOS in the presented through-flow program. Additionally, the wide range (between 0.5 and 1.5) and the dramatic variation (from 0.6 to 1.06) of the compressibility factor exhibit good

robustness of the calculations by means of using the EOS of Span and Wagner. Moreover, this study also verifies the application of JST-scheme for the through-flow method in terms of real gas EOS.

The incorporation of real gas EOS into *tFlow* not only develops the functionality of the program further but also exhibits good potentials for application of real gas EOS in the through-flow method. As the next step, the program is to be further extended for calculation of compressors using real gas as working fluid, e.g. sCO<sub>2</sub> compressors.

## NOMENCLATURE

$A$	area (inch <sup>2</sup> , m <sup>2</sup> )
$c$	absolute flow velocity (m/s)
$f_b$	blade force vector
$f_{blockage}$	volume force vector due to blockage
$f_f$	vector of losses
$f_{cor}$	Coriolis force vector
$f_c$	centrifugal force vector
$\mathbb{F}$	inviscid flux vector in x-direction
$\mathbb{G}$	inviscid flux vector in y-direction
$\mathbb{H}$	inviscid flux vector in z-direction
$h$	specific static enthalpy (J/kg)
$L$	length of nozzle (inch, m)
$\dot{m}$	mass flow rate (kg/s)
$Ma$	Mach number (-)
$n_s$	isentropic volume exponent for real gas
$p$	static pressure (bar)
$R$	specific gas constant (J·kg <sup>-1</sup> ·K <sup>-1</sup> )
$s$	specific entropy (J/kg)
$\$$	additional source term
$T$	temperature (K, °C)
$\mathbb{U}$	vector of conservative variables
$v$	specific volume (m <sup>3</sup> /kg)
$w$	relative flow velocity
$x$	coordinate in x-direction (inch, m)
$y$	coordinate in y-direction (inch, m)
$z$	coordinate in z-direction (inch, m)
$Z$	compressibility factor (-)
$\Delta$	difference (-)
$\kappa$	isentropic exponent (-)
$\rho$	density (kg/m <sup>3</sup> )
$\pi$	the ratio of a circle's circumference to its diameter (-)

## subscript

crit	parameter at critical state
e	parameter at constant internal energy
i	index of density vector
in	inlet
j	index of internal energy vector
out	outlet
p	parameter at constant pressure
ref	reference parameter
t	total parameter / stagnation state
th	parameter at throat of nozzle

$T$	parameter at constant temperature
$x$	parameter in x-direction
$y$	parameter in y-direction
$z$	parameter in z-direction
$\rho$	parameter at constant density

## Abbreviations

CDV	Converging-Diverging-Verification
CFD	Computational Fluid Dynamics
CO <sub>2</sub>	Carbon dioxide
EOS	Equations of State
GIRoe	Generalised Ideal Roe
JST	Jameson-Schmidt-Turkel
LUT	Lookup Table
NASA	National Aeronautics and Space Administration
sCO <sub>2</sub>	Carbon dioxide in supercritical state
1D	one-dimensional
2D	two-dimensional
3D	three-dimensional

## ACKNOWLEDGEMENTS

The authors declare that they have no known competing financial interests or personal relationships that could have appeared to influence the work reported in this paper.

## REFERENCES

- [1] Wu, C.-H. (1952). A General Theory of Three-Dimensional Flow in Subsonic and Supersonic Turbomachines of Axial-, Radial-, and Mixed-Flow Types. NACA Technical Note 2604. Lewis Research Center, Cleveland, Ohio.
- [2] Baralon, S.; Eriksson, L.-E.; Häll, U. (1998). Validation of a Throughflow Time-Marching Finite-Volume Solver for Transonic Compressors. The International Gas Turbine and Aeroengine Congress & Exposition. Sweden, Stockholm.
- [3] Sturmayer, A. and Hirsch, Ch. (1999). Throughflow model for design and analysis integrated in a three-dimensional Navier-Stokes solver. Proceedings of the Institution of Mechanical Engineers, Vol. 213, Part A, pp. 263-273.
- [4] Pacciani, R.; Marconcini, M.; Arnone, A. (2017). A CFD-Based Throughflow Method with Three-Dimensional Flow Features Modelling. International Journal of Turbomachinery, Propulsion and Power 2, no. 3: 11.
- [5] Föllner, S.; Amedick, V.; Bonhoff, B.; Brillert, D.; Benra, F.-K. (2020). Model Validation of an Euler-based 2D-Throughflow Approach for Multistage Axial Turbine Analysis. Proceedings of the ASME 2020 Turbomachinery Technical Conference and Exposition. U. K., London.
- [6] Jenzen, R.; Woiczinski, C.; Schuster, S.; Brillert, D. (2022). An Euler-based Throughflow Approach for Centrifugal Compressors – Part A: Extension and Modifications of Models. Proceedings of the ASME Turbo Expo 2022 Turbomachinery Technical Conference and Exposition, GT2022-82170. The Netherlands, Rotterdam.
- [7] Span, R. and Wagner, W. (1994). A New Equation of State for Carbon Dioxide Covering the Fluid Region from the Triple-

- Point Temperature to 1100 K at pressures up to 800 MPa. *Journal of Physical and Chemical Reference Data* 25, 1509 (1996).
- [8] Hirsch, C. and Warzee, G. (1976). A finite element method for the axisymmetric flow computation in a turbomachine. *International Journal for Numerical Methods in Engineering*, Vol. 10, pp. 93-113.
- [9] Yao, Z. and Hirsch, Ch. (1995). Throughflow model using 3D Euler or Navier-Stokes solver. Verein Deutscher Ingenieure (VDI) – Gesellschaft Energietechnik, VDI-Berichte 1185, pp. 51-61. Germany, Düsseldorf.
- [10] Sturmayer, A. (2004). Evolution of a 3-D Structured Navier-Stokes Solver towards Advanced Turbomachinery Applications. Dissertation, Vrije Universiteit Brussel, Belgium.
- [11] Jameson, A. (2017). The Origins and Further Development of the Jameson-Schmidt-Turkel (JST) Scheme. *Journal of American Institute of Aeronautics and Astronautics (AIAA)*, Vol. 55(5), pp. 1-41.
- [12] Roe, P. L. (1981). Approximate Riemann Solvers, Parameter Vectors, and Difference Schemes. *Journal of Computational Physics*, Vol. 43, pp. 357-372.
- [13] Tegethoff, K.; Schuster, S.; Brillert, D. (2022). Numerical simulation of real gas one-component two-phase flow using a Roe-based scheme. *Computers and Fluids*, Vol. 245 / 105560, pp. 1-9.
- [14] Jr. Oertel, H.; Böhle, M.; Reviol, T. (2013). *Strömungsmechanik für Ingenieure und Naturwissenschaftler*. 7<sup>th</sup> Edition, published by Springer Vieweg.
- [15] Lüdtke, K. H. (2004). *Process Centrifugal Compressors: Basics, Function, Operation, Design, Application*. Published by Springer.
- [16] Pham, H.-S.; Alpy, N.; Ferrasse, J.-H.; Boutin, O.; Tothill, M.; Quenaut, J.; Gastaldi, O.; Cadiou, T.; Saez, M. (2016). An approach for establishing the performance maps of the sc-CO<sub>2</sub> compressor: Development and qualification by means of CFD simulations. *International Journal of Heat and Fluid Flow*, Elsevier, 2016, 61 (Part B), pp. 379 – 394.
- [17] Jr. Anderson, J. D. (2003). *Modern Compressible Flow: With Historical Perspective*. 3<sup>rd</sup> Edition, published by McGraw-Hill.

## ANNEX A

### CALCULATION METHOD OF THE 1D QUASI-ANALYTICAL ANALYSIS

#### GOVERNING EQUATIONS

In this work, a one-dimensional program is developed to predict nozzle flows by using real gas EOS. Although classic correlations exist, such as the correlation between static and total pressure or the correlation between cross-sectional area  $A$  and Mach number  $Ma$  described in [14], assumptions made for ideal gas must be taken into account. If the compressibility factor  $Z$  differs a lot to 1, like 0.3 by  $CO_2$  near the critical point, these assumptions are not valid anymore, and, therefore, the derivation of such correlations for real gas should differ to those mentioned above. Actually, there are some easy ways to incorporate real gas EOS into the existing correlations. One of them is to consider the isentropic volume exponent  $n_s$  for real gas instead of  $\kappa$ . This parameter is mentioned by Lüttke [15] and applied by Pham et al. [16] for predicting performance maps of sCO<sub>2</sub> compressors. This provides an efficient method to develop performance prediction of sCO<sub>2</sub> turbomachines, but it does not show the plausibility of the use of this parameter in the mentioned correlations. Thus, efforts are made to derive the governing equations for real gas nozzle flow.

The 1D quasi-analytical analysis is based on the mean-line method, where the Span and Wagner EOS [7] is employed to solve the fluid states of  $CO_2$ . Because iterations exist during solving the fluid states, it is regarded as a quasi-analytical method. For this analysis, two assumptions are made: 1) the Mach number in front of the throat is less than one (subsonic inlet condition); 2) the nozzle wall is frictionless and adiabatic (isentropic process if there is no shock, and no heat addition). For flow through a nozzle without shock, following equations are valid:

$$\dot{m}(x) = A(x)c(x)\rho(x) = \dot{m}, \quad (8)$$

$$h_t = h_{t,in} = f(p_{t,in}, T_{t,in}), \quad (9)$$

$$s = s_{in} = f(p_{t,in}, T_{t,in}), \quad (10)$$

where  $f$  represents the EOS correlation. Equation (8) considers the mass conservation, eq.(9) considers the energy conservation, and eq.(10) considers the reversible process of a throughflow. However, since both velocity  $c$  and density  $\rho$  are normally unknown, one of them needs to be guess in the first step and updated iteratively. The iterative solution is achieved by considering eq. (8) and equations as follows:

$$h_t = h + \frac{1}{2}c^2, \quad (11)$$

$$h = f(\rho, s) \text{ or } \rho = f(h, s). \quad (12)$$

Once the density  $\rho$  is solved, other thermodynamic parameters can be obtained through the EOS.

Furthermore, equations for solving shock waves are considered. Denoting the fluid properties directly in front of the shock with subscript "1" and directly after the shock with subscript "2", the shock can be described by

$$\rho_1 c_1 = \rho_2 c_2, \quad (13)$$

$$p_1 + \rho_1 c_1^2 = p_2 + \rho_2 c_2^2, \quad (14)$$

$$h_1 + \frac{1}{2}c_1^2 = h_2 + \frac{1}{2}c_2^2. \quad (15)$$

where the conservation of mass, momentum and energy for a normal shock [14] is taken into account. Guessing a parameter after the shock in the first step, e.g.  $c_2$ , the parameters after the shock can be solved with the Newton's method, if the parameters in front of the shock are known. Note that the flow condition before the shock must be supersonic.

#### CALCULATION PROCESS

Normally, the given parameters are the total pressure and temperature at the nozzle inlet, and the static pressure at the nozzle outlet. The 1D quasi-analytical analysis will firstly distinguish the flow condition by calculating the transition points between subsonic, shocked and supersonic flow. If the case is subsonic, the mass flow rate is calculated based on the given pressure at the outlet. Otherwise, the flow is regarded as choked, and the mass flow rate is then calculated by considering  $Ma = 1$  at the throat. The transition point between shocked and supersonic flow is calculated by considering a shock wave directly at the outlet of the nozzle [17]. The determination of the flow condition is necessary, because normally there are two solutions (subsonic and supersonic) for a certain cross-sectional area.

After determining the flow condition, the Mach number distribution can be preliminarily distinguished. For subsonic case, the Mach number is less than one in both converging and diverging part. For supersonic case, the Mach number is less than one in the converging part and greater than one in the diverging part. Subsequently, the Mach number and other fluid properties like pressure, temperature etc. can be calculated based on eq.(8) - (12). Shocked flow is regarded as a special case here since it causes loss (increased entropy) and its location needs to be fixed. However, in this case, properties in the converging part are calculated as same as in the case of supersonic flow, because both the cases have reached the choking condition. In the diverging part, the Mach number is firstly greater than one in front of the shock and thereafter less than one. The shock location is solved with the Newton's method as well, by guessing an  $x$ -coordinate at first and solving the pressure at the nozzle outlet iteratively. In each iteration, the properties after the shock are calculated by eq.(13) - (15), considering a supersonic condition before the

shock at the specified location. The calculation process ends, once the calculated outlet pressure fits to the given one.



## INFLUENCE OF THE EQUATION OF STATE ON THE DESIGN OF sCO<sub>2</sub>-POWER CYCLES

**Sebastian Rath\***

TU Dresden

Dresden, Germany

Email: sebastian.rath@tu-dresden.de

**Uwe Gampe**

TU Dresden

Dresden, Germany

**Andreas Jäger**

TU Dresden

Dresden, Germany

### ABSTRACT

The favorable location of the critical point close to common ambient temperatures makes carbon dioxide (CO<sub>2</sub>) highly attractive to be used as working fluid for supercritical power cycles. The combination of the thereby wide usable range of temperatures with the special fluid properties close to the critical point, e.g. high densities and low viscosities, holds a distinctive potential for significant efficiency increases as well as smaller component sizes compared to the actual state of the art. However, due to the highly non-ideal behavior of the fluid properties in the regions of interest, especially at near-critical conditions, reliable equations of state (EoS) are needed to correctly predict the fluid behavior. This concerns all steps in design and development of supercritical power cycles, from the preliminary modeling of the cycle up to tasks of detailed engineering of individual components. If, in addition, mixtures or impurities are considered instead of a pure substance, the deviation of the EoS of each component is also included in the mixture calculation, which underlines the importance of accurate EoS. Therefore, a certain sensitivity is required to what extent the selection of the EoS may influence the expected results.

In this work, the influence of different equations of state on the thermodynamic design of CO<sub>2</sub> power cycles is investigated. Within this context, five different equations of state were compared to each other by calculating a selection of power cycle configurations, which are typically considered for sCO<sub>2</sub> applications. Aside characteristic process parameters such as relevant fluid properties at each state point of the cycle and the thermal efficiency, differences in the sizes for the internal heat exchangers are considered.

The results show, with some exceptions, a largely good agreement in the cycle efficiencies for most of the considered

EoS. However, it can also be seen, that the thermophysical properties can differ significantly between the EoS, which is also reflected in notable variations in the heat exchanger performance parameters and furthermore may lead to non-negligible deviations in subsequent evaluations.

### INTRODUCTION

The critical point of CO<sub>2</sub> at a pressure of  $p_c = 73.773$  bar and a temperature of  $\vartheta_c = 30.9782$  °C, which is quite close to ambient conditions, facilitates the use of carbon dioxide (CO<sub>2</sub>) as working fluid for supercritical power cycles for a variety of applications. Compared to the actual state-of-the-art, i.e., steam Rankine cycles and gas turbine Brayton cycles, sCO<sub>2</sub> holds a distinctive potential for significant efficiency increases as well as smaller component sizes. Current investigations range from the preliminary modeling of the cycle including thermoeconomic studies [1,2], detailed engineering of individual components [3], up to the selective admixing of dopants in order to influence selected target values [4–6].

However, due to the highly non-ideal behavior of the fluid properties in the regions of interest, especially at near-critical conditions, reliable equations of state (EoS) are needed to correctly predict the fluid behavior. The resulting effects on the design parameters of power cycles have so far received only limited attention.

Zhao et al. [7] has compared selected EoS for a rather simple recuperated cycle investigating six different equations of state. They concluded that concerning cycle efficiency, the influence of different equations of state is not as significant as for other properties, which are important for designing components, as for example the  $UA$ -coefficient of heat exchangers. These findings are in line with investigations of Rath et al. [5,6] who used

\* corresponding author(s)

different mixture models for modeling a simple cycle as well as a recuperated cycle with sCO<sub>2</sub> as working fluid and the findings of Mickoleit et al. [8] for a split air conditioner with internal heat exchanger. In the aforementioned works, different mixture models and their results have been compared and it was found that the influence of the equations of state on the thermal efficiency as well as on the COP was rather limited whereas other properties, such as the  $UA$ -coefficient, differ more significantly when using different equations of state. However, regarding the usage of sCO<sub>2</sub>, mostly the influence of equations of state on rather simple cycle architectures with only limited technical relevance has been investigated in the literature.

Therefore, the purpose of this work is to extend these considerations to more complex cycle configurations, which are commonly discussed for sCO<sub>2</sub> power cycles. Herein, emphasis is placed on the actual impact of different frequently used equations of state on the overall design values of various cycle configurations. Related to the frequent use of even simpler equations of state, it is intended to raise awareness of the importance of a proper selection on exemplary base of the selected commonly discussed cycle architectures. The studied equations of state comprise the Soave-Redlich-Kwong equation of state (SRK), the Peng-Robinson equation of state (PR), the Lee-Kesler-Plöcker equation of state (LKP), the PCP-SAFT equation of state, as well as the actual reference equation of state for CO<sub>2</sub> by Span and Wagner [9].

## EQUATIONS OF STATE

In order to compare the influence of the equations of state (EoS) on various performance parameters of thermodynamic cycles, such as thermal efficiency, and the  $UA$  value as a performance parameter for the heat exchangers, different equations of state have been used in this work. The software TREND 5.0 [10] has been used for the calculation of thermophysical properties. The studied equations of state, which are available in the software TREND, are the Soave-Redlich-Kwong equation of state (SRK) [11,12], the Peng-Robinson equation of state (PR) [13], the Lee-Kesler-Plöcker equation of state (LKP) [14,15], the PCP-SAFT equation of state [16–20], and multiparameter equations of state, i.e., the reference equation for CO<sub>2</sub> by Span and Wagner [9] formulated in the dimensionless Helmholtz energy  $\alpha$ . The used models will be briefly introduced in the following.

Multiparameter equations of state formulated in the dimensionless Helmholtz energy  $\alpha$  can be considered the state-of-the-art in accurate property modeling. These equations of state are empirical in nature and are typically capable of representing all experimental data within the experimental uncertainty of the measurements. The dimensionless Helmholtz energy  $\alpha$  is commonly split into an ideal part  $\alpha^0$ , representing the dimensionless Helmholtz of the ideal gas and a residual part  $\alpha^r$ , accounting for the real behavior of the substance. It is

$$\frac{a}{RT} = \alpha(\tau, \delta) = \alpha^0(\tau, \delta) + \alpha^r(\tau, \delta). \quad (1)$$

In Eq. (1),  $\tau$  denotes the reciprocal reduced temperature

$$\tau = T_c/T \quad (2)$$

and  $\delta$  the reduced density

$$\delta = \rho/\rho_c. \quad (3)$$

with  $T_c$  and  $\rho_c$  being the critical temperature and critical density of the substance, respectively.  $T$  denotes the temperature and  $\rho$  the molar density in Eqs. (2) and (3). The ideal part  $\alpha^0$  can be obtained from experimental (or simulated) data for the isobaric heat capacity of the ideal gas and the ideal gas law. The residual part consists of empirical terms, commonly referred to as polynomial-like terms, exponential terms, Gaussian-bell shaped terms, and non-analytical terms. The reference equation of state by Span and Wagner [9] consists of 42 of these terms.

The cubic equations of state, i.e., the SRK and PR, are implemented in TREND as described by Bell and Jäger [21]. When translating the SRK to the residual dimensionless Helmholtz energy, it reads

$$\alpha^r = -\ln(1 - b\delta\rho_c) - \frac{\tau a \ln(b\rho_c\delta + 1)}{RT_c b}. \quad (4)$$

The PR translated to the residual dimensionless Helmholtz energy becomes

$$\alpha^r = -\ln(1 - b\delta\rho_c) - \frac{\tau a \ln\left(\frac{(1 + \sqrt{2})b\rho_c\delta + 1}{(1 - \sqrt{2})b\rho_c\delta + 1}\right)}{RT_c 2\sqrt{2}b}. \quad (5)$$

In Eqs. (4) and (5),  $a$  is the attraction parameter and  $b$  the co-volume of the SRK and PR, respectively. Details for the calculation of  $a$  and  $b$  can be found in, e.g., [21].

The basic idea of the LKP is to interpolate the compression factor  $z$  of the fluid of interest using the compression factor of a simple fluid (methane, argon, krypton)  $z^0$  with an acentric factor of  $\omega^0 = 0$  and the compression factor of a reference fluid ( $n$ -octane)  $z^r$  with an acentric factor of  $\omega^r = 0.3978$ . The LKP reads

$$z = z^0 + \frac{\omega}{\omega^r}(z^r - z^0). \quad (6)$$

The implementation of the LKP in TREND is described in the work of Herrig [22]. The application of the SRK, PR, and LKP for CO<sub>2</sub> only requires the critical properties as well as the acentric factor. The values used in this work are listed in Table 1.

Table 1: Critical properties and acentric factor of CO<sub>2</sub> used for the SRK, PR, and LKP in this work

$\omega$	$T_c/\text{K}$	$p_c/\text{MPa}$
0.224	304.1282	7.3773

Finally, the PCP-SAFT equation of state for CO<sub>2</sub> reads

$$\alpha^r = \alpha^{hc} + \alpha^{\text{disp}} + \alpha^{\text{QQ}}, \quad (7)$$

where the hard-chain term and the dispersion term are given in Ref. [18] and the quadrupole-quadrupole interaction term is given by Ref. [19]. The parameters for the PCP-SAFT equation of state used for CO<sub>2</sub> in this work are given in Table 2

Table 2: Parameters for the PCP-SAFT equation used for CO<sub>2</sub> in this work

$m$	$\sigma/\text{\AA}$	$(\varepsilon/k_B)/\text{K}$	$Q/\text{D}\text{\AA}$
1.5131	3.1869	163.33	4.4

All of the equations of state used in this work are implemented in TREND according to the form given in Eq. (1). The residual parts of the Helmholtz energy for the SRK, PR, LKP, and PCP-SAFT are given in Eqs. (4)-(7). The ideal part of the dimensionless Helmholtz energy  $\alpha^0$  can be obtained by integrating over the ideal gas isobaric heat capacity  $c_p^0$ . For the multiparameter equation of state, the correlation for  $\alpha^0$  given by Span and Wagner [9] has been used. For all other equations of state,  $c_p^0$  have been calculated with a correlation given in the VDI-Wärmeatlas [23], which reads

$$\frac{c_p^0}{R} = B + (C - B) \left( \frac{T}{A + T} \right)^2 \cdot \left[ 1 - \frac{A}{A + T} \left( D + E \frac{T}{A + T} + F \left( \frac{T}{A + T} \right)^2 + G \left( \frac{T}{A + T} \right)^3 \right) \right]. \quad (8)$$

The parameters for Eq. (8) are given in Table 3

Table 3: Parameters for the ideal gas isobaric heat capacity of CO<sub>2</sub> according to Eq. (8)

A	B	C	D	E	F	G
514.5073	3.4923	-0.9306	-6.0861	54.1586	-97.5157	70.9687

Thermophysical properties of CO<sub>2</sub> can be calculated from Eq.(1) by combining the dimensionless Helmholtz energy and its derivatives with respect to the independent variables  $\tau$  and  $\rho$ . For example, it is [24]

$$p = \rho RT \left( 1 + \delta \left( \frac{\partial \alpha^r}{\partial \delta} \right)_\tau \right), \quad (9)$$

$$h = RT \left[ 1 + \tau \left( \frac{\partial \alpha^0}{\partial \tau} \right)_\delta + \tau \left( \frac{\partial \alpha^r}{\partial \tau} \right)_\delta + \delta \left( \frac{\partial \alpha^r}{\partial \delta} \right)_\tau \right], \quad (10)$$

and

$$s = R \left[ \tau \left( \frac{\partial \alpha^0}{\partial \tau} \right)_\delta + \tau \left( \frac{\partial \alpha^r}{\partial \tau} \right)_\delta - \alpha^0 - \alpha^r \right]. \quad (11)$$

Note that in Eqs. (9), (10), and (11) the intensive variables  $\rho$ ,  $h$ ,  $s$  are molar if the universal gas constant  $R$  is used and these variables are specific, if the specific gas constant is used.

## CYCLE MODELING

To evaluate the influence of the EoS, four supercritical cycle architectures of varying complexity were selected, which have also been considered frequently in recent literature for various applications of sCO<sub>2</sub> power cycles.

The simple recuperated cycle (SRC) represents the most basic configuration of recuperated supercritical Brayton cycles. Compared to the non-recuperated cycle, it promises high efficiencies with a manageable number of components, so that it is often chosen as a basis for investigations in related topics as well as for comparison with cycles of higher complexity (e.g., [25]). As shown in Figure 1, the SRC includes the essential main components to represent a recuperated Brayton cycle. Starting at the compressor inlet in point 1, the fluid is compressed to the upper pressure level. Subsequently, heat is added in the recuperator (2 to 3) and the heater (3 to 4) until the turbine inlet temperature is reached in point 4. After expansion to the lower pressure level in point 5, excess heat is rejected by passing the recuperator (5 to 6) and the cooler (6 to 1) going back to starting conditions. However, one drawback of this simple layout is a certain limitation of the amount of recuperable heat caused by the strong variation of the near critical heat capacities and the resulting mismatch in the temperature changes of the hot and the cold side. To counteract this effect, the recompression cycle (RCC) divides the heat recovery into two separate recuperators, a high temperature unit (HTR) and a low temperature unit (LTR) including a split in the mass flow in between at the cold side (point 8). While the main flow passes the cooler (8 to 1), the main compressor (1 to 2) and the LTR (2 to 3), the second stream bypasses the cooler and gets compressed in a re-compressor (8 to 3) without prior heat rejection, rejoining the main flow at the outlet of the LTR in point 3. In this way, the heat capacity flows in the LTR can be adjusted to prevent the aforementioned mismatch in temperatures. Subsequently, the rejoined mass flow passes the HTR (3 to 4) and the heater until it reaches the turbine inlet temperature (TIT) in point 5 and finally gets expanded in the turbine to the lower pressure level at the inlet of the HTR in point 6. Since with appropriately selected bypass mass flows the re-compressor work input is less than the heat removed in the cooler, higher thermal efficiencies can be achieved compared to the SRC architecture [26].

To further improve the thermal efficiency, the RCC can be expanded to more complex layouts, such as the intercooled cycle (ICC) or the partial cooling cycle (PCC), which are also taken into account in this work. As shown on the bottom left in Figure 1, in the intercooled cycle (ICC) the compression of the main fluid flow is split up to two stages, namely the pre-compressor (9 to 10) and the main compressor (1 to 2). Within this configuration, the fluid rejects heat in an intercooler at intermediate pressure (10 to 1), before entering the main-

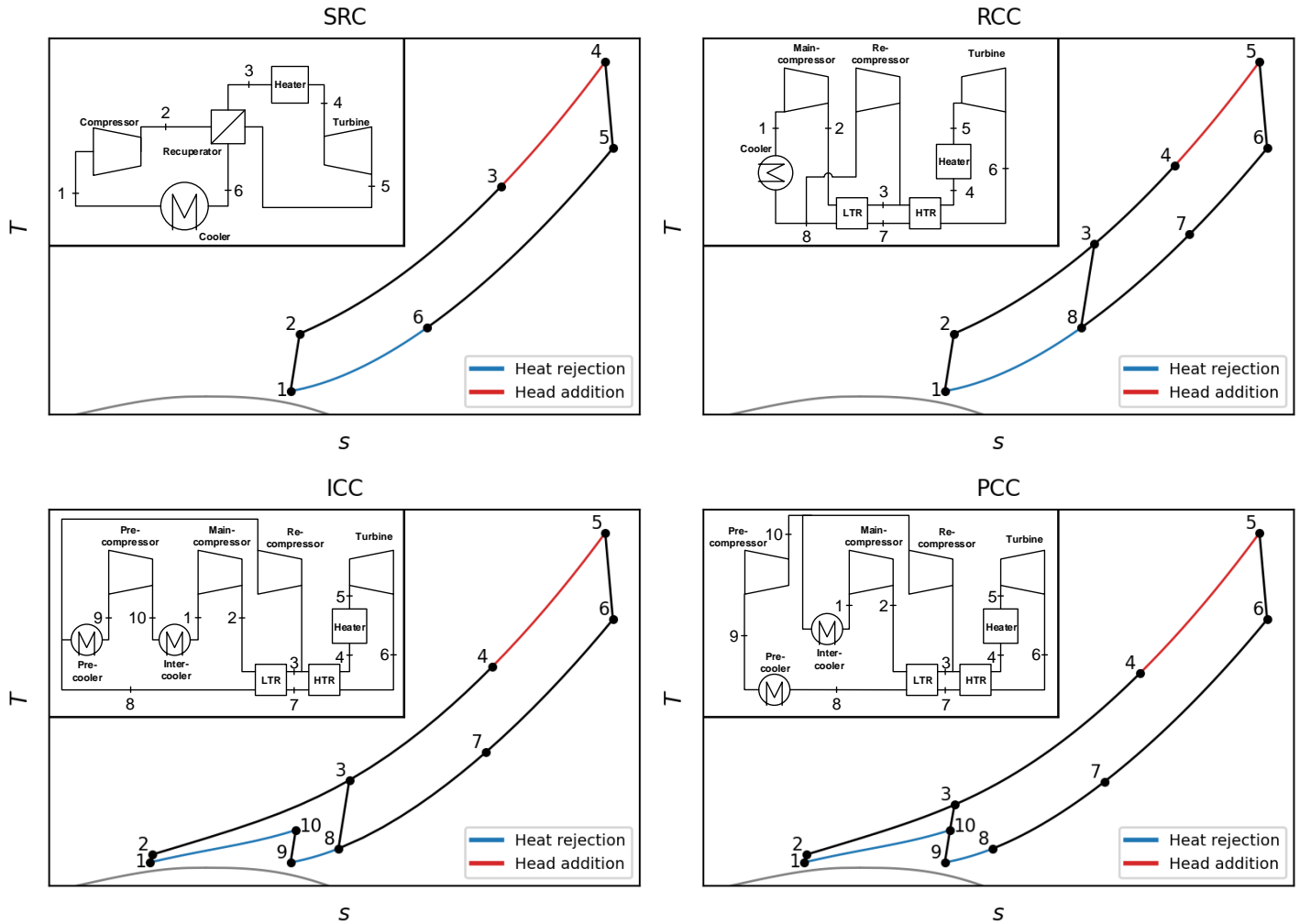


Figure 1:  $T$ - $s$  diagrams and block-layouts of the considered cycle architectures

compressor. This leads to a reduced total compressor work and thus to higher efficiencies [27].

Related to this, the concept of a staged compression is also taken up in the precooled cycle (PCC), shown at the bottom right of Figure 1. Starting at the low pressure side exit of the LTR in point 8, the whole mass flow passes a pre-cooler (8 to 9) and pre-compressor (9 to 10). Subsequently, the split-up takes place at intermediate pressure. Whereas the bypass flow directly gets compressed by the re-compressor (10 to 3), heat is rejected again from the main flow in an inter-cooler (10 to 1) before entering the main compressor (1 to 2).

Using the equations of state described before, calculations were done for all four layouts based on a set of preset values for the inlet of the main compressor, the turbine inlet as well as the mass-flow bypass ratio and the intermediate pressure level for the higher order cycles.

To take account for the strong variation of the flow properties, a step-wise approach was chosen for all recuperators by splitting

up the device into multiple segments of constant enthalpy change (cf. Figure 2). Then, the evaluation was done iteratively by setting a minimum pinch point difference ( $\Delta T_R$ ). Starting from an assumed initial value, e.g.  $T_6 = T_2 + \Delta T_R$  in the SRC, the guess is iteratively adjusted until the pinch-point criterion is met in all sections.

Herein, the  $UA$  value is determined for each recuperator as the product of the heat transfer coefficient  $U$  and the heat exchanger area  $A$ . The  $UA$  value is a common metric for initial classification of heat exchanger size and performance, widely used in common literature, also for  $sCO_2$  applications, e.g. [28–30].

Based on the heat flux given by the enthalpy differences of the fluid on each side it can be calculated by:

$$UA = \frac{\dot{Q}}{LMTD} \quad (12)$$

As no explicit values for the mass flows are set within the thermodynamic analysis of the cycles, and since the absolute values are not relevant for a relative comparison of the EoS within one cycle architecture, a relative formulation for the mass flow is used. Assuming a constant heat input for each cycle, the EoS-specific, relative mass-flow can be calculated by relating the value of the enthalpy difference in the heater for each EoS to the value gained by using the reference equation. This results in:

$$m^* = \frac{h_4 - h_3}{h_{4,\text{ref}} - h_{3,\text{ref}}} \quad (13)$$

for the simple recuperated cycle, and

$$m^* = \frac{h_5 - h_4}{h_{5,\text{ref}} - h_{4,\text{ref}}} \quad (14)$$

for all other cycle configurations. Consequently, in combination with Eqs (12) this results in:

$$UA = \frac{\dot{Q}}{LMTD} = \frac{\Delta h_R \cdot m^*}{LMTD} \quad (15)$$

In Eqs. (12) and (13), LMTD is the mean log temperature difference given by:

$$LMTD = \frac{\Delta T_{\text{hot}} - \Delta T_{\text{cold}}}{\ln(\Delta T_{\text{hot}}) - \ln(\Delta T_{\text{cold}})} \quad (16)$$

With  $\Delta T_{\text{hot}}$  and  $\Delta T_{\text{cold}}$  referring to the temperature differences at the hot and cold side of the recuperator, respectively. With regard to the previously mentioned segment-based approach, the  $UA$  value for the entire device, as shown in Figure 2, arises as the sum of the  $UA$  values of the individual segments:

$$UA_{\text{tot}} = \sum_{i=1}^n UA_i = \sum_{i=1}^n \frac{\Delta h_i \cdot m^*}{LMTD_i} \quad (17)$$

Alternatively, the same result can be obtained by using the averaged logarithmic temperature difference of all segments:

$$UA_{\text{tot}} = \frac{\Delta h_R \cdot m^*}{\overline{LMTD}} \quad (18)$$

With  $\overline{LMTD}$  calculated as the harmonic mean of the individual values of all segments:

$$\overline{LMTD} = \frac{n}{\sum_{i=1}^n LMTD_i^{-1}} \quad (19)$$

In equations (17) and (19)  $n$  refers to the total number of sections. As shown in Figure 2 on an exemplary division into 12 sections and in contrast to the conventional calculation of the heat exchanger as a single section, this allows a better consideration of the changes in the fluid properties and the resulting non-

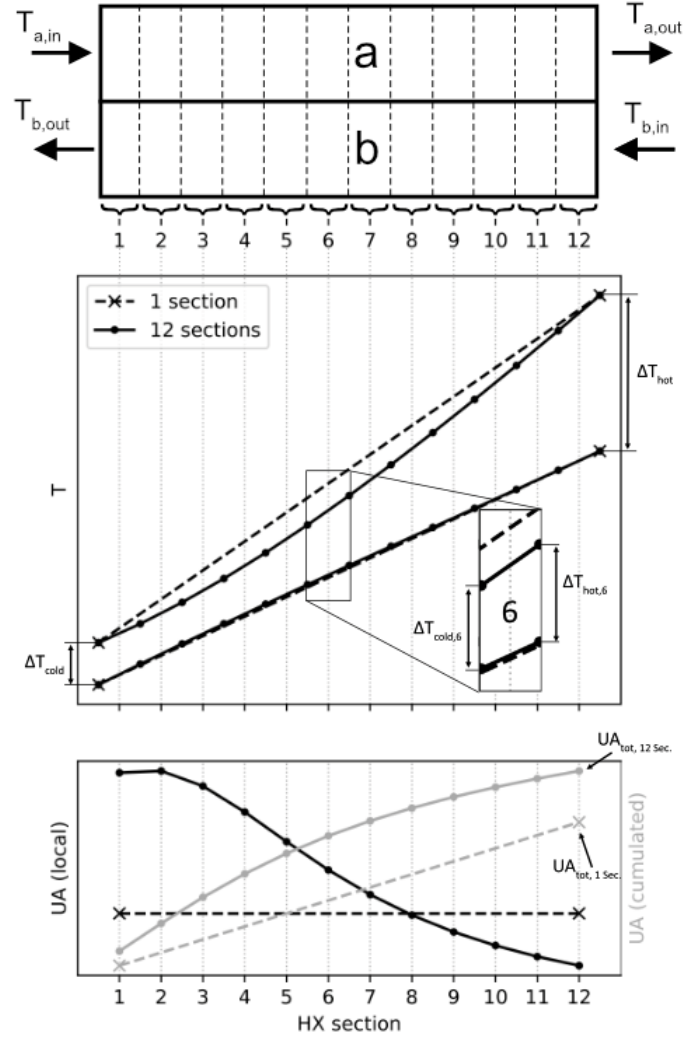


Figure 2: Illustration of the segment-wise evaluation of the  $UA$  value for better consideration of non-ideal (non-linear) fluid properties, including, going through from top to bottom, the schematic segmentation of the heat exchanger, the resulting differences in the temperature lines, and the resulting differences in the local and cumulated values for  $UA$ . In both plots, for  $T$  as well as for  $UA$ , the dashed line refers to the non-segmented (1 segment) approach and the solid line referring to the split up of the device into 12 sections.

linearity of the temperature lines, which finally leads to a more accurate value for  $UA$ . In the calculations performed here, the recuperators were divided into 24 segments each.

As a second parameter to compare the EoS, the thermal efficiency was used which generally can be calculated by relating the heat rejected from the cycle to the cycles heat input:

$$\eta_{\text{th}} = 1 - \frac{|\dot{Q}_{\text{out}}|}{\dot{Q}_{\text{in}}} \quad (20)$$

Related to the cycle architectures described above, this leads to

$$\eta_{\text{th,SRC}} = 1 - \frac{h_6 - h_1}{h_4 - h_3} \quad (21)$$

for the simple recuperated cycle, to

$$\eta_{\text{th,RCC}} = 1 - \frac{(h_8 - h_1) \cdot (1 - m_{\text{BR}})}{h_5 - h_4} \quad (22)$$

for the recompression cycle, to

$$\eta_{\text{th,ICC}} = 1 - \frac{(h_8 - h_9 + h_{10} - h_1) \cdot (1 - m_{\text{BR}})}{h_5 - h_4} \quad (23)$$

for the intercooling cycle, and to

$$\eta_{\text{th,PCC}} = 1 - \frac{(h_{10} - h_1) \cdot (1 - m_{\text{BR}}) + (h_8 - h_9)}{h_5 - h_4} \quad (24)$$

for the partial cooling cycle. Herein, in Equations (22) to (24),  $m_{\text{BR}}$  is the fractional amount of bypassed mass-flow.

The boundary conditions applied to the thermodynamic cycles are listed in Table 4. Temperatures were oriented to an exemplary waste heat recovery application, i.e., acting as a bottoming cycle using the exhaust heat from a gas turbine process. Thus, the higher temperature level, directly corresponding to the turbine inlet temperature, is set to a fixed value of TIT = 550°C which is in the range of typical gas-turbine exhaust temperatures (c.f. Glos et al. [31]). The lower temperature is varied within a range of 32 °C to 40 °C regarding to different recooling conditions. The lower pressure level is set to a near critical value of 7.4 MPa while the higher pressure level is set to 25 MPa corresponding to a typical value for sCO<sub>2</sub> cycles. The intermediate pressure level for the intercooled cycle and the precooled cycle was set arbitrarily to 8.5 MPa. Similarly, the fractional amount of bypassed mass-flow was set to a value of 0.2. Losses were treated in terms of isentropic efficiencies for the compressor and the turbine. For the recuperators, a minimum pinch point difference of  $\Delta T_{\text{R}} = 10$  K was applied. Pressure losses were completely neglected.

Table 4: Boundary conditions applied to the process calculations

Boundary condition	Symbol	Value
Minimum temperature	$\vartheta_{\text{low}} \equiv \text{CIT}_{\text{mc}}$	35 °C (32 .. 40 °C)
Maximum temperature	$\vartheta_{\text{high}} \equiv \text{TIT}$	550 °C
Lower pressure level	$p_{\text{low}}$	7.5 MPa
Upper pressure level	$p_{\text{high}}$	25 MPa
Intermediate pressure (ICC, PCC)	$p_{\text{mid}}$	8.5 MPa
Mass-flow bypass ratio	$m_{\text{BR}}$	0.2
Compressor efficiency	$\eta_{\text{C}}$	0.8
Turbine efficiency	$\eta_{\text{T}}$	0.9
Min. pinch point diff. recuperator	$\Delta T_{\text{R}}$	10 K

## NEAR CRITICAL MODELING CAPABILITIES OF THE SELECTED EQS

For an initial cycle-independent comparison of the near-critical capabilities of the selected equations of state, several sets of isobars were calculated for relevant fluid properties in a temperature range close to critical conditions.

Beginning with the plots for the isobaric heat capacity, shown in Figure 3, it can be seen that all EoS are able to show the general behavior of a peak in the properties flattening with increasing distance from the critical pressure, including its shifts towards higher temperatures. However, compared to the multi-parameter equation of state, all other equations partly show a clear offset from the reference values. Focusing on the cubic equations of state (PR, SRK) and PCP-SAFT, these EoS predict the heat capacity peak at significantly lower temperatures than the other equations of state, resulting in higher values for  $c_p$  for temperatures below the pseudocritical point and lower values for temperatures above. Furthermore, the same EoS show notably lower peaks at higher pressure levels. The trend to lower values continues for higher temperatures, showing only slow convergence to the reference values. In contrast, the LKP shows a comparatively good agreement with the reference equation for the near-critical 7.4 MPa isobar. Nevertheless, for temperatures below the pseudocritical point and higher pressures, obtained values for  $c_p$  are clearly below the reference.

A somewhat similar behavior can be seen for the isobars in the  $\rho$ - $T$  diagram shown in Figure 4. Especially the cubic equations as well as PCP-SAFT show remarkably lower values for the density with increasing differences to the reference EoS for higher pressures. In contrast, also here, the LKP shows good agreement with the reference values on all isobars with only

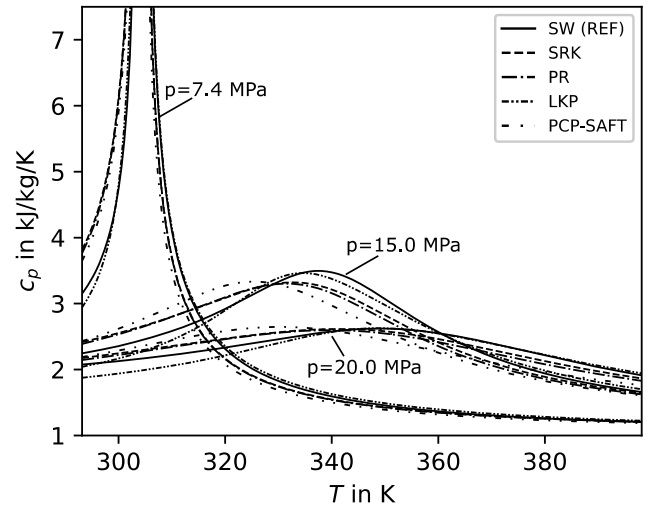


Figure 3: Near critical isobaric heat capacities for several isobars calculated with the selected EoS



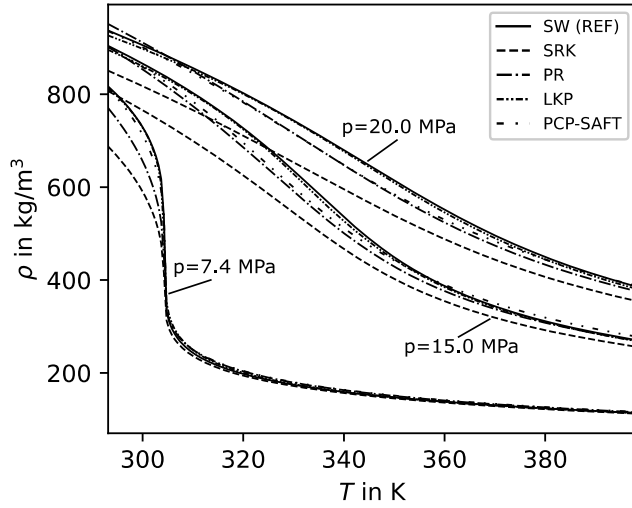


Figure 4: Near critical densities for several isobars calculated with the selected EoS

small deviations. Moreover, for the heat capacity as well as for the density, all equations of state converge to ideal gas behavior at higher temperatures. As expected, at higher pressures the results converge slower to the ideal gas limit, i.e. the differences in the results of the equations of state tend to be greater at greater pressure at the same temperature.

## RESULTS AND DISCUSSION

In order to compare the influence of the selected EoS, calculations were done for all four cycle architectures regarding the boundary conditions specified in Table 4 and for an initially fixed lower temperature level of 35 °C. The results for each equation of state are listed in Table 5 in terms of calculated values for the reference EoS by Span and Wagner and related to this, the percentage relative deviation for all other EoS is given. Starting with the thermal efficiencies, it can be seen that for all cycles all EoS show a fairly good agreement with each other. The largest differences compared to the reference equation are found in the results for the cubic equations and for the usage of PCP-SAFT. Herein, it can be seen that the SRK leads to higher deviations in the efficiency for the simpler layouts (SRC, RCC) than for the more complex cycle architectures (ICC, PCC). PCP-SAFT, on the other hand, shows smaller deviations in the results for the SRC and RCC than for the efficiencies of higher order cycles examined here.

In contrast to the efficiencies, the results for  $UA$  partially show large differences between the individual equations of state. In case of the cubic equations of state (SRK, PR), deviations from the reference EoS of up to 23.3 % can be observed in the results for the high-temperature recuperator of the RCC. Significant differences can also be seen for the application of PCP-SAFT, ranging from about -4 % for the low-temperature recuperator (LTR) of the PCC up to over 40 % for the high-temperature recuperator (HTR) of the RCC. In contrast, also here, the results

Table 5: Relative deviation of the calculated values compared to the reference equation of state

		Relative deviation from the reference value in %				
		$100 \cdot \left( \frac{x - x_{REF}}{x_{REF}} \right)$				
		SW (ref)	SRK	PR	LKP	PCP-SAFT
SRC	$\eta_{th}$	0.377	-1.056 %	0.2089 %	-0.243 %	1.136 %
	$m^*$	1.0	1.223 %	1.565 %	-1.902 %	3.322 %
	$UA_R$	8.16	6.513 %	8.847 %	-2.370 %	13,550 %
	$\Delta h_R$	313.77	0.701 %	0.508 %	0.380 %	-1.713 %
	$\overline{LMTD}_R$	38.44	-4.300 %	-6.843 %	0.862 %	-10.566 %
RCC	$\eta_{th}$	0.398	-1.260 %	0.240 %	-0.309 %	1.088 %
	$m^*$	1.0	1.418 %	1.582 %	-1.846 %	3.288 %
	$UA_{LTR}$	11.57	10.716 %	14.400 %	-1.886 %	25.408 %
	$\Delta h_{LTR}$	229.25	-0.162 %	-1.277 %	2.217 %	-3.058 %
	$\overline{LMTD}_{LTR}$	19.92	-8.667 %	-12.505 %	2.261 %	-20.410 %
	$UA_{HTR}$	4.50	14.214 %	23.274 %	-9.846 %	40.360 %
	$\Delta h_{HTR}$	130.37	2.102 %	3.281 %	-2.207 %	0.612 %
	$\overline{LMTD}_{HTR}$	29.00	-9.336 %	-14.893 %	6.470 %	-25.962 %
ICC	$\eta_{th}$	0.413	-0.308 %	1.050 %	0.108 %	2.335 %
	$m^*$	1.0	3.366 %	4.068 %	-0.373 %	5.423 %
	$UA_{LTR}$	9.89	-2.634 %	4.775 %	1.883 %	8.080 %
	$\Delta h_{LTR}$	250.57	-1.232 %	-2.934 %	1.147 %	-5.498 %
	$\overline{LMTD}_{LTR}$	25.35	-0.527 %	-3.589 %	-1.093 %	-7.821 %
	$UA_{HTR}$	3.07	14.189 %	22.463 %	-1.479 %	33.785 %
	$\Delta h_{HTR}$	179.49	-2.282 %	-0.972 %	-2.741 %	0.453 %
	$\overline{LMTD}_{HTR}$	58.41	-11.544 %	-15.847 %	-1.650 %	-20.843 %
PCC	$\eta_{th}$	0.400	-0.531 %	0.733 %	-0.076 %	2.171 %
	$m^*$	1.0	2.196 %	2.970 %	-1.037 %	4.978 %
	$UA_{LTR}$	6.43	-10.156 %	-9.635 %	-3.973 %	-3.912 %
	$\Delta h_{LTR}$	113.18	-12.995 %	-14.896 %	-6.559 %	-11.094 %
	$\overline{LMTD}_{LTR}$	17.60	-1.034 %	-3.026 %	-3.703 %	-2.868 %
	$UA_{HTR}$	4.63	12.806 %	17.972 %	2.787 %	23.400 %
	$\Delta h_{HTR}$	289.40	1.797 %	2.026 %	1.146 %	0.057 %
	$\overline{LMTD}_{HTR}$	62.46	-7.778 %	-10.948 %	-2.617 %	-14.977 %

of the LKP show much smaller deviations from the results of the reference equation of state. Most of them are in the single-digit percentage range. The highest value with approx. 10 % is obtained again for the high-temperature recuperator of the RCC.

In comparison with the previously discussed results for the near-critical heat capacities in Figure 3, it is noticeable that equations of state, which show significant offsets in the heat capacities, also lead to significant deviations for the calculated  $UA$  values of the recuperators. Taking the 15 MPa isobar in Figure 3 as an example, a clear offset to lower values can be seen for both the cubic equations of state as well as for PCP-SAFT. In addition, the less pronounced shift of the LKP also coincides with the lower deviations in the calculated values for  $UA$  in Table 5. However, a closer look at the deviations of the individual variables associated with the calculation of  $UA$  (cf. Equation (15)), which are also listed in Table 5, reveals different influences on the final value for  $UA$ . Starting with  $m^*$ , which indicates the relative change in the mass-flow regarding the reference equation, for the cubic equations as well as for the PCP-SAFT equation deviations in a positive single digit percentage range can be noted for all cycle architectures. The LKP, on the other hand, shows small negative deviations between  $-1.9\%$  and approx.  $-0.4\%$  in each case. Herein, it is noticeable, that increased values for  $m^*$  are not necessarily linked with increased values for  $UA$ . For instance, in the case of the ICC, the use of the LKP results in a slightly reduced mass flow rate, but still an increased value for  $UA$ .

A contrasting example can be found for the cubic equations of state applied to the pre-compression cycle (PCC), in which higher relative mass flows  $m^*$  result in lowered values in the  $UA$  values for the low-temperature recuperator (LTR) but in elevated ones for the high-temperature unit (HTR). Moreover, for all cycle architectures, the largest deviations in mass flow occur when using the PCP-SAFT equation.

In contrast, a more distinct influence on  $UA$  can be found in the deviations for the mean logarithmic temperature differences ( $\overline{LMTD}$ ), cf. equation (19), as well as for the enthalpy difference  $\Delta h$  between in- and outlet of each device. In case of the simple recuperated cycle and the recompression cycle, also  $\Delta h$  shows only smaller deviations in small single digit percentage ranges. Noticeable higher deviations can be seen for  $\overline{LMTD}$  instead, being in line with the order of magnitude of the deviations in  $UA$ . For example, the previously mentioned 40 % increase in  $UA$  for the high-temperature recuperator of the RCC when using PCP-SAFT results in a deviation of about  $-26\%$  in  $\overline{LMTD}$ , but only 0.612 % in  $\Delta h$  (and approx. 3.3 % in  $m^*$ ). Similar results can be found for the usage of the cubic EoS for both cycle architectures. The results using the LKP are less significant in this aspect, since the deviations, for  $UA$  as well as for  $\Delta h$  and  $\overline{LMTD}$ , are much less pronounced than for the other equations of state.

However, especially when looking at the results of the cubic EoS, effects change partially in case of the ICC and the PCC, depending on the temperature level of the recuperator. While the aforementioned prevalence in the deviation in  $\overline{LMTD}$  is mainly

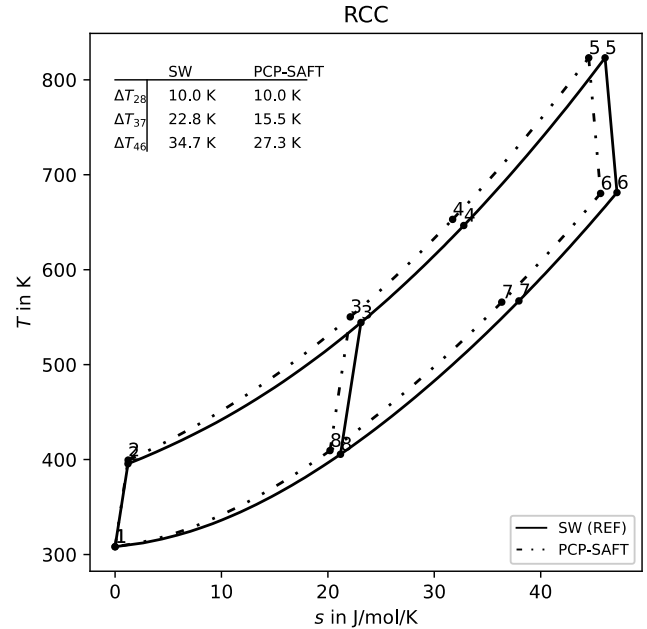


Figure 5:  $T$ - $s$  diagram of the RCC on base of different EoS, including a comparison of the terminal temperature differences of both recuperators

evident for the HTR, relative values for  $\overline{LMTD}_{LTR}$  and  $\Delta h_{LTR}$  are quite close to each other regarding the ICC, up to the case that  $\Delta h_{LTR}$  shows up remarkable higher deviations than  $\overline{LMTD}_{LTR}$  for the PCC. With reference to the latter, for example, deviations in  $UA$  for the low temperature recuperator are about  $-10\%$ , whereas relative deviations for  $\Delta h_{LTR}$  are around 13 % (SRK) to 15 % (PR) while  $\overline{LMTD}_{LTR}$  deviates only in a range from

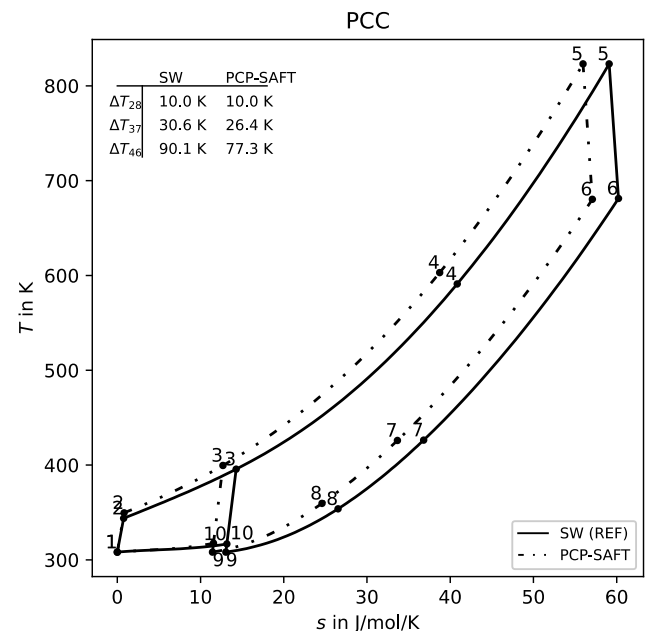


Figure 6:  $T$ - $s$  diagram of the PCC on base of different EoS, including a comparison of the terminal temperature differences of both recuperators

approximately  $-1\%$  (SRK) to  $-3\%$ . Similarly, the same can be noted for the PCP-SAFT and the LKP, although, as before, the effect is less pronounced in case of the LKP equation due to the generally smaller deviations from the reference equation.

Based on the case with the largest deviation in the calculated values for  $UA$ , Figure 5 shows the  $T$ - $s$  diagram of the recompression cycle on the one hand calculated with the reference equation by Span and Wagner and on the other hand calculated with PCP-SAFT using the boundary conditions from Table 4 in each case.

Referring to the aforementioned trend to lower values in the isobaric heat capacities for PCP-SAFT, a faster increase in temperature compared to the reference EoS can be seen, i.e., the

isobar of the PCP-SAFT EoS exhibits a steeper slope than the isobar of the reference EoS in a  $T$ - $s$  diagram.

The comparison of the temperature differences of the state points, corresponding to the terminal temperature differences of the recuperators (c.f. top left in Figure 5) shows that this leads to lower temperature differences in the recuperators, which, in accordance with Eqs. (12) and (13), result in higher values for  $UA$ . Moreover, the mutual influence of the recuperators in the higher order cycles leads to a potential multiplication of the deviation within the calculation process by using the result from the preceding component (e.g. LTR) as a boundary condition for the subsequent component (e.g. HTR).

Additionally, Figure 6 shows the same comparison of  $T$ - $s$  diagrams calculated with the reference EoS and with PCP-SAFT

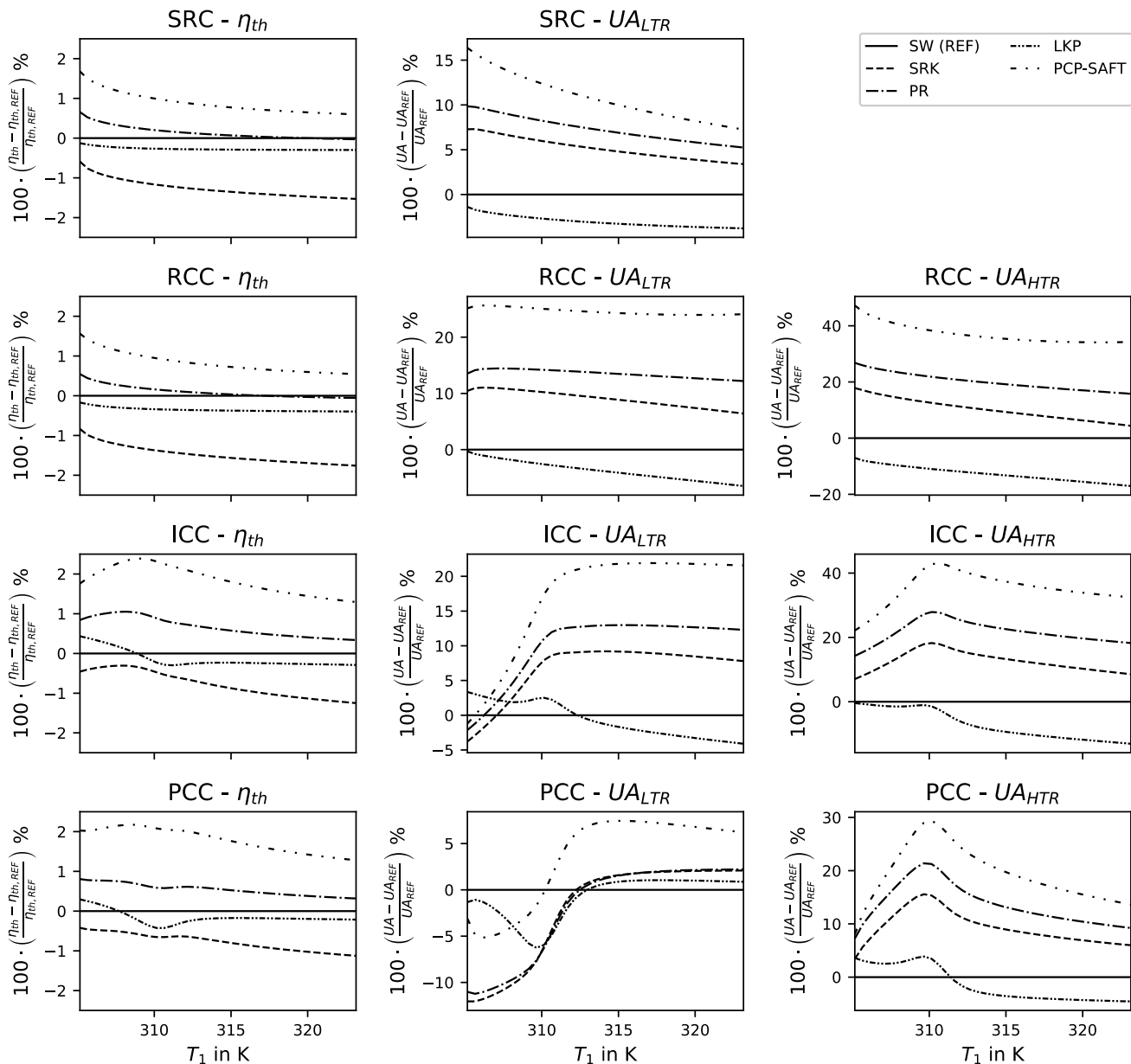


Figure 7: Changes in the relative deviation of the calculated properties for varying compressor inlet temperatures

for the precompression cycle (PCC) and the boundary condition specified in Table 4. As before, the PCP-SAFT equation shows a faster increase in temperature compared to the reference EoS resulting in a shift of the state points and respective changes in the terminal temperature differences of the recuperators. However, it can also be seen that, due to the lower temperature at the compressor outlet in point 2, the temperature range of the LTR (approx. 350 K to 400 K) is significantly lower than in case of the RCC (approx. 400 K to 540 K). Taking again into account the curves for the isobaric heat capacities in Figure 3, it can be noted, that for the higher pressure levels significantly larger deviations in the heat capacity are to be expected in this temperature range. Using the example of the 20 MPa isobar, it is apparent, that this clearly covers the range of the pseudocritical peak of the fluid properties. This in turn infers, that the significantly increased heat capacity in this region combined with the EoS specific shifts in the pseudocritical point itself, leads to the previously noted more prevalent deviations in the enthalpy differences  $\Delta h_{LTR}$  compared to changes in the temperature resulting in deviations of  $\overline{LMTD}_{LTR}$ .

Finally, Figure 7 shows the changes in the deviations of  $\eta_{th}$  and  $UA$  for varying compressor inlet temperatures, as specified within the boundary conditions in Table 4. It can be seen that for the cases considered here, even with reference to a wider temperature range, the deviations in efficiency remain within a small range of  $\pm 2.5\%$ . Beyond that, it is noticeable that the usage of the SRK consistently results in lower efficiencies compared to SW, while using PR and PCP-SAFT mostly yields values above the reference

Regarding the  $UA$  values, the results underline the dependency on the capabilities of the EoS to model supercritical heat capacities. Thus, for values of  $c_p$  well below the reference at higher temperatures (c.f. Figure 3), as is the case for SRK, PR, and PCP-SAFT, comparably high positive deviations in the  $UA$  values of up to over 40% can be seen. Although the compressor inlet temperature only allows limited statements to be made about the recuperator inlet conditions, it can be further assumed, that the change to negative deviations of  $UA$ , especially visible for the low temperature recuperator in the ICC and the PCC, for lower values of  $T_1$  relates to the offset in the heat capacity peak to lower temperatures. Analogous to the efficiencies, a certain tendency towards stabilized values for the deviations can also be seen here for higher temperatures. Nevertheless, the deviations remain at fairly high values.

## CONCLUSION

In summary, in this work the influence of different EoS on the calculation of efficiency and heat exchanger performance of several power cycle architectures frequently considered for applications with  $sCO_2$  as working fluid has been studied. Within this context, five different equations of state were compared to each other. For the calculated efficiencies, even the results of the simpler equations of state show an overall good agreement with the reference values. Nevertheless, especially for more complex

cycle architectures deviations in a single-digit percentage range may occur, which may not be negligible for more detailed evaluations. However, it has also been shown that the choice of the EoS is even more significant when it comes to the calculation of components. Based on the example of the  $UA$  value, as a widely used performance and size indicator for heat exchangers, deviations in the values for the recuperators of more than 40% were noticed. Note that the observed differences in the results of the cycle calculations with the equations of state studied in this work do not reflect the deviations of the different EoS at the same state points but are a result of error propagation, since the different EoS lead to different state points at the inlets and outlets of the components as discussed in Figure 5 and Figure 6. However, the deviations are exclusively due to the use of a different EoS, i.e., there are no other influences which could explain the observed differences.

Both, the good agreement of the calculated efficiencies as well as the deviations found in the calculated values for  $UA$  are in good agreement with the findings of Mickoleit et al. [8] or Zhao [7], which underlines the importance of the use of an appropriate EoS also beyond the scope of the cycles considered here. This becomes especially important if mixtures are considered as working fluids, because usually the reference equation of state (multiparameter equation of state) is used to calculate the base case. Therefore, it is favorable to also use the reference equation of state in the mixture model in order to get consistent results, as the use of other equations of state might result in significant deviations for performance parameters of the cycle as demonstrated in this work.

## NOMENCLATURE

### Symbols

$a$	molar Helmholtz energy ( $J mol^{-1}$ )
	attraction parameter ( $Pa m^6 mol^{-2}$ )
$A$	area ( $m^2$ )
$b$	co-volume ( $m^3 mol^{-1}$ )
$h$	molar enthalpy ( $J mol^{-1}$ )
	specific enthalpy ( $J kg^{-1}$ )
$i$	counting variable for summation (-)
$k_B$	Boltzmann constant ( $J K^{-1}$ )
$LMTD$	logarithmic mean temperature difference (K)
$\dot{m}$	mass flow ( $kg/s$ )
$m^*$	relative mass flow factor ( $kg/s$ )
$n$	number of sections (-)
$p$	pressure (Pa)
$Q$	quadrupole moment ( $D\AA = 3.3356 \cdot 10^{40} Cm^2$ )
$R$	universal gas constant
$s$	molar entropy ( $J mol^{-1} K^{-1}$ )
	specific entropy ( $J kg^{-1} K^{-1}$ )
$T$	temperature (K)
$U$	heat transfer coefficient ( $W m^{-2} K^{-1}$ )
$UA$	$UA$ value as the product of $U$ and $A$ ( $W K^{-1}$ )
$z$	compression factor (-)

### Greek symbols

$\alpha$	dimensionless Helmholtz energy (-)
$\delta$	reduced density (-)
$\varepsilon$	segment energy parameter (J)
$\eta$	efficiency (-)
$\vartheta$	temperature (°C)
$\rho$	molar density (mol m <sup>-3</sup> ) specific density (kg m <sup>-3</sup> )
$\sigma$	segment size parameter (Å)
$\tau$	reciprocal reduced temperature (-)

### Subscripts

1 .. 10	related to the corresponding process point
BR	bypass ratio (fractional amount of the bypassed mass-flow)
c	property at the critical point
HTR	related to the high-temperature recuperator
LTR	related to the low temperature recuperator
mc	related to the main compressor
t	related to the turbine
th	thermal, related to the (thermal) efficiency
R	related to the recuperator
ref	related to the reference (EoS)

### Superscripts

0	ideal gas property
r	residual property

### Chemical Formulas

CO<sub>2</sub> carbon dioxide

### Abbreviations

CIT	(main-) compressor inlet temperature
EoS	equation of State
HTR	high temperature recuperator
ICC	intercooling cycle
LMTD	logarithmic mean temperature difference
LTR	low temperature recuperator
PR	Peng-Robinson equation of state
PCP-SAFT	perturbed-chain polar Statistical associating fluid theory
PCC	partial cooling cycle
RCC	recompression cycle
SRC	simple recuperated cycle
SRK	Soave-Redlich-Kwong equation of state
SW	multi-parameter EoS by Span and Wagner
TIT	turbine inlet temperature

### **ACKNOWLEDGEMENTS**

This work was carried out within the Supercritical Carbon Dioxide-Lab (suCOO-Lab) of the School of Engineering Sciences of TU Dresden. The authors want to thank the School of Engineering Sciences of TU Dresden for partial funding of the presented results.

### **REFERENCES**

- [1] T. Gotelip, U. Gampe, S. Glos, Optimization strategies of different sCO<sub>2</sub> architectures for gas turbine bottoming cycle applications, *Energy*. 250 (2022) 123734. <https://doi.org/10.1016/j.energy.2022.123734>.
- [2] G. Manzolini, M. Binotti, D. Bonalumi, C. Invernizzi, P. Iora, CO<sub>2</sub> mixtures as innovative working fluid in power cycles applied to solar plants. Techno-economic assessment, *Solar Energy*. 181 (2019) 530–544. <https://doi.org/10.1016/j.solener.2019.01.015>.
- [3] S. Unger, J. Müller, M.B. Mohankumar, S. Rath, U. Hampel, Numerical Dimensioning of a Pre-Cooler for sCO<sub>2</sub> Power Cycles to Utilize Industrial Waste Heat, *Energies*. 14 (2021) 8278. <https://doi.org/10.3390/en14248278>.
- [4] M. Binotti, C.M. Invernizzi, P. Iora, G. Manzolini, Dinitrogen tetroxide and carbon dioxide mixtures as working fluids in solar tower plants, *Sol. Energy*. 181 (2019) 203–213. <https://doi.org/10.1016/j.solener.2019.01.079>.
- [5] S. Rath, E. Mickoleit, U. Gampe, C. Breitkopf, A. Jäger, Study of the influence of additives to CO<sub>2</sub> on the performance parameters of a sCO<sub>2</sub>-cycle, in: *Proceedings of the 4th European SCO<sub>2</sub> Conference for Energy Systems, Online-Conference*, 2021. <https://doi.org/10.17185/dupublico/73965>.
- [6] S. Rath, E. Mickoleit, U. Gampe, C. Breitkopf, A. Jäger, Systematic analysis of additives on the performance parameters of sCO<sub>2</sub> cycles and their individual effects on the cycle characteristics, *Energy*. 252 (2022) 123957. <https://doi.org/10.1016/j.energy.2022.123957>.
- [7] Q. Zhao, M. Mecheri, T. Neveux, R. Privat, J.-N. Jaubert, Selection of a Proper Equation of State for the Modeling of a Supercritical CO<sub>2</sub> Brayton Cycle: Consequences on the Process Design, *Ind. Eng. Chem. Res.* 56 (2017) 6841–6853. <https://doi.org/10.1021/acs.iecr.7b00917>.
- [8] E. Mickoleit, C. Breitkopf, A. Jäger, Influence of Equations of State and Mixture Models on the Design of a Refrigeration Process, *Int. J. Refrig.* 121 (2021) 193–205. <https://doi.org/10.1016/j.ijrefrig.2020.10.017>.
- [9] R. Span, W. Wagner, A New Equation of State for Carbon Dioxide Covering the Fluid Region from the Triple-Point Temperature to 1100 K at Pressures up to 800 MPa, *J. Phys. Chem. Ref. Data*. 25 (1996) 1509–1596. <https://doi.org/10.1063/1.555991>.
- [10] R. Span, R. Beckmüller, S. Hielscher, A. Jäger, E. Mickoleit, T. Neumann, S.M. Pohl, B. Semrau, M. Thol, TREND. Thermodynamic Reference and Engineering Data 5.0, (2020).
- [11] O. Redlich, J.N.S. Kwong, On the Thermodynamics of Solutions. V. An Equation of State. Fugacities of Gaseous Solutions., *Chem. Rev.* 44 (1949) 233–244. <https://doi.org/10.1021/cr60137a013>.
- [12] G. Soave, Equilibrium Constants from a Modified Redlich-Kwong Equation of State, *Chem. Eng. Sci.* 27 (1972) 1197–1203. [https://doi.org/10.1016/0009-2509\(72\)80096-4](https://doi.org/10.1016/0009-2509(72)80096-4).

- [13] D.-Y. Peng, D.B. Robinson, A New Two-Constant Equation of State, *Ind. Eng. Chem. Fund.* 15 (1976) 59–64. <https://doi.org/10.1021/i160057a011>.
- [14] B.I. Lee, M.G. Kesler, A Generalized Thermodynamic Correlation Based on Three-Parameter Corresponding States, *AIChE J.* 21 (1975) 510–527. <https://doi.org/10.1002/aic.690210313>.
- [15] U. Plöcker, H. Knapp, J. Prausnitz, Calculation of High-Pressure Vapor-Liquid Equilibria from a Corresponding-States Correlation with Emphasis on Asymmetric Mixtures, *Ind. Eng. Chem. Process Des. Dev.* 17 (1978) 324–332. <https://doi.org/10.1021/i260067a020>.
- [16] W.G. Chapman, G. Jackson, K.E. Gubbins, Phase equilibria of associating fluids: Chain molecules with multiple bonding sites, *Mol. Phys.* 65 (1988) 1057–1079. <https://doi.org/10.1080/00268978800101601>.
- [17] W.G. Chapman, K.E. Gubbins, G. Jackson, M. Radosz, New Reference Equation of State for Associating Liquids, *Ind. Eng. Chem. Res.* 29 (1990) 1709–1721. <https://doi.org/10.1021/ie00104a021>.
- [18] J. Gross, G. Sadowski, Perturbed-Chain SAFT: An Equation of State Based on a Perturbation Theory for Chain Molecules, *Ind. Eng. Chem. Res.* 40 (2001) 1244–1260. <https://doi.org/10.1021/ie0003887>.
- [19] J. Gross, An equation-of-state contribution for polar components: Quadrupolar molecules, *AIChE J.* 51 (2005) 2556–2568. <https://doi.org/10.1002/aic.10502>.
- [20] J. Gross, J. Vrabec, An equation-of-state contribution for polar components: Dipolar molecules, *AIChE J.* 52 (2006) 1194–1204. <https://doi.org/10.1002/aic.10683>.
- [21] I.H. Bell, A. Jäger, Helmholtz Energy Transformations of Common Cubic Equations of State for Use with Pure Fluids and Mixtures, *J. Res. Natl. Inst. Stan.* 121 (2016) 238–263. <https://doi.org/10.6028/jres.121.011>.
- [22] S. Herrig, New Helmholtz-energy equations of state for pure fluids and CCS-relevant mixtures, Dissertation, Ruhr-Universität Bochum, 2018. <https://hss-opus.ub.ruhr-uni-bochum.de/opus4/frontdoor/deliver/index/docId/6284/file/diss.pdf> (accessed February 7, 2019).
- [23] Verein Deutscher Ingenieure, VDI-Gesellschaft Verfahrenstechnik und Chemieingenieurwesen, eds., *VDI-Wärmeatlas*, 11., bearb. und erw. Aufl., Springer Vieweg, Berlin, 2013.
- [24] R. Span, *Multiparameter Equations of State: An Accurate Source of Thermodynamic Property Data*, Springer, Berlin, Germany, 2000.
- [25] F. Crespi, G. Gavagnin, D. Sánchez, G.S. Martínez, Supercritical carbon dioxide cycles for power generation: A review, *Applied Energy.* 195 (2017) 152–183. <https://doi.org/10.1016/j.apenergy.2017.02.048>.
- [26] A. Moisseytsev, J.J. Siemicki, Performance improvement options for the supercritical carbon dioxide brayton cycle., 2008. <https://doi.org/10.2172/935094>.
- [27] J. Yin, Q. Zheng, Z. Peng, X. Zhang, Review of supercritical CO<sub>2</sub> power cycles integrated with CSP, *Int J Energy Res.* 44 (2020) 1337–1369. <https://doi.org/10.1002/er.4909>.
- [28] T. Held, J. Miller, D. Buckmaster, A Comparative Study of Heat Rejection Systems for sCO<sub>2</sub> Power Cycles, in: San Antonio, Texas, USA, 2016.
- [29] S.-I. Na, M.S. Kim, Y.-J. Baik, M. Kim, Optimal allocation of heat exchangers in a Supercritical carbon dioxide power cycle for waste heat recovery, *Energy Conversion and Management.* 199 (2019) 112002. <https://doi.org/10.1016/j.enconman.2019.112002>.
- [30] J.S. Kwon, S. Son, J.Y. Heo, J.I. Lee, Compact heat exchangers for supercritical CO<sub>2</sub> power cycle application, *Energy Conversion and Management.* 209 (2020) 112666. <https://doi.org/10.1016/j.enconman.2020.112666>.
- [31] S. Glos, M. Wechsung, R. Wagner, A. Heidenhof, D. Schlehber, Evaluation of sCO<sub>2</sub> power cycles for direct and waste heat applications, (2018). <https://doi.org/10.17185/DUEPUBLICO/46082>.



## DESIGN AND SETUP OF THE SUCCO-LAB sCO<sub>2</sub> TEST FACILITY AT TU DRESDEN

**Sebastian Rath\***

TU Dresden

Dresden, Germany

Email: sebastian.rath@tu-dresden.de

**Uwe Gampe**

TU Dresden

Dresden, Germany

**Cornelia Breilkopf**

TU Dresden

Dresden, Germany

**Andreas Jäger**

TU Dresden

Dresden, Germany

### ABSTRACT

Compared to the current state of the art, power cycles based on supercritical CO<sub>2</sub> (sCO<sub>2</sub>) offer the potential for significant increases in power density and efficiency and are thus seen as a promising element for a more sustainable and flexible heat utilization in the future. There is a particular need for experimental work in order to bring this technology to market maturity. For instance, it is necessary to validate theoretical approaches and to test and develop components.

As part of the supercritical carbon dioxide laboratory (suCOO-Lab), a test facility was set up at TU Dresden. The aim is to provide a flexibly usable and expandable test infrastructure for basic research, validation work, as well as small-scale component tests and development.

Key components of the system are an electric heater, two compressors and a powerful cooling system. Temperatures up to 300 °C and pressures up to 20 MPa allow covering of a wide range of parameters in the trans- and supercritical fluid region of CO<sub>2</sub>. The integration of a capable measurement and data acquisition system ensures the continuous availability of measurement data at all relevant points in the rig. Experimental setups can be flexibly integrated into the process at various locations, which additionally allows the simultaneous use of different parameter ranges in one or more experimental setups. Furthermore, special care was taken within the selection of the components itself. All parts, including the compressors, are designed for a lubricant free operation ensuring high fluid purities. This is beneficial for experiments with pure CO<sub>2</sub> and also enables investigations of CO<sub>2</sub>-mixtures.

This paper describes the design and the current status of the suCOO-Lab test facility at TU Dresden. Special emphasis is placed on the targeted parameter range, characteristic design aspects of the rig, and on the capabilities of measurement and data acquisition.

### INTRODUCTION

The increasing global demand for energy calls for further development of existing technologies for a more economical, sustainable, and, above all, a more complete usage of available energy sources. Power cycles based on supercritical carbon dioxide (sCO<sub>2</sub>) are a current topic in science and industry for a variety of applications, such as concentrated solar power (CSP), nuclear plants, waste heat recovery, or the utilization of geothermal heat [1–5]. Compared to other working fluids such as, e.g., steam, sCO<sub>2</sub> offers distinct advantages. Its special (non-ideal) properties in the supercritical state, as for example a liquid-like density, a low viscosity, or the absence of a phase change, enable the potential for a significant reduction in complexity and size of the cycle and its components as well as high thermal efficiencies with even simple cycle configurations and moderate temperature levels. Furthermore, the relatively low critical temperature of CO<sub>2</sub> ( $\vartheta_{\text{crit}} \approx 31$  °C), makes it applicable for a wide range of thermal heat sources of both, conventional and renewable origin.

However, there is still a considerable need for research to bring the technology to market maturity. Herein, a major aspect are the strong fluctuations in fluid properties in the near- and the supercritical region, which means that even small changes in temperature may lead to large variations for example in density or heat capacity. This affects all levels of development from fundamental research, process stability and control, up to design, manufacturing, and testing of components.

Referring to the compressor inlet temperature, for instance due to variations in the ambient temperature, this for example can result in significant operating point deviations with corresponding changes in efficiency [6,7]. In terms of the heat exchangers, especially the changes in the heat capacities can massively impede the heat transfer with corresponding effects on the proper performance of the device [8]. As a combination of individual effects, this consequently results in a noticeable

\* corresponding author(s)

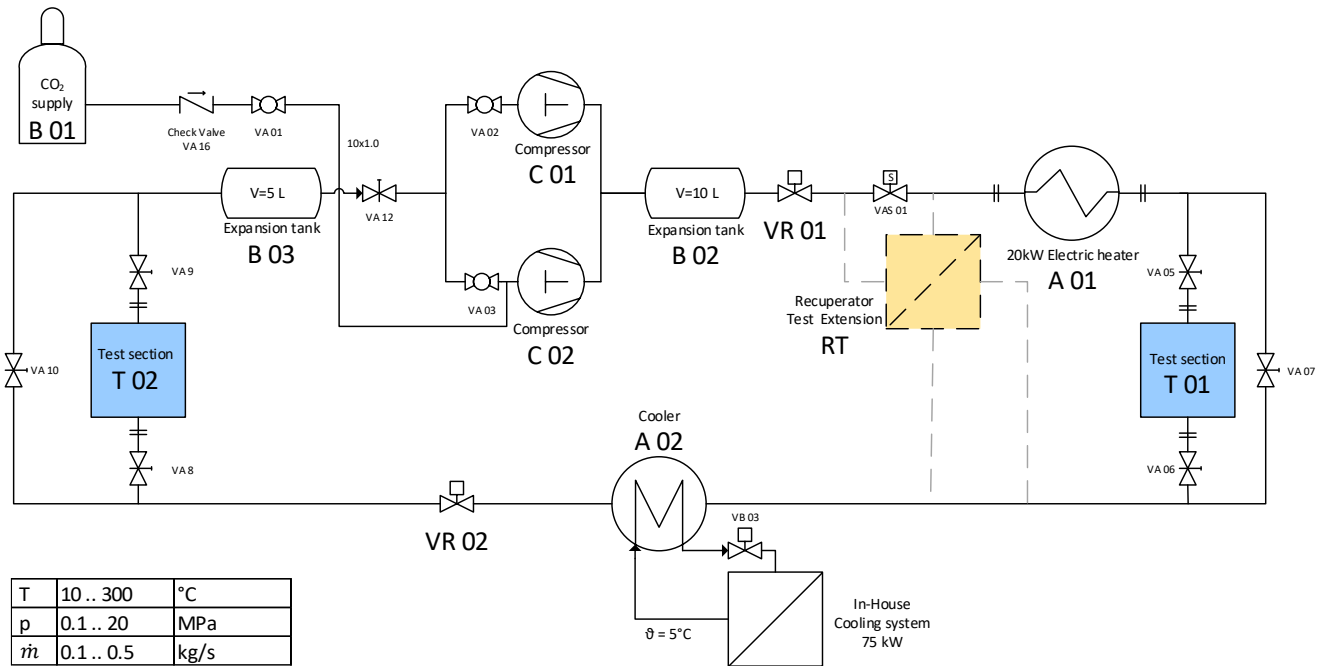


Figure 1: Basic layout of the test rig including targeted design parameters

temperature dependence of the whole cycle's efficiency which needs to be taken into account [9]. Furthermore, it has been (mostly theoretically) shown that CO<sub>2</sub> purity can also have a significant impact on process performance. On the one hand, even minor impurities can unintentionally lead to significant changes in efficiency [10]. On the other hand, efficiency increases are also conceivable through the selective admixture of additives [2,11,12].

For all these reasons, there is a particular need for experimental work to support and validate theoretical approaches, requiring a further expansion of experimental capacities. This includes in particular the previously mentioned aspect of fluid composition, which has so far only been experimentally addressed to a limited extent.

#### suCOO-Lab TEST-FACILITY –BASIC SETUP

To establish sCO<sub>2</sub> as an alternative working fluid in power systems in research and teaching at TU Dresden, the supercritical carbon dioxide laboratory (suCOO-Lab) was founded as a central platform for interdisciplinary sCO<sub>2</sub>-projects with partners from research and development. As a part of this lab, a test facility was set up, providing a flexibly usable and expandable test infrastructure for basic research and validation work, as well as small-scale component tests and development.

Consequently, boundary conditions for the base setup were chosen to cover a sufficiently wide range in the near- and supercritical fluid region as well as to maintain the possibility for future extensions of the facility. As shown along with the block diagram in Figure 1, all components are designed to handle maximum CO<sub>2</sub>-temperatures of 300 °C at pressures of up to 20 MPa. Mass flows of the supercritical fluid were targeted from 0.1 kg/s, for higher compression ratios and/or lower densities, up

to 0.5 kg/s for near-critical compressor inlet states or in the case that the fluid circulates at higher pressures by only compensating pressure losses. Within this context, pipe sizes were set to 18x2.00 mm and 2x 10x1.00 mm for sections of parallel flow. As can be seen in the block diagram in Figure 1, the basic layout of the test rig consists of a closed-loop cycle in which the fluid circulates. Referring to the labels C 01 and C 02, the pressure build-up is realized via two piston compressors connected in parallel. For this purpose, air-driven gas boosters supplied by Maximator are used, which operate according to the principle of a double-acting piston. A principle sketch is given in Figure 2. By charging the large pistons with compressed air as driving medium, the smaller pistons are used to raise the pressure of the CO<sub>2</sub> up to targeted values. Herein, the dry-running principle enables a continuous lubricant-free operation. Furthermore, they are able to cover a wide operating range, from pure gas phase at ambient pressure up to trans- and supercritical regions. A separate connection of the second compressor (C 02) to the CO<sub>2</sub> supply (B 01) (cf. Figure 1) allows initial filling and pressurization of the system as well as simultaneous refilling

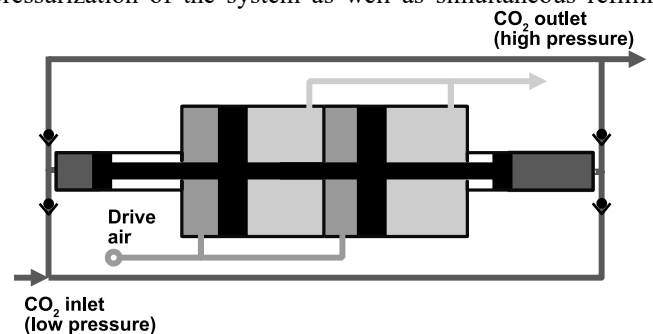
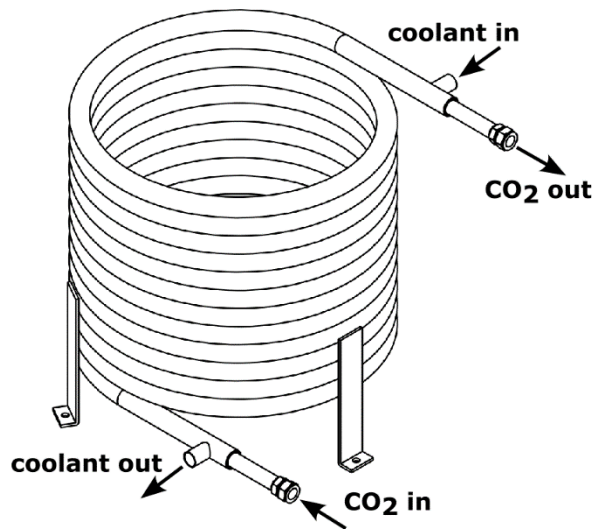


Figure 2: Principle sketch of the compressors



**Figure 3:** Coaxial heat exchanger used as cooler

during test runs. Two expansion tanks, located upstream (B 03) and downstream (B 02) of the compressors, provide hydraulic compensation for pulsations. Driving air is supplied via an in-house compressed air system, allowing volume flows of up to 6500 l(S)/min at pressures up to 10 bar, which fits the estimated requirements of the compressors for the aforementioned mass-flow conditions. However, as mostly lower driving pressures are needed for the gas boosters, upstream regulating valves allow precise control of the driving pressure separately for each device. In this initial stage of the rig, thermal input is provided by a 20 kW electrical heater (A 01), which, based on the previously mentioned mass-flow of 0.1 kg/s, provides sufficient capacities for temperatures up to 250 °C. However, as already mentioned, note that all components are designed for temperatures of up to 300 °C at pressures up to 20 MPa. Therefore, temperatures higher than 250 °C also at higher mass-flows than 0.1 kg/s will be achievable after the planned extensions of the rig.

Heat rejection is achieved by a coaxial heat exchanger (A 02), depicted in Figure 3. The strict implementation of a counterflow design with the CO<sub>2</sub> in the inner tube and the coolant in the outer tube enables precise temperature control as well as investigations of the heat transfer close to the critical point. The integration into the in-house cooling water system gives access to cooling capacities of up to 75 kW at constant coolant inlet temperatures of 5 °C and maximum pressures of up to 5 bar (limited by the coaxial heat exchanger). Temperature control is done by means of the mass flow, allowing the use of increased return temperatures of the coolant of up to 80 °C.

For experimental setups, two test sections are available, consisting of two face seal flanges, which allow a flexible integration of various test assemblies. The arrangement of one section directly after the heater (T 01) and one section downstream of the cooler (T 02) allows simultaneous investigations of different temperature levels. The pressure level in each test section can additionally be set by the two regulation

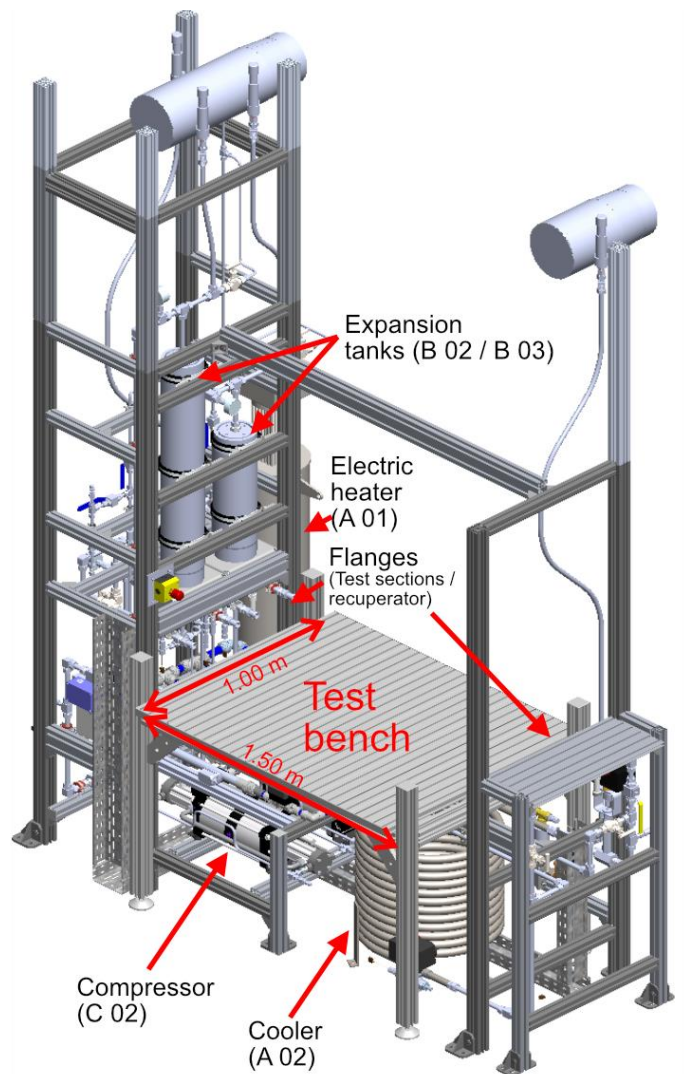


**Figure 4:** Assembly of the test-rig (CAD model)

valves VR 01 and VR 02. In addition to the test sections, further flanges are available which allow the direct integration of recuperator modules (RT).

To meet the space requirements on site and as can be seen in Figure 4, the components are arranged in a rack-like support system around a central test bench. In addition to a space-saving and clear structure, this also allows good accessibility to all components. The compressors (only C 02 visible in Figure 4) are mounted close to the ground and can be removed laterally with comparatively little effort if necessary. The large rack on the left side of the picture contains both expansion tanks as well as all pipe assemblies directly connected to the heater. The back-open construction, as well as a vertical arrangement of the pipes in different tiers, allows easy access to all valves and measurement equipment. The right side of the test-rig, on the other hand, contains the cold end of the system with the cooler situated next to the compressors. Again, the pipe assemblies directly connected to it are mounted in a small rack, which provides

**Table 1:** Measuring device types installed on the test-rig

Fluid	Property	Measurement Device	Range	Uncertainty of the sensor	Location / Purpose
CO <sub>2</sub>	Temperature	Thermocouple Type T, Class 1	-185 °C .. 300 °C	±0.5 K (≤ 125 °C) / ±0.004 ·  T	Process monitoring / Test sections T 01/T 02
CO <sub>2</sub>	Temperature	RTD PT1000, 1/3 DIN B	-100 °C .. 450 °C	±(0.1 + 0.0017 ·  T ) °C	Test sections T 01/T 02
CO <sub>2</sub>	Pressure	Piezoresistive pressure transmitter Keller PA23SY	0 .. 300 bar	±0.25 % FS	Process monitoring
CO <sub>2</sub>	Pressure	Piezoresistive pressure transmitter Keller PA35XHTC	0 .. 300 bar (T <sub>max</sub> = 300 °C)	±0.05 % FS	Process monitoring HT / Test section T 01
CO <sub>2</sub>	Pressure	Piezoresistive pressure transmitter Keller PA33X	0 .. 300 bar	±0.05 % FS	Test section T 02
CO <sub>2</sub>	Mass-flow	Coriolis flow meter Rheonic RHM08L	0.008 .. 0.8 kg/s	±0.2 %	Process monitoring
Air	Temperature / Flow rate	Calorimetric flow meter IFM SD8500	-10 .. 60 °C; 14 -3750 l/min	±0.5 K ± (2 % MV + 0.5 % MEV)	Process monitoring
Air	Pressure	Piezoresistive pressure transmitter Keller PAA21Y	0 .. 10 bar	±0.5 % FS	Process monitoring
Water	Temperature	Thermocouple Type T, Class 1	-185 °C .. 300 °C	±0.5 K (≤ 125 °C) / ±0.004 ·  T	Process monitoring
Water	Flow rate	Magnetic-inductive flow meter IFM SM6000	0.1 .. 25 l/min	± (0.8 % MV + 0.5 % MEV)	Process monitoring

access to all controls and instrumentation at its rear facing away from the test bench.

The central test bench consists of a height-adjustable table situated in-between the two mounting racks that can be used for variable test setups of both test sections. The flanges of the two test sections are placed to face each other along the length of the table, giving a total space for individual setups of approximately 1.50 m x 1.00 m.

### DATA MEASUREMENT AND ACQUISITION

For process monitoring and control, the facility is equipped with a variety of measuring devices, to monitor selected fluid properties at all relevant process points in the loop. With reference to this, Table 1 shows a list of the sensor types used within the rig.

For temperature measurement at a total of 14 locations in the CO<sub>2</sub> part of the rig, type T thermocouples were chosen as they can measure punctually in the core flow, exhibit a high response capability to sudden changes and have a sufficient accuracy for the scoped range of temperatures. For an even better accuracy at the inlet and the outlet of both test sections, PT1000 resistance thermometers are optionally available.

Pressure measurement is performed throughout with piezo-resistive pressure transmitters. For general process monitoring, all relevant system points can be captured with an accuracy of

± 0.25% FS (Full Scale). At the inlet and outlet of the test sections, as well as in the high temperature sections of the rig, transmitters with an extended accuracy of ± 0.05% FS are installed. Furthermore, for safety reasons, all separable system parts are equipped with manual pressure gauges giving a direct information of the system pressure even when the data acquisition system is not running. The mass flow is determined after the compressors, between the expansion tank and the heater inlet. The Coriolis flowmeter used for this purpose covers mass flows of up to 0.8 kg/s, giving calibrated accuracies of ± 0.2%. Within the scope of the secondary media, the inlet and outlet temperature as well as the flow rate for the cooling water are measured. Again, temperature measurement is done by means of type T thermocouples.

For the flow-rate, a magnetic-inductive flow meter is used providing a range of 0.1 .. 25 l/min with accuracies of ± (0.8 % MV + 0,5 % MEV). With regard to the compressed air used to drive the compressors (C 01, C 02), pressure, temperature, and flow rate are monitored separately for each device. This allows a separate control as well as an exact balancing of both compressors, which particularly enables a more detailed analysis of their individual performance. The pressure is measured by piezoresistive pressure transmitters providing an accuracy of ± 0.5% FS for pressures up to 10 bar. Temperature and flow are measured by calorimetric flow meters, which have a measuring range of -10 ... 60°C / 14 - 3750 l/min with accuracies of ± 0.5 K / ± (2 % MV + 0,5 % MEV).

Data acquisition is done via a WAGO 750 industrial IO System in connection with LabVIEW. The measurement data is redundantly available on several local hard disks as well as on a network storage, which also can be accessed remotely.

### SAFETY ASPECTS

For safe operation, a number of precautions have been adopted concerning both the equipment and the installation site. The test rig is equipped with two solenoid valves, which are closed when no voltage is applied. The first one disconnects both compressors from the compressed air supply. The second valve, which is also depicted in Figure 1 (VAS 01), is located directly in the CO<sub>2</sub> line upstream of the heater preventing any circulation of the CO<sub>2</sub> in the closed state. This means that no operation can take place without an explicit and continuous signal by the control system. Similarly, a loss of power supply, e.g. also triggered by a manual emergency stop, causes the implicit closing of the valves.

To protect against impermissibly high operating temperatures, the fluid and the core temperature of the heater as well as the recooling temperature are monitored. If the measured values exceed the allowed temperatures, the heater is disconnected from the power supply and the fluid circulation is stopped by closing the solenoid valves leading to a safe power-off state. For protection against impermissibly high pressures, all separable sections are equipped with safety valves. Their direct connection to a ventilation line provides a safe removal of the blown-off media from the building in case of response.

Regarding the integration on-site and as shown in Figure 5, the space for the test-rig is spatially separated by metal-stud walls to





**Figure 5:** Test facility in housing on-site

adjacent areas. System operation takes place from a separate control room so that no personnel is required within the immediate vicinity of the test rig during runs. Manual emergency stops in every reach in the test- and control room enable a direct and immediate shutdown of the system in any situation, leading to the aforementioned safe power-off scenario by switching off the power-supply for the heater and the solenoid valves. A gas warning system continuously records the CO<sub>2</sub> concentration within the ambient air of the test rig area. At elevated concentrations, a warning is set in the control interface and a ventilation system is switched on, which exchanges the room air via ventilation ducts integrated into the floor. If, nevertheless, higher CO<sub>2</sub> concentrations are reached, a gas alert is triggered giving optical and acoustic warnings to the user and the surroundings. Additionally, if the gas alarm persists over a certain time span, the system is automatically shut down. The system has been designed throughout in accordance with the European Pressure Equipment Directive 2014/29/EU [13]. Additionally, compliance with the regulations is confirmed by a certified authority.

### CURRENT STATE AND FUTURE EXTENSIONS

At time of submission of this paper, the mechanical work has been successfully completed. Current work is concerned with the wiring of the sensors, as well as the integration into the user interface of the control software. In parallel, preparations are being made for approval within the European Pressure Equipment Directive by a certified authority.

Beyond the commissioning and the initial tests, a first use of the test facility is planned within the SHARP-sCO<sub>2</sub> project, which has been started in November 2022 and which is funded by the European Union's HORIZON EUROPE Research and Innovation Programme. Herein, the suCOO-Lab test facility will be used to design and investigate sCO<sub>2</sub>-air heat exchangers for use with concentrated solar power (CSP). As shown in Figure 6, in this context the test rig will be extended by a hot air loop providing a continuous hot air stream within the test sections.

Recirculation of the air is intended to enable cost-efficient supply of the requested air temperatures. By doing so, blower inlet temperatures up to 300 °C and a targeted heater capacity of 60 kW will allow hot air temperatures up to 700 °C at mass flows of 0.15 kg/s and near ambient pressures.

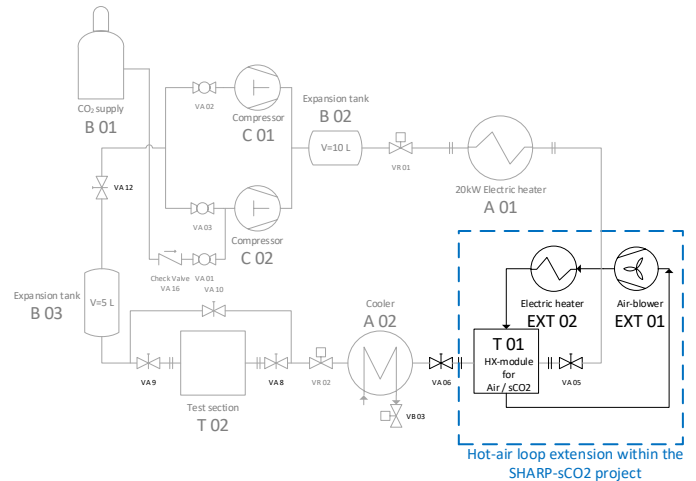


**Figure 6:** Planned hot-air-loop extension of the test-rig within the SHARP-sCO<sub>2</sub> project

### CONCLUSION

As part of the suCOO-Lab at TU Dresden, a test facility was set up, providing a flexibly usable and expandable test infrastructure for basic research and validation work, as well as small-scale component tests and development. In addition to a wide operating range, the system offers flexible integration of experimental setups into two separate, simultaneously usable test sections. As a unique feature, the rig is designed to operate completely free of lubricants. On the one hand, this enables investigations with CO<sub>2</sub> at defined purity without the risk of dissolved lubricant residues influencing the results. On the other hand, this also makes the system suitable for use with CO<sub>2</sub> mixtures, which for instance enables the targeted investigation of the influence of impurities or the use of predefined sCO<sub>2</sub>-blends.

### NOMENCLATURE

#### Symbols

$\dot{m}$	[kg/s] Mass flow
$p$	[Pa] Pressure
$\vartheta$	[°C] Temperature

#### Subscripts

crit	Critical property
------	-------------------

#### Abbreviations

CSP	Concentrated solar power
FS	Full scale
MEV	Measuring range end value
MV	Measured Value
S	Standard state ( $T = 213.15 \text{ K}$ , $p = 101325 \text{ Pa}$ )

## ACKNOWLEDGEMENTS

This project has received funding from the European Union's HORIZON EUROPE Research and Innovation Programme under the Grant Agreement No: 101083899

Disclaimer: "Funded by the European Union. Views and opinions expressed are however those of the author(s) only and do not necessarily reflect those of the European Union. Neither the European Union nor the granting authority can be held responsible for them."



Funded by  
the European Union

The authors would also like to thank the School of Engineering Sciences of TU Dresden for supplying funding for the test rig.

## REFERENCES

- [1] Y. Ahn, S.J. Bae, M. Kim, S.K. Cho, S. Baik, J.I. Lee, J.E. Cha, Review of supercritical CO<sub>2</sub> power cycle technology and current status of research and development, *Nuclear Engineering and Technology*. 47 (2015) 647–661. <https://doi.org/10.1016/j.net.2015.06.009>.
- [2] S.A. Wright, T.M. Conboy, D.E. Ames, CO<sub>2</sub>-based mixtures as working fluids for geothermal turbines., 2012. <https://doi.org/10.2172/1049477>.
- [3] U. Gampe, J. Henoch, G. Gerbeth, F. Hannemann, S. Rath, U. Hampel, S. Glos, Concept and preliminary design of a 600 °C+ sCO<sub>2</sub> test facility, in: Proceedings of the 2nd European SCO<sub>2</sub> Conference 2018, Essen, Germany, 2018. <https://doi.org/10.17185/duublico/46084>.
- [4] Md.J. Hossain, J.I. Chowdhury, N. Balta-Ozkan, F. Asfand, S. Saadon, M. Imran, Design Optimization of Supercritical Carbon Dioxide (s-CO<sub>2</sub>) Cycles for Waste Heat Recovery From Marine Engines, *Journal of Energy Resources Technology*. 143 (2021) 120901. <https://doi.org/10.1115/1.4050006>.
- [5] J. Yin, Q. Zheng, Z. Peng, X. Zhang, Review of supercritical CO<sub>2</sub> power cycles integrated with CSP, *Int J Energy Res*. 44 (2020) 1337–1369. <https://doi.org/10.1002/er.4909>.
- [6] H. Chen, W. Zhuge, Y. Zhang, H. Liu, Effect of Compressor Inlet Condition on Supercritical Carbon Dioxide Compressor Performance, in: Volume 9: Oil and Gas Applications; Supercritical CO<sub>2</sub> Power Cycles; Wind Energy, American Society of Mechanical Engineers, Phoenix, Arizona, USA, 2019: p. V009T38A012. <https://doi.org/10.1115/GT2019-90647>.
- [7] E.M. Clementoni, T.L. Cox, Effect of Compressor Inlet Pressure on Cycle Performance for a Supercritical Carbon Dioxide Brayton Cycle, in: Volume 9: Oil and Gas Applications; Supercritical CO<sub>2</sub> Power Cycles; Wind Energy, American Society of Mechanical Engineers, Oslo, Norway, 2018: p. V009T38A005. <https://doi.org/10.1115/GT2018-75182>.
- [8] G. Musgrove, S. Sullivan, D. Shiferaw, P. Fourspring, L. Chordia, Heat Exchangers, in: Fundamentals and Applications of Supercritical Carbon Dioxide (SCO<sub>2</sub>) Based Power Cycles, Woodhead Publishing, 2017: pp. 217–256.
- [9] A. de la Calle, A. Bayon, Y.C. Soo Too, Impact of ambient temperature on supercritical CO<sub>2</sub> recompression Brayton cycle in arid locations: Finding the optimal design conditions, *Energy*. 153 (2018) 1016–1027. <https://doi.org/10.1016/j.energy.2018.04.019>.
- [10] I. Ali, H. Saari, Investigating the effect of impurities on components and efficiency of the 10 MW S-CO<sub>2</sub> gas turbine power plant, *J Mech Sci Technol*. 36 (2022) 4789–4796. <https://doi.org/10.1007/s12206-022-0837-8>.
- [11] W.S. Jeong, Y.H. Jeong, Performance of supercritical Brayton cycle using CO<sub>2</sub>-based binary mixture at varying critical points for SFR applications, *Nuclear Engineering and Design*. 262 (2013) 12–20. <https://doi.org/10.1016/j.nucengdes.2013.04.006>.
- [12] S. Rath, E. Mickoleit, U. Gampe, C. Breitkopf, A. Jäger, Systematic analysis of additives on the performance parameters of sCO<sub>2</sub> cycles and their individual effects on the cycle characteristics, *Energy*. 252 (2022) 123957. <https://doi.org/10.1016/j.energy.2022.123957>.
- [13] DIRECTIVE 2014/68/EU OF THE EUROPEAN PARLIAMENT AND OF THE COUNCIL of 15 May 2014 on the harmonisation of the laws of the Member States relating to the making available on the market of pressure equipment., n.d. <https://eur-lex.europa.eu/legal-content/EN/TXT/?uri=CELEX%3A02014L0068-20140717>.



## SYSTEM ANALYSIS OF EXPERIMENTAL sCO<sub>2</sub> CYCLE SOFIA

**Daniel Kriz\***  
Research Centre Rez  
Husinec-Rez, Czech Republic  
Email: daniel.kriz@cvrez.cz

**Petr Vlcek**  
Research Centre Rez  
Husinec-Rez, Czech Republic

**Otakar Frybort**  
Research Centre Rez  
Husinec-Rez, Czech Republic

### ABSTRACT

This work describes the one-dimensional, thermo-hydraulic model of the sCO<sub>2</sub> cycle Sofia which was made within the Efekt project to investigate optimal control methods and behaviour of the cycle during its operation. This dynamic model contains all devices like turbomachinery, heat exchangers or valves and piping including heat loss, according to the concept of the 1 MWe sCO<sub>2</sub> cycle, to be realised in the site of a fossil power plant in the Czech Republic.

Model assembly and calculations are performed with the commercial Modelica-based library ClaRaPlus using the simulation environment Dymola and in combination with another Modelica-based library, UserInteraction; the real-time simulations, with some parameter changes during the calculation, are made and described in this paper.

Nominal parameters were achieved during the steady-state simulation, except the lower mass flow of sCO<sub>2</sub>. Transient simulation of power turbine start-up from standby state and results are also presented in this paper. The nominal state is achieved with the semi-automatic procedure in approx. 3 hours. The simulation results allow more detailed analyses of control methods and a better understanding of real device control and behaviour during start-up, shutdown, or other transients.

Careful manipulation with turbine valves in cooperation with the pressuriser operation was identified as crucial for optimal control of the system. Also, the initial amount of CO<sub>2</sub> in the pressuriser affects its behaviour during transients.

### INTRODUCTION

Supercritical (sCO<sub>2</sub>) cycles promise high thermodynamic efficiency and thus more effective use of the primary sources of energy. Moreover, the compactness of sCO<sub>2</sub> cycles and the possibility of combining these cycles with renewable sources of energy could support the decentralisation of the energy industry.

However, these sources of energy are unstable, and it is necessary to balance the fluctuations of power production. From the point of view of the thermal cycles, this creates a requirement for relatively quick reactions of the entire system and its control, safety, and reliability.

The Efekt project supported by the Technology Agency of the Czech Republic is being performed in CVR. The main goal of this project is the development of effective means of bulk energy storage using a sCO<sub>2</sub> cycle to convert stored thermal energy to electricity and validation of the key components or control methods of this system. The turbomachinery, such as the power turbine or the starter and main compressors, were identified as the key components to be tested on a simple recuperative sCO<sub>2</sub> power cycle called Sofia that enables testing of turbines with power up to 1.8 MWe.

The construction of effective and reliable turbomachines, as well as research of capable control strategies for the systems, are significant obstacles to the commercial use of the sCO<sub>2</sub> cycles from the technical point of view. Therefore, the experimental cycle Sofia is being performed within the Efekt project.

For a better understanding of the cycle behaviour, a one-dimensional, thermo-hydraulic model of the Sofia cycle has been prepared. The modelling approach is quite detailed and considers several features like real turbomachines characteristics, including the inertia of the rotors. Also considered are printed circuit heat exchangers (PCHE) and brazed plate heat exchangers (BPHE) with advanced heat transfer models or heat capacity of components structure, including piping.

The thermo-hydraulic model enables verification of proposed strategies for the cycle control, or its behaviour, during both normal operation and transient states. This paper describes the main components of the Sofia cycle, including the modelling approach. Furthermore, a control system proposal for the whole cycle and electric heater will be presented. The last part of this

\* corresponding author

paper presents selected results of the simulations, focused on the nominal steady state of the cycle and the power turbine start-up.

### FACILITY PARAMETERS AND LAYOUT

The Sofia facility is a recuperative Brayton cycle with a compander – the main compressor driven by its radial turbine and the power turbine. The chosen design temperature of 565 °C is a compromise of the maximum working parameters of the modern supercritical Rankine steam cycles (600 – 700 °C) and acceptable investment costs. Operational parameters of 550 °C and 25 MPa were selected, as these parameters are considered suitable even for the energy use of sCO<sub>2</sub> cycles. (Frýbort *et al.*, 2021)

The main modelled devices of the cycle are:

- Heat Supply – Electric Heater (6 MWe)
- Recuperative Heat Exchanger
- Water Cooler
- Pressuriser
- Radial Starter Compressor
- Compander – Main Radial Compressor, mechanically connected to the Radial Turbine
- Axial Power Turbine (1 MWe)

### MODELLING PIPING AND FITTINGS

These main components are connected by pipes, as shown in Figure 1. The piping, including valves, is modelled with respect to the conceptual topology and dimensions of the real cycle. The model allows calculations of the local and friction losses, as well as heat losses and heat accumulation, to the piping walls.

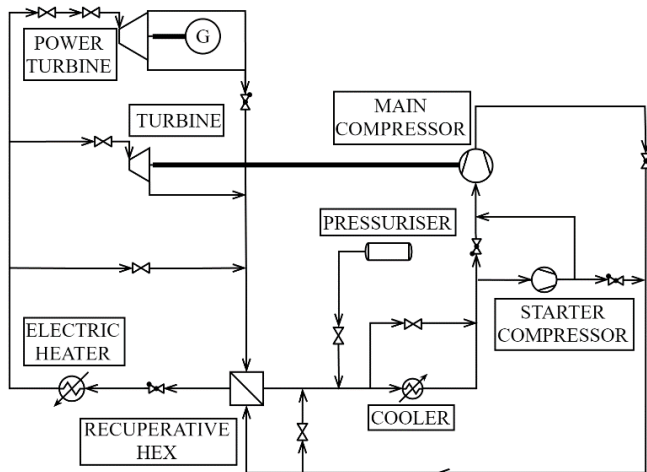


Figure 1: PFD scheme of the Sofia cycle model.

The ClaRa+ library from Dymola contains all the components needed for the pipes and fittings. The whole pipe model assembly in the Dymola environment is shown in Figure 2. One can see two walls in this figure. The first wall represents the steel wall of the pipe; the second wall represents thermal insulation. External heat losses are represented by a convective

boundary condition. The pipeline modelling is important from the standpoint of determining the amount of CO<sub>2</sub> that will fill the facility.

Integral parts of the piping are fittings like control, closing or check valves. For testing the control strategies, it is necessary to include the exact design solution of the given fittings, represented in this case by the volume and closing speed of the valve. For these purposes, the components *GenericValveVLE\_L1* and *ControlValveVLE\_L1* from the ClaRa+ library were used. These models enabled the use of characteristics of the real valves, which were obtained from the manufacturer.

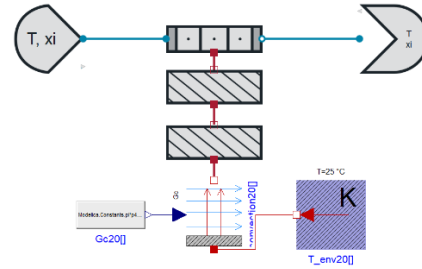


Figure 2: Pipe model assembly in Dymola. (XRG Simulation GmbH, 2022)

### HEAT EXCHANGERS

Heat exchangers are probably the biggest challenge from the modelling point of view. The four heat transfer devices in the cycle all have different designs. Within the electric heater with the shell & tube design, there are electrical heating rods instead of tubes. The recuperative HEX is designed as a printed circuit heat exchanger (PCHE), see Figure 3. The cooler in Figure 4 is designed as a brazed plate heat exchanger (BPHE). Finally, the pressuriser is a shell & tube HEX with an electric heater, but with a combination of electric heating rods and water-cooled tubes. Thermo-hydraulic models of described heat exchangers have been developed in CVR using modified components from the ClaRa+ library.

The recuperative HEX is modelled as pure counter-current PCHE with semi-circular channels. Heat transfer and pressure drop are calculated only in these channels; distribution and collection parts of the HEX are neglected. The geometry is defined by the parameters according to Meshram *et al.* (2016) and described in Figure 3.

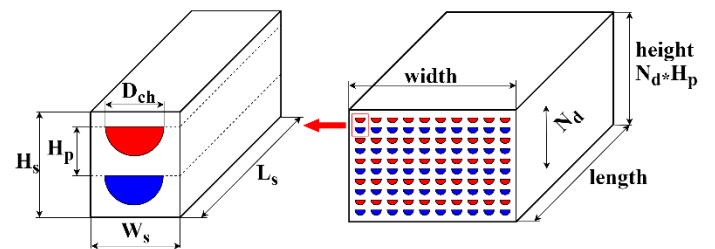


Figure 3: Description of PCHE. (Kriz, 2022)

Gnielinski equation is used for the turbulent flow convective heat transfer. It is

$$Nu = \frac{(\xi/8)(Re - 1000) Pr}{1 + 12.7\sqrt{\xi/8} (Pr^{2/3} - 1)}, \quad (1)$$

where  $\xi$  is the friction coefficient due to the modified equation

$$\xi = (1.82 \log(Re) - 1.64)^{-2}. \quad (2)$$

As shown in Table 1, heat transferred by recuperative HEX at nominal operation exceeds 8 MWt. Nevertheless, due to the microchannel design, the HEX is still relatively compact. Thermodynamic properties of supercritical CO<sub>2</sub> like low viscosity led to relatively low values of pressure drop. However, as mentioned before, distribution and collection parts of the HEX are neglected. Therefore, it is necessary to take the values of pressure drop given in Table 1 with a margin.

**Table 1:** Parameters of the recuperative HEX.

Parameter	Unit	LP	HP
Inlet temperature	°C	458	62
Outlet temperature	°C	101	313
Working pressure	MPa	8.40	25.40
Mass flow	kg/s	20.0	20.0
Pressure drop	kPa	59.91	19.96
Number of channels – one plate	-	201	201
Number of plates	-	66	66
Fluid volume	dm <sup>3</sup>	18.19	18.19
Avg. heat transfer coef.	W/m <sup>2</sup> K	3170	4120
Heat transfer area	m <sup>2</sup>	55.93	
Heat transferred	kW	8308	
HEX width	m	0.503	
HEX height	m	0.211	
HEX length	m	0.820	

Like the recuperative heat exchanger, the smallest possible dimensions are also desirable in the case of the cooler. However, river water is used as a coolant. In this case, the use of PCHE is not an ideal solution because of the higher risk of fouling and the probable higher pressure drop at the water side. Therefore, a brazed plate heat exchanger appears to be a better solution for this type of application.

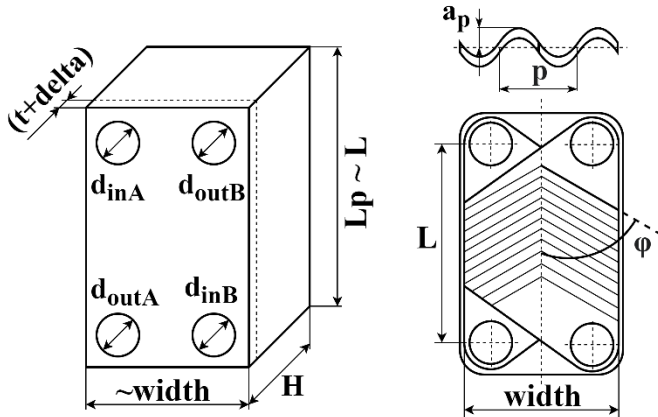


**Figure 4:** Description of BPHE. (Kriz, 2022)

The geometry of the model is shown in Figure 4. The parameters of the cooler are listed in Table 2. The modelling approach of the cooler is based on the methodology described in VDI (2010). Counter current flow is considered. Similar to the PCHE model, heat transfer and pressure drop are calculated only in the channels part. The value of this pressure drop is listed in Table 2.

**Table 2:** Parameters of the cooler.

Parameter	Unit	CO <sub>2</sub>	Water
Inlet temperature	°C	100	16
Outlet temperature	°C	30	30
Working pressure	MPa	8.00	1.10
Mass flow	kg/s	20.0	81.0
Pressure drop	kPa	24.50	101.93
Number of plates	-	380	
Number of channels	-	189	190
Fill volume	dm <sup>3</sup>	128	18.19
Overall heat transfer coef.	W/m <sup>2</sup> K	2564	
Heat transfer area	m <sup>2</sup>	94.55	
Heat transferred	kW	4747	
Width	m	0.386	
H	m	0.878	
L	m	0.875	

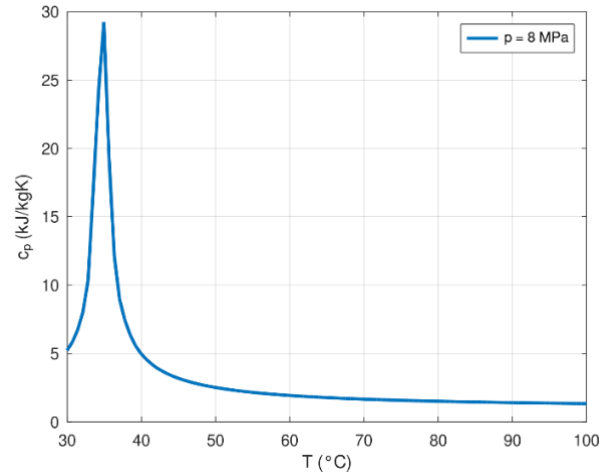


**Figure 5:** Isobaric heat capacity of CO<sub>2</sub> – temperature dependence.

Additional pressure drop in distribution and collection channels are estimated based on the similarity to flow in a circular tube. The heat transfer coefficient between plates is determined by the modified L ev eque basic equation according to VDI (2010).

$$Nu = 1.615 \left[ \left( \frac{\xi Re}{64} \right) Re Pr \frac{d_h}{L} \right]^{1/3} \quad (3)$$

and with the implementation of the Hagen number

$$2Hg = \xi Re^2 = \frac{\rho \Delta p d_h^3}{\mu^2 L_p} \quad (4)$$

has the following form

$$Nu = c_q Pr^{1/3} \left( \frac{\mu}{\mu_w} \right)^{1/6} [2Hg \sin(2\varphi)]^{1/3}. \quad (5)$$

In Table 2, it is also noticeable that the CO<sub>2</sub> temperature decreases below the critical temperature during cooling. This leads to a significant change in the thermodynamic parameters of the CO<sub>2</sub>, especially isobaric heat capacity, as one can see in Figure 5. This phenomenon has a big influence on the temperature field in the cooler, and in some cases can cause problems with pinch point. (Dostál, 2005)

The electric heater is the largest device in the cycle. As mentioned before, it is a shell & tube type, but there are electric heating rods instead of tubes for the heating medium. Various numbers of heating rods are electrically joined to two heating segments with different sizes and power. There is a set of three heating U-rods called the heating cell. It has an output power of 30 kW (10 kW per heating rod). 27 heating U-rods are joined to the heating cluster, with 270 kW of output power.

The whole heating system is divided into three tubular vessels (TOH1, TOH2, TOH3). In each of the vessels, there are two bundles of 10 heating cells and three heating clusters, i.e., 111 electric heated U-rods in each bundle with an overall power of 1110 kW. With six bundles, TS1 – TS6, we have an electric heater with a power of 6660 kW. For modelling purposes, the U-rods were replaced by 222 straight rods. This simplified geometry can be seen in Figure 6.

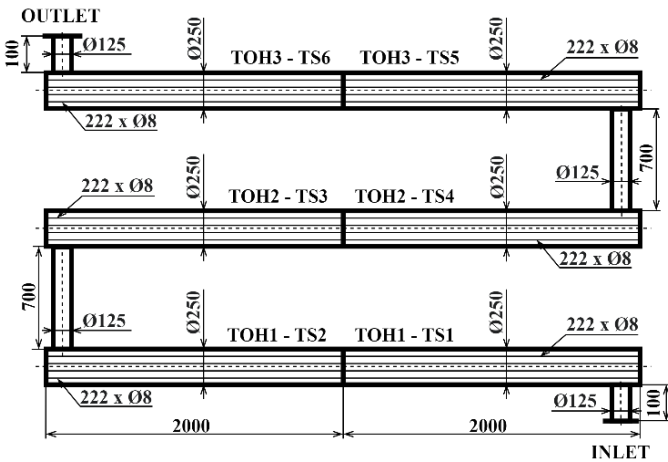


Figure 6: Simplified geometry of the electric heater.

Common semi-circular baffles for the shell & tube HEX are not used, and the longitudinal flow of CO<sub>2</sub> is considered. This approach promises to minimise the risk of the heating rods overheating due to a wake behind the semi-circular baffles. However, baffles cannot be completely omitted because they improve the stability of the heating rods.

Therefore, perforated circular plates are used instead of standard baffles. In the thermo-hydraulic model of the electric heater, no baffles are considered. The pressure drop of the electric heater in several states is determined by CFD simulation, and this is implemented in the Modelica model as a nominal parameter that is used for recalculation of the pressure drop in any other state.

The heat transfer area of the electric heater depends on a number of active heating rods that change during its operation. Therefore, several standard ClaRa+ components were modified. The component *ShellFlowVarBundleVLE\_LA* allows for calculations of heat transfer with temperature and pressure fields in the axial direction during longitudinal flow around a tube bundle. Even the amount of heat accumulated in a heating rod depends on its state. There is a larger amount of heat stored in active rods, with higher temperatures than in disabled rods. The mass of heating rods and the accumulation of heat in them is represented by modified component *CylindricalThinWall\_LA*, where active and disabled rods are distinguished.

## TURBOMACHINES

The turbomachinery, such as the power turbine, starter compressor, main compressor and its turbine were identified as the key components for the development and testing in the Sofia cycle. Development of these machines is challenging, especially from a technical point of view, due to their small size in combination with high performance. Before the Sofia cycle commissioning, it was necessary to perform some numerical studies.

Results from CFD or FEM simulations of a standalone turbomachinery or its parts can help with the optimisation of the geometry and mechanical durability. Other important outputs of the CFD simulations are the hydraulic and performance characteristics of turbomachines, which are used in the 1-D analysis of the whole cycle in Dymola.

With these simulations, it is possible to check the behaviour of turbomachines together with all the cycle devices, even during transient states. For these purposes, 1-D numerical models of a compressor and turbine were developed in CVR, based on ASME (1998) methodology and realised with Modelica code and ClaRa+ library. The model allows non-dimensional hydraulic and performance characteristics implementation. Therefore, it is possible to perform simulations in a wide range of parameters.

## REGULATION AND CONTROL STRATEGIES

There are five main control loops in the Sofia facility. The first one is pressure control at the inlet of the main, or starter, compressor. This pressure is controlled by the pressuriser. The second control loop is temperature control at the inlet of the main, or starter, compressor, provided by the water cooler and its bypass. The pressure at the outlet of the main compressor is controlled by a valve at the compander turbine inlet, which also affects the speed of the whole compander, i.e., main compressor. This pressure can also be controlled with the valve in the bypass of the turbines, which is used in some operation states. The admission temperature of the turbines is provided by the electric

heater. The control system of this facility is extremely complex and will be partly described in the next paragraph. The last control loop is the output power control of the power turbine by a control valve at the power turbine inlet. However, this control loop was not yet used in simulations.

The electric heater described in the previous chapter has several heating elements with variable heating power. In every heating bundle, there are some proportional controlled and some two-position controlled heating cells (a set of three heating U-rods with a maximum power of 30 kW). Moreover, there are some two-position controlled heating clusters (a set of 27 U-rods with a maximum power of 270 kW). Each of the described heating segments is used for outlet temperature regulation. Activation of the specific heating segment depends on boundary conditions, like the mass flow of CO<sub>2</sub>, and on the location of the previously activated heating segment. This approach will provide uniform heating of the filling in all the vessels of the heater. At the same time, the dependence on the mass flow reduces the risk of overheating certain parts of the electric heater.

### THE CYCLE MODEL BENCHMARKS

All of the described sub-models of components and control loops form the overall model of the Sofia cycle. The first test of the model is a steady-state simulation of the nominal operation state that will prove interactions between individual components and the stability of the initialisation setup. It is also the first opportunity to see how the control loops react to small changes in controlled parameters. The results of the simulation were compared with design parameters, as shown in Table 3.

**Table 3:** Nominal parameters of Sofia facility.

	Inlet			Outlet	
	T °C	P MPa	m kg/s	T °C	p MPa
COMPRESSOR C.	30	8.00	20.0	62	25.50
RECUP HEX HP	62	25.47	20.0	312	25.32
EL. HEATER	312	25.26	20.0	550	25.16
TURBINE C.	550	25.06	6.5	448	8.50
POWER TURBINE	550	25.07	13.5	468	8.50
RECUP HEX LP	461	8.41	20.0	100	8.26
COOLER	100	8.23	20.0	30	8.19

From the following results of the steady-state simulation in Table 4, it can be seen, that the nominal mass flow was not reached. This was caused by the design characteristics of the turbomachines and their mutual interaction. According to the CFD characteristics, the compander turbine and power turbine are slightly more effective and need a lower mass flow and pressure ratio to achieve the required performance. This leads to compander turbine throttling and to a reduction of the overall mass flow in the cycle.

**Table 4:** Results of the steady-state simulation.

	Inlet			Outlet	
	T °C	p MPa	m kg/s	T °C	p MPa
COMPRESSOR C.	31	8.00	17.6	62	25.29
RECUP HEX HP	62	25.25	17.6	314	25.32
EL. HEATER	314	25.13	17.6	550	25.08
TURBINE C.	548	20.26	5.1	449	8.25
POWER TURBINE	550	24.98	12.5	460	8.36
RECUP HEX LP	457	8.24	17.6	99	8.14
COOLER	98	8.10	17.6	31	8.09

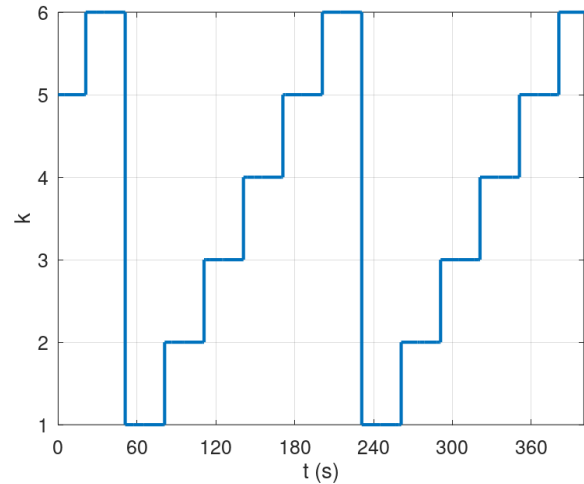


**Figure 7:** Sampling for heating segments control.

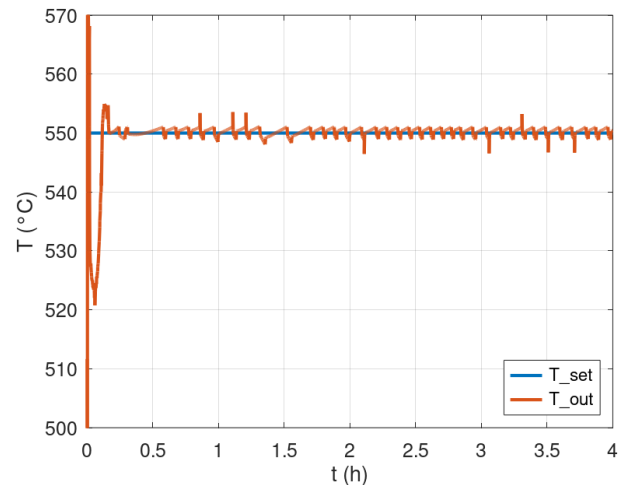


**Figure 8:** Nominal outlet temperature of the electric heater.

The electric heater output temperature can be seen in Figure 8. A large discontinuity at the beginning of the simulation was caused by initialisation. Only two-position control of the electric heater was active during this simulation. Therefore, the output temperature varied within certain limits. These limits were different for heating cells ( $\pm 1$  °C offset) and for heating clusters ( $\pm 10$  °C offset). The wider tolerance for heating clusters



prevented excessive oscillations. The heating segments were triggered at different times across bundles. This was provided by the control sequence, see Figure 7, where the  $k$  means activated bundle (TS1 – TS6). Each bundle regulated the output temperature for 30 seconds. Then it was replaced with the next bundle, according to sequence, to prevent local overheating. The rest of the time bundles held a constant power from the last activation.

As mentioned before, the pressure at the compressor inlet is controlled by the pressuriser. It is a tempered vessel filled with CO<sub>2</sub>. If there is low pressure at the inlet of the main compressor, the pressuriser heats the fluid inside. A specific volume of the fluid will increase and cause the pressure to increase. Alternatively, if the pressure is too high, the fluid in the pressuriser will be cooled and cause the reverse effect. Too large pressure fluctuations do not occur during a normal operation, and temperature in the pressuriser changes minimally, as one can see in Figure 9.

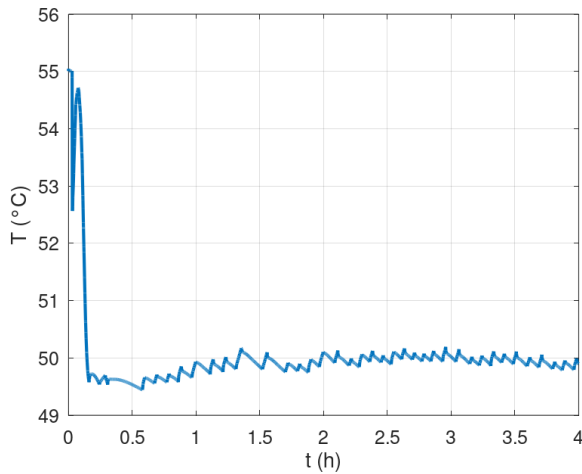


**Figure 9:** Temperature inside the pressuriser.

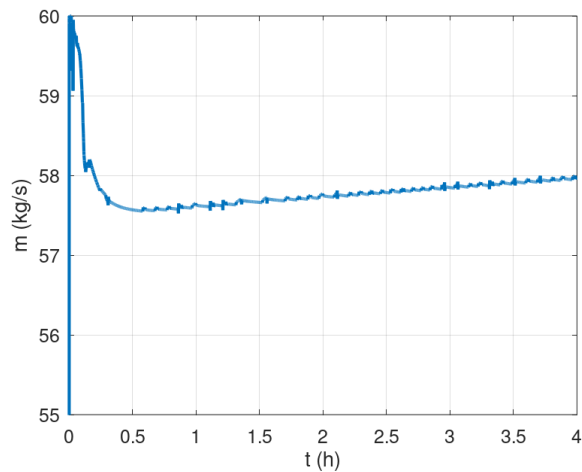


**Figure 10:** Water mass flow in the cooler.

In this case, the inlet temperature of the compressor was controlled by mass flow rate regulation of the cooling water,

which is shown in Figure 10. It is also possible to control this temperature with a bypass of the Cooler for specific operation states. As one can see, the water mass flow is not completely steady, because the CO<sub>2</sub> output temperature from the cooler did not reach the setpoint of 30 °C yet. It has offset about 1 °C but changes slowly. Therefore, in this case, the state of the cycle can be evaluated as a steady state despite a slight increase in water mass flow.

According to the simulation, the power turbine produces about 1200 kW of output power during the nominal operation. The power consumption of the main compressor driven by its turbine ranges around 550 kW. The rotational speed of the whole compander is approx. 66,000 RPM.

### RESULTS OF TRANSIENT SIMULATION

This thermohydraulic model is mainly created for research on the behaviour of the cycle during transient states, such as during start-up or shutdown. One of the tasks during the start-up procedure is the power turbine start-up. This can only be done if the compander turbomachinery works independently of the starter compressor and if there are some excess power and mass flow that can be used to drive the power turbine. This specific “standby” or “initial” state was determined by previous calculations and simulations. In this case, the power turbine start-up is provided by a semi-automatic control system. Some parameters are program-controlled, but several parameters, like valves opening or temperature setpoint, are controlled manually. This approach will most likely even be used for operating the real facility. In *Dymola*, the library *UserInteraction* is used for this type of operation. It allows the parameters of selected components to be changed during the simulation.

Parameters in the cycle in this standby state can be seen in Table 5. The main compressor must provide a sufficient mass flow for both the compander and the power turbine. It is obvious that if the power turbine is not operating, an excess mass flow rate must be diverted with a bypass. Therefore, the first operation during the power turbine start-up is a partial closure of the bypass valve and a partial opening of the valve at the inlet of the power turbine.

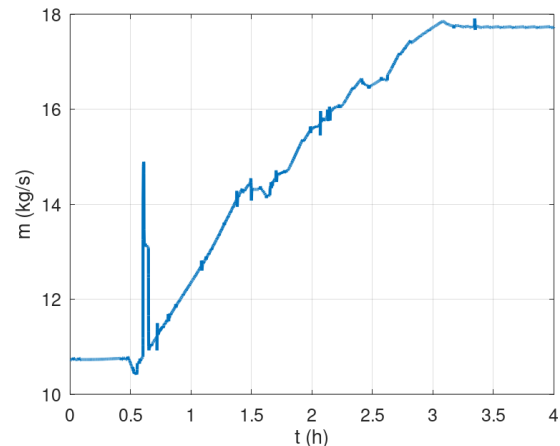


**Figure 11:** The overall mass flow rate development during the power turbine start-up.



In **Figure 11**, from 0.5–0.75 h, it can be seen, that the valve operations caused a temporary increase in the mass flow rate in the cycle. Valve cooperation, according to **Figure 12**, was not optimal; the power turbine valve opened a little bit faster and the pressure at the outlet of the main compressor decreased, but the power of its turbine was not changed. According to the main compressor characteristics, this leads to a higher mass flow rate.

**Table 5:** Standby (initial) state of the Sofia cycle.

	Inlet			Outlet	
	T °C	p MPa	m kg/s	T °C	p MPa
COMPRESSOR C.	28	8.02	10.9	40	14.51
RECUP HEX HP	40	14.49	10.9	161	14.48
EL. HEATER	161	14.45	10.9	300	14.38
TURBINE C.	296	13.02	3.8	257	8.11
POWER TURBINE	-	-	-	-	-
TURBS. BYPASS	298	14.36	7.1	286	8.11
RECUP HEX LP	276	8.10	10.9	55	8.07
COOLER	55	8.06	10.9	28	8.05

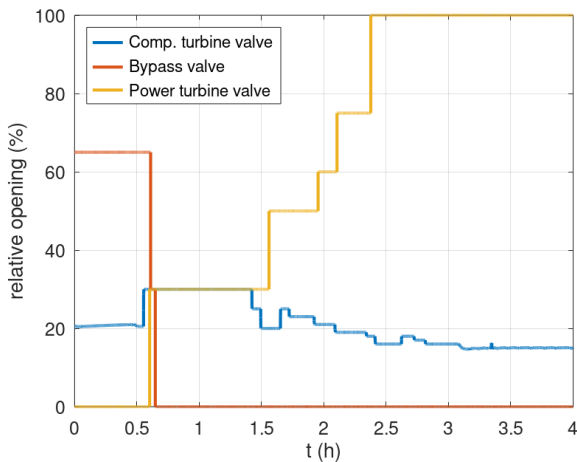


**Figure 12:** Relative opening of involved valves.

After this critical step, it is necessary to gradually reach the nominal parameters in the cycle. Increasing the outlet temperature from the electric heater in combination with manual control of the compander rotational speed using the compander turbine control valve proved to be a suitable way for reaching the nominal parameters. As one can see in **Figure 13**, a setpoint of the temperature was changed manually several times, and the electric heater control system automatically held the required value. According to the sampling in the electric heater control system, various heating segments are activated across the electric heater at different times. For example, **Figure 14** shows how the power of two different heating segments (cell and cluster) in two different bundles is changing during the operation.

As the power of the compander increases, the opening of the valves may not always correspond (**Figure 12**), and there can be a lack of CO<sub>2</sub> in low-pressure parts of the cycle. This results in a decrease of pressure at the inlet of the main compressor, and it

must be balanced by an increase in temperature in the pressuriser, see **Figure 15**. As the temperature increases, the specific volume of CO<sub>2</sub> also increases, which leads to an increase in pressure thus forcing the CO<sub>2</sub> out of the pressuriser to the Low-pressure side, as shown in **Figure 16**, which describes the development of the mass of CO<sub>2</sub> in the cycle during the start-up. The distribution of the volume and mass of CO<sub>2</sub> in the cycle is described in **Table 6**.

**Table 6:** Volume and mass of CO<sub>2</sub> in the cycle

		HP side	LP side	Pressuriser	Overall
Volume	dm <sup>3</sup>	1000	887	659	2546
Mass - start	kg	218	194	110	522
Mass - end	kg	245	167	110	522

However, the pressuriser has limited possibilities to handle these fluctuations due to the maximum operating temperature of 130 °C and a power of 15 kW. Therefore, the operation of valves must be carefully done in concert with the temperature development in the pressuriser. This temperature, in context with pressure at the inlet of the main compressor, is shown in **Figure 15**.

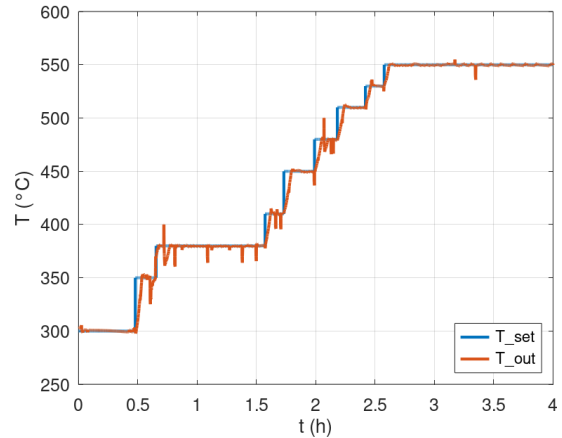


**Figure 13:** The electric heater outlet temperature development.

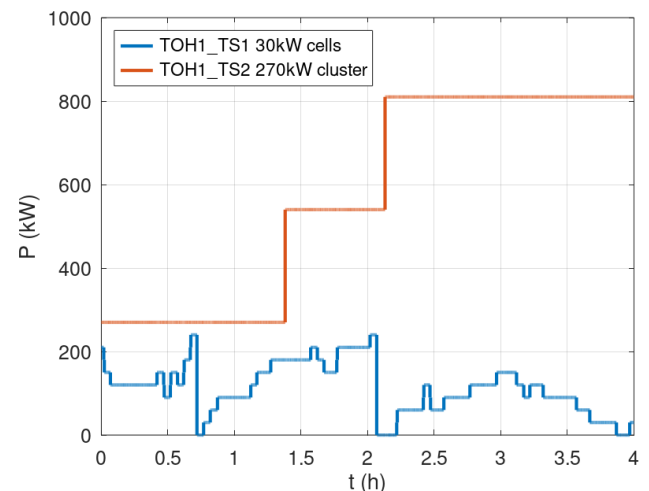


**Figure 14:** The power of selected heating segments.

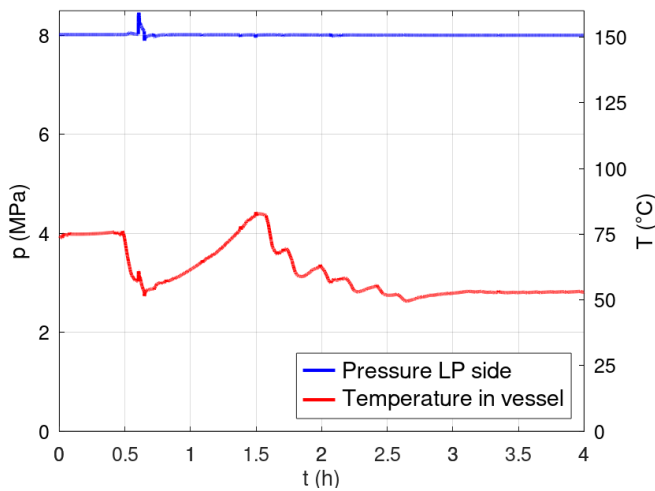


**Figure 15:** Temperature in the pressuriser and the pressure at the inlet of the main compressor.

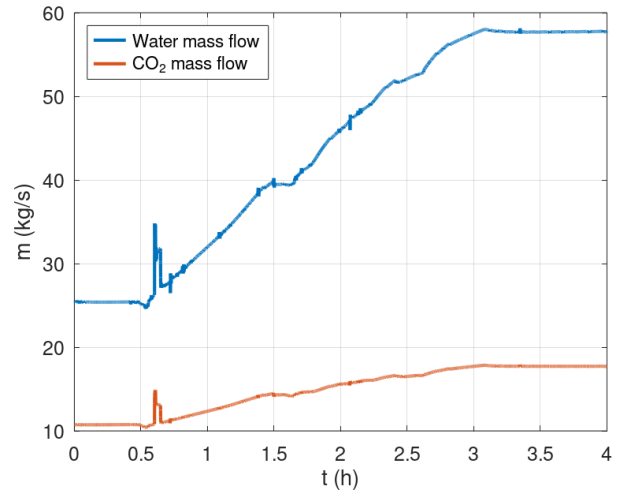


**Figure 17:** Cooling water and CO<sub>2</sub> mass flow.

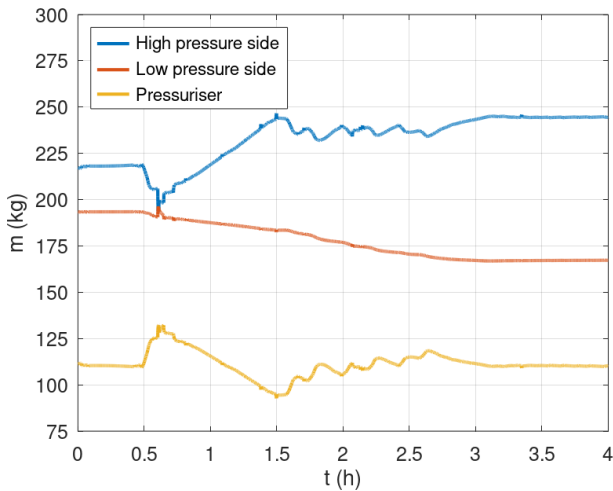


**Figure 16:** Mass of the CO<sub>2</sub> in the cycle

As in the previously described steady-state simulation, the inlet temperature of the main compressor was controlled automatically by regulation of the cooling water mass flow. Of course, more amount of CO<sub>2</sub> requires more amount of cooling water with a constant temperature. Therefore, increases during the simulation, as shown in Figure 17.

The increasing temperature in the system causes a specific volume change that leads to some pressure increase. At the same time, this pressure increase leads to the higher power of the compander, and this leads to another pressure and mass flow increase. Once again, increasing the temperature in the system was identified as the key part of the control. A throttling of the compander turbine requires only small interventions during this kind of start-up and is important mainly for the pressure balancing in low-pressure parts of the cycle. As shown in Figure 18, the main compressor outlet pressure increases by approx. constant gradient to the nominals.

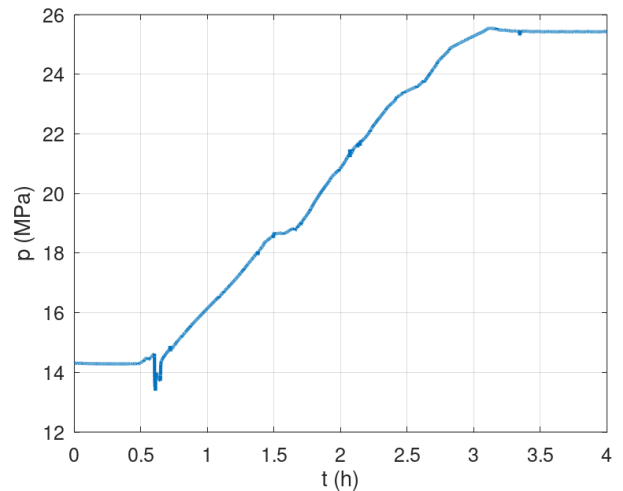


**Figure 18:** Main compressor outlet pressure.

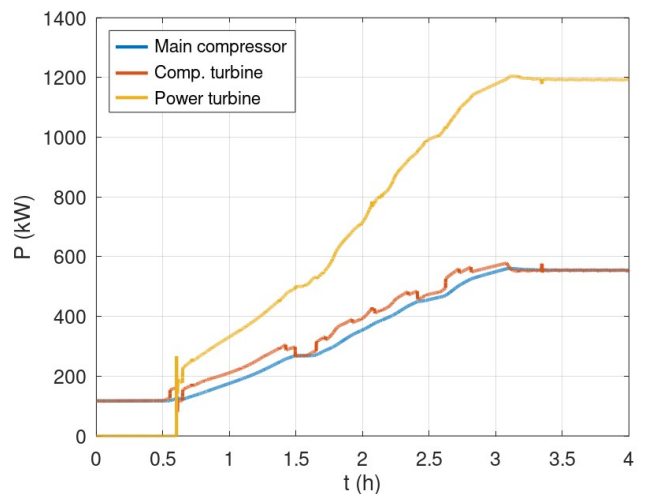


**Figure 19:** The power of turbomachines.

Finally, Figure 19 shows the power development of the turbomachines. The curves of the main compressor and its turbine overlap, according to mechanical connection. The power turbine started at zero power and gradually achieved the nominal power of approx. 1200 kW. During the whole simulated transient, the power turbine is in phase with the generator, and it has a constant, nominal rotational speed. As the admission pressure approached the nominal pressure, the automatic control of the compander turbine valve was triggered; from that moment, the cycle was controlled completely automatically.

## CONCLUSION

Dymola software with ClaRa+ library, based on Modelica code, has been used in CVR for a long time; several numerical models created in it were experimentally verified at sCO<sub>2</sub> facilities by CVR or by its partners. This proves the usability of the mentioned software tools for these types of applications.

The results of the simulations can, therefore, be used with some certainty, even if the Sofia cycle is not yet in operation. The ability to test turbines with power up to 1.8 MWe enables the Sofia cycle to become the key facility for future commercial applications of the sCO<sub>2</sub> cycles. However, the determination of the optimal control strategies and the makeup of the main components are some of the more challenging issues.

For preliminary studies and systemic behaviour analyses of the Sofia cycle, the described 1-D thermo-hydraulic model was built within the Efekt project. All of the key components were created with respect to the concept designs of the real components. For example, complex models of the PCHE and BPHE heat exchangers were prepared, and non-dimensional turbomachines with characteristics determined by CFD simulations were used. Also, the control system of the electric heater, which is the largest facility in the Sofia cycle, was designed. Many steady-state and transient simulations were performed to support the development of the large-scale testing facility. Selected simulations - nominal steady state and power turbine start-up, were described in this paper to show the capabilities of the numeric model. Careful manipulation with turbine valves in cooperation with the pressuriser operation was identified as crucial for optimal control of the system. Also, the initial amount of CO<sub>2</sub> in the pressuriser affects its behaviour during transients. Work on the numerical model continues. There is still some room for optimisation, for example, a more detailed model of the power turbine and its equipment or control loops including delays, etc. However, the results of the performed simulations are already aiding the Sofia cycle realisation.

## NOMENCLATURE

BPHE	Brazed Plate Heat Exchanger
C	Compander
$c_q$	Coefficient for Nusselt Number Calculation (-)
CVR	Research Centre Rez
$\Delta p$	Pressure Drop (kPa)
$d_h$	Hydraulic Diameter (m)
e	Electrical
$\varphi$	Wave Angle of Inclination (°)
HEX	Heat Exchanger
Hg	Hagen Number (-)
HP	High-Pressure Side
$\xi$	Friction Coefficient
L, L <sub>p</sub>	Length of the Plate (m)
LP	Low-Pressure Side
$\mu$	Dynamic Viscosity (Pas)
$\mu_w$	Dynamic Viscosity at Wall (Pas)
Nu	Nusselt Number (-)
PCHE	Printed Circuit Heat Exchanger
Pr	Prandtl Number (-)
Re	Reynold Number (-)
$\rho$	Fluid Density (kg.m <sup>-3</sup> )
sCO <sub>2</sub>	Supercritical Carbon Dioxide
t	Thermal, Time (-, h)
TACR	Technology Agency of the Czech Republic

## ACKNOWLEDGEMENTS

This work was supported by TACR THETA2, project no. TK02030059 (Efekt).

## REFERENCES

- [1] ASME (1998) 'Performance Test Code on Compressors and Exhausters: An American National Standard'. New York: ASME.
- [2] Dostál, V. (2005) 'A supercritical carbon dioxide cycle for next generation nuclear reactors /', 154.
- [3] Frýbort, O. *et al.* (2021) 'Sofia – sCO<sub>2</sub> facility for supercritical Brayton cycle research', *4th European sCO<sub>2</sub> Conference for Energy Systems: March 23-24, 2021, Online Conference*. Edited by D. Brillert, pp. 185–193. Available at: <https://doi.org/10.17185/dupublico/73942>.
- [4] Kriz, D. (2022) *Thermodynamic cycles working in supercritical region*. Czech Technical University in Prague.
- [5] Meshram, A. *et al.* (2016) 'Modeling and analysis of a printed circuit heat exchanger for supercritical CO<sub>2</sub> power cycle applications', *Applied Thermal Engineering*, 109, pp. 861–870. Available at: <https://doi.org/10.1016/J.APPLTHERMALENG.2016.05.033>.
- [6] VDI (2010) *VDI Heat Atlas*. Berlin, Heidelberg: Springer Berlin Heidelberg. Available at: <https://doi.org/10.1007/978-3-540-77877-6>.
- [7] XRG Simulation GmbH (2022) 'ClaRaPlus'. Hamburg: XRG Simulation GmbH.

## DYNAMIC SIMULATION AND EXPERIMENTAL VALIDATION OF A 35 MW HEAT PUMP BASED ON A TRANSCRITICAL CO<sub>2</sub> CYCLE

**Leonhard Wolscht\***

MAN Energy Solutions Schweiz AG  
Zurich, Switzerland  
Email: Leonhard.wolscht@man-es.com

**Kai Knobloch\***

Technical University of Denmark  
Copenhagen, Denmark  
Email: kaikn@dtu.dk

**Emmanuel Jacquemoud**

MAN Energy Solutions Schweiz AG  
Zurich, Switzerland

**Philipp Jenny**

MAN Energy Solutions Schweiz AG  
Zurich, Switzerland

### ABSTRACT

Replacing the baseload providers on the energy market with decarbonized renewable solutions increases frequency dynamics on the grid. In order to handle the concomitant risks and chances linked with this change of paradigm between energy producers and consumers, complex dynamic models are required to optimize energy management strategies. Industrial transcritical carbon dioxide (CO<sub>2</sub>) heat pumps, such as the one developed by MAN Energy Solutions Schweiz AG (MAN ES), offer a proven solution for the decarbonization of the district heating sector. Furthermore, they are associated with pathways to increase the usage of this solution for sector coupling applications. This work presents a detailed Modelica model of the high-temperature CO<sub>2</sub> heat pump, focusing on the thermodynamic states of the refrigerant during load variations of the system. In a consecutive step, the model is validated against testbed data of a heat pump from MAN ES with over 35 MW heat supply and a lift from 40 to 100 K. The model results match the testbed data with an accuracy of over 95 % and demonstrate a full coverage of the performance map minimum to maximum speed, providing water-side supply temperatures of 50 to 109 °C. Realistic dynamics in fast load balancing operation are demonstrated where power consumption was varied by 80 % compared to maximum power within 30 s. Models of this kind are essential for an accurate prediction how decarbonized energy networks react by linking electricity and heat supply together. These predictions are ultimately useful to upgrade or optimize complex control strategies.

### 1. INTRODUCTION

Three-quarters of the emissions that have pushed global average temperatures 1.1 °C higher since the pre-industrial age stem from the energy sector [1]. Taking into consideration that the provision of heat for homes and industry accounted for more

than half of the total energy consumption in 2021 [2], making it the largest energy end-use, throws into sharp relief the significance of sustainable heat supply for a transition towards a carbon-neutral future [3]. In this context, district heating networks receive particular attention from cities and communities which are leading the energy transition and are increasingly replacing conventional fossil-based heat plants with large-scale heat pumps [4]. Large-scale industrial heat pumps represent an emerging solution for future district energy networks and sector coupling, not only providing heat but also having the potential for cooling applications and ancillary services on the electric grid.

Heat pumps are usually classified according to their working fluid, heat source, temperature level, and physical working principle. Following the work from Lorentzen in 1994 [5], an increasing amount of work investigated CO<sub>2</sub> as a natural refrigerant with low global warming potential, flammability, and toxicity [6]. While large temperature glides in the heat source increase the potential of zeotropic mixtures due to their non-isothermal phase change [7], the high transcritical temperature glide in the gas cooler makes CO<sub>2</sub> particularly suitable for large temperature differences in the heat sink, for example for domestic hot water heating [8]. Unlike ammonia (NH<sub>3</sub>) based heat pumps, CO<sub>2</sub> heat pumps can easily achieve sink temperatures above 90 °C and up to more than 130 °C, ideally with heat sink inlet temperatures not too far above the relatively low critical temperature of 31 °C. Moreover, the high volumetric heat capacity of CO<sub>2</sub> allows the use of compact compressors and heat exchangers (HEX) [9]. Besides, using a natural refrigerant like CO<sub>2</sub> for large scale industrial systems reduces environmental and operating risks as well as capital costs compared to synthetic refrigerants or widely used NH<sub>3</sub>.

As elaborated in a survey amongst 25 Danish operators and manufacturers of large-scale heat pumps [10], more than 25 %

\* joint first and corresponding author(s)

of the faults during operation are related to the compressor, accounting for the largest share overall and making it the most crucial component of the heat pump system. Additionally, the survey highlights that 38 % of the considered heat pumps are already operating electricity price driven, as well as partly providing ancillary services based on agreements with the utilities.

In conclusion, the key design factors for a district heating heat pump are the selected working fluid and the compressor component. With a focus on these key factors, i) the demonstration of a large-scale system testing with ii) a suitable dynamic model for both, control system and energy management concept, is required. This work presents the dynamic simulation of an industrial high-temperature CO<sub>2</sub> heat pump validated with latest full-scale testbed data from MAN ES.

### 1.1 Dynamic heat pump modeling

While the first dynamic modeling of heat pumps dating back to the 1980s was using lumped parameter models [11], distributed parameter models, for example, to investigate the dry evaporator for control purposes [12], emerged one decade later.

Already in 1995, Vargas et al. used a mathematical model for a heat pump operating with a variable-speed compressor in a transient regime to propose a closed-loop control (feedback control) instead of the traditional on-off control [13]. Since then, dynamic modeling of heat pumps and their control gained track, ranging from empirical compressor models in heat pumps [14] and performance maps for the entire heat pump [15] to various characteristic maps used to describe each compressor/expander stage individually [16]. However, the ability to provide ancillary services through load variation has only been tested with rapid dynamics on a small scale (kW-scale in seconds [17]) or with moderate dynamics on medium scale (100 s of kW in 1 to 3 minutes [18]).

A large variety of programming and modeling languages is generally used for dynamic modeling of heat pumps, such as Amesim [19], Fortran [9], TRNSYS [20], and Modelica/Dymola [21]. Recently, Modelica based object-oriented model libraries and their application come to the fore due to the availability of commercial simulation environments, with linearization remaining a numerically advantageous and required procedure [22]. Moreover, seminal approaches such as hardware-in-the-loop test benches [23] and reinforcement learning for control optimization [24] seem to have found their common ground in Modelica. Despite the latest advancements, current literature lacks validation on a large scale and for fast operational changes. Dynamic heat pump models are required to fill this gap and are crucial for accurate prediction and design of a variety of emerging application cases including the combination with cold [25] and/or hot [26] thermal storages that could even be used in a successive step for the reconversion to electricity [27].

Figure 1 offers an overview of a general methodology for model-based simulations with the steps presented in this work marked in red.

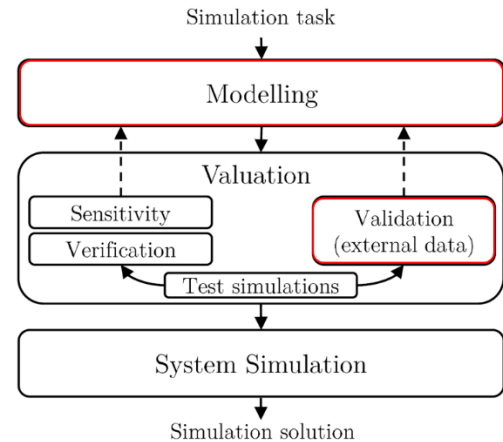


**Figure 1** General modeling methodology. In red the steps presented in this work.

After the introduction in section 1, section 2 provides background on the heat pump unit (HPU) layout used for the experimental validation. The modeling part is elaborated on in section 3. Experimental data from a testbed is used to validate the dynamic model in section 4. A general conclusion and an outlook are given in section 5.

## 2. SYSTEM DESCRIPTION

### 2.1. HPU Design and Experimental Setup

The HPU layout investigated in this work is a CO<sub>2</sub> transcritical heat pump cycle. Based on the schematic flow diagram in Figure 2, the main components employed and the thermodynamic cycle are illustrated in Figure 3. The multi-stage HOFIM™ radial turbo-compressor (A) brings the CO<sub>2</sub> from a gaseous (1) to a supercritical state (2). In the hot heat exchanger (B), also referred to as the heat sink HEX, heat is transferred to the hot consumer. Still in a supercritical state (3), the CO<sub>2</sub> enters either the turbo-expander (C) or the expander bypass valve (D) where it is expanded into a liquid state (4). A second expansion into the two-phase region takes place across the expansion valve (E). Exiting the expansion valve, the CO<sub>2</sub> mixture at low temperatures (5) is evaporated by heat transfer with a cold consumer through the evaporator heat exchanger (F), also referred to as the heat source HEX.

The core component of the HPU is the high-speed, oil-free integrated motor HOFIM™ compressor which is more compact than conventional compressors, hermetically sealed, and equipped with magnetic bearings. The variable frequency drive allows continuous performance variation over a wide speed range without a gearbox. The motor is cooled with the process medium and reintegrates thermal motor losses into the process.

The selection of both HEXs is mainly determined by the external consumer circuits. The control valves D and E, however, have to be designed to match the turbo-expander. Both valves provide control flexibility to secure that the turbo-expander remains in a single-phase condition and within its pressure-ratio and flow limitations independent from the compressor operation.



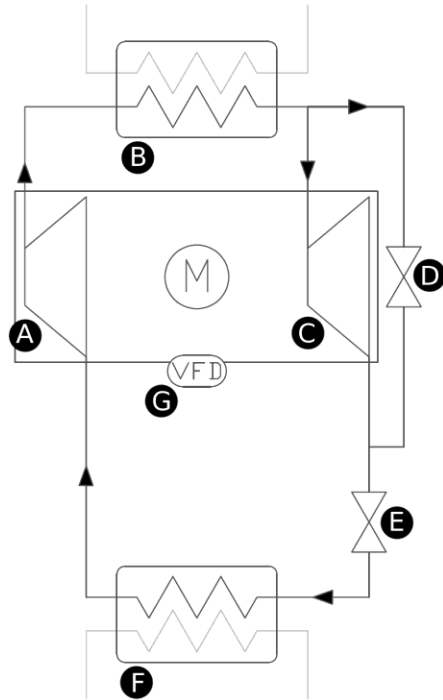


**Figure 2:** Flow diagram of the HPU. (A) turbo-compressor; (B) hot HEX; (C) turbo-expander; (D) expander bypass valve; (E) expansion valve; (F) evaporator HEX; (G) variable frequency drive.

In 2022, a full-scale HPU prototype was built by MAN ES and tested under various operating conditions. Table 1 gives an informative overview of the process parameters applicable for this kind of experimental setup. Test results have been used to validate the simulation model introduced in Section 4. A picture of the central part of the test setup with the HOFIM™ is shown in Figure 4. The heat sink was integrated using a full-scale printed circuit HEX unit [28] short-circuited with the heat source over several parallel shell-and-tube HEX connected to a water-glycol closed cooling loop. Any surplus of heat was extracted from the water-glycol loop with open air-to-water cooling tower. Redundant piping has been installed for high process flexibility for motor cooling gas flows and is more complex than Figure 2 shows.

For data acquisition, 256 industrial-grade sensors were integrated into the loop, including more than 200 temperature and pressure sensors. Each of the measurement points has been equipped redundantly with double or four-fold sensors to

**Table 1:** HPU testbed process parameters.

Parameter	Unit	Max. Value
Motor Active Power	MW <sub>el</sub>	10.5
Heating Duty	MW <sub>th</sub>	35
Cooling Duty	MW <sub>th</sub>	25
CO <sub>2</sub> Pressure	bar	140
CO <sub>2</sub> Temperature	°C	130
Min. CO <sub>2</sub> Evaporation Temperature	°C	-2

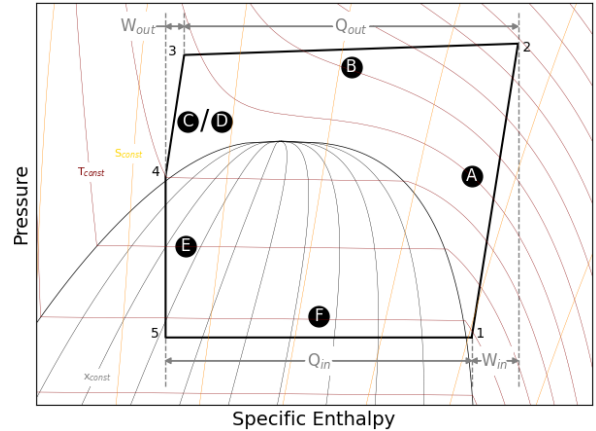


**Figure 3:** State diagram of CO<sub>2</sub>. (1) Superheated gas at compressor suction; (2) hot supercritical state at compressor discharge; (3) cooled supercritical CO<sub>2</sub> at expander inlet; (4) liquid state at expander outlet; (5) subcooled liquid and gas mixture (two-phase) at evaporator inlet.

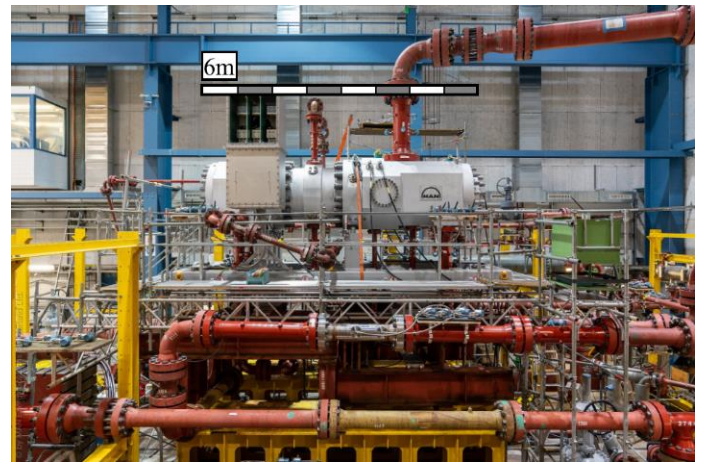


**Figure 4:** Picture of the turbomachinery part of the testbed setup in MAN ES facility, incl. scale.

minimize measurement errors and risks of hardware failure. The process data is collected via OPC Unified Architecture [29] and is continuously recorded with a sample time of 0.5 Hz.

## 2.2. Figures of Merit

Turbomachines are described by their characteristic performance maps. This work uses the pressure ratio  $\Pi = p_{\text{outlet}}/p_{\text{inlet}}$  as the work coefficient and the volumetric flow  $\dot{v}$  as the flow coefficient spanning a map shown in Figure 6. The performance of both, the compressor and expander, can be expressed in a single point each in their respective characteristic, yielding a compressed comparative value pair containing information on the process conditions at points 1, 2, 3, and 4 of Figure 3 combined. The turbomachine characteristics in this work are based on volume flow instead of reduced mass flow since the compressor is a volumetric machine.



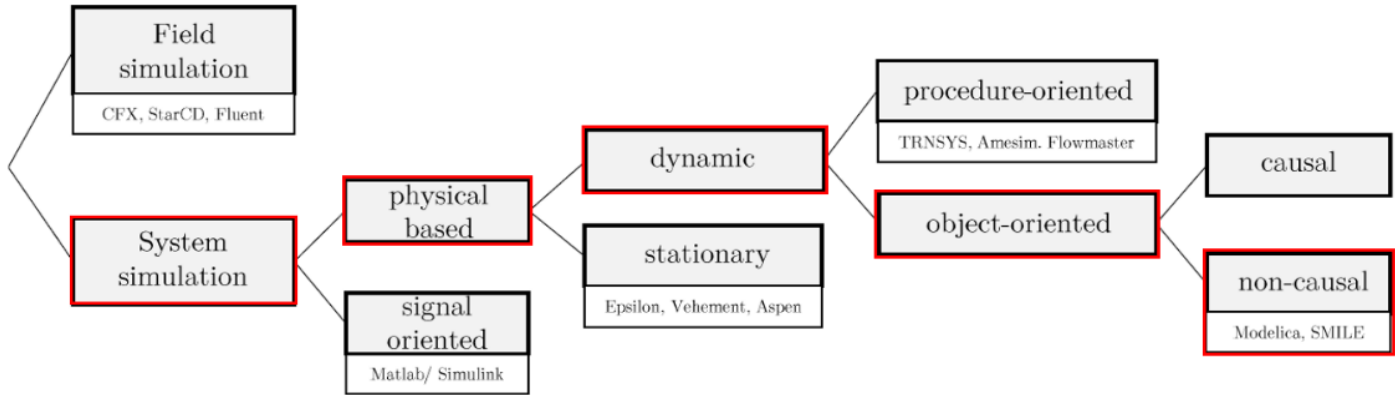


**Figure 5:** Categorization of simulation approaches (adapted from [30]). In red Modelica as the programming language used here.

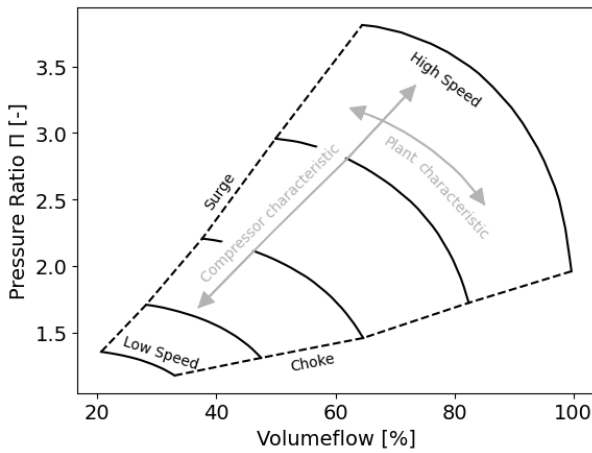


**Figure 6:** Exemplary characteristic map of a compressor with different lines of constant speed spanning between the choke and surge limit.

Nevertheless, the pressures and temperatures, before and after the compressor, as well as the mass flows at the compressor suction and the motor active power – which is the actual shaft power after the VFD - are more suitable to identify dynamics and shall be referred to as evaluation parameters.

The coefficient of performance (*COP*) is defined based on Figure 3 as

$$COP = \frac{Q_{Out}}{W_{In} - W_{Out}} .$$

The values in Table 1 indicate that the approximate *COP* of the investigated system is roughly 3.3.

For each measured and calculated testbed value, an uncertainty analysis has been performed in order to evaluate the reliability of data and maximum achievable validation accuracy. The acquired data with a sampling time of 0.5 Hz has been grouped and analyzed in sets of one minute. Within this minute, the standard deviation based on mean, minimum, and maximum has been computed and a relative uncertainty to the average data value was calculated. For each test operation, the maximum

relative uncertainty of the related minutely datasets has been selected as a maximum confidence interval.

### 3. MODELLING

#### 3.1. Language and environment

According to the classification by [30], the HPU model is categorized as a non-causal, object-oriented, dynamic, physical-based system simulation, see Figure 5.

The applied object-oriented programming language Modelica is widely used for modeling physical systems. The system components are described by differential-algebraic equations and stored in libraries. The result of the translation is an equation system that is solved by a selected algorithm. One main advantage of Modelica is the multi-domain modeling allowing for the simultaneous modeling and simulation of electric, thermal, mechanic, hydraulic, and pneumatic components. The process-relevant parameters like pressure, temperature, or composition are transferred by connectors between objects. In this context, the acausality of Modelica is worth mentioning. Compared to signal flow oriented software systems like Matlab/Simulink, system circuits are generated faster and in a clear manner. However, some circuit rules need to be considered [31].

In contrast to the programming language Modelica, the simulation environment Modelon Impact used in this work is not open source. In addition to the Modelica Standard Library [32], the modeling in this work is supported by the commercial libraries VaporCycle, ThermalPower, and ThermoFluidPro from Modelon [33].

#### 3.2. Implementation

In preparation for modeling the full HPU, all single components have been validated individually against available datasheets from manufacturers. The full-loop HPU has been composed of the described models in a structure as displayed in Figure 7. Table 2 lists the auxiliary models used, including their underlying physics and associated limitations or advantages, while the main components are explained below.

### 3.2.1. Medium Model

The media model is based on a spline-based table lookup (SBTL) method. The simulation is much faster compared to the Helmholtz approach which calculates the media properties from equations of state. Especially the stability along the transition between single- and two-phase regions gives the advantage to the table-based approach. Increased speed is achieved by fast access to pre-calculated properties defined in the spline coefficient tables computed with the REFPROP database [34]. Spline coefficient tables are loaded as external objects at the initialization of a simulation. In general, property functions from SBTL (as well as their first derivatives and inverse functions) are continuous and numerically consistent with each other, hence used for various computationally extensive process simulations whenever conventional multi-parameter equations of state are unsuitable due to their computing time consumption, as extensively described by Kunick [35].

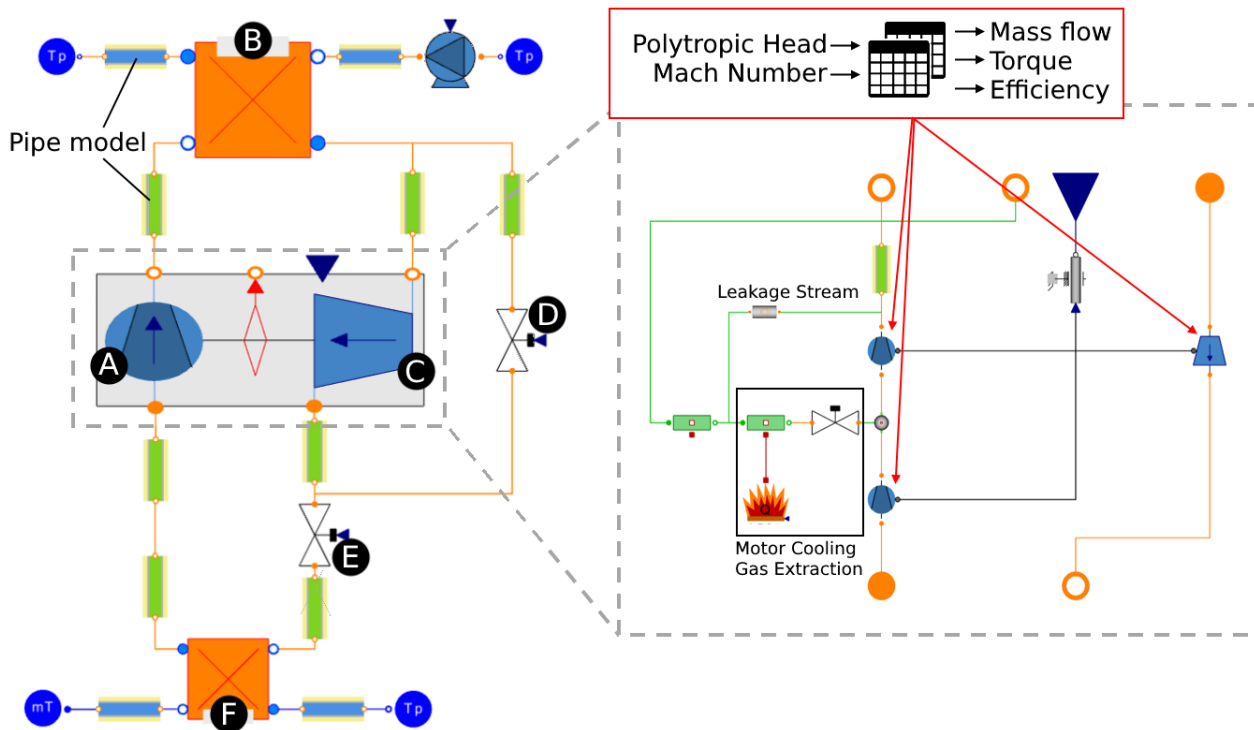
### 3.2.2. Turbomachine Model

The main focus lies on the implementation of the turbomachine as it is the core of the heat pump system. Since the compressor, expander, and motor are physically one unit, there is an individual model for the whole unit. This allows a simple exchange of the turbomachine from the heat pump model and separate validation and testing of the high-speed machine model. As can be seen on the right-hand side close-up in Figure 7, the compressor and expander stream are strictly separated. The compressor is separated into two sections representing different

numbers of stages. Each of the turbo machines is described by a table of polytropic efficiency and a flow table. Based on the polytropic head over the model and the impeller tip speed relative to the mediums Mach number, mass flow, torque, and efficiency are computed from 2D tables. While the expander has no leakage streams, the compressor side respects extraction of motor cooling gas over a control valve from between the compressor stages as well as a leakage stream from the high-pressure side into the motor. Motor losses are calculated with a given motor efficiency from the accumulated total shaft power and transferred into the motor cooling stream by a heat flow source.

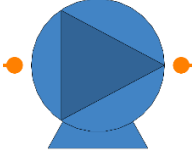
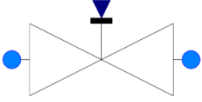
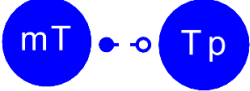

### 3.2.3. Heat Exchanger Models

The heat exchangers have been modeled based on the generic model of the Modelon Thermal Power library for two-phase media. It basically represents a pipe-wall-pipe system where pipes can be arbitrarily multiplied and discretized. The heat sink model is discretized into 10 segments, while the heat source model has only 3 segments. The pressure drop over the heat exchangers is calculated based on the friction of a nominal operating point. The heat exchanger model can be fine-tuned with correction factors for both pressure drop and heat transfer. For the hot heat exchanger, the heat transfer correlation of Shah [36] and Akers [37] was used for CO<sub>2</sub>.



**Figure 7:** Overview of the HPU in Modelon Impact. The illustrated models correspond to the models described in Subsection 3.2 and Table 2. Please note that detailed piping, control components and cooling gas streams are excluded from this figure.

**Table 2:** List of used auxiliary models.

Illustration	Description	Limitation
ThermoFluid.Pumps.Pump 	To integrate some control features, this pump model defines the water flow between two pressure sources on the district heating. Characteristics (flow rate, head, and power consumption) are provided in a table for a nominal rotational speed.	<ul style="list-style-type: none"> <li>• Simplified adaption from nominal conditions with similarity equations.</li> <li>• Speeds outside the table data are extrapolated.</li> </ul>
ThermoFluid.Valves.ValveCompressible 	Linear $C_V$ characteristics, following the IEC 534/ISA S.75 standards for sizing including choked conditions.	<ul style="list-style-type: none"> <li>• Compressible fluid.</li> <li>• Turbulent flow.</li> <li>• No phase change.</li> </ul>
VaporCycle.Sources.LiquidPressureSource VaporCycle.Sources.LiquidFlowSource 	Prescribes an absolute pressure and temperature or a mass flow and temperature, both possible as source or sink.	<ul style="list-style-type: none"> <li>• Homogeneous liquid.</li> <li>• Temperature and mass fractions set in the component only affect the rest of the system when the component acts as a source.</li> </ul>
ThermalPower.Thermal.Sources.HeatFlowSource 	A uniform heat flow source converts a power signal input into a heat flow rate.	

### 3.2.4 Pipe Models

The pipe models of Modelon's VaporCycle library have been manipulated to include a pipe wall and an optional insulation layer as well as an additional flow resistance accounting for all pipe fittings which are not modeled in detail. Pipe elements between major components are represented as straight pipes of constant diameter with a two-phase correlation for friction as proposed by [38] and confirmed for CO<sub>2</sub> by [39]. Additional losses due to fittings such as bends and reductions are summed up into a theoretical resistance factor  $\zeta$  which imposes

$$dp = \zeta \left( \frac{\rho \cdot v^2}{2} \right).$$

Geostatic height differences between the inflow and outflow of the pipe section are also respected in this model. Heat losses to the environment are included by a constant heat transfer coefficient over the pipe surface to a constant ambient temperature. Pipe models have been parameterized for sections of similar pipe diameter, which results in two consecutive pipe elements at the compressor suction. Short pipe sections such as the framing of the expander bypass valve have been neglected for simplification.

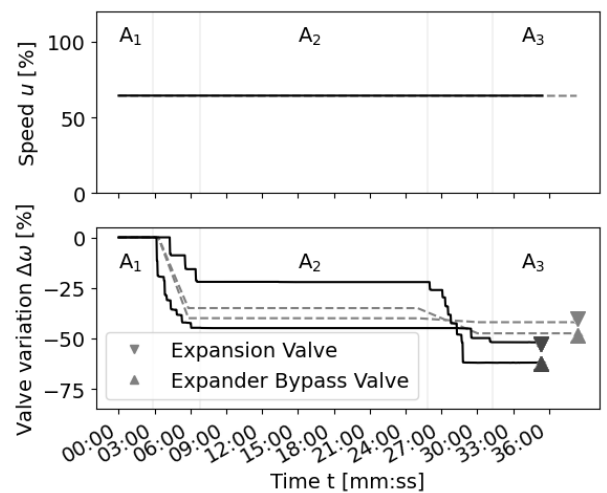
## 4. VALIDATION

The validity of the dynamic model is tested for the full range of achievable operating conditions which are predominantly defined by the compressor map, see Figure 6. Since the main operational changes in order to move the operating point within the compressor map are identified as the rotational speed of the compressor and the loop resistance, subsection 4.1 and 4.2 compare the model and testbed HPU behavior for large

individual changes of these two inputs. While subsection 4.3 validates the simultaneous change of both inputs, the main observations are discussed in subsection 4.4.

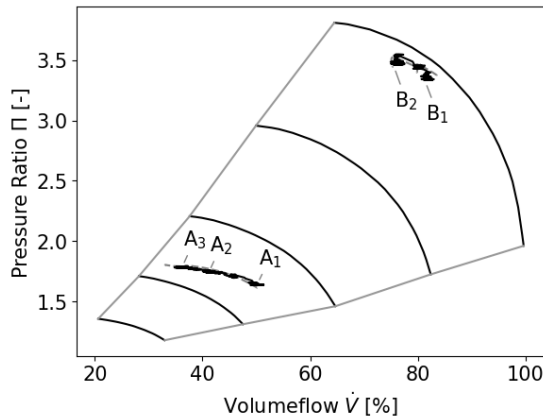
### 4.1 Loop resistance variation

For the validation of system behavior along the plant characteristic, the valve openings have been varied while keeping a constant speed. This variation was performed at the minimum speed (Figures 8, 9, 10) as well as at nominal speed (Figures 9, 11, 12).



**Figure 8:** System inputs during the loop resistance variation at low speed by closing the expansion valve; simulated (---) and testbed data (—).

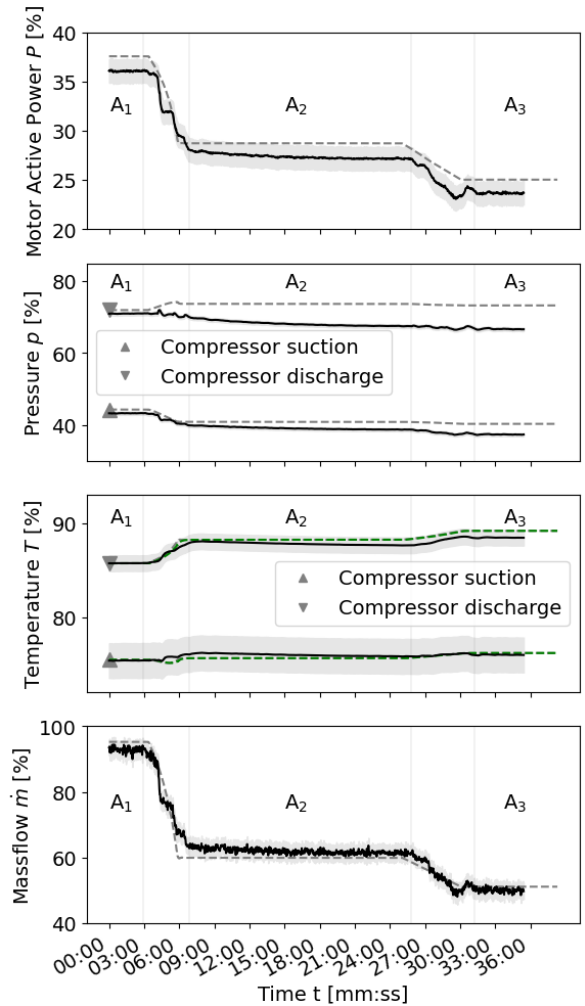
Figure 8 shows the system inputs. The turbomachine speed was constant at the minimum allowed rotation of 60 % of the nominal speed. The operation starts at the low loop resistance A1 with the expansion valve and expander bypass valve open at 80 and 62 %, respectively. Successively, the valves are shut to a medium resistance point A2 and finally to a high resistance point A3. These three operating points cover most of the compressor's characteristic maps speed line as depicted in Figure 9. Since the characteristic map is composed of multiple stages, it varies with changing suction condition, the indicated surge and choke line can only serve as an orientation, not exact values.



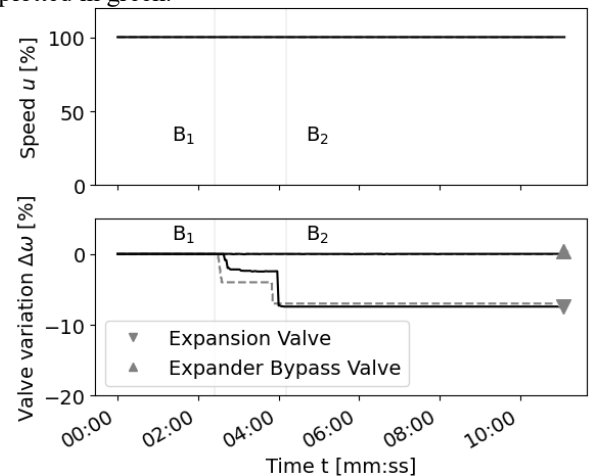
**Figure 9:** Characteristic compressor map during the low- (A) and high-speed (B) loop resistance variation; simulated (---) and testbed data (—).

Figure 10 compares the main physical quantities of the simulation and testbed data. The simulated compressor performance, temperatures, and mass flow are more than 95 % accurate (based on the system inputs from Figure 8).

For nominal speed, the allowed resistance variation was limited due to testbed restrictions of the cooling water system. The valve variation is therefore constrained to a slight closing of the expansion valve as shown in Figure 11 and results in only a small movement in the theoretical characteristic map from Figure 9. The agreement between simulation and testbed results in Figure 12 is consistently satisfactory over every parameter with an accuracy of 95 %. The testbed data uncertainty during these rather slow dynamics is below 2 % throughout all data points.



**Figure 10:** Physical quantities during the low-speed loop resistance variation; simulated (---) and testbed data (—) with a confidence interval (■) as defined in subsection 2.2. Results of adding a time delay on the simulation output of the temperature are plotted in green.



**Figure 11:** System inputs during the loop resistance variation at high speed by closing the expansion valve; simulated (---) and testbed data (—).

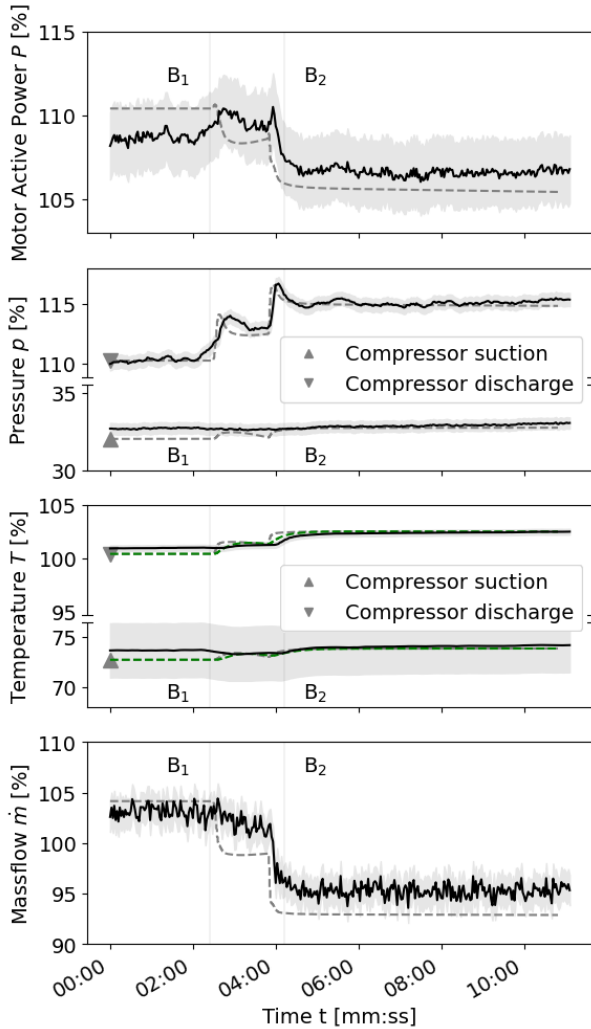


**Figure 12:** Physical quantities during the high-speed loop resistance variation; simulated (---) and testbed data (—) with a confidence interval (■) as defined in subsection 2.2. Results of adding a time delay on the simulation output of the temperature are plotted in green.

#### 4.2 Rotational speed variation

In order to validate the system behavior along the compressor characteristic (see Figure 6), the speed was varied rapidly while keeping all other parameters (e.g. valves, water temperatures) constant, imitating a primary frequency reserve operation on European markets [40]. In Figure 13, the speed as input in the simulation and testbed procedure is shown. From nominal speed, at 100 %, the rotation of the turbomachine shaft was reduced to 60 % within 30 s and restored after a settle-out period of 50 s. Similarly, a speed variation increasing from nominal to 105 % was performed.

While the transient dynamics demonstrate high accuracy, the visualization in the characteristic compressor map in Figure 14 suffers mainly from the smallest deviations in absolute pressure measurements. Both curves resemble an 8-shape where

the larger, lower loop is related to the speed decrease operation 100 %-60 %-100 % and the much smaller, upper loop is caused by the speed increase operation 100 %-105 %-100 %.

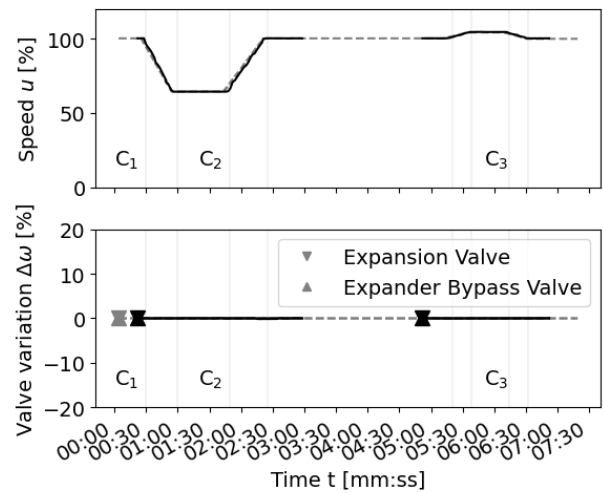


**Figure 13:** System inputs during the high-speed loop resistance variation; simulated (---) and testbed data (—).

The power consumption of the HPU – as a result – falls to 26 % of the nominal duty. The transient dynamics are in good agreement between the simulation and testbed system, showing only a small deviation when settling after the large speed increase from 60 % to nominal. A similar agreement can be found in the fluid state measurements as presented in Figure 15. The transient behavior is captured well in absolute numbers and dynamics. A larger deviation is found in the temperature, where the dynamics of the simulation are much quicker than what testbed data shows. Adding a first-order transfer function with a delay of 15 s to the simulation temperature data yields the green result and much better agreement with the testbed measurements.

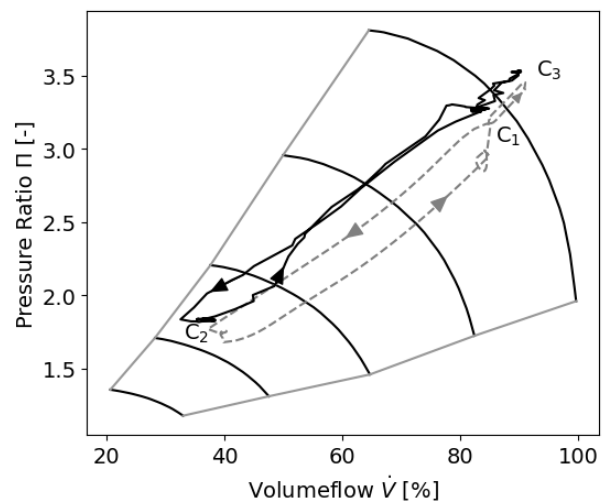


**Figure 14:** Characteristic compressor map during the speed variation; simulated (---) and testbed data (—).



The testbed measurements show a high uncertainty of up to 20% for mass flow and temperatures during these fast dynamics. Generally, it is concluded that the simulation results show a good qualitative agreement with the testbed data. Over wide ranges, especially during steady states, the quantitative values also reach a high accuracy of more than 95%. Several result deviations are discussed in subsection 4.4.

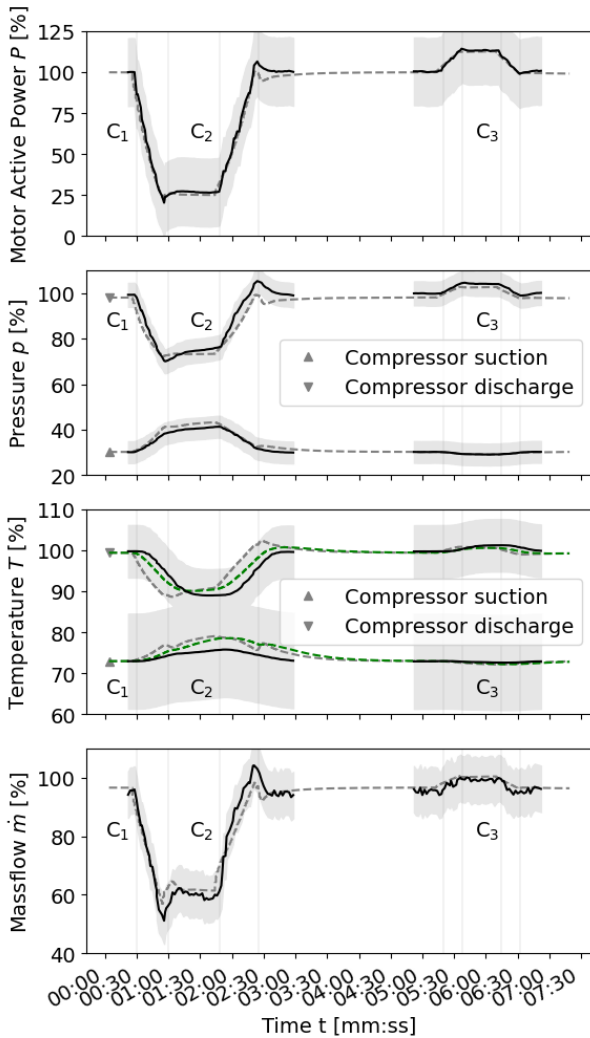


**Figure 15:** Physical quantities during the speed variation; simulated (- -) and testbed data (—) with a confidence interval (■) as defined in subsection 2.2. Results of adding a time delay on the simulation output of the temperature are plotted in green.

#### 4.3 Combined variation of rotational speed and loop resistance

After the validation of transient operation with a single input variation, the response of a simultaneous change of both, speed and valve position, is investigated. A fast load-balancing operation is performed, reducing the speed by 60% within 30 s and at the same time opening both valves, expansion and expander bypass, as given in Figure 16.

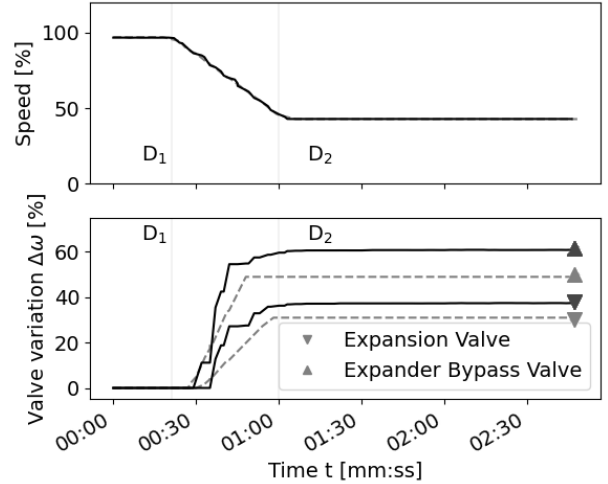


**Figure 16:** System inputs during the speed as well as loop resistance variation; simulated (- -) and testbed data (—).

Figure 17 shows the transition in the characteristic map. The operating point moves diagonally from a high-speed point at high resistance to a minimum speed closer to the choke line. A slight offset of the simulation is present again, but the shape of the path is in good agreement between experimental data and simulation.

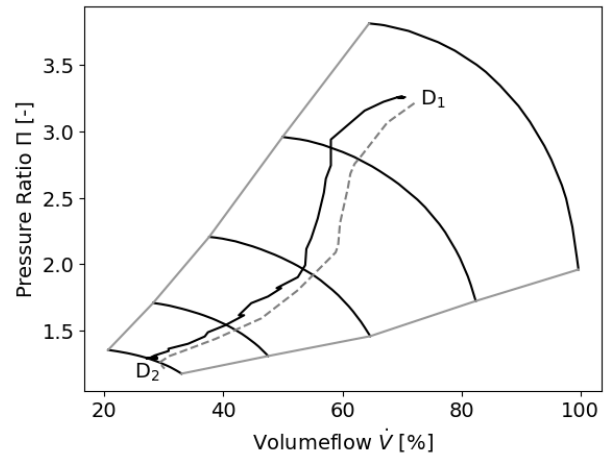


**Figure 17:** Characteristic compressor map during the speed as well as loop resistance variation; simulated (- -) and testbed data (—).

The power consumption of the testbed HPU falls by over 80% within 45 s and is well matched by the simulation. Also, compressor pressures, temperatures, and mass flow remain in agreement with the experimental data in highly dynamic transitions as shown in Figure 18. As seen above, the hot temperature measurement on the compressor discharge is delayed on the testbed but can be compensated with an imposed time delay to the simulation output.



**Table 3:** Summary of the most relevant observations together with potential causes as well as proposed measures.

Observation (corresponding subsection)	Root	Measure
Pressure drift for slow dynamics (4.4.1)	Thermal shift on the water-glycol loop impacts the evaporation pressure	None – physical testbed limitation
Loop resistance uncertainties (4.4.2)	Simplified pipe modeling, challenging valve characteristics	Linear valve model based on testbed or improved manufacturer data
Elevated testbed path in the characteristic compressor map (4.4.3)	Overperformance of the manufactured compressor (conservative compressor model)	Regenerate compressor maps based on testbed measurements
Temperature deviations (4.4.4)	Thermal inertia of temperature sensors	Implementation of first-order transfer function(s)
High sensitivity to total CO <sub>2</sub> mass (4.4.5)	Inaccurate mass balance measurement on the testbed	None – physical testbed limitation

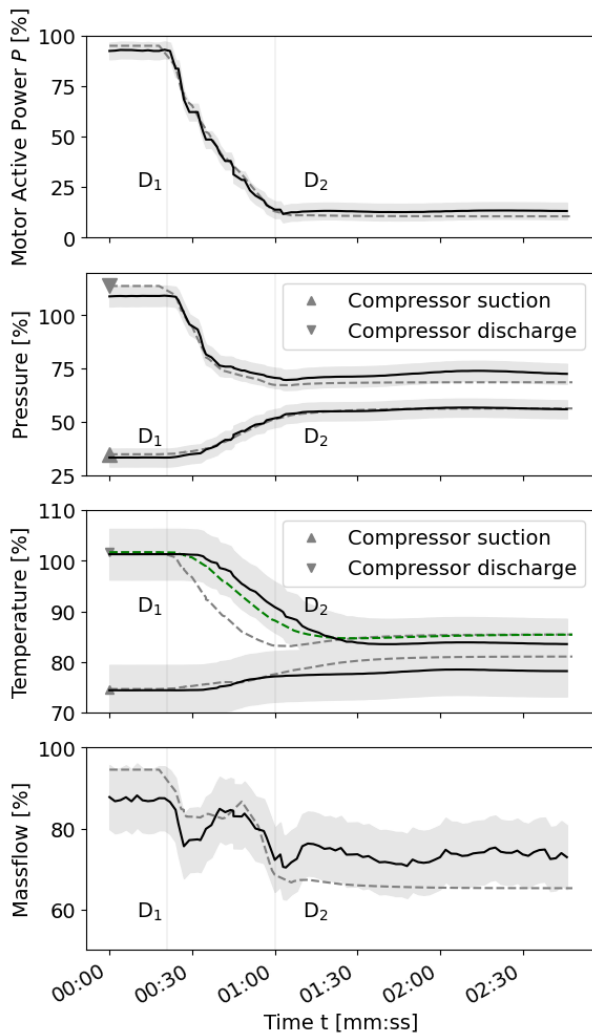


**Figure 18:** Physical quantities during the speed as well as loop resistance variation; simulated (---) and testbed data (—) with a confidence interval (■) as defined in subsection 2.2. Results of adding a time delay on the simulation output of the temperature are plotted in green.

#### 4.4 Discussion of the results

The most relevant observations during the validation, together with their root and potential measures, are summarized in Table 3 as well as elaborated in the following subsections.

##### 4.4.1 Pressure drift for slow dynamics

In Figure 10, a strong pressure drift, defined as a gradual, unintended deviation of the process from the expected performance, can be observed. This unsteady drift can be linked to challenges in manually adjusting the cooling water flow in the testbeds interlinked heat sink and source. Balancing the thermal energy of the testbed loop is complex and results in a thermal shift on the evaporator. This directly influences the evaporation pressure and can project to all of the closed-loop states. Further, this limitation of the interlinked heat sink and source also restricts the loop resistance variation at high speeds, resulting in the rather short path in Figure 9.

##### 4.4.2 Loop resistance uncertainties

Another major discrepancy between the simulation and testbed is the overall loop resistance, visible in the deviating valve positions throughout all validation cases in Figures 8, 11, 13, and 16. A fundamental cause lies in the simplifications of pipe modeling. Additional pipes and armatures on the testbed as well as varying surface conditions on different pipe elements and a high number of flange connections are difficult to model accurately. On top of this comes the poor quality of the valve characteristics. In ever-changing fluid properties from liquid to multiphase to supercritical and even gaseous states, the correlation between opening,  $C_v$ , and actual resistance is non-trivial. The choice of a simple linear valve model in correspondence with the manufacturer is a conscious decision to allow for tuning flexibility on the loop resistance. While a fitting valve opening can be easily found based on measurement data, it limits the control application of the model at this stage to qualitative use only.

#### 4.4.3 Elevated testbed path in the compressor map

The paths of the testbed and the simulation data in the characteristic map for the load-balancing operation are slightly shifted. The data translation into pressure ratio emphasizes small deviations and measurement inertia on the testbed projects onto the volume flow. In Figure 14 the simulation gives a nearly ideal path, while the path of the testbed data appears morphed. On one hand, this is caused by a fast pressure measurement and a comparably slow temperature sensor which results in a temporarily wrong combination of data points. The dominating shift of the experimental data to higher pressure ratios is explained by a conservative compressor model. The manufactured compressor wheels reach higher pressures than designed for a given volume flow. The compressor look-up tables should be recalculated and updated based on the testbed experience.

#### 4.4.4 Temperature deviations

The dynamic response of the temperature differs significantly between the simulation results in the dotted gray and the testbed results in solid black as described in section 4.2 and is visible in Figure 15 and Figure 18. By adding a first-order transfer function with a time constant of 15 s to the temperature output of the simulation, the resulting temperature curve in dotted green is in much better agreement. This could be explained by the thermal inertia of the temperature sensors, which had not been in direct contact with the medium but placed in an insertion sleeve, leading to a delay. The impact of measurement inertia is non-negligible and contributes to the systematic validation uncertainty. Especially computed values from the testbed such as volume flow, enthalpy and ultimately *COP* propagate this error and inhibit a higher uncertainty during transient operation.

#### 4.4.5 Total refrigerant charge

It is challenging to accurately monitor the total mass of refrigerant present in the test loop. Therefore, it can only be roughly estimated based on weight inventory measurements during the charging procedure. Moreover, some refrigerant was added or removed during the multiple days of testing, resulting in significant uncertainties of the refrigerant charge at a certain time. The actual refrigerant mass varied in the range between 5.5 to 6.5 tons. This relatively large uncertainty creates, however, a degree of freedom for the simulation which can have an impact on the results.

## 5. CONCLUSION

Large-scale industrial heat pumps are crucial solutions for the decarbonization of district energy networks or process heat applications. An optimal integration in complex operating frameworks must take into consideration the system dynamics. Hence, transient simulation is one of the key tools to provide accurate predictions of future heat pump operation. More specifically, application services such as seasonal load planning, day-to-day heat balancing, and highly dynamic grid services can be supported by the concept and tool elaborated in this work. The

presented model improves on the current state-of-the-art by its validation with full-scale experimental testing results. For fast self-induced operational changes, the major results can be summarized as follows:

- The developed Modelica HPU model matches the testbed measurements with an accuracy of 95 % in the discussed physical quantities (with few exceptions as discussed).
- Fast dynamic changes of the power consumption up to 80 % within 30-45 s by varying the loop resistance and the speed have been validated both, individually and combined.
- The validated HPU model is qualified to predict transient plant operation and control responses.

As the next step of development, the integration of elaborated valve characteristics can provide dynamic models for even more accurate system predictions. Besides ensuring the scalability of such models, future studies should investigate control strategies on different time scales. A validated dynamic model as presented here can serve as the foundation for more complex energy management systems connecting long-term resource planning with fast dynamics of ancillary services on an industrial scale.

## NOMENCLATURE

CO <sub>2</sub>	Carbon Dioxide
COP	Coefficient of Performance
C <sub>v</sub>	Valve Flow Coefficient
$\rho$	Density [kg/m <sup>3</sup> ]
$dp$	Pressure Loss [Pa]
HEX	Heat Exchanger
HPU	Heat Pump Unit
IEC	International Electrotechnical Commission
ISA	International Society of Automation
MAN ES	MAN Energy Solutions Schweiz AG
NH <sub>3</sub>	Ammonia
SBTL	Spline-based Table Lookup
$Q_{in/out}$	Specific Heat [J/kg]
$v$	Median Flow Velocity [m/s]
$W_{in/out}$	Specific Work [J/kg]
$\zeta$	Flow Resistance Factor [-]

## CREDIT AUTHOR STATEMENT

**Leonhard Wolscht** Conceptualization, Data curation, Software, Model, Writing, Visualization **Kai Knobloch** Conceptualization, Data curation, Software, Writing, Visualization, Funding acquisition **Emmanuel Jacquemoud** Resources, Supervision, Writing - Review **Philipp Jenny** Writing - Review.

## ACKNOWLEDGMENTS

The authors would like to express their gratitude to MAN Energy Solutions Schweiz AG for supporting this work with resources as well as experimental data. Kai Knobloch acknowledges the financial support from the Danish Energy Technology Development and Demonstration Program (EUDP 64016-0027) and the Otto Mønstedts Fund. The authors would like to thank Christian Hermsdorf, George Kleynhans, Zeno Antonini, and Luis Sanz Garcia for their valuable engineering expertise and support.

## REFERENCES

- [1] International Energy Agency. World Energy Outlook. Paris; 2021.
- [2] International Energy Agency. Heating. Paris; 2021.
- [3] van Vuuren DP, van Soest H, Riahi K, Clarke L, Krey V, Kriegler E et al. Carbon budgets and energy transition pathways. *Environ. Res. Lett.* 2016;11(7):75002.
- [4] International Energy Agency. District Heating. Paris; 2021.
- [5] Lorentzen G. Revival of carbon dioxide as a refrigerant. *International Journal of Refrigeration* 1994;17(5):292–301.
- [6] Gabrielli P, Sansavini G, Singh S, Garcia LS, Jacquemoud E, Jenny P. Off-Design Modeling and Operational Optimization of Trans-Critical Carbon Dioxide Heat Pumps. *Journal of Engineering for Gas Turbines and Power* 2022;144(10).
- [7] Zühlsdorf B, Jensen JK, Cignitti S, Madsen C, Elmegaard B. Analysis of temperature glide matching of heat pumps with zeotropic working fluid mixtures for different temperature glides. *Energy* 2018;153:650–60.
- [8] Arpagaus C, Bless F, Uhlmann M, Schiffmann J, Bertsch SS. High temperature heat pumps: Market overview, state of the art, research status, refrigerants, and application potentials. *Energy* 2018;152:985–1010.
- [9] Diniz HAG, Paulino TF, Pabon JJG, Maia AAT, Oliveira RN. Dynamic Model of a Transcritical CO<sub>2</sub> Heat Pump for Residential Water Heating. *Sustainability* 2021;13(6):3464.
- [10] Aguilera JJ, Meesenburg W, Ommen T, Poulsen JL, Kramer KR, Markussen WB et al. Operational challenges in large-scale ammonia heat pump systems. In: Amano Y, Sciubba E, Elmegaard B, editors. 34th International Conference on Efficiency, Cost, Optimization, Simulation and Environmental Impact of Energy Systems (ECOS 2021). Tokyo, Japan: ECOS 2021 Program Organizers; 2022, p. 1842–1853.
- [11] Chi J, Didion D. A simulation model of the transient performance of a heat pump. *International Journal of Refrigeration* 1982;5(3):176–84.
- [12] Nyers J, Stoyan G. A dynamical model adequate for controlling the evaporator of a heat pump. *International Journal of Refrigeration* 1994;17(2):101–8.
- [13] Vargas J, Parise J. Simulation in transient regime of a heat pump with closed-loop and on-off control. *International Journal of Refrigeration* 1995;18(4):235–43.
- [14] Dechesne B, Bertagnolio S, Lemort V. Development of an empirical model of a variable speed vapor injection compressor used in a Modelica-based dynamic model of a residential air source heat pump. *IOP Conf. Ser.: Mater. Sci. Eng.* 2015;90:12031.
- [15] Thomasen S, Sørensen K, Bojesen C, Vinther K. Sensitivity Analysis of Optimised Large Scale District Heating Heat Pump Concepts. In: Proceedings of The 61st SIMS Conference on Simulation and Modelling SIMS 2020, September 22-24, Virtual Conference, Finland: Linköping University Electronic Press; 2021, p. 63–70.
- [16] Thermal Power Library - Experiments - HeatPump: Example of a MW-scale, two-stage district heating heat pump system based on R134a: Modelon Inc; 2022.
- [17] Kim Y-J, Norford LK, Kirtley JL. Modeling and Analysis of a Variable Speed Heat Pump for Frequency Regulation Through Direct Load Control. *IEEE Trans. Power Syst.* 2015;30(1):397–408.
- [18] Meesenburg W, Markussen WB, Ommen T, Elmegaard B. Optimizing control of two-stage ammonia heat pump for fast regulation of power uptake. *Applied Energy* 2020;271:115126.
- [19] Watanabe Y, Traverso A. Dynamic modeling and simulation of a heat pump system for enhancing cycle flexibility. *E3S Web Conf.* 2019;113:1007.
- [20] Byrne P, Miriel J, Lenat Y. Design and simulation of a heat pump for simultaneous heating and cooling using HFC or CO<sub>2</sub> as a working fluid. *International Journal of Refrigeration* 2009;32(7):1711–23.
- [21] Ko J, Takata N, Thu K, Miyazak T. Dynamic Modeling and Validation of a Carbon Dioxide Heat Pump System. *Evergreen* 2020;7(2):172–94.
- [22] Gräber M, Kosowski K, Richter C, Tegethoff W. Modelling of heat pumps with an object-oriented model library for thermodynamic systems. *Mathematical and Computer Modelling of Dynamical Systems* 2010;16(3):195–209.
- [23] La Tejada De Cruz A, Riviere P, Marchio D, Cauret O, Milu A. Hardware in the loop test bench using Modelica: A platform to test and improve the control of heating systems. *Applied Energy* 2017;188:107–20.
- [24] Peirelinck T, Ruelens F, Decnoninck G. Using reinforcement learning for optimizing heat pump control in a building model in Modelica. In: 2018 IEEE International Energy Conference (ENERGYCON): IEEE; 2018, p. 1–6.
- [25] Selvnes H, Allouche Y, Hafner A. Experimental characterisation of a cold thermal energy storage unit with a pillow-plate heat exchanger design. *Applied Thermal Engineering* 2021;199:117507.
- [26] Knobloch K, Muhammad Y, Costa MS, Moscoso FM, Bahl C, Alm O et al. A partially underground rock bed

- thermal energy storage with a novel air flow configuration. *Applied Energy* 2022;315:118931.
- [27] Vecchi A, Knobloch K, Liang T, Kildahl H, Sciacovelli A, Engelbrecht K et al. Carnot Battery development: A review on system performance, applications and commercial state-of-the-art. *Journal of Energy Storage* 2022;55:105782.
- [28] Le Pierres R, Southall D, Osborne S. Impact of Mechanical Design Issues on Printed Circuit Heat Exchangers. *Proceedings of sCO<sub>2</sub> Power Cycle Symposium* 2011.
- [29] OPC Foundation. The Industrial Interoperability Standard™.
- [30] Gerhard S. Energy storages: Presentation during the International Joint Graduate Course on Sustainable Energy. Seoul.
- [31] Wischhusen S. *Dynamische Simulation zur wirtschaftlichen Bewertung von komplexen Energiesystemen*. 1st ed. Göttingen: Cuvillier; 2005.
- [32] Modelica Association. *Modelica Standard Library 3.2.1*.
- [33] Modelon Inc. *Modelon Library Suite 2022*.
- [34] Huber M, Harvey A, Lemmon E, Hardin G, Bell I, McLinden M. *NIST Reference Fluid Thermodynamic and Transport Properties Database (REFPROP) Version 10 - SRD 23: National Institute of Standards and Technology; 2018*.
- [35] Kunick M. *Fast Calculation of Thermophysical Properties in Extensive Process Simulations with the Spline-Based Table Look-Up Method (SBTL)*: VDI Verlag; 2018.
- [36] Shah MM. A general correlation for heat transfer during film condensation inside pipes. *International Journal of Heat and Mass Transfer* 1979;22(4):547–56.
- [37] Akers, W.W., Deans, H.A., Crosser, O.K. Condensing heat transfer within horizontal tubes. *Chem. Eng. Progr.* 1959(55).
- [38] Friedel L. Improved friction pressure drop correlations for horizontal and vertical two-phase pipe flow. *Proceedings of European Two-Phase Flow Group Meeting; 1979(2)*.
- [39] Park CY, Hrnjak PS. CO<sub>2</sub> and R410A flow boiling heat transfer, pressure drop, and flow pattern at low temperatures in a horizontal smooth tube. *International Journal of Refrigeration* 2007;30(1):166–78.
- [40] ENTSO-E. European association for the cooperation of transmission system operators (TSOs) for electricity; Available from: <https://www.entsoe.eu/>.

## PERFORMANCE AND COST POTENTIAL FOR DIRECT-FIRED SUPERCRITICAL CO<sub>2</sub> NATURAL GAS POWER PLANTS

**Sandeep R Pidaparti**

National Energy Technology Laboratory/NETL  
Support Contractor  
Pittsburgh, USA

**Charles W. White**

National Energy Technology Laboratory/NETL  
Support Contractor  
Fairfax, USA

**Eric Liese\***

National Energy Technology Laboratory  
Morgantown, USA  
[Eric.Liese@netl.doe.gov](mailto:Eric.Liese@netl.doe.gov)

**Nathan T. Weiland\***

National Energy Technology Laboratory  
Pittsburgh, PA  
[Nathan.Weiland@netl.doe.gov](mailto:Nathan.Weiland@netl.doe.gov)

### ABSTRACT

Direct-fired supercritical CO<sub>2</sub> (sCO<sub>2</sub>) power cycles are being explored as an attractive alternative to natural gas combined cycle (NGCC) plants with carbon capture and storage (CCS). Therefore, understanding their performance and cost potential is important for the commercialization of the technology. This study presents the techno-economic optimization results of natural gas-fired, utility-scale power plants based on the direct sCO<sub>2</sub> power cycle, which are lacking in public literature. To identify the optimum plant configuration, the study considered multiple cases with varying levels of thermal integration with the plant air separation unit (ASU). Several design variables for each power cycle configuration were identified and optimized to minimize the levelized cost of electricity (LCOE) for each case. The optimization design variables include the sCO<sub>2</sub> cooler outlet temperatures, recuperator approach temperatures, and pressure drops. High fidelity models for recuperators, coolers, and turbines were developed and used to capture the impact of design variables on plant efficiency and capital costs. The optimization was conducted using a combination of manual sensitivity analyses and automated derivative-free optimization algorithms available under NETL's Framework for Optimization and Quantification of Uncertainty and Sensitivity platform.

The optimized direct sCO<sub>2</sub> power plants offered similar or slightly higher plant efficiencies than the reference NGCC plants based on the F-class gas turbine with carbon capture and storage (CCS). The LCOE of the optimized direct sCO<sub>2</sub> plants is 13 to 17% higher than the reference NGCC plants with CCS due to high capital costs associated with the ASU and sCO<sub>2</sub> power

block, though there is significant room for improvement due to the high uncertainty in component capital costs for these new plants. Recuperators make up over 50% of the sCO<sub>2</sub> power block costs. Consequently, any research and development efforts to reduce the recuperator capital costs will benefit the technology's commercialization. The study also presents preliminary results showing the impact of co-firing landfill gas and natural gas on plant efficiency, LCOE, and CO<sub>2</sub> emissions.

### INTRODUCTION

Direct-fired sCO<sub>2</sub> power cycles are an attractive alternative to NGCC plants (with CCS) due to their high efficiency and inherent ability to capture CO<sub>2</sub> at high rates. A simplified schematic of the direct-fired sCO<sub>2</sub> power cycle is shown in Figure 1. In these cycles, gaseous fuel is burned with oxygen in a highly dilute sCO<sub>2</sub> environment, with the combustion products driving a turbine to generate power. The thermal energy in the turbine exhaust is recuperated to heat the CO<sub>2</sub> diluent flow to the combustor. After recuperation, water is condensed out of the product stream, and a portion of the stream (primarily CO<sub>2</sub>) is drawn from the cycle for further purification, compression, and storage. The rest of the stream is compressed to a pressure near the critical pressure, followed by additional cooling, and pumping to the cycle maximum pressure before pre-heating in the recuperator.

Allam and colleagues extensively studied the direct sCO<sub>2</sub> power cycles. [1, 2, 3] Commercialization of this technology is being pursued by NET Power, 8 Rivers Capital, and their collaborators, who built a 25 MWe demonstration plant in Laporte, Texas. In the natural gas-fired version of this cycle, their literature

\* corresponding author(s)

suggests that net power plant efficiencies > 53% (HHV basis) are achievable with near 100% carbon capture. [3] Under slightly different assumptions, Foster Wheeler/IEAGHG modeling of this system yielded a net plant efficiency of 49.9% with 90% carbon capture. [4] Scaccabarozzi et al. performed sensitivity analyses and cycle optimization of the system modeled by IEAGHG and reported an HHV efficiency of 49.5–50.0%. [5, 6] SwRI evaluated alternative natural gas-fired direct sCO<sub>2</sub> cycles with reported plant HHV thermal efficiencies ranging 46.5–51.1 percent. [7]

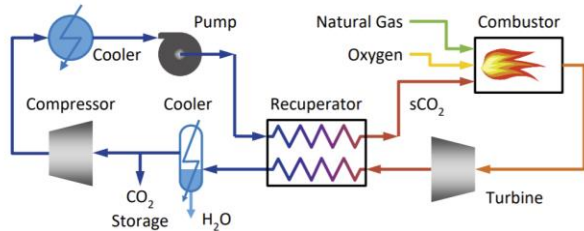


**Figure 1:** Schematic of a natural gas-fueled direct-fired sCO<sub>2</sub> power cycle

Prior NETL study presented a techno-economic analysis (TEA) of natural gas-fired version of the direct-fired sCO<sub>2</sub> power cycle. [8] Plant efficiency (HHV basis) was reported at 48.2%, which is higher than, or similar to, the reference NGCC plants with CCS (using F-frame and H-frame gas turbines). The COE of this plant is estimated at \$79.2/MWh, compared to \$83.3/MWh for the reference NGCC plant with CCS (using F-frame gas turbine). [8] These studies made several assumptions for modeling of the recuperators, turbine, and turbine blade cooling based on the best data available at the time. The primary objective of this paper is to build on the prior NETL natural gas-fired direct sCO<sub>2</sub> power cycle analyses to improve the accuracy of performance and economic modeling for components such as ASU, recuperators, coolers, and turbine. In particular, this study uses a high-fidelity cooled sCO<sub>2</sub> turbine model to estimate the turbine output and required turbine coolant flow. High-fidelity recuperator and cooler models are used to study the impact of design parameters such as temperature approach and pressure drop on both the plant efficiency and COE. The study also presents a pre-screening level analysis showing the impact of landfill gas (LFG) and natural gas co-firing on direct sCO<sub>2</sub> power plant efficiency, COE, and emissions.

### SCO<sub>2</sub> POWER PLANTS DESCRIPTION

A block flow diagram of the natural gas-fired direct sCO<sub>2</sub> plant modeled in this study is shown in Figure 2. Compressed natural gas (stream 14), pre-heated oxidant (stream 12), and pre-heated recycle diluent (stream 32) are fed to the sCO<sub>2</sub> oxy-combustor where combustion of the natural gas increases the temperature of mixture to the TIT. The effluent from the combustor (stream 34) is expanded in sCO<sub>2</sub> turbine. It is also important to emphasize that the combustion system for direct-fired sCO<sub>2</sub> plants is vastly different compared from that of traditional NGCC plants. Traditional NGCC plant combustors are air-fired and operate at pressures ~3.5 MPa [9] whereas direct-fired sCO<sub>2</sub> plant

combustors are oxy-fired and operate at an order of magnitude higher pressures (~30 MPa) than traditional NGCC plant combustors. These differences will lead to vastly different combustion kinetics and combustor designs which can have a major impact on plant performance as well as capital costs.

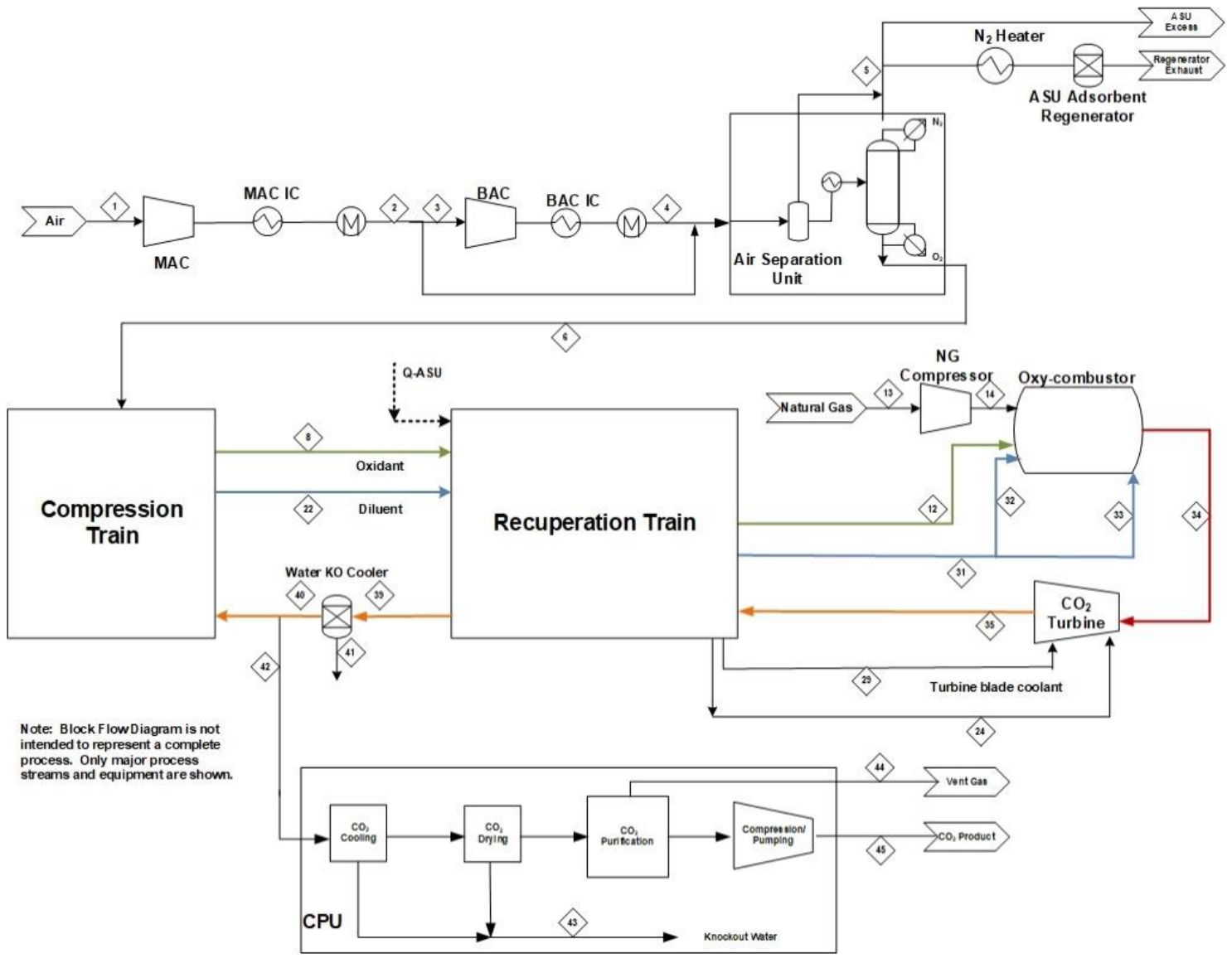
The turbine exhaust (stream 35) pre-heats the incoming oxidant (stream 8) and recycle diluent (stream 20) streams in the recuperation train. Exiting the recuperation train, the cooled turbine exhaust (stream 39) is passed through the water knockout (KO) cooler to condense out water (stream 41) from the mixture. A portion of the recycle stream is purged from the cycle (stream 42) for further purification and compression in the CPU, to meet CO<sub>2</sub> pipeline standards for O<sub>2</sub>, CO, H<sub>2</sub>O, and other contaminants. The rest of the recycle stream is sent to the compression train. The recycle and purge stream flows are controlled to attain a TIT of 1204°C. In the compression train, a pre-compressor increases the pressure of recycle stream (stream 15) to ~100 bar and the compressed stream (stream 16) is cooled in the main cooler. A portion of the recycle stream (stream 18) is mixed with O<sub>2</sub> (stream 6) from the ASU to generate the oxidant stream (stream 7). The maximum mole fraction of O<sub>2</sub> in the oxidant stream is set to 23.5% based on guidance from ASU vendors. The oxidant stream (stream 7) and rest of the recycle stream (stream 19) are compressed to cycle maximum pressure in the oxidant compressor and boost pump respectively. Oxygen for the plant comes from a cryogenic ASU. An O<sub>2</sub> purity of 99.5% is chosen to minimize N<sub>2</sub> and Ar impurities, which increase the required compression power in the sCO<sub>2</sub> cycle, thereby reducing cycle efficiency. [9] This is partially offset by the increase in ASU power requirement needed to produce high-purity O<sub>2</sub> and also increases the cost of the ASU. The recuperation train is split into four stages to better manage thermal pinch points, provide the necessary turbine coolant flows, reduce high temperature material use, and for thermal integration with the ASU.

The LTR is designed to achieve condensation of water vapor from the hot, LP turbine exhaust stream (stream 36). To avoid an internal pinch point in the LTR, the hot side inlet (stream 38) temperature is typically at or close to its dew point so that water begins to condense at the ITR outlet. Integration of the process heat from the ASU occurs in parallel to the LTR and the ITR, where the specific heat capacity difference between hot and cold sides is highest. Ideally, the thermal integration should occur in the temperature range of LTR, ITR, and HTR2 to maximize heat recovery; however, due to lack of high temperature heat sources from the ASU, the thermal integration is limited to the LTR and ITR. The temperature of the diluent (stream 25) and oxidant (stream 10) streams exiting the ITR is set to 213.3°C. A portion of the diluent stream exiting the ITR is drawn (stream 24) to provide the necessary turbine blade coolant flow. The temperature of the diluent (stream 28) and oxidant (stream 11) streams exiting the HTR2 is set to 327.8°C. The rest of the turbine blade coolant (stream 29) is withdrawn from the diluent stream exiting the HTR2. An upper limit of 760°C was chosen for the turbine exhaust (stream 35) based on high temperature and pressure limits of nickel-based alloys, which represent a



major constraint on the system design. [8] Three different cases with varying levels of thermal integration with the ASU were considered in this study to systematically understand the impact of ASU thermal integration on plant efficiency and LCOE. The case description and matrix are presented in Table 1. Modeling assumptions for ASU compressors and intercoolers are based on a discussion with ASU vendors. For Case A, no thermal integration with the ASU was considered and the ASU main air compressor (MAC) and boost air compressor (BAC) were intercooled with water. For Case B, the intercooled MAC was

replaced with an adiabatic compressor (no intercooling) for thermal integration with relatively hot air exiting the MAC. Heat is recovered from air exiting the MAC followed by an aftercooler to cool the air to the desired temperature. For Case C, thermal integration with both the ASU MAC and BAC was considered. The MAC is an adiabatic compressor (no intercooling, similar to Case B) and the BAC is a multi-stage intercooled compressor with the intercooler (IC) temperature set to have 5.6°C approach to the diluent stream temperature exiting the compression train (stream 20) to allow for thermal integration with ASU BAC ICs.



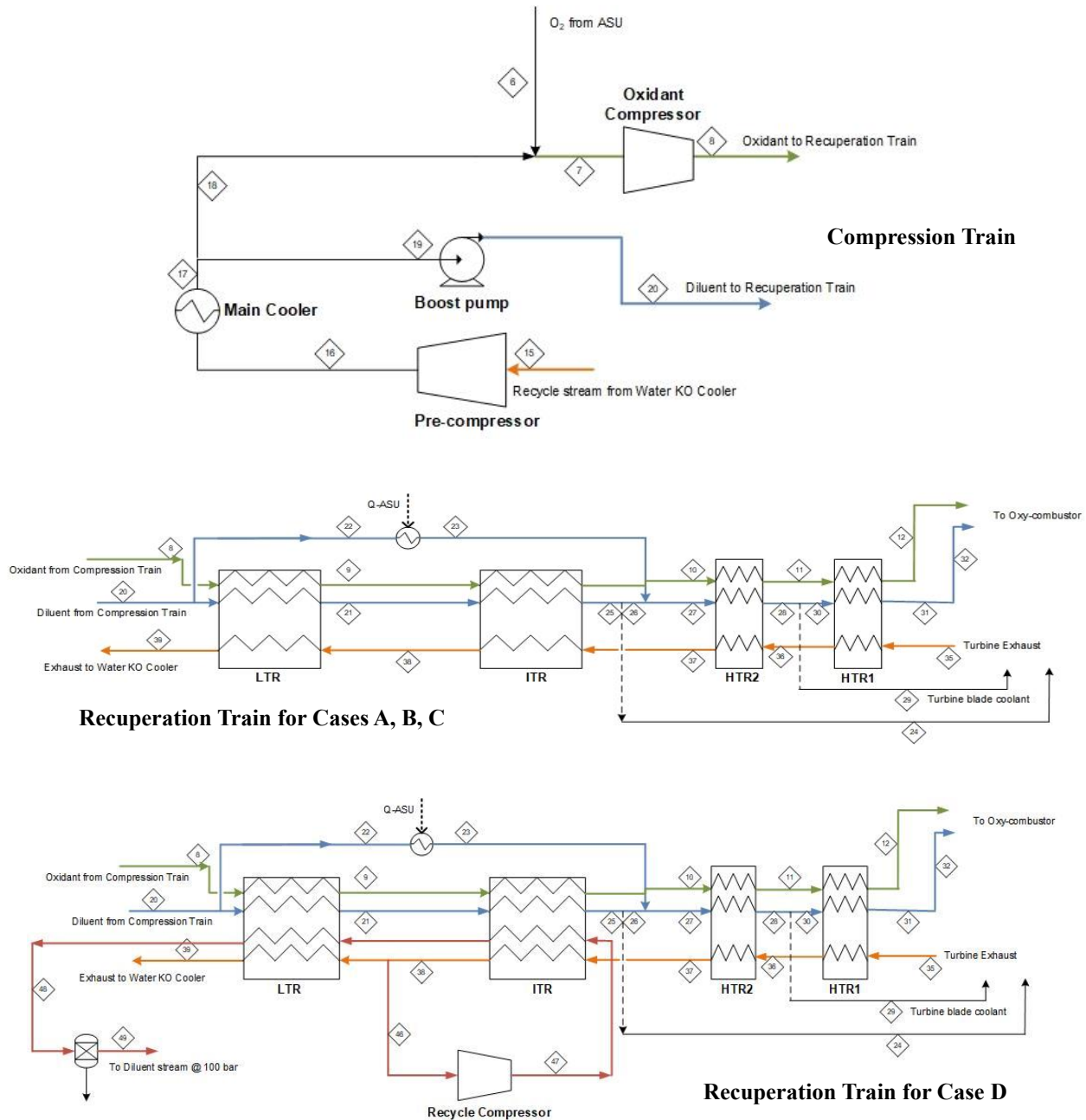


**Figure 2:** Block flow diagrams for natural gas-fueled direct-fired sCO<sub>2</sub> power plants considered in this study

In addition to the three cases presented in Table 1, an alternative case based on a patent from 8 Rivers was considered to increase the amount of heat recovered to the recuperation train. [10] This case is represented as Case D in the paper. A diagram of the recuperation train for Case D is shown at the bottom of Figure 2. A portion of the turbine exhaust exiting the ITR (stream 36) is bypassed and compressed in a recycle compressor to 100 bar (1,460 psi) that matches with the O<sub>2</sub> delivery pressure from the ASU. The hot CO<sub>2</sub> stream exiting the recycle compressor (stream

47) is sent back to the recuperation train to provide additional heat for the ITR and LTR. After exiting the LTR, the compressed CO<sub>2</sub> stream (stream 48) is cooled in a separate water knockout cooler and the resulting dried stream (stream 49) is mixed with the compressed CO<sub>2</sub> stream exiting the pre-compressor (stream 16). In addition to the heat supplied by the compressed recycle stream (stream 47), the recuperation train for Case D is also thermally integrated with the ASU MAC and BAC (similar to Case C). Based on the case descriptions, it can be noted that the

amount of additional heat supplied to the recuperation train increases from Case A to Case D, which improves the cycle efficiency but at the expense of increased auxiliary loads for the ASU and the recycle compressor (only for Case D).

Case Description	ASU MAC Heat Recovery	MAC Intercooler Temperature	ASU BAC Heat Recovery	BAC Intercooler Temperature
Case A	No (Isothermal MAC)	21.1°C	No (Isothermal BAC)	21.1°C
Case B	Yes (Adiabatic MAC)	No intercooling	No (Isothermal BAC)	21.1°C
Case C	Yes (Adiabatic MAC)	No intercooling	Yes (Isothermal BAC)	5.6°C approach to diluent temperature entering LTR

**Table 1:** Direct sCO<sub>2</sub> plants configuration matrix

### MODELING APPROACH

The design bases from NETL’s Fossil Energy Baseline study [11] and Quality Guidelines for Energy System Studies (QGESS) series were adopted so that the results from this study would be consistent with the established results for reference NGCC plants. All the plants are assumed to be located at a generic plant site in the midwestern United States at sea level with an ambient dry bulb temperature of 15°C and 60% relative humidity. All the plants are assumed to have an 85% capacity factor with net power output of 650 MWe. Natural gas properties used in this study are taken from 2019 revision of the NETL QGESS document “Specification for Selected Feedstocks”. [12]

### Performance Modeling Methodology

The thermodynamic performances of all the plants described in this study are based on the output from a steady-state model developed using Aspen Plus® software. In addition to the overall plant model, sub-system models for the cooled sCO<sub>2</sub> turbine, recuperators, CO<sub>2</sub> coolers/ICs were used for estimating their performance and cost. These sub-system models will be described briefly in the subsequent sections. For direct-fired sCO<sub>2</sub> power cycles, the working fluid is not pure CO<sub>2</sub> and changes composition at various points in the cycle. Due to limitations of the REFPROP property method for sCO<sub>2</sub> mixtures, the LK-PLOCK property method (based on the Lee-Kesler-Plöcker EOS) was used for modeling the direct sCO<sub>2</sub> power cycle. [13] For ASU and CPU components, the PENG-ROB physical property method was used.

For Case A, the ASU MAC was modeled as a three-stage compressor with two intercooling stages. The discharge pressure of the MAC was assumed to be 0.586 MPa with an isentropic efficiency of 87% for each stage. For the rest of the cases, the multi-stage water intercooled model was replaced with an

adiabatic compression train with aftercoolers. As described earlier, the aftercooler uses recycle CO<sub>2</sub> exiting the compression train as the cold sink. The ASU BAC was modeled as a six-stage compressor with five intercooling stages. The discharge pressure of the BAC was assumed to be 11.38 MPa with an isentropic efficiency of 87% for each stage. The cold sink for Cases A and B is process water cooling whereas for Cases C and D, recycle CO<sub>2</sub> exiting the compression train is the cold sink.

Table 2 summarizes the sCO<sub>2</sub> power cycle design conditions used for all the cases in this study. [4, 5, 8] The oxy-combustor was modeled in Aspen Plus with a series of combustion reactions for the oxidizable components of the fuel and assuming 100 percent conversion of these fuel components. The amount of excess O<sub>2</sub> is based on the stoichiometric amount needed for complete combustion of the fuel stream entering the process, without regard to any oxidizable components in the recycle sCO<sub>2</sub> stream. The turbine inlet temperature (TIT) selected in Table 2 (1,204°C) is slightly lower than that of reference F-class gas turbine (TIT ≈ 1,371°C) selected in this study. Follow-on studies should consider TIT as a design variable for optimization.

Section	Parameter	Value
<b>Combustor</b>	O <sub>2</sub> purity	99.5%
	Excess O <sub>2</sub>	0.1%
	Stages	1
	Pressure drop	300 kPa
	Heat loss	Zero
<b>Turbine</b>	Inlet temperature	1,204°C
	Inlet pressure	30.0 MPa
	Outlet pressure	2.98 MPa
	Blade cooling	See below
<b>CO<sub>2</sub> Pre-Compressor</b>	Stages	5
	Intercooling stages	4
	Isentropic efficiency	85%
<b>Oxidant/Recycle compressor</b>	Stages	1
	Intercooling stages	0
	Isentropic efficiency	85%
<b>Boost Pump</b>	Stages	2
	Intercooling stages	1
	Isentropic efficiency	85%

**Table 2:** sCO<sub>2</sub> power cycle design parameters [4, 5, 8]

The cooled sCO<sub>2</sub> turbine includes four stages and was modeled in Aspen Custom Modeler (ACM) based on a high-fidelity turbomachinery design to estimate the necessary coolant flowrates, cooled turbine efficiencies, turbine exhaust temperature (as well as stage temperature distribution), and power output. A cooled turbine analysis, which was originally

developed and validated for air-breathing gas turbines, [14] was reviewed and modified for sCO<sub>2</sub> working fluid. An analytical thermal stress analysis was conducted to determine coolant temperatures and cooling configurations to ensure safe operation for the disks and blades (i.e., without causing excessive thermal stress loads). The design for this study only considered internal cooling since the viability of film cooling in an sCO<sub>2</sub> environment has not yet been verified. Figure 3 shows the sCO<sub>2</sub> turbine configuration and introduction of coolant streams. As mentioned earlier, two coolant streams at 213.3°C and 327.8°C are drawn from the recuperation train (diluent stream exiting ITR, HTR2) for turbine blade cooling. The lower temperature stream is used to cool the third stage and the higher temperature stream is used to cool the first two stages to reduce thermal stresses. The fourth stage of the turbine is not cooled. Purge cooling is used to provide cooling to the rims and seals of the turbine and supplemental cooling for the disks and blades. The fraction of the purge flow varies for each stage, but it is in the range of 0.2–0.5 percent of the diluent flowrate. The range of purge cooling flow is determined from the typical ranges used in conventional gas turbines. The coolant used to cool the stator is directed to the casing to cool the turbine outer casing to reduce tip clearance related losses of the rotors. The purge cooling between the stator and rotor blades is supplied from the casing, whereas the purge cooling for the stator is supplied from the disk cavity. The cooling analysis showed that a thermal barrier coating is needed to provide thermal protection. Further details about the cooled turbine design equations and calculations can be found in Uysal et al. [15, 16]

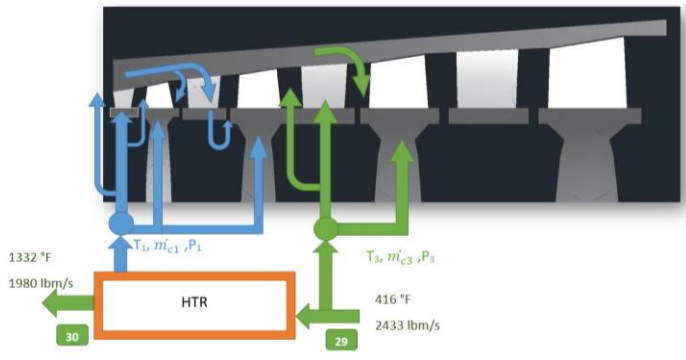


**Figure 3:** Single flow sCO<sub>2</sub> turbine configuration

The sCO<sub>2</sub> recuperators are envisioned to be compact diffusion-bonded heat exchangers, commercially known as printed circuit heat exchangers (PCHEs). A one-dimensional PCHE model was developed in the ACM platform for the design of the cycle recuperators. The cross-section of PCHE etched channels is mostly semi-circular with a channel width/diameter ( $D_c$ ) varying from 1 – 5 mm. In this study,  $D_c$  was varied for each of the recuperators to reduce the capital cost of the recuperation train. A high-angle channel design was adopted for the cold side and a low-angle channel design was adopted for the hot side using thermal-hydraulic correlations developed based on experimental data available in open literature. [17] The low-angle channel

design for the hot side results in significantly lower pressure drops, which is advantageous despite having lower heat transfer coefficients compared to the high-angle channel design. The ratio between the number of hot and cold plates ( $R_p$ ) was set to 2 for a more uniform distribution of pressure drop on hot and cold sides. To capture the sharp variation in thermo-physical properties near the critical point, the number of nodes along the z direction was set to 50. Further details of the PCHE model and validation can be found in Jiang et al. [18]

The sCO<sub>2</sub> cycle coolers and ICs are made up of adiabatic cooler bays. Adiabatic coolers are used in the CO<sub>2</sub> refrigeration industry to enhance the performance of CO<sub>2</sub> coolers during hot conditions. An Excel-based performance model of an adiabatic cooler bay was developed. The heat exchanger tube bundles are discretized into multiple sub-sections ( $N=10$ ) to account for the non-linear variation in thermo-physical properties of CO<sub>2</sub>. The model was validated to the data provided by the vendor. The adjustable inputs include CO<sub>2</sub> operating conditions, ambient air dry and wet bulb temperatures, and the number of discretization points ( $N$ ) along the tube bundle length. The model iteratively calculates the number of required bays, total auxiliary fan power consumption and total water consumption rate to meet the desired operating conditions. Further modeling details, CO<sub>2</sub>-side and air-side heat transfer and pressure drop correlations, can be found in Pidaparti et al. [19]

### Economic Analysis Methodology

Plant capital costs in this study are estimated according to NETL’s QGESS document [20]. The capital costs are defined at two levels: bare erected cost (BEC) and total plant cost (TPC), which are overnight costs expressed in 2018 base-year dollars. No process contingency costs are applied to sCO<sub>2</sub> specific components during optimization, which are more reflective of Nth-of-a-kind (NOAK) cost estimates.

All the sCO<sub>2</sub> power cycle components costs follow a general power law form:

$$C = aSP^b \times f_T$$

where  $SP$  is the scaling parameter,  $a$  and  $b$  are the scaling coefficients, and  $f_T$  is a temperature correction factor of the following form:

$$f_T = \begin{cases} 1 & \text{if } T_{max} < T_{bp} \\ 1 + c(T_{max} - T_{bp}) + d(T_{max} - T_{bp})^2 & \text{otherwise} \end{cases}$$

where  $T_{bp}$  is the temperature breakpoint which is 550°C, and  $T_{max}$  is the maximum temperature rating of the component. The scaling parameters and coefficients are listed in Table 3. Except for recuperators and coolers, these values are taken from Weiland et al. [21]. Recuperators cost correlation use recuperator mass ( $M_{recup}$ ) as the scaling parameter derived from vendor quotes.  $M_{recup}$  is calculated using the PCHE model described earlier and captures the impact of design variables such as temperature approach, pressure drops etc. The recuperator cost correlation shown in Table 3 is only valid for PCHEs constructed

out of stainless steel 316. However, HTR1 experiences temperatures  $>700^{\circ}\text{C}$  due to exposure to turbine exhaust. In order to withstand such high temperatures, HTR1 is broken into two separate sections (HTR1-LT and HTR1-HT). HTR1-LT is constructed out of stainless steel 316 (SS316) and HTR1-HT is constructed out of Inconel 740H (IN740H) to withstand temperatures as high as  $760^{\circ}\text{C}$ . The IN740H PCHE cost is calculated using the following cost algorithm, which includes a correction factor ( $CF$ ) to account for difference in material costs for SS316 (material cost =  $\$6.8/\text{lb}$ ) and IN740H (material cost =  $\$30.0/\text{lb}$ ):

$$C = 1,371 M^{0.7842} * (CF)$$

$$CF = \left(\frac{30}{6.8}\right)$$

It should be noted the IN740H PCHE cost correlation is not compared/validated against any vendor quote and also does not consider the difference in fabrication costs between IN740H and SS316 PCHEs. Therefore, it carries a high degree of uncertainty compared to the SS316 PCHE cost correlation. To reduce the total capital cost of HTR1, a sensitivity analysis was conducted to determine an appropriate breakpoint temperature between HTR1-LT and HTR1-HT sections. As shown in Figure 4, HTR1 capital cost exhibits a minimum around temperature breakpoint of  $\sim 600^{\circ}\text{C}$ .

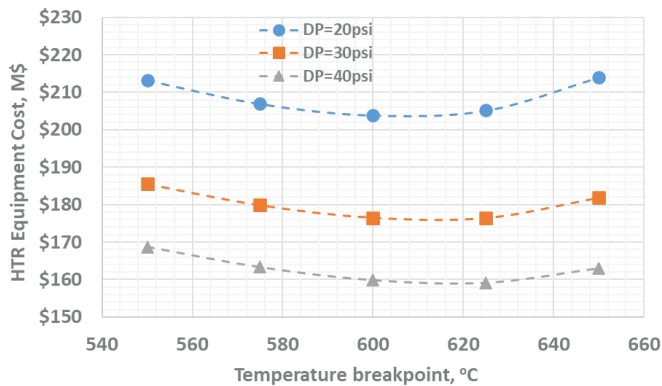


**Figure 4:** HTR1 capital cost as a function of breakpoint temperature for various pressure drops

Component	Scaling parameter (Units)	Coefficients			
		$a$	$b$	$c$	$d$
Recuperators (HTR2, ITR, LTR)	$M_{Recup}$ (kg)	1,371	0.78	0	0
sCO <sub>2</sub> compressors	$\dot{V}_{in}$ (m <sup>3</sup> /s)	6,220,000	0.11	0	0
Generator	$\dot{W}_e$ (MW <sub>e</sub> )	108,900	0.55	0	0
Compressor motor	$\dot{W}_e$ (MW <sub>e</sub> )	399,400	0.61	0	0
Adiabatic coolers	$N_{bays}$	124,933	1.00	0	0
Water Knockout cooler	$UA$ (W/K)	49.45	0.76	0	0

**Table 3:** Cost scaling parameters and coefficients for the sCO<sub>2</sub> power cycle components

The equipment cost of coolers and intercoolers are scaled linearly with the number of adiabatic cooler bays ( $N_{bays}$ )

calculated by the cooler model. The coefficient  $a$  for the coolers represents the cost per bay quoted by the vendor. The most novel component of the cycle is the combustor and turbine, for which no cost estimates exist in the public domain at any scale. The approach taken with this component is to combine the cost of a similarly-sized gas turbine (without the compressor) with the cost of a high-pressure outer casing similar to those used for HP steam turbines. Costs for these components are well-known and combine to constitute a cost estimate for a mature, NOAK direct sCO<sub>2</sub> turbine and combustor, albeit with a high degree of uncertainty. Any cost adjustments based on turbine output were calculated using the scaling exponent from NETL's QGESS. [22]

ASU capital cost was derived from an existing vendor quote for IGCC applications. The capital cost was scaled based on the O<sub>2</sub> flowrate using the scaling parameter from NETL's QGESS [22] and the costs are adjusted to 2018 dollars using the Chemical Engineering Plant Cost Index. It should be noted that the cryogenic ASU requirements for direct sCO<sub>2</sub> plants is different from the requirements for IGCC applications. IGCC applications require higher N<sub>2</sub> product pressure, which require use of higher-pressure columns in the ASU. Therefore, there might be significant uncertainty associated with use of this vendor quote for direct sCO<sub>2</sub> plant applications.

Operation and maintenance (O&M) costs are divided into two categories: fixed O&M costs that are independent of plant operation hours (e.g., labor, overhead, etc.), and variable O&M costs that are proportional to the power generation (e.g., consumables, waste disposal, maintenance materials). The variable O&M and fuel costs are multiplied by an assumed capacity factor of 85% to arrive at the actual annual expenditure. The captured CO<sub>2</sub> transportation and storage (T&S) costs are estimated as  $\$10/\text{tonne}$  [23]. The assumed levelized natural gas price is  $\$4.19/\text{GJ}$  ( $\$4.42/\text{MMBtu}$ ), on an HHV basis, delivered to the Midwest, and reported in 2018 U.S. dollars. Fuel costs are levelized over an assumed 30-year plant operational period with an assumed on-line year of 2023.

The levelized cost of electricity (LCOE) is reported on a  $\$/\text{MWh}$  basis and consists of contributions from the O&M costs (fixed, variable, and fuel)

, CO<sub>2</sub> T&S costs, and the annualized capital over the assumed 30-year lifetime of the plant. Additional details on the cost estimating methodology and other economic assumptions can be found in Gerdes et al. [20]. All the economic assumptions are consistent with the reference NGCC plants to ensure a fair comparison between both the technologies.

## OPTIMIZATION APPROACH

The overall plant optimization was conducted in two steps. In the first step, design parameters related to the recuperation train were optimized. This includes conducting a manual sensitivity analysis with respect to LTR cold end approach temperature, oxidant O<sub>2</sub> mole fraction, and recuperation train total pressure drops. To optimize the recuperation train total pressure drop, a manual sensitivity analysis was conducted assuming the same



pressure loss ( $P_{Loss}$ ) for each recuperator as the starting point; the distribution of  $P_{Loss}$  across the recuperation train was optimized using automated optimization solvers in the FOQUS platform [24] to minimize the recuperation train capital cost. For automated optimization, the covariance matrix adaption evolution strategy (CMA-ES) solver, which belongs to the class of evolutionary algorithms, was selected. [25] Recuperator channel diameters were also optimized using the CMA-ES optimization solver to minimize the recuperation train capital costs. Once the recuperation train design parameters were optimized, the compression train-related design parameters were optimized in the second step. The compression train optimization included conducting manual sensitivity analyses with respect to cooler/IC temperatures, and cooler/IC pressure drops. For each cooler temperature, the compression pressure profiles were optimized using the CMA-ES optimization solver to minimize the compression train power consumption. Once the compression train optimization was complete, the optimum recuperation train design parameters were verified by conducting a perturbation analysis as the final step of optimization.

### Sample Optimization Results

Figure 5 presents sample optimization results showing the impact of LTR cold end approach temperature ( $T_{App,LTR}$ ) and recuperator pressure loss ( $P_{Loss}$ ) on the plant efficiency and LCOE. These sample results are generated for Case C (thermal integration with ASU MAC and BAC), but similar trends were noticed for all the cases. For these sample results,  $P_{Loss}$  (defined below) is assumed to be same for all the recuperators (LTR, ITR, HTR2, HTR1-LT, HTR1-HT).

$$P_{Loss} = \frac{\Delta P_{cold} + \Delta P_{hot}}{P_{hot,in} + P_{cold,in}}$$

From Figure 5, increasing  $T_{App,LTR}$  or  $P_{Loss}$  reduces the plant efficiency but the plant LCOE presents an optimum value with respect to both  $T_{App,LTR}$  and  $P_{Loss}$ . Increasing  $T_{App,LTR}$  reduces the recuperation train effectiveness and results in lower combustor inlet temperature. This leads to higher natural gas and  $O_2$  flow requirements to achieve the desired TIT of 1204°C, thereby reducing the plant efficiency. Likewise, increasing  $P_{Loss}$  directly contributes to lower plant efficiency by increasing the compression train power consumption to make up for the pressure losses in the recuperation train. However, increasing  $T_{App,LTR}$  and  $P_{Loss}$  also leads to lower recuperation train capital costs due to higher driving forces and lower heat transfer area requirements. These competing factors lead to optimum LCOE values with respect to both  $T_{App,LTR}$  and  $P_{Loss}$ . From these sample results, it is clear that Case C considered in this study can achieve plant efficiencies as high as 50 percent (HHV basis) reported in the literature. However, the resulting capital costs and LCOE would be high in order to achieve these higher plant efficiencies.

The next step of the recuperation train design optimization is to conduct an automated optimization of the recuperation train to identify appropriate PCHE channel diameters and  $P_{Loss}$  for

individual recuperators to minimize the total recuperation train capital costs. Table 4 shows the  $P_{Loss}$  for individual recuperators before and after optimization using the CMA-ES solver in the FOQUS platform. Before the optimization,  $P_{Loss}$  for all the recuperators was assumed to be 0.2975%. After the optimization, a significantly higher  $P_{Loss}$  is calculated for the Inconel 740H PCHE (HTR1-HT);  $P_{Loss}$  is lowest for LTR, which has the lowest design temperature. As a result of the optimization, recuperation train equipment cost decreased from 345.5 M\$ to 238.0 M\$ and the LCOE decreased from \$84.4/MWh to \$80.5/MWh. These results highlight the importance of recuperation train optimization to reduce the direct sCO<sub>2</sub> plant LCOE, albeit at the expense of reduced plant efficiency.

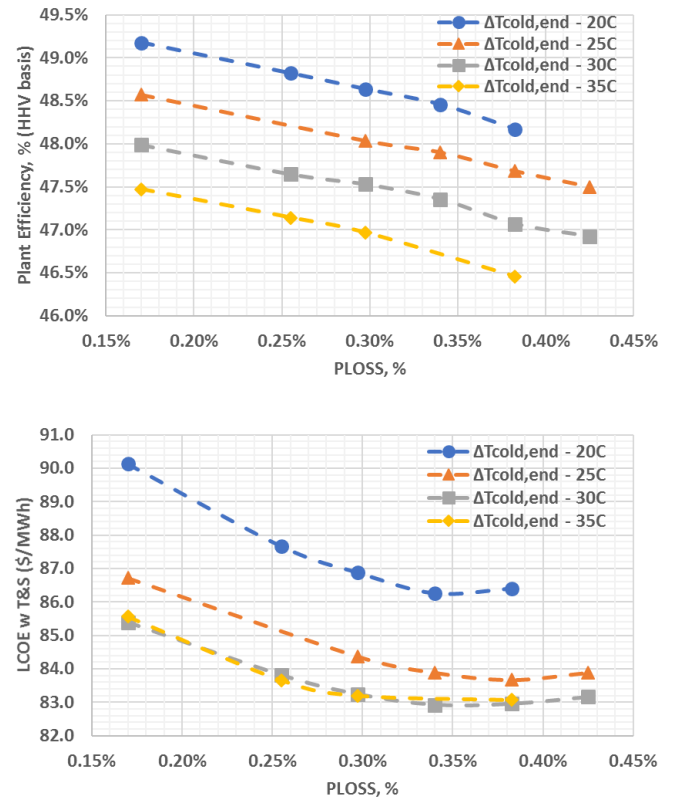


Figure 5: Impact of LTR cold end approach temperature and recuperator pressure loss on plant efficiency and LCOE

Design Variables	Pre-Optimization	Post-Optimization
$P_{Loss,LTR}$	0.2975%	0.188%
$P_{Loss,ITR}$	0.2975%	0.226%
$P_{Loss,HTR2}$	0.2975%	0.226%
$P_{Loss,HTR1-LT}$	0.2975%	0.329%
$P_{Loss,HTR1-HT}$	0.2975%	0.973%
Recuperation train equipment cost, M\$	345.5	238.0
LCOE with T&S (\$/MWh)	84.4	80.5

Table 4: Optimization of  $P_{Loss}$  distribution using CMA-ES optimization solver



Figure 6 presents the impact of sCO<sub>2</sub> cooler/IC temperature ( $T_{cooler}$ ) on the plant efficiency and LCOE. For each cooler temperature, the compression train pressure profiles as well as cooler/IC pressure drops are optimized to minimize the plant LCOE. Optimum compression pressure profiles for each cooler temperature are presented in Table 5. The pre-compressor outlet pressure is set to 10 MPa for all the cases to provide necessary mixing with O<sub>2</sub> from the ASU to generate the oxidant stream. The pre-compressor stage outlet pressures decrease with the cooler temperature. The pre-compressor stage 4 outlet pressure is close to the saturation/pseudo-critical pressure of the mixture. From Figure 6, decreasing  $T_{cooler}$  from 26°C to 20°C improves the plant efficiency by 1.4 percentage points and reduces the LCOE by ~3.8%. Any further reduction in  $T_{cooler}$  below 20°C improves the plant efficiency but increases the LCOE due to higher capital costs associated with coolers/ICs. It should be noted that these results are only valid for fixed ambient design conditions used in this study.

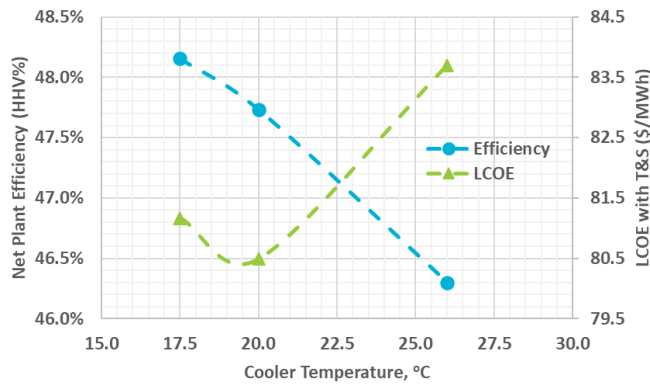


**Figure 6:** Impact of cooler/IC temperature on plant efficiency and LCOE

$T_{cooler}$	17.5°C	20.0°C	26.0°C
Pre-compressor stage1 outlet	3.58	3.67	3.66
Pre-compressor stage2 outlet	4.67	4.92	4.87
Pre-compressor stage3 outlet	5.84	6.19	6.23
Pre-compressor stage4 outlet	6.50	6.82	7.45
Boost pump stage1 outlet	17.51	17.74	17.51

**Table 5:** Optimization pressure profiles (in MPa) for different cooler/IC temperatures

### OPTIMIZED DIRECT sCO<sub>2</sub> PLANTS

Table 6 presents optimized design variables for all the cases (Case A through Case D) considered in this study. Optimized compression train design parameters are similar for all the cases, but the optimized recuperation train design parameters are impacted by the amount of thermal integration with the ASU. Optimum  $T_{App,LTR}$  increases with the amount of thermal integration with the ASU due to tighter approach temperatures within the recuperation train. For example, optimum  $T_{App,LTR}$  for Case A (no heat recovery from the ASU) is 1.5°C but that value increases to 25.0°C for Case C (heat recovery from both the ASU

MAC and BAC) to reduce the recuperation train capital cost. Likewise, the optimum  $P_{Loss}$  distribution is also impacted by the amount of thermal integration with the ASU. For example, optimum  $P_{Loss}$  for Inconel 740H PCHE (HTR1-HT) increases from 0.872% to 0.973% going from Case A to Case C, again, to reduce the recuperation train capital cost.

Design Variables	Case A	Case B	Case C	Case D
<b>Recuperation Train Design Parameters</b>				
$T_{App,LTR}$ , °C	1.5	15.0	25.0	25.0
$D_{C,LTR}$ , mm	1.1	1.0	1.2	1.1
$D_{C,ITR}$ , mm	1.1	1.1	1.3	1.1
$D_{C,HTR2}$ , mm	2.6	2.5	2.3	2.0
$D_{C,HTR1-LT}$ , mm	1.7	1.7	1.6	1.4
$D_{C,HTR1-HT}$ , mm	1.6	1.6	1.4	1.1
$P_{Loss,LTR}$	0.276%	0.224%	0.188%	0.183%
$P_{Loss,ITR}$	0.273%	0.255%	0.226%	0.211%
$P_{Loss,HTR2}$	0.204%	0.224%	0.226%	0.217%
$P_{Loss,HTR1-LT}$	0.307%	0.316%	0.329%	0.312%
$P_{Loss,HTR1-HT}$	0.872%	0.949%	0.973%	0.957%
Oxidant O <sub>2</sub> mole fraction	13.3%			
<b>Compression Train Design Parameters</b>				
$T_{cooler}$ , °C	20.0			
$\Delta P_{PCIC1}$ , kPa	103.4			
$\Delta P_{PCIC2}$ , kPa	103.4			
$\Delta P_{PCIC3}$ , kPa	34.5			
$\Delta P_{PCIC4}$ , kPa	13.8			
$\Delta P_{MC}$ , kPa	103.4			
$\Delta P_{IC}$ , kPa	103.4			
Pre-compressor stage1 outlet, MPa	3.67			
Pre-compressor stage2 outlet, MPa	4.92			
Pre-compressor stage3 outlet, MPa	6.19			
Pre-compressor stage4 outlet, MPa	6.82			
Boost pump stage1 outlet, MPa	17.74			

**Table 6:** Optimized design variables for cases A through D

Table 7 (Refer to ANNEX A) provides a summary of the performance and detailed auxiliary power breakdown for the optimized direct sCO<sub>2</sub> plants along with reference NGCC plants. The reference B31B.90 and B31B.97 cases are state-of-the-art F-class NGCC plants with 90% and 97% CO<sub>2</sub> capture respectively. Details regarding performance modeling and economic analysis for the reference cases can be found in NETL’s Fossil Energy Baseline report. [11] For comparison purposes, the natural gas flow rate for all the direct sCO<sub>2</sub> plants is set to the value used in the reference F-class NGCC plants. The following observations can be made when comparing the performance of the direct sCO<sub>2</sub> power plants with the reference NGCC plants:

- The optimized direct sCO<sub>2</sub> plants offered plant efficiencies in the range of 46.4 – 48.2%. These efficiencies are in line with the state-of-the-art F-class NGCC plants with CO<sub>2</sub> capture rates of 97%. However, direct sCO<sub>2</sub> plants can achieve capture rates as high as 99%.
- All the direct sCO<sub>2</sub> plants have a higher gross power output than the reference B31B.90, B31B.97 cases. However, the auxiliary power requirement for the direct sCO<sub>2</sub> plants is significantly higher than the reference NGCC plants primarily due to the ASU auxiliary load and natural gas compression. The ASU is not needed for the reference

NGCC plants due to the use of a post-combustion CO<sub>2</sub> capture system.

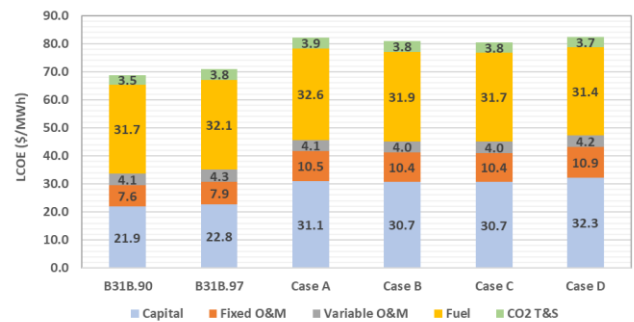
- The ASU power consumption increases as the heat recovery from the ASU increases. For example, ASU MAC and BAC power consumption increases from ~128 MWe to ~146 MWe going from Case A to Case C. However, this higher ASU power consumption is more than offset by the higher gross power output due to increased heat recovery.
- Thermal integration with the ASU is needed to achieve higher plant efficiencies. For example, optimized Case A has plant efficiency of 46.4% but that value increases to 47.7% for Case C despite having higher LTR cold approach temperatures (see Table 6). The likelihood of achieving >50% plant efficiency (HHV basis) is low for the direct sCO<sub>2</sub> plants without thermal integration with the ASU.
- Out of all the direct sCO<sub>2</sub> plants, Case D, which is based on the patent from 8 Rivers, offered the highest plant efficiency. This case also represents maximum heat integration with the ASU as well as heat integration with compressed recycle CO<sub>2</sub> gas.
- Water consumption of all the direct sCO<sub>2</sub> plants is significantly lower than the reference NGCC plants. Significant water reduction for the sCO<sub>2</sub> plants is primarily due to differences in cooling technologies (adiabatic versus wet cooling) as well as elimination of intrinsic water losses arising from the bottoming Rankine cycle such as from blowdown.

Table 8 (Refer to ANNEX A) shows the capital cost summary for all the optimized direct sCO<sub>2</sub> plants along with the reference NGCC plants. Figure 7 shows the LCOE breakdown for these cases. The following observations can be made when comparing the economics of the direct sCO<sub>2</sub> power plants with the reference NGCC plants:

- LCOE of the direct sCO<sub>2</sub> power plants are 13–23% higher than the reference NGCC plants. The higher LCOE is primarily due to higher capital costs associated with the cryogenic ASU and sCO<sub>2</sub> power block.
- TPCs of the direct sCO<sub>2</sub> power plants are 35–50% higher than the reference NGCC plants on a \$/kWe basis. From Table 8, TPC of the cryogenic ASU for the direct sCO<sub>2</sub> plants is on par with the post-combustion CO<sub>2</sub> capture system TPC (Flue Gas Cleanup & Piping sub-account from Table 8) used in the reference NGCC plants. However, as noted earlier, there is uncertainty associated with the ASU vendor quote used for this study. BOP capital costs for the direct sCO<sub>2</sub> power plants are similar to that of the reference NGCC plants.
- sCO<sub>2</sub> power block capital costs are over twice that of the combined gas turbine, HRSG, and steam turbine capital costs in the NGCC plants. These differences arise from the need for additional heat exchangers (recuperators, multiple coolers, and ICs within the compression train) for direct sCO<sub>2</sub> power cycles. From Table 8, recuperators (HTR, ITR, and LTR) make up nearly 50% of the total sCO<sub>2</sub> power block

costs. Coolers and ICs make up an additional 23 percent. Therefore, combined together, heat exchangers makeup 70–75% of the total sCO<sub>2</sub> power block costs.

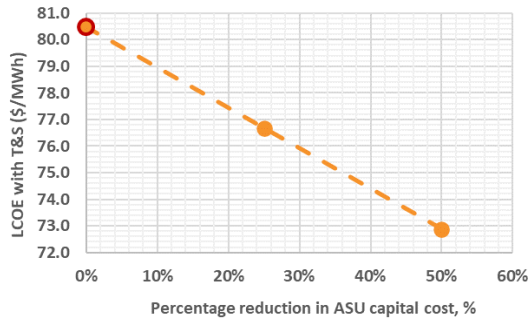
- Thermal integration with the ASU not only improves the plant efficiency but also improves the plant economics and LCOE. For example, going from Case A to Case C, the plant TPC (\$/kWe basis) and LCOE decreases by 1.3% and 2%, respectively. Thermal integration with the ASU increases the recuperation train capital costs as can be seen in Table 8. However, this increase in the power block capital costs is more than offset by higher power generation resulting from thermal integration with the ASU.
- Out of all the direct sCO<sub>2</sub> plants, Case C offered the lowest LCOE. Despite having higher plant efficiency, LCOE of the Case D is higher than the rest of the cases primarily due to additional capital expenses associated with the recycle compressor, additional water knockout cooler, etc. Therefore, heat integration with compressed recycle gas might not be an economical choice. However, if low-cost recuperators are developed in the future, the concept might present an attractive opportunity for additional heat beyond what can achieved with ASU thermal integration alone.



**Figure 7:** LCOE breakdown for all the optimized direct sCO<sub>2</sub> plants and reference NGCC plants

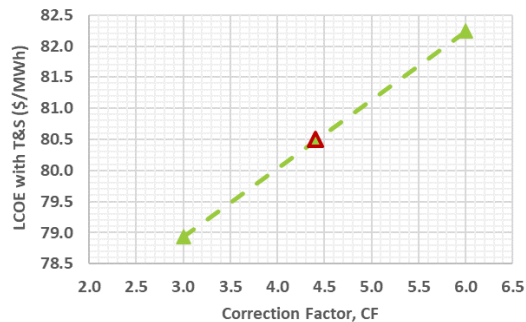
### Additional Sensitivities

Figure 8 presents the impact of ASU capital cost reduction on the plant LCOE. As mentioned earlier, the ASU capital cost might carry a large degree of uncertainty due to the use of a vendor quote that is intended for IGCC applications. For example, the ASU capital cost used in the current study is ~\$843/kWe but the ASU capital cost reported in the IEAGHG study is nearly 50 percent lower (~\$440/kWe). [4] Consequently, a 50% reduction in the ASU capital cost leads to nearly 10% reduction in the plant LCOE making the technology much more competitive with the reference NGCC plants using a post-combustion capture system.



**Figure 8:** Impact of ASU capital cost reduction on LCOE

Another area of uncertainty in this study is associated with the Inconel 740H PCHE cost correlation. As described previously, the IN740H PCHE cost correlation includes a correction factor (*CF*) to account for the difference in material costs between IN740H and stainless steel 316. However, this approach is largely unvalidated and a sensitivity analysis was conducted to the *CF* as presented in Figure 9. Decreasing the *CF* from the base case of 4.4 to 3.0 reduces the LCOE by 2%. A lower correction factor can be a result of a more accurate cost algorithm accounting for differences in material as well as fabrication costs for IN740H PCHE. Alternatively, low-cost nickel alloys such as Inconel 625 can be used in place of IN740H to reduce the cost of the HTR.



**Figure 9:** Impact of IN740H PCHE correction factor on LCOE

### IMPACT OF LANDFILL GAS CO-FIRING

This section presents the impact of LFG and natural gas co-firing on the direct sCO<sub>2</sub> plant efficiency, LCOE, and CO<sub>2</sub> emissions. LFG is a product of the decomposition of organic material (e.g., municipal solid waste) under anaerobic conditions. For a typical U.S. municipal solid waste, LFG contains 50–55% methane, 45–50% CO<sub>2</sub>, and 2–5% other gases such as N<sub>2</sub> and sulfides, etc., along with less than 1% of non-methane organic compounds and trace amounts of inorganic compounds. For this study, the LFG composition was assumed to be 50% methane and 50% CO<sub>2</sub> (vol% basis) representing a generic site based on EPA recommendation. [26] Most landfills in the United States capture and flare the LFG to reduce methane emissions since methane is a significantly more potent greenhouse gas than CO<sub>2</sub>. However, energy recovery systems can make use of this captured LFG to produce heat (boilers, kilns), generate electricity, or produce renewable natural gas.

For this study, the LFG gas collection and control system (GCCS) capital costs and annual O&M costs are estimated using EPA's LFGcost-Web Excel-based application. [27] LFG fuel price depends on the amount of treatment needed among other factors. For this study, the EPA-recommended value of \$1.75/MMBtu was used as the LFG fuel price. [27] This is ~40% cheaper than the natural gas price assumed in the current study. LFG pre-purification steps (such as water and siloxanes removal) were assumed to be part of the assumed LFG fuel price.

Captured LFG is compressed from near atmospheric pressure to the combustor pressure of ~300 bar in a multi-stage intercooled compressor (total stages = 10). The maximum compression temperature is limited to 150°C to avoid LFG autoignition at high temperatures due to O<sub>2</sub> intrusion from air during compression. [28] Compression of LFG also presents an additional opportunity for thermal integration with the recuperation train and to improve plant efficiency. The LFG compressor intercooler temperature is set to have a 5.6°C approach to the recycle CO<sub>2</sub> stream exiting the power cycle compression train to allow for thermal integration. The stage isentropic efficiency is assumed to be 85%.

Figure 10 shows the impact of LFG and natural gas co-firing on the plant efficiency. Increasing the LFG co-firing from 0% to 50% decreases the plant efficiency by 0.3 percentage points. As the amount of LFG co-firing increases, the auxiliary loads associated with LFG compression, CPU increase. This is partially offset by higher cycle efficiency due to higher heat recovery from LFG compression. Consequently, the overall impact of LFG co-firing on plant efficiency is minimal.

Plant LCOE increases with LFG co-firing primarily due to the higher capital costs associated with the sCO<sub>2</sub> power block, LFG GCCS, and CPU. The power block capital cost increases with the LFG co-firing primarily due to higher capital costs associated with HTR. As the LFG co-firing increases, the amount of heat recovered from LFG compression increases leading to tighter approach temperatures within the recuperation train. The minimum temperature approach decreases from 6.9°C for 0% LFG co-firing to 3.1°C for 50% LFG co-firing. However, it should be pointed out that no attempt was made to optimize the recuperation train for different levels of LFG co-firing. Optimizing the LTR cold end approach temperature and the recuperators  $P_{Loss}$  distribution can lead to lower LCOEs than the values presented in Figure 10. In addition to higher capital costs, O&M costs increase with LFG co-firing due to costs associated with the LFG GCCS. Increased LFG co-firing also leads to higher levels of CO<sub>2</sub> capture, which increases the CO<sub>2</sub> T&S costs. Overall, the increase in capital costs, O&M costs, and CO<sub>2</sub> T&S costs is partially offset by the lower fuel costs (due to lower LFG fuel price). As a result, increasing LFG co-firing from 0% to 50% increases the LCOE by 3% with only a marginal LCOE increase up to 30% LFG co-firing.

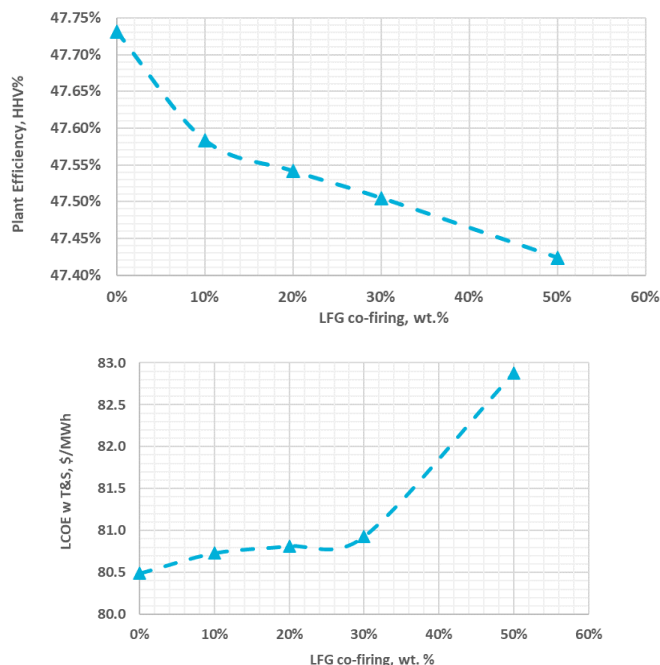


**Figure 10:** Impact of LFG co-firing on plant efficiency and LCOE

Figure 11 presents the impact of LFG co-firing on the net CO<sub>2</sub> emissions. The net CO<sub>2</sub> emissions for the plant are calculated using two methods from the literature. In Method1, the CO<sub>2</sub> emissions from LFG co-firing are offset from the plant CO<sub>2</sub> emissions. [28] Flaring of 1 kg of LFG generates 1.46 kg of CO<sub>2</sub> emissions assuming 100% combustion of the methane in LFG. Net CO<sub>2</sub> emissions are calculated by assuming that 50% of these flared CO<sub>2</sub> emissions are from biomass sources. [28] In Method2, the avoided CO<sub>2</sub> emissions from the use of LFG instead of natural gas are offset from the plant CO<sub>2</sub> emissions to calculate the net CO<sub>2</sub> emissions. Since LFG is considered as a renewable energy source, use of LFG can offset the need for natural gas fuel. The avoided CO<sub>2</sub> emissions from use of LFG instead of natural gas are calculated using EPA's LFGCost-Web Excel-based application. [27] Using both of the methods, the direct sCO<sub>2</sub> plants have the potential to achieve net-zero CO<sub>2</sub> emissions for 3–4% LFG co-firing. Due to high inherent CO<sub>2</sub> capture rates, direct sCO<sub>2</sub> plants have a strong potential for net negative CO<sub>2</sub> emissions when co-firing LFG and natural gas. For example, increasing the LFG co-firing rate to 50% results in net negative CO<sub>2</sub> emissions of 78–94 kgCO<sub>2</sub>/MWh. It should be noted the net CO<sub>2</sub> emissions presented in Figure 11 did not consider the CO<sub>2</sub> emissions associated with the upstream chain aspects of LFG and natural gas supply. For example, CO<sub>2</sub> emissions associated with LFG leakage from the gas collection system or natural gas transportation are ignored in the calculations. As such, these results should be treated as a screening type analysis to utilize LFG for power generation at utility scale. Future studies should consider a life-cycle analysis in order to estimate the net CO<sub>2</sub> emissions more accurately.

Conducting a life-cycle analysis will likely lead to higher required LFG co-firing rates in order to achieve net-zero CO<sub>2</sub> emissions.

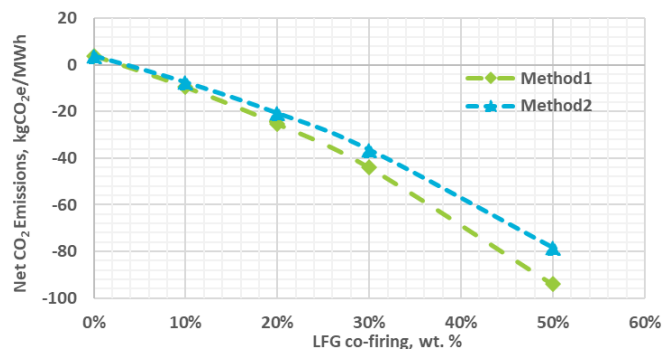


**Figure 11:** Impact of LFG co-firing on net CO<sub>2</sub> emissions

## SUMMARY AND CONCLUSIONS

This study presented the techno-economic optimization results for natural gas fueled direct sCO<sub>2</sub> plants. To improve the modeling accuracy, the plant Aspen Plus model included high-fidelity sub-system models for the air separation unit, cooled sCO<sub>2</sub> turbine, PCHE recuperators, and adiabatic coolers. Plant optimization was conducted using a combination of manual sensitivity analyses and automated optimization wherever possible to minimize the plant LCOE. Optimization variables included parameters related to the recuperation train (temperature approach, pressure drops, PCHE channel diameters) and the compression train (cooler temperature, compression pressure profiles, cooler/IC pressure drops). The study also considered various levels of thermal integration between the ASU and the recuperation train to investigate the impact on plant efficiency and LCOE. Results indicate that thermal integration of power cycle with both the ASU MAC and BAC is needed to achieve high plant efficiencies (>50% on HHV basis). However, achieving such high plant efficiencies would require tight recuperator approach temperatures and low CO<sub>2</sub> pressure drops, which increases the sCO<sub>2</sub> power block capital costs and the plant LCOE. Optimizing the design parameters while considering their impact on both plant efficiency and LCOE resulted in a plant efficiency (HHV basis) of 47.7% and LCOE (with CO<sub>2</sub> T&S) of \$80.5/MWh. Compared to a state-of-the-art NGCC plant with CCS (using an F-class gas turbine and 97% CO<sub>2</sub> capture), the optimized direct sCO<sub>2</sub> plant has a 0.7 percentage point higher plant efficiency and 13.5% higher LCOE while offering a higher CO<sub>2</sub> capture rate of 98.5%. Uncertainty might exist in the ASU capital cost estimates and based on the sensitivity analysis conducted, a 50% reduction in the ASU capital cost would decrease the direct sCO<sub>2</sub> plant LCOE by 9.5%, which makes the technology competitive with the state-of-the-art NGCC plants with CCS. Additional economic improvements can be achieved by reducing the capital cost of PCHE recuperators operating at temperatures > 600°C, which would require the use of nickel alloys.



A screening type analysis was conducted to investigate the impact of co-firing LFG and natural gas on direct sCO<sub>2</sub> plant efficiency, LCOE, and emissions. Increasing the LFG co-firing rate from 0% to 50% (weight basis), decreased the plant efficiency by 0.3 percentage points and increased the LCOE by 3%. Due to high inherent CO<sub>2</sub> capture rates, direct sCO<sub>2</sub> plants have the potential to achieve net-negative CO<sub>2</sub> emissions from LFG and natural gas co-firing. Overall, this study presents the clearest picture of the cost and performance potential for direct sCO<sub>2</sub> power cycles in the public literature and identifies areas of research and development that could expedite the commercialization of this technology.

## NOMENCLATURE

Ar	- Argon
ASU	- Air separation unit
BAC	- Boost air compressor
BFD	- Block flow diagram
BOP	- Balance of Plant
CCS	- Carbon capture and storage
CMA-ES	- Covariance matrix adaption evolution strategy
COE	- Cost of electricity
CPU	- CO <sub>2</sub> purification unit
CTM	- Cooled turbine model
DP	- Pressure drop
EPA	- Environmental protection agency
FOQUS	-Framework for Optimization and Quantification of Uncertainty and Sensitivity
GCCS	- Gas collection and control system
HHV	- Higher heating value
HRSG	- Heat recovery steam generator
HTR	- High temperature recuperator
IC	- Intercooler
IEAGHG	- International Energy Agency Greenhouse Gas Research Programme
IGCC	- Integrated gasification combined cycle
ITR	- Intermediate temperature recuperator
LCOE	- Levelized cost of electricity
LFG	- Landfill gas
LTR	- Low temperature recuperator
MAC	- Main air compressor
NETL	- National Energy Technology Laboratory
NGCC	- Natural gas combined cycle
NOAK	- Nth-of-a-kind
O&M	- Operation and maintenance
PCHE	- Printed circuit heat exchanger
QGESS	- Quality Guidelines for Energy System Studies
R&D	- Research and development
sCO <sub>2</sub>	- Supercritical carbon dioxide
T&S	- Transport and storage
TEA	- Techno-economic analysis
TIT	- Turbine inlet temperature
TPC	- Total plant cost

## DISCLAIMER

This project was funded by the Department of Energy, National Energy Technology Laboratory an agency of the United States Government, through a support contract. Neither the United States Government nor any agency thereof, nor any of its employees, nor the support contractor, nor any of their employees, makes any warranty, express or implied, or assumes any legal liability or responsibility for the accuracy, completeness, or usefulness of any information, apparatus, product, or process disclosed, or represents that its use would not infringe privately owned rights. Reference herein to any specific commercial product, process, or service by trade name, trademark, manufacturer, or otherwise does not necessarily constitute or imply its endorsement, recommendation, or favoring by the United States Government or any agency thereof. The views and opinions of authors expressed herein do not necessarily state or reflect those of the United States Government or any agency thereof.

## ACKNOWLEDGEMENTS

The authors would like to thank Travis Shultz (NETL), Richard Dennis (NETL), Can Uysal and Mark Woods (NETL support contractors) for their support and assistance in performing this work.

## REFERENCES

- [1] R. Allam, S. Martin, B. Forrest, J. Fetvedt, X. Lu, D. Freed, G. W. Brown Jr, T. Sasaki, M. Itoh and J. Manning, "Demonstration of the Allam Cycle: an update on the development status of a high efficiency supercritical carbon dioxide power process employing full carbon capture," *Energy Procedia*, vol. 114, pp. 5948-5966, 2017.
- [2] R. J. Allam, J. E. Fetvedt, B. A. Forrest and D. A. Freed, "The oxy-fuel, supercritical CO<sub>2</sub> Allam Cycle: New cycle developments to produce even lower-cost electricity from fossil fuels without atmospheric emissions," in *Turbo Expo: Power for Land, Sea, and Air*, 2014.
- [3] R. J. Allam, M. R. Palmer, G. W. Brown Jr, J. Fetvedt, D. Freed, H. Nomoto, M. Itoh, N. Okita and C. Jones Jr, "High efficiency and low cost of electricity generation from fossil fuels while eliminating atmospheric emissions, including carbon dioxide," *Energy Procedia*, vol. 37, pp. 1135-1149, 2013.
- [4] International Energy Agency Greenhouse Gas (IEAGHG), "Oxy-Combustion Turbine Power Plants," Cheltenham, United Kingdom, August 2015.
- [5] R. Scaccabarozzi, M. Gatti and E. Martelli, "Thermodynamic analysis and numerical optimization of the NET Power oxy-combustion cycle," *Applied energy*, vol. 178, pp. 505-526, 2016.
- [6] R. Scaccabarozzi, M. Gatti and E. Martelli, "Thermodynamic optimization and part-load analysis of

- the NET Power Cycle," *Energy Procedia*, vol. 114, pp. 551-560, 2017.
- [7] A. McClung, K. Brun and J. Delimont, "Comparison of supercritical carbon dioxide cycles for oxy-combustion," in *Turbo Expo: Power for Land, Sea, and Air*, 2015.
- [8] C. White and N. Weiland, "Preliminary cost and performance results for a natural gas-fired direct sCO<sub>2</sub> power plant," in *The 6th International Supercritical CO<sub>2</sub> Power Cycles Symposium*, 2018.
- [9] Electric Power Research Institute (EPRI), "Performance and Economic Evaluation of Supercritical CO<sub>2</sub> Power Cycle Coal Gasification Plant," (300200374), Palo Alto, California, December, 2014.
- [10] R. J. Allam, B. A. Forrest and J. E. Fetvedt, *Method and system for power production with improved efficiency*, Google Patents, 2017.
- [11] R. E. James III PhD, D. Kearins, M. Turner, M. Woods, N. Kuehn and A. Zoelle, "Cost and performance baseline for fossil energy plants volume 1: bituminous coal and natural gas to electricity," 2019.
- [12] National Energy Technology Laboratory, "Quality Guidelines for Energy System Studies: Specification for Selected Feedstocks," U.S. Department of Energy, Pittsburgh, PA, 2019.
- [13] C. W. White and N. T. Weiland, "Evaluation of Property Methods for Modeling Direct-Supercritical CO<sub>2</sub> Power Cycles," *Journal of Engineering for Gas Turbines and Power*, vol. 140, p. 011701, 2018.
- [14] S. C. Uysal, Analytical Modelling of the Effects of Different Gas Turbine Cooling Techniques on Engine Performance, West Virginia University, 2017.
- [15] S. C. Uysal and N. Weiland, "Turbomachinery design of an axial turbine for a direct fired sCO<sub>2</sub> cycle," *Energy Conversion and Management*, vol. 267, p. 115913, 2022.
- [16] S. C. Uysal, C. W. White, N. Weiland and E. A. Liese, "Cooling analysis of an axial turbine for a direct fired sCO<sub>2</sub> cycle and impacts of turbine cooling on cycle performance," *Energy Conversion and Management*, vol. 263, p. 115701, 2022.
- [17] R. Le Pierres, D. Southall and S. Osborne, "Impact of mechanical design issues on printed circuit heat exchangers," in *Proceedings of SCO<sub>2</sub> Power Cycle Symposium*, 2011.
- [18] Y. Jiang, E. Liese, S. E. Zitney and D. Bhattacharyya, "Design and dynamic modeling of printed circuit heat exchangers for supercritical carbon dioxide Brayton power cycles," *Applied Energy*, vol. 231, p. 1019–1032, 2018.
- [19] S. Pidaparti, C. W. White, A. C. O'Connell and N. Weiland, "Cooling Technology Models for Indirect sCO<sub>2</sub> Cycles," 2020.
- [20] K. Gerdes, W. M. Summers and J. Wimer, "Quality Guidelines for Energy System Studies: Cost Estimation Methodology for NETL Assessments of Power Plant Performance," 8 2011.
- [21] N. T. Weiland, B. W. Lance and S. R. Pidaparti, "sCO<sub>2</sub> Power Cycle Component Cost Correlations From DOE Data Spanning Multiple Scales and Applications," in *ASME Turbo Expo 2019: Turbomachinery Technical Conference and Exposition*, 2019.
- [22] National Energy Technology Laboratory, "Quality Guidelines for Energy System Studies: Cost Estimation Methodology for NETL Assessments of Power Plant Performance," U.S. Department of Energy, Pittsburgh, PA, 2019.
- [23] T. Grant, "Quality Guidelines for Energy System Studies: Carbon Dioxide Transport and Storage Costs in NETL Studies," 8 2019.
- [24] J. C. Eslick, B. Ng, Q. Gao, C. H. Tong, N. V. Sahinidis and D. C. Miller, "A framework for optimization and quantification of uncertainty and sensitivity for developing carbon capture systems," *Energy Procedia*, vol. 63, pp. 1055-1063, 2014.
- [25] N. Hansen, S. D. Müller and P. Koumoutsakos, "Reducing the time complexity of the derandomized evolution strategy with covariance matrix adaptation (CMA-ES)," *Evolutionary computation*, vol. 11, pp. 1-18, 2003.
- [26] [Online]. Available: <https://www3.epa.gov/ttnatcat1/dir1/lan dgem-v302-guide.pdf>.
- [27] [Online]. Available: [https://www.epa.gov/sites/default/files/2016-12/documents/lfgcost-webv3.1manual\\_113016.pdf](https://www.epa.gov/sites/default/files/2016-12/documents/lfgcost-webv3.1manual_113016.pdf).
- [28] G. V. Brigagão, J. L. Medeiros, F. A. Ofélia de Queiroz, H. Mikulčić and N. Duić, "A zero-emission sustainable landfill-gas-to-wire oxyfuel process: Bioenergy with carbon capture and sequestration," *Renewable and Sustainable Energy Reviews*, vol. 138, p. 110686, 2021.
- [29] X. Lu, B. Forrest, S. Martin, J. Fetvedt, M. McGroddy and D. Freed, "Integration and optimization of coal gasification systems with a near-zero emissions supercritical carbon dioxide power cycle," in *Turbo Expo: Power for Land, Sea, and Air*, 2016.
- [30] X. Lu, "Flexible Integration of the sCO<sub>2</sub> Allam Cycle with Coal Gasification Low-Cost Emission-Free Electricity Generation," in *GTC*, 2014.
- [31] N. T. Weiland and C. W. White, "Techno-economic analysis of an integrated gasification direct-fired supercritical CO<sub>2</sub> power cycle," *Fuel*, vol. 212, pp. 613-625, 2018.



**ANNEX A**

Parameter	Reference NGCC Plants		Optimized Direct sCO <sub>2</sub> Plants			
	B31B.90	B31B.97	Case A	Case B	Case C	Case D
Gross Power Output (MWe)	692	687	793	822	830	836
Auxiliary Power Requirement (MWe)	47	51	164	180	183	182
Net Power Output (MWe)	645	637	629	642	647	654
Natural Gas Flow Rate (lb/hr)	205,630	205,630	205,626	205,626	205,626	205,626
HHV Thermal Input (kWth)	1,354,905	1,354,905	1,355,866	1,355,866	1,355,866	1,355,866
Net Plant HHV Efficiency (%)	47.6%	47.0%	46.4%	47.3%	47.7%	48.2%
Raw Water Consumption (gpm)	2,965	3,029	1,464	1,335	1,310	1,255
CO <sub>2</sub> Capture Rate (%)	90%	97%	98.5%	98.5%	98.5%	98.5%
CO <sub>2</sub> Emissions (lb/MWh-net)	85	26	8.9	8.8	8.7	8.6
<b>Auxiliary Power Breakdown</b>						
ASU MAC, kWe	-	-	84,150	100,770	100,780	100,780
ASU BAC, kWe	-	-	42,730	42,730	44,770	44,770
Other ASU Auxiliaries, kWe	-	-	1,000	1,000	1,000	1,000
Natural Gas Compressor Power, kWe	-	-	13,830	13,780	13,790	13,790
CO <sub>2</sub> Capture/Removal Auxiliaries, kWe	13,600	15,200	-	-	-	-
CO <sub>2</sub> Compression, kWe	17,900	19,290	10,440	10,470	10,470	10,480
Miscellaneous BOP, kWe	570	570	570	570	570	570
Combustion/sCO <sub>2</sub> Turbine Auxiliaries, kWe	1,020	1,020	1,020	1,020	1,020	1,020
Steam Turbine Auxiliaries, kWe	200	200	-	-	-	-
Feedwater Pumps, kWe	4,830	4,830	-	-	-	-
Condensate Pumps, kWe	170	170	-	-	-	-
Circulating Water Pumps, kWe	4,830	4,390	1,400	1,180	1,100	1,090
Ground Water Pumps, kWe	400	410	160	150	140	140
Cooling Tower Fans, kWe	2,240	2,270	740	620	580	570
Adiabatic Cooling System Fans, kWe	-	-	3,867	3,973	4,381	3,836
Transformer Losses, kWe	2,220	2,210	2,760	2,890	2,920	2,940
<b>Total Auxiliaries, kWe</b>	<b>47,492</b>	<b>50,562</b>	<b>163,917</b>	<b>180,403</b>	<b>182,771</b>	<b>182,236</b>

**Table 7:** Performance summary for the optimized direct sCO<sub>2</sub> plants and reference NGCC plants

Parameter	Reference NGCC Plants		Optimized Direct sCO <sub>2</sub> Plants			
	B31B.90	B31B.97	Case A	Case B	Case C	Case D
Feedwater & Miscellaneous BOP	\$113,279	\$113,414	\$71,069	\$69,016	\$68,396	\$67,940
Cryogenic ASU	-	-	\$545,498	\$545,497	\$545,522	\$545,522
Flue Gas Cleanup & Piping	\$507,564	\$539,258	\$48,756	\$48,813	\$48,313	\$48,832
Combustion/sCO <sub>2</sub> Turbine & Accessories	\$113,760	\$113,760	\$660,102	\$667,077	\$678,894	\$777,288
HRSR, Ductwork, & Stack	\$110,033	\$109,850	-	-	-	-
Steam Turbine & Accessories	\$82,513	\$80,986	-	-	-	-
Cooling Water System	\$50,697	\$51,068	\$23,398	\$21,040	\$20,128	\$19,989
Accessory Electric Plant	\$69,316	\$71,385	\$139,736	\$148,536	\$148,875	\$149,760
Instrumentation & Control	\$23,725	\$23,951	\$25,162	\$25,550	\$25,604	\$25,592
Improvements & Site	\$28,811	\$28,715	\$30,671	\$31,176	\$31,316	\$31,420
Building & Structure	\$18,378	\$18,232	\$8,004	\$8,023	\$8,022	\$8,035
<b>Total</b>	<b>\$1,118,075</b>	<b>\$1,150,619</b>	<b>\$1,552,386</b>	<b>\$1,564,728</b>	<b>\$1,576,569</b>	<b>\$1,674,377</b>
<b>Total, \$/kWe</b>	<b>1,734</b>	<b>1,807</b>	<b>2,467</b>	<b>2,439</b>	<b>2,436</b>	<b>2,561</b>
<b>sCO<sub>2</sub> Power Cycle Capital Cost Breakdown</b>						
Turbine	-	-	\$58,724	\$58,724	\$58,724	\$58,724
HTR	-	-	\$235,541	\$246,442	\$264,343	\$311,264
ITR	-	-	\$42,004	\$43,351	\$41,717	\$45,609
LTR	-	-	\$40,798	\$45,757	\$38,476	\$42,980
Water KO Cooler	-	-	\$9,235	\$10,149	\$10,785	\$30,810
Pre-compressor	-	-	\$56,128	\$56,786	\$56,966	\$56,753
Adiabatic Coolers	-	-	\$142,083	\$147,824	\$149,259	\$156,913
Boost Pump	-	-	\$16,586	\$16,905	\$16,973	\$17,083
Oxidant/Recycle Compressor	-	-	\$17,481	\$17,481	\$17,494	\$31,355
Natural Gas Compressor	-	-	\$5,391	\$5,391	\$5,391	\$5,391
Piping	-	-	\$5,315	\$5,315	\$5,315	\$5,315
Foundations	-	-	\$12,816	\$12,951	\$13,180	\$15,091

**Table 8:** Capital cost (TPC/\$1,000) summary for the optimized direct sCO<sub>2</sub> plants and reference NGCC plants

## REVIEW OF HAYNES® 282® ALLOY FOR SUPERCRITICAL CO<sub>2</sub> STRUCTURAL APPLICATIONS

**Brett Tossey**

Haynes International, Inc  
Kokomo, Indiana USA

**BTossey@HaynesIntl.com:**

**Vinay Deodeshmukh**

Haynes International, Inc  
Kokomo, Indiana USA

**VDeodeshmukh@HaynesIntl.com**

**Bruce Pint**

Oak Ridge National Laboratory  
Oak Ridge, TN

**Pintba@ornl.com**

### ABSTRACT

In this paper, HAYNES® 282® alloy (282® alloy) properties, microstructure, high temperature oxidation resistance, weldability, and American Society of Mechanical Engineers (ASME) code case highlights are reviewed. The long term performance of high temperature, high strength, creep resistant alloys is critical to the success of supercritical carbon dioxide equipment. Several modern power generation technologies require alloys that can operate continuously at or above 700°C. 282® alloy is a precipitation strengthened nickel based super alloy that meets these requirements. The results of 282® alloy research reviewed in this paper include long-term cyclic oxidation behavior in air and sCO<sub>2</sub>, independent research and validation of 100k hour creep life, and successful welding of the alloy in the age hardened condition. The latter is critical for joining of hardened components (flanges, piping, heat exchanger internal, etc.) and field repair. Several highlights from the code case for this ASME-approved material are also presented.

### INTRODUCTION

This paper presents a comprehensive overview of a nickel-based alloy that is qualified for long term, high temperature service in super critical carbon dioxide.

HAYNES®<sup>1</sup> 282® alloy was first available for commercial use in 2005. 282® alloy is a precipitation strengthened alloy whose primary alloying elements are Ni-Cr-Co-Mo-Ti-Al. Its primary commercial applications are in the aerospace, industrial gas turbine, and automotive industries. Heat treatments applied to the 282 alloy have the purpose of forming chromium-rich M<sub>23</sub>C<sub>6</sub> carbides and of precipitating gamma-prime particles. Detailed information about the alloy's development, thermal stability, microstructure, and properties has been explained in a previous paper [1,2].

The operating conditions of supercritical carbon dioxide (sCO<sub>2</sub>) power cycles and advanced supercritical steam cycles (A-USC) require high pressure, high temperature plant components to be manufactured from nickel-based superalloys. Research conducted by the U.S. Department of Energy (DoE) proved HAYNES® 282® alloy (UNS N07208), a Ni-Cr-Co-Mo-Ti-Al precipitation strengthened alloy was a leading choice for A-USC applications [3]. Research performed by the DoE and Haynes International, Inc. led to the production of required American Society of Mechanical Engineers (ASME) code case data. The data generated focused on a single step age hardening treatment, which is a four hour single step age hardening heat treatment at 800°C (1472°F) followed by air cooling (800°C

---

<sup>1</sup> HAYNES and 282 are registered trademarks at Haynes International, Inc.

(1472°F)/4 hr/AC). The 282® alloy ASME code case is 3024 and the Code Case is applicable to Section I and Section VIII, Division 1 construction.

Research efforts parallel to DoE code case efforts [4-6] have been heavily supported by Haynes International, Inc. through several pathways. One pathway included Haynes International, Inc. providing alloy product forms (bar, plate, forgings, cast stock, powder, pipe, and tube) to private and federally-funded research programs. The programs have produced many demonstrations of potential end use products for demonstration scale and laboratory scale 282® alloy components. These components include a forged rotor shaft, a cast turbine rotor casing, heat exchanger tube bundles, advanced manufactured microchannel heat exchangers, and micro turbine components with blades integrated with the rotor shaft to produce one-piece turbine internals. A second pathway is that Haynes International often provides internally-generated data to selected research programs and customer applications in support of their goals.

**COMPOSITION AND MICROSTRUCTURE**

Table 1 contains the ASME chemical composition of 282® alloy in weight percent.

Element	Nominal Composition, %
Ni	Remainder
Cr	18.5-20.5
Fe	1.5 max
Mn	0.3 max
Co	9.0 - 11.0
C	0.04 - 0.08
Si	0.15 max
S	0.015 max
P	0.015 max
Al	1.38-1.65
B	0.003-0.010
Cu	0.1 max
Mo	8.0-9.0
Ta	0.1 max
Ti	1.9-2.3
Nb	0.2 max
W	0.5 max

Zr	0.02 max
----	----------

**Table 1.** Nominal alloy composition in HAYNES® 282® alloy. UNS N07208.

282® alloy is supplied in the wrought, solution annealed condition; see Figure 1 for a representative micrograph of the anneal grain structure [7]. Some residual carbide stringers are evident in the micrograph. Figure 2 shows the location of carbides in a higher magnification micrograph. Figure 3 shows the intragrain structure of solution annealed 282® alloy prior to heat treatment; very fine nano-scale gamma prime particles are evident in the grains. Complete suppression of nano-scale precipitation of gamma prime upon cooling is practically impossible. This fact has little effect on the ability to cold work the alloy in the mill annealed condition, as the annealed hardness is often in the range of 90 Rockwell B.

The alloy mechanical properties depend on the formation of beneficial secondary phases in the microstructure, namely carbides and gamma prime. The carbides begin to precipitate upon cooling below 1120°C (~2050°F) after solution annealing in the range of 1121 to 1149°C (2050 to 2100°F). Carbides are primarily of the form M<sub>23</sub>C<sub>6</sub> that are rich in chromium, although nickel, cobalt, and molybdenum substitution is often present. M<sub>6</sub>C are also present; they are rich in molybdenum with nickel and chromium substitution possible.

A single step heat treatment at 800°C for four hours followed by air cooling, which is also the ASME code-approved heat treatment, creates chromium rich M<sub>23</sub>C<sub>6</sub> carbides that are discrete globular blocks; see Figure 4. Figure 4 shows the grain boundary carbide structure after aging and preferential etching to highlight the carbides. Gamma prime is a coherent Ni<sub>3</sub>Al intragranular precipitate that forms at temperatures below approximately 1000°C; see Figure 5. Figure 5 is a micrograph of heat-treated and etched 282® alloy. Gamma prime is evident in intragranular regions.

The single step heat treatment co-precipitates carbide and gamma prime networks in one step. This is important because a single stage heat treatment, compared to a two stage heat treatment, can provide significant time and cost savings to equipment owners.

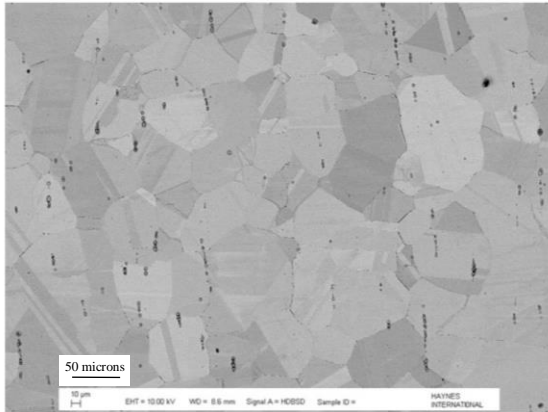


**Figure 1.** SEM image of mill annealed 282® alloy. Primary carbide stringers are evident in the microstructure.

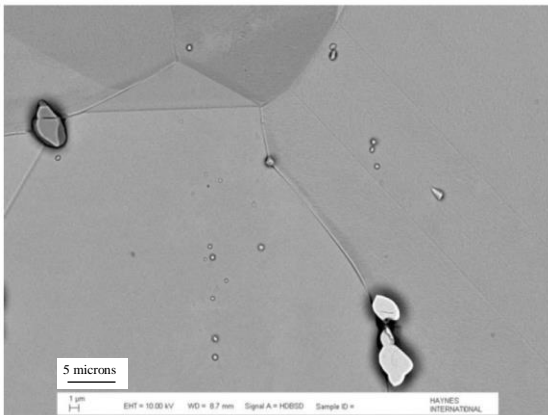


**Figure 2.** High magnification SEM image of mill annealed 282® alloy. Primary carbides are evident in the microstructure; dark carbides in the image are MC-type while bright carbides are M6C carbides.



**Figure 3.** High magnification of mill annealed 282® alloy showing well dispersed very fine intragranular gamma prime particles. Particle sizes are typically less than 5 microns.

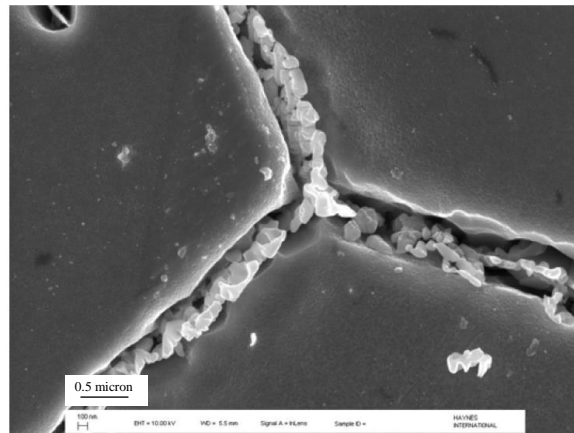


**Figure 4.** SEM images showing an etched triple point grain boundary in 4 hours single aged 282® alloy. Grain boundaries are decorated with globular carbide blocks.

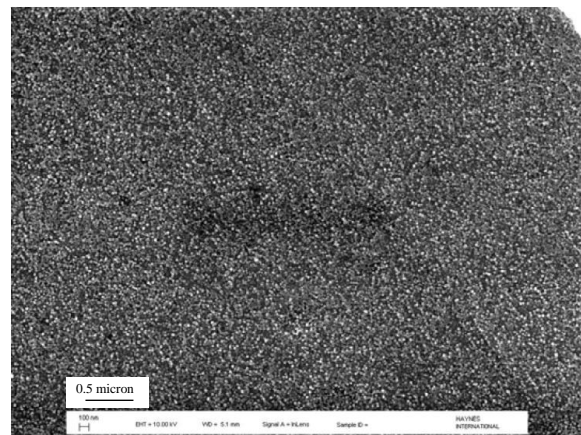


**Figure 5.** SEM image of etched 4 hours aged 282® alloy intragranular gamma prime precipitation. The typical gamma prime particle size is < 1 micron.

**MECHANICAL PROPERTIES**

sCO<sub>2</sub> high temperature equipment requires an alloy with excellent high temperature strength, creep resistance, and elongation. The properties must be persistent following long-term thermal exposure. The average tensile properties from room temperature to 900°C are in Table 2. Tensile testing was conducted on precipitation strengthened 282® alloy plate from three heats of alloy.

Temperature (°C)	0.2% Yield Strength (MPa)	Ultimate Tensile Strength (MPa)	% Elongation
RT	733	1170	34
100	684	1123	34
200	655	1095	35
300	640	1060	35
400	639	1021	36
500	628	998	36
600	626	1002	32
700	620	952	23
800	577	745	16
900	406	480	30

**Table 2.** Tensile properties of HAYNES® 282® alloy from room temperature to 900°C

Retained tensile strength of 282 alloy is a key mechanical property that makes the alloy suitable for high temperature sCO<sub>2</sub> applications. The data show that 282® alloy is very strong across a broad range of temperatures, and the ductility remains above 15% for all tests. It is important to note that the values in Table 2 are larger than the published ASME codes case data. The values are larger because the published code case data are often minimum values from multiple heats of testing, and sometimes an alloy owner (such as Haynes International, Inc.) requests that published values to be slightly lower than the actual minimums to impart conservatism. Figure 6 contains the ASME allowable stress for 282® alloy and other alloys often used in high temperature ASME applications; HAYNES® 230® alloy, HAYNES® 617 alloy, and 800HT alloy.

760°C is the target temperature for sCO<sub>2</sub> applications and 282® alloy exceeds the creep life requirement to

surpass 100,000 hours at 100 MPa (14.5 ksi) at 1400°F (760°C).

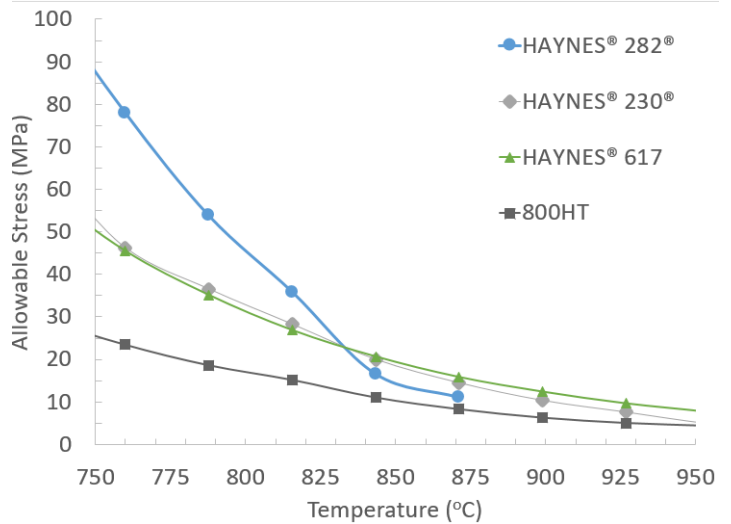


**Figure 6.** ASME allowable stress versus temperature for selected alloys, including HAYNES® 282® alloy.

In fact, 282® alloy is stronger [8] than its closet peer in this alloy group, UNS N07740, and all of the ASME approved nickel based solid solution strengthened alloys for high temperature service. It is also notable that 282® alloy ASME maximum allowable temperature is 871°C, whilst UNS N07740 is 815°C.

The creep properties of 282® alloy demonstrate that the alloy is capable of long term service in high temperature sCO<sub>2</sub> applications up to 871°C. A Larson Miller Parameter (LMP) plot is presented in Figure 7. The LMP plot (C=16.6) in Figure 7 contains data generated by ORNL [9] on single step aged 0.5” plate. These data also were used for a portion of the ASME code case. The plot clearly shows that across multiple heats, 282® alloy delivers very consistent long term creep properties in the single aged wrought condition.



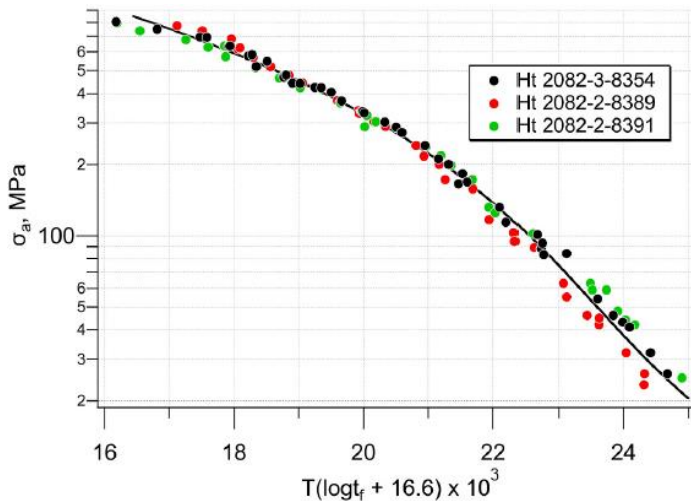


**Figure 7.** Larson Miller Parameter plot versus applied stress for HAYNES® 282® alloy. Data courtesy of Oak Ridge National Laboratory in support of 282® alloy ASME code case 3024.

Table 3 contains stress rupture data for 282® alloy from 649°C to 927°C and stress rupture times of 100 hours and 1,000 hours [10]. Data are presented for single step precipitation strengthened base metal and all weld metal. Welded 282® alloy properties are explored more fully in the next section.

Property	Test Temperature		282 Alloy Base ksi (MPa)	282 Alloy Weld ksi (MPa)
	°F	°C		
Stress-to-Produce Rupture, in 100 h ksi (MPa)	1200	649	104 (715)	101 (693)
	1300	704	80 (550)	76 (522)
	1400	760	58 (401)	54 (375)
	1500	816	41 (280)	37 (253)
	1600	871	26 (179)	23 (156)
	1700	927	14 (97)	13 (87)
Stress-to-Produce Rupture, in 1000 h ksi (MPa)	1200	649	86 (591)	101 (693)
	1300	704	62 (428)	76 (522)
	1400	760	43 (298)	54 (375)
	1500	816	27 (189)	37 (253)
	1600	871	15 (102)	23 (157)
	1700	927	7 (51)	13 (87)

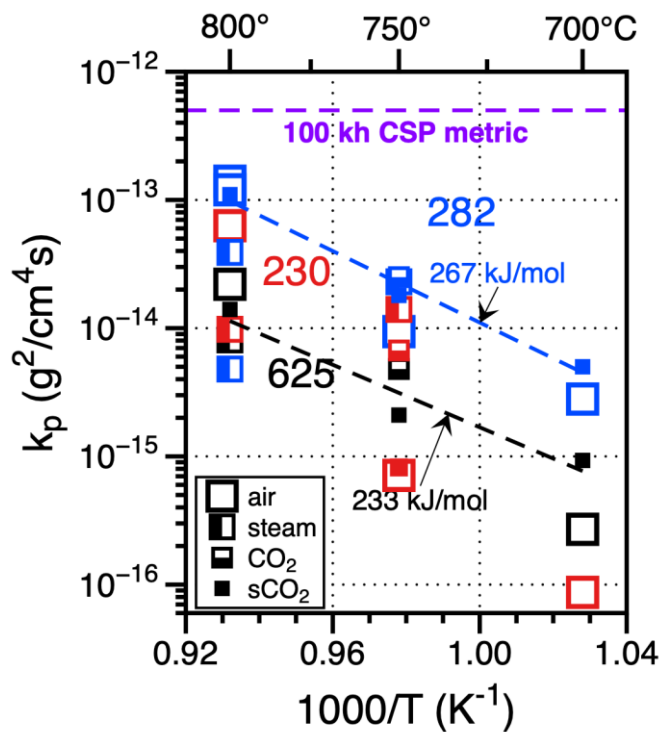
**Table 3.** Comparative average creep-rupture properties of single step age hardened HAYNES® 282® alloy base metal and weld metal. Weld metal data comprised of GMAW and GTAW data.

Table 3 shows that the alloy stress-to-produce rupture values at 871°C are 179 MPa for 100 hours, 102 MPa in a 1,000 hour test. The stress-to-produce rupture in 10,000 hours is 55MPa and the ASME allowable stress at the same temperature is 11MPa for 100khr service. The weld data show that although the wrought metallurgy was changed by welding, the stress-to-produce rupture at 100 and 1,000 hours are not negatively affected. In fact, there is little change in the alloy performance when comparing wrought creep properties to the properties in the as welded condition.

## OXIDATION

282® alloy can resist oxidation in sCO<sub>2</sub> at time scales relevant to long-term operation of high temperature equipment. Several research programs focused on alloy oxidation in sCO<sub>2</sub> environments conducted over approximately the past fifteen years. Short-term oxidation tests were commonly near 500 hours and long-term tests were over 10,000 hours. The range of the testing pressures were one bar to 400 bar and temperatures ranged from 650°C to 900°C. Figures 8 through 10 are oxidation data generated by Oak Ridge National Laboratory [6] with support of Haynes International for 282® alloy. HAYNES® 625 alloy and HAYNES® 230® alloy are also included for context. The plots include oxidation kinetics using the parabolic rate constant versus inverse temperature (Figure 8), oxidation rate as mass gain versus time (Figure 9), and oxidation mass gain at 750°C and 800°C versus alloy aluminum and titanium composition (Figure 10). As mentioned earlier, 282® alloy is an ASME code approved alloy, but the code does not require oxidation rates be specified. The impact of oxidation on creep life is incorporated, in a sense, into the short and long term creep tests (in air). Long-term oxidation study of 282 alloy showed minimal metal loss, or thickness reduction, over 10kh exposure. Accordingly, 282 alloy could provide long-term oxidation resistant performance of a component operating near 760°C.





**Figure 8.** Plot of oxidation rate constant,  $k_p$ , versus inverse temperature. The 100khr metric line from the advanced ultra supercritical program is also included for reference.

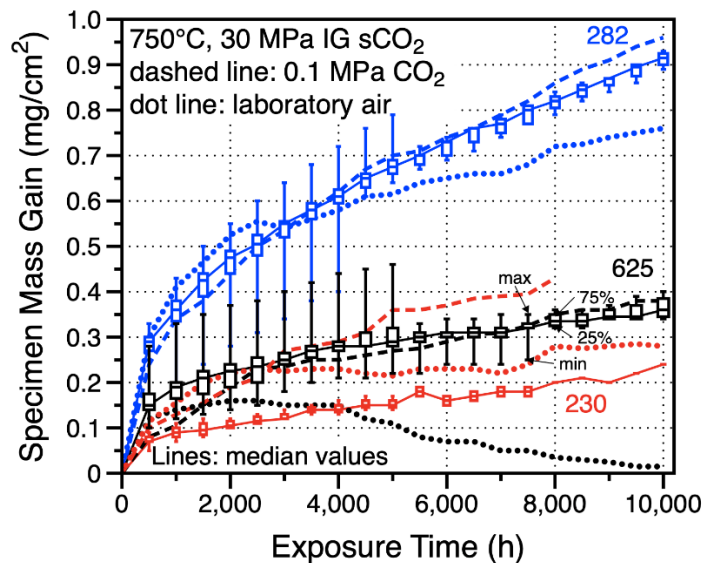


**Figure 9.** Oxidation mass gain versus time for selected alloys including HAYNES® 282® alloy.

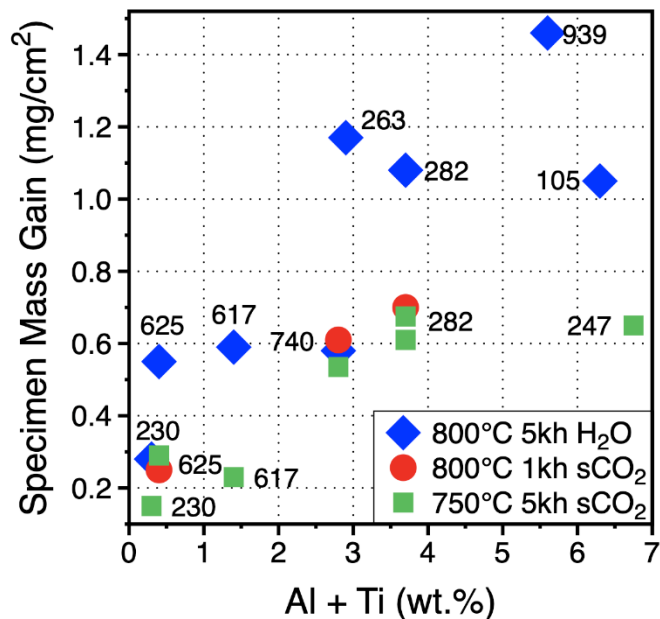


**Figure 10.** Oxidation mass gain versus alloying content of aluminum plus titanium. At 705°C and 800°C in sCO<sub>2</sub> and water for various exposure times.

### WELDING 282® alloy

282® alloy is easily fabricated and welded. The alloy's high level of creep strength is attained at a relatively low volume fraction of the strengthening gamma-prime phase, resulting in outstanding resistance to strain-age cracking. Additionally, slow gamma-prime precipitation kinetics allow for the alloy to have excellent ductility in the solution annealed condition. The preferred welding processes are gas tungsten arc (GTAW or TIG) and gas metal arc (GMAW or MIG), using 282 alloy bare filler wire. Preheating of HAYNES® 282® alloy is not required, as long as the base metal to be welded is above 32°F (0°C). Interpass temperatures should be less than 200°F (93°C).

After welding, 282® alloy should be age-hardened. The use of a full solution anneal (typically at 2075°F/1135°C) after welding and prior to age-hardening treatment is neither required nor prohibited. For heavy section weldments, or complex weldments with high residual stress, a full solution anneal prior to the age-hardening treatment may be advisable to minimize the threat of cracking.

282® alloy weldability has been explored by several companies and organizations (United States Department of Energy, the Electric power Research Institute(EPRI), nickel alloy fabricators such as Babcock and Wilcox, Haynes International, Inc, several universities. It has been demonstrated that wrought product can be welded in thick sections up to 3.3 inches (84mm) [11].

Figure 11 is a micrograph of a welded cross section of a gas tungsten arc welded (GTAW) specimen. Two 19 mm (0.75”) thick plates in the solution-annealed condition were welded together and then aged at 800°C for four hours. The sample was polished, electrolytically etched in HCl – oxalic acid, and subjected to Rockwell C hardness testing. A hardness profile was collected across the sample; the locations of the measurements are identify in red numbers (1 through 11) in the figure. The hardness data are in Table 4.

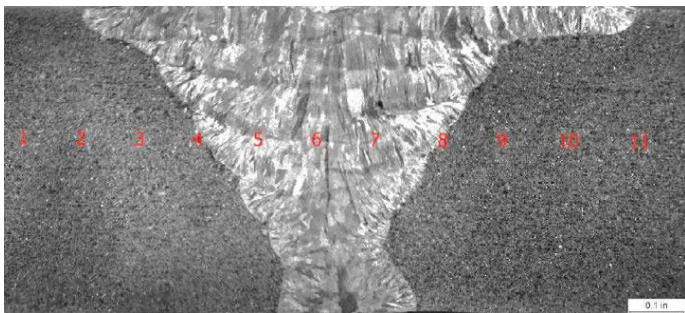


**Figure 11.** Micrograph of welded HAYNES® 282® alloy plate. Cross section is polished and etched; red labels are hardness measurement locations.

GTAW Specimen	
Location	Hardness (HRC)
1	34.9
2	35.8
3	36.8
4	37.6
5	36.5
6	37.0
7	36.1
8	38.6
9	36.9
10	36.9
11	35.1

**Table 4.** Hardness profile data of 282 alloy weldment.

The hardness profile data show that the welding and precipitation hardening treatment has little effect on the cross-weld hardness. There is some indication that the weld is at most 3.7 HRC point higher than the parent alloy, although the regions near the weld line indicated by numbers 4 and 8 were hardest. The fusion zone was at most 2.1 HRC higher compared to the lowest base metal hardness measurement of 34.9.

It is important to note that large power generation components and piping may not be able to be heat treated in the as welded, fully fabricated condition. This can be due to system size, the requirement to fabricate on site, and parts with complex geometries. To address this need, Haynes developed guidelines to weld precipitation hardened 282® alloy parts. Once welded, the local welded area can be heat treated on site in accordance with the single step heat treatment.

ASME code case activities also included bend testing of wrought and welded 282® alloy plate. Each specimen was precipitation strengthened prior to welding and no post weld heat treatment was performed before bend testing. The weld processes were GTAW and gas metal arc welding (GMAW). A 4T radius mandrel (mandrel radius is equal to 4X the plate thickness) and the wrap-around test method (ASME Boiler and Pressure Vessel Section IX, figure QW-466.3) were recommended for qualification purposes. Figure 12 is a photograph of representative welded bend specimens. The face side, root side, and side bend orientations are shown. No cracking was evident in any specimen.



**Figure 12.** Photograph of bend test specimens. No cracks were evident in the single step heat treated HAYNES® 282® alloy specimens.

Another important parameter within ASME code is the Weld Strength Reduction Factor (WSRF), which needs to be applied when calculating design stresses and pressure boundary thicknesses. The WSRF methodology in STP-PT-077 acknowledges that WSRFs can be calculated by comparing the time-temperature-strengths relationships from data generated using all base metal specimens, welded specimens, and all weld metal specimens where:

$$WSRF = \frac{Rupture\ Stress\ (weld)}{Rupture\ Stress\ (base\ metal)}$$

282® alloy creep test results show that WSRFs depend on temperature. The WSRF for 282® alloy are in Table 5. It is worth noting that the WSRF for UNS N07740 is 0.7 for all temperature ranges up to its maximum allowable temperature in accordance with ASME, which is 815°C (1500°F). Also, Table 5 includes WSRF up to 927°C (1700°F), the ASME Code Case only specifies WSRF up to 871°C (1600°F), which is the maximum use temperature for 282® alloy.

Temperature (°C)	Weld strength reduction factor
593 - 620	0.99
621 - 815	0.93
816 - 870	0.86
871 - 927	0.84

**Table 5:** WSRF for HAYNES® 282® alloy.

Figure 13 is a plot of 282 LMP data for base alloy and weld alloy creep rupture data [12] collected over a temperature range of 593°C – 927°C (1100°F – 1700°F). The plot shows the base alloy performance and weld alloy performance are very similar, which is crucial for the alloy performance in sCO2 power generation applications.

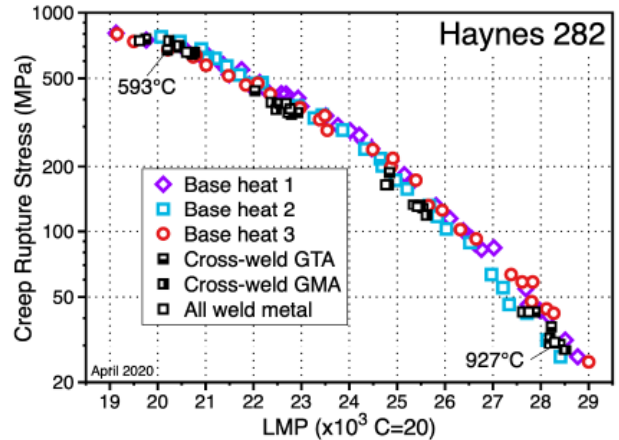


**Figure 7.** Larson-Miller parameter plot of the creep data.

**Figure 13.** Larson Miller Parameter plot for base alloy and welded HAYNES® 282® alloy specimens.

### SUMMARY

282® alloy is precipitation hardenable alloy whose primary alloying elements are Ni-Cr-Co-Mo-Ti-Al. Heat treatments applied to the 282 alloy have the purpose of forming chromium-rich M<sub>23</sub>C<sub>6</sub> carbides and of precipitating gamma-prime particles.

The operating conditions of supercritical carbon dioxide (sCO2) power cycles and advanced supercritical steam cycles (A-USC) require high pressure, high temperature plant components to be manufactured from nickel-based superalloys. Research conducted by the U.S. Department of Energy proved HAYNES® 282® alloy (UNS N07208) is a leading choice for sCO2 applications. Research performed by the DoE and Haynes International, Inc. led to the production of required American Society of Mechanical Engineers (ASME) code case data. The data generated focused on a single step age hardening treatment, which is a four hour single step age hardening heat treatment at 800°C (1472°F) followed by air cooling (800°C (1472°F)/4 hr/AC). The 282® alloy ASME code case is 3024.

## REFERENCES

[1] Pike, Lee. *100+ Years of Wrought Alloy Development at Haynes International. 8th International Symposium on Superalloy 718 and Derivatives.*

[2] L.M. Pike, "Development of a Fabricable Gamma-Prime ( $\gamma'$ ) Strengthened Superalloy," (Paper presented at *Superalloys 2008*, Champion, PA, September 14-18, 2008) 191-200.

[3] Srivastava, S.K. & Caron, J.L. & Pike, L.M.. (2014). Recent developments in the characteristics of HAYNES 282 alloy for use in A-USC applications. pp. 120-130, *Advances in Materials Technology for Fossil Power Plants*, Proceedings from the Seventh International Conference October 22-25, 2013, Waikoloa, Hawaii, USA

[4] D.L. Klarstrom and L.M. Pike, "Material Solutions for Advanced Steam Power Plants," *Advances in Materials Technology for Fossil Power Plants, Proc. Fifth Int. Conf.*, October 2007, pp.107-118, EPRI 2008.

[5] V. P. Deodeshmukh and B. A. Pint, "Long-Term Performance of High Temperature Alloys in Oxidizing Environments and Supercritical CO<sub>2</sub>," in Proceedings of the Joint EPRI – 123HiMAT International Conference on Advances in High Temperature Materials,

[6] Pint, B.A. (2018). Performance of Wrought Superalloys in Extreme Environments. In: , et al. Proceedings of the 9th International Symposium on Superalloy 718 & Derivatives: Energy, Aerospace, and Industrial Applications. The Minerals, Metals & Materials Series.

[7] Robertson, JR. "Continued Developments in the Characteristics of HAYNES® 282® Alloy for Use in A-USC Applications." *Proceedings of the ASME 2018 Symposium on Elevated Temperature Application of Materials for Fossil, Nuclear, and Petrochemical Industries. ASME 2018 Symposium on Elevated Temperature Application of Materials for Fossil, Nuclear, and Petrochemical Industries.*

Seattle, Washington, USA. April 3–5, 2018. V001T01A007. ASME.

[8] ASME Boiler and pressure vessel code Section VIII Division 1.

[9] Michael L. Santella, Peter F. Tortorelli, Mark Render, Bruce Pint, Hong Wang, Vito Cedro, Xiang (Frank) Chen, Effects of applied stress and grain size on creep-rupture lifetime prediction for Haynes 282 alloy, *Materials Science and Engineering: A*, Volume 838, 2022

[10] Haynes International, Inc. data submitted in part to support ASME Code Case 3024.

[11] A-USC Report on thick section Welding of Haynes® 282® alloy.

[12] Pint, Bruce A., Wang, Hong, Hawkins, Charles Shane, and Unocic, Kinga A. Technical Qualification of New Materials for High Efficiency Coal-Fired Boilers and Other Advanced FE Concepts: Haynes® 282® ASME Boiler and Pressure Vessel Code Case. United States: N. p., 2020. Web. doi:10.2172/1649169.

## TECHNO-ECONOMIC ANALYSIS OF sCO<sub>2</sub> POWER CYCLE FOR COAL-FIRED POWER SYSTEM

**In Woo Son**

*Department of Nuclear and Quantum Engineering,  
Korea Advanced Institute of Science and Technology  
373-1 Guseong-dong Yuseong-gu, Daejeon, 305-701,  
Korea*

Email: siw4139@kaist.ac.kr

**Jeong Ik Lee\***

*a Department of Nuclear and Quantum Engineering,  
Korea Advanced Institute of Science and Technology  
373-1 Guseong-dong Yuseong-gu, Daejeon, 305-701,  
Korea*

mail: jeongiklee@kaist.ac.kr

**Yongju Jeong**

*Department of Nuclear and Quantum Engineering,  
Korea Advanced Institute of Science and Technology  
373-1 Guseong-dong Yuseong-gu, Daejeon, 305-701,  
Korea*

Email: jyj7317@kaist.ac.kr

### ABSTRACT

Supercritical CO<sub>2</sub> (sCO<sub>2</sub>) power cycles are considered one of the promising candidates to replace a steam Rankine cycle. The sCO<sub>2</sub> power cycle has compact component size and minimum compression work because the supercritical state of CO<sub>2</sub> has a density similar to that of a liquid and a viscosity similar to that of a gas. Considering these advantages, many countries and institutions around the world are conducting research on the sCO<sub>2</sub> power cycle. However, most studies have focused on the thermal performance optimization of the power cycle, and an economic analysis and optimization is limited since experiences with sCO<sub>2</sub> power cycle commercial operation are not abundant. Fortunately, previous researchers have proposed expected component cost correlations for sCO<sub>2</sub> power cycle from cost data and literature survey [1]. In this paper, by utilizing the previously proposed component cost correlations, a sensitivity analysis of an sCO<sub>2</sub> power cycle with respect to the system's power output, cycle maximum temperature, fuel cost and cycle layout is conducted. From this study, a relation between the thermal performance optimization and the minimum cost is understood for the current technology level.

### INTRODUCTION

The Supercritical Carbon dioxide (sCO<sub>2</sub>) power cycle is a next-generation high-efficiency power cycle and is expected to be a candidate to replace the steam Rankine cycle [2]. Carbon dioxide is non-toxic, non-flammable, and has the critical point of 304.13K, 7.38 MPa, which is easily achievable.

Carbon dioxide in a supercritical state has a density similar to that of liquid and a viscosity similar to that of a gas at the same time. Therefore, the sCO<sub>2</sub> power cycle can have compact component size and minimum compression work, so it can be used in various energy sectors such as nuclear power, renewable energy, waste heat recovery, and marine propulsion [2]. Due to these advantages, the sCO<sub>2</sub> power cycle is being developed in many countries and institutions around the world, and pilot and demonstration plants are being constructed such as the STEP Demo pilot project [3], Sandia National Laboratories (SNL)'s test loop [4], sCO<sub>2</sub> HeRO Loop [5], etc.

Studies on the sCO<sub>2</sub> power cycle are mainly focused on thermal performance evaluation, and relatively fewer studies on the economic analysis of the cycle are founded. This is because the current Technology Readiness Level (TRL) of the sCO<sub>2</sub> power cycle is 7 stages, so no commercial operation has been carried out [6]. The research on the economic analysis of the sCO<sub>2</sub> power cycle is an essential process before entering the TRL 8 and 9 stages which is the commercial operating stage.

\* corresponding author(s)



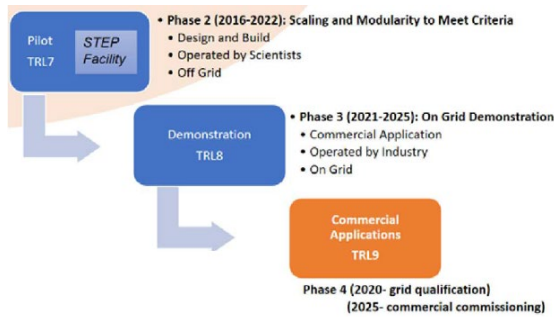


Fig. 1 Roadmap phase for the sCO<sub>2</sub> power cycle of the SNL [6]

Nevertheless, some studies performed an economic analysis of the power cycle by developing cost models for the sCO<sub>2</sub> power cycle components [7-12]. However, few researches have studied the relationship between cost and performance for the sCO<sub>2</sub> power cycle rather than calculating the minimum power cycle cost [13, 14]. In the work of Benjelloun et al., a techno-economic analysis was performed on the direct and indirect recompression cycles and confirmed that both are suitable as a power cycle for next-generation nuclear power plants [13]. Alfani et al. performed techno-economic optimization of the sCO<sub>2</sub> power cycle integrated with CSP [14]. Among the four cycle layouts, they suggested that the recompression cycle with intercooling is the most promising from a perspective of the techno-economic and presented the optimal solution of the cycle.

In the previous studies, variables such as cycle component efficiency, pressure ratio and pinch temperature of a recuperator were set as parameters of sensitivity study [13, 14]. However, the power output and fuel cost for heat sources can also be set as parameters of the sensitivity study. This is because the power output affects the cost of cycle components, and the cycle performance determines the required fuel cost for electricity generation. Therefore, in this study, a techno-economic sensitivity study of the sCO<sub>2</sub> power cycle is performed with the power output and fuel cost. In addition, the previous studies have not examined whether a complex cycle is economically more effective compared to a simple recuperated cycle layout which is one of the simplest layouts [13, 14]. Therefore, in this study, a techno-economic analysis is aimed to observe whether the improvement in cycle performance due to the addition of components can be also economically beneficial.

To perform the economic analysis of the sCO<sub>2</sub> power cycle, data on the components' cost of the cycle are required. Fortunately, through cost data, literature surveys, and vendor quotes, the previous researchers have suggested the expected component cost of the sCO<sub>2</sub> power cycle concerning the component design [1]. The cost correlation for the cycle components is suggested and calculated for the total equipment cost of a 10MWe plant [15] and a 550MWe plant [16] as examples. In addition, the cost model has temperature correction factors to reflect the structural material change when the operating temperature is high.

$$f_T = \begin{cases} 1 & \text{if } T_{\max} < T_{bp} \\ 1 + c(T_{\max} - T_{bp}) + d(T_{\max} - T_{bp})^2 & \text{if } T_{\max} \geq T_{bp} \end{cases} \quad (1)$$

In the previous studies, the temperature breakpoint of the temperature correction factor is set to 550°C, which the temperature is better to use a thinner nickel-based superalloy than the commonly used thicker stainless steel [1, 17]. Therefore, to consider this effect, the cycle maximum temperature is added as a parameter in the sensitivity study.

In this study, four variables are selected to be in total for the sensitivity study: cycle layout, cycle maximum temperature, fuel cost, and cycle power output, which significantly affect the Levelized Cost Of Energy (LCOE) of the sCO<sub>2</sub> power cycle and the corresponding cycle performance. The analysis of the sCO<sub>2</sub> power cycle is performed by using the component cost correlation of the sCO<sub>2</sub> power cycle suggested in the previous studies [1].

## SCO<sub>2</sub> POWER CYCLE COST MODEL

In this study, the cycle thermal efficiency and the LCOE need to be calculated. To calculate these values, the sCO<sub>2</sub> power cycle design parameters should be set first. However, before setting the cycle design parameters, it is necessary to consider the cost model proposed in the previous study [1]. It is noted that this section will focus on the discussion of the application to Weiland's cost model presented in Ref. [1], since the major cost models utilized in this study is based on the Weiland's cost model.

From a material point of view, stainless steel is used for components operating below 550°C, and if not, nickel-based superalloy is used for higher temperatures components. This is incorporated to the cost model by using the high-temperature correction factor in equation (1) [1].

Weiland's research developed cost correlations for two types of primary heaters: natural gas-fired and coal-fired heaters [1]. These correlations include burners, fans, air preheaters, ductwork, headers, and connecting piping. In this study, the cost model for coal-fired heaters is used. This is because, the natural gas-fired heaters exist in the primary heater cost model of the previous study, but the valid range is too narrow (10 to 50 MW<sub>th</sub>) [1] for this study. In this study, the heat source is limited to the coal-fired power field due to the limitation of the cost correlation equation of the primary heater in the previous study. However, in further study, the application areas can be expanded by using the cost correlations for other heat sources when more data is accumulated. The power range of the sCO<sub>2</sub> power cycle is set from 60MW<sub>e</sub> to 500MW<sub>e</sub> considering the valid range of the model for the coal-fired heaters.

As for the pre-cooler cost model, the direct air cooler type was provided in the previous study [1]. However, in this study, water/sCO<sub>2</sub> PCHE is used for the pre-cooler. Fortunately, in the previous study, the recuperator cost model can be used conservatively for water/sCO<sub>2</sub> PCHE pre-cooler [1]. Therefore,



in this study, the cost model for the recuperator is used for the cost model of the pre-cooler.

The model selection of compressors and motors is more complicated than other components. In the previous study, the compressor cost model consists of integrally geared (IG) centrifugal type and barrel-type centrifugal compressors [1]. For the cost model of motor, three types are suggested in the previous study [1]: explosion-proof motors (EPM), synchronous motors (SM), and open drop-proof motors (OM). The cost model of each motor is as follows. The EPM cost model has the lowest cost and that of the OM has the highest cost. Therefore, it is necessary to subdivide the motor for the required compressor work. For the recompression cycle layout, since the main compressor and re-compressor exist, it is necessary to consider whether the shaft is separated or single. The maximum valid range of the motor cost model is 37MW<sub>e</sub>, so if the combined work of the main compressor and re-compressor is less than 37MW<sub>e</sub>, it can be operated with one motor. However, if not, the shaft of the compressor must be separated and operated with each motor.

If the work of one compressor exceeds the maximum motor model range of 37MW<sub>e</sub>, additional calculation is required. In the previous study, the calculations were performed using multiple barrel-type compressors and assuming each fitted with a motor [1]. Therefore, in this study, when one compressor work exceeds 37MW<sub>e</sub>, a multiple barrel-type compressor is used by dividing the compressors' work. To comply with the limits of the valid range of the cost models for motors and compressors, the divided compressor work is less than 37MW<sub>e</sub> and the divided compressor volumetric flowrate is less than 2.4 m<sup>3</sup>/s. The detailed compressor and motor cost calculation process is as follows.

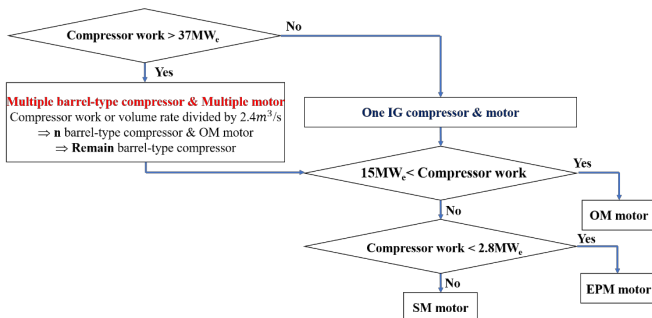


Fig. 2 Compressor and motor cost model selection algorithm

Therefore, the purchased equipment cost (PEC) of the sCO<sub>2</sub> power cycle can be calculated as follows. The process for obtaining the LCOE is covered in detail in the LCOE calculation section.

$$PEC = C_{PHX} + C_{Recup} + C_{Turb} + C_{Comp} + C_{Motor} + C_{Generator} \quad (2)$$

## SCO<sub>2</sub> POWER CYCLE OPTIMIZATION

The cost models are summarized in Table 1. Three cycle power outputs within the valid range of cost models are set as shown. Therefore, a fair comparison of the power cycle could be

made within the valid range of the cost model. In addition, to study the effect of the temperature correction factor in the cost model, two different maximum cycle temperature was reviewed: 550 and 650 °C. Other parameters are set as shown in Table 1 based on the references [18, 19]. Two different sCO<sub>2</sub> power cycle layouts are selected for comparison: simple recuperated cycle layout and recompression cycle layout as shown in Fig 3 and 4, respectively.

Table 1. Cycle design parameters and optimization variables

Maximum Temperature (°C)	550, 650
Cycle output (MW <sub>e</sub> )	60, 100, 500
Maximum pressure (MPa)	25
Minimum temperature (°C)	35
Turbine efficiency (%)	85
Compressor efficiency (%)	80
Component pressure drop (Kpa)	100-150
HTR, LTR effectiveness (%)	90
Generator efficiency (%)	98
Optimization variables	
Pressure ratio (2.62~3.24 for simple recuperated cycle) (2.49~3.05 for recompression cycle)	
Flow split ratio (0.5~0.99 for recompression cycle layout)	

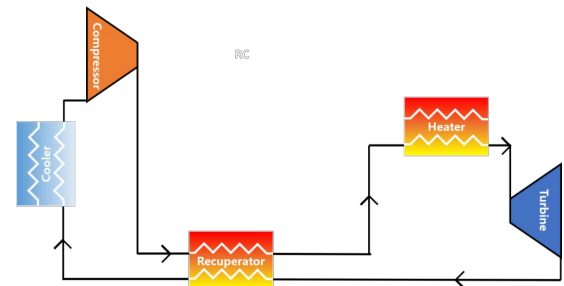


Fig. 3 simple recuperated cycle layout

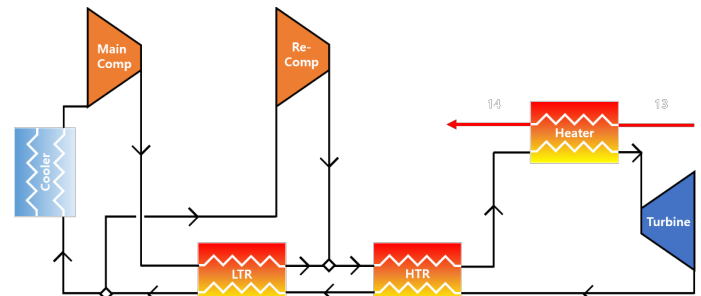


Fig. 4 Recompression cycle layout

Therefore, cycle optimization is performed using the KAIST-CCD code. The KAIST-CCD code is a MATLAB-based in-house code and has been developed by the KAIST research

team. The physical properties of the sCO<sub>2</sub> are calculated with NIST-REFPROP database for accurate calculation of properties [20]. The operation algorithm of the KAIST-CCD code is shown in Figure 5, and the error of the algorithm is as follows.

$$\text{Error} = \frac{[\text{heat input}(n) - \text{heat input}(n-1)]}{\text{heat input}(n)} \quad (3)$$

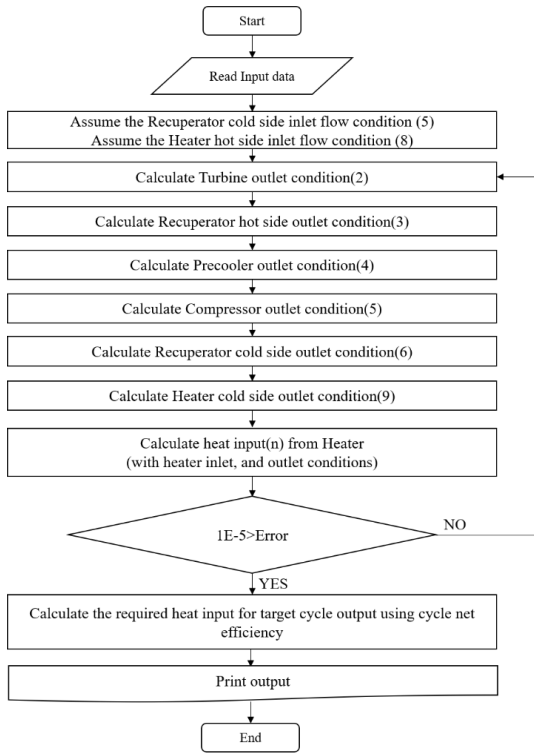


Fig. 5 Operation algorithm of the KAIST-CCD code

The optimization results for each cycle maximum temperature, output, and layout are summarized in Tables 2 and 3, and the cycle optimization results are shown in Fig 6,7 and 8. Fig. 6 (a) is the pressure ratio-efficiency graph for the cycle maximum temperature of 550°C, and Fig. 6 (b) is the same graph for the cycle maximum temperature of 650°C. For the recompression cycle, the optimization variables are the pressure ratio and flow split ratio. Fig. 7 shows the optimization result graph for the maximum cycle temperature of 550°C, and Fig. 8 shows the graph for the maximum cycle temperature of 650°C.

Table 2. Cycle optimization results for simple recuperated cycle

Cycle maximum temperature (°C)	550	650
Cycle thermal efficiency (%)	31.85	34.47
Cycle output (MW <sub>e</sub> )	60 / 100 / 500	60 / 100 / 500
Required thermal power (MW <sub>th</sub> )	188 / 314 / 1570	174 / 290 / 1450

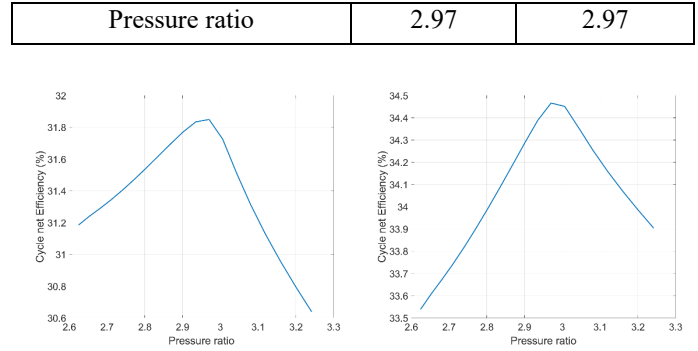


Fig. 6 Cycle optimization results for simple recuperated cycle by cycle maximum temperature (a) 550°C (b) 650°C

Table 3. Cycle optimization results for recompression cycle

Cycle maximum temperature (°C)	550	650
Cycle thermal efficiency (%)	38.17	41.80
Cycle output (MW <sub>e</sub> )	60 / 100 / 500	60 / 100 / 500
Required thermal power (MW <sub>th</sub> )	157 / 262 / 1310	144 / 239 / 1196
Pressure ratio	2.74	2.81
Flow split ratio	0.7	0.7

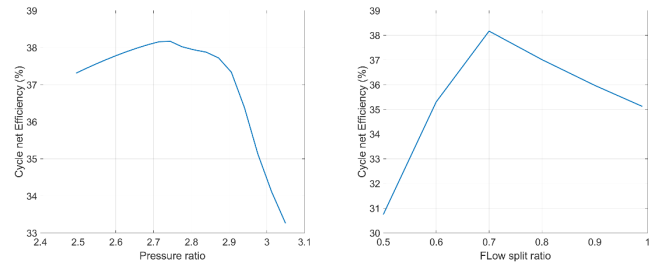


Fig. 7. Cycle optimization results for recompression cycle for cycle maximum temperature 550°C (a) Pressure ratio-Efficiency (b) Flow split ratio-Efficiency

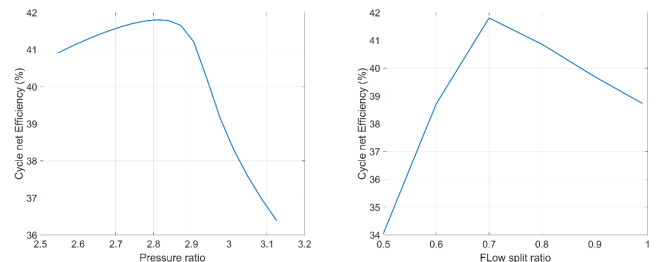


Fig. 8 Cycle optimization results for recompression cycle for cycle maximum temperature 650°C (a) Pressure ratio-Efficiency (b) Flow split ratio-Efficiency

## RECUPERATOR AND PRE-COOLER CONDUCTANCE-AREA CALCULATION

To utilize the cost model of the recuperator and pre-cooler, the conductance-area product, UA, of each heat exchanger should be calculated. The cycle design points within the optimization range are obtained by performing cycle optimization. Therefore, the conductance-area product UA can be calculated using the heat exchanger inlet and outlet temperatures and pressures. In the previous study, as a result of calculating UA through the discretized heat exchanger model using the REFPROP database [20], precise calculations can be performed even with 20 nodes [1]. Therefore, in this study, a discretized heat exchanger model with 200 nodes is developed to accurately calculate UA. This code uses the NIST REFPROP database [20], and the conductance-area product UA of each node can be calculated through the following LMTD method using the inlet and outlet temperature of the heat exchanger. Therefore, the UA of the heat exchanger can be calculated.

$$\dot{Q}_{Re}(W) = UA_{\text{heat transfer}} \Delta T_m \quad (4)$$

$$\Delta T_m = \frac{(T_{\text{hot in}} - T_{\text{cold out}}) - (T_{\text{hot out}} - T_{\text{cold in}})}{\ln((T_{\text{hot in}} - T_{\text{cold out}}) / (T_{\text{hot out}} - T_{\text{cold in}}))} \quad (5)$$

Since it is difficult to show the UA at the all design point within optimization variables, only the UA at the cycle optimum point is shown in Table 4 and 5. The UA of the recuperator and pre-cooler at the optimal point for each cycle layout are as follows.

Table 4. UA calculation results for simple recuperated cycle layout

Cycle maximum temperature (°C)	550	650
Cycle output (MW <sub>e</sub> )	60 / 100 / 500	60 / 100 / 500
Required thermal power (MW <sub>th</sub> )	188 / 314 / 1570	174 / 290 / 1450
Recuperator UA (MW/K)	3.1 / 5.2 / 25.8	2.7 / 4.4 / 22.3
Pre-cooler UA (MW/K)	12.6 / 21.1 / 105.4	10.8 / 18.0 / 89.8

Table 5. UA calculation results for recompression cycle layout

Cycle maximum temperature (°C)	550	650
Cycle output (MW <sub>e</sub> )	60 / 100 / 500	60 / 100 / 500
Required thermal power (MW <sub>th</sub> )	157 / 262 / 1310	144 / 239 / 1196
Hot Temp Recuperator	4.8 / 8.0 / 40.2	4.3 / 7.2 /

UA (MW/K)		35.9
Low Temp Recuperator UA (MW/K)	7.8 / 13.0 / 65.2	5.4 / 9.0 / 44.9
Pre-cooler UA (MW/K)	19.2 / 31.7 / 158.5	16.8 / 27.9 / 139.7

## LCOE CALCULATION

The Levelized Cost Of Energy (LCOE) is a measure of the average net present cost of electricity production over the lifetime of a power plant. The LCOE is defined with the following equation (17). In the equation,  $I_t$  is the Fixed Capital Cost (FCI),  $M_t$  is the Operation and Maintenance (O&M,  $M_t$ ) costs,  $F_t$  is the fuel expenditures in year t,  $E_t$  is the electricity energy generated in the year t, r is the discount rate, and t is the expected life time. The load factor used in this study is 53.5%, which is the load factor of coal-fired power plants worldwide in 2019 [21].

$$LCOE = \frac{\sum_{t=1}^n \left[ \frac{I_t + M_t + F_t}{(1+r)^t} \right]}{\sum_{t=1}^n \frac{E_t}{(1+r)^t}} \quad (6)$$

According to references, FCI consists of direct cost (DC) and indirect cost (IC), and O&M cost is a cost related to FCI [21]. The direct cost refers to the cost that directly affects the system, such as structural, piping, and civil costs. Indirect cost means the cost that is indirectly related to the system, such as contingency, supervision, and engineering. The DC is the cost associated with the purchased equipment cost (PEC) in equation (13), and IC is the cost affected by DC [22]. The purchased equipment installation cost for each component referred to Weiland's research [1]. The piping cost is 20% of the PEC when the maximum cycle temperature exceeds 550°C, and 5% of the PEC otherwise [1]. Therefore, direct cost, indirect cost, and operating maintenance cost are summarized in Table 6 [1, 22].

$$I_t = FCI \text{ (Fixed Capital Cost)} = DC + IC \quad (7)$$

$$M_t = O\&M = \text{function}(FCI)_{\text{Table 6}} \quad (8)$$

$$DC \text{ (Direct Cost)} = \text{function}(PEC)_{\text{Table 6}} \quad (9)$$

$$IC \text{ (Indirect Cost)} = \text{function}(DC)_{\text{Table 6}} \quad (10)$$

Table 6 O&M, IC, DC cost [1, 22]

O&M cost (M <sub>t</sub> )	
Fixed operating and maintenance	6.8% of FCI
Various operating and maintenance	6.1% of Fixed O&M

Indirect Cost (IC)	
Engineering and supervision	8% of DC
Construction cost and contractor's profit	15% of DC
Contingency	15% of DC
Direct Cost (DC)	
Purchased equipment installation [1]	50% of PEC [Primary heat exchanger]
	20% of PEC [Other components]
	5% of PEC [Recuperator]
Piping [1]	5% of PEC ( $T_{max} < 550^{\circ}C$ ) 20% of PEC ( $T_{max} > 550^{\circ}C$ )
Instrumentation & controls	10% of PEC
Civil, structural, and architectural factor	30% of PEC
Service facilities	30% of PEC

In this study, the fuel is coal. The cost of coal is referred a trading site [23]. since the fuel price is used as a variable in the sensitivity analysis, the lowest and the highest fuel costs for one year are used for 1st August 2022.

Table 7. Fuel cost of the sCO<sub>2</sub> power cycle

Fuel cost ( $F_f$ ) [23]		
Fuel (Coal)	18.4~51.6	\$/MWh <sub>th</sub>

### SENSITIVITY STUDY

The relation between the optimum cycle thermal efficiency and the LCOE minimum point is investigated with a sensitivity analysis in this study. Table 8 shows the range of variables for sensitivity analysis. The discount rate and lifetime of the sCO<sub>2</sub> power cycle required for LCOE calculation are set to 5% [24-26] and 40 years [27, 28], respectively.

Table 8. The variable range used for sensitivity analysis

Cycle output (MW <sub>e</sub> )	6-500
Cycle Maximum Temperature, $T_{max}$ (°C)	550-650
Fuel (Coal) cost (\$/MWh <sub>th</sub> )	18.4-51.6



### CASE 1: SIMPLE RECUPERATED CYCLE ( $T_{max} = 550^{\circ}C$ )

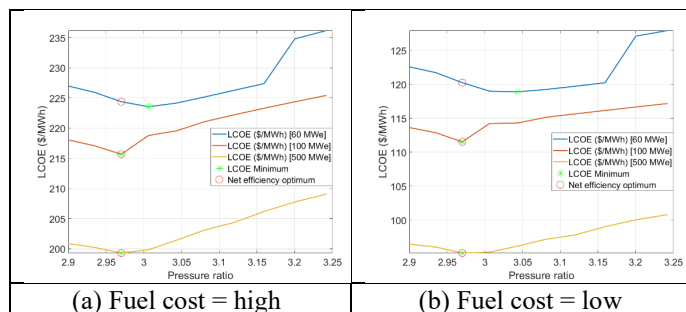


Fig. 9 sCO<sub>2</sub> power cycle LCOE results for pressure ratio and fuel cost ( $T_{max} = 550^{\circ}C$ , Cycle output = 60, 100, 500MW<sub>e</sub>)

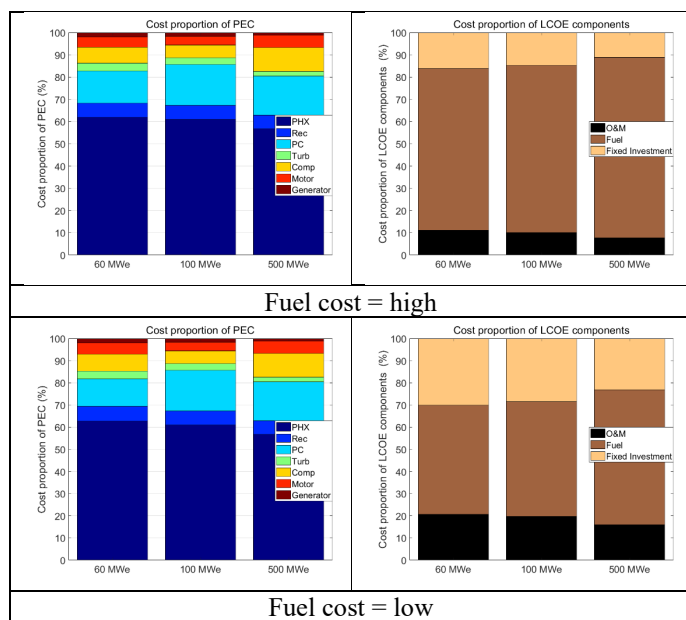


Fig. 10 PEC (a) and LCOE (b) of the sCO<sub>2</sub> power cycle ( $T_{max} = 550^{\circ}C$ , Cycle output = 60, 100, 500MW<sub>e</sub>)

The results for each fuel cost and cycle output are shown for a simple recuperated cycle layout with a cycle maximum temperature of 550°C. The larger the cycle output, the closer the cycle thermal performance optimum point and the LCOE minimum point is. This is because the component costs take the form of a function of cost =  $x^n$  ( $n < 1$ ), so the cost converges as the output of the system increases. Therefore, the percentage of fixed investment cost which related to the component cost decreases as the cycle output increases as shown in Fig. 10. In other words, as the cycle output increases, the fixed investment

cost converges to a certain value. On contrary, as the cycle output increases, the cost of fuel increases linearly. These results suggest that the fuel costs have a significant impact on LCOE when the cycle output is large enough. Therefore, the LCOE minimum point with large the cycle output approaches the optimum point of cycle thermal efficiency requiring the least additional heat sources.

The LCOE decreases as the system output increases as shown in Fig. 9. However, due to the limitation on the valid range of the compressor and motor cost models; it is necessary to use multiple compressors and motors. Therefore, it can be seen that the LCOE for the pressure ratio increases stepwise depending on whether multiple compressors and motors are used. As can be seen from the bar graph for percentage change in component cost in PEC, as the system output increases, unlike other components, the cost fraction of compressor as well as motor increases.

When the fuel cost is low, LCOE decreases. The percentage of fuel in LCOE shows a large difference such that about 22% decreases compared to that of the high fuel cost case. As fuel cost decreases, the cost for additional heat sources required at non-optimal cycle efficiencies decreases. This effect smooths the slope of the LCOE with respect to the pressure ratio.

### CASE 2: SIMPLE RECUPERATED CYCLE ( $T_{max} = 650^{\circ}C$ )

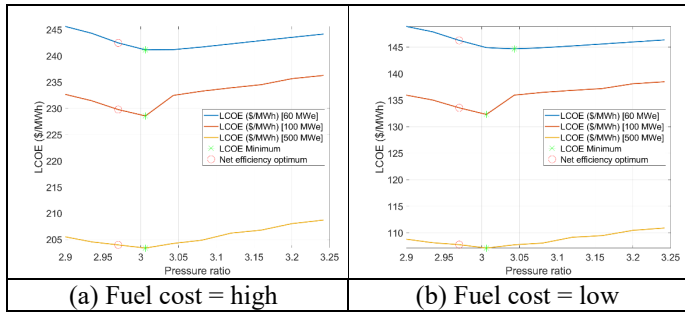


Fig. 11  $sCO_2$  power cycle LCOE results for pressure ratio and fuel cost ( $T_{max} = 650^{\circ}C$ , Cycle output = 60, 100, 500MWe)

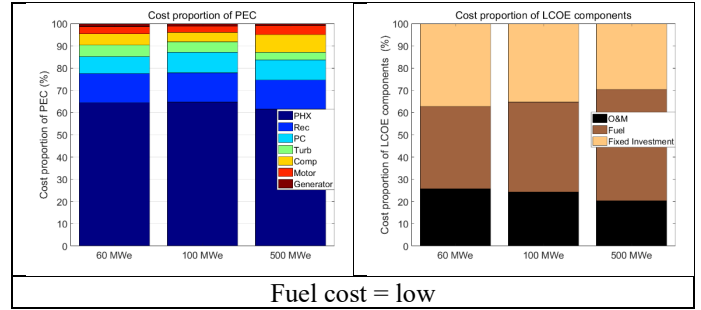
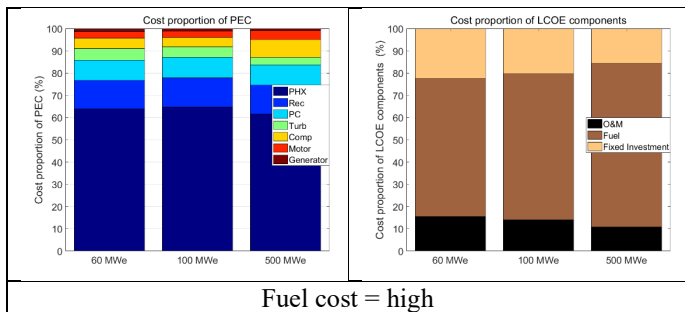


Fig. 12 PEC (a) and LCOE (b) of the  $sCO_2$  power cycle ( $T_{max} = 650^{\circ}C$ , Cycle output = 500MWe)

For the cycle maximum temperature  $650^{\circ}C$  case, the costs of high-temperature components, such as primary heater, turbine, and recuperator, increase due to the temperature correction factor. As shown in Fig. 12 (a), the fraction of primary heater, turbine, and recuperator increases compared to the case with  $550^{\circ}C$ .

As shown in Fig.12 (b), it is confirmed that the fraction of the fixed investment cost related to the component cost increases. Therefore, the effect of fuel cost on the LCOE is reduced compared to that of  $550^{\circ}C$  case, and this effect can be confirmed with the fact that the cycle efficiency optimum point and the minimum LCOE point do not match with each other, which is in contrast with the  $550^{\circ}C$  result.

If the fuel cost is low, the LCOE decreases, and the fraction of fuel in the LCOE is reduced by 24%. The fuel cost affects the cost of the additional heat required to produce the same cycle power output with the lower cycle efficiency cases. Therefore, when the fuel cost is low, the effect of the cycle optimum efficiency on the LCOE becomes small. This effect confirmed that the cycle optimum point and the LCOE minimum point do not match in the case of a low fuel cost as shown in Fig. 11.

### CASE 3: RECOMPRESSION CYCLE ( $T_{max} = 550^{\circ}C$ )

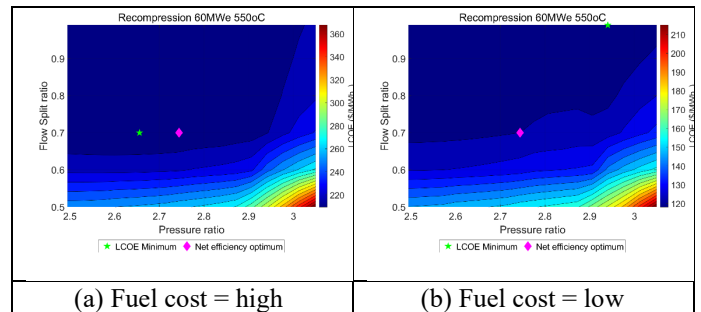


Fig. 13  $sCO_2$  power cycle LCOE results for pressure ratio and fuel cost ( $T_{max} = 550^{\circ}C$ , Cycle output = 60MWe)

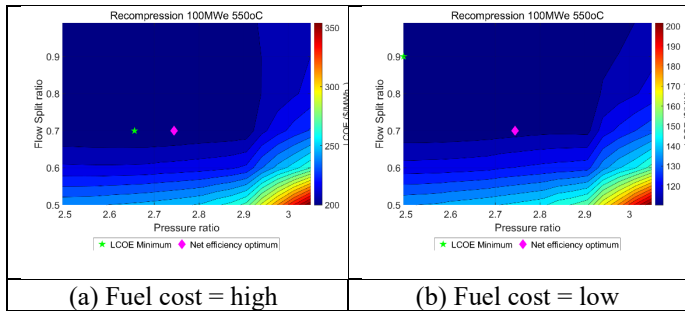


Fig. 14 sCO<sub>2</sub> power cycle LCOE results for pressure ratio and fuel cost ( $T_{max} = 550^{\circ}\text{C}$ , Cycle output =  $100\text{MW}_e$ )

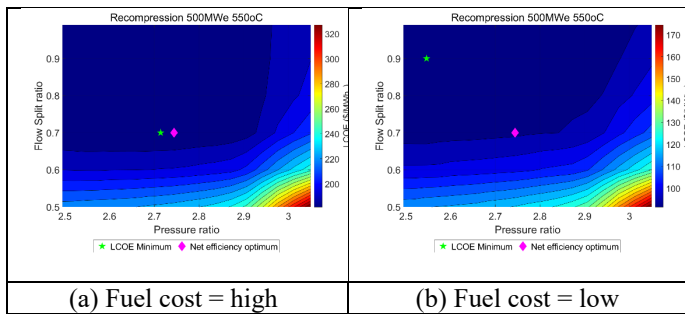


Fig. 15 sCO<sub>2</sub> power cycle LCOE results for pressure ratio and fuel cost ( $T_{max} = 550^{\circ}\text{C}$ , Cycle output =  $500\text{MW}_e$ )

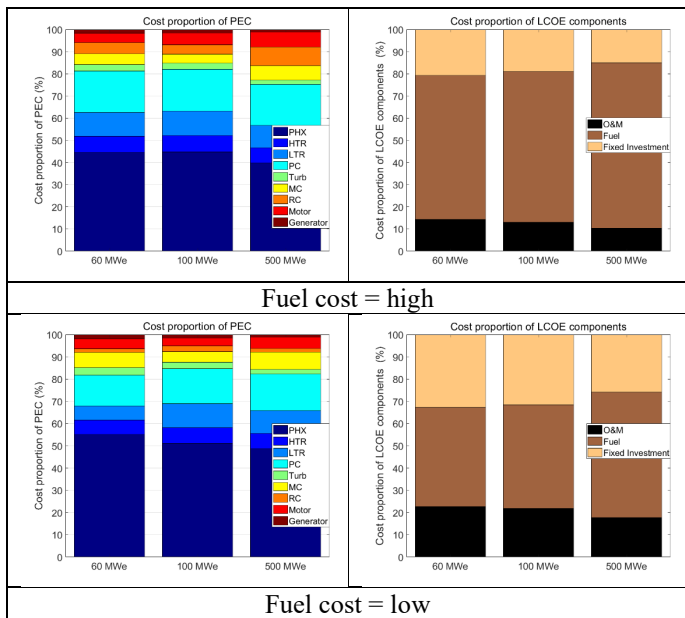


Fig. 16 PEC (a) and LCOE (b) of the sCO<sub>2</sub> power cycle ( $T_{max} = 550^{\circ}\text{C}$ , Cycle output =  $60, 100, 500\text{MW}_e$ )

The recompression cycle improves the cycle efficiency by adding recompressing process. In this cycle, heat rejection can be reduced by splitting the mass flow rate before the pre-cooler as shown in Fig. 4. Compared to the simple recuperated cycle layout, the recompression cycle has more components. Therefore, the fraction of fixed investment cost in LCOE increases compared to the simple recuperated cycle layout.

When the cycle output and fuel cost is small, the increase in component cost is larger than the increase in work due to the recompression effects, resulting in higher LCOE compared to that of the simple recuperated cycle. Therefore, the minimum LCOE occurred in the direction of the simple recuperated cycle (FSR = 100%) at low power output ( $60, 100\text{MW}_e$ ) and low fuel cost as shown in Fig. 13(b). Conversely, if the cycle output is larger than  $100\text{MW}_e$ , the component cost does not significantly affect the LCOE. This is because the component cost function has the form  $x^n$  ( $n < 1$ ). In other words, when the system output is large enough, the minimum LCOE point converges to a cycle optimal point with the lowest fuel cost. Therefore, it is confirmed that the larger the system output and the higher the fuel cost are, the greater the effect of recompression becomes.

The fraction of fuel cost in LCOE decreases by 20% when the fuel cost decreases as shown in Fig. 16. This result shows that the fraction of the fuel cost in LCOE is reduced, so that the LCOE is more sensitive to the cycle component cost. Therefore, the lowest point of the LCOE is not closer to the optimum cycle efficiency point compared to when the fuel cost is high.

#### CASE 4: RECOMPRESSION CYCLE ( $T_{max} = 650^{\circ}\text{C}$ )

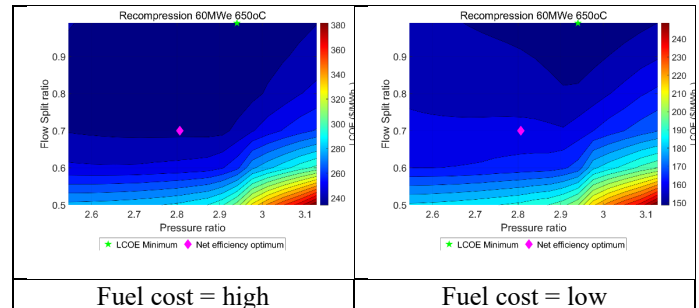


Fig. 17 sCO<sub>2</sub> power cycle LCOE results for pressure ratio and fuel cost ( $T_{max} = 650^{\circ}\text{C}$ , Cycle output =  $60\text{MW}_e$ )

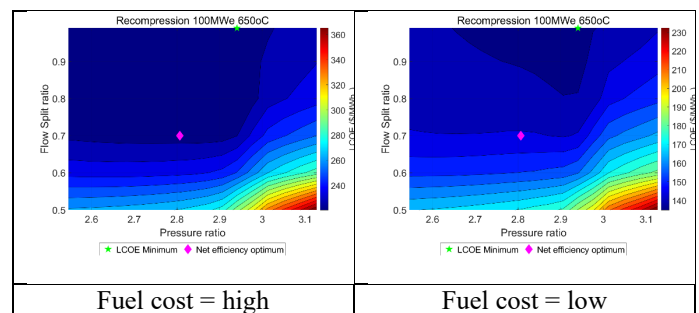


Fig. 18 sCO<sub>2</sub> power cycle LCOE results for pressure ratio and fuel cost ( $T_{max} = 650^{\circ}\text{C}$ , Cycle output =  $100\text{MW}_e$ )



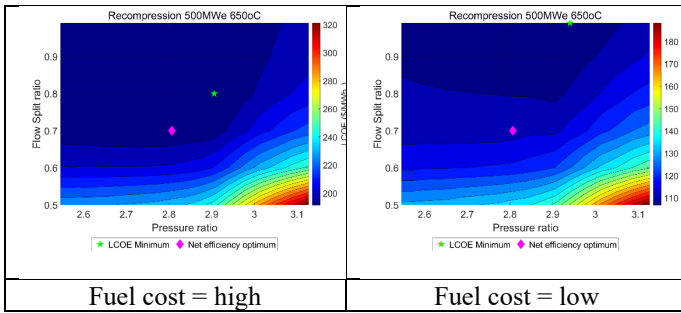


Fig. 19  $s\text{CO}_2$  power cycle LCOE results for pressure ratio and fuel cost ( $T_{\max} = 650^\circ\text{C}$ , Cycle output =  $500\text{MW}_e$ )

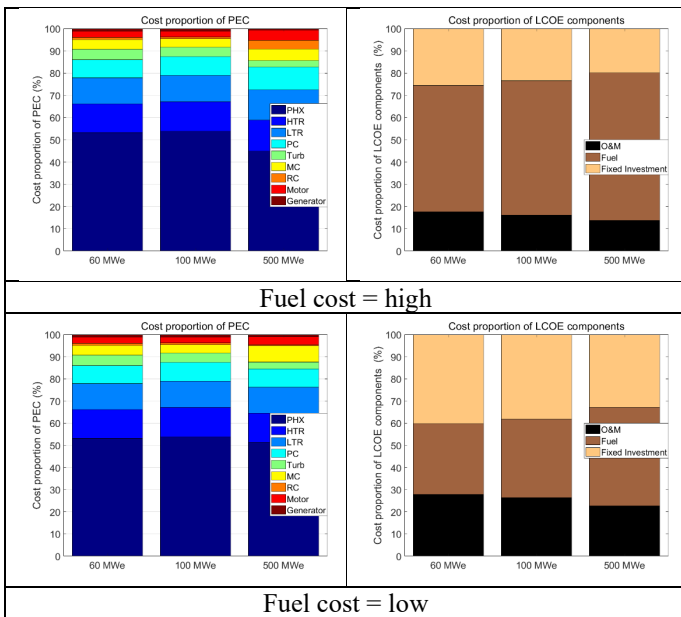


Fig. 20 PEC and LCOE of the  $s\text{CO}_2$  power cycle ( $T_{\max} = 650^\circ\text{C}$ , Cycle output = 60, 100,  $500\text{MW}_e$ )

In the case of  $650^\circ\text{C}$  case, the cost and the cost escalation of high-temperature components increase due to the temperature correction factor. Therefore, the effect of fixed investment costs on LCOE increases as shown in Fig. 20 (b).

When the fuel cost is low, component costs have a significant impact on LCOE. Therefore, the effect of recompression is hardly seen in the case of low fuel cost and  $650^\circ\text{C}$  as shown in Figs. 17, 18, 19.

## SUMMARY AND CONCLUSIONS

In this study, techno-economic sensitivity analysis is performed on the correlation between the LCOE minimum point and the optimum cycle performance for the  $s\text{CO}_2$  power cycle.

The correlation between the best cycle performance and the lowest LCOE point is determined by the impact of the following key variables on fixed investment costs and fuel costs: 1. Cycle power output, 2. Cycle maximum temperature, 3. Fuel cost, 4. Cycle layout. The sensitivity analysis for cycle performance and LCOE is performed for these four factors.

First, it is confirmed that the LCOE minimum point converges to the optimum point of cycle efficiency as the cycle power output increases. This is because, as the cycle power output increases, the cost of the cycle component converges, while the cost of the required fuel increases proportionally to the cycle power output.

Second, as the maximum cycle temperature exceeds  $550^\circ\text{C}$ , the cost of the component increases due to the temperature correction factor. As the maximum cycle temperature increases (over  $550^\circ\text{C}$ ), the fraction of fixed investment costs in the LCOE increases, so the LCOE minimum point becomes distant from the cycle efficiency optimum point.

Third, as the fuel cost increases, the fraction of fuel cost in LCOE increases. As the cycle efficiency approaches the optimum efficiency, the fuel required to generate the same cycle power output decreases. Therefore, the higher the fuel cost is, the greater the effect of cycle efficiency on LCOE is. Therefore, as the fuel cost increases, it is confirmed that the cycle efficiency optimum point and the LCOE minimum point are close.

Finally, as a result of comparing the cycle layout, it is confirmed that the recompression effect increases as the system output and the fuel cost increases. That is, a sufficiently large power cycle output or a high fuel cost for a heat source is required to benefit from the addition of a recompression process. However, in the current level of technology, the thermal performance optimum and the LCOE minimum of the recompression cycle do not match with each other under ranges of variables considered in this study.

In conclusion, it is confirmed that the cycle best performance and the minimum LCOE points generally do not coincide as the cycle becomes more complex and the cycle maximum temperature becomes high. The discrepancy between the cycle performance and the LCOE shows that cycle design optimization should consider not only the cycle performance, but also the economic performance as well at the current technology level. When the cost data is more accumulated after the  $s\text{CO}_2$  power cycle enters higher technology readiness level in the future, it can be expected that the cost model will be improved even at higher temperatures and smaller sizes. As the proposed future study, the techno-economical sensitivity of the  $s\text{CO}_2$  power cycle will be performed for considering wider range of variables, such as recuperator conductance-area product UA, updated material costs, pipe costs and, discount rate, etc [9].

## NOMENCLATURE

$\Delta T_m$	Log mean temperature
C	Component cost
$F_t$	Fuel expenditures in year t
$f_T$	Temperature correction factor
$I_t$	Fixed capital cost in year t
$M_t$	Operation and maintenance cost in year t

r	Discount rate
T	Temperature
t	Power cycle life time
$T_{max}$	Cycle maximum temperature
UA	Conductance-area product

## ACKNOWLEDGEMENTS

This research was supported by Civil-Military Technology Cooperation Program (iCMTC) funded by the Agency for Defense Development – South Korea (17-CM-EN-04).

## REFERENCES

[1] Weiland, Nathan T., Blake W. Lance, and Sandeep R. Pidaparti. "sCO<sub>2</sub> power cycle component cost correlations from DOE data spanning multiple scales and applications." *Turbo Expo: Power for Land, Sea, and Air*. Vol. 58721. American Society of Mechanical Engineers, 2019.

[2] Ahn, Yoonhan, et al. "Review of supercritical CO<sub>2</sub> power cycle technology and current status of research and development." *Nuclear engineering and technology* 47.6 (2015): 647-661.

[3] Marion, John, et al. "The STEP 10 MWe sCO<sub>2</sub> Pilot Demonstration Status Update." *Turbo Expo: Power for Land, Sea, and Air*. Vol. 86083. American Society of Mechanical Engineers, 2022.

[4] Pasch, James Jay, et al. Supercritical CO<sub>2</sub> recompression Brayton cycle: completed assembly description. No. SAND2012-9546. Sandia National Laboratories (SNL), Albuquerque, NM, and Livermore, CA (United States), 2012.

[5] Hacks, Alexander Johannes, et al. "Operational experiences and design of the sCO<sub>2</sub>-HeRo loop." 3rd European supercritical CO<sub>2</sub> Conference. 2019.

[6] Mendez Cruz, Carmen Margarita, and Gary E. Rochau. sCO<sub>2</sub> Brayton Cycle: Roadmap to sCO<sub>2</sub> Power Cycles NE Commercial Applications. No. SAND-2018-6187. Sandia National Lab.(SNL-NM), Albuquerque, NM (United States), 2018.

[7] Wright, Steven A., Chal S. Davidson, and William O. Scammell. "Thermo-economic analysis of four sCO<sub>2</sub> waste heat recovery power systems." Fifth International SCO<sub>2</sub> Symposium, San Antonio, TX, Mar. 2016.

[8] Meybodi, Mehdi Aghaei, et al. "Techno-economic analysis of supercritical carbon dioxide power blocks." *AIP Conference Proceedings*. Vol. 1850. No. 1. AIP Publishing LLC, 2017.

[9] Neises, Ty, and Craig Turchi. "Supercritical carbon dioxide power cycle design and configuration optimization to minimize leveled cost of energy of molten salt power towers operating at 650 C." *Solar Energy* 181 (2019): 27-36.

[10] Thanganadar, Dhinesh, et al. "Techno-economic analysis of supercritical carbon dioxide cycle integrated with coal-fired power plant." *Energy Conversion and Management* 242 (2021): 114294.

[11] Marchionni, Matteo, et al. "Techno-economic comparison of different cycle architectures for high temperature waste heat to power conversion systems using CO<sub>2</sub> in supercritical phase." *Energy Procedia* 123 (2017): 305-312.

[12] Wang, Xurong, and Yiping Dai. "Exergoeconomic analysis of utilizing the transcritical CO<sub>2</sub> cycle and the ORC for a recompression

supercritical CO<sub>2</sub> cycle waste heat recovery: A comparative study." *Applied energy* 170 (2016): 193-207.

[13] Benjelloun, M., G. Doulergis, and R. Singh. "A method for techno-economic analysis of supercritical carbon dioxide cycles for new generation nuclear power plants." *Proceedings of the Institution of Mechanical Engineers, Part A: Journal of Power and Energy* 226.3 (2012): 372-383.

[14] Alfani, Dario, et al. "Techno-economic analysis of CSP incorporating sCO<sub>2</sub> brayton power cycles: Trade-off between cost and performance." *AIP Conference Proceedings*. Vol. 2445. No. 1. AIP Publishing LLC, 2022.

[15] White, Charles W., et al. Techno-economic Evaluation of Utility-Scale Power Plants Based on the Indirect sCO<sub>2</sub> Brayton Cycle-Report. No. 21490. National Energy Technology Laboratory (NETL), Pittsburgh, PA, Morgantown, WV (United States), 2017.

[16] Zitney, Stephen E., and Eric Liese. Dynamic Modeling and Simulation of a 10MWe Supercritical CO<sub>2</sub> Recompression Closed Brayton Power Cycle for Off-Design, Part-Load, and Control Analysis. No. NETL-PUB-21414. National Energy Technology Laboratory (NETL), Pittsburgh, PA, Morgantown, WV (United States), 2017.

[17] Mecheri, Mounir. "sCO<sub>2</sub> closed Brayton cycle for coal-fired power plant: An economic analysis of a technical optimization." 2nd European sCO<sub>2</sub> Conference 2018: 30-31 August 2018, Essen, Germany. 2018.

[18] SunShot Vision Study. N.p.: U.S. Department of Energy, Feb. 2012. PDF.

[19] Le Moullec, Yann, et al. "Shouhang-EDF 10MWe supercritical CO<sub>2</sub> cycle+ CSP demonstration project." 3rd European Conference on Supercritical CO<sub>2</sub> (sCO<sub>2</sub>) Power Systems 2019: 19th-20th September 2019.

[20] E.W. Lemmon, M.L. Huber, and M. O. McLinden, "NIST Standard Reference Database 23," NIST Reference Fluid Thermodynamic and Transport Properties –REFPROP, version, vol.9, p.55, 2010.

[21] "Carbonbrief", CabonBrief.org, last modified March 26, 2020, accessed December 27, 2022, <https://www.carbonbrief.org/mapped-worlds-coal-power-plants/>

[22] Bejan, Adrian, George Tsatsaronis, and Michael J. Moran. Thermal design and optimization. John Wiley & Sons, 1995.

[23] "TRADING ECONOMICS", TRADING ECONOMICS, last modified August 1, 2022, accessed August 1, 2022, <https://tradingeconomics.com/commodity/coal>

[24] Arrow K, Cropper M, Gollier C, Groom B, Heal G, Newell R, et al. Determining benefits and costs for future generations. *Science* 2013;341:349–50.

[25] Locatelli G, Boarin S, Fiordaliso A, Ricotti ME. Load following of Small Modular Reactors (SMR) by cogeneration of hydrogen: a techno-economic analysis. *Energy* 2018;148:494–505.

[26] Rath Michael, Granger Morgan M. Assessment of a hybrid system that uses small modular reactors (SMRs) to back up intermittent renewables and desalinate water. *Prog Nucl Energy* 2020;122:103269.

[27] Bundesnetzagentur. Power plant list. 2019. [https://www.undesnetzagentur.de/EN/Areas/Energy/Companies/SecurityOfSupply/GeneratingCapacity/PowerPlantList/PubliPowerPlantList\\_node.html](https://www.undesnetzagentur.de/EN/Areas/Energy/Companies/SecurityOfSupply/GeneratingCapacity/PowerPlantList/PubliPowerPlantList_node.html). Accessed March 14, 2019.

[28] Fiebrandt, Marc, Julian Röder, and Hermann-Josef Wagner. "Minimum loads of coal-fired power plants and the potential suitability for energy storage using the example of Germany." *International Journal of Energy Research* 46.4 (2022): 4975-4993.

PARAMETRIC ANALYSIS OF HEAT EXCHANGER DESIGN IN A TECHNO-ECONOMIC OPTIMIZATION OF A sCO<sub>2</sub> SYSTEM.

**Thiago Gotelip\***

Technische Universität Dresden  
Dresden, Germany  
Email: Thiago.Gotelip\_Correa\_Veloso@tu-dresden.de

**Uwe Gampe**

Technische Universität Dresden  
Dresden, Germany

**Sebastian Rath**

Technische Universität Dresden  
Dresden, Germany

**Andreas Jäger**

Technische Universität Dresden  
Dresden, Germany

**Stefan Glos**

Siemens Energy AG  
Mülheim, Germany

**ABSTRACT**

The investigation of favorable operating conditions for sCO<sub>2</sub> cycles for waste heat recovery is a process that requires a proper analysis of operating parameters, component design, and economic performance. In this aspect, examining the heat exchanger has preponderant significance. In this study, as part of the Carbosola project, a thermo-economic multiobjective optimization of the sCO<sub>2</sub> cycle is analyzed based on a one-dimensional design of the heat exchangers, focusing on the recuperator. The main objective is to investigate the effect of the non-linearity of the CO<sub>2</sub> properties in the heat exchanger geometry and on the cycle performance. The results highlight the significance of the one-dimensional investigations in the optimization process, while sensitivity analyses indicate the recuperator as key equipment for the optimal cycle operation. Furthermore, the examination reveals the influence of the CO<sub>2</sub> properties characteristics at different operating ranges and its effects on the system's equipment design and thermo-economic performance. Finally, the results indicate a prominent potential of the sCO<sub>2</sub> Preheating architecture for heat recovery from gas turbines.

**INTRODUCTION**

The more recent development of the supercritical carbon dioxide (sCO<sub>2</sub>) power cycle has enhanced its potential for efficient power generation. Especially for waste heat recovery applications, sCO<sub>2</sub> systems stand out as a technically and economically competitive alternative for gas turbine bottoming cycles.

According to Huck *et al.* [1] sCO<sub>2</sub> can outperform the steam bottoming cycle at more feasible pressure levels (250) bar for operation temperatures of 500 °C. The sCO<sub>2</sub> power cycle for waste heat recovery (WHR) from a gas turbine can achieve higher efficiency than a steam/water cycle, despite its simplicity and compactness [2].

Li *et al* [3] propose a comparative investigation on the supercritical carbon dioxide power cycle for waste heat recovery of gas turbine is carried out. The results indicate that turbine dominates the investment cost of power cycle. The partial heating cycle is recommended due to its balanced overall performance. Ancona *et al* [4] investigated sCO<sub>2</sub> potential as bottoming recovery cycles in combined heat and power plant configuration comparing several gas turbines models at part-load operation.

Heat exchangers are an enabling technology for efficient power generation with a closed, recuperated Brayton cycle using supercritical carbon dioxide (sCO<sub>2</sub>) as the working fluid. Heat exchangers influence the overall system efficiency and system size. The heat exchanger designs must balance between heat exchanger effectiveness and pressure drop to achieve the desired tradeoff between system efficiency and system size. This tradeoff between system efficiency and system size will vary with each energy conversion system application.[5]

Guo [6] employed a segmental design method to accurately capture the drastic variations of properties in the supercritical carbon dioxide (sCO<sub>2</sub>) recuperator. According to the authors, both fluids' local heat capacity flow rates have drastic changes in sub-heat exchangers, even though the mass flow rates of both fluids remain unchanged. The segmented method for heat exchangers is largely applied to investigate sCO<sub>2</sub> applications. [7–9]

The thermodynamic properties suffer significant variations near the critical point, and the determination of these characteristics in this region as transfer and pressure drop of carbon dioxide (CO<sub>2</sub>) are difficult to predict. These are crucial issues for the design of the cycle. The investigations in [10–12] also present the characteristics of the sCO<sub>2</sub> cycle near the pseudo-critical point.

\* corresponding author(s)

Kwon [7] developed a model for PCHE off-design quasi-steady state performance for the recuperator and pre-cooler in a supercritical CO<sub>2</sub> (sCO<sub>2</sub>) Brayton cycle, respectively, to optimize power system operation strategies under off-design conditions. The developed model evaluates the performance of the sCO<sub>2</sub> system to establish operation strategies such as inventory control and heater bypass control under off-design conditions.

The present investigation is part of the CARBOSOLA project. The project aims to design the components and system of a technology demonstrator for waste heat recovery applications, besides investigating the methods required for further technology development up to commercial maturity.

## METHODOLOGY

The thermal source investigated in this study is the waste exhaust gas from two SGT-A65 gas turbines. Heat recovery from gas turbines represents a significant potential for sCO<sub>2</sub> cycling applications. Table 1 presents the main characteristics of the thermal source adopted in the calculation model.

Table 1 Exhaust Gas Characteristics

Heat Source	2 x AGT on 1 sCO <sub>2</sub>
Pressure [bar]	1,04
Temperature [°C]	432
Cold Flue Gas Temperature [°C]	≥ 75
Mass Flow [kg/s]	337
Wet cooling tower parameters:	
Ambient Temperature [°C]	15
Wet Bulb Temperature [°C]	10,8
Approach Temperature [°C]	5
Warm Up Range [°C]	7

### 2.1 Cycle Architecture

The Regenerative architecture is a general arrangement of the cycle sCO<sub>2</sub>, comprising a turbine, recuperator, cooler, and compressor Figure 1. It is a typical closed regenerative Brayton cycle. For most authors, the regenerative cycle is considered the simplest potential architecture.

Due to the difference between the specific heat capacity of the high-pressure stream (2) and low-pressure stream (4), the equipment deal with high irreversibility. Therefore, the temperature of stream (2) will be limited. [13–16].

This effect limits the temperature ( $T_3$ ) at the heater outlet. Furthermore, this architecture does not allow satisfactory exploitation of the heat source. As a result, a considerable amount of energy is rejected in the stack. These characteristics limit the efficiency of the architecture and its economic performance, especially for WHR.

According to Kim *et al.* [17], in waste heat recovery (WHR), the purpose of cycle optimization is not to maximize the thermal efficiency of the cycle, but to maximize the power output from the waste heat source. Therefore, it is essential to incorporate the thermal efficiency of the cycle (cycle efficiency) and the utilization efficiency of the waste heat (heat recovery efficiency) to maximize the power output of the WHR system from the given heat source (system efficiency).

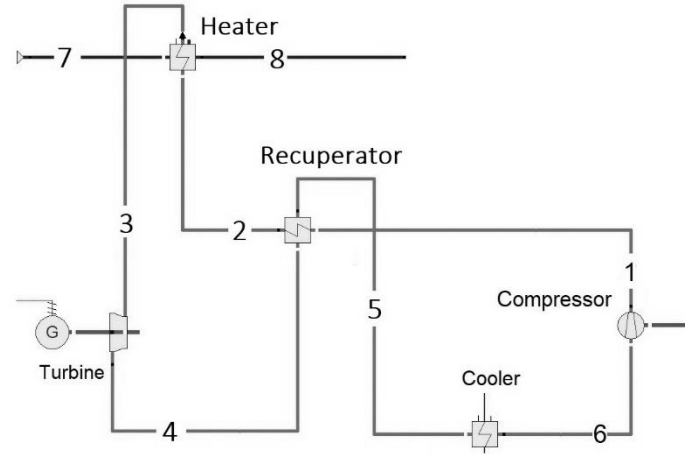


Figure 1 Schematic layout of Regenerative Cycle.

The architectures of sCO<sub>2</sub> cycles characterized by flow-split before heating, such as Recompression, and Preheating cycles, allow for overcoming the Regenerative cycle limitations.

In the Preheating architecture, an additional heater (Preheater) is introduced to the system for heat recovery from the heat source, Figure 2. This architecture splits the CO<sub>2</sub> stream into two primary paths after the compression: one through the recuperator and the second through the preheater.

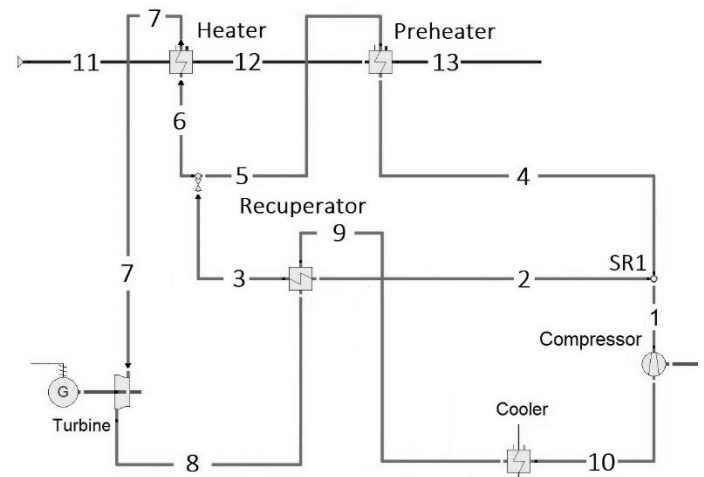


Figure 2 Schematic layout of Preheating Cycle.

In a split flow cycle, the recuperator is divided into low- and high-temperature parts. Each part has different flow rates to accommodate the large variations in the heat capacity of the fluid. If there is an additional low-temperature heat source, it can be used to compensate for the low specific heat of the turbine exhaust stream to minimize the internal irreversibility in the recuperator [2].

The preheating architecture allows better use of the thermal source, recovering heat at two temperature levels (heater and preheater). In addition, the higher mass flow rate ( $\dot{m}_{recup_H}$ ) of the stream (8), which combines the mass flow rate of the

recuperator ( $\dot{m}_{recupC}$ ) and the preheater ( $\dot{m}_{preh.}$ ), allows for greater heat recovery and increases the equipment's efficiency.

The combined mass flow rate in stream (8) will be represented as:

$$\dot{m}_{recupH} = \dot{m}_{recupC} + \dot{m}_{preh.} \quad (1)$$

While the mass ratio between  $\dot{m}_{recupC}$  and  $\dot{m}_{recupH}$  is expressed as:

$$\phi = \frac{\dot{m}_{recupC}}{\dot{m}_{recupH}} \quad (2)$$

The ratio ( $\phi$ ) significantly impacts the recuperator's performance and system optimization.

An in-house calculation tool (OptDesign) developed in MATLAB is used to investigate different sCO<sub>2</sub> cycle architectures thermo-economically. The model analyzes the system at cycle and component levels using the Refprop data library to determine the thermodynamic properties. The subroutines determine the heat exchanger design and the turbine isentropic efficiency estimation (related to the equipment inlet's volumetric flow rate). The maximum isentropic efficiency of the turbine is limited to 90%. On the other hand, the efficiency of the pump/compressor is assumed to be 80%.

This study evaluates the operation of supercritical (sCO<sub>2</sub>) and transcritical (tCO<sub>2</sub>) cycles. In the sCO<sub>2</sub> systems, the compressor inlet temperature is defined as 35°C. While in the tCO<sub>2</sub> system, the minimum temperature is 20°C. Both cycles operate above the critical pressure. The pressure range of the investigation is (75-100 bar) for the low-pressure streams and (200-300) for the high-pressure streams. The minimum temperature difference is limited to 5K in the recuperator and 10K in the heater and preheater.

The OptDesign tool performs a genetic algorithm-based multi-objective optimization (NSGAI) for determining the optimal outcome set.

In this study, two investigations were defined assuming objective functions:

- Maximization of net power and minimization of Fixed Capital Investments (FCI).
- Maximization of Net Present Value and minimization of the Levelized Cost of Energy (LCOE).

The economic analysis of this study addresses the Net Present Value (NPV) methodology and Levelized Cost of Energy (LCOE) as parameters for the thermo-economic evaluation of the investigated sCO<sub>2</sub> systems. In addition, the analysis provides an understanding of the effect of the main operating parameters and architectural characteristics on the system's economic performance.

The equipment cost models are based on the literature of [18,19], which explores an extensive analysis of vendor quotes.

The general equation for component cost is determined by:

$$C = aSP^b \times f_T \quad (3)$$

where C is the component cost, a and b are fit coefficients, SP is the scaling parameter, and f<sub>T</sub> is a temperature correction factor [20]. Table 1 presents the scaling parameters for the primary equipment costs.

Table 1 Summary of the scaling parameters for cost correlation.

Equipment	a	SP		b
Heater	-	$UA_{Heater}$	$[W_t/K]$	0.7544
Recuperator	49.45	$UA_{Recu}$	$[W_t/K]$	0.7544
Cooler	32.88	$UA_{Cooler}$	$[W_t/K]$	0.75
Axial Turbine	182600	$P_{mec}$	$[MW_t]$	0.5561
Generator	108900	$P_e$	$[MW_e]$	0.5463
Gearbox	177200	$P_{mec}$	$[MW_t]$	0.2434
Compressor (centrifugal)	1230000	$P_{shaft}$	$[MW_t]$	0.3992
Motor	399400	$P_e$	$[MW_e]$	0.6062

Source: Adapted from [18]

In the NPV analysis, revenue values are calculated annually according to the product's selling price (electricity). The capital expenditure of main equipment (Capex) indicators contemplate the costs of main equipment, site preparation, facility construction, indirect project costs, contingency fees, and others. At the same time, operational expenditure (Opex) determines the fixed and variable costs of the operation as well as maintenance costs.

According to Drennen and Lance [19], these costs contribute significantly to an LCOE estimation; however, they are often ignored. Therefore, the mentioned study contributes a detailed methodology for calculating LCOE.

In this way NPV is defined as:

$$NPV = \sum_{n=1}^{n=20 \text{ years}} \frac{Revenue - (Capex - Opex)}{(1 + interestrate)^n} \quad (4)$$

CAPEX: Capital expenditure of main components.

OPEX: Operational expenditure including operation and maintenance.

The LCOE approach indicates the overall process costs levelized during the economic lifetime of the technology [21]. The LCOE calculation is expressed by:

$$LCOE = \frac{CAPEX \times f_a + OPEX}{P_e \times Hour_{year}} \quad (5)$$

$f_a$ : The discount factor considers both the risk aversion of the investor and the investment distribution over the plant lifetime.

$P_e$ : The electrical power output of the power plant.

$Hour_{year}$ : The plant availability.

The LCOE allows quantifying different trade-offs like Capex/Opex or production/annual cost trade-offs [21]. Moreover, this procedure allows economic comparison of different technologies [19].

## HEAT EXCHANGER MODEL

The CO<sub>2</sub> thermodynamic properties variation in the vicinity of the critical point is a preponderant aspect of the heat exchangers' design and evaluation of the cycle's operating characteristics.

The  $\epsilon$ -NTU, P-NTU, and MTD methods of exchanger heat transfer analysis, assuming the overall heat transfer coefficient (U) as constant and uniform, do not apply to sCO<sub>2</sub> investigation due to highly variable fluid properties.

- PCHE Tool

For the analysis of the sCO<sub>2</sub> operation, a one-dimensional Matlab tool was developed for the heat exchanger performance evaluation. The tool holds a 1-D discretized method, splitting the heat exchanger into 100 nodes. The local thermodynamic properties are determined for each node. The size of individual segments should be sufficiently small so that all fluid properties and other variables/ parameters can be considered constant within each segment [22]. The assessment analyzes a pair of straight semi-circular channels of the heat exchanger. The channel can represent the behavior of the heat exchanger, assuming a uniform flow.

The heat exchanger analysis considers a pressure drop target as an inlet condition while the tool executes the calculation looping to reach the established performance target. The optimization analysis set a 2% pressure drop for each heat exchanger. The unidimensional model was validated using the CFD solver of ANSYS CFX 21.0, and the one-dimensional model demonstrated satisfactory compatibility.

The number of nodes determined in this analysis aims to adequately represent the local effects of the non-linearity of CO<sub>2</sub> properties, mainly in the recuperator. According to [23], the method's main disadvantage is the longer computational time and the iterative temperature derivative of the properties of interest. Therefore, the authors in [18] consider discretizing each heat exchanger model with 20 nodes. The same methodology is adopted by Held [24] for 25 sub-elements.

According to [20], the calculation of overall thermal conductance (UA) based on the log-mean temperature difference (LMTD) for sCO<sub>2</sub> is a poor assumption in many cases, especially for the recuperator and the cooler. This analysis can cause an error in the (UA) prediction of approximately 10% for HTR and 80% for LTR compared to the discretized heat exchanger model.

## IDEAL RECUPERATOR

The investigation of [15,16,25] adopts an ideal recuperator model to define the theoretical limit of heat exchanger performance. The theoretical limit is an effect of the differences in thermal properties of both CO<sub>2</sub> streams in the recuperator, in particular specific heat.

As the specific heats of these two flows are different, the change in temperature for one flow will be less than that of the other since the amount of heat is the same for both flows.

The aspects of the recuperator irreversibility are known attributes of sCO<sub>2</sub> operation. Therefore, the present study extends the analysis to explore important features and behavior of the transcritical operation. The lower operating temperatures of the tCO<sub>2</sub> cycle represent a challenge to the recuperator operation since the CO<sub>2</sub> property variations in the vicinity of the critical point are very representative.

Finally, this analysis encompasses the aspects of different mass flow rates between streams in the recuperator. The splitting flow architectures are practical alternatives to overcome the irreversibility limitation in the recuperator. However, the operating ranges of the tCO<sub>2</sub> cycles lead to significant changes in the CO<sub>2</sub> properties. These different characteristics result in additional criteria that are significant for the recuperator analysis, especially in thermo-economic considerations.

The present analysis proposes a similar approach considering an ideal heat exchanger with an infinity length. However, for a more meaningful analysis, considers the recuperator terminal temperature difference (LTTD) as 10 K, defined in equation 6.

$$LTTD = T_9 - T_2 \quad (6)$$

Therefore, the terminal temperature difference (UTTD) express the temperature difference between the stream (3) and stream (8). The UTTD minimum defined in the model is 5K.

$$UTTD = T_3 - T_8 \quad (7)$$

The study of [15,16,25] uses the recuperator temperature effectiveness concept to determine how close the cold outlet temperature  $T_3$  is to the hot inlet  $T_8$  in an ideal recuperator. The temperature effectiveness is defined as:

$$TE = \frac{T_3 - T_2}{T_8 - T_2} \quad (8)$$

This concept does not apply to the recuperator calculation model for non-ideal equipment analysis (finite length). The realistic analysis of the heat exchangers follows the effectiveness equation proposed in [22].

The parametric analysis estimates the temperatures  $T_8$  and  $T_2$  for each operating pressure evaluated in the range: of 7.5-9.5 MPa (low pressure) and 20-30 MPa (high pressure), with a 0.1 MPa step.

The turbine inlet temperature will be  $T_1 = 634$  K throughout the analysis. At the same time the compressor inlet temperature is set to  $T_{10} = 308$  K in sCO<sub>2</sub> cycles and  $T_{10} = 293$  K in tCO<sub>2</sub> systems. The efficiencies of the turbine ( $\eta_T = 0.9$ ) and the compressor ( $\eta_C = 0.8$ ) are constant. For instance, the temperature range  $T_2$  is (314 to 323 K) at the tCO<sub>2</sub> and (337 to 419 K) at the sCO<sub>2</sub> cycle.

Figure 3 represents this operating range for the inlet side of the recuperator (lower temperature side). Furthermore, the specific heat capacity shows a significant variation, especially in transcritical cycle design.



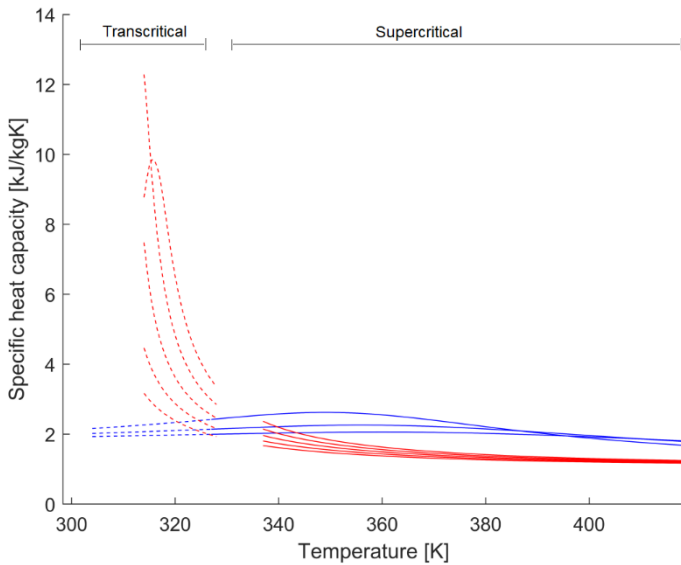


Figure 3: CO<sub>2</sub> specific heat capacity profile at the transcritical and supercritical recuperator range of operation.

## RESULTS

### Parametric Analysis

The parametric analysis of the idealized recuperator aims to investigate various operating conditions of the sCO<sub>2</sub> and tCO<sub>2</sub> cycles. The analysis based on the idealized recuperator model uses the one-dimensional PCHE tool to evaluate the thermodynamic properties of each operating condition. The mass and energy balance defines the temperature distribution along the equipment. The model determines the heat capacity characteristics, and the temperature difference between the recuperator flows over 100 calculation sections representing the equipment. This approach allows for a quick investigation of several operating conditions as critical characteristics of the recuperator's operation. In particular, the analysis aims to investigate the effect of the nonlinear behavior of the CO<sub>2</sub> properties on the characteristics of the recuperator, especially in transcritical operation.

#### - Supercritical cycle

The contour diagram in Figure 4 represents the parametric analysis of the idealized recuperator. The independent variable (temperature effectiveness) levels are presented in a color scale, referring to each pair of the operating pressure (high pressure and low pressure) evaluated.

The results of 4.a referring to the Regenerative architecture ( $\phi=1$ ) at supercritical condition point to the well-known characteristic of sCO<sub>2</sub> cycles: the remarkable irreversibility of the equipment due to the imbalance of heat capacity. For the analysis's boundary conditions, the recuperator's temperature effectiveness was restricted to 0.54-0.64. A widely discussed alternative to overcome this limitation is employing different levels of mass flow between the equipment streams. Thus, Figure 4b presents the analysis of increasing the mass flow

rate of the low-pressure stream ( $\phi=0.7$ ). The results point to a significant increase in temperature effectiveness (0.84-0.98) for the same independent variables evaluated.

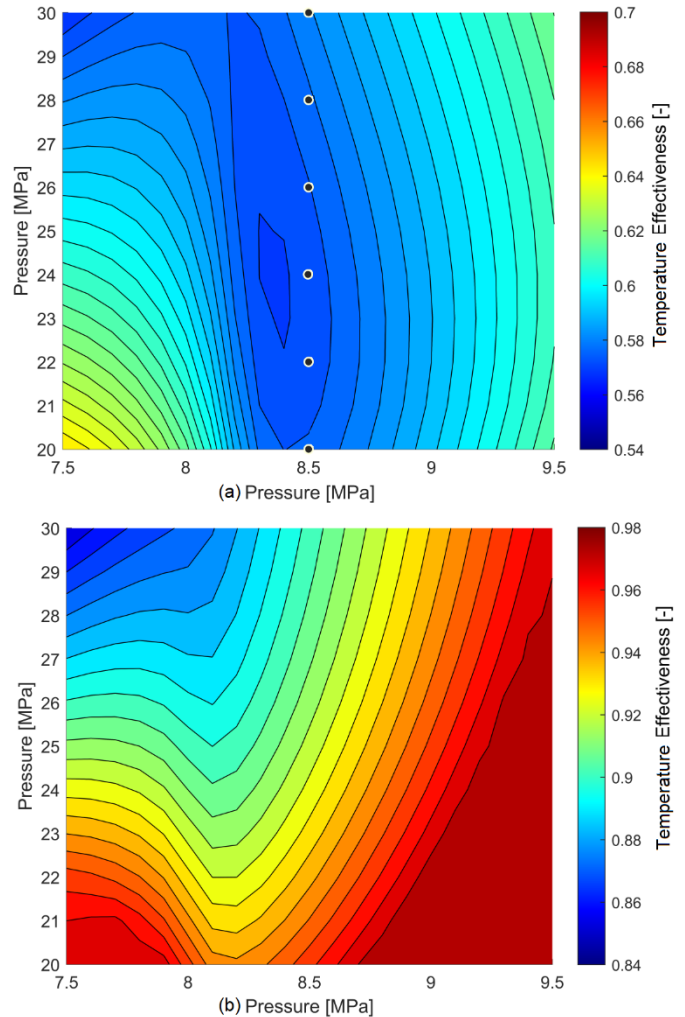


Figure 4: Temperature effectiveness of the sCO<sub>2</sub> idealized recuperator. (a)  $\phi = 1$ . (b)  $\phi = 0.7$ .

Figure A1 (Annex A) points out the characteristics of the operation referring to the sCO<sub>2</sub> cycle and  $\phi=1$ , with low pressure of 85 bar and six high-pressure levels from 200 to 300 bar (points represented in graph 4.1a). Segment 1 refers to the recuperator inlet, low-temperature side. In this configuration, the higher heat capacity value on the heat exchanger's high-pressure side restricts heat transfer, limiting the output temperature of the high-temperature side.

Similarly, the operation with Preheating architecture, Figure A2 (Annex A), allows a better balance of the heat capacity, increasing the equipment's effectiveness and allowing higher temperature at the output. Its indicated by the lower temperature difference. The temperature difference distribution is not linear due to the characteristics of the CO<sub>2</sub> properties combined with the different mass flow rates.

**- Transcritical Cycle:**

The parametric analysis proposed is particularly insightful when evaluating the characteristics of the transcritical operation. Figure 5 presents the distribution of properties across the exchanger for the same pressure conditions as the previous analysis, whereas for the transcritical cycle.

Furthermore, Figure 5a presents the results of the tCO<sub>2</sub> with  $\phi=1$ . Similarly to the sCO<sub>2</sub> cycle, the effects of the higher specific heat capacity in the high-pressure stream lead to the same irreversible characteristics.

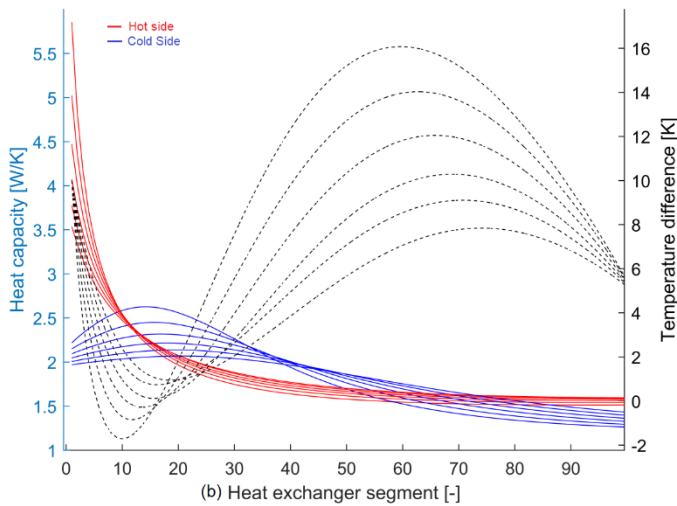
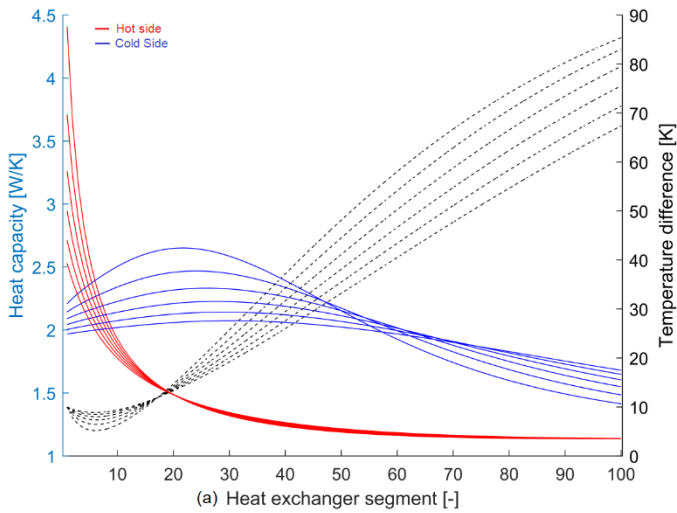


Figure 5: Properties distribution along the tCO<sub>2</sub> idealized recuperator. (a)  $\phi = 1$ . (b)  $\phi = 0.7$ .

Although at the recuperator inlet, there is a remarkable increase in the specific heat capacity on the low-pressure side. This characteristic is associated with the influence of the vicinity of the critical point. As a result, the deviation of the temperature difference curve in the inlet region (segments 1 to 10) of the recuperator is noticeable.

Consequently, a higher mass flow rate of the low-pressure stream, as represented in Figure 5b ( 0.7), accentuates the heat capacity difference in this region. Thus the temperature

difference at the recuperator tends to zero, as indicated by the temperature distribution. This characteristic implies an exponential increase in the heat exchange area. Similarly, as indicated, some operating conditions tend to pinch point violations, which is not thermodynamically possible.

Figure 6 shows the contour diagram for the analysis of the transcritical operation. The gray areas indicate the operating conditions leading to a pinch-point violation, which is, therefore, thermodynamically unacceptable.

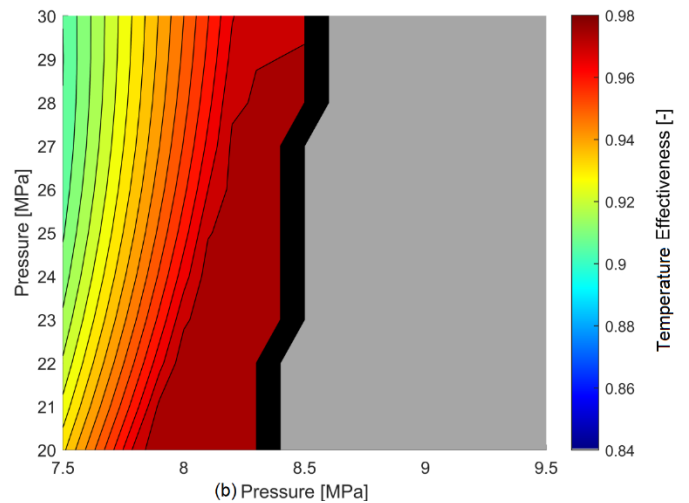
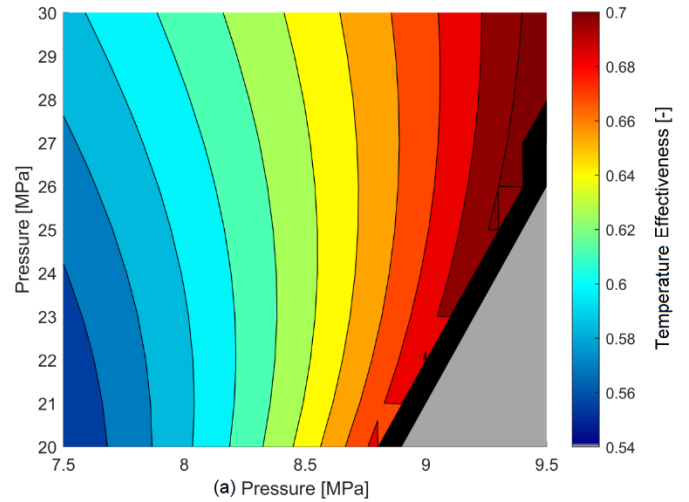


Figure 6: Temperature effectiveness of the tCO<sub>2</sub> idealized recuperator. (a)  $\phi = 1$ . (b)  $\phi = 0.7$ .

It is notorious that the temperature effectiveness is higher under transcritical operating conditions. However, especially in the split-flow architecture (Figure 6b), a significant portion of the operating conditions lead to pinch point violation internally in the exchanger.

The parametric study reveals significant features for the transcritical operation analysis. Foremost, the split flow characteristics allow for less irreversibility in the recuperator. Therefore providing a higher temperature at the recuperator outlet enhances the cycle's performance. However, unlike the

supercritical operation, the characteristics of higher specific heat capacity in the low-pressure stream are exacerbated by the higher mass flow of this stream. Then, it leads to a pinch temperature inside the equipment while restricting the range of possible operating conditions. The temperature pinch refers to a local temperature difference within an exchanger that is lower than either of the two terminal temperature differences and is minimum in the equipment [22].

Figure 7 shows important features in the recuperator analysis for this operating condition. The heat exchanger evaluation considered a dimensionless mass flow during the analysis. Therefore, the overall thermal conductance, heat transferred, and heat transferred area at the recuperator calculated by the PCHE tool are demonstrated in representative terms, products of these parameters by a factor (ft).

Figure 7a presents the minimal temperature differences in the recuperator inlet regions. It can be observed that the pinch temperature decreases with increasing low pressure, until the pinch point violation conditions.

It is noticeable that the temperature pinch inside the equipment is considerably lower than LTTD (10K). Thus, these operating conditions suggest a significantly higher overall conductance.

Therefore, the increase in overall conductance (Figure 7c) is more closely related to the decrease of the temperature difference in the pinch point region than to the total heat absorbed at the equipment (Figure 7b).

The analysis of the area factor according to the one-dimensional analysis of the recuperator shows the same outcome (Figure 7d). Similarly, the significant increase in UA relates to the increase in the heat exchange surface area due to the enlargement of the pinch-point effect, which requires a larger heat transfer area.

An operation at the high-pressure 280 bar leads to UA values 4.4 times higher at low-pressure 85 bar than at 75 bar, even though this indicates better recuperator effectiveness.

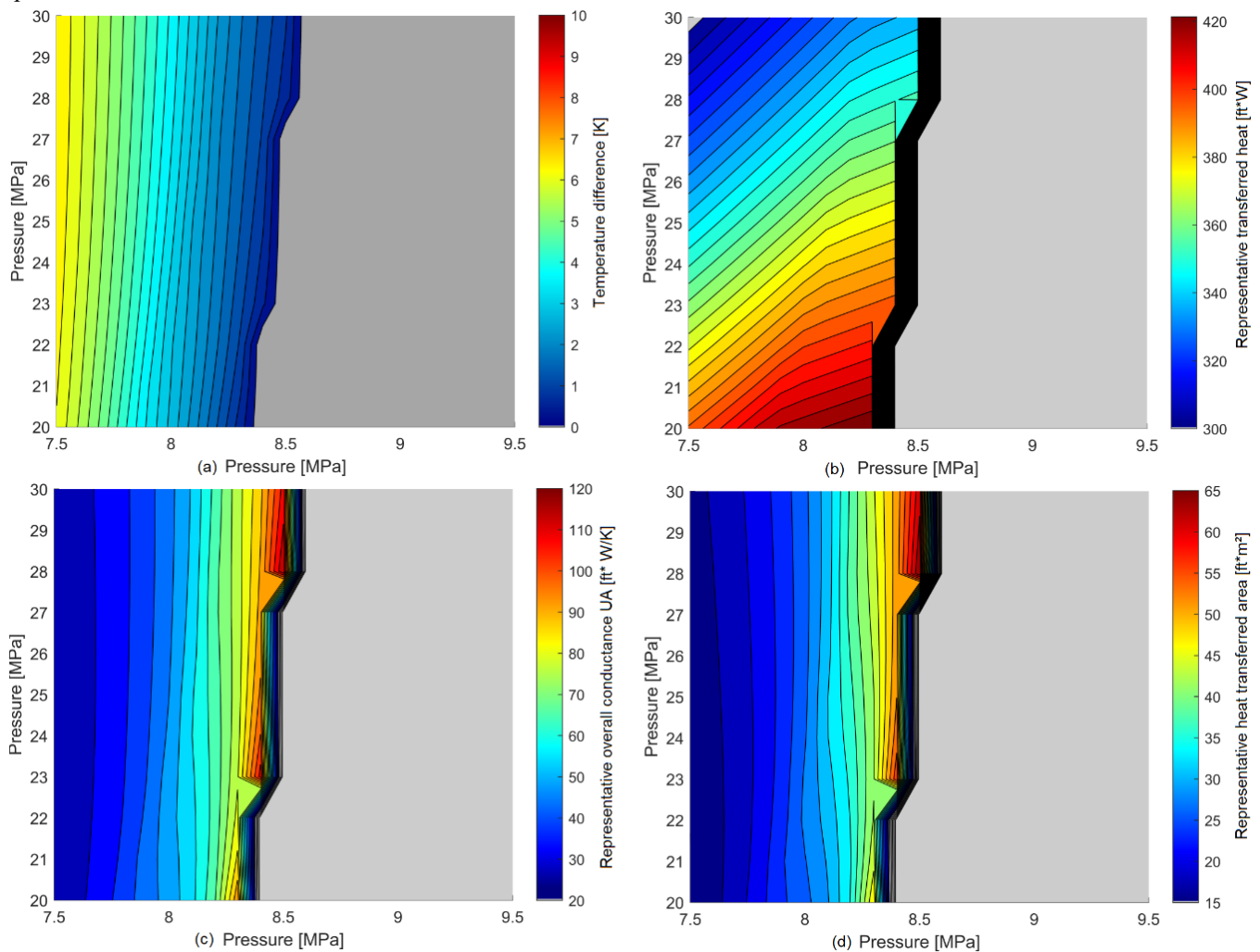


Figure 7: Features of the idealized tCO<sub>2</sub> recuperator indicated in the parametric analysis. (a) Minimal temperature difference. (b) Representation of transferred heat. (c) Representation of overall conductance. (d) Representation of transferred area.

In addition, although this provides 12.3% more heat recovery, this operating condition leads to a pinch point of 0.7 K, in contrast to a pinch point of 6.5 K at 75 bar.

The effects of mass ratio on preheating architecture provide conflicting results for recuperator design. While reducing  $\phi$  allows for a reduction in irreversibility, it can also lead to a pinch-point, a significant increase in the heat exchanger area, and, consequently, an increase in equipment cost.

Furthermore, the performance gains expected by the different mass ratios in the recuperator can drastically restrict the design operating range of the equipment and limit the off-design operations.

Therefore, the effects of the nonlinearity of the CO<sub>2</sub> properties enhanced by the mass ratio by the Preheating transcritical cycle demand a more complex analysis for cycle optimization. These effects have a relevant impact on equipment analyses and system optimization.

### MULTIOBJECTIVE OPTIMIZATION

This study performed a multiobjective optimization analysis of the sCO<sub>2</sub> cycle for waste heat recovery based on different thermo-economic criteria comparing two sets of the objective function:

- 1- Maximization of NPV and minimization of LCOE.
- 2- Maximization of net power and minimization of Fixed Capital Investment (FCI).

The results demonstrate that the economic analysis criteria are crucial for defining the optimal operating conditions. The Pareto's frontier from the optimization adopting the first set of objective functions corresponds to a fraction of the optimal results of the net power analysis (set 2). Therefore, the operating conditions of the first analysis are not associated with the highest power generation of the cycle.

Figure 8 presents the multiobjective optimization results with the Pareto for the sCO<sub>2</sub> and tCO<sub>2</sub> systems. The most prominent frontier, with power generation between 31.9-35.7, corresponds to the tCO<sub>2</sub> cycle designs.

Therefore, the scope of the present analysis encompasses range-I (which allows the best thermo-economic performance of the system) up to the designs with the highest power generation (range-III). Furthermore, the analysis aims to demonstrate which parameters influence the economic depreciation at the higher power generation designs. A parametric evaluation of the results indicates that the operating conditions of the recuperator have a decisive effect on the best thermo-economic performance.

Tables 3 and 4 present the main operating parameters of the transcritical and supercritical cycle designs. A previous study evaluates a wider range of thermo-economic results and concludes that designs with lower power generation than Range-I demonstrate lower thermo-economic performance [26].

The transcritical operation generally provides a higher potential for the investigated operating conditions. The optimum results for the thermo-economic analysis (Range-I) indicate that the transcritical system allows more efficient cycles, with higher net power (up to 20.2%) and three times higher NPV associated

with lower LCOE (10.7% lower) compared to the sCO<sub>2</sub>. Furthermore, the tCO<sub>2</sub> design is generally associated with lower compression work and higher power in the turbine as it operates with lower minimum temperatures.

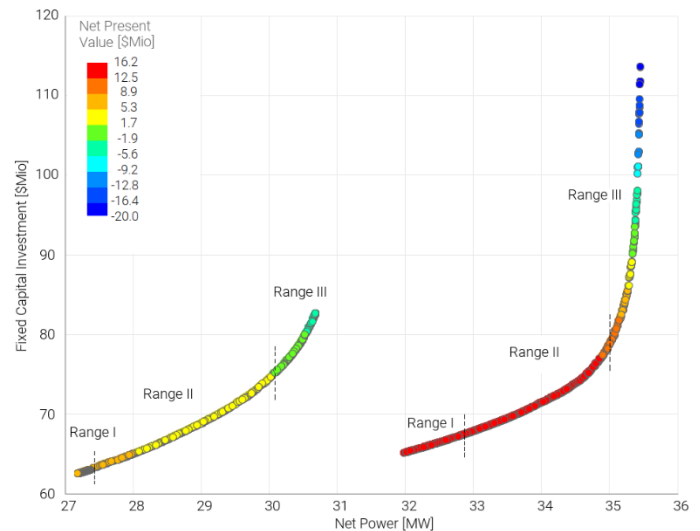


Figure 8 Optimization results of sCO<sub>2</sub> and tCO<sub>2</sub> operation.

The parametric analysis of the results of the transcritical operation, Table 3, indicates that the net power on Range I (31.9 to 32.8 [MW]) is, on average, 10% inferior to the maximum net power of Range III (35 to 35.7 [MW]). However, the gain in net power and thermal efficiency of the cycle is associated with a significant increase in equipment cost, consolidating in the decrease of NPV and increased LCOE.

Table 3 Parameters of tCO<sub>2</sub> optimization results.

	Range-I	Range-II	Range-III
Net Power [MW]	31.9–32.8	32.7 - 35	35 – 35.7
NPV [Mio\$]	16.2	16.1–0.2	10.1–(-20.0)
LCOE [\$ /MWh]	34.1–34.2	34.2–37.0	37.1–48.9
Efficiency [%]	26.2–26.9	26.9–28.7	28.8–29.1
Pressure [Bar]	267–272	258–280	249–258
Temp. T1 [K]	633–634	617–634	609–618
UTTD [K]	14–10	10–5	5
LTTD [K]	25–24	24–10	10 – 8
$\dot{m}_{recupc}$ [kg/s]	249-252	248-316	318-342
$\dot{m}_{preh.}$ [kg/s]	160-165	162–171	159-163
$\phi$ Ratio [-]	60.3-60.9	59.3-66.0	66.2-68.2
$UA_{recup}$ [MW/K]	3.62-4.2	4.2-13.7	14-57.4
$UA_{heater}$ [MW/K]	2.0–2.2	2.1-2.8	2.4-2.5
$UA_{preheater}$ [MW/K]	1.60-1.9	1.8-2.6	2.3-2.4

The increase in the thermodynamic performance of the system (range-I to range-III) is mainly associated with the higher heat recovery in the recuperator. For instance, at the tCO<sub>2</sub> operation, the heater has a 2.1% increase in absorbed heat, while in the recuperator, it represents 35.3%. This higher exploitation also evidences the decrease in the UTDD and LTTD.

Thus, the reduction of LTTD (24°C to 10°C) and UTTD (10°C to 5°C) at range-II results in up to 3.2 times higher  $UA_{recup}$ . While in range-III, reducing LTTD from (10°C to 7°C) results in 13.6 times higher UA. In this last range, the combined increase of UAheater and UAprheater is only 15.6%.

The increase in  $UA_{recup}$  in these ranges is largely responsible for the equipment cost rise. In this way, there is a reduction in NPV in Range-II from 16.1 Mio\$ to -0.2 Mio\$. While in range-III, the exponential increase in recuperator cost would result in NPV of -20Mio\$. Similarly, the LCOE values increase from (34.1-34.2) to (37.1- 48.9).

The exponential increase of  $UA_{recup}$  in the range-III frontier is associated with the pinch point effect in the equipment. This characteristic is mainly responsible for the exponential increase in system and LCOE costs, and the decrease in NPV.

The effect of the internal pinch point in the recuperator becomes evident in the tCO<sub>2</sub> designs at range-III. Although these designs range the LTTD between 7 and 10, the minimum temperature difference occurs inside the equipment, as evidenced by the parametric analysis. Thus, the pinch temperatures in these cases vary between 5 and 0.5. Consequently, once the temperature difference in the equipment tends to zero, the heat exchange surface of the equipment would tend to infinity.

Therefore, this reflects in the characteristic of the exponentially increasing equipment cost. The NPV decreases from 9.9 \$Mio for a net power of 35 MW to -20 \$Mio for a net power of 35.7 MW. Thus these conditions are not technoeconomically realistic.

The sCO<sub>2</sub> cycle optimization results described in Table 4 follow the same characteristics of the previous analysis for the tCO<sub>2</sub> system. The range-I compose the optimal designs in NPV maximization and LCOE minimization.

Table 4 Parameters of sCO<sub>2</sub> optimization results.

		Range-I	Range-II	Range-III
Net Power	[MW]	27.1–27.3	27.4-30.2	30.2 – 30.7
NPV	[Mio\$]	5.42-5.45	5.41-0.54	0.54–(-4.0)
LCOE	[\$/MWh]	38.2-38.3	38.3-40.8	40.7-40.9
Efficiency	[%]	22.3-22.5	22.5-24.9	24.7-25.2
Pressure	[Bar]	275-276	236-280	220-240
Temp. T1	[K]	634-635	604-640	594-605
UTTD	[K]	12–10	10-5	5.0
LTTD	[K]	25–24	25-10	10 – 5.0
$\dot{m}_{recupc}$	[kg/s]	262–263	258-369	369- 424
$\dot{m}_{preh.}$	[kg/s]	155–159	152-192	188 - 196
Ø Ratio	[ - ]	62.1-62.4	60.9-66.0	65.9-68.7
$UA_{recup}$	[MW/K]	3.3 - 3.4	3.3-9.3	9.3-14.5
$UA_{heater}$	[MW/K]	2.0–2.1	2.1–2.6	2.1–2.2
$UA_{preheater}$	[MW/K]	1.3–1.4	1.2-3.6	3.6-4.2

Similarly, the power increase from range-I is accompanied by better thermodynamic performance, although penalizing the techno-economic criteria. The NPV values decrease from (5.42 to 5.45 Mio\$) to (0.54 to -4.0 Mio\$) in range-III. As well as,

LCOE increase from (38.2 to 38.3 \$/MWh) to (40.7 to 40.9 \$/MWh). As in the previous analysis, these characteristics also result from the higher heat recovery at the recuperator.

Thus, as a common characteristic between both cycles, the increase in net power and thermodynamic performance is associated with more intensive use of the recuperator. However, these designs are associated with higher costs and do not configure the optimal results of the thermo-economic analysis.

The higher internal heat recovery of the cycle correlates to systems with higher mass flow rates. In order to accommodate these characteristics, the designs indicate an increase in the recuperator's mass ratio, a decrease in temperature and pressure at the main heater outlet, a decrease in specific work, and modify the cost ratio with other heat exchangers.

These characteristics will be discussed in the following topics.

- Specific net power

Range-I designs converge to operate at higher turbine inlet pressures and temperatures than in the range (II, III) designs. Meanwhile, the operating conditions occur at lower mass flow rates and larger temperature differences in the heat exchangers. These characteristics provide a better thermodynamic and economic performance ratio.

The net power gain in the range (II, III) increasing the flow rate in the recuperator path restricts the heater's and preheater's operating conditions. Thus, high pressure and temperature operation conditions are not achievable.

Therefore, maximizing the recuperator exploitation demands lower pressure and temperature operations at the heater outlet. Thus, although these designs provide higher power generation, they conduct lower specific power.

- Pinch Point Restriction:

The increase of the CO<sub>2</sub>-specific heat capacity in the vicinity of the critical region directly impacts the recuperator operating conditions. This characteristic is especially aggravated in Preheating architecture at transcritical operation. Therefore, the maximization of the recuperator usage tends to the temperature pinch occurrence and pinch-point violations.

Thus, the designs of range-III imply an exponential increase in the UA in the recuperator. The one-dimensional analysis of the recuperator evidence that the temperature difference between the streams in the recuperator tends to zero under these operating conditions.

Although these operating conditions (range-III) are thermodynamically accepted, they would be impractical. However, when the equipment analysis does not correctly consider the properties variation, it may not observe these characteristics, which leads to erroneous decision-making in cycle evaluation

- Matching performance of recuperator and preheater:

The maximal use of the recuperator and the highest exploitation of the heat source characterize the higher net power achieved in range-III. In this way, the residual gases from the gas turbine leave the preheater with the minimum temperature established in the calculation model (348K).



However, the increase of the mass flow of the recuperator path is higher than that of the preheater. For instance, at the tCO<sub>2</sub>, the split flow ratio decreases from 0.65 at range-I to 0.46 at range-III. Similarly, the rate reduces from 0.60 to 0.45 in the sCO<sub>2</sub>.

In this way, it is evident that the operating conditions of the recuperator and the preheater stream are complementary for better cycle performance. However, they compete regarding the use of the thermal source.

The increase in the mass flow of the recuperator path associated with higher power generations implies lower temperatures of the thermal source at the heater's outlet (stream 12), decreasing the availability of energy in the preheater. Thus, due to the lower temperature differences in the preheater, the specific cost of the equipment increases.

The reduction of the CO<sub>2</sub> operating pressure and temperature at the heater outlet mentioned before is related to accommodating the operating conditions of the preheater stream to the increased mass  $\dot{m}_{recupC}$ .

- Mass flow Ratio:

The parametric analysis pointed out how the imbalanced flow levels in the recuperator can compensate for the different CO<sub>2</sub> properties in the recuperator leading to improved performance, but can also aggravate certain characteristics leading to unacceptable operating conditions.

The multiobjective optimization has highlighted in the tCO<sub>2</sub> system that the effects of pinch temperature decrease inside the recuperator are the major responsible for the exponential increase of costs. Thus, it is evident that the mass flow ratio significantly impacts the system design analysis.

Therefore, this analysis evaluates the effects on cycle performance of varying the mass flow ratio in the recuperator for the optimal thermal-economic performance design (DP-Range 1,  $\phi=0.60$ ; Net Power= 32.8 MW; NPV= 16.2 Mio\$) and the highest net power generation design (DP-Range 3,  $\phi=0.68$ ; Net Power= 35.4 MW; NPV= -20.0 Mio\$). The operating pressure and temperature levels at the turbine inlet were maintained for these reference design conditions. Figure 9 presents the results.

In the DP-Range1 design, the increase from  $\phi=0.60$  to  $\phi=1$  negatively impacts net power and economic performance (NPV and LCOE). The net power reduction is associated with the irreversibility increase in the recuperator and less heat recovery in the preheater.

However, for the DP-Range 3 design point, the increase in mass flow ratio ( $\phi$ ) also leads to a net power reduction, although initially, it improves economic performance.

The better match of mass flow ratio modifies the heat capacity ratio at the recuperator's inlet, avoiding the pinch-point effect. Therefore, the novel operation condition would result in a net power of 30.0 MW (as opposed to 35.4 MW) and an NPV value of 8.71 Mio\$.

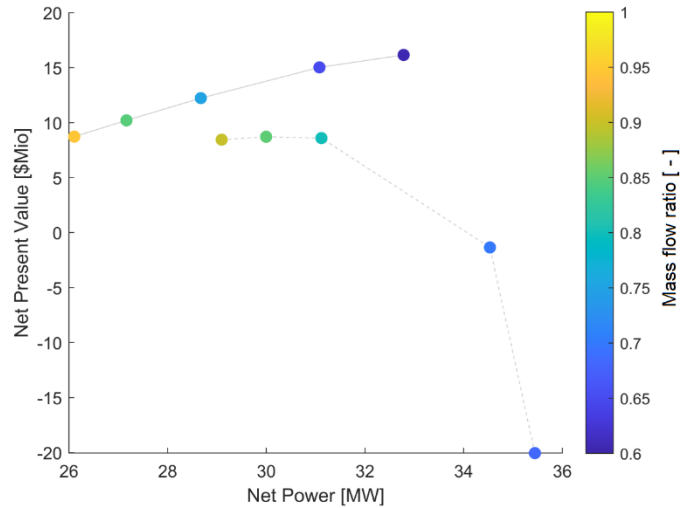


Figure 8 Mass flow ratio impact on cycle performance.

## CONCLUSION

The study presents a parametric analysis to investigate the effect of the non-linear behavior of the CO<sub>2</sub> properties on the recuperator characteristics. The approach analyzes supercritical and transcritical CO<sub>2</sub> cycles in a Preheating architecture.

In general, the operation with different mass flow levels in each stream of the recuperator, compensates the differences in the CO<sub>2</sub> properties between the low and high-pressure flow, reducing irreversibility in the equipment.

Although these characteristics contribute to conflicting effects in transcritical operations. The investigation of the transcritical operation points out that while the split flow reduces irreversibility, it can also conduct a lower temperature pinch inside the equipment, a significant increase in the heat exchanger area and consequently, an increase in equipment cost.

The study describes a thermo-economic optimization of both systems for waste heat recovery from a gas turbine (medium-temperature thermal source). According to the multiobjective optimization, the transcritical operation allows a 20.1% improvement in net power, 10.7% reduction of LCOE and three times higher NPV, compared to the supercritical cycle. Furthermore, the analysis indicates that maximizing the recuperator's heat recovery leads to higher power generation and more efficient cycles. However, the highest net power range designs are associated with lower specific work, higher specific costs, and unfavorable economic performance for both cycles.

In the tCO<sub>2</sub> system, the designs that provide the best thermal-economic performance range between 31.9 and 32.8 MW of net power. An 8.8% increase in net power from this range entails a 69% higher cost. Mostly due to the costs of the recuperator. As a result, NPV values decrease dramatically from the optimal result of 16.2 Mio\$ to negative values.

In addition, to accommodate and allow for more significant recuperator exploitation and consequently increased efficiency, the designs operate with lower pressure and temperature at the turbine inlet, which decreases the net power by 11.1%. In this



range, the characteristics of the recuperator also negatively impact the performance of the preheater.

The parametric analysis followed by multiobjective optimization indicates that the operating characteristics of the recuperator are crucial for optimal system performance. While for the transcritical cycle, the effects of the non-linear CO<sub>2</sub> properties on the recuperator are a challenge to system optimization and off-design operation.

#### ACKNOWLEDGEMENTS

These investigations were conducted as part of the research project CARBOSOLA. The authors would like to thank the German Federal Ministry of Economics and Energy (BMWi) for the financial support as per resolution of the German Bundestag under grant numbers 03EE5001A (Siemens) and 03EE5001B (TU Dresden). The authors alone are responsible for the content of this paper.

#### NOMENCLATURE

<i>C</i>	<i>Component Cost</i>
<i>CAPEX</i>	<i>Capital expenditure of main C</i>
<i>DC</i>	<i>Direct costs</i>
<i>FCI</i>	<i>Fixed Capital Investment</i>
<i>HT</i>	<i>High temperature</i>
<i>HP</i>	<i>High pressure</i>
<i>HTR</i>	<i>High temperature recuperator</i>
<i>Hx</i>	<i>Heater</i>
<i>IC</i>	<i>Indirect cost</i>
<i>LCOE</i>	<i>Levelized Cost of Energy</i>
<i>LMTD</i>	<i>Log Mean Temperature Difference</i>
<i>LTTD</i>	<i>Lower Terminal Temperature Difference</i>
<i>LP</i>	<i>Low pressure</i>
<i>LT</i>	<i>Low temperature</i>
<i>LTR</i>	<i>Low temperature recuperators</i>
<i>m</i>	<i>Mass flow</i>
<i>NPV</i>	<i>Net Present Value</i>
<i>OPEX</i>	<i>Operational expenditure</i>
<i>PEC</i>	<i>Purchased Equipment Cost</i>
<i>Pe</i>	<i>Electrical power output</i>
<i>SR</i>	<i>Split ratio</i>
<i>U</i>	<i>overall heat transfer coefficient</i>
<i>UA</i>	<i>Overall thermal conductance</i>
<i>UTTD</i>	<i>Upper Terminal Temperature Difference</i>
<i>WHR</i>	<i>Waste Heat Recovery</i>

#### REFERENCES

- [1] Huck P, Freund S, Lehar M, Peter M. Performance comparison of supercritical CO<sub>2</sub> versus steam bottoming cycles for gas turbine combined cycle applications. 5th Int Symp - Supercrit CO<sub>2</sub> Power Cycles 2016.
- [2] Kim YM, Sohn JL, Yoon ES. Supercritical CO<sub>2</sub> Rankine cycles for waste heat recovery from gas turbine. *Energy* 2017;118:893–905. <https://doi.org/10.1016/j.energy.2016.10.106>.
- [3] Li B, Wang S, Wang K, Song L. Comparative investigation on the supercritical carbon dioxide power cycle for waste heat recovery of gas turbine. *Energy Convers Manag* 2021;228. <https://doi.org/10.1016/j.enconman.2020.113670>.
- [4] Ancona MA, Bianchi M, Peretto A, Torricelli N, Branchini L, Pascale A De, et al. *Power Plants for Energy Harvesting in Industrial Gas Turbines* 2021.
- [5] Musgrove G, Sullivan S, Shiferaw D, Fourspring P, Chordia L. *8-Heat exchangers*. Elsevier Ltd; 2017. <https://doi.org/10.1016/B978-0-08-100804-1.00008-6>.
- [6] Guo J. Design analysis of supercritical carbon dioxide recuperator. *Appl Energy* 2016;164:21–7. <https://doi.org/10.1016/j.apenergy.2015.11.049>.
- [7] Kwon JS, Bae SJ, Heo JY, Lee JI. Development of accelerated PCHE off-design performance model for optimizing power system operation strategies in S-CO<sub>2</sub> Brayton cycle. *Appl Therm Eng* 2019;159:113845. <https://doi.org/10.1016/j.applthermaleng.2019.113845>.
- [8] Xie J, Liu D, Yan H, Xie G, Boetcher S. A review of heat transfer deterioration of supercritical carbon dioxide flowing in vertical tubes- Heat transfer behaviors, identification methods, critical heat fluxes, and heat transfer correlations.pdf. *Int J Heat Mass Transf* 2019;149.
- [9] Marchionni M, Chai L, Bianchi G, Tassou SA. Numerical modelling and performance maps of a printed circuit heat exchanger for use as recuperator in supercritical CO<sub>2</sub> power cycles. *Energy Procedia* 2019;161:472–9. <https://doi.org/10.1016/j.egypro.2019.02.068>.
- [10] Cabeza L, Gracia A de, Fernández I, Farid M. Supercritical CO<sub>2</sub> as heat transfer fluid: A review. *Appl Therm Eng* 2017;125:799–810.
- [11] Xu XY, Wang QW, Li L, Chen YT, Ma T. Study on thermal resistance distribution and local heat transfer enhancement method for SCO<sub>2</sub>-water heat exchange process near pseudo-critical temperature. *Int J Heat Mass Transf* 2015;82:179–88. <https://doi.org/10.1016/j.ijheatmasstransfer.2014.11.029>.
- [12] Xiao G, Xing K, Zhang J, Yang T, Ni M, Cen K. Heat Transfer Characteristics of Sco<sub>2</sub> and Dynamic Simulation Model of Sco<sub>2</sub> Loop. 3 Rd Eur Supercrit CO<sub>2</sub> Conf 2019:1–11. <https://doi.org/10.17185/dupublico/48881>.
- [13] Feher EG. The Supercritical Thermodynamic Power Cycle. *Energy Convers* 1967;8:85–90.
- [14] Moisseytsev A, Sienicki JJ. Investigation of alternative layouts for the supercritical carbon dioxide Brayton cycle for a sodium-cooled fast reactor. *Nucl Eng Des* 2009;239:1362–71. <https://doi.org/10.1016/j.nucengdes.2009.03.017>.
- [15] Dostal V, Hejzlar P, Driscoll MJ. High-performance supercritical carbon dioxide cycle for next-generation nuclear reactors. *Nucl Technol* 2006;154:265–82. <https://doi.org/10.13182/NT154-265>.

- [16] Moisseytsev A. Passive Load Follow Analysis of the STAR-LM and STAR-H2 Systems. 2003.
- [17] Kim YM, Lee YD, Ahn KY. Parametric study of a supercritical CO<sub>2</sub> power cycle for waste heat recovery with variation in cold temperature and heat source temperature. *Energies* 2021;14. <https://doi.org/10.3390/en14206648>.
- [18] Weiland NT, Lance BW, Pidaparti S. SCO<sub>2</sub> POWER CYCLE COMPONENT COST CORRELATIONS FROM DOE DATA SPANNING MULTIPLE SCALES AND APPLICATIONS. Proc ASME Turbo Expo 2019 Turbomach Tech Conf Expo 2019:1–17.
- [19] Drennen T, Lance B. An integrated techno-economic modeling tool for sCO<sub>2</sub> Brayton cycles. 2019.
- [20] Weiland N, Thimsen D. A Practical Look at Assumptions and Constraints for Steady State Modeling of sCO<sub>2</sub> Brayton Power Cycles. 5th Int Symp - Supercrit CO<sub>2</sub> Power Cycles 2016:1–14.
- [21] Zhao Q. Conception and optimization of supercritical CO<sub>2</sub> Brayton cycles for coal-fired power 2019.
- [22] Shah RK, Sekulic DP. Fundamentals of Heat Exchanger Design. 2003.
- [23] Hoopes K, Sánchez D, Crespi F. A NEW METHOD FOR MODELLING OFF-DESIGN PERFORMANCE OF sCO<sub>2</sub> HEAT EXCHANGERS WITHOUT SPECIFYING DETAILED GEOMETRY. 5thInternational Symp - Supercrit CO<sub>2</sub> Power Cycles 2016:1–14.
- [24] Held TJ. Supercritical CO<sub>2</sub> cycles for gas turbine combined cycle power plants. *Power Gen Int* 2015.
- [25] Mylavarapu SK. Design, Fabrication, Performance Testing, and Modeling of Diffusion Bonded Compact Heat Exchangers in a High-Temperature Helium Test Facility. Ohio State University, 2011.
- [26] Gotelip T, Gampe U, Glos S. Optimization strategies of different SCO<sub>2</sub> architectures for gas turbine bottoming cycle applications. *Energy* 2022;250:123734. <https://doi.org/10.1016/j.energy.2022.123734>.

## ANNEX A

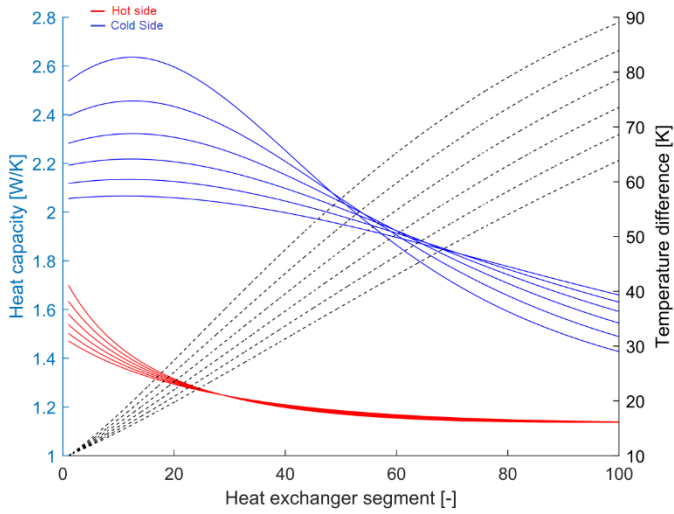


Figure A1: Properties distribution along the sCO<sub>2</sub> idealized recuperator ( $\phi = 1$ ).

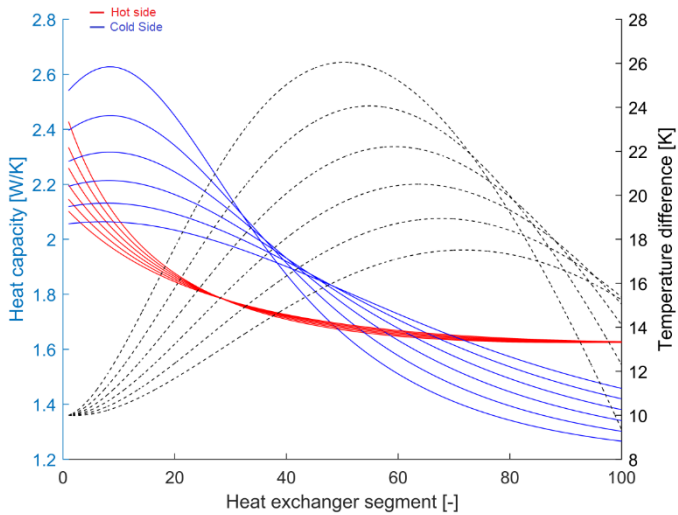


Figure A2: Properties distribution along the sCO<sub>2</sub> idealized recuperator ( $\phi = 0.7$ ).

## PERFORMANCE COMPARISON OF TEMPERATURE SENSORS FOR CLOSED CYCLES OPERATING WITH SUPERCRITICAL CO<sub>2</sub>

**Pierre Belleoud\***

Cranfield University  
Bedfordshire, United-Kingdom  
Email: pierre.belleoud@cranfield.ac.uk

**Eduardo Anselmi Palma**

Cranfield University  
Bedfordshire, United-Kingdom

**Jason Chetwynd-Chatwin**

Rolls Royce plc  
Bristol, United-Kingdom

**Ioannis Roumeliotis**

Cranfield University  
Bedfordshire, United-Kingdom

### ABSTRACT

Near the critical point of carbon dioxide (CO<sub>2</sub>), small changes in temperature or pressure can result in large changes in the calculation of its thermodynamic properties, thus the right choice of instrumentation is of importance. This paper addresses the challenges related to CO<sub>2</sub> temperature measurement in small-diameter pipes and assesses different sensors utilizing Cranfield University's supercritical CO<sub>2</sub> test rig capabilities. In order to compare temperature sensor types for supercritical CO<sub>2</sub>, a test tube has been designed to fit different sizes of temperature probes at the discharge of the transcritical compressors at the sCO<sub>2</sub> test rig. Different diameters of thermocouples (0.75 to 4.5 mm), Resistance Temperature Detectors (RTDs) and surface sensors were tested and compared in terms of amplitude and adaptability to sudden temperature changes. Results for different fluid conditions in the supercritical region of CO<sub>2</sub> were derived. The use of thermowell is discussed as it can offer a suitable compromise between practicality and 'internal' measurements. The results presented in this paper aim to provide a comparison of temperature sensors' performances for different regimes, transient or steady state.

**Keywords:** Instrumentation, Uncertainties, Thermocouples, Supercritical CO<sub>2</sub>, Transient.

### INTRODUCTION

An accurate knowledge of the total temperature variation through turbomachinery is essential in quantifying its performance in understanding its operation and in applying efficient control. By measuring temperatures and pressures at various planes throughout a rotating machine, the performance of compressors and expanders may be calculated. This implies the selection of instruments being mounted on purposely

designed supports and strategic positions. The selection of these instruments shall also address turbomachinery performance scenarios: steady-state or transient. The second scenario, measuring changing temperatures, is bounded by a specific concern: the sensor should ideally change its temperature at the same rate as the stream (or body) being measured. The relevance of this concern increases when considering the potential implications in control strategies for turbomachinery, specifically for closed cycles operating with supercritical CO<sub>2</sub>. In the case of centrifugal compressors operating with this working fluid, on top of the classical challenges of avoiding surge, sits the ambition of keeping the inlet temperature within certain ranges near the critical point (7.4 MPa and 31 °C).

During the initial development of the test rig at Cranfield University in 2015, the available references of operative rigs were predominantly: Sandia National Laboratories [1], Naval Nuclear Integrated System Test [2] and Korea's rigs (by Korean Atomic Energy Research Institute [3], Korea Advanced Institute of Science and Technology and Korean Institute of Energy Research). These references plus paired conversations during the 1st European Seminar on sCO<sub>2</sub> Power Systems in 2016 [4], led to select RTDs Pt100 ( $\pm 0.2$  °C for CO<sub>2</sub> stream) as temperature sensors for Cranfield's rig. However, as the rig commissioning progressed and more rigs started to report their operative results, see Table 1, it became a concern that for testing future turbomachinery, RTDs might not be the obvious selection for dynamic phenomena. On top of that, the location and mechanical features of the probes were also to be considered.

\* corresponding author(s)

**Table 1:** Reported temperature sensors from test rig facilities used as references by Cranfield University

Facility	Temperature Measurement Technology	Device error (°C)	Temperature range investigated
SANDIA SNL [1]	RTD	± 1.1	Ambient to 811 K
KAPL / BAPL IST [5]	Thermocouple Type T (Special Limit of Error)	± 0.4	309 to 554 K
KAIST [3]	RTD	± 0.2	Ambient to 573 K
SCARLETT [6]	Thermocouple Type T RTD	± 0.1 ± 0.3	Ambient to 350 K
sCO <sub>2</sub> -HeRo [7]	Pt100	± 0.15	Up to 823 K
SUSEN [8]	Thermocouple Type K	± 0.5	Up to 823 K
Brunel [18]	RTD Type K	±0.03 to 0.06 ±1.5	223 to 523K 273 to 1273K
TU Wien [19]	RTD class AA RTD class A	0.1+0.0017T 0.15+0.002T	223 to 523K 173 to 723K

For example, Hexemer et al. [2] acknowledged the challenges for matching measurements against the pre-defined by the compressor manufacturer (Barber Nichols Inc) “total” compressor inlet conditions. Two different inlet flow areas (pipe and inlet compressor) needed to be considered when defining or measuring fluid conditions upstream of the compressor. The measured temperature and pressure should be “consistent” with the reference conditions stated in the compressor’s map. Moreover, the preliminary transient results also demonstrated the importance of fast temperature monitoring of cooling water pre-cooler inlet temperature (ramped from 35 to 18 °C in 5 to 60 seconds) to keep compressor CO<sub>2</sub> temperature within ± 1 °F (± 1.8 °C) [2]. Later results provided by Clementoni in 2017 [9], confirmed that their rig sensors (thermocouples type T) were able to register small fluctuations of the compressor inlet temperature in the operations of up and down-power transient; specifically, 96 ± 1 °F (35.5 ± 1 °C) in windows of 50 seconds.

Similarly, on the topic of mechanical installation, Southwest Research Institute [10] previously pointed out the challenges of dynamic excitation of inserted thermocouples due to periodic vortex shedding. Suggesting performing FEA in thermowell design “to ensure sufficient separation between vortex shedding and mechanical natural frequencies and also that non-resonant probe stresses are well below the material’s endurance limit operating temperatures” on p251 of [10]. Stuttgart [6] also disclosed their mechanical settings for estimating heat transfer and pressure drop near the critical point in a Ø 2 mm (inner diameter) copper tube. Including a discussion about the error

impact of soldering their T-type thermocouples into milled channels on the surface of the test tube. More recently, SANDIA [11] exemplified the impact on transient measurement in the discharge of their Peregrine’s turbine, due to improper insertion depth of their RTDs. Interestingly, the mechanical arrangement shown seemed simple but effective. Not much information has been found about the installation of Kiel-type probes, the use of exposed junction thermocouples or recommended types of shields for total temperature measurements in CO<sub>2</sub> streams. Even, in 2021, the uncertainty assessment about instrumentation and measuring techniques for sCO<sub>2</sub> compressors using ASME PTC-10 by Mortzheim [17]; indicated the use of T-type thermocouples inside custom-made thermowell configurations, which caused obstruction bigger than 30 % in the pipelines. A few more references, [18] and [19] can be found in Table 1 that complete this non-exhaustive list of sCO<sub>2</sub> test facilities.

The right selection (and mechanical design) of temperature measurement for transient operation implies an iterative process of trial and error. At Cranfield University, it has been decided to inform the selection process for future turbomachinery with a series of experiences using the available test rig. A test tube and two measurement stations on the gas side of the rig have been monitored with different sensors to register and identify their time responses. This is relevant, as it seems that the selection of temperature sensors for monitoring closed cycles operating with supercritical CO<sub>2</sub>, will imply selecting two or three types of sensors, addressing primarily two challenges: accuracy and response time.

This paper will focus on relatively easy installations: surface, in-line tip insulated and thermowell; to create a measuring experience before attempting other approaches such as: bare exposed junction, grounded junction, radiation shield, or Kiel-type installation. After presenting the experimental setup and the condition of how the measurements were performed, this paper will discuss the different responses of the temperature sensors in terms of time response and in terms of value. A discussion on the impact of the sensor accuracy on the calculation of thermodynamic properties such as the density and the specific enthalpy will then be provided.

## EXPERIMENTAL SETUP

The analysis conducted herein utilizes the Cranfield university sCO<sub>2</sub> test rig capabilities. This rig, shown in Figure 1, is composed of two 45 kW semi-hermetic compressors (1), one of which is regulated in frequency via an inverter, electronic expansion valves for high pressure (2a), liquid expansion (2c), flash gas (not shown), an industrial controller which regulates operating modes of compressors and fans (on/off, speed) and valve positioning (3), a liquid receiver of 60 L (4), a gas cooler of 200 kW (5) and a brazed plate heat exchanger of 95 kW (6). More details can be found in [12].

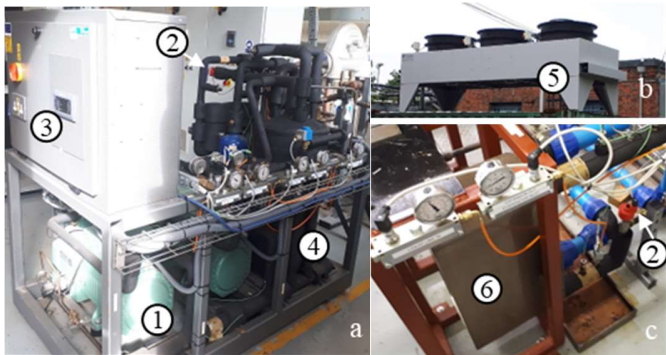


**Figure 1:** Cranfield supercritical CO<sub>2</sub> rig main components: compressors, liquid receiver and controller (a), gas cooler (b) and evaporator (c).

To compare the performance of different types of temperature sensors, a specifically designed test tube has been placed in parallel to the discharge of the compressor. This test tube includes a system of valves allowing isolation and depressurisation, which facilitates the replacement and inspection of the sensors. The testing section has been set in a straight run of the main discharge tube, away from 20 internal diameters of any elbows or t-pees, up and downstream, to avoid severe changes in flow direction that could modify the flow locally. The tube is equipped with two connections of 1/4" BSPP and one of 1/2" BSPP to be able to vary sensor sizes as shown in Figure 2. The test tube is made of a high-copper alloy that is 28.57 mm in outside diameter with a wall thickness of 1.78 mm (thermal conductivity of 260 W.m<sup>-1</sup>.K<sup>-1</sup>). A thermowell has been mounted on connection 1 and compression fittings have been placed on connections 2 and 3 to place the sensor element directly in the flow. Two sensors were placed at the surface of the tube. One of them is a K-type thermocouple of 0.75 mm placed on the surface of the tube with thermal paste and aluminium tape, see Figure 3, then covered with an additional layer of insulation foam of 13 mm of thickness and thermal conductivity of 0.033 W.m<sup>-1</sup>.K<sup>-1</sup> at 0 °C. The second one is another K-type thermocouple designed to be installed on pipes. Due to its orientation and size, it was not insulated which will underline the effect of the natural convection within the laboratory room.

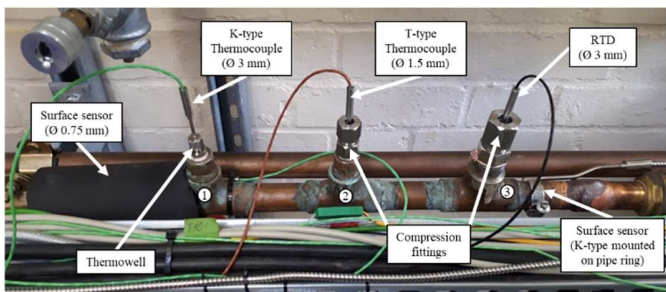


**Figure 2:** Test tube equipped with compression fittings, thermowell and temperature probes.



**Figure 3:** Installation of Ø 0.75 mm thermocouple at the surface of the pipe with a layer of thermal paste (right) and covered with aluminium tape (left).

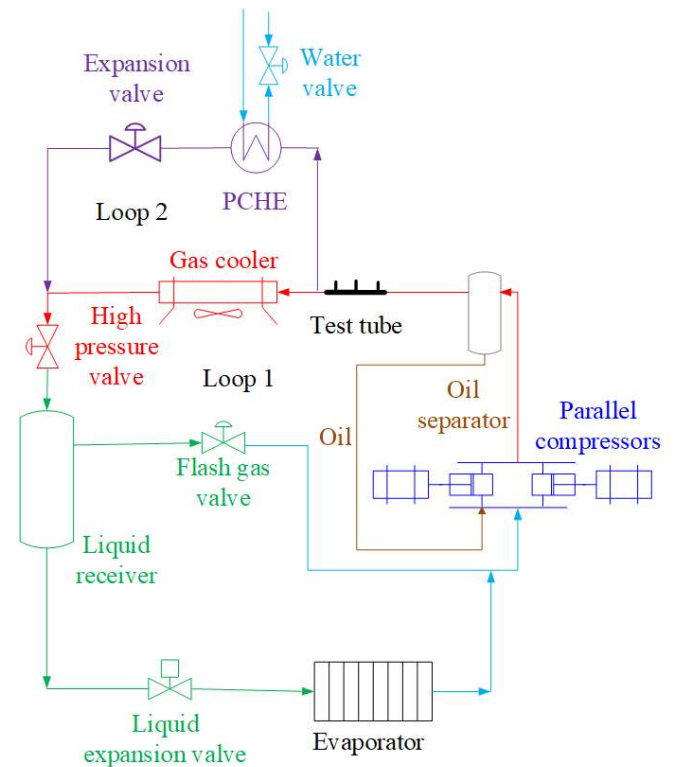


**Figure 4:** Diagram of the main experimental set-up and additional measurements.

### TEMPERATURE PROBES

Different probes have been selected to be compared in this paper: RTD, K-type thermocouple and T-type thermocouple as a non-exhaustive list of common temperature probes in use. A summary of their characteristics is given in Table 2. When available, the manufacturer's typical time response is provided and compared against in-house tests in the same conditions. The



sensors were submitted to a step temperature change from the ambient (around 20 °C) to a boiling water bath at 100 °C. The time response given is the time to reach 63 % of the final temperature. The resulting dimensionless temperature for the five sensors,  $\theta$  calculated via (1), has been plotted in Figure 5.

$$\theta = \left( \frac{T - T_{amb}}{T_{100^\circ C} - T_{amb}} \right) \quad (1)$$

The response times thus measured have been added to Table 2. At first sight, measured values differ to some extent from the manufacturer's values which could be due to differences in the calibration protocol. However, the relative 'order' in the sensors is consistent, the RTD has the longest time response of 2.1 s and the thermocouples' time response is following the size of the sensor, the 0.75 mm in diameter has the fastest response and the 4.5 mm, the longest. These considerations can be useful when selecting the sensor as thin thermocouples may not support flow conditions (severe changes of flow momentum for instance) but if placed at the surface of the pipe, the lower the time response is, the better it is to compensate for the conduction through the pipes' wall.

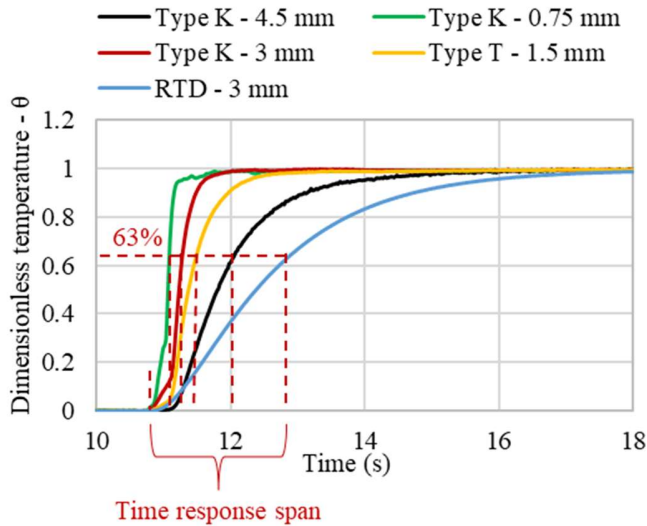


Figure 5: Step of temperature from ambient to 100°C.

To provide a theoretical value of the sensor time response within the test tube we can as well express the ratio (2), considering that the Biot Number,  $B_i$ , (3) is below one according to [19].

$$\frac{T - T_\infty}{T_i - T_\infty} = e^{-\frac{t}{\tau}} \quad (2)$$

$$B_i = \frac{h_{CO_2} L_{c_{sensor}}}{k_{sensor}} \quad (3)$$

The sensor used here has an insulated junction protected with a grade 316L stainless steel (SS) sheath filled with

Magnesium Oxide (MgO). It is then possible to estimate the overall thermal conductivity (4),  $k_{sensor} = 11 \text{ W.m}^{-1}\text{.K}^{-1}$ , density (6),  $\rho_{sensor} = 5785 \text{ kg/m}^3$ , and heat capacity (5),  $c_{p_{sensor}} = 688.5 \text{ J.kg}^{-1}\text{.K}^{-1}$ , of the sheath, assuming that the two materials are equally represented, as a first approximation:

$$k_{sensor} = \frac{1}{\frac{1}{k_{SS}} + \frac{1}{k_{MgO}}} \quad (4)$$

$$\rho_{sensor} = \frac{1}{2}(\rho_{SS} + \rho_{MgO}) \quad (5)$$

$$c_{p_{sensor}} = \frac{1}{2}(c_{p_{SS}} + c_{p_{MgO}}) \quad (6)$$

The Biot number in the worst-case scenario ( $\varnothing 4.5 \text{ mm}$ ) in the flow condition of the reference case described next section is then  $0.16 < 1$ .

The time constant,  $\tau$ , is then expressed as per (7):

$$\tau = \frac{\rho_{sensor} V_{sensor} c_{p_{sensor}}}{h_{CO_2} A_{sensor}} \quad (7)$$

Taking 3 times the value of  $\tau$  gives us an approximation of the theoretical time response at 63 % within the test tube in the reference conditions for each sensor and be compared with the manufacturer and measured ones in water in Table 2.

In addition, all sensors received a 3-points calibration (0 °C, ambient and 100 °C) against the platinum RTD before being installed on the test tube.

Table 2: Selected probes' specifications

Sensor type	$\varnothing$ (mm)	Manufacturer time response (s)	Manufact. uncertainty (°C)	Meas. time resp. (s)	Theoretical time resp. (s)
Pt100	3	Not given	Not given	2.1	
K	0.75	0.09	1.5	0.3	0.59
	1.5	0.3		0.5	1.18
	3	0.9		0.8	2.36
	4.5	1.4		1.0	3.54
T	1.5	0.3		0.6	1.18

It is to be noted that the data acquisition system – a mix analogue, digital and sensor measurements device equipped with a high-density thermocouple module – used has an accuracy of 50 ppm per sample rate and between  $\pm 0.02 \text{ }^\circ\text{C}$   $\pm 0.25 \text{ }^\circ\text{C}$  on the

temperature measurement depending on the acquisition mode. Measurements have been done with an acquisition frequency of 40 Hz.

### MEASUREMENT TEST CONDITIONS

The measurements provided in this paper, for the test tube, have been taken during the start-up of the rig going from no CO<sub>2</sub> circulation to established regimes. From a set of five tests, a reference case scenario is detailed below to describe the flow of CO<sub>2</sub> within the tube when the steady regime is achieved. In this reference case, CO<sub>2</sub> state variables are: T = 77.9 °C and P = 6.4 MPa and thermodynamic properties, calculated from the National Institute of Standards and Technology database [20], are gathered in Table 3 along with the reference mass flow of CO<sub>2</sub> and tube dimensions.

**Table 3:** CO<sub>2</sub> and tube properties

Density	$\rho_{CO_2} = 120.97 \text{ kg/m}^3$
Kinematic viscosity	$\nu = 1.58 \times 10^{-7} \text{ m}^2/\text{s}$
Thermal conductivity	$k = 26.12 \times 10^{-3} \text{ W/m.K}$
Prandtl number	$Pr = 0.97$
CO <sub>2</sub> mass flow	$\dot{m}_{CO_2} = 0.34 \text{ kg/s}$
Tube internal diameter	$D = 26.18 \times 10^{-3} \text{ m}$
Tube thickness	$e = 1.2 \times 10^{-3} \text{ m}$
Test section length	$L = 5 \times 10^{-1} \text{ m}$

From these data, it is then possible to calculate the Reynolds number of the flow going through the tube using the inner diameter with (8)

$$Re_D = \frac{uD}{\nu} \quad (8)$$

With a CO<sub>2</sub> velocity of 5.20 m/s within the section of the tube, a Reynolds number of  $8.6 \times 10^5$  is reached for our reference case confirming that the flow is fully turbulent in the test section.

To evaluate the heat transfer within the tube we are using the Dittus-Boelter correlation (9) as the Reynolds Number is above  $10^4$ , the Prandtl number is between 0.7 and 160 and the test section aspect ratio (L/D) is superior to 10 [13].

$$Nu_D = 0.023 Re_D^{4/5} Pr^n \quad (9)$$

With n = 0.4 as the fluid is mainly heated during the experiments, we obtain a Nusselt number of 1269.6 which allows us to evaluate the heat transfer coefficient within the tube (10),  $h_{CO_2}$ :

$$h_{CO_2} = \frac{Nu_D k}{D} \quad (10)$$

The heat transfer coefficient in the test section is close to  $1.27 \times 10^3 \text{ W/m}^2\text{K}$  which is around 2 orders of magnitude above the typical heat transfer coefficient in our standard laboratory room with free air flow (typically 2.5 to 25 [14]).

To generate a less severe change of temperature in the test tube, an additional scenario was generated. The stream properties in the test tube varied between conditions named state 1 and state 2 (presented in Table 4). This was achieved by bypassing the rig's gas cooler and using a Printed Circuit Heat Exchanger (PCHE) connected to a water-cooling circulation (see 'Loop 2' in Figure 4). This sudden change of boundary conditions at the sink level was enough to cause a variation of 9 kW of heat rejection, allowing to evaluate temperature variations in the test tube.

**Table 4:** State 1 and 2 flow conditions.

	State 1	State 2
Temperature (°C)	110	113
Pressure (MPa)	7.10	7.45
Density, $\rho_{CO_2}$ , (kg/m <sup>3</sup> )	116.13	123.21
Kinematic viscosity, $\nu$ , (m <sup>2</sup> /s)	$1.77 \times 10^{-7}$	$1.70 \times 10^{-7}$
Thermal conductivity, $k$ , W/m.K	$28.17 \times 10^{-3}$	$28.76 \times 10^{-3}$
Prandtl number, $Pr$	0.90	0.91
CO <sub>2</sub> mass flow, $\dot{m}_{CO_2}$ , kg/s	0.19	0.19
Reynolds number, $Re_D$	$4.5 \times 10^5$	$4.4 \times 10^5$
Nusselt number, $Nu$	732.1	726.0
Heat transfer coefficient, $h_{CO_2}$ , (W/m <sup>2</sup> K)	$7.88 \times 10^2$	$7.98 \times 10^2$

### RESULTS

The first test to be conducted was to follow the temperature transition of the different sensors from an inactive state to the reference case described above at the compressor discharge, see Figure 6. These signals give us a reference for the temperature time evolution of typical uses of the rig detailed in this paper. This elevation of temperature corresponds to the pressure build-up first with one compressor between 70 s and 160 s where the second compressor enters into action, which causes the drop in temperature around 160 s. Despite the delay observed, all the sensors follow the same trend with a certain delay depending on the sensor itself and its location.

A first observation to be drawn is that despite the different time responses, the configuration of the installation of the probe appears to have a major impact. As could be expected, the fastest probes to react are the two directly inserted into the tube type T "in line" in Figure 6. followed by the RTD 1.6 s later. Then with a delay of 2.8 s the 3 mm K-type thermocouple in the thermowell

and the 0.75 mm at the surface of the tube start to measure a temperature rise. A delay that can be explained by the additional inertia induced by the wall of the thermowell and the pipe. The temperature rise is detected by the ring thermocouple 7.1 s after the first one (T-type thermocouple) due, in addition to the pipe wall's thermal inertia, to the convective heat exchanges within the room, highlights the expected necessity of thermal lagging on pipes around surface sensors.

This reference experiment gives us a first hint concerning the typical time evolution of the temperature within the tube. As a matter of fact, among the two probes to react first are the two directly in contact with the flow, as stated above, there is the RTD with the highest measured time response. Based on this observation we can estimate that this time evolution is above the 2.1 s time response of the RTD.

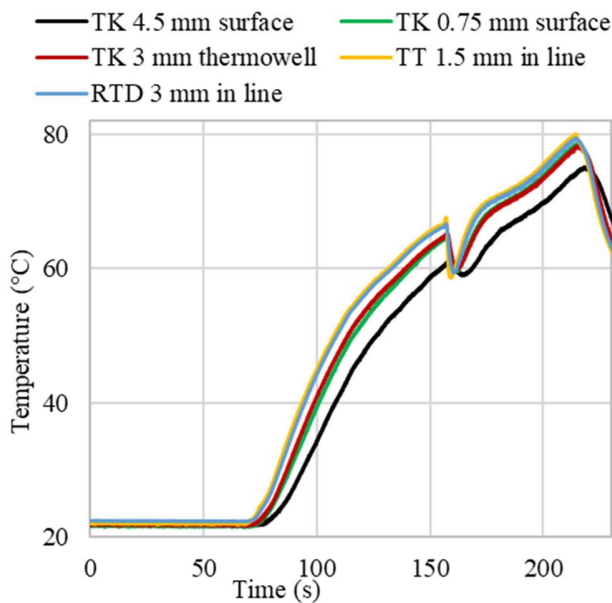


**Figure 6:** Typical temperature rise within the test tube from rest to the reference case of the cycle.

The results plotted in Figure 7 represent the temperature evolution of CO<sub>2</sub> when the system is stabilised around the condition of the reference case scenario described above. This illustrates how uneasy it is to get a fully steady state (at least in temperature) depending on the system, as the capacity of the different equipment, like the compressor, keeps adjusting to maintain the different setpoints. With these results, we notice that the three 'levels' of temperature highlighted in Figure 6 are maintained: the two sensors directly in line, TT 1.5 mm and RTD 3 mm, which keep running ahead of TK 0.75 mm at the surface and TK 3 mm in the thermowell with a temperature difference from 2 to 5 °C, and a difference between 6 and 12 °C with the TK 4.5 mm mounted on the adjustable ring.

This shows how different time responses can affect transient regimes as well as steady states. Indeed, as the different components of the rig are equipped with modulating devices and

regulated via PI and PID, it is most likely that the levels of temperature and pressure never reach a smooth line but keep adjusting. Slow time responses could then introduce delays which will alter the accuracy of the temperature measurement reaching a couple of degrees. The difference with TK 4.5 mm is also most likely due to the effect of the natural convection within the test room. This could explain why the temperature never reaches the same level as the other 4.

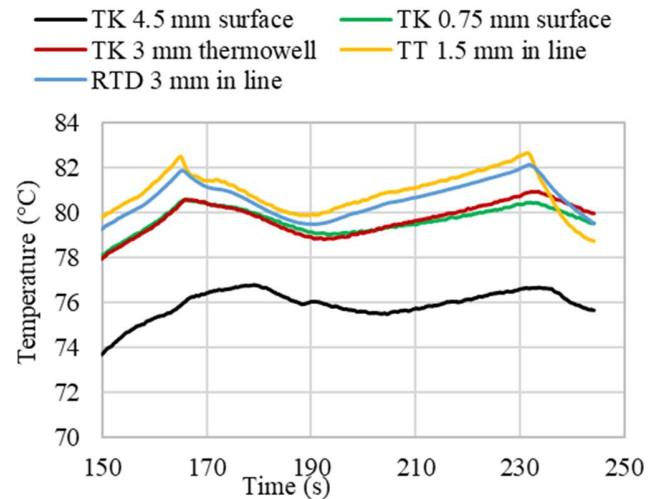


**Figure 7:** Temperature of CO<sub>2</sub> when a quasi-steady state is achieved

The second test concerns a sudden change of heat load at the sink level of the cycle from state 1 conditions to state 2 conditions (Table 4) from 25 s to around 127 s and back to state 1 from this time. This leads to a variation in the CO<sub>2</sub> high-pressure which comes along with an elevation or a reduction of the temperature within the test tube, see Figure 8.

A first qualitative remark is that during the rise in temperature, as no steady regime is reached, TK 0.75 mm at the surface (in green) and TK 3 mm in the thermowell (in red) never achieve the temperature of the inline RTD 3 mm (in blue) and TT 1.5 mm (in yellow) with a consistent temperature difference of 0.4 °C. However, during the step down to the lower pressure and lower temperature conditions of stage 1, the temperature, measured by the two sensors in line, drops quicker than the other two reducing the relative error between these four sensors to 0.05 °C. This means that, depending on the transition direction, if the temperature is increasing or decreasing the bias in the measurement will be higher or lower and it will not be straightforward to correct the temperature during the different transient scenarios.

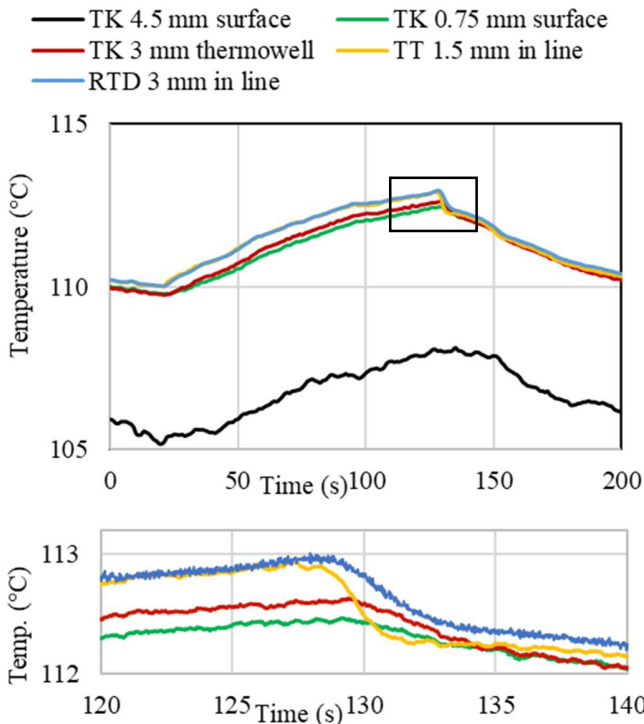


**Figure 8:** Temperature of CO<sub>2</sub> from test tube sensors during sudden flow changes between state 1 and state 2 (top) and closeup between 120 and 140 s (bottom).

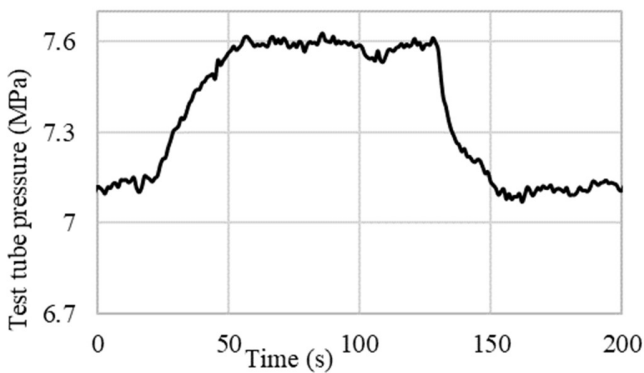


**Figure 9:** Measured pressure within the test tube.

The next question that can be asked is to what extent these temperature differences have an impact on calculated properties like the density or the specific enthalpy. To obtain these quantities we used the NIST database [20] considering the temperature acquired by 5 sensors of the test tube and the pressure measured during the test given in Figure 9. Calculated density and specific enthalpy are then plotted in Figure 10 and Figure 11.

To be compared, the reference properties are calculated using the temperature measured via the RTD which is supposed to have the best accuracy. Due to its interaction with the ambient air, TK 4.5 mm leads to property calculation with the highest

relative error (1 % for the enthalpy and 2.2 % for the density). For the 4 other sensors, the relative error stays below 0.2 % for the calculation of the specific enthalpy and below 0.4 % for the calculation of the density.

However, the accuracy level of the sensors should be approached with more care when investigating critical conditions as CO<sub>2</sub> properties can rapidly change around the critical point [15] and [16].

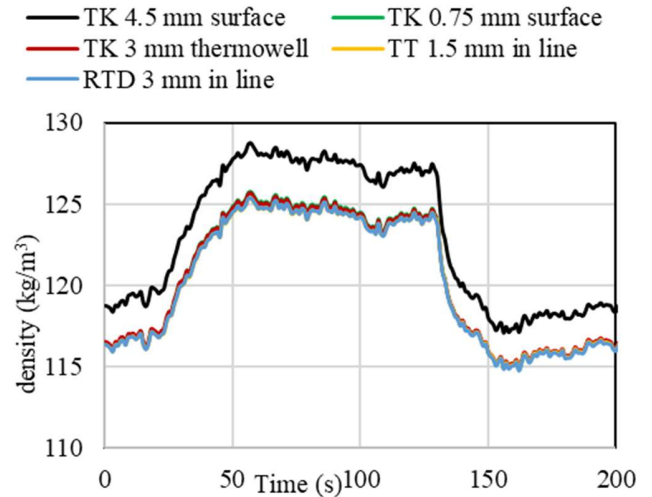


**Figure 10:** Calculated density of CO<sub>2</sub> from measurements of pressure and temperatures using the NIST database [20].

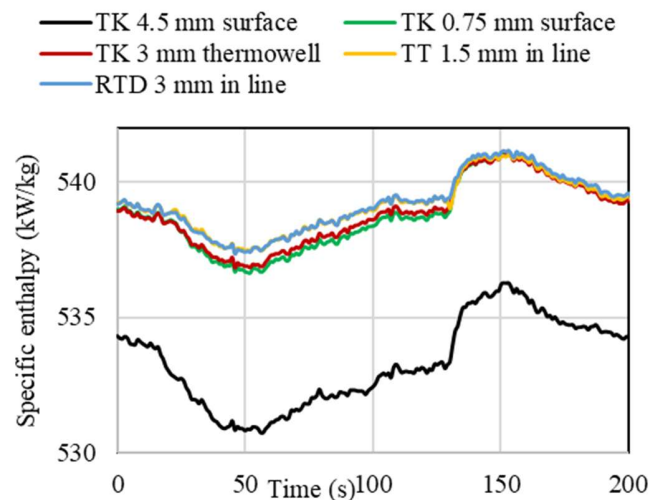


**Figure 11:** Calculated specific enthalpy of CO<sub>2</sub> from measurements of pressure and temperatures using the NIST database [20].

## CONCLUSION

Although finding the best compromise between accuracy for performance analysis, or fast response when transient operations need to be monitored in real-time is not an easy task, the results gathered in Table 5 have the purpose to give an informed review of commonly used sensors to acquire temperature on our rig using CO<sub>2</sub> in a transcritical state as a working fluid.

It has been shown that, at least away from the critical point, the accuracy of the measurement implies an error on the calculation of thermodynamic properties between 0.4 and 2.2 % error for the density and 0.2 and 1 % for the enthalpy. In addition, it has been demonstrated that in the case of interaction between different regulations causing low-frequency oscillations of the steady state, slow time response sensors may introduce additional inaccuracy due to their delay to react. This makes it then trickier to provide a compensation factor to correct the measurement. To return to the introduction example, the question of keeping the compressor inlet within  $\pm 1$  °F ( $\pm 1.8$  °C) becomes then very real and this additional inaccuracy turns out to be an issue to consider with care. It, thus, requires complementary measurements varying the levels of pressure and temperature to provide a complete study of the functioning conditions of the compressor.

**Table 5:** Summary of temperature sensors comparison results.

Sensor	Location	$\Delta t$ from ref (s)	$\Delta T$ from ref (°C)
Pt 100 3 mm	In-line	1.6	Ref
TT 1.5 mm	In-line	Ref	0.5
TK 3 mm	Thermowell	2.8	2 to 5
TK 0.75 mm	Surface	2.8	2 to 5
TK 4.5 mm	Surface	7.1	6 to 12

Finally, the question of the maintenance of the sensor can be a critical parameter while selecting the right balance between a fast response or accuracy and a fast response sensor at a surface of a pipe may be advantageous compared to slow response sensor in-line as the replacement of the probe may require stopping the rig for depressurization, sensor replacement, vacuum and CO<sub>2</sub> refill of the pipe section.

## NOMENCLATURE

$A_{\text{sensor}}$	Sensor surface (m <sup>2</sup> )
D	Test tube diameter (m)
e	Test tube wall thickness (m)
h	Heat transfer coefficient (W.K <sup>-1</sup> .m <sup>-2</sup> )
k	Thermal conductivity (W.K <sup>-1</sup> .m <sup>-1</sup> )
L	Test tube length (m)
$L_c$	Characteristic length, $L_c = \frac{V_{\text{sensor}}}{A_{\text{sensor}}}$ (m)
$\dot{m}$	Mass flow (kg/s)
Nu	Nusselt number (-)
NIST	National Institute of Standards and Technology

P	Relative pressure (MPa)
ppm	Part per million
Pr	Prandtl number (-)
PCHE	Printed Circuit Heat Exchanger
RTD	Resistance Temperature Detector
T	Temperature (°C)
T <sub>i</sub>	Initial temperature (°C)
TK	Thermocouple type K
TT	Thermocouple type T
T <sub>∞</sub>	Final temperature (°C)
u	Velocity (m/s)
$V_{\text{sensor}}$	Sensor volume (m <sup>3</sup> )
$\Delta t$	Time difference (s)
$\Delta T$	Temperature difference (°C)
$\nu$	Kinematic viscosity (m <sup>2</sup> /s)
$\rho$	Density (kg/m <sup>3</sup> )
$\theta$	Dimensionless temperature (-)

## ACKNOWLEDGEMENTS

This research has received funding from Innovate UK under project reference 113263. The authors are grateful to Rolls-Royce plc for its support during the project.

## REFERENCES

- [1] Pasch, J., Conboy, T., Fleming, D., Rochau, G. (2012). Supercritical CO<sub>2</sub> Recompression Brayton Cycle: Completed Assembly Description. SANDIA Report SAND2012-9546. October 2012, Albuquerque, New Mexico and Livermore, California, USA.
- [2] Hexemer, M. J. Hoang, H. Y., Rahner, K. D., Siebert, B. W., Wahl, G. D. (2009). Integrated Systems Test (IST) S-CO<sub>2</sub> Brayton Loop Transient Model Description and Initial Results Proceedings of S-CO<sub>2</sub> Power Cycle Symposium 2009, RPI, Troy, NY, USA, April 29-30, 2009.
- [3] Baik, S., Gu Kim, S., Jun Bae, S., Ahn, Y., Lee, J., Lee, J. I. (2015). Preliminary experimental study of precooler in supercritical CO<sub>2</sub> Brayton Cycle. Proceedings of ASME Turbo Expo 2014: Turbomachinery Technical Conference and Exposition, Montreal, Canada, June 15-19, 2015. Paper GT2015-42915.
- [4] Anselmi, E., Zachos, P., Collins, R., Hassan, M. (2016). Development of an experimental S-CO<sub>2</sub> loop for bottoming cycle applications. 1st European Seminar on SCO<sub>2</sub> Power Systems, Vienna, Austria, 29-30 September 2016.
- [5] Clementoni, E. M., Cox, T. R. L. (2014). Comparison of Carbon Dioxide property measurements for an operating supercritical Brayton Cycle to the REFPROP physical properties database. Proceedings of ASME Turbo Expo 2014: Turbomachinery Technical Conference and Exposition, Dusseldorf, Germany, June 16-20, 2014. Paper GT2014-25338.
- [6] Wahl, A., Mertz, R., Laurien, E., Straflinger, J. (2019). Experimental investigation of heat transfer and pressure drop in tubes to cool CO<sub>2</sub> near the critical point. 3rd European supercritical CO<sub>2</sub> Conference, Paris, France, September 29-10, 2019. Paper 2019-sCO<sub>2</sub>.eu-131.

- [7] Hacks, A. J., Vojacek, A., Dohmen, H. J., Brillert, D. (2018). Experimental investigation of the sCO<sub>2</sub>-HeRo compressor. 2nd European supercritical CO<sub>2</sub> Conference, Essen, Germany, August 30-31, 2018. Paper 2018-sCO<sub>2</sub>.eu-115.
- [8] Vojacek, A., Melichar, T., Hajek, P., Doubek, F., Hoppe, T. (2019). Experimental investigation and simulations of the control system in supercritical CO<sub>2</sub> loop. 3rd European supercritical CO<sub>2</sub> Conference, Paris, France, September 29-10, 2019. Paper 2019-sCO<sub>2</sub>.eu-148.
- [9] Clementoni, E. M., Cox, T. R. L., King, M. A., Rahner, K. D. (2017). Transient Power Operation of a Supercritical Carbon Dioxide Brayton Cycle. Proceedings of ASME Turbo Expo 2017: Turbomachinery Technical Conference and Exposition, Charlotte, NC, USA, June 26-30, 2017. Paper GT2017-63056.
- [10] Moore, J. (2017). Chapter 9: Auxiliary Equipment in Fundamentals and applications of supercritical carbon dioxide (sCO<sub>2</sub>) based power cycles, from Brun, K., Friedman, P., Dennis, R. Woodhead Publishing, Elsevier Ltd. UK. ISBN 978-0-08-100805-8.
- [11] Rapp, L. (2022). Experimental testing of a 1MW SCO<sub>2</sub> Turbocompressor. The 7<sup>th</sup> International Supercritical CO<sub>2</sub> Power Cycles Symposium. San Antonio, Texas, USA. February 21-24, 2022. Paper #32.
- [12] Anselmi, E., Bunce, I., Pachidis, V. (2019). An overview of initial operating experience with the closed-loop sCO<sub>2</sub> test facility at Cranfield University. Proceedings of ASME Turbo Expo 2019, Phoenix, Arizona, USA, June 17-21, 2019, ASME Paper No. GT2019-91391.
- [13] Mills, A. F. (1992). Heat Transfer, United States, Los Angeles.
- [14] Kosky, P., Balmer, R., Keat, W., Wise, G. (2013). Exploring Engineering.
- [15] Polikhronidi, N., Batyrova, R., Aliev, A., Abdulagatov I. (2019). Supercritical CO<sub>2</sub>: Properties and Technological Applications - A Review. Journal of Thermal Science, 28, pages 394-430.
- [16] Abdulagatov, I. M., Skripov, P. V. (2021). Thermodynamic and Transport Properties of Supercritical Fluids. Part 2: Review of Transport Properties. Russian Journal of Physical Chemistry B volume 15, pages 1171-1188.
- [17] Mortzheim, J., Hofer, D., Priebe, S., McClung, A., Moore, J. J., Cich, S. (2021). Challenges with measuring supercritical CO<sub>2</sub> compressor performance when approaching the liquid-vapor dome. Proceedings of ASME Turbo Expo 2021: Turbomachinery Technical Conference and Exposition, Virtual, Online, June 7-11, 2021. Paper GT2021-59527.
- [18] Marchionni, M. (2021). PhD Thesis, page 88
- [19] Illyés, V., Morosini, E., Doninelli, M., David, P.-L., Guerif, X., Werner, A., Di Marcoberardino, G., Manzolini, G. (2022). Design of an air-cooled condenser for co<sub>2</sub>-based mixtures: model development, validation and heat exchange gain with internal microfins. Proceedings of ASME Turbo Expo 2022, June 13-17 2022. Paper GT2022-82438.
- [19] Incropera, F. P., DeWitt, D. P., Bergman, T. L., Lavine, S. L. (2006). Fundamental of Heat and Mass Transfer.
- [20] Lemmon, E. W., Bell, I. H., Huber, M. L., Mc Linden, M.O. (2018). NIST Standard Reference Database 23: Reference Fluid Thermodynamic and Transport Properties-REFPROP, Version 10.0, National Institute of Standards and Technology, Standard Reference Data Program, Gaithersburg.



DESIGN OF AN AXIAL SCO<sub>2</sub> TURBINE FOR A DEMO PLANT  
IN AN INDUSTRIAL ENVIRONMENT

**Stefan Glos**  
Siemens-Energy  
Mülheim an der Ruhr, Germany  
stefan.glos@siemens-energy.com

**Christian Musch**  
Siemens-Energy  
Mülheim an der Ruhr, Germany

**Carmen Stueer**  
Siemens-Energy  
Mülheim an der Ruhr, Germany

**Dominic Schlehuber**  
Siemens-Energy  
Mülheim an der Ruhr, Germany

**Michael Wechsung**  
Siemens-Energy  
Mülheim an der Ruhr, Germany

**ABSTRACT**

Energy conversion processes based on supercritical carbon dioxide (sCO<sub>2</sub>) are being investigated in the field of scientific and industrial power engineering due to the great potential in terms of compactness and efficiency.

The working fluid CO<sub>2</sub> poses a number of challenges for turbine design and aerodynamic optimization. Due to the high density of the working fluid CO<sub>2</sub>, which is associated with high losses at high velocities, special attention must be paid to aerodynamic optimization. In addition, fluid density can affect rotordynamic stability. The significantly higher demands on seals, both within the turbine and for sealing against the environment, require new sealing concepts that meet the requirements for performance and operational safety.

In this paper the development of an axial turbine for a demo plant application in an industrial environment is discussed in terms of topology, technology and optimization approaches and the resulting design concept is presented. Aero- and rotodynamic details of the specific challenges coming from the working fluid CO<sub>2</sub> are discussed as well as material aspects and the system integration in a power cycle concept. Furthermore, the scalability to larger power output and process temperatures is described.

**INTRODUCTION**

The potentials of the sCO<sub>2</sub> technology with respect to compactness and performance are well known in science and the energy industry. Development is taking place in parallel for several application areas with the involvement of industry and science. Disruptive significance is seen in CSP applications, where the use of sCO<sub>2</sub> is expected to significantly increase

competitiveness [1] as well as for fossil fired and waste heat recovery applications [2].

Due to the high maturity of existing gas and steam power plants with high efficiencies and the market situation for energy prevailing in the past, the demand and market for alternative technologies was low for a long time, especially in Europe. This has changed, especially against the background of the energy transition and several research projects have been started within the innovation program "Horizon 2020" [3-6].

In order to establish sCO<sub>2</sub> technology in energy technology in the long term, sophisticated technical solutions with high reliability of the corresponding systems are necessary. It is therefore necessary to adapt existing design and analysis methods to the special thermodynamic properties of sCO<sub>2</sub> and to supplement and expand the existing wealth of experience from the development and operation of conventional steam-based systems [9]. Topics include, in the field of materials engineering and mechanical engineering, the development and analysis of suitable heat exchangers, turbomachinery concepts and process modeling, with the special challenges derived in particular from compression and heat transfer near the critical point.

With the CARBOSOLA project, funded by the German BMWK, a sCO<sub>2</sub> technology development has started in 2019. In the first two working packages an analysis of the expected advantages has been carried out for two use cases in the fields of waste and exhaust heat recovery (bottoming cycles of combined cycle gas turbine plants) and solar-thermal power plant technology (CSP). For that, a technical-economic evaluation and optimization has been performed for both use cases [7-8] where particularly for the waste heat recovery case a benefit could be derived.

Beside a further work package in which the development and the commissioning of a modular sCO<sub>2</sub> test-rig for

\* corresponding author(s)

component development and generic experimental studies has been accomplished [9], the basic design considerations of a potential demonstration plant have been addressed. The gained knowledge, especially concerning the turbine design, defines the basis for the detailed design and realization of a small scaled sCO<sub>2</sub> turbine in a demo plant for an industrial application within the Horizon 2020 framework. For the implementation of this EU funded research project, called CO<sub>2</sub>OLHEAT, a broad consortium of academics and industrial experts covering the necessary equipment such as compressor, turbine, heat exchanger, control systems and system integration has been founded.

The focus in this publication is the design of the 2 MW axial sCO<sub>2</sub> turbine for the demonstration plant. In the next section the thermodynamic boundary conditions for the design are briefly described followed by the explanations of the different design aspects in terms of topology, technology, optimization approaches and finally the outlook on upscaling for larger outputs.

### THERMODYNAMIC CYLCE DESIGN

A demonstration plant in an industrial environment should be small enough to limit the overall costs and the commercial risks of such an advanced research project. On the other hand, it should be scalable for higher power output and deviating temperatures, so that the knowledge gained can be transferred to commercial systems. Therefore, the thermodynamic boundary conditions were selected for the further procedure based on a use case providing waste heat from an industrial process in the magnitude of 10 MW thermal. The thermodynamic layout of the sCO<sub>2</sub> cycle as shown in figure 1 has two expansion sections in series, one driving the turbo-compressor and the other as power generation turbine.

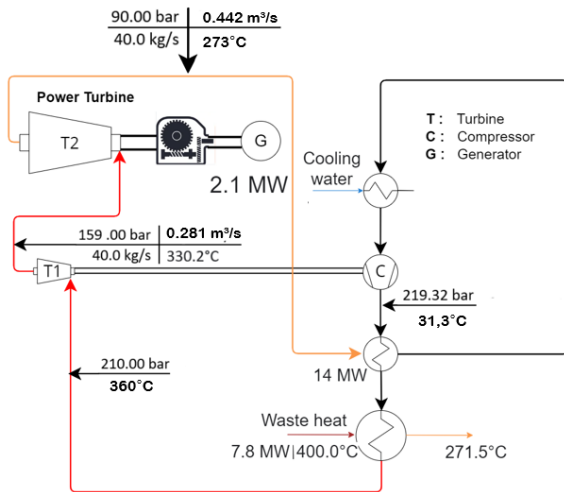


**Figure 1:** Preliminary thermodynamic cycle layout used for turbine design study. The thermodynamic parameters of the CO<sub>2</sub>OLHEAT project deviate from this to a certain extent due to the project-specific boundary conditions.

This concept requires on the one hand a very detailed alignment of the characteristics and operational aspects between both machines. On the other hand, the thermodynamic conditions at the inlet and the outlet of the power generation turbine still allow a feasible axial turbine design with an output of approximately 2,1 MW, which can be upscaled to larger power outputs.

### TURBINE DESIGN STUDY

A design study for the sCO<sub>2</sub> power turbine was initiated based on the assumed thermodynamic requirements according to figure 1. To this end three alternative concepts were designed according to figure 2 and evaluated with respect to manufacturing and assembly aspects, rotordynamic and mechanical criteria, costs and scalability. These are two variants in barrel design (1,3) and one concept with a horizontal split joint (2).

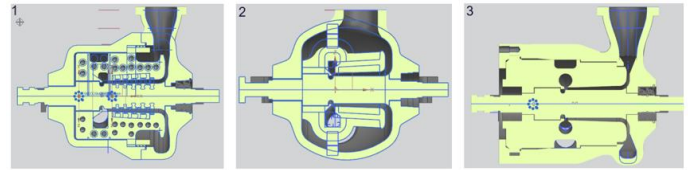


**Figure 2:** Comparison of design concepts for a sCO<sub>2</sub> turbine

In principle, barrel type turbines exhibit lower radial deformations and are therefore particularly suitable for high-pressure applications. However, production and assembly are comparatively complex. In this respect, turbines with a horizontal parting line are more favorable, but they react less favorably to high pressure differences. Consequently, it can become quite challenging to avoid leakage at the half-joint for such a design. Particularly the gas tightness to the ambient is seen to be a decisive factor, which could not be fully guaranteed for design 2. The relatively large space that needs to be provided for the dry gas seals makes it hardly possible for design 2 to place the stud bolts at the half joint in such a way to avoid leakage. Additionally, this also imposes further difficulties with respect to scalability. This described contact separation is shown in figure 3 for design 2.

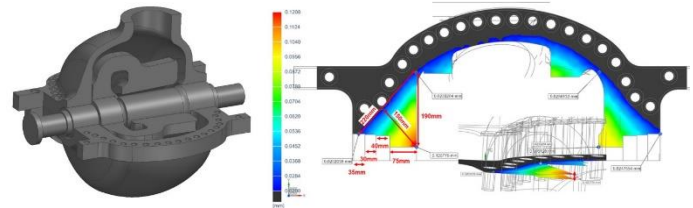


**Figure 3:** Contact separation at horizontal joint for design 2

The aerodynamic design, which will be discussed in more detail in the following section, is also unfavorable in design 2. Finally, the larger radial deformation leads to larger requirements in radial clearances and therefore give rise to higher losses. The resulting decision matrix according to table 1 documents the choice for design 1 as the favorable concept for the sCO<sub>2</sub> turbine

**Table 2:** Decision matrix for the three designs

	Gas Tightness	Pressure Losses	Rotorforce	Procurability	Manufacturability	Assembly	Scalability	Sealing
D 1	+	++	+	+	+	o	+	+
D 2	--	-	o	+	++	++	-	--
D 3	+	++	+	+	-	o	+	-

As mentioned above dry gas seals have been selected and an in-House solution was integrated in the outer casing of the barrel turbine. Dry gas seals are referenced in most sCO<sub>2</sub> applications due to their low leakage, and friction losses [10] and in a previous assessment [11] it was as well concluded that dry gas seals seem to be the best technology for sCO<sub>2</sub> turbines. On the other hand, the remaining leakages are not to be neglected from an operational point of view, as regular replenishment would be necessary, and a recovery system is inevitable. As sealing gas CO<sub>2</sub> is chosen which is extracted from the cycle upstream the turbine and thus must be purified or treated to meet the necessary pressure and temperature requirements. The resulting system technology must safely supply the seal with gas in all operating and fault conditions. An illustration of the basic design for the 2MW CO<sub>2</sub> turbine is shown in figure 4, which also shows the compactness of the machine very well.

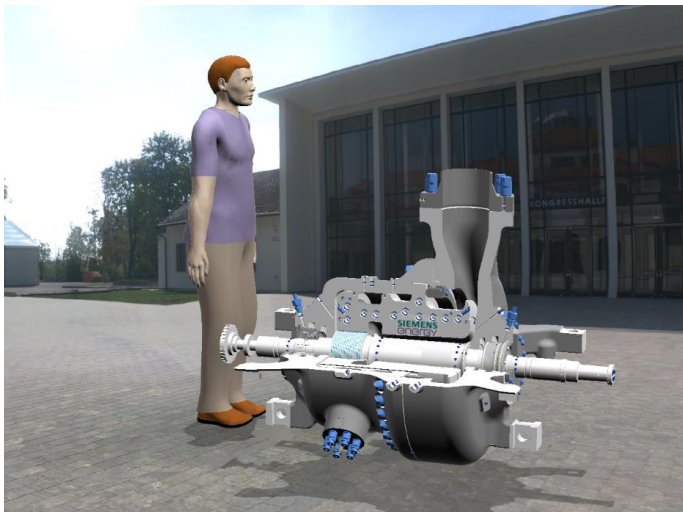


**Figure 4:** 2 MW sCO<sub>2</sub> demo turbine

Furthermore, current dry gas seal concepts are limited in size so that for larger upscaling a further technology development might be necessary.

#### AERODYNAMICS – TURBINE INFLOW & EXHAUST

Particular attention must be paid to the aerodynamic design of such a sCO<sub>2</sub> turbine, since the specific thermodynamic properties of the working medium show major differences compared to steam. Especially the high fluid density leads to

increased flow losses. Under the simplifying assumption of an incompressible fluid the pressure loss can be deduced from energy conservation and written as,

$$\Delta p_{tot} = \zeta \frac{\rho}{2} c^2 \quad (1)$$

with  $\zeta$  being the dimensionless pressure loss coefficient, the density  $\rho$  and the flow velocity  $c$ . Although, the loss coefficient is depending on the Reynolds Number, this effect is not very strong, when comparing a regular steam cycle to sCO<sub>2</sub>. The Reynolds Number is already very high for steam and thus the loss coefficient is not changing much for higher Reynolds Number as present in this application. However, it can be seen that the pressure loss is linearly proportional to the density. Depending on the exact thermodynamic boundary conditions, the fluid density of the presented turbine is up to 4 times higher than the density in a comparable steam driven turbine. Thus, it is necessary to reduce the flow velocity by a factor of roughly two, in order to keep the overall losses on a similar level. Additionally, care should be taken to avoid regions with locally high flow velocities as these are usually the main sources for increased pressure loss. Particular attention is therefore paid to the aerodynamic design of the inflow and exhaust flow of the turbine.

The size of the turbine, and the corresponding mass flow, requires only one feed pipe to fulfil the demand on the flow velocity mentioned in the former section. From an aerodynamics point of view, an inlet volute is the preferred solution of such a one pipe arrangement, as the volute gives a very homogeneous flow field. Consequently, the losses in such a design are on a very low level as well (e.g. shown by Hecker [12]). The main advantage of design 1 over design 2 is the much easier possibility to realize this feature. In particular, the resulting torque from the flow in the volute can be transferred to the outer casing much easier in design 1, whereas in design 2 usually a dead-end opposite to the feed pipe is introduced to reduce the torque. However, this dead end mostly results in increased flow losses.

The flow field for both designs has been investigated with the help of computational fluid dynamics (CFD) methods to determine the exact flow losses. Total pressure and total temperature are set at the inlet of the model; the design mass flow is prescribed at the outlet. The upstream effect due to the flow blockage of the blading has been modelled via a porous medium. This can be shown to accurately predict the flow in the inlet chamber itself (see Sievert [13] and Hecker [12]). Meshing has been done with a hybrid approach, i.e., an unstructured tetrahedral mesh in the inlet chamber and an extruded mesh for the porous medium. All walls adjacent regions are meshed with prism elements to accurately account for the boundary layer of the flow. The overall mesh size is approximately 3 Mio nodes. Grid element size and boundary layer size were defined according to [15]. CFD calculation has been done as steady state analysis using Ansys 19.2 and CFD solver CFX. All walls have no-slip boundary condition. Convergence has been considered to



be achieved when average residuals were less than  $10^{-4}$  and mass flow and energy imbalances were below 0.01%. Turbulence was modeled applying  $k-\omega$  turbulence model with wall functions (Hecker [11]). Accurate resolution of the boundary layer can be shown from the  $y^+$  values (dimensionless wall distance of mesh node next to wall) which have a maximum of 45. This is well within the logarithmic region of the turbulent boundary layer and therefore sufficient for the usage of wall functions. The fluid is modelled with real gas properties from a gas table using the REFPROP [14] library. Spatial discretization is done using a hybrid scheme of almost second order accuracy.

The flow field for both design variants is shown in figure 5

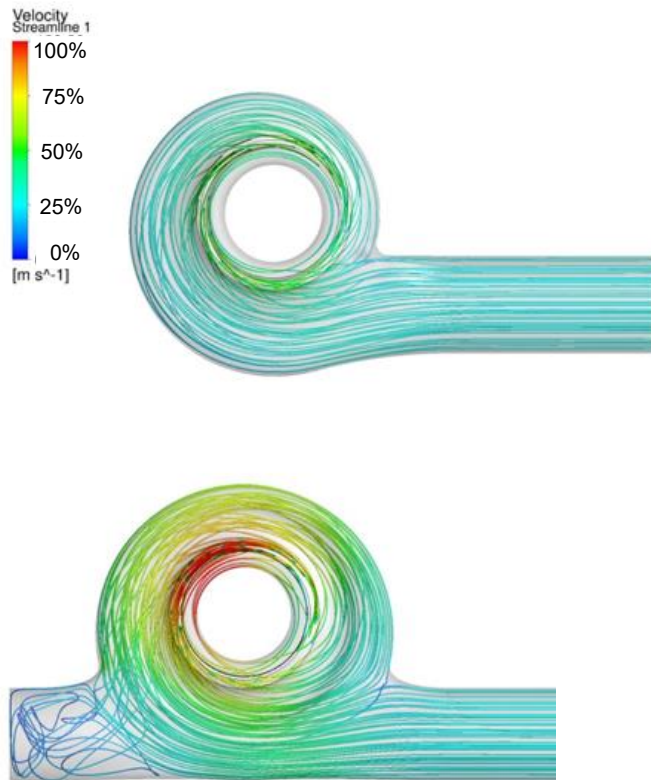


**Figure 5:** Comparison of inlet flow fields for design 1 and 2

It can be seen from the streamline plot, that the flow field in the volute of design 1 is much more homogeneous around the circumference, with flow incidence angles to the first stator vane only varying between  $-6^\circ$  to  $3^\circ$ . Additionally, the maximum velocity in design 2 is much higher. Consequently, the pressure loss coefficient for design 1 ( $\zeta=0.2$ ) is reasonably lower compared to design 2 ( $\zeta=2.1$ ). As a nice-to-have the resulting forces on the rotor are also lower for design 1.

The turbine exhaust flow has also been investigated with care to reduce pressure losses and transient effects caused by flow separation in the diffuser section of the exhaust. A preliminary layout of the diffuser has been done with the help of a very simplistic 2D-CFD approach based on a potential flow solver combined with a boundary layer solver to predict flow separation. This preliminary design is then investigated and

further improved with a fully 3D-CFD approach like the one described in the former section. The velocity profiles in axial, radial and circumferential direction, and the total temperature, which are taken from a separate simulation of the last stage alone, are used as boundary conditions at the diffuser inlet. At the outlet of the exhaust the static pressure is prescribed. Again, a hybrid mesh with prism elements in the near wall region has been used, resulting in an overall mesh count of 6 million nodes. Turbulence closure has been done using the  $k-\omega$  turbulence model (compare Musch [15]). Fluid properties are taken from the REFPROP library again. The approach for discretization and convergence control are the same as applied for the inlet. It can be seen from the flow field in figure 6, that the objective to avoid flow separation in the diffuser could be achieved. Overall flow losses are on an acceptable level, with a pressure loss coefficient of  $\zeta=0.3$  according to the definition above.

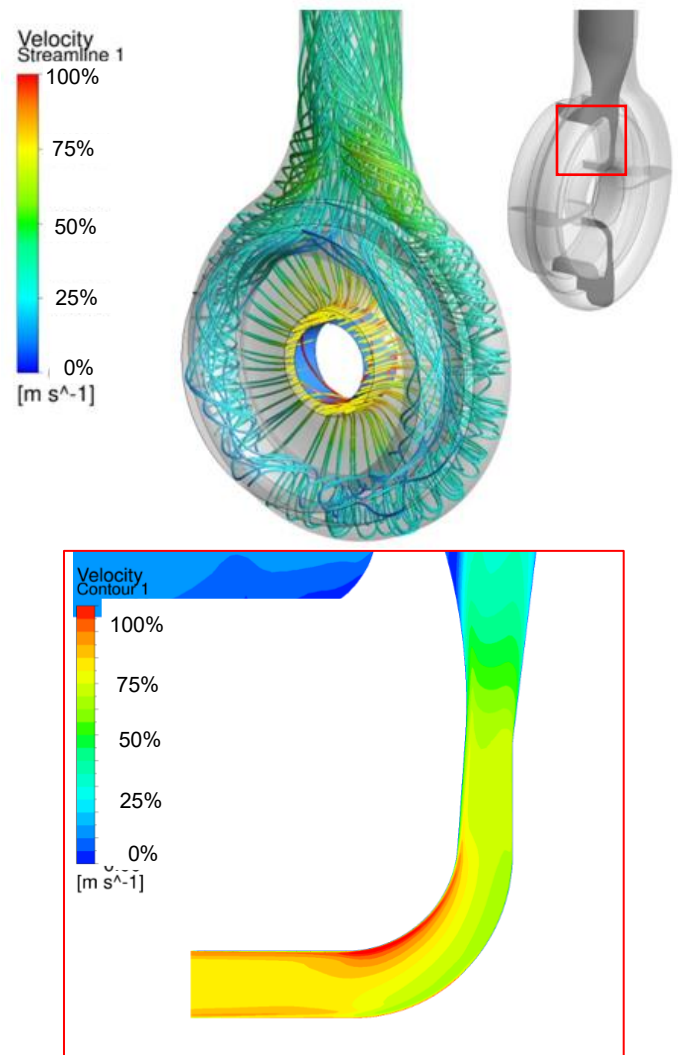


**Figure 6:** Flow field in turbine exhaust and diffuser

## ROTOR DYNAMICS

As for the aerodynamics design, also for the rotordynamic calculations special care must be taken to consider the more challenging fluid properties of sCO<sub>2</sub>. These fluid properties have a major impact on the fluid forces on the rotor and therefore on possible flow excitation in the seals. The very high fluid density, and the low viscosity, do not allow to use the same semi-empirical methods, applied for steam, to determine the rotordynamic coefficients, which are vital for the assessment of the shaft train. As the standard correlations could not be applied directly, it has been decided to evaluate all seals for the demonstration turbine with the help of 3D-CFD. As an example, the numerical approach is described for the dummy piston seal. Figure 7 shows an overview of the examined sealing section. An eccentricity of 10 μm has been assumed for the simulations. Meshing is done applying a sweep method in circumferential direction. Again, an eddy viscosity approach has been applied for turbulence closure, this time using the Baseline (BSL) model by Menter [16], which has been proven by Musch [17] to produce reliable results for CFD simulations of labyrinth seals. From the calculated forces on the shaft, the rotordynamic coefficients for stiffness and damping of the seal can be derived and considered in the shaft train design.

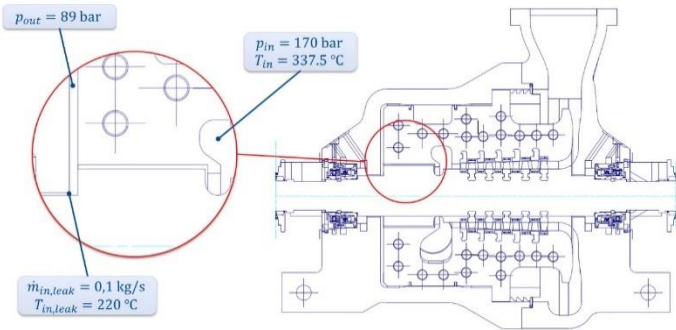


**Figure 7:** Cross Section of turbine with close-up of dummy piston

## MATERIALS

For the design and the manufacturing of a turbine, operating with supercritical CO<sub>2</sub> as working fluid, materials must be selected assuring a safe and reliable operation. To answer the question, whether conventional materials used for (steam) turbines are also suitable for the operation with sCO<sub>2</sub>, the effects of oxidation and carbonization need to be evaluated. Many scientific studies were carried out in the field of interest in different institutes all over the world in the past about 50 years. Available oxidation data in sCO<sub>2</sub> was assessed and published in [2]. In figure 8, published in [2] a limit of suitability of  $5 \times 10^{-13} \text{ g}^2/\text{cm}^4 \text{ s}$  has been defined. However, corrosion rates of  $5 \times 10^{-12} \text{ g}^2/\text{cm}^4 \text{ s}$  are experienced for 9-12% Cr. steels in steam atmosphere. From that it is concluded that these material class can even be operated up to approximately 560 °C.

Positive corrosion resistance is reported based on small additions of silicon [18] and a further improvement can be

achieved by oxidation protection layers. For further technology development these measures should be further evaluated by experiments. Initial measurement campaigns are carried out within the CO<sub>2</sub>OLHEAT project. However, for the above-described waste heat recovery application with inlet temperatures below 400 °C, it is assumed that proven materials can be used without any restrictions.

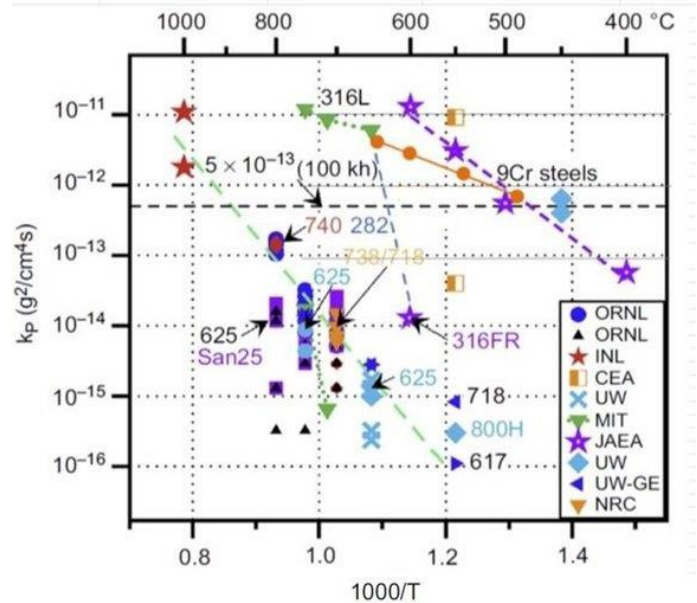


**Figure 8:** Corrosion rates of different materials in CO<sub>2</sub> atmosphere [2]

## SYSTEM INTEGRATION

To integrate the sCO<sub>2</sub> turbine into the overall system, it is connected to a generator on a base frame via a gearbox and equipped with the necessary auxiliary systems such as the oil module and the sealing and leakage gas system. Figure 9 shows the overall package of the sCO<sub>2</sub> turbine.

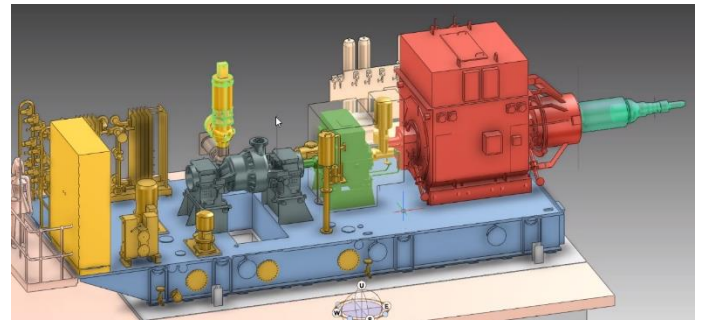


**Figure 9:** Preliminary set-up of complete sCO<sub>2</sub> -turbine train

As already mentioned above, the sealing system is designed to minimize leakages and assures a safe operation in each operational condition of the plant. The chosen dry gas seal (DGS), integrated in the outer casing as shown in figure 7, requires clean sealing gas with defined requirements in terms of

purity, pressure and temperature. For that, CO<sub>2</sub> is extracted from the high-pressure side of the cycle and processed as shown in the preliminary and simplified P&ID in figure 10, whereas redundancies of the components needs to be considered in order to assure a reliable operation of the system. The main portion of leakage gas discharged in a first stage at low overpressure and sent to the recovery compressor of the system. The remaining leakage of  $\ll 10^{-4}$  kg/s is vented into the atmosphere.

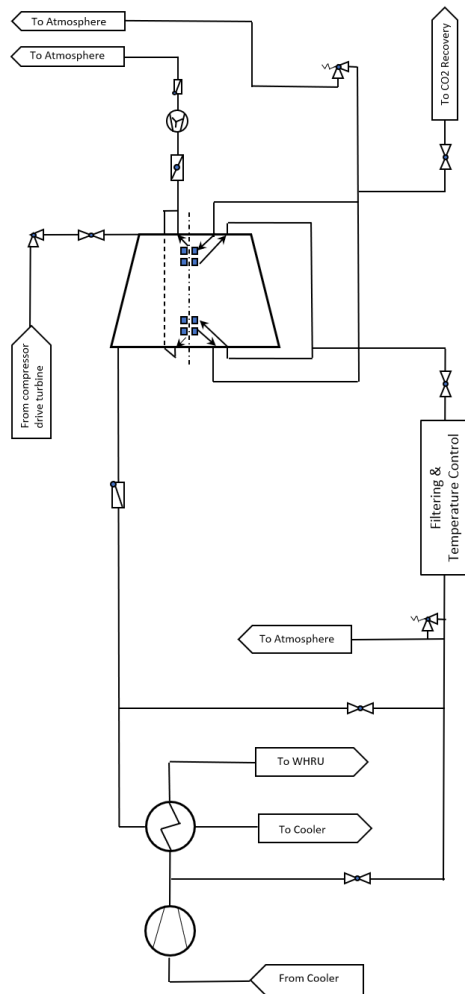


**Figure 10:** Preliminary and simplified P&ID of sealing system

In addition to the development of the components, the integration and coordination of the respective designs is one of the main challenges in the development of closed Brayton cycles. In this context, off-design load cases, transient processes such as startup and shutdown, and malfunctions are of particular importance. In contrast to the water-steam cycle, there is no integrated storage of the working medium, such as in the hotwell of the condenser or in the feedwater tank. Such an accumulator is therefore essential to enable transient processes such as start-up or shut-down. The further elaboration of the process

technology including the corresponding logics and control loops of the entire system will be an essential focus of the joint development of the CO<sub>2</sub>OLHEAT consortium for the next phase of the project.

### UPSCALING

The presented design of a 2 MW sCO<sub>2</sub> demo turbine is at the lower end of the sensible application range of axial turbines. Due to the low volume flow and thus low blade-heights, the leakage losses are dominating and leading to a moderate efficiency. However, the goal is to validate a scalable design that can be applied for larger-scale power range. In table 2 the basic results for upscaling the 2MW bladepath design to 10 MW and 50 MW is shown. This leads to a significant improvement of the achievable efficiency. A more detailed description of the blading design methodology can be shown in [11].

**Table 2:** Basic results of upscaling the developed turbine design

	2 MW	10 MW	50 MW
Di	160 mm	300 mm	500 mm
h <sub>1st stage</sub>	16 mm	35mm	60 mm
stages	6	4	11
n	175 Hz	110 Hz	50Hz
η <sub>Bld</sub>	~ 83 %	~ 91 %	~ 93 %

In figure 11 the sketch of the 50 MW variant is compared with the 2 MW demo turbine in terms of size and the compactness of the 50 MW variant becomes obvious. Upscaling the power output by a factor of 25 increases the rotor length by a factor of ~ 2 only.

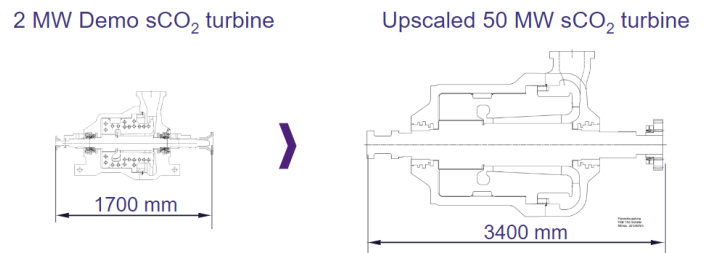


**Figure 11:** Comparison of scaled 50 MW turbine with 2 MW demo turbine

The basic feasibility of the scaled variants was investigated, whereby technological aspects must be the subject of further investigations and optimizations. For example, the sealing concept must be examined in detail for larger diameters and higher temperatures. In addition, the cycle architecture might be changed for larger applications due to potential restrictions of the



serial connection of compressor drive turbine and power turbine for higher outputs and temperatures.

## NOMENCLATURE

Bld	Blading
c	Velocity
CSP	Concentrated Solar Power
D	Diameter
DGS	Dry-Gas Seal
h	Height
P	Power [MW]
p	Pressure [bar]
P&ID	Piping & Instrumentation drawing
n	rotational speed [1/s]
sCO <sub>2</sub>	Supercritical Carbon Dioxide
T	Temperature [°C or K]
tot	Total
Δ	Difference
η	isentropic Efficiency (total/total)
ζ	Pressure loss coefficient
ρ	Density

## ACKNOWLEDGEMENTS

This paper combines the results of the CARBOSOLA project, and the first realizations derived in the CO<sub>2</sub>OLHEAT project. The authors would like to thank the Federal Ministry of Economics and Climate (BMWK) for the financial support of the CARBOSOLA project as per resolution of the German Bundestag under grant numbers 03EE5001A. The authors alone are responsible for the content of this paper. The CO<sub>2</sub>OLHEAT project has received funding from the European Union's Horizon 2020 research and innovation program under grant agreement No 101022831. This publication reflects only the author's views and the European Union is not liable for any use that may be made of the information contained therein.

## REFERENCES

[1] V. Bush, (2018). GTI STEP forward on sCO<sub>2</sub> Power - Supercritical Transformational Electric Power project. Pittsburgh, Pennsylvania, USA.

[2] K. Brun, P. Friedman, und R. Dennis (2017). Fundamentals and applications of supercritical carbon dioxide (sCO<sub>2</sub>) based power cycles, 1st edition. Waltham, MA: Elsevier.

[3] J. Starflinger, D. Brillert, O. Frybort, P. Hajek, A. Hennink, T. Freutel (2017). Raising Nuclear Reactor Safety to a Higher

Level – The Supercritical CO<sub>2</sub> Heat Removal System – sCO<sub>2</sub>-HeRo. Slovenia.

[4] V. Maquart, B. Valentin (2017) Environmental assessment of a 25 Mwe fossil-fired supercritical CO<sub>2</sub> cycle. Prague, Czech Republic

[5] M. Binotti et al. (2019). Supercritical Carbon Dioxide/Alternative Fluid Blends for Efficiency Upgrade of Solar Power Plant. Paris, France.

[6] R. Guédez et al. (2019). First Year of the EU SolarSCO<sub>2</sub>OL Demonstration Project – Enabling Hybrid Supercritical CO<sub>2</sub> CSO Plants integrated with PV. San Antonio, Texas, USA.

[7] T.G. Gothelip, U. Gampe, S. Glos (2021). Techno-economic optimization method and its application to a sCO<sub>2</sub> gas turbine bottoming cycle”. 4th European sCO<sub>2</sub> Conference

[8] L. Heller, R. Buck, S. Glos (2021). sCO<sub>2</sub> power cycle design without heat source limitations: “Solar thermal particle technology in the CARBOSOLA project”, 4th European sCO<sub>2</sub> Conference

[9] S. Unger et. al. (2021). Aufbau einer Versuchsanlage mit superkritischen Kohlenstoffdioxid (sCO<sub>2</sub>) als Arbeitsmedium in Kraftkreisläufen“, In: Kraftwerkstechnik ISBN 978-3-949169-02-1.

[10] A. Laxander, A. Fesl, B. Hellmig (2019). Development and testing of dry gas seals for turbomachinery in multiphase CO<sub>2</sub> application, 3rd European sCO<sub>2</sub> Conference, Paris, France.

[11] Glos et al. (2021). Design considerations of sCO<sub>2</sub> turbines developed within the Carbosola project, 4th European sCO<sub>2</sub> Conference.

[12] S. Hecker (2011). Strömungs- und strukturmechanische Untersuchung der Einströmung einer Dampfturbine, PhD Thesis, Ruhr-Universität Bochum, Bochum

[13] R. Sievert et al. (2007). Porous Media Simulating the Stator Row in Steam Turbine Inlet Flow Calculations, 7th European Turbomachinery Conference, ETC.

[14] E. W. Lemmon et al. (2018), NIST Standard Reference Database 23: Reference Fluid Thermodynamic and Transport Properties-REFPROP, Version 10.0, National Institute of Standards and Technology, <https://www.nist.gov/srd/refprop>.

[15] C. Musch et al., Impact of the Exhaust Geometry on Flow Losses in a High-Pressure Steam Turbine, Int. J. Turbomach. Propuls. Power 2016, 1, 2; doi:10.3390/ijtp1010002

[16] F. R. Menter. (1994). Two-equation eddy-viscosity turbulence models for engineering applications. AIAA-Journal. 32 (8): 1598–1605. <http://dx.doi.org/10.2514/3.12149>.

[17] C. Musch (2008). Beitrag zur gekoppelten Auslegung von Endstufen mit Deckband und anschließendem Diffusor in Niederdruck-Dampfturbinen, PhD Thesis, Ruhr-Universität Bochum, Bochum

[18] D. Young (2008). High temperature oxidization and corrosion of metals. ISBN 978-0-08-044587-8. Elsevier

## ANALYSIS OF THE POTENTIAL OF CO<sub>2</sub> BASED MIXTURES TO IMPROVE THE EFFICIENCY OF COGENERATIVE WASTE HEAT RECOVERY POWER PLANTS

**Ettore Morosini\***  
Politecnico di Milano  
Milano, Italy

**Michele Doninelli**  
Università degli studi di Brescia  
Brescia, Italy

**Dario Alfani**  
Politecnico di Milano  
Milano, Italy

**Marco Astolfi**  
Politecnico di Milano  
Milano, Italy

**Gioele Di Marcoberardino**  
Università degli studi di Brescia  
Brescia, Italy

**Giampaolo Manzolini**  
Politecnico di Milano  
Milano, Italy

### ABSTRACT

The waste heat potentially available from a wide range of industrial processes still represents a significant fraction of the primary energy consumption related to the processes.

Some of the most energy intensive processes can be categorized in the iron, steel and glass production, the fine chemical industry, and the production of non-ferrous materials such as cement, polymers, paper or in the textile industry. Of the overall thermal energy rejected in the environment, a part of it is feasibly exploitable from a technical and economical point of view in waste heat recovery plants. This work proposes innovative solutions for waste heat recovery cycles working with sCO<sub>2</sub> cycles and transcritical cycles adopting CO<sub>2</sub>-mixtures. As the heat rejection from these cycles is non-isothermal, these power plants are particularly suitable to be used in CHP configuration, therefore transferring heat to a stream of pressurized water at high temperature, up to 200°C.

When a waste heat source available at 450°C is considered, assuming a stack temperature of 125°C, the proposed sCO<sub>2</sub> power cycle can convert around 12% of the thermal input in electricity and 87% in useful heat above 60°C, while a cycle working with the CO<sub>2</sub>+Acetonitrile mixture can deliver 15.5% of the thermal input in electricity while still recovering the remaining more than 80% in useful heat above 60°C.

CO<sub>2</sub> based mixtures are therefore suggested for power cycles in CHP configuration to reach nominal electric efficiencies higher than sCO<sub>2</sub>, avoiding the consumptions of natural gas to produce the same amount of electricity and heat with separated systems.

### INTRODUCTION

All across the developed and developing countries an increasing amount of waste heat from industrial processes can be recovered in Waste Heat Recovery (WHR) plants. Especially for small scale applications, these plants normally consist of power

cycles, as the Organic Rankine Cycles (ORC), producing electric power by cooling down the exhaust gases released in the environment as much as possible, before releasing them at the stack [1]. The state of the art of ORCs can be identified in subcritical cycles operating with organic fluids, allowing for maximum temperatures decisively lower than the ones achieved in steam cycles. ORCs can be designed as cogeneration units in Combined Heat and Power (CHP) plants by increasing the condensation temperature, entailing a non-negligible penalization of electric efficiency, while, thanks to their flexibility, can switch to pure electric mode when heat is not required by the thermal user.

As a matter of fact, considering the soaring prices of natural gas and other fuels for conventional fossil fuels-based boilers, alternative solutions to produce low temperature heat are considered increasingly attractive. The potential of supercritical carbon dioxide (sCO<sub>2</sub>) power cycles for electricity generation in the industrial WHR sector has been already investigated in several works [2–4]. However, differently than ORC, sCO<sub>2</sub> power cycles do not show iso-thermal heat rejection from the cycle, and therefore they can be employed in CHP plants for WHR applications without a strong penalization in electrical efficiency, without any bleeding, unlike steam cycles. The produced useful heat from the sCO<sub>2</sub> cycle, in the 60-200°C range, can be released in part at low temperature for space heating in district heating networks and in part exploited at higher temperature as industrial process heat, adaptable to a variety of applications such as drying, carbon capture with amines, sterilization or thermal desalination. In the US this technological solution was proposed to the market by Echogen Power Systems [5], which manufactured and commercialized sCO<sub>2</sub>-based systems also in CHP configuration.

In addition to sCO<sub>2</sub> cycles, transcritical cycles adopting CO<sub>2</sub>-based mixtures as working fluid are also investigated in this work for CHP applications: a more innovative family of power cycles gaining ground in the last few years among various

\* ettore.morosini@polimi.it

literature works regarding concentrated solar power, as in the SCARABEUS project [6] and the DESOLINATION project [7], two H2020 EU projects. The performances of these innovative solutions for WHR plants are examined in this work: as the working fluid is compressed in liquid phase (instead of supercritical phase like in  $s\text{CO}_2$  cycles), the cycle efficiency can likely increase and the temperature difference in the compression step reduces drastically, allowing for a better coupling with the hot sources and reducing the stack temperature on the exhaust gases side, at constant boundary conditions, with respect to  $s\text{CO}_2$  solutions.

In this work, for all the configurations proposed, the totality of the waste heat is recovered and partially or fully converted in electric power and useful heat in different fractions, depending on the technical solution adopted as bottom cycle. In conclusion, tanking for granted the good performances of ORC for electric-only WHR cycles [8], this work stresses the flexibility and efficient capability of  $\text{CO}_2$ -based cycles to convert waste heat into useful thermal power, while keeping satisfactory levels of electric power produced.

## POTENTIAL OF WASTE HEAT IN THE INDUSTRIAL SECTOR AND THE COGENERATION BENEFITS

The EU carbon neutrality targets require an improvement of the primary energy conversion efficiency of the industrial processes to reduce their carbon footprint, and the exploitation of the available waste heat is a key strategy to meet the targets. According to a 2020 Eurostat report [9], the EU industrial sector is responsible for more than 26% of the total primary energy consumption, closely after the transport sector at 28%.

More than 70% of the energy consumption in industries is used for heating processes [10], which results in a remarkable amount of waste heat (up to 50%) dissipated in the environment [11].

Bianchi et al [12] analyzed the WHR potential in EU both in terms of technical potential (heat available from effluents and exhaust gases) and Carnot potential by considering the temperature levels of the wasted heat and converting it into mechanical power with each corresponding Carnot efficiency. It highlighted that the EU industrial sector dissipates into the environment nearly half of the primary energy consumed. According to the authors, the industrial WHR available accounts for about 920  $\text{TWh}_{\text{th}}$ , which is 29% of the industrial consumption, while the Carnot potential is around 279  $\text{TWh}_{\text{el}}$ .

Papapetrou [13] examined the waste heat potential in EU per sectors, temperature levels and countries, showing that one third is available at a temperature level below 200°C, 25% in the range 200–500°C and the rest above 500°C.

Moreover, power generation plants also reject large amounts of valuable heat which is currently dissipated in the environment. For instance, small scale gas turbines (5-60  $\text{MW}_{\text{el}}$ ) typically have exhaust gases in the temperature range between 450 and 560°C. Internal combustion engines (ICE) convert 30% to 40% of the primary energy into useful mechanical work, while the remaining part is released to the environment through exhaust gases and cooling systems. Exhaust gases of ICEs also have

temperatures in the range 450-600 °C and they can be exploited in a WHR unit.

According to a study on the final energy demand in Europe in 2015 [14], the demand for heating and cooling (H&C) is nearly 50% of the overall final energy demand: in particular, space heating has the largest portion (53%) of the H&C demand, followed by process heating (32%).

Of the overall H&C demand, more than 20% can be located in the 100-200°C temperature range, a challenging range for any applications that has the goal of decarbonization. This fraction of heat demand is then divided in sectors, such as: pulp and paper production (230  $\text{TWh}_{\text{th/y}}$ ), food and beverage industry (123  $\text{TWh}_{\text{th/y}}$ ), the chemical (119  $\text{TWh}_{\text{th/y}}$ ) and non-metallic minerals (43  $\text{TWh}_{\text{th/y}}$ ) sectors.

Accordingly, in this work the heat recovered from the cycle heat rejection unit is differenced in heat above 100°C and below 100°C, both technically obtainable due to the high temperature difference of the working fluid across the heat rejection step, to highlight the capability of the proposed technology to also reduce the primary energy consumption of the H&C demand in the 100-200°C range and the related  $\text{CO}_2$  emissions.

## ADVANTAGES IN THE ADOPTION OF $\text{CO}_2$ -BASED CYCLES FOR WHR APPLICATIONS

This work presents various cycle simulations where a generic waste heat source (exhaust gases) is available at a temperature higher than 420°C and can be cooled down to 125°C. The power from the exhaust gases is transferred to a heat transfer fluid (HTF) that is heated from 110°C to 420°C, used to separate the power block to the upstream process and to hypothetically adopt a thermal energy storage system. Finally, the HTF provides thermal input to the cycle, that can have a maximum temperature up to 400°C and a temperature at primary heat exchanger inlet up to 100°C, to completely exploit the available thermal power. This solution is not always optimal for only-electric configurations, where a tradeoff between the heat source exploitation and cycle thermodynamic efficiency must be considered. However, this is not the case for CHP systems where, to maximize the sum between heat and power produced, it is beneficial to completely cool down the heat source.

As detailed later in this work, ORC can efficiently be employed in WHR plant in an only-electric configuration. A graphical representation of the temperature profile of the waste heat source and a generic saturated ORC power cycle is reported in Figure 1 in a  $T$ - $s$  diagram, where the nature of working fluid is not specified for generalization purposes. As evident from the figure, the heat rejection from the ORC is dominated by the isothermal condensation, rejecting heat into the ambient at temperatures lower than 45°C, a temperature level not of interest for CHP configurations. Moving from the ORC to  $\text{CO}_2$ -based mixtures used in transcritical cycles, Figure 2 depicts the power cycle behavior on a  $T$ - $s$  diagram for this application. In these cases, the heat rejection from the cycle is not isothermal, and, while the fraction of heat below 60°C is still rejected by means of an air-cooled condenser, a wide fraction of this heat is at a temperature

level valuable to be exploited in a CHP plant: the first contribution is ideally exploitable in a district heating network, while the second one can have other industrial uses, as described in the previous chapter. The fraction of heat rejected through the air-cooled condenser can be neglected if the cycle minimum temperature is sufficiently higher than 60°C: in this condition, the thermal input to the cycle is almost completely converted in the CHP plant, with the exception of a small fraction of electro-mechanical losses.

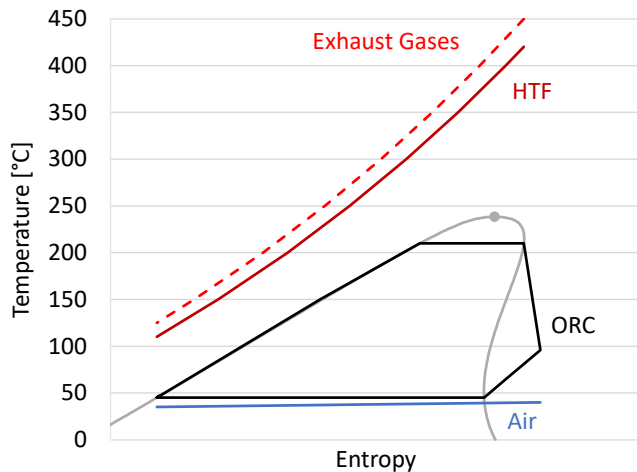


**Figure 1.** Temperature - Specific Entropy and heat recovery characterization of an ORC representing the state of the art of small scale WHR cycles for electricity production

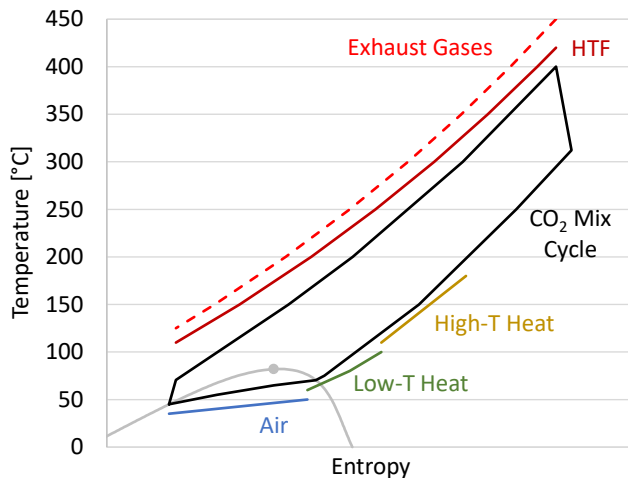


**Figure 2.** Temperature - Specific Entropy and heat recovery characterization of the innovative WHR transcritical cycle with a generic CO<sub>2</sub>-based working fluid for CHP applications

While analogous considerations can be drawn also for pure sCO<sub>2</sub> cycles, supercritical cycles normally present lower cycle efficiency with respect to transcritical cycles especially when, as in the considered cases, the difference between the maximum and minimum cycle temperature is not considerable. In addition, the most efficient conditions for CHP applications are the ones at high cycle minimum temperature (above 60°C): in these cases

the compressor power, operating far from the critical temperature of CO<sub>2</sub>, increases non-linearly with the cycle minimum temperature and it negatively affects both the cycle efficiency and the specific work. In conclusion, underlining the concepts behind the two *T-s* diagrams proposed, Figure 3 depicts an indicative breakdown of the conversion of the thermal input performed by the two different categories of power cycles for a cycle minimum temperature above 60°C (the figures reported are indicative). As noticeable, moving from an ORC to a CO<sub>2</sub>-based cycle solution, it is possible to better exploit the available waste heat at the expenses of a slightly lower electrical efficiency.

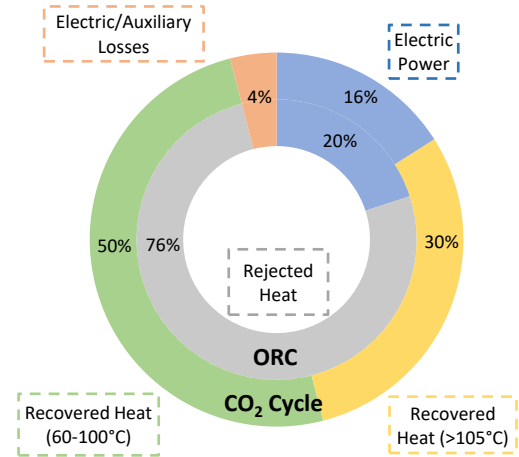


**Figure 3.** Indicative comparison between ORC and CO<sub>2</sub>-based cycles in the conversion of the heat introduced in the cycle

## MODELLING OF THE WORKING FLUIDS FOR THE CO<sub>2</sub>-BASED CYCLES

Two CO<sub>2</sub>-based mixtures are reported in this work as working fluid for transcritical cycles in CHP applications, along with the performances of pure CO<sub>2</sub> in supercritical cycles. The first mixture is the CO<sub>2</sub>+Acetonitrile mixture: this dopant (CAS: 75-05-8) is a flammable, non-toxic and commonly adopted fluid for many applications as solvent and in the production of chemicals. The CO<sub>2</sub>+Acetonitrile mixture is already studied, as many VLE experimental data are available in literature, and the dopant has a thermal stability well above 400°C, suitable for this application. The mixture is modelled in ASPEN PLUS (v.11) with the standard Peng Robinson (PR) equation of state (EoS) and a binary interaction parameter ( $k_{ij}$ ) of 0.055, retrieved from experimental data [15]. The second dopant considered is referred to “unnamed compound” (UC) in this work. The compound will be object of publications in the near future within the SCARABEUS and DESOLINATION framework (H2020 EU projects), and it is currently IPR protected. The dopant is considered thermally stable over 400°C, it has a low toxicity, it is not flammable and suitable for power cycles applications as it is commonly adopted as solvent for organic materials. The mixture is also modelled with the PR EoS in Aspen Plus with no binary interaction parameter, as no mixture experimental data are

available in literature, while for the pure CO<sub>2</sub> the Span and Wagner EoS is adopted [16], as it is considered the gold standard thermodynamic model for pure CO<sub>2</sub>. The CO<sub>2</sub>+UC mixture is presented as an alternative to acetonitrile as dopant for circumstances where non-flammable fluids are of interest.

## MODELLING OF THE CO<sub>2</sub>-BASED CYCLES FOR CHP APPLICATIONS

The methodology developed to compute the nominal electric and thermal performances of the innovative CO<sub>2</sub> based power cycles is described in this chapter. All cycles are always optimized, in any condition, to reach the highest electric efficiency, since the heat recovery efficiency from the exhaust gases is always maximized by default, as already specified. The optimization parameters for each configuration are the cycle minimum pressure and the split ratio of the cycle splitter valve for the sCO<sub>2</sub> cycles; the mixture composition and the split ratio, on the other hand, for the CO<sub>2</sub> mixture cycles. For transcritical cycles adopting mixtures the minimum pressure is set at the bubble condition at any cycle minimum temperature.

The various CO<sub>2</sub>-based power cycles are modelled in this work according to the assumptions listed in Table 1, assuming a unitary value of HTF mass flow rate (1 kg/s) in the ASPEN modeling tool. The quite conservative values for the cycle non idealities (mainly the turbomachinery efficiencies) are indicative of small-scale applications, in the range between 15 to 30 MW<sub>th</sub>, while, at the same time, the high maximum pressures, typical of large-scale power plants for power generation, are strictly necessary for this category of power plants.

**Table 1.** Cycles characteristics and non-idealities

Parameter	Value
Cycle maximum temperature	400°C
Pressure at turbine inlet	250 bar
PHE/PCHE pinch point (MITA)	10°C
Compression isentropic efficiency	80%
Expansion isentropic efficiency	85%
Pressure drops (PHE / HRU)	3 bar / 1 bar
Pressure drops PCHE (HP / LP)	1 bar / 2 bar
Generator/Motor efficiency	97% / 97%
Auxiliary HRU Electric Consumption	1% of $\dot{Q}_{COND,AIR}$

Two plant layouts are adopted in this analysis: the dual recuperative layout (proposed in Figure 4) and the cascade layout (reported in Figure 5). These two layouts, which are particularly suitable for WHR applications, are modified in this work separating the heat rejection section in two different heat exchangers, one for low temperature heat and one for high temperature heat (already identified in the qualitative *T-s* diagram of Figure 2). The calculations are carried out in the simulation software ASPEN PLUS, assuming a minimum temperature difference of 5°C between the heat rejected by the cycle and the various cold sinks (the air and the two streams of pressurized water for the cogeneration uses).

In conclusion, six different cases are proposed in this work, as two plant layouts are combined with three working fluids (pure CO<sub>2</sub> and the two mixtures).

In addition to that, as the variability in the electric and thermal power demand is strongly case-specific for CHP plants (especially if dedicated to the industrial sector), a sensitivity analysis on the cycle minimum temperature is proposed.

As water scarcity is becoming one of the most defining global environmental problems, and water availability cannot be taken for granted in any location, water has not been adopted within this work as cold sink for the power plants. Accordingly, with only air-cooled heat rejection units, minimum cycle temperatures below 45°C are not considered. On the other hand, since the application for the low temperature heat recovered is district heating with a minimum temperature of 60°C (underlined in Figure 3), considering a pinch point of 5°C between the heat rejected and the pressurized water for the district heating would result in maximum cycle minimum temperatures of 65°C, as higher temperatures will penalize the electric efficiency with no advantages on the cogenerative section. For these reasons, the sensitivity analysis on the cycle minimum temperature is carried out in the range 45°C-65°C. When the cycle minimum temperature is lower than 65°C, the fraction of heat below this threshold is rejected in the environment with an air-cooled heat rejection unit. In this case, an electric auxiliary consumption is included to model the fan power of the heat exchanger, fixed at 1% of the rejected heat, as reported in Table 1.

Finally, as for the dual recuperative layout it is not suitable to abundantly recover heat above 105°C in conditions characterized by a low cycle minimum temperature, only the low temperature thermal user is considered at 45°C minimum temperature for this plant layout, while both the high temperature and low temperature one is modelled for higher cycle minimum temperatures.

## PERFORMANCES OF THE CO<sub>2</sub>-BASED CYCLES FOR CHP APPLICATIONS

In this chapter the main parameters to define a CHP power plant are defined and reported for the proposed solutions. The definitions of electric efficiency and thermal efficiencies considered in this work are detailed from Equation (1) to (5).

$$\eta_{el} = \frac{\dot{W}_{Turbine} \cdot \eta_{Gen} - \frac{\dot{W}_{Compression}}{\eta_{Motor}} - \dot{W}_{Aux,HRU}}{\dot{Q}_{HTF}} \quad (1)$$

$$\eta_{Th,HT} = \frac{\dot{Q}_{Rejected,HT}}{\dot{Q}_{HTF}} \quad (2)$$

$$\eta_{Th,LT} = \frac{\dot{Q}_{Rejected,LT}}{\dot{Q}_{HTF}} \quad (3)$$

$$\eta_{Th} = \eta_{Th,HT} + \eta_{Th,LT} \quad (4)$$

$$\eta_{Overall} = \eta_{el} + \eta_{Th} \quad (5)$$

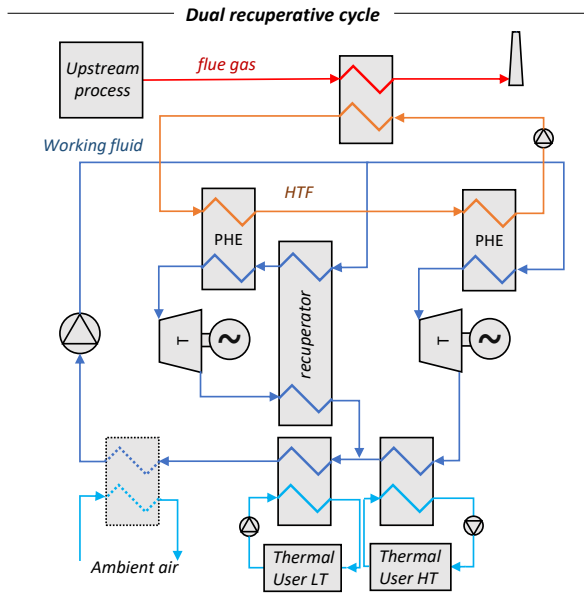


**Figure 4.** Dual recuperative layout for WHR power cycles.

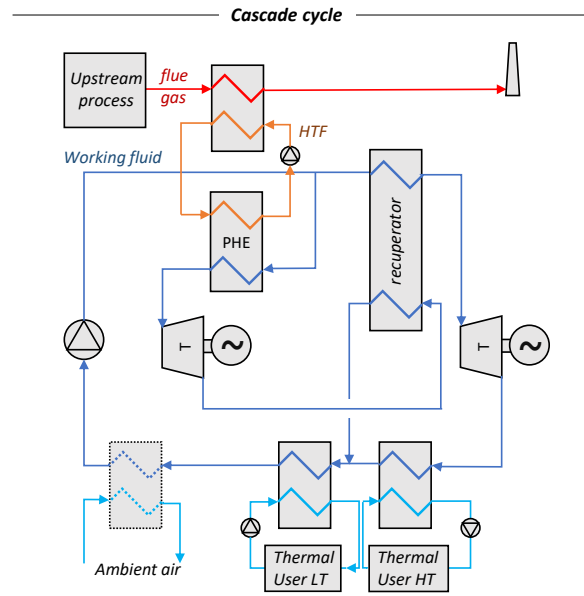


**Figure 5.** Cascade layout for WHR power cycles.

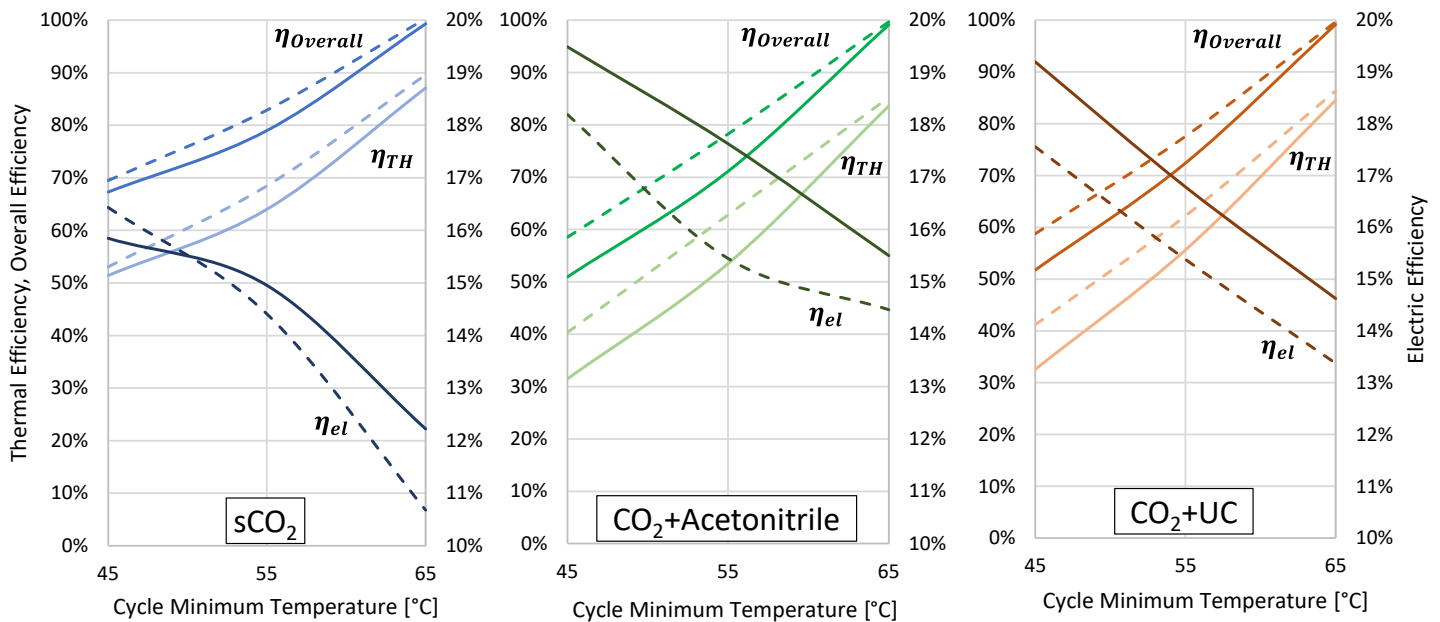


**Figure 6.** Trends of the electric, thermal and overall efficiency of the CO<sub>2</sub>-based cycles adopted in CHP configuration. (Dotted line: Cascade Cycle. Solid line: Dual recuperative Cycle).

The resulting performances of the three working fluids are evidenced in Figure 6. In general, sCO<sub>2</sub> cycles present a more modest electric efficiency and a slightly higher thermal efficiency for the CHP applications. Especially for high cycle minimum temperatures (65°C) sCO<sub>2</sub> can achieve a 12.2% electric efficiency, which is 3.3% lower with respect to the mixture with acetonitrile (more than 27% lower in relative terms). The drop of electric efficiency of the proposed sCO<sub>2</sub> cycles is significant, in particular where the cycle minimum temperature is far from the CO<sub>2</sub> critical temperature. In addition,

the resulting optimal molar compositions of the power cycles adopting mixtures varies with the minimum temperature. The molar composition of the CO<sub>2</sub>+Acetonitrile mixture ranges from 94% (at T<sub>MIN</sub>=45°C, 95% on a mass basis) to 89% (at T<sub>MIN</sub>=65°C, 90% on a mass basis) of CO<sub>2</sub> content, significantly reducing the flammability risks associated to pure acetonitrile. By contrast, the heat released from the sCO<sub>2</sub> cycle is slightly higher than the one from the configurations adopting the mixtures. As no thermal power is rejected into the environment when the cycle minimum temperature is set at 65°C, and no



auxiliary consumptions of the air-cooled condenser are involved, these conditions present an overall efficiency of the CHP system ( $\eta_{Overall}$ ) close to 100%, where only the turbomachinery electromechanical losses contribute to the power lost.

Examining the thermal power recovered in the two HRUs of the cascade cycle (taken as a reference for sake of representation), in Figure 7, it is evident that the fraction recovered at low temperature (60-100°C range) is dominant with respect to the one at high temperature (above 105°C), as defined in Equation (2) and Equation (3). For higher cycle maximum temperatures, nevertheless, the high temperature recovery efficiency can exceed 30%, becoming technically of interest for a user interested in high quality heat. The maximum temperatures of the higher quality heat vary from 170°C to 220°C, depending on the cycle minimum temperature, considering a stream at the inlet of the HT HRU unit at 105°C.

Assuming a reasonable value of thermal power from the exhaust gases for these power plant sizes (between 15 to 30 MW<sub>th</sub>) the power produced from these CHP systems can be around 3-4 MW<sub>el</sub> and 10-25 MW<sub>th</sub>, that can be divided into 4-7 MW<sub>th</sub> in the 105-200°C range and 6-16 MW<sub>th</sub> for state-of-the-art district heating applications.

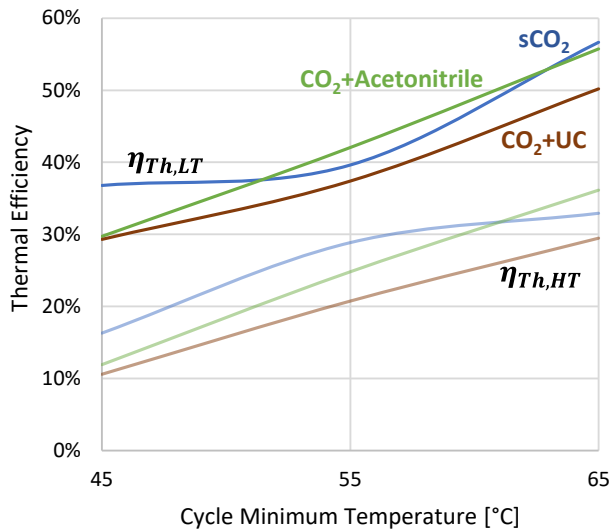


**Figure 7.** Thermal fraction of the thermal input recovered from the cycle HRUs for the cascade layout (Figure 5).

### AVOIDED CO<sub>2</sub> EMISSION AND GAS CONSUMPTION OF THE CHP SYSTEMS

CHP systems are natively adopted with the advantage of reducing both primary energy consumption and carbon emissions. As a matter of fact, carbon emissions related to the thermal sector nowadays are estimated to be around 56 kgCO<sub>2</sub>/GJ<sub>LHV</sub> for natural gas (202 kgCO<sub>2</sub>/MWh<sub>LHV</sub>), while, considering the European energy mix and the share of renewable power production, for the electric sector are estimated at 74 kgCO<sub>2</sub>/GJ<sub>el</sub> (266 kgCO<sub>2</sub>/MWh<sub>el</sub>) [17]. In this work, the avoided carbon emissions are computed for the proposed CHP systems

adopting CO<sub>2</sub>-based cycles, considering as base case a condition where the electric and thermal power are produced separately with two dedicate reference plants.

Figure 8 reports the resulting avoided emissions for the cycle configurations considered in this work. The calculations are carried out assuming only 5 months per year of utilization of the thermal power for district heating purposes, considering as reference scenario a natural gas boiler with an efficiency of 90%. From the figure it is possible to notice that avoided emissions up to 30 or 35 kgCO<sub>2</sub>/GJ<sub>th</sub> of exhaust gases are possible with these systems. sCO<sub>2</sub> cycles allow for a higher share of avoided emissions for cycles minimum temperatures around 45°C, close to the CO<sub>2</sub> critical point, due to the higher fraction of thermal energy recovered with respect to the CO<sub>2</sub>-mixtures power plants (around 50% higher in relative terms). On the other hand, CO<sub>2</sub> mixtures in cycles adopted for CHP configurations present higher avoided carbon emissions when the cycle minimum temperature is high and the overall recovery efficiency is close to 100%, as electricity covers a higher share of the overall power produced from the CHP plant with respect to sCO<sub>2</sub>.

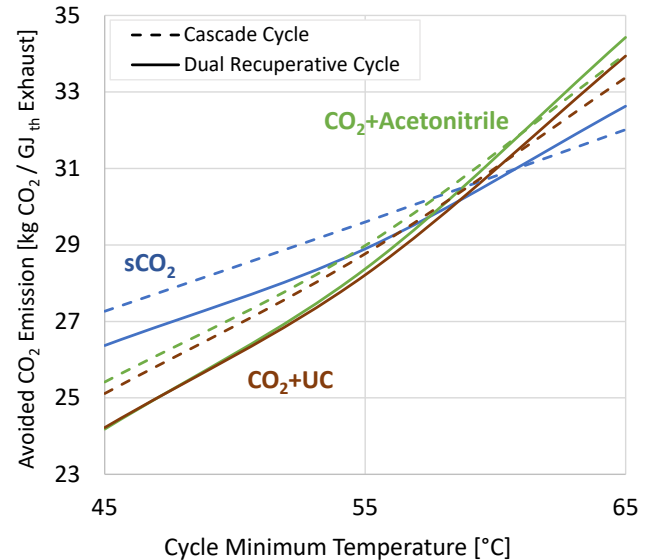


**Figure 8.** Avoided carbon emissions per GJ<sub>th</sub> available from the exhaust gases for the various CHP solutions proposed.

Ultimately, the avoided natural gas consumption is proposed in Figure 9 since it is the main drive of the economic feasibility of any WHR power plant, both for only electricity production and for CHP applications. In practice, for each unit of thermal power released by the exhaust gases in the WHR plant, the CHP systems can avoid the consumption of 0.7 to 1.2 unit of natural gas on LHV terms. The avoided natural gas consumption is computed assuming a reference electric efficiency of 52.5% from natural gas plants (typical of a combined cycle), and the boiler efficiency previously mentioned of 90% for the thermal power generation. Coherently with the carbon emissions trends, a higher avoided fuel consumption is possible for high cycle minimum temperatures, where all heat is recovered and transformed into a useful product and no fraction is rejected in the environment with

air-cooled heat rejection units. As for the avoided emissions, also in terms of natural gas consumption the CO<sub>2</sub>-based mixtures show a slight edge over pure CO<sub>2</sub> in power cycles at high cycle minimum temperatures, in addition to provide a +3.3% electric production from the exhaust gases (more than 27% in relative terms).

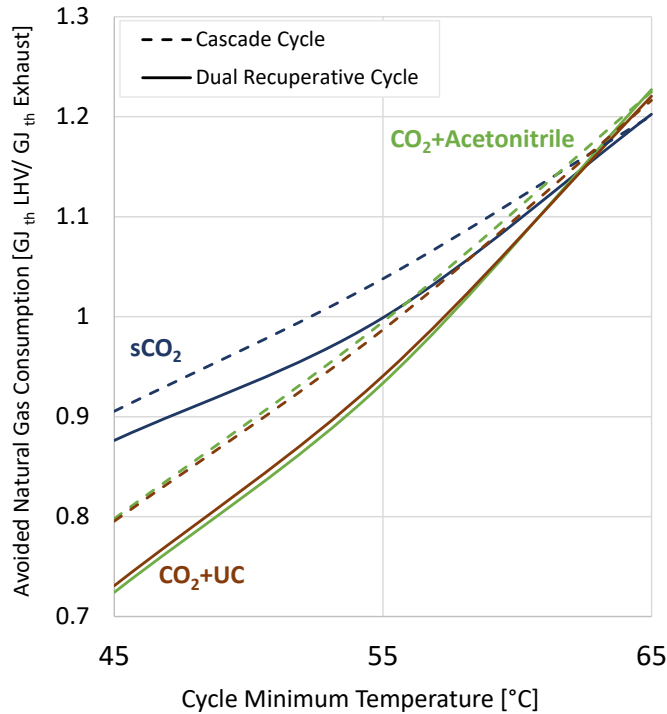


**Figure 9.** Avoided natural gas consumption per GJ<sub>th</sub> available from the exhaust gases for the various CHP solutions proposed.

## COMPARISON WITH ORC FOR ONLY-ELECTRIC WHR SYSTEMS

A comparison between the reported results of CO<sub>2</sub>-based systems and a more conventional ORC for WHR applications is detailed in this chapter. The purpose of this comparison is to investigate the maximum obtainable electric power from the available waste heat with a category of power cycle different than CO<sub>2</sub>-based systems and with a higher level of commercial maturity.

The electric efficiencies of Figure 6 at 45°C of cycle minimum temperature can be already considered as the maximum electric power output of the CO<sub>2</sub>-based systems considered in this work, as all the parameters involved (cycle minimum pressure, molar compositions and mass split ratio) are already optimized to have the maximum electric efficiency for any ambient temperature, in any conditions. At the lowest cycle minimum temperature, the heat recovered in the HRUs for district heating is considered an unavoidable by-product, determined by the high temperature difference across the compression step and the non-negligible pinch point of the recuperator (PCHE), which determines a

certain temperature difference that necessarily must be compensated during the heat rejection. Higher electric efficiencies are theoretically possible with the same working fluids (at constant hot source, ambient temperature and HTF temperature range) only adopting plant layouts different than the one proposed in Figure 4 and Figure 5. Nevertheless, a wider sensitivity analysis on different plant layouts is considered out of the scope in this work. For these reasons, the highest electric efficiency of the proposed CO<sub>2</sub>-based systems for WHR applications adopting air-cooled heat rejection unit are, respectively, 16.5% for the sCO<sub>2</sub> cycle (cascade layout), 19.6% for the CO<sub>2</sub>+Acetonitrile cycle (dual recuperative layout) and 19.2% for the CO<sub>2</sub>+UC cycle (dual recuperative layout).

In contrast to CO<sub>2</sub>-based cycles, ORC systems are investigated in this work only for electricity production from WHR plants adopting the model of Astolfi [18]: nonetheless, future works can potentially explore also ORC in CHP configurations.

Regarding the ORC plant configurations, as the vast majority of the installed ORC plants is based on subcritical cycle, it has been decided to limit the comparison to either saturated or superheated subcritical cycles adopting internal recuperator for pressurized liquid preheating from expanded vapor cooling. The optimization variables considered are the working fluid selected (among a pool of 47 candidate fluids), the evaporation temperature  $T_{eva}$ , the degree of superheating  $\Delta T_{SH}$ , (equal to difference between the maximum temperature of the cycle and the evaporation temperature) and the condensation temperature  $T_{cond}$ . Coherently with CO<sub>2</sub> and CO<sub>2</sub> mixtures cases, an air-cooled condenser is considered also for ORCs, setting the minimum condensation temperature to 45°C and an auxiliary electrical consumption equal to 1% of the rejected heat. For each fluid a different upper bound on the maximum cycle temperature representative of the fluid thermal stability limit has been adopted and set equal to the maximum temperature of the experimental dataset at the base of the reduced Helmholtz energy Equation of State (EOS) provided by Refprop 9.2[19].

Adopting the same assumptions on the cycle non-idealities of Table 1 and the heat source modelling previously described, the numerical tool defines the optimal ORC operating parameters and configurations for each working fluid aiming to maximize the electric power production. Regarding condensation pressure, two cases have been considered: in case A, the lower bound is set to 1 bar in order to prevent air in-leakages due to sub-atmospheric pressures in the condenser while in CASE B this limit has been removed. Table 2 reports the results for the two cases: if minimum pressure is bounded to 1 bar the optimal cycle is cyclopentane showing for this pressure value a saturation temperature (49°C) very close to 45°C that is the lowest possible value. Lower critical temperature cycles are penalized in terms of maximum evaporation pressure that consequently limits cycle pressure ratio, while fluids having a higher critical temperature must condensate at higher temperature with a consequent performance decrease. Differently, if the minimum cycle pressure is not constrained the optimal fluid is Toluene, with a condensing temperature of 45°C and a minimum pressure of around 0.1 bar being able to reach higher evaporation

temperatures. Both cycles are optimized in saturated condition since the inclusion of a superheating for this application is not convenient and it would result in a lower working fluid mass flow rate and a higher turbine outlet temperature that cannot be really exploited without penalizing the heat recovery from the heat source.

**Table 2.** Only-electric ORC solutions for WHR in this work

	CASE A	CASE B
Working fluid	Cyclopentane	Toluene
Flammability / Toxicity	Yes / No	Yes / Yes
Electric efficiency, $\eta_{el}$	19.5%	23.9%
Maximum Pressure [bar]	40	36
Minimum Pressure [bar]	1	0.099
Evaporation temperature [°C]	229	309
Condensation temperature [°C]	49	45

Comparing these results to the ones of CO<sub>2</sub>-based systems, no apparent improvements in cycle efficiency are evident when the ORC with cyclopentane is compared to the two CO<sub>2</sub> mixtures, while a +3.5% in electric efficiency is reported when adopting toluene as working fluid. However, in this case, the cycle minimum pressure results to be sub-atmospheric, leading to criticalities related to air in-leakages in the condenser (an issue not present in CO<sub>2</sub>-based systems). It must be reminded that in ORCs it is not possible to remove the non-condensable gases by venting them in the environment using a deaerator, but instead a vacuum pump and a gas treatment unit are adopted to solve this issue, increasing the cost and complexity of operation of the plant. On the other hand, considering CHP configurations, the most favorable condition shown in this work is the transcritical CO<sub>2</sub>+Acetonitrile cycle at 65°C minimum temperature (15.5% of electric efficiency). The drop in net electric production from the waste heat is not so drastic when moving from an only-electric configuration (ORC) to a CHP plant (CO<sub>2</sub>+Acetonitrile), even considering toluene as adopted working fluid for the ORC. These results suggest a robust performance of the CO<sub>2</sub>-based solutions for CHP plant in WHR applications, as, even with an abundant thermal power recovered, the electric efficiency can still compete with traditional only electric ORC solutions, at least when over-atmospheric ORCs are employed with non-toxic working fluids.

## CONCLUSIONS

An innovative concept of CHP plants is presented in this paper, applied to a waste heat source of a generic industrial process. In fact, CO<sub>2</sub>-based power cycles (both pure sCO<sub>2</sub> cycles and transcritical cycles working with binary CO<sub>2</sub> mixtures) allow for non-isothermal heat rejection from the power cycle, in any condition. Thanks to this characteristic they can be adopted efficiently both for WHR applications and in CHP configuration (by recovering the rejected heat at a temperature higher than 60°C), simply by imposing a high cycle minimum temperature. This work underlines the beneficial aspects derived from the selection of CO<sub>2</sub>-based working fluids for low-temperatures

(< 400°C) power cycles adopted in WHR applications. It details these advantages especially when the plant location allows for a district heating network and the use of high temperature heat for additional industrial processes, both from a technical point of view and an environmental one. In fact, the recovery of a large contribution of sensible useful heat from the heat rejection unit of the cycle is the main focus of this work. These CHP systems can also be adopted in a trigenerative perspective to produce cold thermal load for residential applications, with the adoption of an absorption chiller fed by the hot thermal power normally distributed through the district heating network.

In addition, the higher electric efficiency of the WHR cycles based on CO<sub>2</sub>-mixtures are evidenced with respect to sCO<sub>2</sub> cycles due to the adoption of transcritical cycles in place of supercritical ones, an effect that intensifies at low temperature difference between the hot source and cold sink of the cycle. In addition, innovative working fluids like CO<sub>2</sub>-mixtures are proposed as an attractive technical solution for conditions where cogeneration is of interest without drastically compromising the electric efficiency of the CHP plant with respect to a more conventional solution for WHR applications, like a state-of-the-art ORC-based power system.

The mixture CO<sub>2</sub>+Acetonitrile is highlighted as an efficient working fluid in these conditions, converting 15.5% of the waste heat in electric power and more than 80% in thermal power, both for district heating (60-100°C range) and potentially to supply high quality heat for industrial needs (105-220°C range). Future works will certainly expand the pool of possible dopants for CO<sub>2</sub>-mixtures to be adopted in such applications, characterized by a working fluid maximum temperature in the order of 400°C. The thermal and electric power produced by these CO<sub>2</sub>-based power cycles in CHP configuration can potentially avoid the emission of up to 34 kg<sub>CO2</sub> and the consumption of more than 1.1 GJ<sub>th,LHV</sub> per unitary GJ<sub>th</sub> recovered from the exhaust gases, if compared to a reference scenario where the thermal and electric power are produced, separately, from conventional natural gas-based plants.

## NOMENCLATURE

### *List of abbreviations*

CAS – Chemical Abstracts Service number  
CHP – Combined Heat and Power  
EoS – Equation of State  
EU – European Union  
H&C – Heating and Cooling  
HE or HX – Heat Exchanger  
HRU – Heat Rejection Unit  
HT – High Temperature  
HTF – Heat Transfer Fluid  
HP – High Pressure  
ICE – Internal Combustion Engines  
MITA – Minimum Internal Temperature Approach  
ORC – Organic Rankine Cycle  
LHV – Lower Heating Value  
LP – Low Pressure  
LT – Low Temperature  
PCHE – Printed Circuit Heat Exchanger  
PHE – Primary Heat Exchanger  
PR – Peng Robinson  
sCO<sub>2</sub> – supercritical CO<sub>2</sub>  
SH – SuperHeating  
TIT – Turbine Inlet Temperature [°C]  
WHR – Waste Heat Recovery  
UC – Unnamed Compound  
VLE – Vapor Liquid Equilibrium

### *List of symbols*

$h$  – Specific enthalpy [kJ/kg]  
 $\dot{m}$  – Mass flow rate [kg/s]  
 $p$  – Pressure [bar]  
 $Q$  or  $\dot{Q}$  – Thermal Power [MW]  
 $s$  – Specific entropy [kJ/(kg·K)]  
 $T$  – Temperature [°C]  
 $\eta_{el}$  – Electric efficiency [-]  
 $\eta_{Th}$  – Thermal efficiency [-]

## ACKNOWLEDGEMENTS

This paper is part of the DESOLINATION project that has received funding from the European Union's Horizon 2020 research and innovation programme under grant agreement N. 101022686.

## REFERENCES

- [1] A. Mahmoudi, M. Fazli, and M. R. Morad, "A recent review of waste heat recovery by Organic Rankine Cycle," *Appl Therm Eng*, vol. 143, pp. 660–675, Oct. 2018, doi: 10.1016/J.APPLTHERMALENG.2018.07.136.
- [2] D. Alfani, M. Binotti, E. Macchi, P. Silva, and M. Astolfi, "sCO<sub>2</sub> power plants for waste heat recovery: design optimization and part-load operation strategies," *Appl Therm Eng*, vol. 195, p. 117013, Aug. 2021, doi: 10.1016/J.APPLTHERMALENG.2021.117013.
- [3] G. Manente and M. Costa, "On the Conceptual Design of Novel Supercritical CO<sub>2</sub> Power Cycles for Waste Heat Recovery," *Energies 2020, Vol. 13, Page 370*, vol. 13, no. 2, p. 370, Jan. 2020, doi: 10.3390/EN13020370.
- [4] S. A. Wright, C. S. Davidson, and W. O. Scammell, "Thermo-Economic Analysis of Four sCO<sub>2</sub> Waste Heat Recovery Power Systems," *The 5th International Symposium - Supercritical CO<sub>2</sub> Power Cycles*, pp. 1–16, 2016.
- [5] "Waste Heat Recovery Power Generation | Echogen Power Systems." <https://www.echogen.com/> (accessed Oct. 25, 2022).
- [6] "Scarabeus H2020 Project." <https://www.scarabeusproject.eu/> (accessed Oct. 01, 2021).
- [7] "Desolination H2020 Project." <https://desolination.eu/> (accessed Oct. 25, 2022).
- [8] E. Macchi and M. Astolfi, *Organic Rankine Cycle (ORC) Power Systems - Technologies and applications*. Elsevier, 2017. doi: 10.1016/C2014-0-04239-6.
- [9] Eurostat, "Energy statistics-an overview Statistics Explained".
- [10] J. Malinauskaite, H. Jouhara, L. Ahmad, M. Milani, L. Montorsi, and M. Venturelli, "Energy efficiency in industry: EU and national policies in Italy and the UK," *Energy*, vol. 172, pp. 255–269, Apr. 2019, doi: 10.1016/J.ENERGY.2019.01.130.
- [11] H. Jouhara and A. G. Olabi, "Editorial: Industrial waste heat recovery," *Energy*, vol. 160, pp. 1–2, Oct. 2018, doi: 10.1016/J.ENERGY.2018.07.013.
- [12] G. Bianchi *et al.*, "Estimating the waste heat recovery in the European Union Industry," *Energy Ecol Environ*, vol. 4, no. 5, pp. 211–221, Oct. 2019, doi: 10.1007/s40974-019-00132-7.
- [13] M. Papapetrou, G. Kosmadakis, A. Cipollina, U. La Commare, and G. Micale, "Industrial waste heat: Estimation of the technically available resource in the EU per industrial sector, temperature level and country," *Appl Therm Eng*, vol. 138, pp. 207–216, Jun. 2018, doi: 10.1016/J.APPLTHERMALENG.2018.04.043.
- [14] T. Fleiter, "Profile of heating and cooling demand in 2015," 2017.
- [15] M. J. Lazzaroni, D. Bush, J. S. Brown, and C. A. Eckert, "High-pressure vapor-liquid equilibria of some carbon dioxide + organic binary systems," *J Chem Eng Data*, vol. 50, no. 1, pp. 60–65, Jan. 2005, doi: 10.1021/JE0498560.
- [16] R. Span and W. Wagner, "A New Equation of State for Carbon Dioxide Covering the Fluid Region from the Triple-Point Temperature to 1100 K at Pressures up to 800 MPa," *J Phys Chem Ref Data*, vol. 25, no. 6, pp. 1509–1596, Nov. 1996, doi: 10.1063/1.555991.
- [17] "Greenhouse gas emission intensity of electricity generation in Europe — European Environment Agency." <https://www.eea.europa.eu/data-and-maps/indicators/overview-of-the-electricity-production-3/assessment> (accessed Oct. 25, 2022).
- [18] M. Astolfi, D. Alfani, S. Lasala, and E. Macchi, "Comparison between ORC and CO<sub>2</sub> power systems for the exploitation of low-medium temperature heat sources," *Energy*, vol. 161, pp. 1250–1261, Oct. 2018, doi: 10.1016/J.ENERGY.2018.07.099.
- [19] NIST - National Institute of Standards and Technology, "REFPROP - Reference Fluid Thermodynamic and Transport Properties."

## PART LOAD ANALYSIS OF A CONSTANT INVENTORY SUPERCRITICAL CO<sub>2</sub> POWER PLANT FOR WASTE HEAT RECOVERY IN CEMENT INDUSTRY

**Dario Alfani**  
Politecnico di Milano  
Milano, Italy

**Marco Astolfi\***  
Politecnico di Milano  
Milano, Italy  
Marco.astolfi@polimi.it

**Marco Binotti**  
Politecnico di Milano  
Milano, Italy

**Paolo Silva**  
Politecnico di Milano  
Milano, Italy

**Giacomo Persico**  
Politecnico di Milano  
Milano, Italy

### ABSTRACT

*The present work investigates the part-load performance of a MW-scale sCO<sub>2</sub> power plant designed as heat recovery unit for an existing cement plant located in Czech Republic, in the framework of the H2020 funded project CO2OLHEAT. The study firstly presents the selected power plant configuration and then focuses on the evaluation of its part load operation due to variation of flue gas mass flow rate and temperature. The range of flue gas conditions at the outlet of the upstream process is retrieved from a preliminary statistical analysis of historical trends obtained through the cement plant monitoring. The numerical model developed for this study aims at providing realistic results thanks to the adoption of turbomachinery performance maps provided by the project partners. Moreover, heat exchangers have been modelled through a discretized approach which has been validated against manufacturer data, while piping inventory and pressure losses have been assessed through a preliminary sizing that considers the actual distances to be covered in the cement plant. Performance decay is estimated for the whole range of flue gas conditions, reporting the most significant power cycle parameters, and identifying the main causes of efficiency loss. The part-load analysis is carried out considering a constant CO<sub>2</sub> inventory, in order to reduce the system complexity and capital cost and simplify plant operation. Results show that the operation entails minor variation of the compressors operative points in the whole range of operating conditions of the cement plant, avoiding the risk of anti-surge bypass activation. Moreover, the plant is able to work at nearly constant thermodynamic cycle efficiency (20.5%-23.0%) for most of the year and benefits from part-load operation in terms of overall performance. These predictions will be used, in next steps of the project, to guide the definition of power plant control during transients related to changes of upstream process conditions or specific needs of power output control.*

\* marco.astolfi@polimi.it

### INTRODUCTION AND SCOPE OF WORK

Waste heat-to-power is one of the main assets to improve the energy efficiency and reduce the footprint of the industrial sector [1][2]. Although the presence of commercial technologies (i.e. Organic Rankine Cycles - ORC for small-scale low-temperature [3] and steam power plants for larger and higher temperature applications [4]), a huge market potential is available for new concepts especially when waste heat is available at mid-to-high temperature [5][6], as for example in the cement production sector [7]. Supercritical carbon dioxide (sCO<sub>2</sub>) power plants are widely recognized as a very promising technology for several applications based on solar energy [8][9], IV<sup>th</sup> generation nuclear reactors [10][11], fossil fuels [12][13] and also waste heat recovery [14], thanks to more compact and less expensive turbomachinery, higher flexibility than steam power plants [15] and higher performance with respect to ORCs [14].

This study focuses on the off-design simulation of a sCO<sub>2</sub> power plant designed as heat recovery unit for an existing cement plant in the framework of the H2020 funded project CO2OLHEAT [16]. The selected cement plant is located in Prachovice, Czech Republic, and its operation undergoes variable conditions depending on the load and the activation of raw mills. This implies a variation in the thermodynamic conditions of the hot flue gas available for the waste heat recovery process, eventually affecting the performance and the operation of the bottoming sCO<sub>2</sub> power unit. The knowledge of the expected trend for sCO<sub>2</sub> cycle main thermodynamic quantities and operating parameters is of fundamental importance for both finalizing the design of each component and for the definition of the control system ensuring a safe, reliable, and efficient operation of the power plant. The understanding of the power plant adaptation to a variation of a specified boundary condition requires a properly developed numerical tool and the

DOI: 10.17185/dupublico/77288



knowledge of detailed information on the design of the main components, namely the turbomachinery and heat exchangers. This paper aims at providing such information, so to demonstrate the potential of sCO<sub>2</sub> power units in the cement production sector and to provide insights on general industrial waste heat recovery characterized by similar waste heat potential. The off-design analysis investigates both the effect of flue gas flow rate and temperature variations that have been retrieved from a preliminary statistical analysis of historical trends obtained from the cement plant monitoring. Mass flow rate of flue gas released from the cement plant are mainly affected by the number of active raw mills, while flue gas temperature simply varies in a narrow range between 400°C and 370°C. The most representative operating conditions of the selected cement plant are reported in Table 1. The nominal flue gas conditions are assumed for the cement plant running with no active raw mills: flue gas mass flow rate of 230'000 Nm<sup>3</sup>/h (situation occurring approximately 5% of the year) and flue gas temperature equal to 400°C.

Table 1: Most representative cases of the cement plant operation (in brackets the fraction of time in which each condition occurs in a year).

	T <sub>FG</sub> =400°C	T <sub>FG</sub> =370°C
<b>No raw mills in operation (5%)</b> 230'000 Nm <sup>3</sup> /h of FG available	Case A (nominal)	Case D
<b>One raw mill in operation (85%)</b> 165'000 Nm <sup>3</sup> /h of FG available	Case B	Case E
<b>Two raw mills in operation (10%)</b> 100'000 Nm <sup>3</sup> /h of FG available	Case C	Case F

### NOMINAL POWER PLANT DESIGN

The nominal design of the power plant is based on the assumptions defined in the framework of the CO2OLHEAT project and agreed with all the consortium partners, including constraints and specifications of component manufacturers as Baker Hughes (BH), Siemens Energy (SIE), Bosal and Heatric. The plant is based on a simple recuperated cycle without neither recompression nor recuperator bypass, as reported in Figure 1: the choice is motivated by the relatively low maximum temperature of the heat source (i.e., the flue gas) and the high minimum stack temperature in order to avoid acid condensates (150°C). Minimum cycle thermodynamic conditions are set to 32°C and 85 bar to properly exploit the high density of CO<sub>2</sub> in the proximity of the critical point and improve thermodynamic cycle efficiency. The maximum cycle pressure at compressor outlet is set to 216.9 bar, which correspond to a turbine inlet pressure of around 210 bar, a value considered a good tradeoff between cycle performance, component manufacturability and techno-economic feasibility. Resulting cycle pressure ratio is equal to 2.55 and it is achieved with two centrifugal compressors in series that have been designed by BH. The compressors are installed on the same shaft and are mechanically driven by two centripetal turbines in series, thus creating a compact turbo-expander unity. To ensure a safe start-up of the system and to properly balance the power required by the compressors and the power delivered by BH turbine in all operating conditions, an

electric motor (“helper”) is connected to the shaft, consuming 246 kW of electric power in nominal conditions. In this study a direct flue gas-pressurized CO<sub>2</sub> primary heat exchanger has been preferred to the use of an heat transfer fluid (HTF) loop based on diathermic oil. Goal is to maximize turbine inlet temperature, reduce the complexity of the system and avoid a large inventory of flammable liquid on site eventually leading to a possible reduction of capital and operational cost related to additional equipment, piping and fire protection. On the other hand, the use of a HTF loop would be preferable in case of lack of space close to the upstream process or in case of discontinuous process where the use of thermal storage allows to decouple waste heat recovery and power production. According to the use of direct heat introduction, maximum temperature of the cycle is set at 360°C, namely 40°C lower than the flue gas nominal temperature in order to design with a reasonable heat transfer area. The expansion is then completed in a power turbine, designed by SIE, that exploits the residual pressure ratio and produces the electrical power output by means of an electrical generator. Power turbine operation can be controlled with an admission valve that involves a pressure drop of 0.3 bar in wide open position. A CO<sub>2</sub> mass flow rate of 1 kg/s is extracted downstream of the compressors and reintroduced in the power cycle to compensate for Dry Gas Seals (DGS) leakages in the turbines (0.5 kg/s for mechanical drive turbine and 0.4 kg/s for power turbine) and injected in minor amount upstream of the cooler (0.1 kg/s). Turbomachinery efficiencies are assumed equal to the preliminary nominal values provided by manufacturers: 73% for the compressors, 84% for the mechanical-drive turbines, and 82% for the power turbine. An additional efficiency loss equal to 5% is accounted for mechanical and electrical losses in both shafts.

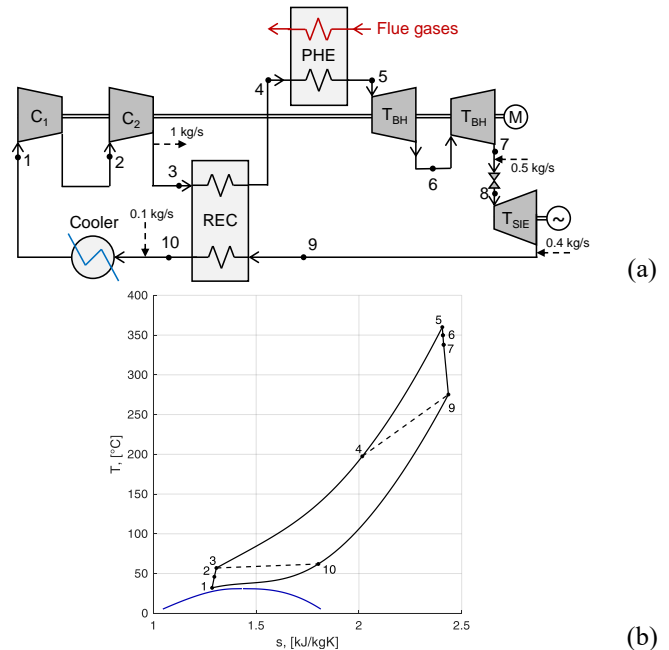


Figure 1: Layout (a) and T-s (temperature-specific entropy) diagram (b) of the sCO<sub>2</sub> power cycle.

The heat transfer surfaces and internal volumes of the different heat exchangers are calculated by matching the assumed pressure drops by means of numerical routines proprietary of Politecnico di Milano, mostly based on previous experience from the H2020 sCO<sub>2</sub>-Flex project [17].

The Primary Heat Exchanger (PHE) consists of a finned tube HX with direct heat transfer between flue gas and the CO<sub>2</sub>, modelled through the same methodology presented in [14]. Supercritical carbon dioxide flows inside the tubes while the flue gas stream flows across the finned tubes bundles. The recuperator is designed as a printed circuit heat exchanger (PCHE) with a pinch point temperature difference of 5°C and pressure losses on the low pressure (LP) side and high pressure (HP) side of 1.25 bar and 0.75 bar respectively, as suggested by the consortium partner Heatric, responsible of the recuperator design. The cooler is designed as several dry air-cooled heat exchangers bays arranged in parallel: each single unit is made up of batteries consisting of different rows of small diameter aluminum finned copper tubes through which air is blown or sucked by fans. The CO<sub>2</sub> side pressure drop in the component is estimated to be equal to 4 bar.

Piping length and diameter have been determined by consortium partner Simerom through a preliminary analysis of the distances to be covered in the cement plant. This data is particularly useful for an accurate evaluation of the pressure losses of the sCO<sub>2</sub> power cycle as well as for the estimation of the CO<sub>2</sub> inventory held within the system, equal to 1551.7 kg. The resulting net power output is 2.17 MW, with a cycle efficiency of 23.17% referred to the inlet thermal power and 11% if referred to the maximum power available from flue gas cooling down to 150°C, a limit generally imposed to avoid the condensation of acid compounds.

## OFF DESIGN SIMULATION NUMERICAL APPROACH

In this work the use of a CO<sub>2</sub> tank/vessel for active inventory change is not implemented in order to maintain the control strategy of the plant as simple as possible and to reduce the system capital cost. The compressors are operated at fully open (0°) Inlet Guide Vanes (IGV) and their efficiency is calculated based on the operating maps provided in Figure 2. During off-design operation the first compressor inlet temperature is maintained equal to the nominal value (32°C) by regulating the cooling air mass flow rate in the HRU, while cycle minimum pressure is not controlled and varies according to the constant inventory operation. Mechanical drive turbines work in sliding pressure operation: their isentropic efficiency and reduced mass flow rate (see Equation (1)) are characterized with the correlations reported in Figure 3.a as function of the ratio  $u/c$  between the peripheral speed  $u$  and the spouting velocity  $c$ , defined according to Equation (2). The power turbine operation is computed through the same methodology but using the turbine pressure ratio as the input parameter (see Figure 3.b). The admission valve at power turbine inlet is not employed in steady-state operation in order to maximize cycle performance and CO<sub>2</sub> leakages mass flow rates due to DGS are considered constant and equal to design values for all off-design operation.

Finally, the heat exchangers in off-design conditions are simulated computing the heat transfer coefficients for both the CO<sub>2</sub> and the flue gas while the HXs pressure drops are updated with the simplified correlation reported in Equation (3).

$$m_{red,turb} = \frac{\dot{m}\sqrt{T}}{p} \Big|_{in,turb} \quad (1)$$

$$c = \sqrt{2 \cdot \Delta h_{is,turb}} \quad (2)$$

$$\Delta p = \Delta p_{nom} \left( \frac{\rho_{nom}}{\rho} \right) \left( \frac{\dot{m}}{\dot{m}_{nom}} \right)^2 \quad (3)$$

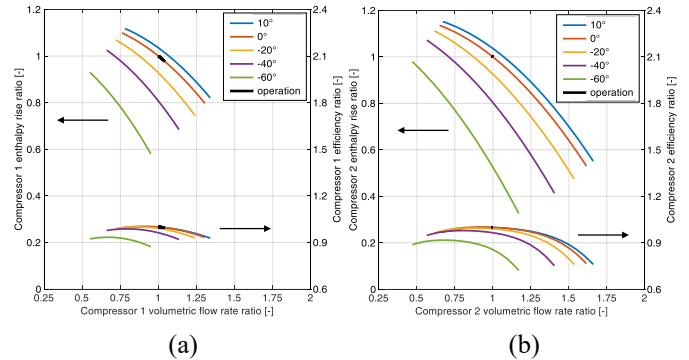


Figure 2: First (a) and second (b) compressor operating maps (normalized enthalpy rise and efficiency) as function of the normalized volumetric flow rate.

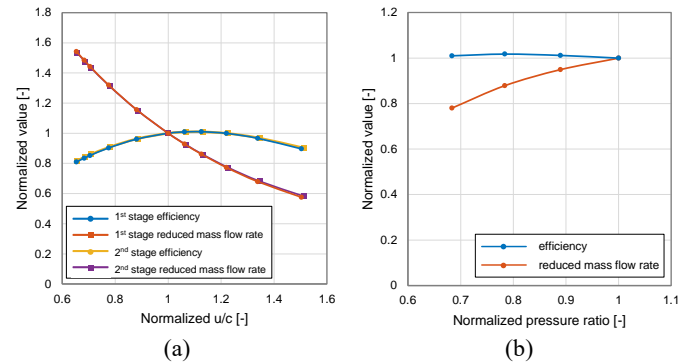


Figure 3: Baker Hughes (a) and Siemens (b) turbine operating curves (normalized reduced mass flow rate and efficiency) as function of the normalized ratio ( $u/c$ ) and turbine pressure ratio, respectively.

## OFF DESIGN RESULTS

The off-design analysis investigates both the effect of flue gas flow rate and temperature deviation from nominal conditions. In particular, in the numerical simulations these two parameters are varied in the following ranges as suggested by the statistical analysis of historical data:

- Flue gas flow rate is varied from the nominal value (230'000 Nm<sup>3</sup>/h, no raw mills in operation) to 40% of the nominal value, corresponding to 92'000 Nm<sup>3</sup>/h.
- Flue gas temperature is varied from the nominal value, equal to 400°C, to 370°C.

As the combined effect of these two flue gas condition variations is investigated, the results of the off-design analysis

are presented as contour maps displaying how the main parameters and figures of merit of the sCO<sub>2</sub> power cycle vary in off-design operation. Cases A to F (see Table 1) are reported with markers and letters on the displayed maps.

### Heat recovery from flue gas

The flue gas temperature at PHE outlet is not controlled and tend to decrease during part-load operation (see Figure 4.a) due to the fact that the PHE surface results oversized in part-load conditions. For this reason, the thermal power input to the cycle decreases less than the flue gas mass flow rate for the same heat source temperature, as reported in Figure 4.b. For example, Case C, characterized by nominal flue gas temperature equal to 400°C and a reduction of 56% of the mass flow rate, implies a decrease of heat input to the cycle of only ~14%. During part load operation the plant tends to exploit a larger fraction of the thermal power available from the exhausts, whose maximum amount can be calculated considering a minimum stack temperature of the exhausts  $T_{FG,min}$  equal to 150°C. As a result, reducing the flue gas mass flow rate allows increasing the heat recovery factor  $\chi_{rec}$  (see Equation (4) and Figure 4.c) from the nominal value of 0.47 to a value close to 1 for case F.

$$\chi_{rec} = \frac{\dot{Q}_{in,cycle}}{\dot{Q}_{FG,max}} = \frac{\dot{m}_{FG} c_{p,FG} (T_{FG,max} - T_{stack})}{\dot{m}_{FG} c_{p,FG} (T_{FG,max} - T_{FG,min})} \quad (4)$$

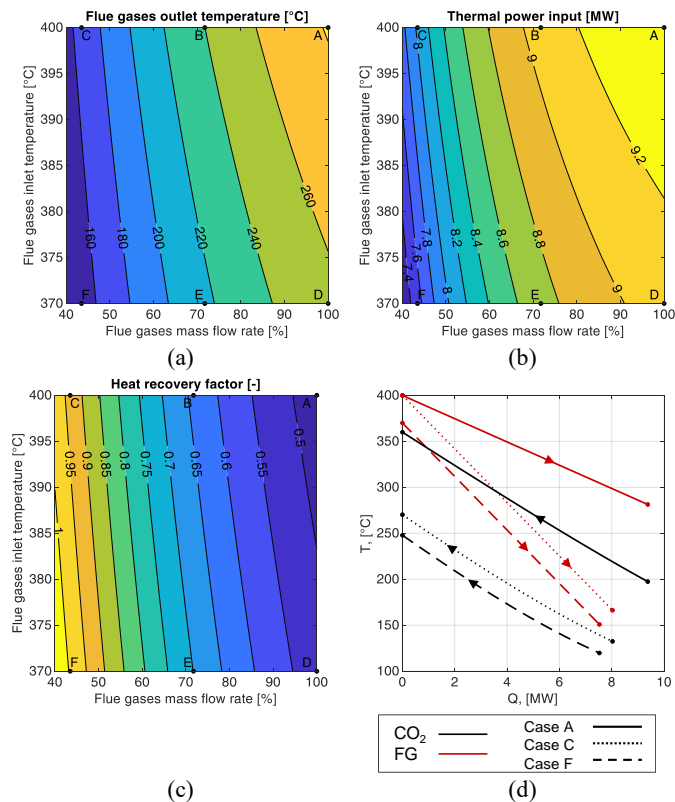


Figure 4: Flue gas temperature at PHE outlet (a), thermal power transferred in the PHE (b) and heat recovery factor as function of off-design flue gas conditions. PHE T-Q diagram for cases A, C, F (d).

This aspect is also clearly visible from the T-Q diagrams (temperature – thermal power) of the PHE which is depicted for case A (nominal), case C (minimum FG flow rate) and F (minimum FG flow rate and minimum temperature) in Figure 4.d. Cases with minimum FG flow rate are characterized by smaller duty but a lower FG minimum temperature and thus a larger heat recovery factor. Moreover, it is also noticeable how the CO<sub>2</sub> temperature at the outlet of PHE (i.e., the maximum cycle temperature) tends to decrease for low flue gas mass flow rates (cases C and F in Figure 4.d).

### Power plant operating conditions

The CO<sub>2</sub> temperature at the outlet of PHE (first turbine inlet temperature) and the CO<sub>2</sub> mass flow rate processed in the power cycle are reported in Figure 5.a and Figure 5.b, respectively. While maximum cycle temperature decreases rapidly when FG mass flow rate reduces, the CO<sub>2</sub> mass flow rate in the power cycle tends to remain fairly constant, as it is proportional to the slope of the CO<sub>2</sub> profile in the T-Q diagram, which remains similar. Its value passes from 45.5 kg/s of the nominal conditions to a value equal to 40.4 kg/s in case F (-11.2%).

Figure 5.c and Figure 5.d depict the cycle maximum and minimum pressure as function of the flue gas conditions. It is possible to notice that, as the flue gas mass flow rate and temperature decrease, both pressure levels decrease as a result of the sliding pressure operation of the turbines and the strong reduction of average CO<sub>2</sub> temperature in the PHE.

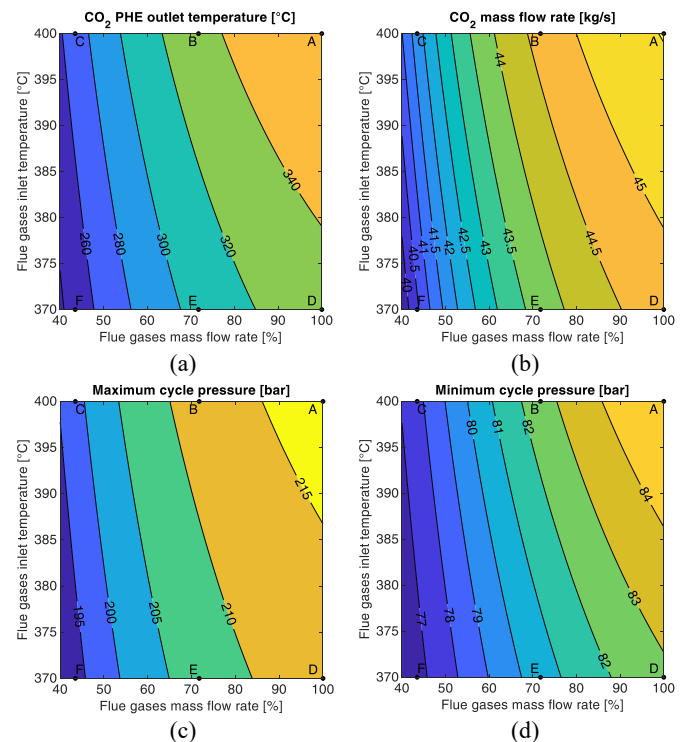


Figure 5: CO<sub>2</sub> temperature at PHE outlet (a), CO<sub>2</sub> mass flow rate processed by the cycle (b), cycle maximum (c) and minimum pressure (d) as function of the off-design flue gas conditions.

The cycle maximum pressure passes from a nominal value of 216.9 bar to a value of 193.2 bar for case F while, for the same case, the minimum pressure decreases from 85 bar to 76.7 bar. On the other hand, the cycle pressure ratio variation in the whole off-design operation is limited, with a maximum variation range restricted to  $-2.3/+0.9\%$ .

### Turbines, generator and electrical helper operation

Figure 6.a depicts the power required by the electric helper balancing the turbo-expander shaft. The electric consumption increases from 246 kW (Case A nominal condition) to 330 kW (Case F), mainly due to the decrease of the maximum cycle temperature (i.e., the first turbine inlet temperature) at nearly constant cycle pressure ratio.

Maximum cycle temperature reduction leads to a consequent decrease of CO<sub>2</sub> temperature at power turbine inlet (Figure 6.c) and also a reduction of its specific work as it is possible to notice from Figure 6.d, where power turbine isentropic enthalpy drop varies from a design point condition of 69.0 kJ/kg to a value of 47.8 kJ/kg (-31%) in case F. As a consequence, although the CO<sub>2</sub> mass flow rate is little affected, the SIE turbine power output appreciably decreases from more than 2.4 MW in the design condition down to slightly less than 1.6 MW in condition F (see Figure 6.b).

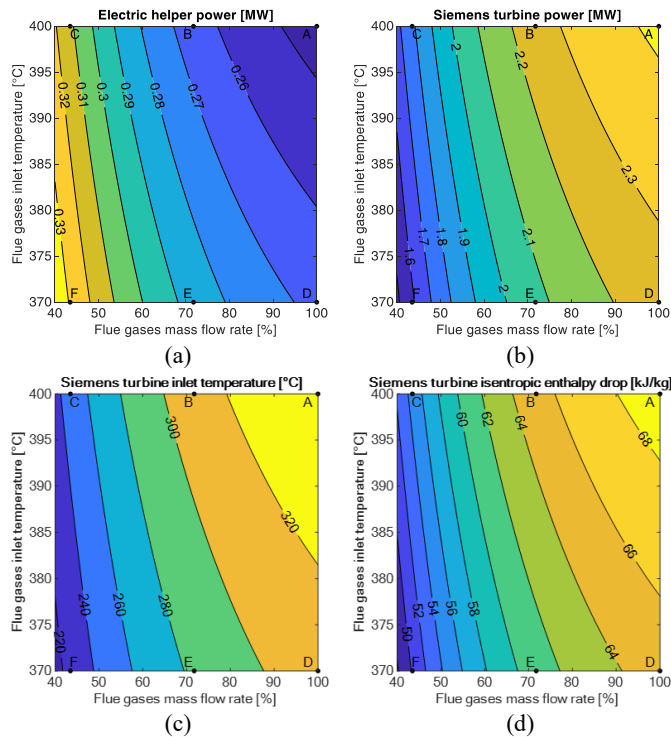


Figure 6: Electric helper power consumption (a), Siemens turbine power (b), Siemens turbine inlet temperature (c) and isentropic enthalpy drop (d) as function of the off-design flue gas conditions.

### Compressors operation

Considering the whole range of off-design operation of the plant, while the first compressor operating point deviates only slightly from the nominal conditions, for the second compressor the variation is almost negligible, as noticeable from Figure 2.a and Figure 2.b, respectively.

This aspect is due to the almost constant volumetric flow rate at both compressors inlet, due to the combined effect of the slight decrease of both the CO<sub>2</sub> mass flow rate and the cycle minimum pressure, which cause a consequent reduction of the inlet density to the compressors (Figure 7.a and Figure 7.b). As a consequence, the efficiency variation during off-design operation of these two components is very limited.

### Net power output and cycle performance

In part load operation cycle efficiency (Figure 8.b) decreases from a nominal value of 23.2% (case A) to a minimum value of 16.7% (case F), corresponding to  $-28\%$  in relative terms. However, the performance decay is not constant across the operation range and there is a wide span of conditions where the performance remains close to the nominal one. In particular, considering the actual cement plant operation, the sCO<sub>2</sub> power system can be operated with a conversion efficiency above 20% for most of the year, as the cases B and E, which represent 85% of the yearly operation, feature a cycle efficiency of 21.9% and 20.5%, respectively. On the other hand, in these two conditions the waste heat recovery plant can achieve a lower net power output, ranging from 1.79 MW to 1.99 MW.

Considering the whole range of the cement plant operation, the net power output (Figure 8.a) decreases from a nominal value of 2.17 MW to 1.26 MW ( $-41.8\%$ ) of electricity generated in the most penalizing condition (case F) as a consequence of the consumption increase of electric helper installed on the turbo-expander shaft as well as of the decrease of SIE power turbine electric output. Nevertheless, this result can be considered encouraging as it is obtained with both a reduction of the available flue gas mass flow rate, equal to  $-56\%$ , and a decrease of 30°C of their maximum temperature.

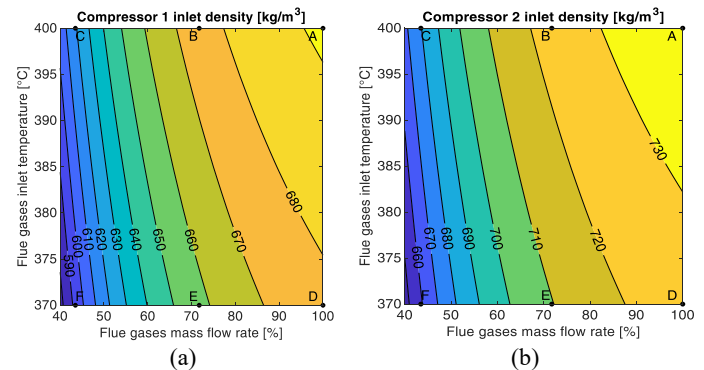


Figure 7: First (a) and second (b) compressor CO<sub>2</sub> inlet density as function of the off-design flue gas conditions.



Actually, it is possible to notice that the overall plant efficiency (Figure 8.c), defined as the product of the cycle efficiency and the heat recovery factor, increases in part load operation, and presents a maximum close to case C operating conditions (around 17.1% vs. 11% in nominal conditions, equal to +55.5% in relative terms), thanks to the increase of heat source exploitation. In such condition the flue gases have a stack temperature very close to the temperature limit to avoid acid condensates (150°C). Table 2 reports a summary of the main results for the most representative cases.

## CONCLUSIONS

This paper presents the numerical assessment of the part-load performance of a sCO<sub>2</sub> power plant for a waste heat recovery application in a cement plant, in the frame of the H2020 funded project CO2OLHEAT. This study demonstrates the possibility to operate waste heat recovery unit based on sCO<sub>2</sub> power cycles at constant CO<sub>2</sub> inventory. This solution not only allows to decrease the installation cost, but also largely simplifies the system operation at part-load and the power plant control system. Numerical results show how the pressure ratio and CO<sub>2</sub> mass flow rate remain relatively constant in the whole range of the cement plant operation, allowing to limit turbomachinery off-design performance decay. As a result, even operating the compressors with fixed IGV aperture, their operative points remain very close to nominal conditions, limiting the issues related to loss of performance and anti-surge bypass activation. This brings to the possibility to operate the plant for most of the year (90%) with an efficiency close to the nominal one.

Furthermore, in spite of a reduction of cycle conversion efficiency at part load operation, the overall plant efficiency actually increases as the sCO<sub>2</sub> power cycle tends to exploit a larger fraction of the thermal power available from the exhausts.

For example, by reducing by about 50% the flue gas mass flow rate at the nominal temperature, even if the cycle efficiency decreases by approximately 5 points (from the nominal value of

23.2% to 18.3%), the heat recovery factor almost doubles (from 47.5% to 93.5%), thus resulting in an overall plant efficiency increase of more than 50 % in relative terms (passing from 11.0% to 17.1%). These results will provide useful insights in the next steps of the CO2OLHEAT project, in particular to guide the definition of power plant control system.

A techno-economic analysis of the plant will represent the following step of this work.

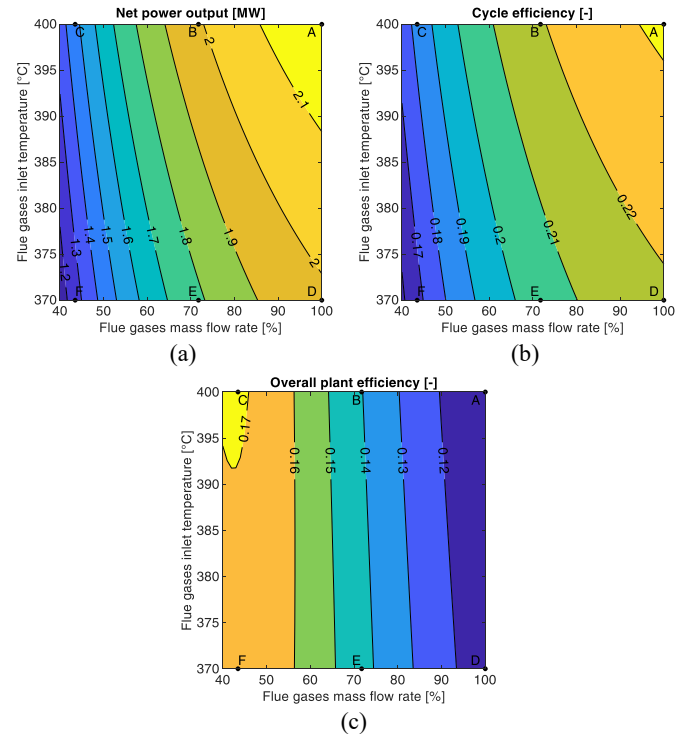


Figure 8: Net power output of the plant (a), cycle efficiency (b) and overall conversion efficiency (c) as function of the off-design flue gas conditions.

Table 2: Summary of the main results for the most representative cases

	A	B	C	D	E	F
<b>sCO<sub>2</sub> thermodynamic cycle</b>						
CO <sub>2</sub> mass flow rate [kg/s]	45.52	44.66	41.74	44.76	43.71	40.42
Maximum pressure [bar]	85.00	82.57	77.72	82.80	80.50	76.71
Minimum pressure [bar]	216.90	211.99	198.41	212.48	207.18	193.24
CO <sub>2</sub> temperature at PHE outlet [°C]	360.0	333.1	270.2	331.4	305.7	247.9
<b>Heat and power balance</b>						
Flue gas thermal power [MW]	19.76	14.17	8.59	17.39	12.47	7.56
Cycle thermal power input [MW]	9.38	9.07	8.03	9.08	8.72	7.53
Compressor 1 power [MW]	0.574	0.562	0.519	0.563	0.548	0.500
Compressor 2 power [MW]	0.547	0.537	0.503	0.538	0.526	0.488
BH turbine power [MW]	0.875	0.834	0.711	0.834	0.788	0.658
Siemens turbine power [MW]	2.42	2.25	1.78	2.25	2.07	1.59
Electric helper power [MW]	0.246	0.265	0.312	0.268	0.286	0.329
Net power output [MW]	2.17	1.99	1.47	1.98	1.79	1.26
<b>Heat and power balance</b>						
Cycle efficiency [%]	23.17	21.91	18.30	21.81	20.47	16.69
Heat recovery factor [%]	47.46	64.03	93.48	52.23	69.93	99.59
Overall plant efficiency [%]	11.00	14.03	17.11	11.39	14.31	16.63

## NOMENCLATURE

### List of abbreviations

DGS – Dry Gas Seals  
EU – European Union  
FG – Flue gas  
HP – High Pressure  
HTF – Heat Transfer Fluid  
HX or HE – Heat Exchanger  
IGV – Inlet Guide Vanes  
LP – Low Pressure  
PCHE – Printed Circuit Heat Exchanger  
PHE – Primary Heat Exchanger  
sCO<sub>2</sub> – supercritical CO<sub>2</sub>  
WH2P – Waste Heat to Power  
WP – Work Package

### List of symbols

$c_p$  – Specific heat capacity [kJ/kgK]  
 $h$  – Specific enthalpy [kJ/kg]  
 $\dot{m}$  – Mass flow rate [kg/s]  
 $m_{red,turb}$  – Turbine reduced mass flow rate  
 $p$  – Pressure [bar]  
 $Q$  or  $\dot{Q}$  – Thermal Power [MW]  
 $s$  – Entropy [kJ/kgK]  
 $T$  – Temperature [°C]  
 $v$  – Velocity [m/s]  
 $\dot{V}$  – Volumetric flow rate [m<sup>3</sup>/h]  
 $\rho$  – Density [kg/m<sup>3</sup>]  
 $\chi_{rec}$  – Heat recovery factor [-]

## ACKNOWLEDGEMENTS

The CO<sub>2</sub>OLHEAT project has received funding from the European Union's Horizon 2020 research and innovation programme under grant agreement N° 101022831.

## REFERENCES

- [1] M. Papapetrou, G. Kosmadakis, A. Cipollina, U. La Commare, and G. Micale, "Industrial waste heat: Estimation of the technically available resource in the EU per industrial sector, temperature level and country," *Appl. Therm. Eng.*, vol. 138, no. July 2017, pp. 207–216, 2018.
- [2] U.S. Department of Energy, "Waste Heat Recovery: Technology Opportunities in the US Industry," 2008.
- [3] E. Macchi and M. Astolfi, *Organic Rankine Cycle (ORC) Power Systems*. Elsevier Science, 2016.
- [4] F. Raab, H. Klein, and F. Opferkuch, "Steam Rankine cycle instead of organic Rankine cycle for distributed high temperature waste heat recovery – pros and cons," in *6th International Seminar on ORC power systems*, 2021, no. 2011, pp. 1–10.
- [5] M. T. White, G. Bianchi, L. Chai, S. A. Tassou, and A. I. Sayma, "Review of supercritical CO<sub>2</sub> technologies and systems for power generation," *Appl. Therm. Eng.*, vol. 185, no. July 2020, p. 116447, Feb. 2021.
- [6] M. Astolfi, D. Alfani, S. Lasala, and E. Macchi, "Comparison between ORC and CO<sub>2</sub> power systems for the exploitation of low-medium temperature heat sources," *Energy*, vol. 161, pp. 1250–1261, Oct. 2018.
- [7] International Finance Corporation and Institute for Industrial Productivity, "Waste Heat Recovery for the Cement Sector: Market and Supplier analysis."
- [8] T. Neises and C. Turchi, "Supercritical carbon dioxide power cycle design and configuration optimization to minimize levelized cost of energy of molten salt power towers operating at 650 °C," *Sol. Energy*, vol. 181, no. November 2018, pp. 27–36, 2019.
- [9] D. Alfani, T. Neises, M. Astolfi, M. Binotti, and P. Silva, "Techno-economic analysis of CSP incorporating sCO<sub>2</sub>brayton power cycles: Trade-off between cost and performance," in *AIP Conference Proceedings*, 2022, vol. 2445.
- [10] V. Dostal, "A supercritical carbon dioxide cycle for next generation nuclear reactors," Massachusetts Institute of Technology, 2004.
- [11] J. J. Sienicki, A. Moiseyev, and L. Krajtl, "A Supercritical CO<sub>2</sub> Brayton Cycle Power Converter for a Sodium-Cooled Fast Reactor Small Modular Reactor," in *ASME 2015 Nuclear Forum*, 2015, pp. 1–10.
- [12] R. J. Allam *et al.*, "High Efficiency and Low Cost of Electricity Generation from Fossil Fuels While Eliminating Atmospheric Emissions, Including Carbon Dioxide," *Energy Procedia*, vol. 37, pp. 1135–1149, 2013.
- [13] D. Alfani, M. Astolfi, M. Binotti, and P. Silva, "Part-Load Strategy Definition and Preliminary Annual Simulation for Small Size sCO<sub>2</sub>-Based Pulverized Coal Power Plant," *J. Eng. Gas Turbines Power*, vol. 143, no. 9, 2021.
- [14] D. Alfani, M. Binotti, E. Macchi, P. Silva, and M. Astolfi, "sCO<sub>2</sub> power plants for waste heat recovery: design optimization and part-load operation strategies," *Appl. Therm. Eng.*, vol. 195, no. April 2021, p. 117013, Aug. 2021.
- [15] M. Persichilli, A. Kacludis, E. Zdankiewicz, and T. Held, "Supercritical CO<sub>2</sub> Power Cycle Developments and Commercialization: Why sCO<sub>2</sub> can Displace Steam Steam," *Power-Gen India Cent. Asia*, pp. 1–15, 2012.
- [16] "CO<sub>2</sub>OLHEAT: Supercritical CO<sub>2</sub> power cycles demonstration in Operational environment Locally valorising industrial Waste Heat. Available online at: <https://co2olheat-h2020.eu/>."
- [17] "sCO<sub>2</sub>-Flex: Supporting the electricity system by making fossil fuel based electricity production more flexible. Available online at: <http://www.sco2-flex.eu/>."



## MODELING OF AUTONOMOUS BRAYTON CYCLE LOOP WITH GAMMA+ CODE FOR MICRO MODULAR REACTOR SIMULATION APPLICATION

**Sungwook Choi**

Department of Nuclear and Quantum Engineering,  
Korea Advanced Institute of Science and Technology  
373-1 Guseong-dong Yuseong-gu, Daejeon, 305-701, Korea  
Email: swchoi2000@kaist.ac.kr

**Jeong Ik Lee\***

Department of Nuclear and Quantum Engineering,  
Korea Advanced Institute of Science and Technology  
373-1 Guseong-dong Yuseong-gu, Daejeon, 305-701, Korea  
Email: jeongiklee@kaist.ac.kr

### ABSTRACT

The Supercritical carbon dioxide (S-CO<sub>2</sub>) cycle is considered as a promising power conversion system for numerous power applications, because it has relatively high thermal efficiency and compact component size. This paper shows the validation of GAMMA+ code, which was originally developed by Korea Atomic Energy Research Institute to analyze the gas-cooled reactors, by comparing the experimental data obtained from Autonomous Brayton Cycle (ABC) loop constructed in Korea Advanced Institute of Science and Technology (KAIST) and calculation result from the code. ABC loop is a simple recuperated closed S-CO<sub>2</sub> Brayton cycle constructed by the KAIST research team. ABC loop consists of a turbine-alternator-compressor (TAC), electric heater, recuperator, pre-cooler and control valves. Previously, GAMMA+ code was already validated with the experimental data obtained from SCO<sub>2</sub>PE and SCIEL facilities. In contrast to the ABC loop, only cooling and compression of the S-CO<sub>2</sub> were tested. With ABC loop, not only cooling and compression of the S-CO<sub>2</sub> were tested, but also the heating and recuperation were experimented. The ABC loop was modeled using GAMMA+ code and the calculation from the code is in accordance with the experimental data. Thus, GAMMA+ code can accurately simulate the S-CO<sub>2</sub> system in the future, for example a Micro Modular Reactor (MMR) utilizing as S-CO<sub>2</sub> power system.

### INTRODUCTION

With the development of technologies, the Small Modular Reactors (SMRs) are receiving more attention due to their advantages, such as modularity and siting flexibilities. Previously, for the conventional nuclear power plants, the steam Rankine cycles were widely used. However, with the ongoing

\* corresponding author(s)

research on the nuclear power plant, more compact, yet effective nuclear reactors were designed, which caused the increase of the nuclear reactor outlet temperature. The nuclear reactor outlet temperature of the previous nuclear reactors was near 330°C, whereas, that of the advanced reactors are above 500°C. With the increased core outlet temperature, the turbine inlet temperature (TIT) also increases in the power conversion system. As shown in Figure 1, as the turbine inlet temperature increases, the cycle efficiency of the steam Rankine cycle is less than the Supercritical Carbon dioxide (S-CO<sub>2</sub>) cycle.

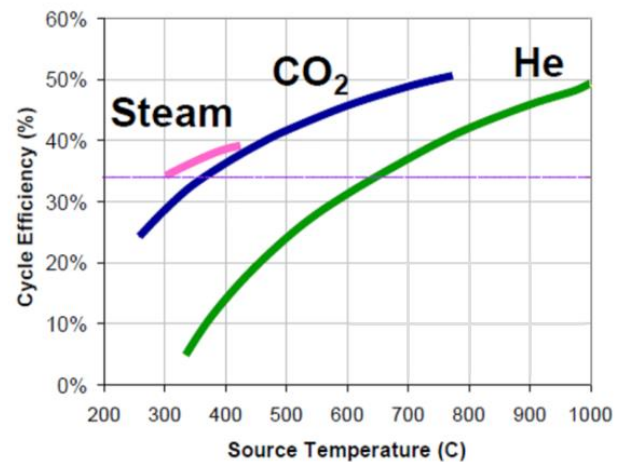
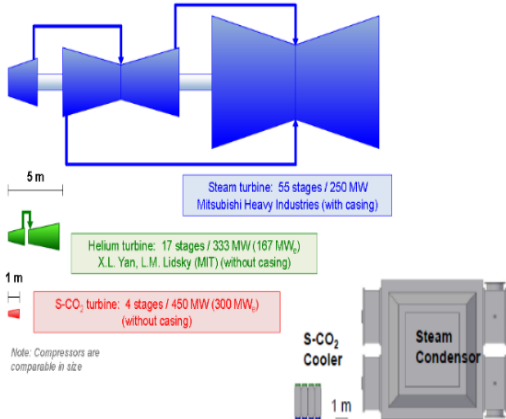


Figure 1. Comparison of cycle efficiency along different TIT

Thus, the S-CO<sub>2</sub> power cycles are regarded as a promising power cycle for the next generation nuclear reactors, because they have high thermal efficiency with compact component size, as shown in Figure 2. The size of S-CO<sub>2</sub> cycle main components,

DOI: 10.17185/duerpublico/77289

including turbine, compressor and cooler, can be compact, because CO<sub>2</sub> behaves as an incompressible fluid, reducing compression work dramatically [1].



**Figure 2.** Main Component Size comparison for S-CO<sub>2</sub> and Rankine Cycle

Based on the advantages of S-CO<sub>2</sub> power cycle and next generation nuclear reactor, Korea Advanced Institute of Science and Technology (KAIST) research team has developed a direct S-CO<sub>2</sub> cooled Small Modular Reactor, KAIST-MMR. KAIST-MMR is an SMR to generate required energy in remote regions [2]. One of the most important features of KAIST-MMR is that it is designed to be controlled autonomously [3].

During the previous researches, the transient analysis and autonomous control of KAIST-MMR have been studied with system simulation code [3-4]. Based on the simulation results, KAIST-MMR can be operated safely and autonomously with reduced loads. However, the validity of the system code used to simulate KAIST-MMR system could be questioned. In this paper, the validation of GAMMA+ code was validated with the Autonomous Brayton Cycle (ABC) Loop experiment data.

**GAMMA+ CODE**

General Analyzer for Multi-component and Multi-dimensional Transient Application (GAMMA+) code was originally developed by Korea Atomic Energy Research Institute (KAERI) to simulate the gas-cooled reactors [5]. The original GAMMA+ code calculated the fluid thermal properties based on the ideal gas correlations. Since the CO<sub>2</sub> behaves as a real gas near the critical point (7.38 MPa, 30.98 °C), the thermal properties calculated by the code deviated from the real values. Thus, NIST-REFPROP fluid thermal property database was implemented to GAMMA+ code. In addition, turbomachinery modeling module was added to predict the off-design performance of the turbomachineries. Figure 3 shows the overview of the modified GAMMA+ code.

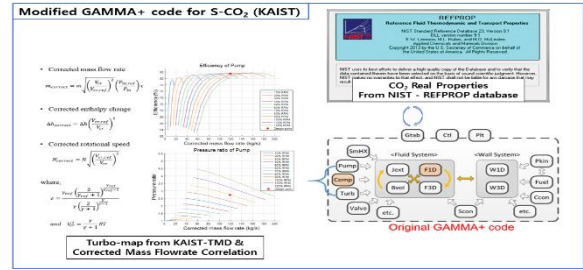


**Figure 3.** Modified GAMMA+ code Overview

The modified GAMMA+ code was initially validated with two different experiment facility: Supercritical CO<sub>2</sub> Brayton Cycle Integral Experiment Loop (SCIEL) and Supercritical CO<sub>2</sub> Pressurization Experiment (SCO<sub>2</sub>PE) [6].

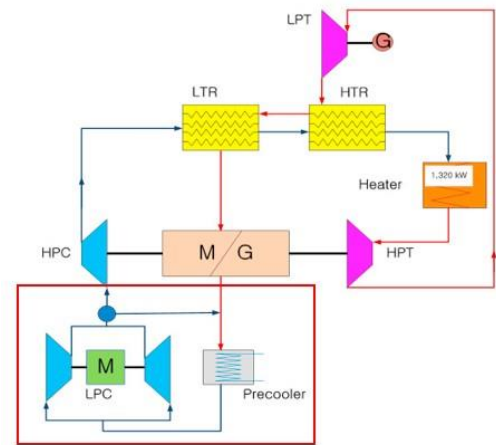


**Figure 4.** Layout of SCIEL Experiment Facility

Figure 4 shows the layout of SCIEL experiment facility located in KAERI, and the components in the red box are simulated by GAMMA+ code and compared with the experiment results. During the experiment, the heat sink water flow was slightly varied, and the whole experiment was conducted at compressor rotational speed of 35000RPM. Figure 5 shows the compressor pressure predicted by the GAMMA+ code simulation and the experiment data [7].

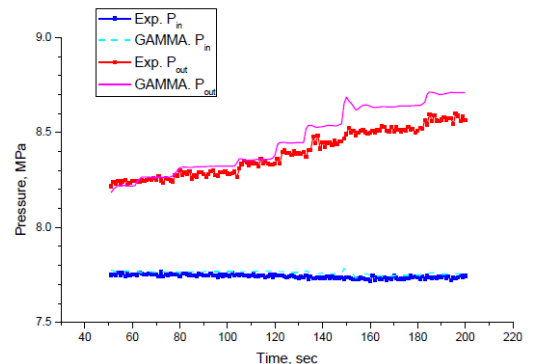


**Figure 5.** Compressor Pressure comparison between SCIEL experiment and GAMMA+ code

Figure 6 shows the SCO<sub>2</sub>PE experiment facility. It is a S-CO<sub>2</sub> experiment facility built by KAIST research team to conduct experiments for S-CO<sub>2</sub> compression and cooling. It consists of canned-motor type compressor, spiral type pre-cooler and globe valve.



Figure 6. General view of SCO<sub>2</sub>PE

Similar to the SCIEL experiment, the SCO<sub>2</sub>PE experiment was conducted by reducing the mass flow rate of the cooling water in the facility, and experimental data, such as compressor pressure and pre-cooler temperature, were obtained. Using GAMMA+ code, the SCO<sub>2</sub>PE was modeled as Figure 7.

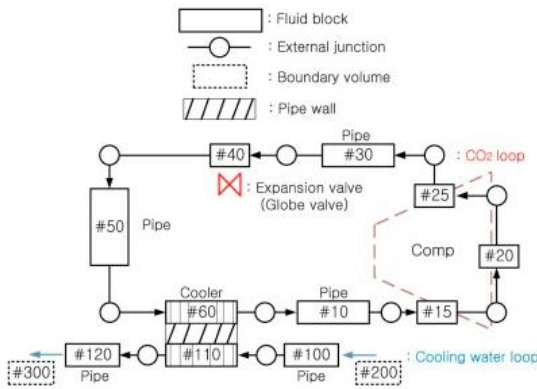


Figure 7. SCO<sub>2</sub>PE modeling for GAMMA+ code

With the nodal shown in the figure, the SCO<sub>2</sub>PE experimental data was predicted by GAMMA+ code, and the results are shown in the following figures. As shown in Figures 8 and 9, the calculation result of GAMMA+ code is in accordance with the actual experiment data. Thus, based on the SCIEL and SCO<sub>2</sub>PE experiments, the GAMMA+ code is well validated about the compression and cooling of the S-CO<sub>2</sub>.

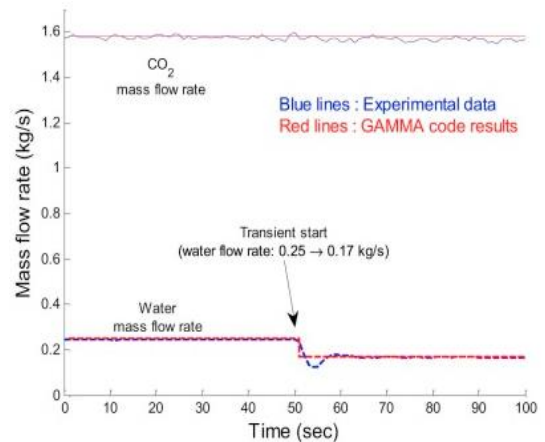


Figure 8. Mass Flow Rate of SCO<sub>2</sub>PE

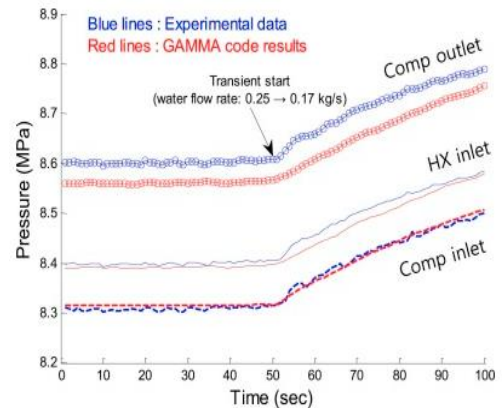
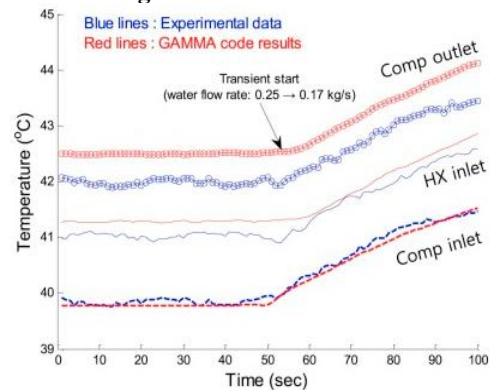


Figure 9. Pressure and Temperature of SCO<sub>2</sub>PE

### ABC LOOP

The ABC loop is a closed S-CO<sub>2</sub> simple recuperated Brayton cycle constructed by KAIST team. It consists of Turbine-Alternator-Compressor (TAC), electric heater, and PCHE type pre-cooler and recuperator. Also, there are several control valves in the cycle to test the autonomous control of the system. Based on the two previous experiments, GAMMA+ code is validated for the compression and cooling of S-CO<sub>2</sub>. In this study, GAMMA+ code will be validated for the heating and



recuperation of S-CO<sub>2</sub> with the data taken during a compressor surge control experiment.

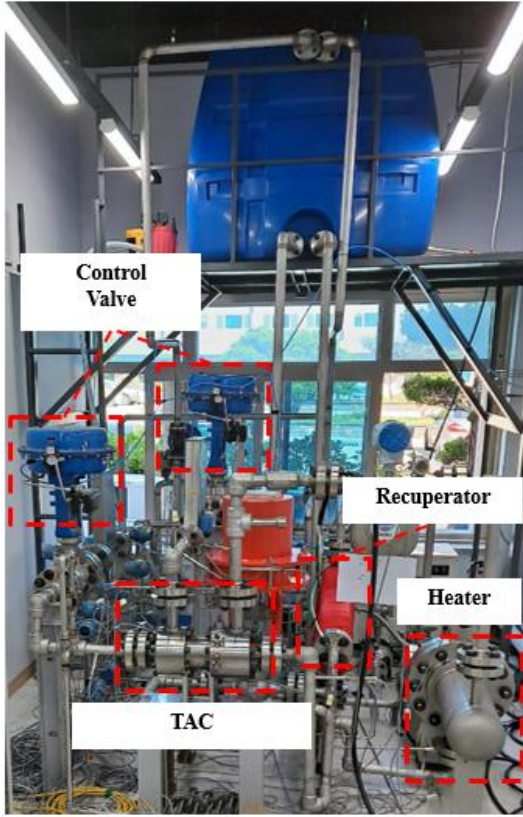


**Figure 10.** General View of ABC Loop

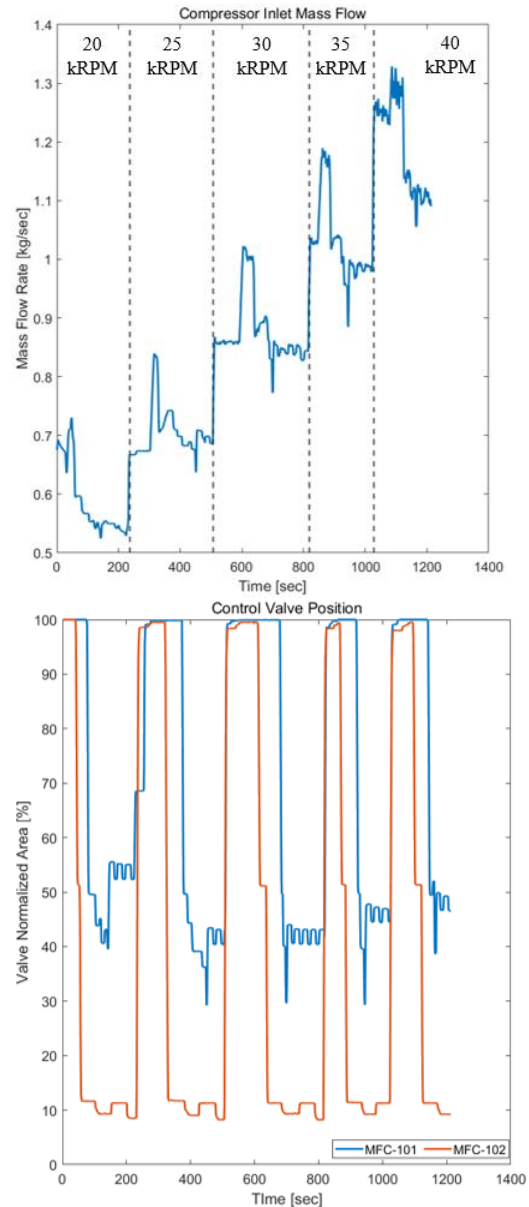
Figure 10 shows the general view of ABC loop experiment facility. Two control valves, MFC-101 and 102, are at the inlet and outlet of the compressor, respectively. For the modeling of GAMMA+ code, the cooling water mass flow rate and the valve opening area of MFC 101 and 102 were as the boundary conditions.

The experiment performed with the ABC loop is the compressor surge control experiment. Compressor surge can be regarded as the compressor operating limit in low mass flow rate region [8]. If compressor surge occurs, the structural integrity of the facility cannot be secured. Thus, there should be enough margin for the compressor mass flow rate. The compressor surge margin can be calculated from the equation below:

$$\text{Surge Margin [\%]} = \frac{\dot{m}_{comp} - \dot{m}_{surge}}{\dot{m}_{comp}} \times 100$$

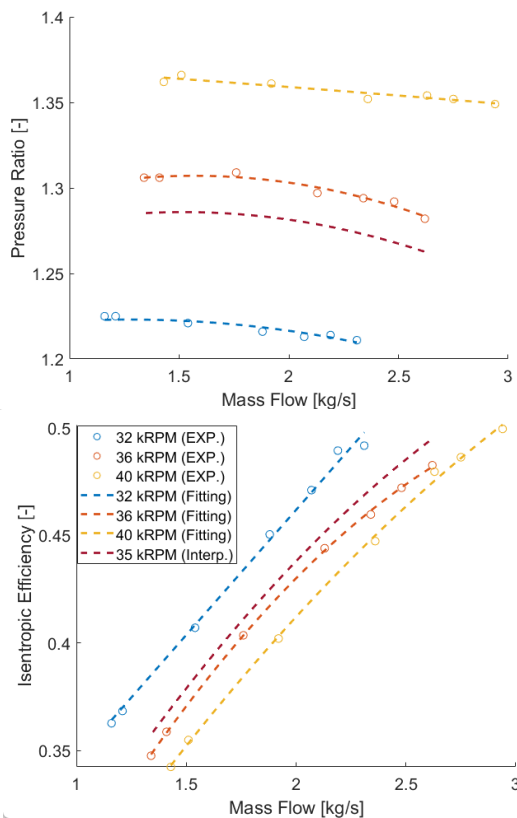
For the experiment, the control valves at the inlet and outlet of the compressor are gradually closed to reduce the compressor mass flow rate. Due to this induced surge condition, the compressor surge margin will gradually drop. As the compressor surge margin becomes lower than 15%, the control valve at the compressor inlet is automatically opened to provide enough compressor mass flow rate. The experiment was conducted for

five different compressor rotational speed as shown in figure 11. For the validation of GAMMA+ code, the experiment result at 35000 RPM was compared with the GAMMA+ code prediction.



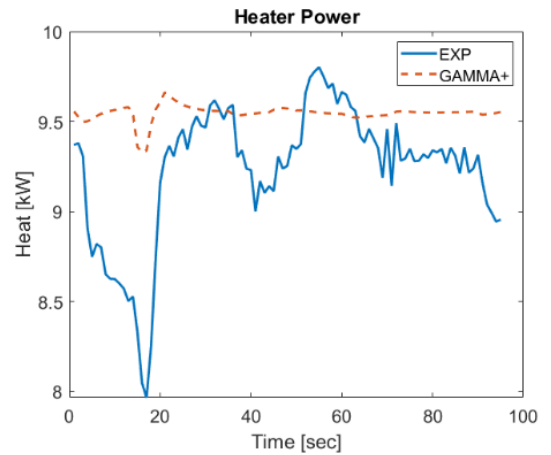
**Figure 11.** Compressor mass flow rate and control valve position during surge control experiment

To simulate the ABC loop compressor surge control experiment, the compressor off-design performance map is required. Figure 12 represents the compressor off-design performance map drawn from the data points. The data points were taken from the previous experiment facility at compressor rotational speed of 32, 36, and 40 kRPM. Since the compressor off-design performance data for 35000 RPM is not included in the data point, data points at 32 kRPM and 36 kRPM were interpolated to produce new data points at 35 kRPM.

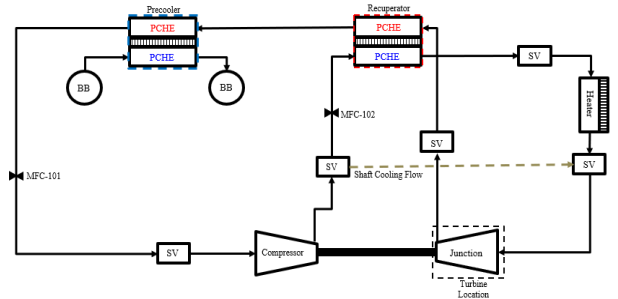


**Figure 12.** Off-design performance map of compressor

The power of the heater was given by the table to imitate the electric heater. Figure 13 shows the heater power calculated by the product of the heater mass flow rate and heater inlet and outlet enthalpy difference. The heater power shown in Figure 13 is data indirectly measured from mass flowrate and enthalpy difference instead of electric power input to the heater. Therefore, the heater thermal inertia and heat loss can reduce heating to the coolant even though constant heat power was applied. In the future, the system will be better insulated and more detail model will be developed to capture these effects with better accuracy. The other components, including the piping, were carefully modeled with the design or measured values. Figure 14 shows the nodalization of the ABC loop modeled in the GAMMA+ code. At this time, the turbine wheel was excluded from the experiment, thus the turbine wheel location was modeled with a single junction in the GAMMA+ code.

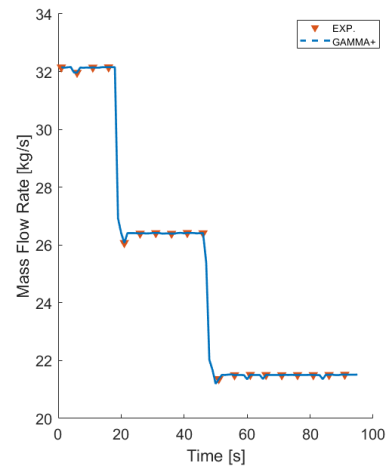


**Figure 13.** Heater Power Profile



**Figure 14.** Nodalization of ABC loop for GAMMA+ Code

With the ABC loop nodalization modeled for GAMMA+ code, the compressor surge control experiment was simulated. The simulation results are shown in the figures below.



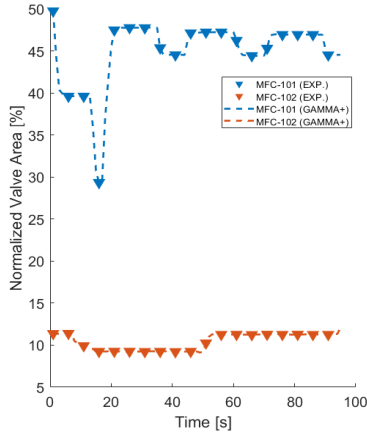


**Figure 15.** Cooling water mass flow rate and control valve opening area

As mentioned before, the cooling water mass flow rate and the compressor control valve opening area are given as the boundary condition. Based on these boundary conditions, the transient condition of the ABC loop was analyzed.

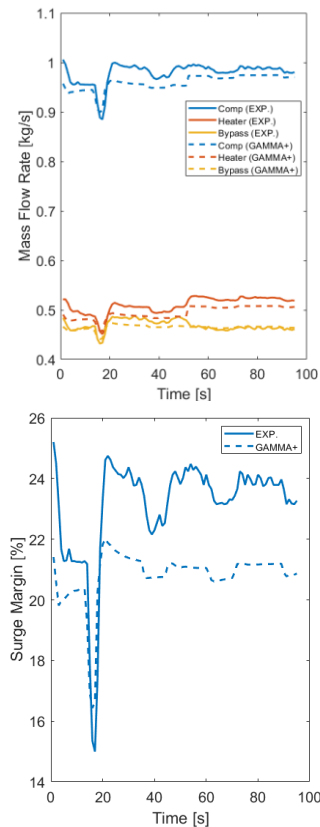


**Figure 16.** S-CO<sub>2</sub> mass flow rate and compressor surge margin at 35 kRPM

Figure 16 shows the mass flow rate of S-CO<sub>2</sub> and compressor surge margin calculated by the equation above. As the control valve at the compressor inlet and outlet closes, the compressor mass flow rate and the compressor surge margin

decrease. When the compressor surge margin falls below 15%, the control valve at the compressor inlet is opened, securing enough compressor mass flow rate. The compressor pressure and temperature predicted by GAMMA+ code were compared with the actual compressor pressure and temperature from the experiment data in Figure 16. As shown in the figure, GAMMA+ code accurately predicted the compressor inlet and outlet pressure. Also, the compressor temperature calculated by the GAMMA+ code reflected the temperature change in the real experiment data.

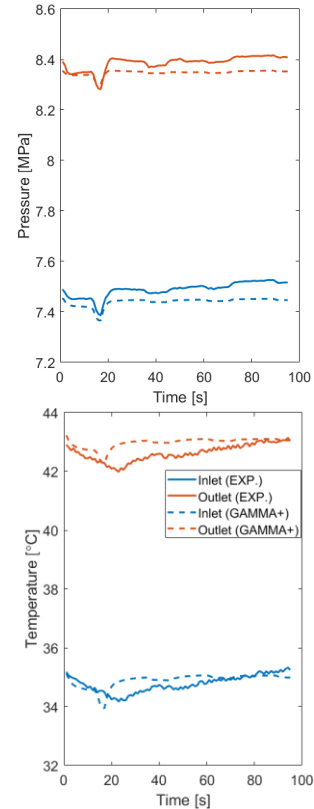


**Figure 17.** Compressor pressure and temperature

The calculation results of heater and recuperator part of the ABC loop are shown in Figures 19 and 20. The pressure and the temperature of each heat exchanger have subtle difference between the GAMMA+ prediction and the actual experiment value. However, the overall trend of the GAMMA+ prediction value is in accordance with the experiment value. For the recuperator temperature predicted by GAMMA+ code seems quite different from the actual recuperator temperature. The difference comes from the error in the steady-state condition modeling. Therefore, the amount of heat transferred in the recuperator was calculated by the following equation:

$$Q_{transferred} = \dot{m}\Delta H$$



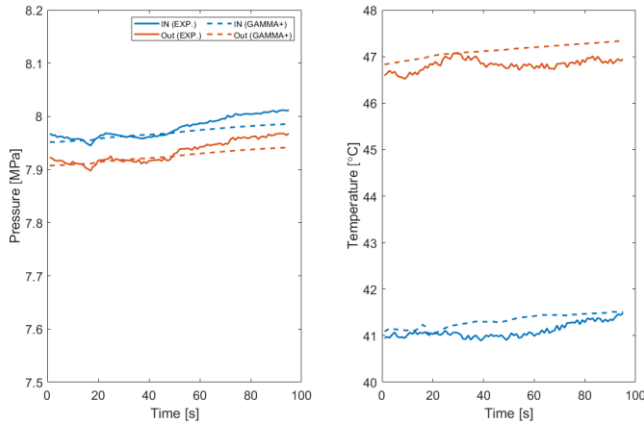


**Figure 18.** Heater pressure and temperature

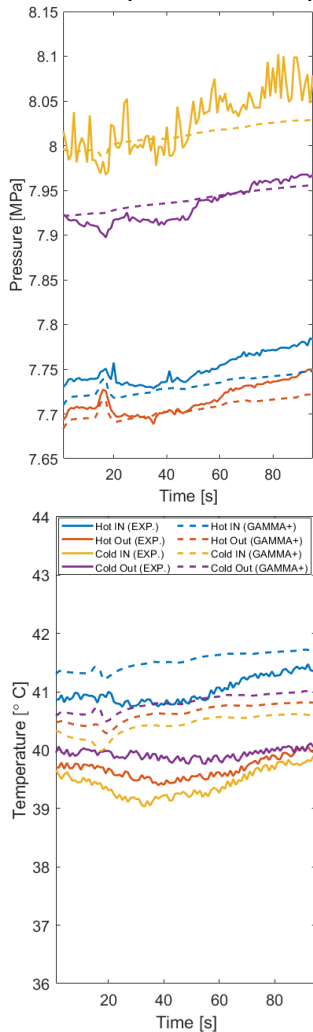


**Figure 19.** Recuperator pressure and temperature

By comparing the amount of heat transferred in the recuperator hot side and cold side, it is concluded that the GAMMA+ can predict the experiment data reasonably well for the heated condition as well. The source of error in the heat transferred is the error in the mass flow rate and the recuperator temperature

difference. Therefore, with ABC loop experiment facility, the GAMMA+ code is validated not only for the compression and cooling of S-CO<sub>2</sub>, but also for the heating and recuperation of the S-CO<sub>2</sub>.

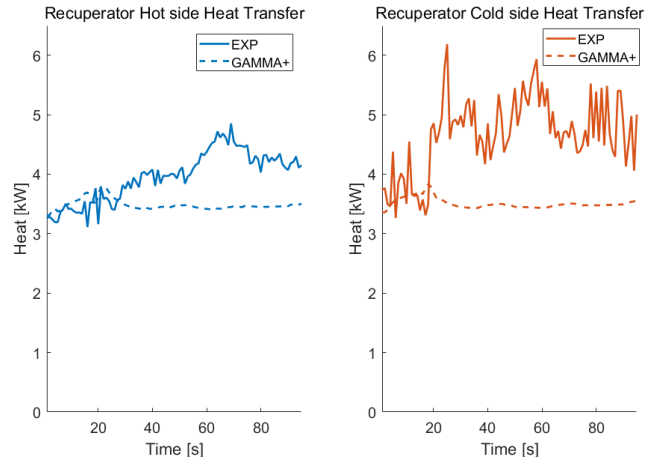


**Figure 180.** Recuperator heat transferred

## CONCLUSIONS & FURTHER WORK

GAMMA+ code is a system simulation code developed by KAERI to simulate gas-cooled reactors. The NIST-REFPROP database was implemented to GAMMA+ code to accurately obtain the thermal property of CO<sub>2</sub> near the critical point. Using the modified code, various simulations for compact nuclear systems, including the transient analysis of KAIST-MMR was conducted previously. To examine how well the simulation result reflects the real operating condition, the code was validated with the compression and cooling data previously. With the newly constructed ABC loop at KAIST, the GAMMA+ code was again validated not only about the compression and cooling of S-CO<sub>2</sub>, but also for the heating and recuperation processes of S-CO<sub>2</sub> power cycle. As the future work, experimental data with turbine will be obtained and will be again compared to GAMMA+ code prediction for validating the turbine model in the code.

As shown in this study, the GAMMA+ code is validated using the ABC loop with the data taken during a compressor surge control experiment. However, the experiment conditions were limited to the low pressure range and small temperature difference due to the hardware limitations on the ABC loop facility at the time. Currently, the ABC loop is being improved to expand capability of the facility. In near future, the experiment will be conducted in wider operating range (i.e. higher pressure ratio and larger temperature difference), and GAMMA+ code will be validated with new experiment data.

## ACKNOWLEDGEMENTS

This research was supported by Civil-Military Technology Cooperation Program (iCMTC) funded by the Agency for Defense Development – South Korea (17-CM-EN-04).

the effect of different back sweep angle and Exducer width on the impeller outlet flow pattern of a centrifugal compressor with Vaneless diffuser,” J. Turbomach., 129 (2006), pp. 421-433

## NOMENCLATURE

$\dot{m}$ : mass flow rate  $\left[\frac{kg}{s}\right]$

$C_p$ : Specific Heat capacity  $\left[\frac{J}{kg \cdot K}\right]$

$\Delta T$ : Temperature difference [K]

$\dot{m}_{comp}$ : Compressor mass flow rate  $\left[\frac{kg}{s}\right]$

$\dot{m}_{surge}$ : Compressor surge mass flow rate  $\left[\frac{kg}{s}\right]$

$Q_{transferred}$ : Transferred Heat [W]

## REFERENCES

- [1] V. Dostal, M. J. Driscoll, and P. Hejzlar, "A supercritical carbon dioxide cycle for next generation nuclear reactors," *USA: Massachusetts Institute of Technology*, vol. MIT-ANP-TR-100, 2004
- [2] S.G. KIM, H. YU, J. MOON, S. BAIK, J.I. LEE, Y. KIM, Y.H. JEONG. (2016). A concept design of supercritical CO2 cooled SMR operating at isolated microgrid region.
- [3] B.S. Oh, and J. I. Lee, "Study of Autonomous Control System for S-CO<sub>2</sub> Power Cycle", 3<sup>rd</sup> European supercritical CO<sub>2</sub> Conference, September 19-20, 2019, Paris, France
- [4] J.Y. Baek, J.J. Lee, and J. I. Lee, "Transient Analysis of the Super-critical Carbon Dioxide Cycle coupled to Pressurized Water Reactor for Nuclear Powered Ships", 4<sup>th</sup> European supercritical CO<sub>2</sub> Conference for Energy Systems, March 23-24, 2021, Online Conference
- [5] "General Analyzer for Multi-Component and Multi-dimensional Transient Application-GAMMA+1.0 Volume 1,2: User's and Theory manual," Korea Atomic Energy Research Institute, 2016
- [6] Y.H. Ahn, S.J. Bae, M. Kim, S. K. Cho, S. Baik, J. I. Lee and J. E. Cha, "Review of supercritical CO2 power cycle technology and current status of research and development," Nuclear Engineering and Technology, 2015
- [7] Y.H. Ahn and J. I. Lee, "Study of innovative Brayton cycle design and transient analysis for Sodium-cooled fast reactor application," Korea Advanced Institute of Science and Technology, 2016
- [8] A. Hildebrandt, and M. Genrup, "Numerical investigation of

## OPTIMISATION OF THE AIR CHANNELS ON THE DIVERSE ULTIMATE HEAT SINK FOR SCO<sub>2</sub> POWER CYCLES

**Radomír Filip**  
Research center Řež  
Husinec-Řež, Czech Republic  
Email: radomir.filip@cvrez.cz

**Sarah Tioual-Demange**  
Fives Cryo  
Golbey, France

**Guillaume Taiclet**  
Fives Cryo  
Golbey, France

### ABSTRACT

During the Horizon 2020 sCO<sub>2</sub>-4-NPP project, several key components for the sCO<sub>2</sub> power cycle as an option for the innovative decay heat removal system for nuclear power plants were developed. One of them was the diverse ultimate heat sink (DUHS), which is an air/sCO<sub>2</sub> plate and fin heat exchanger with straight fins. A representative DUHS mock-up was manufactured and its thermal-hydraulic performance was tested using the sCO<sub>2</sub> loop at Research Centre Rez (CVR) at parameters of 8 MPa of pressure and temperatures up to 170°C on the sCO<sub>2</sub> side. The main findings were the acquisition of the heat transfer correlation on the air side of the heat exchanger and the fanning friction factor in the tiny channels. The collected data were used to verify the heat exchanger design and, moreover, a mathematical model was developed and validated. Furthermore an optimisation study was done using the validated model to find the best channel geometry with the trade-off between high heat transfer coefficient and low pressure losses.

### INTRODUCTION

In the framework of the Horizon 2020 sCO<sub>2</sub>-4-NPP project [1], where the goal was to utilise the self-sustaining sCO<sub>2</sub> power cycle to serve as an additional safety system within the current nuclear power plants, to remove the decay heat during a station blackout (SBO) scenario, several key components were developed. The key components of such a system are schematically shown in Figure 1. These are the compact heat exchanger, turbomachinery and air-cooled diverse ultimate heat sink (DUHS).

The work presented in this paper is focused on the heat removal between the sCO<sub>2</sub> and the ambient air, which is mediated in the DUHS. The DUHS is required to cool the sCO<sub>2</sub> from 240°C down to 55°C at 8 MPa pressure to maintain the cycle functionality, even at some extreme ambient conditions <-45; 45°C>, while maintaining low pressure losses and having light and compact design. To meet these requirements, a plate and fin heat exchanger (PFHE) design with straight fins was proposed

and a 500 kW unit was designed. The preliminary design of the DUHS unit is 2 m in width, 0.64 m in length and 0.98 m in height. It contains 64 layers of sCO<sub>2</sub> channels wound up into eight passes and 128 layers of straight-passage air channels (schematically shown in Figure 2). Where one layer of sCO<sub>2</sub> is stacked between two air layers, the stacking pattern is known as ‘double-banking’ and it is schematically presented in Figure 3.

To validate the thermal-hydraulic design, a small DUHS mock-up unit was fabricated and tested, using the experimental sCO<sub>2</sub> loop [2] at Research Centre Rez (CVR). The experimental data were used to extrapolate the heat transfer and fanning friction coefficient correlations. A special focus was placed on the air side of the DUHS, since the overall heat transfer coefficient is mainly governed by the heat transfer coefficient on the air side, due to the higher convective heat transfer resistance. Thus, improving the channel geometry on the air side would have major impact on the required heat transfer area. For this reason, a 1D numerical model was developed and validated with the experimental results, which was further employed for the optimisation study, that aims to get a channel geometry with an optimal trade-off between heat transfer coefficient and low pressure losses.

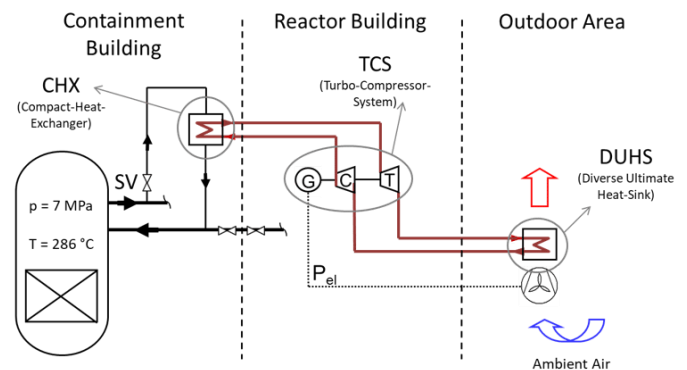


Figure 1: sCO<sub>2</sub> heat removal system attached to a BWR [3].

\* corresponding author(s)

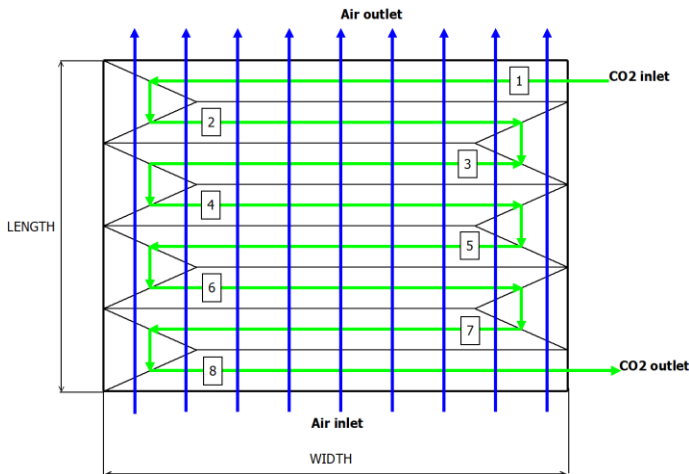


Figure 2: Scheme of DUHS core with cross flow configuration.

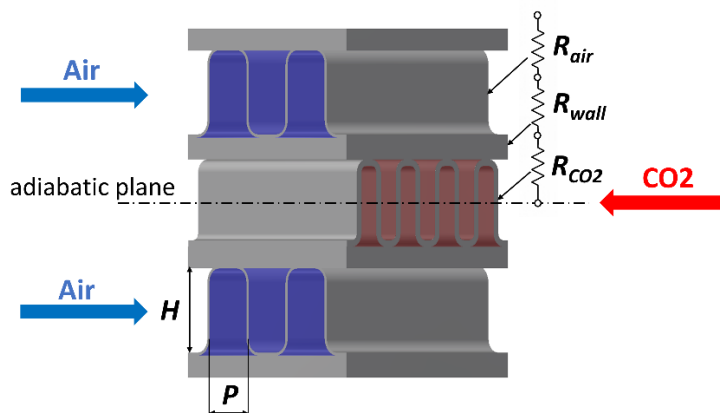


Figure 3: Scheme of DUHS channels 'double-banking' arrangement.

### EXPERIMENTAL VERIFICATION

The fabricated DUHS mock-up (shown in Figure 4) is 305 mm in width, 224 mm in length and 52 mm in height and consists of three layers per CO<sub>2</sub> side with four passes and effective passage length of 1.22 m and six layers per air side with effective passage length of 0.24 m. Each layer is separated with a 1 mm thick sheet made of stainless steel. The channels on the air side contain 0.15 mm thick fins with 2.54 mm spacing, and the sCO<sub>2</sub> channels contain 0.3 mm thick fins with 1.27 mm spacing. The height of both channels is 4 mm. The heat exchanger testing took place at CVR using an sCO<sub>2</sub> experimental loop, which was constructed within the SUSEN (Sustainable Energy) project [2]. The sCO<sub>2</sub> loop is a large-scale experimental facility in the form of a simple Brayton cycle with a heating power of 110 kW, sCO<sub>2</sub> temperatures up to 550°C, pressure up to 25 MPa and mass-flow rate up to 0.3 kg/s. The facility has been used within various R&D projects focused on the development of sCO<sub>2</sub> cycles and components testing. The DUHS mock-up was implemented in the low-pressure part of the sCO<sub>2</sub> loop, which corresponds to an appropriate location in the real sCO<sub>2</sub> cycles.

For the experiments, the DUHS mock-up's air side was equipped with flange ducts on both sides, where the inlet side was connected to the blower and the outlet side was left to the ambient. The sCO<sub>2</sub> side was connected to the low-pressure section of the sCO<sub>2</sub> experimental loop, which was operated at 8 MPa with inlet temperatures in range of <100; 172°C>, to ensure the CO<sub>2</sub> was above its critical point. The experimental PID layout is schematically shown in Figure 5. The installed instrumentations with their measurement errors are listed in Table 1. To minimize the thermal losses, the whole DUHS mock-up was for the experiments wrapped in 5cm thick thermal insulation.

Table 1: List of used instrumentation.

Variable	Description	Range	Units	Measurement error
T1,2,3	K-type Thermocouple class 1	0–300	°C	± 1.5°C
T4,5,6,7, 8,9,10,11	Pt100 class A	0–300	°C	± 0.35°C
F1	Thermic flow sensor	0–465	m <sup>3</sup> /h	± 5% of measured value
F2	Coriolis flow meter	0–0.7	kg/s	± 10% of measured value
P	Absolute pressure transducer	0–30	MPa	± 0.3 bar
PD1	Pressure difference transducer	0–15	mbar	± 0.1 mbar
PD2	Pressure difference transducer	0–500	mbar	± 0.4 mbar



Figure 4: Fabricated DUHS mock-up.

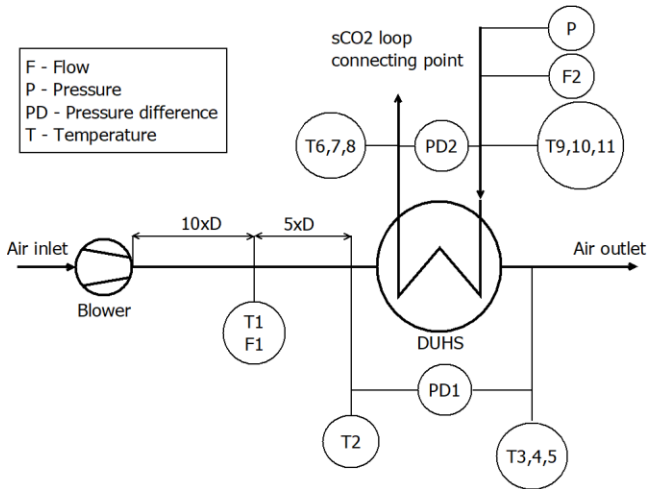


Figure 5: PID of the DUHS experimental setup.

### EXPERIMENTAL RESULTS

During the experimental campaign, the sCO<sub>2</sub> mass-flow and inlet temperature were kept constant at six different levels, while the absolute pressure was kept at 8 MPa. Then for each sCO<sub>2</sub> state, a different air mass-flow setting was applied at five different levels. Hence, a total of 30 steady state data points were obtained. Indicators for determining a steady state were the outlet temperatures gradients of both media. Where each data point was considered steady state when there was no significant temperature gradient change. Final inlet/outlet temperatures were obtained by averaging measured data at given location. As for example the outlet sCO<sub>2</sub> temperature is considered as arithmetic average of measured values T<sub>6</sub>; T<sub>7</sub>; T<sub>8</sub>. The final averaged temperatures are present for each steady state in Figure 6. The measured mass-flows of both media are present in Figure 7 together with their range of measurement error bar given by the devices measurement error from Table 1. Furthermore the measured pressure drop for the sCO<sub>2</sub> side and the air side are plotted in Figure 8 and Figure 9 respectively. The entire overview of the measured data is present for validation purposes in Appendix A.

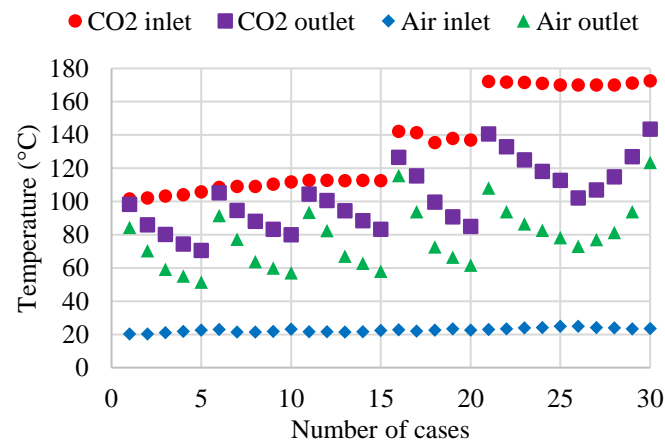


Figure 6: Experimental data: Temperatures.

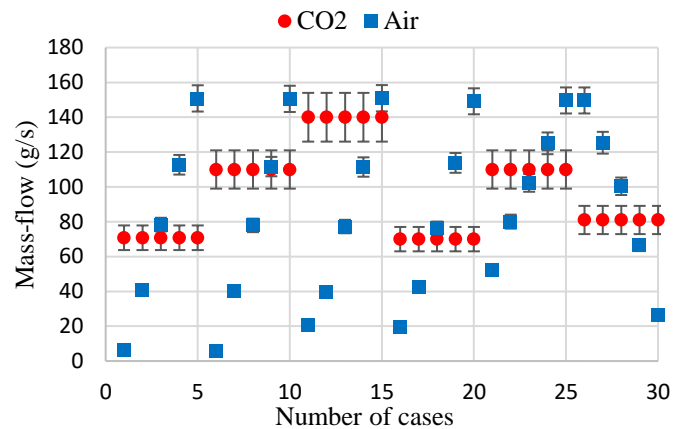


Figure 7: Experimental data: Mass-flow.

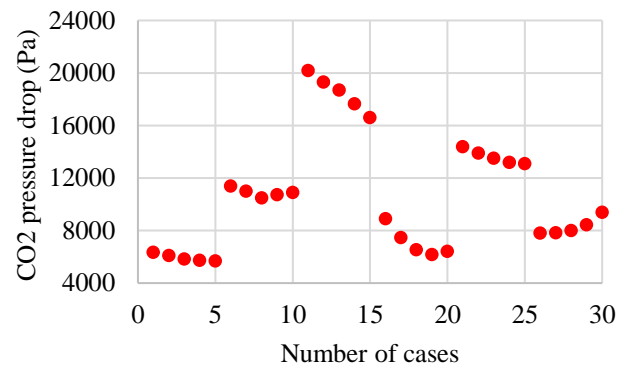


Figure 8: Experimental data: CO<sub>2</sub> side pressure loss.

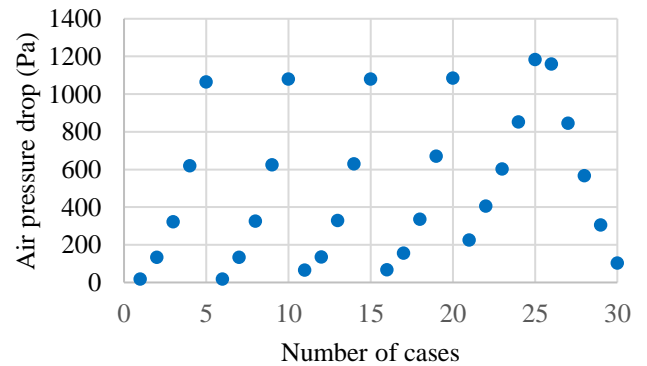
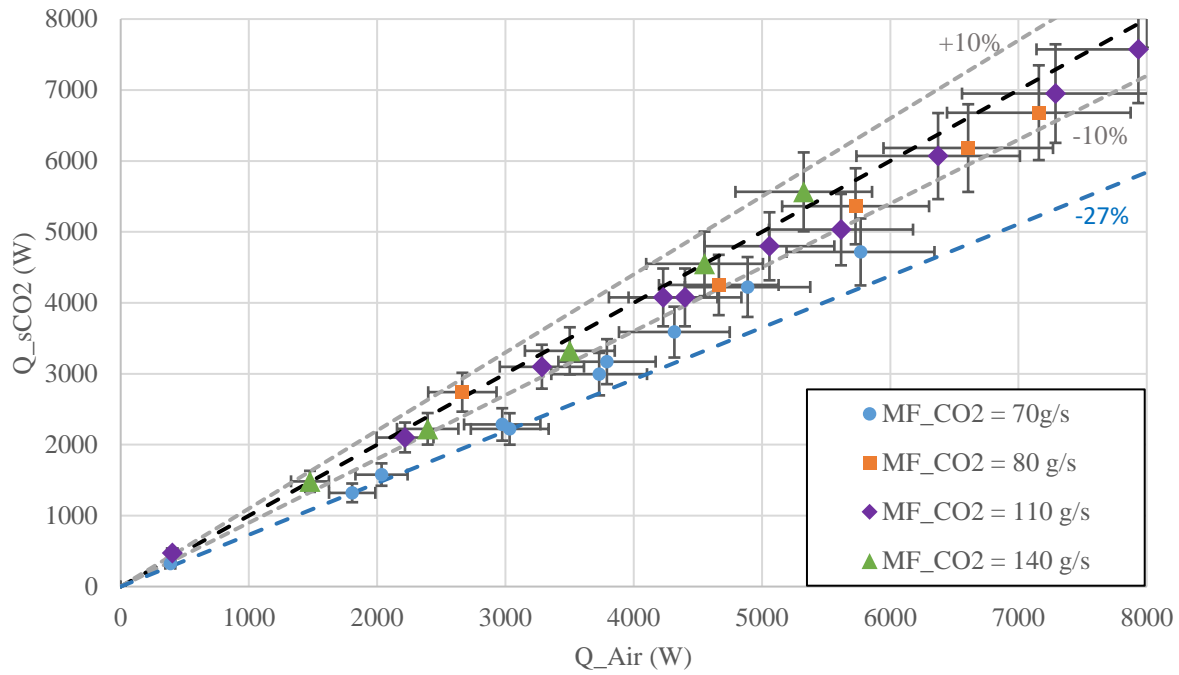


Figure 9: Experimental data: Air side pressure loss.

Heat transfer rate was calculated according to Eq. 1, using the measured mass-flow and the enthalpy difference between the inlet and outlet for each medium. The enthalpies were obtained with NIST REFPROP [4], inputting the measured temperatures and pressures. In case of air, the ambient pressure of 1 bar was considered.



**Figure 10:** Calculated heat transfer rates according to the experimental results at different sCO<sub>2</sub> mass-flow rates.

$$Q = \dot{m} \cdot \Delta i \quad (1)$$

The thermal losses were with respect to the used insulation, outer surface area and the highest temperature gradient estimated to be less than 1% of the average heat transfer rate and thus were neglected.

The heat transfer rate uncertainty  $\sigma_Q$  was considered as an error propagation function of three independent parameters (mass flow, inlet/outlet enthalpy). The error propagation function was linearized by approximation to a first order Taylor series expansion that can be calculated as follows:

$$\sigma_Q = \sqrt{(\Delta i \cdot \sigma_{\dot{m}})^2 + (\dot{m} \cdot \Delta \sigma_i)^2} \quad (2)$$

Where  $\Delta \sigma_i$  is the enthalpy uncertainty difference between the values at the inlet and outlet. Each enthalpy uncertainty can be generally expressed as :

$$\sigma_i = \frac{\sqrt{(i_{(T,Pmax)} - i_{(T,Pmin)})^2 + (i_{(Tmax,P)} - i_{(Tmin,P)})^2}}{2} \quad (3)$$

The heat transfer rate error propagation was calculated in this manner for both media. Resulted heat transfer rates of both media with their errors are plotted in Figure 10, where it can be seen a black dashed line that stands for  $Q_{sCO_2}/Q_{Air} = R = 1$ . Resulted sCO<sub>2</sub> heat transfer, that was measured with mass-flows > 80g/s, lies within the range from  $R \pm 10\%$  (grey dashed lines). However it can be noted that the measured data with sCO<sub>2</sub> mass-flow of 70g/s shows higher dispersion from R, up to -27% (blue

dashed line). This seems to be problem of the Coriolis flow meter that is used to measure the sCO<sub>2</sub> mass flow and its accuracy, measuring in range of less than 10% of its measure span. For this reason the total heat transfer rate is considered  $Q_T = Q_{Air}$ , when sCO<sub>2</sub> mass flow is < 80g/s, when is above, the total heat transfer rate is consider as follows:

$$Q_T = 0.5 (Q_{CO_2} + Q_{Air}) \quad (4)$$

## HEAT TRANSFER COEFFICIENT

The heat transfer coefficient on the air side can be expressed from the experimental data, knowing the heat transfer resistances, then the following expression is valid:

$$R_{air} = R_{tot} - R_{wall} - R_{CO_2} \quad (5)$$

This can be written as:

$$R_{air} = \frac{LMTD}{Q_t} - \frac{t}{(kA)_{wall}} - \frac{1}{(\eta_0 h_{tc} A)_{CO_2}} \quad (6)$$

Assuming the sum of the thermal resistances  $R_{wall}$  and  $R_{CO_2}$  is an order of magnitude smaller than the resulting thermal resistance on the air side of the heat exchanger, the overall heat transfer coefficient will be mainly affected by the heat transfer coefficient on the air side. Therefore, in order to determine the heat transfer coefficient on the sCO<sub>2</sub> side, some general  $h_{tc}$  correlation for



forced convection can be used. For this purpose, Gnielinsky correlation is used and is valid in the range  $10^4 < Re < 10^6$  [5]:

$$htc = \frac{(\xi/8)RePr}{1 + 12.7\sqrt{(\xi/8)}(Pr^{2/3} - 1)} \cdot \left[ 1 + \left(\frac{D_h}{L}\right)^{2/3} \right] \left(\frac{k}{D_h}\right) \quad (7)$$

where  $\xi$  is defined as:

$$\xi = (1.8 \log_{10} Re - 1.5)^{-2} \quad (8)$$

Since the heat exchanger contains fins, the total heat transfer rate is evaluated through a concept of total surface effectiveness  $\eta_0$  defined as :

$$\eta_0 = 1 - (1 - \eta_f) \frac{A_f}{A} \quad (9)$$

where  $A_f$  is the fin surface area and  $A$  is the total surface area, and  $\eta_f$  is the fin efficiency defined as:

$$\eta_f = \frac{\tanh(h'X)}{h'X} \quad (10)$$

where  $X$  is defined as:

$$X = \sqrt{\frac{2 htc}{k_s t}} \quad (11)$$

The value of the  $h'$  term for the 'double-banking' pattern will differ for the air and CO<sub>2</sub> channel. In the case of the air channel,  $h' = h - t$ , but in the case of the CO<sub>2</sub> channel, the adiabatic plane is in the middle of the channel (shown in Figure 3), thus  $h' = h/2 - t$ .

The fin surface area  $A_f$  is considered as:

$$A_f = 2(H - t) \cdot L \cdot N \quad (12)$$

where  $N$  is the number of channels and  $L$  is their effective length. The total area is considered as:

$$A = 2(P - t) \cdot L \cdot N + A_f \quad (13)$$

Finally, the heat transfer coefficient on the air side can be calculated by iterating the following expression:

$$htc_{air} = \frac{1}{(\eta_0 A R)_{Air}} \quad (14)$$

Obtained heat transfer coefficients are converted into the Colburn factor form according to [6]:

$$j = \frac{htc_{air}}{\rho \bar{v} c_p} Pr^{2/3} \quad (15)$$

The Colburn factor was correlated as a function of Reynolds number, using the least square linear regression method. The

following function was found, to best match the extrapolated data:

$$j = 0.084 \cdot Re^{-0.47} \quad (16)$$

The stated Colburn factor correlation is valid for air and straight fins in the range of Reynolds numbers  $<500; 4000>$ . Figure 11 shows the extrapolated and correlated values of the Colburn factor coefficients as a function of the Reynolds number. The comparison of the correlated and the extrapolated data is shown in Figure 12, where the correlation matches the extrapolated data with an average absolute deviation of 6.1% and lies within the maximum error band of  $\pm 15\%$ .

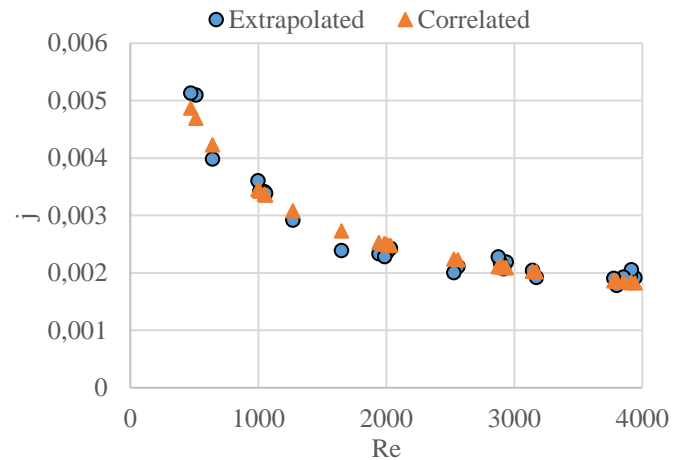


Figure 11: Colburn factor as a function of Reynolds number.

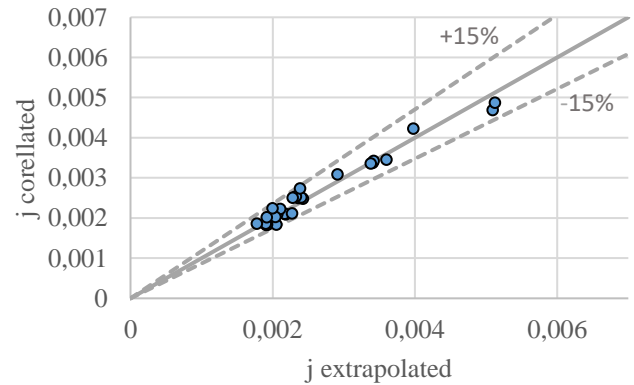


Figure 12: Correlation field between extrapolated and correlated Colburn factors.

## FANNING FRICTION FACTOR

The fanning friction factor can be determined from the experimental data with the following equation [7]:

$$f = \frac{D_h}{2L} \frac{1}{(1/\rho)_m} \left[ \frac{2\Delta p}{G^2} - \frac{1}{\rho_i} (1 - \sigma^2 + K_c) - 2 \left( \frac{1}{\rho_o} - \frac{1}{\rho_i} \right) + \frac{1}{\rho_o} (1 - \sigma^2 + K_e) \right] \quad (17)$$

where  $\sigma$  is the contraction/expansion ratio, which is the ratio of the total front flow area over the total front area at the entrance/exit.  $K_c$  and  $K_e$  are entrance/exit friction factors that were determined from graph [8]. The fanning friction factor was calculated according to Eq. (13) and correlated using the least square linear regression method. The resulting correlation for the fanning friction factor on the air side is as follows:

For laminar region  $Re < 2000$ :

$$f = \frac{18.3}{Re} \quad (18)$$

For turbulent region  $2000 < Re < 4000$

$$f = 0.017 Re^{-0.07} \quad (19)$$

The comparison between extrapolated and correlated friction factors is shown in Figure 13. The correlation field is shown in Figure 14, where the average absolute deviation between extrapolated and correlated data is 5.3% and all the data lie within the maximum error band of  $\pm 15\%$ .

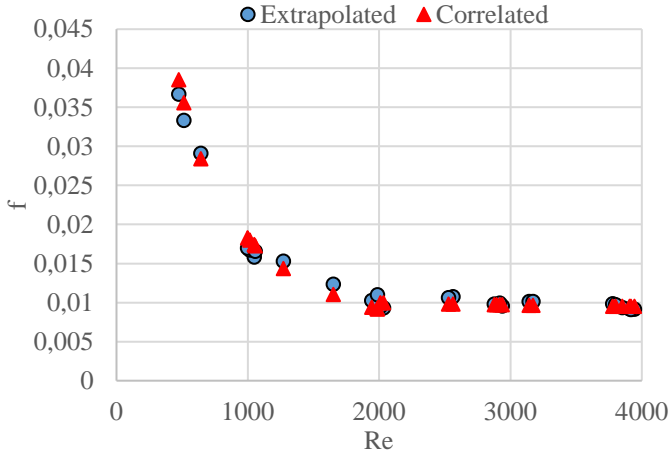


**Figure 13:** Friction factor as a function of Reynolds number.

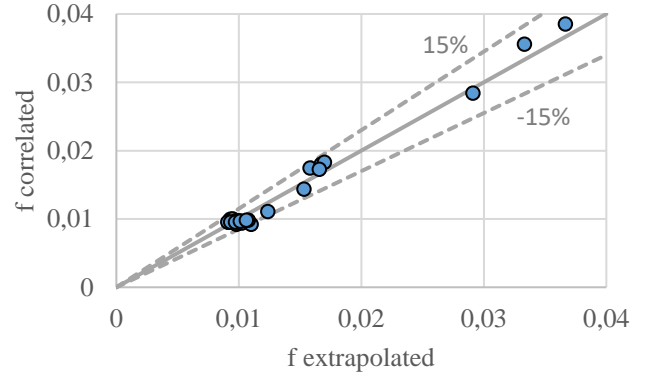


**Figure 14:** Friction factor as a function of Reynolds number.

## MATHEMATICAL MODELLING

To validate the thermal-hydraulic performance of the DUHS mock-up and potential design of different channel geometries, a 1D mathematical model was developed, utilising the correlations obtained from the experimental results. To calculate the heat transfer, an  $\varepsilon$ -NTU method was employed [8]. The heat exchanger was discretised into smaller net transfer units, where the number of rows corresponds to the index  $i$ , which is equal to the number of  $sCO_2$  passages, then the index  $j$  corresponds to the number of columns (shown in Figure 15). In this case, the flow arrangement can be considered as unmixed crossflow, where the heat exchanger effectiveness is given by expression:

$$\varepsilon = 1 - \frac{\exp(-NTU^{0.78}W^*) - 1}{W^*} NTU^{0.22} \quad (20)$$

where  $NTU$  and  $W^*$  are given as follows:

$$NTU = \frac{UA_{i,j}}{W_{min}} \quad (21)$$

$$W^* = \frac{W_{min}}{W_{max}} \quad (22)$$

where  $W$  is a flow heat capacity rate with units (W/K). With the current arrangement, the minimal flow heat capacity will be, in this case, always at the air side; thus, the following expressions for the inlet/outlet NTU temperatures in the first row are valid:

$$T_{air(i+1,j)} = T_{air(i,j)} + \varepsilon_{(i,j)} \cdot (T_{CO2(i,j)} - T_{air(i,j)}) \quad (23)$$

$$T_{CO2(i,j+1)} = T_{CO2(i,j)} + W^* \cdot (T_{air(i+1,j)} - T_{air(i,j)}) \quad (24)$$

The temperatures are iteratively calculated in this manner until certain accuracy is reached. The thermo-physical properties of each medium were obtained from the NIST database [4] and are considered at the average inlet/outlet temperature of each NTU at constant operating pressure.

The mass-flows and flow heat capacities for each medium are calculated as:

$$\dot{m}_i = \frac{\dot{Q}}{\Delta t_i} \quad (25)$$

$$W_i = \frac{\dot{Q}}{\Delta T_i} \quad (26)$$

The DUHS geometrical parameters are listed in Table 2. The channel's *flow area*, the hydraulic diameter  $D_h$  and total number of channels  $N$  are calculated as:

$$\text{Flow area}_i = (P_i - t_i)(H_i - t_i) \quad (27)$$

$$D_{h_i} = 4 \cdot \text{Flow area}_i / (2((P_i - t_i) + (H_i - t_i))) \quad (28)$$

$$N_i = (FPM_i \cdot \text{Effective width} + 1) \cdot \text{number of layers} \quad (29)$$

The channel velocities and Reynolds numbers are calculated as:

$$v_i = \frac{\dot{m}_i}{\text{Flow area}_i \rho_i N_i} \quad (30)$$

$$Re_i = \frac{v_i D_{h_i} \rho_i}{\mu_i} \quad (31)$$

As for the heat transfer coefficients and the overall heat transfer coefficient, these can be calculated from Eq. (6), where the new heat transfer correlation was utilised. For the hydraulic calculation, Eq. (17) can be rewritten into the following form to obtain a formula for the pressure losses:

$$\Delta p = \frac{G^2}{2} \frac{1}{\rho_i} \left[ (1 - \sigma^2 + K_c) + f \frac{2L}{D_h} \rho_i \left( \frac{1}{\rho} \right)_m + 2 \left( \frac{\rho_i}{\rho_o} - 1 \right) - \frac{\rho_i}{\rho_o} (1 - \sigma^2 + K_e) \right] \quad (32)$$

During the pressure loss calculations, the correlated fanning friction factors from Eq. (18) and Eq. (19) were used.

**Table 2:** DUHS mock-up - geometrical parameters.

	Air	sCO <sub>2</sub>
FPM	388.2	787.4
P (mm)	2.576	1.27
H (mm)	4	4
t (mm)	0.2	0.3
number of layers	6	3
Effective width (mm)	281	50
Effective length (mm)	214	1,220

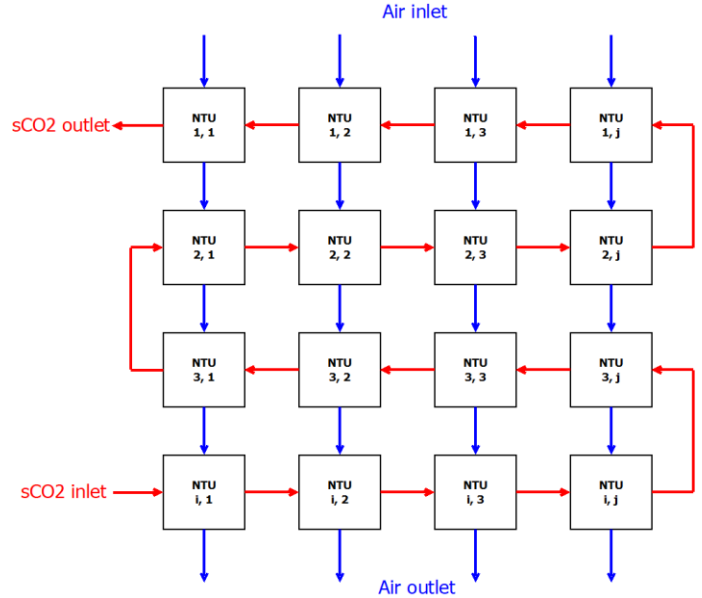


**Figure 15:** Discretisation of DUHS mock-up used in the  $\epsilon$ -NTU method.

## MATHEMATICAL MODEL RESULTS

To validate the numerical 1D model, it was fed with the measured experimental data, namely the total transferred heat  $Q_T$ , input/output CO<sub>2</sub> temperatures and input air temperature. For the heat transfer model validation, the air outlet temperatures predicted by the model and measured during the experiment were compared. The air outlet temperatures comparison is shown in Figure 16, where the predicted air outlet temperatures are matching the experimental data with reasonably good precision, where the predicted temperatures fit within  $\pm 10\%$  error band together with the measured values. The absolute average deviation, comparing measured and modelled data was 3.8%. Regarding the hydraulic model validation, the pressure differences on the air side, predicted by the model were compared with the experimental measurement. The comparison of the pressure difference on the air side is shown in Figure 17, where the predicted pressure losses fit within  $\pm 30\%$  error band. While comparing the measured and modelled data, the absolute average deviation was 11.8%. Slightly higher deviations of the pressure loss predictions on the air side are mainly caused by the initial uncertainty of the mass-flow measurements and resulting

calculation of the average heat transfer, which was the main model input. Despite this fact, the numerical model predicts the thermal and hydraulic performance reasonably well and can be considered valid.

- constant air thermo-physical properties at mean temperature  $T_m = 70^\circ\text{C}$
- contraction/expansion ratio  $\sigma = 0.5$

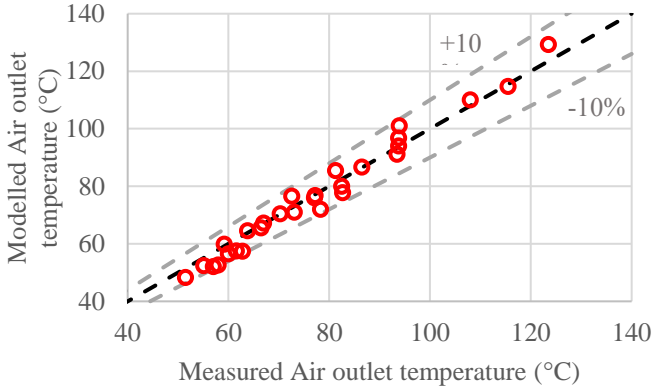


**Figure 16:** Comparison of the air outlet temperatures predicted by the model vs. measured values.

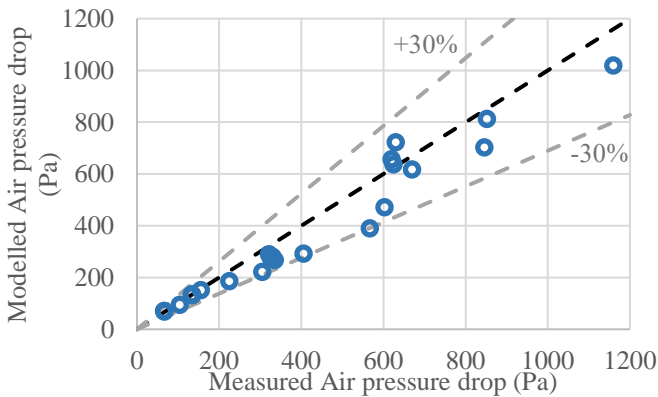


**Figure 17:** Comparison of the pressure difference on the air side predicted by the model vs. measured values.

### AIR SIDE CHANNEL OPTIMISATION

An optimisation task was carried out in order to find a straight fin channel geometry that maintains a high heat transfer coefficient with low pressure losses. New heat transfer and friction factor correlations obtained from the experimental results were used for this purpose. The optimisation parameters are the pitch, height and thickness of the channel’s fins. The limits for these parameters that are present in Table 3, were chosen according to the discussion with the HX manufacturer FIVES Cryo, where the manufacturability was the main consideration. For the optimisation task, a single channel was considered with the following constraints:

- channel length 1m
- constant flow velocity 8 m/s
- maximum allowable pressure 600 Pa/m

**Table 3:** Intervals of the air channel optimisation parameters.

Channel parameter	Interval (mm)
Pitch – P	<1; 5>
Height – H	<2; 8>
Fin thickness – t	<0.1; 0.3>

The velocity value of 8 m/s was chosen as a reasonable trade-off between heat transfer and pressure losses. The pressure loss limit of 600 Pa/m was chosen with respect to the flow characteristics of some commercial axial fans, which are characterised with high flow rates and lower static pressures.

A channel’s hydraulic diameter for each possible combination of  $P(i)$ ,  $H(j)$  and  $t(k)$  was calculated as:

$$D_{h,i,j} = \frac{2 \cdot (P_i - t_k) (H_j - t_k)}{(P_i - t_k) + (H_j - t_k)} \quad (33)$$

An array of Reynolds numbers was obtained using Eq. (31), then the heat transfer coefficient was calculated as a function of the Reynolds number as follows:

$$htc_{i,j} = \frac{Re_{i,j} \mu c_p j}{D_{h,i,j} Pr^{2/3}} \quad (34)$$

where Eq. (16) was used to obtain the Colburn factor  $j$ . The pressure losses were calculated according to Eq. (32), where fanning friction factors from Eq. (18) and Eq. (19) were utilised. To find an optimum between high heat transfer coefficient and low pressure losses, a weight ratio system was utilised. The pressure losses were linearly scaled between values in  $<0; 1>$ , where the zero value was assigned to an array with value lower than the pressure loss limit of 600 Pa/m and a value of one was assigned to the minimum calculated pressure loss. The same was done with heat transfer coefficient, where one was considered the maximum calculated  $htc$  value and zero was considered the minimum  $htc$  in the array. This results in obtaining two arrays with values in the interval  $<0; 1>$ . The final weight was obtained by element-wise multiplication of the two arrays.

### OPTIMISATION RESULTS

According to the results, an increase in given dimensions of the fin thickness has a positive effect on the fin efficiency (shown in Figure 18), which is projected into a slight increase of the effective heat transfer coefficient, presented in Figure 21. Hence, a fin thickness of 0.3 mm can be proposed for the channel design. Combining the smallest given pitch and height values, a maximum effective heat transfer coefficient of  $htc = 41.7 \text{ W/m}^2\cdot\text{K}$  for the given boundary conditions can be reached.

However, this combination also contains a point with the highest calculated pressure loss, with a value of  $\Delta p = 3110$  Pa, which exceeds the given allowable limit by a factor of five (shown in Figure 19). When utilising the weight ratio system with the maximum allowable pressure loss of 600 Pa/m, a surface contour is obtained, as shown in Figure 20. The presented surface has a visible hyperbolic ridge, where the final weight reaches its maximum. This zone represents an area with optimum trade-off between the heat transfer coefficient and sufficiently low pressure losses. The preliminary design point was marked on this surface alongside three other points lying near the region with a local maximum, shown in Figure 22. The values of the effective heat transfer coefficient and the pressure losses for each point, as

well as the preliminary design point, are presented in Table 4. It can be noted that the preliminary design point has the highest value of the effective *htc* from the given points, namely 10.8% more than the average of the three points. However, the pressure loss is also the highest, at 35.4% more than the average. The differences of the values between the considered points are negligible; therefore, the final design can be proposed according to the matching aspect ratio H/P as the same geometry of the DUHS mock-up, where the experimental results were obtained and thus the results should match more closely. Hence, according to the data, the geometry at point two can be recommended for the future design.

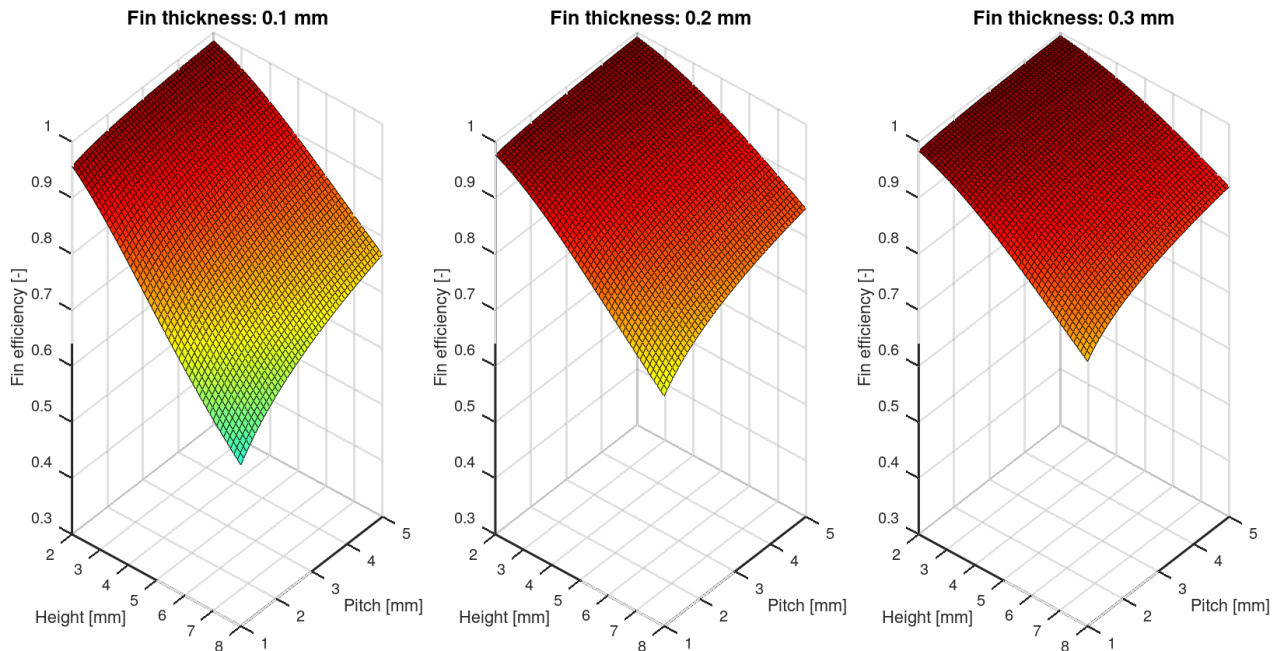


**Figure 18:** Comparison of a fin efficiency for different fin thicknesses (0.1; 0.2; 0.3 mm respectively).

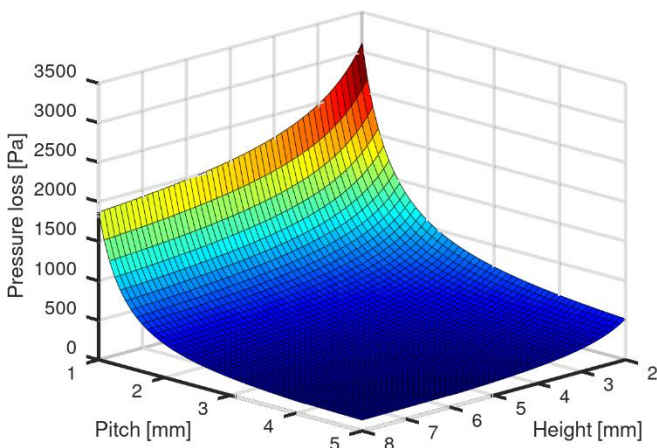


**Figure 19:** Pressure losses surface contour.

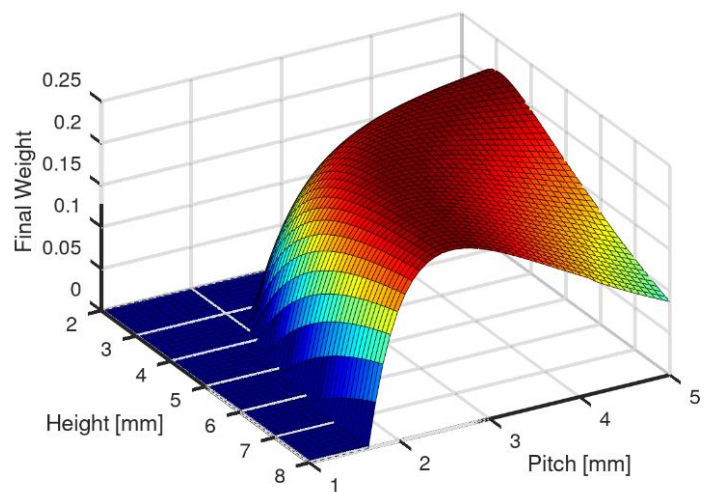


**Figure 20:** Final weight ratio surface contour.



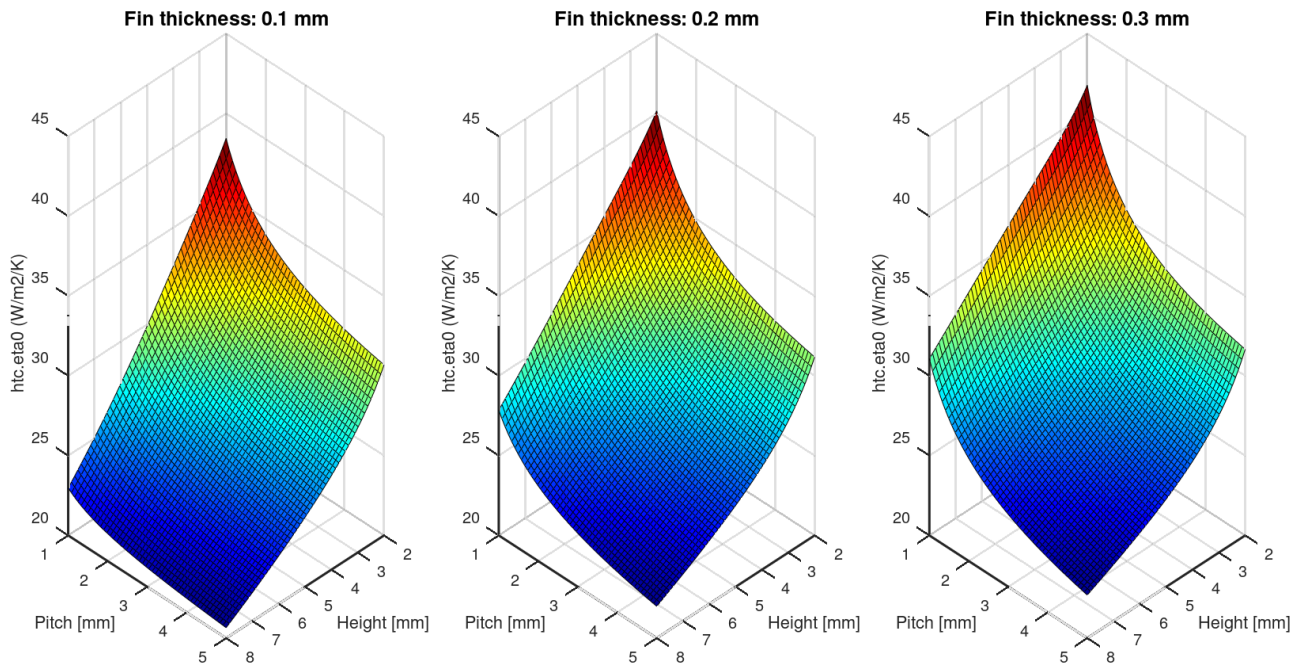


**Figure 21:** Comparison of an effective heat transfer coefficient for different fin thicknesses

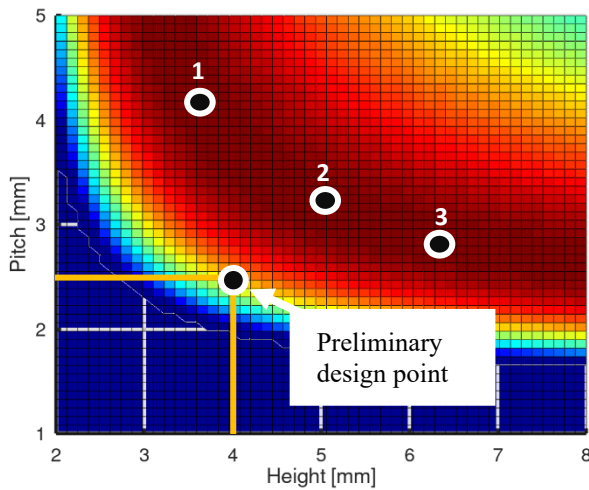


**Figure 22:** Final weight ratio surface contour - top view.

**Table 4:** Air channel optimisation points.

	<b>P (mm)</b>	<b>H (mm)</b>	<b>H/P</b>	<b>htc.n<sub>0</sub> (W/m<sup>2</sup>K)</b>	<b>Δp (Pa/m)</b>
Preliminary design	2.54	4	1.57	32.2	412
1	4.2	3.7	0.88	28.5	257
2	3.2	5	1.56	28.7	265
3	2.8	6.3	2.25	29	276

## CONCLUSION

The present work contains findings and results from the experimental campaign, verifying the thermal–hydraulic design of the plate and fin heat exchanger (PFHE) mock-up, which was designed and fabricated in the framework of the Horizon 2020 sCO<sub>2</sub>-4-NPP project. The preliminary PFHE concept was designed to exchange the heat between air and sCO<sub>2</sub>, where the sCO<sub>2</sub> side was operated at 8 MPa of pressure and a temperature range of <100; 172°C>. The main findings include the heat transfer and the fanning friction coefficients correlations on the air of the PFHE. Furthermore a 1D mathematical model was proposed and validated with the experimental data. Based on the results, an optimisation study of the air channels was made to find the channel geometry with optimal heat transfer and sufficiently low pressure losses. The results of this study show that increasing the fin thickness has a positive effect on the increase of the heat transfer coefficient. Moreover, an optimum field of the optimised parameters exists, for the given boundary conditions. Data points from this optimum field show a slight decrease in heat transfer coefficient compared to the preliminary design; however, they show in average up to 35% lower pressure losses.



## ACKNOWLEDGEMENTS

This project has received funding from the Euratom research and training programme 2014-2018 under grant agreements No 662116 (sCO<sub>2</sub>-Hero), No 764690 (sCO<sub>2</sub>-Flex) and No 847606 (sCO<sub>2</sub>-4-NPP).

The presented results were obtained using the CICRR infrastructure, which is financially supported by the Ministry of Education and Culture - project LM2023041



## DISCLAIMER

This text reflects only the author's view and the Commission is not liable for any use that may be made of the information contained therein.

## NOMENCLATURE

$A$	Total heat transfer area; m <sup>2</sup>
$A_f$	Fins heat transfer area; m <sup>2</sup>
$c_p$	Isobaric heat capacity; J/(kg.K)
$D_H$	Hydraulic diameter; m
$f$	Fanning friction coefficient; (-)
$G$	Mass-flow per flow cross-section; kg/(s.m <sup>2</sup> )
$H$	Channel height; m
$i$	Enthalpy; (J/kg)
$j$	Colburn factor; (-)
$k$	Thermal conductivity; W/(m.K)
$K_c$	Entrance friction factor; (-)
$K_e$	Exit friction factor; (-)
$L$	Effective length; m
$\dot{m}$	Mass flow; kg/s
$Nu$	Nusselt number; $Nu = h.D_p/k_f$ (-)
$N$	Number of channels; (-)
$Re$	Reynolds number; $Re_p = v \rho D_p/\mu$ (-)
$R$	Thermal resistance; W/(m <sup>2</sup> .K)
$p$	pressure; (Pa)
$P$	Channel Pitch; m
$Pr$	Prandtl number; $Pr = c_f.\mu/k$ (-)
$Q$	Transferred heat; W
$T$	Temperature; °C
$U$	Over all heat transfer coefficient; W/(m <sup>2</sup> .K)
$t$	Fin thickness; m
$v$	Flow velocity; m/s
$W$	Flow heat capacity; W/K
<b>Greek letters</b>	
$\varepsilon$	Heat exchanger effectiveness; (-)
$\Delta$	Difference
$\rho$	Density; kg/m <sup>3</sup>
$\mu$	Dynamic viscosity; Pa.s

$\eta_o$	Total surface effectiveness; (-)
$\eta_f$	Fin efficiency; (-)
$\sigma$	Contraction/expansion ratio
<b>Acronyms and abbreviations</b>	
<i>BWR</i>	Boiling water reactor
<i>DUHS</i>	Diverse ultimate heatsink
<i>htc</i>	Heat transfer coefficient, W/(m <sup>2</sup> .K)
<i>HX</i>	Heat exchanger
<i>LMTD</i>	Logarithmic mean temperature difference; °C/K
<i>NTU</i>	Net transfer unit; (-)
<i>FPM</i>	Fins per meter
<i>PFHE</i>	Plate and fin heat exchanger
<i>PID</i>	Piping and instrumentation diagram
<i>SBO</i>	Station blackout
<b>Subscripts</b>	
<i>s</i>	Solid
<i>m</i>	Mean value
<i>i</i>	Inlet/rows in array
<i>o</i>	Outlet

## REFERENCES

- [1] "sCO<sub>2</sub>-4-NPP." <https://www.sco2-4-npp.eu/> (accessed Aug. 09, 2022).
- [2] A. Vojáček, "SCO<sub>2</sub> EXPERIMENTAL LOOP AND CVR R&D ACTIVITIES," Sep. 01, 2017. [http://www.sco2-hero.eu/wp-content/uploads/2017/09/03\\_Vojacek\\_CVR\\_sCO2-experimental-loop-and-CVR-RD-activities.pdf](http://www.sco2-hero.eu/wp-content/uploads/2017/09/03_Vojacek_CVR_sCO2-experimental-loop-and-CVR-RD-activities.pdf) (accessed Aug. 09, 2022).
- [3] J. Venker, "Development and validation of models for simulation of supercritical carbon dioxide Brayton cycles and application to self-propelling heat removal systems in boiling water reactors," 2015.
- [4] E. W. Lemmon, and Ian H. Bell, M. L. Huber, and M. O. McLinden, "NIST Standard Reference Database 23: Reference Fluid Thermodynamic and Transport Properties-REFPROP, Version 10.0, National Institute of Standards and Technology." 2018. doi: <https://doi.org/10.18434/T4/1502528>.
- [5] V. Gnielinski, "Heat Transfer in Pipe Flow," in *Heat Atlas VDI*, 2010, pp. 693–699.
- [6] A. P. Colburn, "A method of correlating forced convection heat-transfer data and a comparison with fluid friction," *Int J Heat Mass Transf*, vol. 7, no. 12, pp. 1359–1384, Dec. 1964, doi: 10.1016/0017-9310(64)90125-5.
- [7] W. M. Rohsenow, James. P. Hartnett, and Y. I. Cho, "Heat exchangers," in *Handbook of heat transfer*, 1993, pp. 1277–1308.
- [8] W. M. Kays and A. L. London, *Compact Heat Exchangers, 3rd edition*. New York: McGraw-Hill, 1998.

## Appendix A

Exp.	F <sub>air</sub> (m <sup>3</sup> /h)	Δp <sub>air</sub> (Pa)	T <sub>in_Air</sub> (°C)	T <sub>out_Air</sub> (°C)	MF <sub>CO2</sub> (kg/s)	P <sub>abs_CO2</sub> (MPa)	Δp <sub>CO2</sub> (Pa)	T <sub>in_CO2</sub> (°C)	T <sub>out_CO2</sub> (°C)
1	18.15	18	20.3	84.4	0.0708	8	6340	101.6	98.2
2	122.4	133	20.3	70.3	0.0708	8	6100	102.2	86
3	235	322	21	59.2	0.0708	8	5830	103.3	80.2
4	339	620	21.8	55.1	0.0708	8	5750	104	74.3
5	455	1065	22.7	51.5	0.0708	8	5680	105.7	70.5
6	17.8	19	23	91.6	0.11	8	11400	108.5	105.2
7	120	134.5	21.4	77.2	0.11	8	11000	109	94.6
8	234	326	21.4	63.8	0.11	8	10480	109	88.1
9	336	625	21.9	60	0.11	8	10730	110.4	83.2
10	455	1080	23.2	57	0.11	8	10900	111.8	80
11	62	66	21.6	93.5	0.14	8	20200	112.7	104.5
12	119	135	21.7	82.5	0.14	8	19300	112.7	100.5
13	232	330	21.4	67	0.14	8	18700	112.5	94.5
14	335	630	21.7	62.8	0.14	8	17650	112.7	88.4
15	455	1080	22.5	58	0.14	8	16600	112.5	83.2
16	59	67	22.8	115.5	0.07	8	8900	142.2	126.6
17	128	156	22.1	93.8	0.07	8	7480	141.3	115.4
18	230	336	22.6	72.6	0.07	8	6540	135.5	99.6
19	344	670	23.3	66.5	0.07	8	6180	138	90.8
20	450	1085	22.7	61.6	0.07	8	6410	137	85
21	157	225	23	108	0.11	8	14400	172.2	140.6
22	242	406	23.3	93.8	0.11	8	13900	171.8	133
23	310	603	23.9	86.5	0.11	8	13500	171.6	125.1
24	379	852	24.1	82.7	0.11	8	13200	171	118.1
25	455	1183	25	78.3	0.11	8	13100	170	112.7
26	455	1160	25	73.1	0.081	8	7800	170	102.2
27	380	846	24.1	77.1	0.081	8	7840	170	106.9
28	304	567	23.9	81.3	0.081	8	8000	170	114.8
29	201	305	23.4	93.9	0.081	8	8450	171.3	127
30	81	104	23.6	123.5	0.081	8	9400	172.5	143.6

## PERFORMANCE ANALYSIS OF PTES LAYOUTS EVOLVING sCO<sub>2</sub> FOR INDUSTRIAL WHR INTEGRATION

**Simone Maccarini\***

Thermochemical Power Group, Department of  
Mechanical Engineering, University of Genova,  
Genova, Italy

Email: [simone.maccarini@edu.unige.it](mailto:simone.maccarini@edu.unige.it)

**Stefano Barberis**

Thermochemical Power Group, Department of  
Mechanical Engineering, University of Genova,  
Genova, Italy

**Syed Safer Mehdi Shamsi**  
Thermochemical Power Group,  
Department of Mechanical  
Engineering, University of Genova,  
Genova, Italy

**Lorenzo Gini**  
Thermochemical Power Group,  
Department of Mechanical  
Engineering, University of Genova,  
Genova, Italy

**Alberto Traverso**  
Thermochemical Power Group,  
Department of Mechanical  
Engineering, University of Genova,  
Genova, Italy

### ABSTRACT

A consistent amount of renewable energy (RES) from non-predictable sources in the energy mix brings an increasing need of energy storage technologies to support grid stability. At the same time, electrification of industrial processes as well as the more and more common habit of industries to self-produce power via RES or CHP, can make industries a partner in disrupting grid stability. Thermo-mechanical storages can contribute through the use of traditional technologies (rotating machinery) employed in power plants, which are currently used to manage peak demand and grid services, and typically classify as hours-size storages, also capable of providing spinning reserve services to the electrical grid. Among such type of storages, Pumped Thermal Energy Storages (PTES) are a promising technology that enhance the concept of power-to-heat-to-power and long duration energy storage, and presents also different layouts and applications. This paper analyse the thermal performance of Pumped Thermal Electricity Storage (PTES) evolving supercritical CO<sub>2</sub> (sCO<sub>2</sub>), comparing different layouts, while valorising waste heat (WH) sources, which are typically in temperature ranges of 100-400°C. WH temperature in this range are difficult to be exploited for traditional energy generation, but they are currently under investigation for the possibility to be valorised via High Temperature Heat Pump. In this sense this quality of Waste Heat could be valorised via PTES. In fact, the use of additional heat, otherwise dumped to ambient, may make the system capable of an apparent round-trip efficiency (RTE) higher than 100%. The use of sCO<sub>2</sub> could enhance the techno-economic features of these systems, if compared to similar plants evolving steam or air. Starting from an identified reference case (a cement production plant with WH temperature to be valorized around 350°C), a sCO<sub>2</sub>-based PTES cycle is presented and analysed in this paper. The waste heat integration to the PTES system has been found to add an undeniable value in terms of RTE. The use of sCO<sub>2</sub> enhances the

techno-economic features of these systems, the independent charging and discharging system proposed in this study can also provide a keen sense of flexibility. At the same time, the valorisation of low temperature waste heat enables industries to enhance their energy efficiency, limit their operational costs and environmental impact, whilst becoming an active part in the regulation of the grid. Nevertheless, CAPEX of the proposed systems are still quite relevant and only a robust exploitation of the PTES in ancillary service market could attract industrial customers interest on sCO<sub>2</sub> PTES.

### INTRODUCTION

Waste heat recovery (WHR) is a direct way to increase industrial energy efficiency and promote EU industry decarbonization and it is already recognized as a best practice in many different industrial sectors particularly to valorise high temperature Waste heat (WH). Nevertheless, as shown in Figure 1, most of the discharged WH during industrial processes is qualified as low-grade heat (under 200 °C) which poses several technical challenges for its exploitation towards power production or internal re-use.

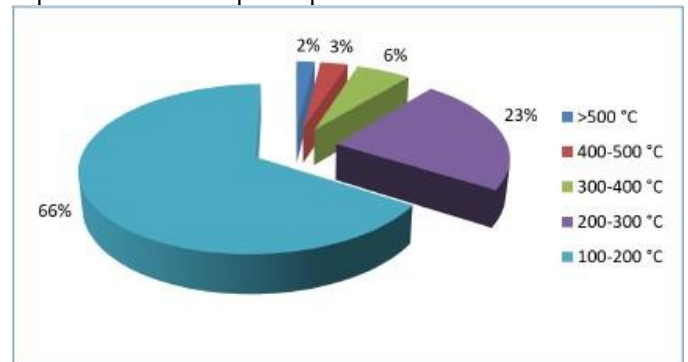


**Figure 1:** EU Industrial Waste Heat Potential Temperature distribution [1]

\* corresponding author(s)

A number of different technologies are available on the market depending on the source type, temperature range and end-use requirements, as shown in Figure 2.

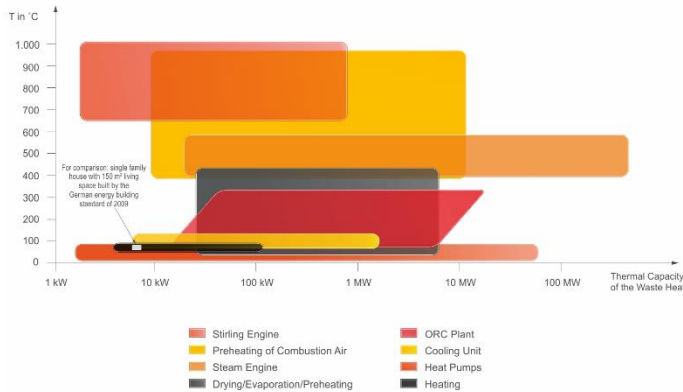


**Figure 2:** Waste Heat Recovery Technologies: temperature and thermal capacity classification [2]

Looking at medium grade WH (temperature ranges between 200-400 °C), which accounts for around 1/3 of EU WH, ORC (with quite low efficiency) seems to be the only way to valorise such WH. Nevertheless, sCO<sub>2</sub> power cycles are gaining more and more interest as WH-to-Power [3], even if the higher conversion efficiencies are reached with WH temperature higher than 350-400°C [4] [5].

WH utilization can be better addressed via Heat Pumps (HPs), in which field CO<sub>2</sub> (in trans critical and supercritical status) as a working fluid is being investigated for high temperature HPs [6]. The possibility to couple sCO<sub>2</sub> HPs and power cycles for bulky energy storage [7] in so called Carnot Batteries [8], while integrating external heat inputs for example coming from Concentrated Solar Power (CSP) [9], has been recently more and more investigated.

Even if the possibility to exploit sCO<sub>2</sub> power cycles for WHR applications is widely analysed [10], including different demonstration projects in US [11] and EU [12], the possibility of valorising WH via a sCO<sub>2</sub> HP for Power-to-heat-to-power (P2H2P) purposes has not been investigated so far. Looking at the fact that: 1) there are more and more fluctuating/non-predictable RES that un-stabilize the grid; 2) self-generation of power via CHP and RES systems is becoming a best practice in different industrial sectors; 3) Electrification of industrial processes seems to be a relevant technological option to reduce fossil fuel consumption in industries, it is quite important to identify solutions that could make industries as grid flexibility actors, while enabling them the possibility to valorise local WH at this purpose.

sCO<sub>2</sub> could make this possible, via WH P2H2P solutions exploiting sCO<sub>2</sub> HPs and power cycles. Basing on previous thermoeconomic analysis of advanced sCO<sub>2</sub> power cycles [13] and energy storage solutions [14], in this paper an innovative layout and concept is proposed, aiming at valorising industrial WH and achieving attractive Round-Trip Efficiency (RTE).

## PURPOSE OF THE STUDY AND CASE STUDY DESCRIPTION

In order to compare from a performance perspective the proposed WH driven P2H2P system with an existing sCO<sub>2</sub> plant for WH2P system (CO<sub>2</sub>OLHEAT project [12]), a cement plant is considered as case study [15].

On a typical cement plant with a capacity of 5,000 t/day, the flue gas flow rate is 300,000 Nm<sup>3</sup>/h with a temperature of 330°C and around 1/3 of exhaust air - “quaternary air” - representing 116,000 Nm<sup>3</sup>/h, which can be exploited thus having a WH source of around 10 MWth of maximum exploitable power at 330°C.

The idea is therefore to study a WH driven P2H2P system in which the waste heat acts as a heat source for the heat pump cycle that operates between the waste heat and the storage unit. The model is composed by: 1) a high temperature HP operating with sCO<sub>2</sub> able to valorise available WH (CHARGING CYCLE); 2) a Molten-Salt (MS) High temperature Thermal Energy Storage (TES) able to store heat produced by the HP (STORAGE ASSET); 3) a sCO<sub>2</sub> power cycle able to produce power once required exploiting the heat stored in the TES (DISCHARGING CYCLE). The goal of the study is to: 1) define sCO<sub>2</sub> cycles operating conditions and design parameters considering the proposed test case, also investigating different WH2P sCO<sub>2</sub> layouts (with or without recuperator); 2) analyse via a sensitivity analysis sCO<sub>2</sub> cycles operating conditions and design parameters towards RTE maximization and WH optimal valorisation; 3) compare from a thermodynamic performance point of view the proposed WH driven P2H2P solution with “state of the art” sCO<sub>2</sub> WH2P cycles.

## PROPOSED CYCLE LAYOUTS

Figure 3 shows the charging cycle where the heat from the WH source of the cement plant is valorised via a heat pump increasing its temperature. Such heat is then stored in a Molten Salt TES (HITEC commercial molten salt). The arrows on the heat exchangers show the direction of transfer of heat. The heat is picked up from the waste heat recovery heat exchanger (WH HEX) and transferred to the thermal energy storage heat exchanger (TES HEX) to be then stored in the TES.

As a result of TES charging, the hot effluents from the cement process are released to the ambient at much lower temperature, for instance from 330°C down to 150-80°C, depending on the HP operating conditions.

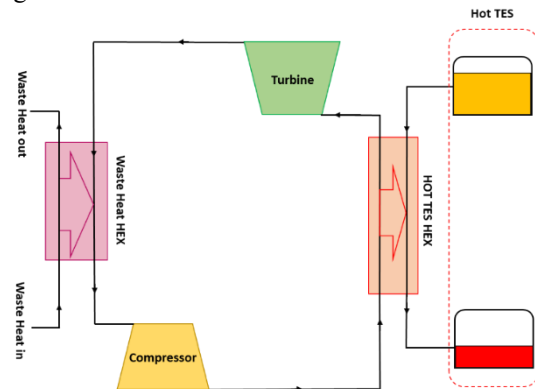


**Figure 3:** Charging cycle configuration

The charging cycle is followed by a discharging cycle. Figure 4 shows the three different configurations of the discharging cycle that will be studied to find out the most suitable configuration for this case study. Figure 4(a) shows a simple sCO<sub>2</sub> discharging cycle valorising the heat stored in the TES: the sCO<sub>2</sub> working fluid gets compressed and absorbs heat along TES HEX entering the sCO<sub>2</sub> turbine, expanding and dissipating the remaining heat in the cooling HEX. The cooling HEX for the discharging operates at a much lower temperature than the WH temperature, thus significantly reducing the compressor work even if working with the same compression ratios.

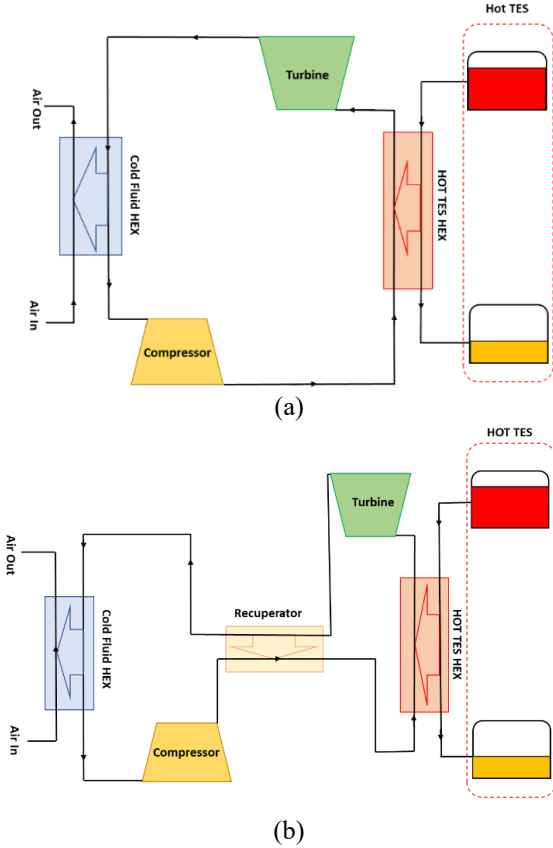


**Figure 4:** Discharging cycle configurations: (a) simple discharge cycle (b) recuperated discharging cycle

In order to maximise the efficiency of the discharging cycle, a recuperated sCO<sub>2</sub> cycle was analysed too. The recuperated heat is utilized right after the compressor, which makes the discharging heat utilization more efficient. The discharging cycle configurations were analysed searching for optimum performance in terms of electrical RTE.

## MODELLING APPROACH DESCRIPTION

The modelling procedure used to get the thermodynamic properties of the cycles is mentioned in this section. Furthermore the economic assumptions and approach used for the component cost calculation are described in detail.

## Cycle modelling technique and information flow

All the thermodynamic computations were done using a modified version of WTEMP-EVO, a component-based in-house thermo-economic simulation tool. It is developed in MATLAB<sup>®</sup>, integrating Coolprop [16] libraries for fluid properties, and it can simulate energy systems through the assembly of the desired layout, as explained in [17]. The tool evolves the solution of each component using simple characteristic equations for mass and energy balances, and pressure computation; some of them are reported in the followings.

$$p_{Out} = p_{In} \cdot \beta_{Compr} \quad (1)$$

$$p_{Out} = p_{In} * (1 - \Delta p_{\%Loss}) \quad (2)$$

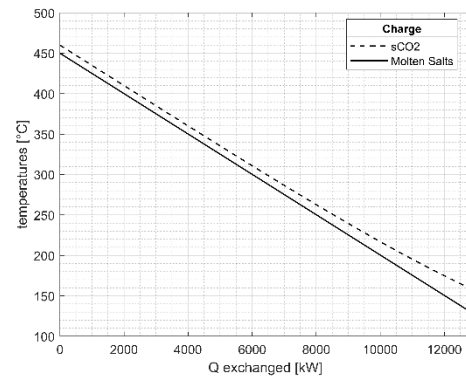
$$h_{Out} = h_{In} + \eta_{Turb} \cdot (h_{Out-isoentr} - h_{In}) \quad (3)$$

$$h_{Out} = h_{In} + (h_{Out-isoentr} - h_{In}) / \eta_{Comp} \quad (4)$$

$$\varepsilon_{HEX} = Q_{HEX} / Q_{HEX-max} \quad (5)$$

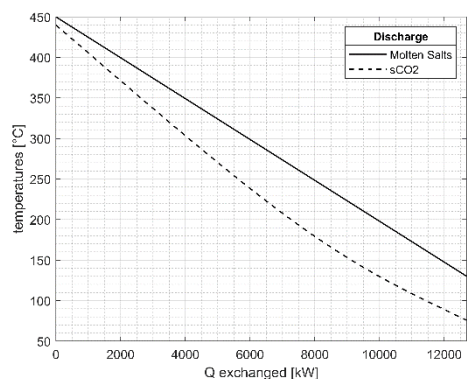
$$Q_{HEX} = \dot{m}_{cold} * (h_{Out-cold} - h_{In-cold}) \quad (6)$$

The maximum heat that can be exchanged by an heat exchanger ( $Q_{HEX-max}$ ) is computed as the maximum amount of heat that can be transferred, from the hot to the cold fluid, in a counterflow heat exchanger that has an infinite area, thus leading to a temperature difference between the hot and cold fluid which is equal to zero in a certain point. If the properties of the fluids change throughout the heat exchanger, an internal pinch point can appear (e.g., when a peak is present in the value of the specific heat capacity of the hot fluid), and the computation of the maximum heat with this method allows to spot the temperature at which the internal pinch point can appear in the case of an ideal counterflow heat exchanger, and assign that value of that heat as the maximum possible.



(a)





(b)

**Figure 5:** High temperature (TES HEX) Heat exchanger thermal exchange behaviour – (a) charging, (b) discharging

Once the desired cycle layout is defined, it is assembled by calling the functions corresponding to the necessary components in the layout (turbomachinery, heat exchangers, etc), and a system of nonlinear equations is formed accordingly. Then, some of the variables are set, accordingly to the assumptions, to define the degrees of freedom of the layout, and the system of equations is solved numerically until convergence is achieved.

Following the thermodynamic resolution of the cycle, it is possible to compute the geometry and the cost of the main equipment necessary to realize the layout, as described in [17].

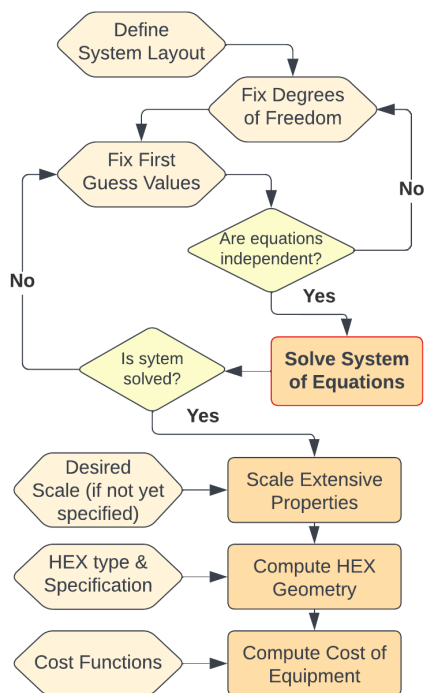


**Figure 6:** Algorithm flowchart of the modified WTEMP-EVO tool

### Thermodynamic modelling assumptions

Since the PTES systems basically consist of two separate cycles, one for charge and one for discharge, the simulation use this approach of separating the computation of the two cycles, connecting the two by imposing the equivalence of the temperatures of the TES, and the amount of energy and mass stored in it.

In practice, the code firstly computes the discharge cycle, and then uses the results to initialize the computation of the charge cycle. To be more precise, since the discharge layout consists of a recuperated cycle, the minimum temperature of the TES depends, for both charge and discharge, on the inlet temperature of the Hot HEX in the discharging cycle, and thus on the effectiveness of the recuperator. For this reason the discharge is computed as first, and then minimum temperature of the TES is used to initialize the discharge cycle.

Modelling approach for this specific study consisted in separate calculations of the charging and the discharging cycles, in order to perform a sensitivity analysis on some identified parameters among the most relevant ones for each layout.

Considering WH available temperature, the commercial TES MS storage media HITEC XL, capable of operating temperatures between 130°C and 450°C [18], was identified giving thus priority to the utilisation of a commercial fluid.

In the charging cycle, the following variables has been selected to be varied in the sensitivity analyses: the two cycle operating pressures (maximum and minimum ones, considered at compressor extremes), and the maximum and minimum temperature of the TES material.

The assumptions for the charging and discharging cycle are shown in Table 1, while TES material properties are presented in Table 2.

**Table 1 – Thermodynamic modelling assumptions**

Assumptions	Value	UoM
TES Max temperature	450	°C
Recuperator Effectiveness	60 ; 80	%
Isentropic efficiency turbomachinery	80	%
Thermal losses of the TES	1	%
Electrical efficiency	98	%
Mechanical efficiency	98	%
Pressure loss in heat exchanger	2	%
Min $\Delta T$ Heat Exchangers	10	K
Compressor Inlet Temp.	35	°C
Ambient Temperature $T_0$	25	°C
Air Temperature Cooler Exit	45	°C
Waste Heat Temperature	330	°C
Waste Heat mass flow rate	38.6	kg/s

**Table 2 – HITEC XL TES Material properties [19]**

Maximum Temperature [°C]	450
Minimum Temperature [°C]	130
Density [kg/m <sup>3</sup> ]	1877
Specific Heat [kJ/kgK]	1.426
Thermal conductivity [W/mK]	0.52
Cost [\$/kg]	1.6



The temperature and pressure levels of the discharging phase where chosen in order to maximise the behaviour of this cycle, and then a corresponding charging cycle was properly studied and selected. In fact, this was possible due to the fact that the charging and discharging cycles were considered fully decoupled, with respect to a standalone PTES, because of the possibility of integration with WH at high temperature.

In the following paragraphs, performance sensitivity analyses of charging and discharging cycles are presented, targeting the matching of the two cycles, and starting from the discharging phase.

Performance is judged mainly in terms of electrical RTE (i.e. accounting only for the electrical energy flows) and in terms of exergetic RTE (i.e. accounting for electrical and thermal exergy flows); the exergetic efficiency of a cycle  $\eta_{ex}$  is used for the evaluation of the direct utilisation of the waste heat. These parameters are defined by the following equations, where E is the energy, P the power,  $\Delta t$  is the charging and discharging time,  $T_0$  is the ambient temperature, and  $\dot{Q}_{WH}$  is the heat flow rate absorbed from the waste heat gases:

$$RTE_{el} = \frac{E_{DC}}{E_{CC}} = \frac{P_{DC} \cdot \Delta t_{DC}}{P_{CC} \cdot \Delta t_{CC}} = \frac{P_{DC}}{P_{CC}} \quad (1)$$

$$RTE_{ex} = \frac{P_{DC}}{P_{CC} + \dot{Q}_{WH} \cdot \left(1 - \frac{T_0}{T_{avg}}\right)} \quad (2)$$

$$\eta_{ex} = \frac{P}{\dot{Q}_{WH} \cdot \left(1 - \frac{T_0}{T_{avg}}\right)} \quad (3)$$

$$T_{avg} = \frac{\int_{in}^{out} T ds}{s_{out} - s_{in}} \cong \frac{h_{out} - h_{in}}{s_{out} - s_{in}}; \quad \text{if } p \cong \text{const.} \quad (4)$$

In fact, considering equal duration of charging and discharging phases, the electrical RTE can be easily calculated on the electrical total power (consumed and produced respectively) of the two cycles (instead of based on total electrical energy values), as the two cycles are obtained considering the same storage dimension and thus the same mass flow rate of the TES fluid, in this case. Similarly, the exergetic RTE can be derived basing on electrical power and exergy flows. The exergetic RTE is computed considering the actual WH input to the cycle and, since the heat exchange does not occur at constant temperature, the corresponding thermodynamic-average temperature  $T_{avg}$  at which the heat exchange can be considered to occur, computed as in Eq. 4 [20].

### Cost assumptions

In order to evaluate the CAPEX of the system, further than HEX cost functions as presented in [18-19], typical sCO<sub>2</sub> power cycle components (turbine – compressor – recuperator) cost functions have been considered here, properly correcting them (particularly once studying “hot compressor” and “cold turbines” in HP/charging cycles) according to literature “correction factor”

approach [21] in order to take into account different materials used to manufacture components in operating conditions that are different than usual ones. Cost function presented in [22] were therefore multiplied and divided by a correction factor of 2.035 and 1.764 respectively to evaluate compressor and turbine CAPEX, considering the different material/operating temperature once such components are operating in HP charging cycle.

### DISCHARGING CYCLE (DC) - SUPERCRITICAL CO<sub>2</sub> POWER CYCLES (WITH/WITHOUT RECUPERATOR)

For what concerns the discharging cycles, typical values for sCO<sub>2</sub> where selected, leading to a maximum pressure considered of 250 bar (this value has been identified by the authors following their experiences in previous study [13], for technological reasons in order not to face too much challenging operation conditions – e.g. manageable compression ratios, use of pressurized HEXs...). Moreover, considering aforementioned assumptions, the maximum CO<sub>2</sub> temperature was selected to be 440°C, while a typical value of 35°C was selected for the compressor inlet temperature, to ensure a stable behaviour of the compressor itself.

The objective of the analysis was to investigate the points in which a match with the charging cycle (to be presented hereafter) can lead to a maximisation of the electrical RTE.

Figure 7 shows the electrical power achievable by a simple CO<sub>2</sub> cycle given a constant mass of molten salts as heat source, with respect to the minimum pressure of the cycle and the minimum TES temperature. From this analysis, while keeping constant all the other variables, the best point for the discharging cycle is identified targeting maximisation of produced power: not surprisingly, the best minimum pressure corresponds closely to the CO<sub>2</sub> critical pressure.

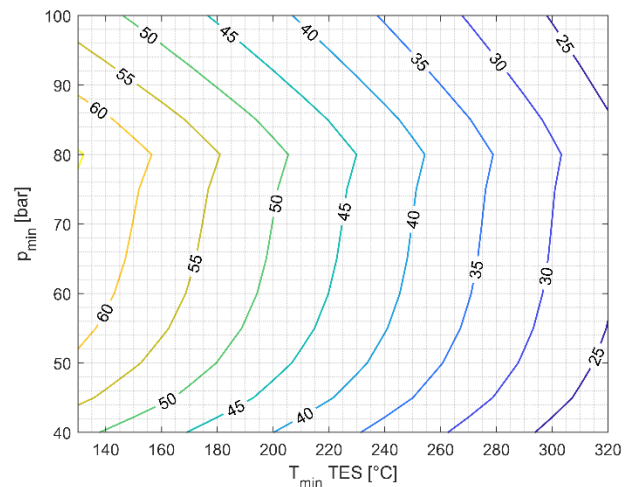


**Figure 7:** Total net power that can be achieved by a simple cycle for a 1 kg/s mass flow rate of the molten salts.

Looking at a recuperated cycle, the value of the minimum temperature of the TES is dependent mainly on the grade of recuperation chosen for the cycle.

The following figures represent the values of this temperature (Fig. 8) and the values of efficiency (Fig.9) and net power (fig.10) that can be achieved by the systems.

The best results are achieved near 80 to 85 bar. While the efficiency of the cycle increases with the recuperator effectiveness, this parameter does not influence much the total power that can be extracted by the TES source, given a constant total mass.

Two extreme values of the recuperator effectiveness are then chosen to represent the behaviour of the recuperated layout: 60% and 80% effectiveness. From those, an optimal value of minimum pressure ensuring the maximum achievable power was chosen equal to 83 bar, being in the above mentioned range as well as guaranteeing a proper compressor operation according to authors' experience [13].

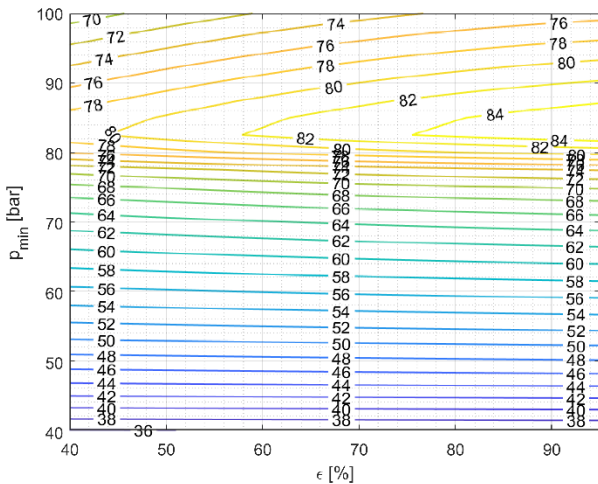


**Figure 8:** Total net power that can be achieved by a recuperated cycle for a 1 kg/s mass flow rate of the molten salts; abscissa is the effectiveness of the recuperator.

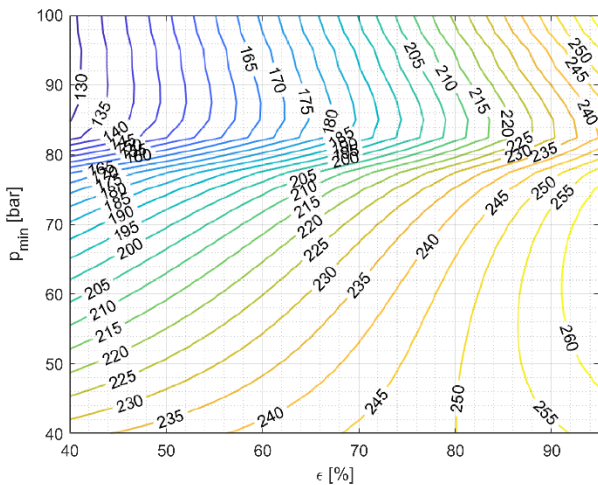


**Figure 9:** Heater inlet temperature in a recuperated cycle; abscissa is the effectiveness of the recuperator.

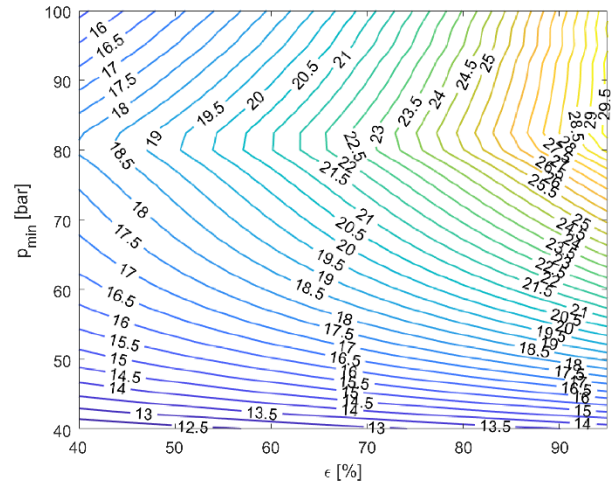


**Figure 10:** Thermal efficiency in a recuperated cycle; abscissa is the effectiveness of the recuperator.

### CHARGING CYCLE (CC) – SUPERCRITICAL CO<sub>2</sub> HEAT PUMP CYCLES

The analyses of the discharging cycles (targeting net power maximisation) allowed to select three values of minimum temperature of the TES to be analysed in the charging cycle.

For each discharging case, a corresponding charging one was analysed, fixing the minimum temperature of the TES at 130°C for the first case, related to the simple discharging one. For the second and third charging cases, corresponding respectively to discharging cycles with low (60%) and high (80%) effectiveness of the recuperator, the TES minimum temperature was assumed equal to 183°C and 222°C, respectively. Since the behaviour of the analysed parameters is similar in all the cases, only the simple discharging and the 80% recuperated discharging cycles results are presented in the following paragraphs.

A common operating performance value to be monitored during the charging phase for all these cases is the compressor outlet temperature. Such temperature, having set the values of the other temperatures, varies with the pressures, but only the values higher than or equal to 460°C were taken into account, given the initial assumptions related to the identified MS TES storage media. In all the following figures the line related to the minimum temperature is drawn in red, separating the not-acceptable values (above) and the real values (below), while the blue region represents a zone with pressure ratio too close to 1 or even lower.

Thus, it is clear that the initial hypothesis on the temperature strongly affects the behaviour of the charging cycle HP and a sensitivity on different values of temperature were needed. Moreover, this behaviour is also highly related to the assumptions on the machinery efficiency, which affect the performance of the heat pump cycle.

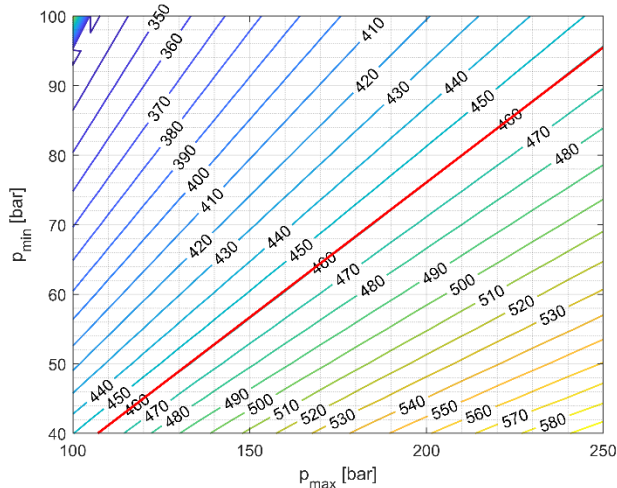


**Figure 11:** sCO<sub>2</sub> Maximum temperature in the charging cycle. The minimum allowable value is 460 °C.

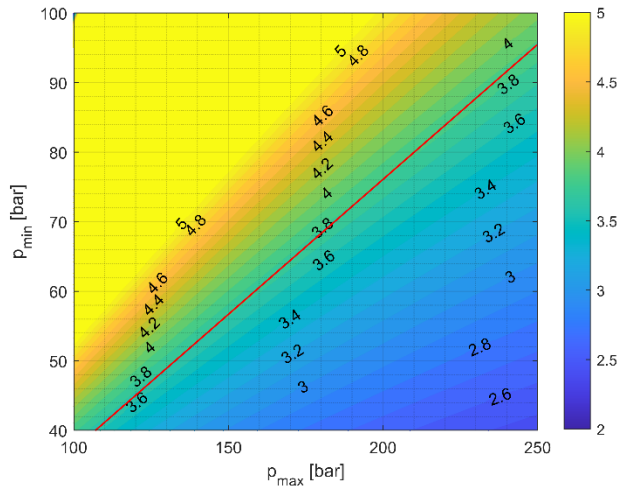


**Figure 12:** COP of a charge with min Temp of the TES equal to 130°C (acceptable area is below the red line).

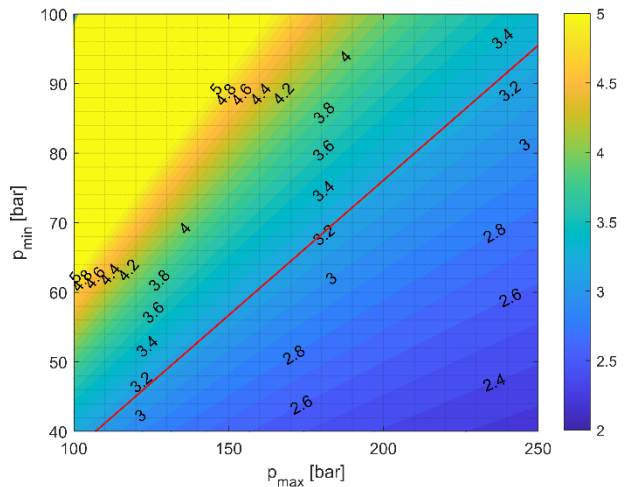


**Figure 13:** COP of a charge with min Temp of the TES equal to 222°C (acceptable area is below the red line).

Analysing the figures representing the HP net power consumption trend, it is worth highlighting that, as for the COP behaviour, power values are quite aligned with temperature values. For example, a value close to 460°C (lowest acceptable sCO<sub>2</sub> temperature) foresees a pressure ratio close to 2.6, and leads to a COP between 3.7 and 3.9.

This is interesting mainly for two reasons: first, a simple thermodynamic optimum would lead to choose high pressure, while a thermo-economic point of view could move the selected point towards lower pressures only for the charging cycle; second, operating at low pressure can increase the influence of the variation of thermophysical properties of sCO<sub>2</sub>, and in particular of the specific heat, potentially leading the heat exchangers to an internal pinch point lower than the assumed values of temperature difference at the extremes. This would imply a more detailed analysis of the heat exchangers, potentially involving introduction of multiple heat exchanger and TES units, carrying different mass flows to better couple the CO<sub>2</sub> heat capacity rate variation.

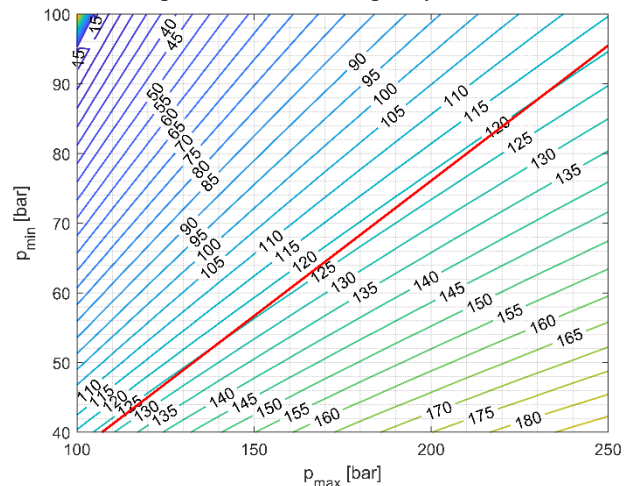


**Figure 14:** Net Power absorbed in a charge with min Temp of the TES equal to 130°C (acceptable area is below the red line).

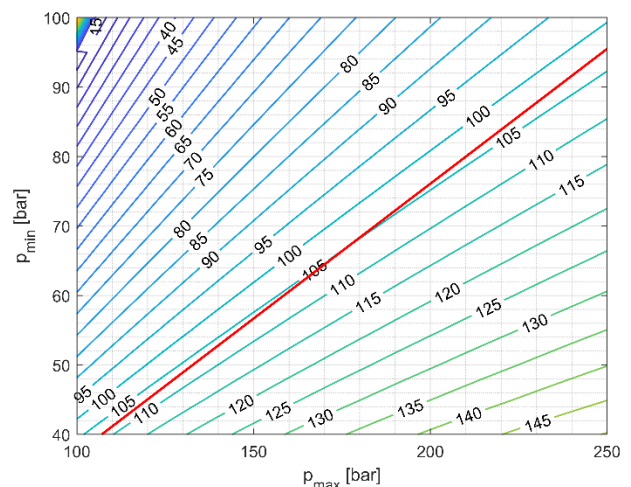


**Figure 15:** Net Power absorbed in a charge with min Temp of the TES equal to 222°C (acceptable area is below the red line).



## WH DRIVEN P2H2P SYSTEM

All the previous analyses conducted for the discharging and the related charging cycles led to the definition of the most effective P2H2P cycle operating points (Figure 16), starting from the initial assumptions and targeting the maximisation of the apparent electrical RTE, thus not considering the amount of the used WH.

The results obtained are then presented in the following tables, always presenting three cases for the discharging cycles:

- I) simple cycle
- II) recuperated cycle with 60% recuperator effectiveness
- III) recuperated cycle with 80% recuperator effectiveness

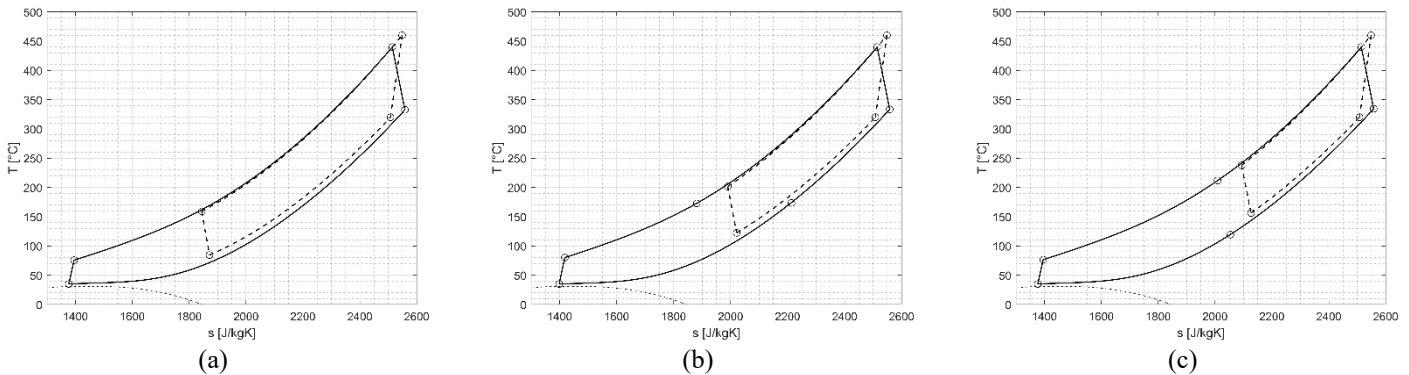


Figure 16: T-s Diagrams for CASE I (a), II (b), III (c)

First, Table 3 presents the values of minimum pressures and TES temperature identified as the best operating parameters. The maximum optimal pressure resulted to be 250 bar for all the cycles (both in charging and discharging phase), i.e. the maximum allowed. Table 4 instead presents the values obtained in CC for the absorbed heat power from waste heat and the resulting temperature at which it is then released, and the values, for DC, of the temperature at which the heat is released. These temperatures are all above 100°C and this is due to the fact that the cycle layouts analysed rely on a Brayton-like configuration and thus they release heat to the cold source in a sensible way. These values suggest a possible further utilisation as process heat, or even the investigation of different layouts here not considered.

Table 3 - Minimum pressures and minimum TES temperature, for the best operating conditions

CASE	Layout	CC $p_{min}$	DC $p_{min}$	TES $T_{min}$
I	CC + SDC	95.5 bar	83 bar	130 °C
II	CC + RDC (60%)	95.5 bar	83 bar	183 °C
III	CC + RDC (80%)	95.5 bar	83 bar	222 °C

Table 4 - Main parameters of heat exchange with the cold sources

CASE	CC WH Power	CC TES HEX Power	CC WH min Temp	DC $T_{in}$ Cooler
I	9.35 MW <sub>th</sub>	12.8 MW <sub>th</sub>	94.5 °C	332.7 °C
II	7.87 MW <sub>th</sub>	11.2 MW <sub>th</sub>	132 °C	173.5 °C
III	6.54 MW <sub>th</sub>	9.6 MW <sub>th</sub>	166 °C	119 °C

The values of electrical RTE (presented in Table 5) show low performance for the case I, the one coupling a simple charging cycle (CC) and a simple discharging one (SDC). Better results are instead achieved using a recuperated discharging cycle (RDC), leading to values even higher than 70%. The utilisation of WH in a PTES is thus confirmed to allow reaching values of electrical RTE otherwise impossible with standalone PTES configuration, considering similar general assumptions. This comes at the cost of using the source of heat, and thus the exergetic RTE better represents the actual use of all the energy inputs involved in the process. Between the solutions investigated, the highly recuperated one shows to be most efficient exergetic RTE, despite the result does not show a good utilisation of the energy inputs, reaching values lower than 40%.

Table 5 – Net Powers and electrical RTE for the optimum points applied to the specific case study

CASE	DC Net Power	CC Net Power	RTE (electrical)	RTE (exergetic)
I	1.63 MW	3.34 MW	49.0%	24.8 %
II	2.10 MW	3.16 MW	66.4%	34.0 %
III	2.18 MW	2.98 MW	73.3%	38.8 %

Finally, it is worthy to underline the relevance of heat exchanger assumptions (Fig.5), since their design performance significantly impacts on cycle performance and should take into account the sCO<sub>2</sub> real-gas behaviour. This aspect would deserve a separate dedicated investigation.

## CAPEX ESTIMATIONS

Table 6 shows the capital cost of the components needed for the three analysed cases. All the values are in M\$ and they are

calculated using the cost functions described in previous sections as well as components sizes from thermodynamic calculations. A 100 MWh TES have been considered. Cost of the compressor and turbine depends on the power output. Heat exchangers costs are based on the UA. The UA value was calculated for the counter flow for all the heat exchangers using log mean temperature difference (LMTD) method, even though this can cause an under-sizing of the heat exchangers where a consistent change of fluid properties occur. According to the power requirement internally geared (IG) centrifugal compressor were used for both charging and discharging while axial turbines were used in both the cases.

The highest cost for all the components is of the TES System, both in terms of TES capacity and TES HEX.

**Table 6 – Estimated CAPEX**

Components	I CC + SDC	II CC + RDC (60%)	III CC + RDC (80%)	WH2P (RC 80%)
CC Compressor	4.58	4.66	4.69	\
CC Turbine	0.11	0.13	0.15	\
WH HEX	1.58	1.39	1.21	1.59
DC Compressor	1.08	1.25	1.24	1.33
TES HEX	1.29	1.80	1.60	\
DC Turbine	0.29	0.34	0.35	0.33
Air Cooler HEX	0.36	0.48	0.54	0.65
Recuperator	/	0.16	0.31	0.35
TES	4.34	4.34	4.34	/
<b>OVERALL</b>	<b>13.65</b>	<b>14.55</b>	<b>14.43</b>	<b>4.26</b>

This is evident by the figure 5, which shows the internal features of the heat exchanger. The temperature difference between the hot side fluid and cold side fluid remain more or less 10K for the whole duration of heat transfer, which tend to make the area of the heat exchanger unusually large. This TES heat exchanger referred in table 6 as TES HEX is similar for the charge and discharge cycle. Although the pressures are not similar for charge and discharge, the UA is calculated for the larger value of pressure which belongs to the discharge cycle. The parameters of pressure and mass flow rate are different, whereas the temperature difference between the inlet and the outlet of TES HEX are same for the charging and the discharging cycle.

Although reversible machinery is being tested for lab scale PTES systems [23], large scale reversible sCO<sub>2</sub> machinery are not technologically ready yet for large scale plants. Therefore separate turbomachinery for charging and discharging are considered-

## BENCHMARKING WITH OTHER WHR ENERGY SYSTEMS SOLUTIONS

A first comparison of the proposed WH driven P2H2P with direct utilisation of the WH for power production can be done basing on one of the cycle layouts used for the P2H2P solution, in particular the simple recuperated cycle. In fact, despite a recuperated cycle does not maximise the WH exploitation, it has been proven to be a viable solution on a thermo-economic point of view [17]. As it can be seen by comparing the tables, the utilisation of the P2H2P system leads to an increase of the net power in discharging phase, if compared to a WH2P sCO<sub>2</sub> system, due to the fact that sCO<sub>2</sub> TIT is higher.

**Table 7 - Results of recuperated cycles applied to the case-study waste heat source**

CASE	p <sub>min</sub>	Net Power	Efficiency	WH T <sub>out</sub>	Exergetic efficiency
RDC (60%)	83 bar	1.71 MW	16.2 %	137 °C	42.6 %
RDC (80%)	83 bar	1.76 MW	18.6 %	157 °C	47 %

Looking at exergy utilisation as a term of comparison for the two different solutions applied to the available waste heat, it can be seen that the direct WH2P solutions are able to achieve higher values for the case study analysed. Thus, this can lead to the conclusion that the system analysed is not competitive with a WH2P utilisation on a purely thermodynamic point of view.

It is also worthy to mention that such a WH2P cycle (if whose costs are estimated via the same costs functions as reported in Table 6) could have a CAPEX around 4.26 M\$ which is significantly lower (at least around -60% of CAPEX) if compared to PTES CAPEX expressed in table. Nevertheless, it is relevant to highlight that such type of plant could not be operated in a flexible way on the electric market, thus not featuring any grid support service which are usually more remunerative power production revenue lines. A more detailed thermo-economic analysis needs to be carried out for a more comprehensive comparison.

## CONCLUSIONS

This work analyses, from a thermodynamic performance and CAPEX point of view., WH driven sCO<sub>2</sub> P2H2P cycles layouts at on-design conditions, presenting a specific case study on cement industry. Sensitivity analyses were made in order to explore the performance features of the charging and the discharging cycles that constitute a PTES system. Performance has been judged mainly in terms of electrical RTE (i.e. accounting only for the electrical energy flows) and in terms of exergetic RTE (i.e. accounting for electrical and thermal exergy flows). In particular, attention is paid to the electrical RTE enhancement potential when the P2H2P system is coupled with industrial waste heat recovery. Based upon the results obtained from such analyses, the most effective operating conditions (targeting electrical RTE maximisation) for the integrated system are presented, for each of the combinations investigated.

Electrical RTE higher than 70%, are obtained envisaging the use of a recuperated cycle in the discharging phase, higher than what can be achieved with standalone PTES systems working in similar conditions. Moreover, a recuperated solution achieves a better result with a limited increase of the TES minimum temperature and thus of its dimension. Actually, the presented solution, leveraging on availability of WHR, can also achieve the elimination of a TES at low temperature, necessary in standalone PTES configurations (thus bringing to a CAPEX saving of the PTES). These results come of course at the cost of the utilisation of WH together with the net power of the charging phase: exergetic RTE shows that even the best of the analysed configurations cannot achieve a result higher than 45%. For the same WHR case study condition, a simple WH2P configuration using the same recuperated cycle layout achieve exergetic efficiencies of 45-50%, showing a better exploitation of its exergetic inputs with respect to the PTES system, for the same case study. This suggest further analyses to be conducted to investigate different temperature levels (also at high Temperature TES level), or even different cycle layouts, to achieve a more comprehensive comparison of the solutions. On the other side, it is worthy to remark that the utilisation of WH PTES is able to decouple the “power production” and the “power utilization/storage” with respect to a traditional WH2P solution, . Therefore, despite higher CAPEX, the attractiveness of the more complex WH PTES solution against the conventional WH2P solution might become clear from a more focused and dedicated thermoeconomic analysis, considering the additional possibility of selling services to the electrical grid and/or the additional flexibility in modulating the electrical power flows depending on the electrical market prices (night/day price profiles).

## NOMENCLATURE

CC	Charging Cycle
COP	Coefficient of Performance
DC	Discharging Cycle
HEX	Heat Exchanger
HP	Heat Pump
MS	Molten Salt
P2H2P	Power to Heat to Power
$p_{max}$	Maximum Pressure
$p_{min}$	Minimum Pressure
PTES	Pumped Thermal Energy Storage
RDC	Recuperated Discharging Cycle
RES	Renewable Energy Sources
RTE	Round Trip Efficiency
TES	Thermal Energy Storage
WH	Waste Heat
WH2P	Waste Heat to Power
WHR	Waste Heat Recovery

## REFERENCES

[1] C. Haddad, C. Périlhon, A. Danlos, M.-X. François, and G. Descombes, “Some Efficient Solutions to Recover Low

- and Medium Waste Heat: Competitiveness of the Thermoacoustic Technology,” *Energy Procedia*, vol. 50, pp. 1056–1069, Jan. 2014, doi: 10.1016/j.egypro.2014.06.125.
- [2] <https://www.waste-heat.eu/about-waste-heat/waste-heat-technologies> - Accessed: 11 Jan. 2023. [Online].
- [3] M. T. White, G. Bianchi, L. Chai, S. A. Tassou, and A. I. Sayma, “Review of supercritical CO2 technologies and systems for power generation,” *Appl. Therm. Eng.*, vol. 185, p. 116447, Feb. 2021, doi: 10.1016/j.applthermaleng.2020.116447.
- [4] D. Alfani, M. Binotti, E. Macchi, P. Silva, and M. Astolfi, “sCO2 power plants for waste heat recovery: design optimization and part-load operation strategies,” *Appl. Therm. Eng.*, vol. 195, p. 117013, Aug. 2021, doi: 10.1016/j.applthermaleng.2021.117013.
- [5] M. Marchionni, G. Bianchi, and S. A. Tassou, “Review of supercritical carbon dioxide (sCO2) technologies for high-grade waste heat to power conversion,” *SN Appl. Sci.*, vol. 2, no. 4, p. 611, Mar. 2020, doi: 10.1007/s42452-020-2116-6.
- [6] C. Mateu-Royo, C. Arpagaus, A. Mota-Babiloni, J. Navarro-Esbrí, and S. S. Bertsch, “Advanced high temperature heat pump configurations using low GWP refrigerants for industrial waste heat recovery: A comprehensive study,” *Energy Convers. Manag.*, vol. 229, p. 113752, Feb. 2021, doi: 10.1016/j.enconman.2020.113752.
- [7] P. Tafur-Escanta, R. Valencia-Chapi, M. López-Guillem, O. Fierros-Peraza, and J. Muñoz-Antón, “Electrical energy storage using a supercritical CO2 heat pump,” *Energy Rep.*, vol. 8, pp. 502–507, Jun. 2022, doi: 10.1016/j.egypr.2022.01.073.
- [8] T. Liang *et al.*, “Key components for Carnot Battery: Technology review, technical barriers and selection criteria,” *Renew. Sustain. Energy Rev.*, vol. 163, p. 112478, Jul. 2022, doi: 10.1016/j.rser.2022.112478.
- [9] “Supercritical CO2 Heat Pumps and Power Cycles for Concentrating Solar Power: Preprint,” *Renew. Energy*, p. 13, 2020.
- [10] L. Liu, Q. Yang, and G. Cui, “Supercritical Carbon Dioxide(s-CO2) Power Cycle for Waste Heat Recovery: A Review from Thermodynamic Perspective,” *Processes*, vol. 8, no. 11, Art. no. 11, Nov. 2020, doi: 10.3390/pr8111461.
- [11] Alex Kcludis, Sean Lyons, Dan Nadav, and Edward Zdankiewicz, “Waste Heat to Power (WH2P) Applications Using a Supercritical CO2-Based Power Cycle.,” in *Proceedings of Power-Gen International 2012*, Orlando, FL U.S.A., Dec. 2012.
- [12] “Home,” *CO2OLHEAT*. <https://co2olheat-h2020.eu/> (accessed Oct. 27, 2022).
- [13] Guédez, R, Barberis, S, Maccarini, S, López-Román, A, Milani, A, Pesatori, E, Oyarzábal, U, & Sánchez, A. "Design of a 2 MW Molten Salt Driven Supercritical CO2 Cycle and Turbomachinery for the SOLARSCO2OL Demonstration Project." Proceedings of the ASME Turbo Expo 2022: Turbomachinery Technical Conference and



- Exposition. Volume 9: Supercritical CO<sub>2</sub>. Rotterdam, Netherlands. June 13–17, 2022. V009T28A008. ASME. <https://doi.org/10.1115/GT2022-82013>
- [14] M. Manzoni, A. Patti, S. Maccarini, and A. Traverso, “Analysis and comparison of innovative large scale thermo-mechanical closed cycle energy storages,” *Energy*, vol. 249, p. 123629, Jun. 2022, doi: 10.1016/j.energy.2022.123629.
- [15] “Waste heat recovery - FIVES PILLARD - PDF Catalogs | Technical Documentation | Brochure.” <https://pdf.directindustry.com/pdf/fives-pillard/waste-heat-recovery/196705-752096.html> (accessed Oct. 27, 2022).
- [16] Welcome to CoolProp — CoolProp 6.4.3 documentation.” <http://www.coolprop.org/> (accessed Jan. 04, 2023).
- [17] G. Baglietto, S. Maccarini, A. Traverso, and P. Bruttini, “Techno-Economic Comparison of Supercritical CO<sub>2</sub>, Steam, and Organic Rankine Cycles for Waste Heat Recovery Applications,” *J. Eng. Gas Turbines Power*, vol. 145, no. 4, Dec. 2022, doi: 10.1115/1.4055727.
- [18] A. Caraballo, S. Galán-Casado, Á. Caballero, and S. Serena, “Molten Salts for Sensible Thermal Energy Storage: A Review and an Energy Performance Analysis,” *Energies*, vol. 14, no. 4, Art. no. 4, Jan. 2021, doi: 10.3390/en14041197.
- [19] Deliverable D3.3\_2019.01 "Thermal storage for improved utilization of renewable energy in steam production " - HighEFF- Centre for an Energy Efficient and Competitive Industry for the Future - Norway's Centre for Environment-friendly Energy Research (FME) - Project co-funded by the Research Council of Norway and Industry partners
- [20] Bejan, A., Tsatsaronis, G. and Moran, M. (1996) Thermal Design & Optimization. John Wiley & Sons Inc., New York.
- [21] N. T. Weiland, B. W. Lance, and S. R. Pidaparti, “sCO<sub>2</sub> Power Cycle Component Cost Correlations From DOE Data Spanning Multiple Scales and Applications,” presented at the ASME Turbo Expo 2019: Turbomachinery Technical Conference and Exposition, Nov. 2019. doi: 10.1115/GT2019-90493.
- [22] Richard Turton, Richard C. Bailie, Wallace B. Whiting, Joseph A. Shaeiwitz, *Analysis Synthesis and Design of Chemical Processes 5th Edition*. Pearson Education.
- [23] D. Steger, M. Feist, and E. Schlücker, “Using a screw-type machine as reversible compressor–expander in a Carnot Battery: An analytical study towards efficiency,” *Appl. Energy*, vol. 316, p. 118950, Jun. 2022, doi: 10.1016/j.apenergy.2022.118950.

## THE STEADY BEHAVIOR OF THE SUPERCRITICAL CARBON DIOXIDE NATURAL CIRCULATION LOOP

**Marko Draskic**

Process & Energy - 3mE  
Delft University of Technology  
Delft, The Netherlands  
[m.draskic@tudelft.nl](mailto:m.draskic@tudelft.nl)

**Benjamin Bugeat**

Process & Energy - 3mE  
Delft University of Technology  
Delft, The Netherlands

**Rene Pecnik\***

Process & Energy - 3mE  
Delft University of Technology  
Delft, The Netherlands  
[r.pecnik@tudelft.nl](mailto:r.pecnik@tudelft.nl)

### ABSTRACT

The steady state behavior of thermodynamically supercritical natural circulation loops (NCLs) is investigated in this work. Experimental steady state results with supercritical carbon dioxide are presented for reduced pressures in the range of 1.1-1.5, and temperatures in the range of 20-65 °C. Distinct thermodynamic states are reached by traversing a set of isochors. A generalized equation for the prediction of the steady state is presented, and its performance is assessed using empirical data. Changes of mass flow rate as a result of changes of thermodynamic state, heating- and driving height are shown to be accurately captured by the proposed predictive equation. However, the enhanced viscous losses in the instrumentation of the loop and in the proximity of heat transfer equipment are shown to significantly limit the steady state flow rate. Subsequently, the findings are put forward in aid of the development of safe, novel supercritical natural circulation facilities.

### INTRODUCTION

When a flow loop is heated at one of its vertical legs and cooled at the other, a natural convection is induced. The flow- and cooling rates of single phase natural circulation facilities are generally orders of magnitude too small to serve any purpose in industrial applications. However, if the operating fluid is in a thermodynamically supercritical state, considerable flow rates can be obtained due to strong density variations in the vicinity of the critical point. The flow rates generated with these simple systems can be used in settings in which an otherwise moderate flowrate is required, but where problems stemming from leakages, power outages and mechanical noise associated with forced convective flows need to be avoided. As such, supercritical fluid NCLs can act as reliable, off-grid cooling solutions for nuclear reactors, in case large heat sinks are present. Additionally, these systems can be used for the passive removal of heat from solar heater assemblies, or for the generation of steady, pulseless flows for sensitive experiments. However, as the properties of supercritical media vary greatly with state, the prediction of the steady state of supercritical NCLs for their potential implementation is not straightforward.

The steady state of supercritical natural circulation loops has previously been investigated using both numerical and experimental approaches. In the numerical literature, a one-dimensional transient model is most commonly used to predict both the steady and unsteady behavior of the considered loops [1]–[4], although three-dimensional approaches have also been undertaken [5]. The mass flow rate of a natural convection loop has been predicted to attain a maximum with varying heating rates [1], [2]. Furthermore, a rise in mass flow rate is expected with increasing loop heights, and increasing channel diameters [1], [3], [5]. On the contrary, an increase of the loop length is expected to have a limiting effect on the flow rate of the loop [5]. The influence of thermodynamic state on the steady behavior of supercritical NCLs is briefly touched upon in [4]. Here, increases in both the filling mass and the heating rate are predicted to result in an increase in loop pressure and subsequently loop flow rate for the range of considered parameters. Similar conclusions can be drawn from experimental investigations of NCLs with supercritical media. An increase in mass flow rate with increasing heating rate was first measured by Tokanai et al., [6]. The broader range of results presented in Liu et al. [7] also show the previously discussed maximum in the mass flow rate with increasing heating. As predicted, an increase in system temperature yields an increase in static pressure at a set charge [8], [9], and an increase in mass flow rate for the considered parameters in the work of Sadhu et al., as shown in [9].

The above findings only consider and discuss an NCL's sensitivity to changes in specific parameters. A generalized consideration of all variables that affect the steady state is however needed in aid of the reliable design of future facilities. A first correlation of the flow rate of a liquid-like supercritical carbon dioxide NCL, in terms of Grashof and Prantl numbers, was presented by Yoshikawa et al., [10]. A more elaborate approach was put forward by Swapnalee et al. [11], following the modus operandi of Vijayan et al. for single-phase fluids [12], [13]. Here, an expression for the mass flow rate is derived from the one-dimensional steady state momentum equation. In order to characterize the distribution of density in the equation

\* corresponding author

that follows, the change in loop density has to be expressed as a function of the change in enthalpy in the heater. For this, the relationship between dimensionless density and dimensionless enthalpy introduced by Ambrosini et al. [14] is used. Here, the adequate overlap of the dimensionless quantities for a broad range of supercritical pressures makes that a single curve can be used to express the relationship between density and enthalpy. Swapnalee et al. [11] use three distinct linear fits of the constitutive curve to express an expected change of density for three separate ranges of subcooling. From this, a straightforward equation for the NCL flow rate follows, which can be expressed in terms of a pipe diameter based Grashof ( $Gr_D$ ) and a Reynolds ( $Re_D$ ) number. A very similar approach is followed in the work of Liu et al. [15], where a two-region linear fit of Ambrosini's [14] curve is used to derive an expression for the steady mass flow rate. As the true evolution with state is however continuous, the chosen discrete description of thermodynamic properties is expected to introduce significant errors in the prediction of the flow rate. Additionally, the absence of the characterization of experimental loop minor losses in both works makes that the found relationship between  $Gr_D$  and  $Re_D$  is configuration specific. As the driving forces are generally limited in comparison with forced convective systems, setup-specific pressure losses in equipment can be expected to have a considerable effect on the flow rates of NCLs.

In this work, a revised generalized equation for the prediction of the steady flow rate of natural circulation loops with supercritical media is proposed. Consequently, the generalized formula is assessed using the experimental results of a new supercritical carbon dioxide natural circulation facility at the Process & Energy laboratory of the Delft University of Technology. In order to find the causes for possible disagreement between theory and experiment, the contributions of state, heating rate, configuration and pressure losses are independently considered.

## GENERALIZED FLOW EQUATION

Away from regions with considerable radial temperature gradients, the flow in a NCL is expected to display behavior similar to that of a developed pipe flow. As such, a generalized equation is sought from the mass- and momentum balance of a one-dimensional flow. Here, a constant-area pipe, and negligible viscous heating are assumed. A geometry that can be described with figure 1 is considered. Here, a heater and a cooler are consecutively placed along a closed flow loop. In the figure, the heater and cooler are indicated with red and blue circles, respectively.

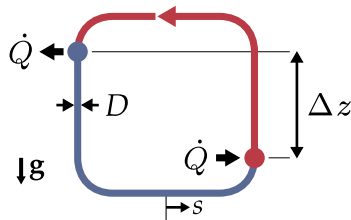


Figure 1: Schematic of simplified NCL. Low- and high density sections indicated in red and blue, respectively. Preferential flow direction indicated with red arrow.

The mass- and momentum balance equations for the considered system are described as a function of streamwise coordinate  $s$ :

$$\frac{1}{A_{cs}} \frac{d}{ds} (\dot{m}) = 0, \quad (1)$$

$$\frac{d}{ds} \left( \frac{1}{A_{cs}^2} \frac{\dot{m}^2}{\rho} + P \right) = \gamma \rho g - \frac{2f}{D} \frac{1}{A_{cs}^2} \frac{\dot{m}^2}{\rho}. \quad (2)$$

Here, the coefficient  $\gamma(s) \in [-1, 1]$  is used to account for the direction of gravity with respect to the flow at coordinate  $s$ . The rightmost term in equation (2) serves to describe viscous losses in the system, using dimensionless Fanning factor  $f$ . Given that the mass flow rate  $\dot{m}$  is a constant, and that  $\oint d(1/\rho)$  and  $\oint dP$  are zero for a closed loop, the path integral of equation (2) reduces to

$$\oint \rho g ds = \frac{2}{DA_{cs}^2} \oint \frac{f \dot{m}^2}{\rho} ds. \quad (3)$$

A force balance with only contributions from the driving buoyancy distribution and viscous losses in the loop remains. The system is ultimately driven by the density difference  $\Delta\rho$  over the vertical section between the cooler and heater with equivalent length  $\Delta z$ . Here,  $\Delta z$  is the vertical distance between the cooler and the heater, if they were to be modeled as point sources and point sinks for heat transfer. In reality, a vertical distribution of  $\rho$  is found in both heat exchangers. As such,  $\Delta z$  depends on the heat transfer mode- and rate, and will attain a value close to the vertical centerline distance. Given the above, equation (3) can be rewritten to

$$\Delta\rho g \Delta z A_{cs} = \frac{1}{L} \frac{A_p}{A_{cs}^2} \frac{\dot{m}^2}{2\rho_m} \sum_{i=1}^n (f_i L_i). \quad (4)$$

Here, the viscous loss contributions of all sections  $i$  are to be summed. By linearizing the change in density with varying enthalpy at the mean loop temperature  $T_m = 1/L \int T(s) ds$  and mean loop pressure  $P_m$ , and assuming constant pressure in the heat transfer equipment,  $\Delta\rho$  can be expressed as a function of a change in enthalpy  $\Delta h$ :

$$\left. \frac{\partial \rho}{\partial h} \right|_p \Delta h g \Delta z A_{cs} = \frac{A_p}{A_{cs}^2} \frac{\dot{m}^2}{2\rho_m} \frac{\Sigma (f_i L_i)}{L}. \quad (5)$$

Using the chain rule, the thermodynamic quantity  $\partial\rho/\partial h|_p$  can be rewritten to  $\rho_m \beta_m / c_{p,m}$ . Here, all thermodynamic quantities are to be evaluated at  $T_m$ . Lastly, given that  $\Delta h = \dot{Q}/\dot{m}$ ,  $A_{cs} = \pi D^2/4$  and  $A_p = \pi DL$  an equation as a function of design parameters of a supercritical fluid NCL follows:

$$\dot{m}^3 = \frac{\pi^2 g}{32} \cdot \underbrace{\frac{\rho_m^2 \beta_m}{c_{p,m}}}_{\text{Fluid properties}} \cdot \underbrace{\frac{\dot{Q} \Delta z D^5}{\Sigma (f_i L_i)}}_{\text{Configuration}} \cdot \underbrace{\frac{1}{\Sigma (f_i L_i)}}_{\text{Viscous losses}}. \quad (6)$$

Equation (6) expresses expected mass flow rate  $\dot{m}$  as a function of a state dependent group of variables, a configuration and geometry specific group, and a viscous loss term. The viscous loss term  $\Sigma (f_i L_i)$  accounts for both viscous losses in developed sections, and for additional losses in loop equipment and bends. Equation (6) has to be solved for iteratively, since the viscous loss term is a function of mass flow rate  $\dot{m}$ . Furthermore, as the Reynolds numbers for the warm and the cold leg of the system

differ at constant  $\dot{m}$ , their viscous losses have to be solved for independently. The fluid properties of the respective sections can be solved for at  $h_{h,c} = h_m \pm \frac{1}{2}\Delta h|_P$ , the value of which follows from the guess for  $\dot{m}$ .

In order to allow for ease of experimental fitting, equation (6) should be rewritten in dimensionless form. For this purpose, dimensionless quantities  $Gr_D$  and  $Re_D$  are introduced:

$$Gr_D = \frac{\rho_m^2 \beta_m \dot{Q} g D^3}{c_{p,m} \mu_m^2 \dot{m}}, \quad Re_D = \frac{\rho_m U D}{\mu_m}. \quad (7)$$

Consequently, the Grashof number can be expressed as a function of the Reynolds number:

$$Gr_D = 2 \frac{\Sigma(f_i L_i)}{\Delta z} \cdot Re_D^2. \quad (8)$$

In case the pressure losses in loop equipment attain negligible magnitudes, and a fanning factor expression of the form  $f = p/Re_D^b$  is used, equation (8) reduces to

$$Re_D = \left( \frac{\Delta z}{2pL} \cdot Gr_D \right)^{\frac{1}{2-b}}. \quad (9)$$

## EXPERIMENTAL FACILITY & METHODOLOGY

The experimental facility designed for- and used in this work is depicted schematically in figure 2. As the heater and cooler are located along the vertical legs of the system, a preferential flow direction prevails. For steady flows, a counter-clockwise circulation is expected in the perspective of the figure. The dimensions of the flow loop and the range of conditions within which it has been designed to operate are specified in table 1. Whereas most of the system is joined using detachable stainless steel tube fittings, EPDM or PTFE is used in components where non-metallic soft seals are required [16]. Heat is supplied to the system using a series of movable electric band heaters. In order to minimize heat losses to the surroundings, the circulation loop is insulated with a 40 mm thick annulus of rockwool. The loop is cooled using a tube-in-tube counter-current heat exchanger. Here, the outer annulus is equipped with baffles to aid in the distribution of the coolant. The inlet temperature of the cooler is controlled using a Julabo FP51-SL refrigerated circulator. Whilst mostly simplistic of nature, the loop is also equipped with flow- and state control devices. An adjustable local pressure loss is introduced using a regulating needle valve. Additionally, the volume in the loop can be varied using a 1 l piston accumulator, indicated below ⑤ in the figure. Here, nitrogen is used as the secondary medium.

Parameter & Description	Value/Range	Unit
H Loop height	4.0	m
L Loop length	10.0	m
D Inside diameter	21.1	mm
$\Delta z$ Driving height	$\leq 2.5$	m
$P$ Design pressure	$\leq 140$	bar
$T$ Design temperature	$-20 \leq T \leq 65$	$^{\circ}\text{C}$

Table 1: Test loop description

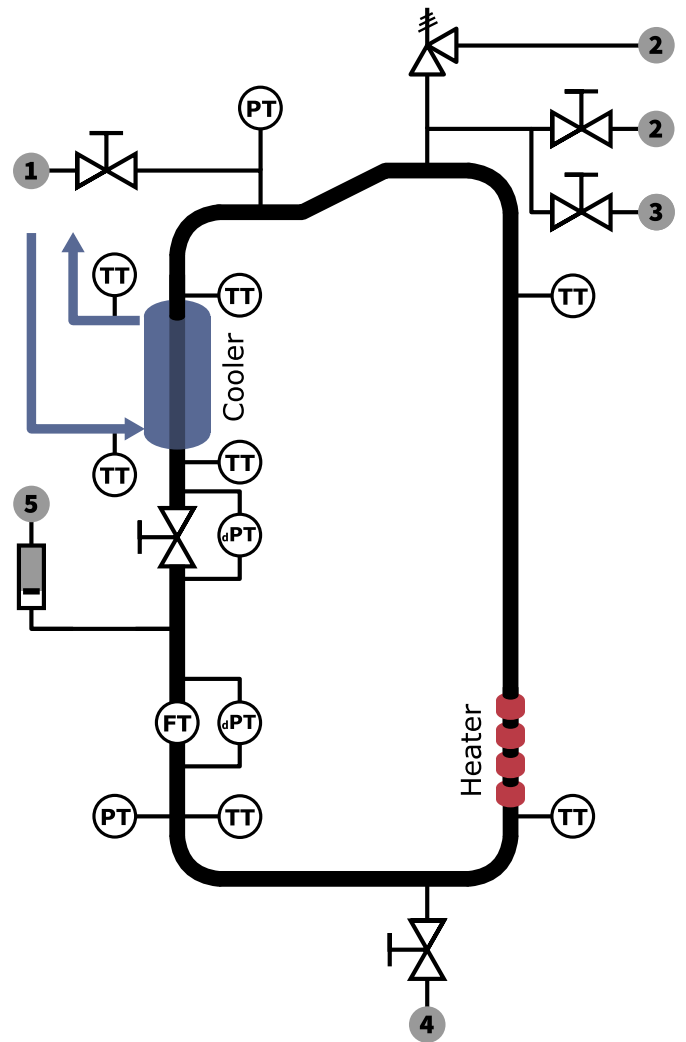


Figure 2: Schematic depiction of the TU Delft Process & Energy  $s\text{CO}_2$  natural circulation loop. As indicated in grey, the system is connected to ① a  $\text{CO}_2$  bottle with dip tube, ② a  $\text{CO}_2$  purge that is connected to the lab's gas vent system, ③ a vacuum pump, ④ a drain, and ⑤ a nitrogen bottle. The electric heater and annular cooler are indicated in red and blue, respectively.

The facility is equipped with a series of transmitters for the continuous monitoring of its performance. Bulk temperatures are measured using PT100 resistance thermometers with a nominal accuracy of  $\pm 0.1\text{ }^{\circ}\text{C}$ , which are laterally inserted into the flow. Absolute pressure measurements are taken using welded STS ATM.1st transmitters, with a nominal uncertainty of  $\pm 0.16\text{ bar}$  or  $0.1\%$ . Furthermore, the loop includes a Rheonik

RHM08 Coriolis mass flow meter with a nominal uncertainty of  $0.2\%$ . Finally, two Siemens SITRANS P420 differential pressure sensors were used for the quantification of the viscous losses in both the Coriolis meter and the regulating valve. The transducer data are acquired at  $1\text{ Hz}$  using a NI cRIO-9074, with RTD module NI-9216, analog in- (NI-9208) and output (NI-9266) modules, and digital input module NI-9421. A Labview user-interface for the real-time visualization of the data was developed to complement the data acquisition structure. Here, the interpolation of tabulated thermodynamic properties allows for the live monitoring of various compound quantities.

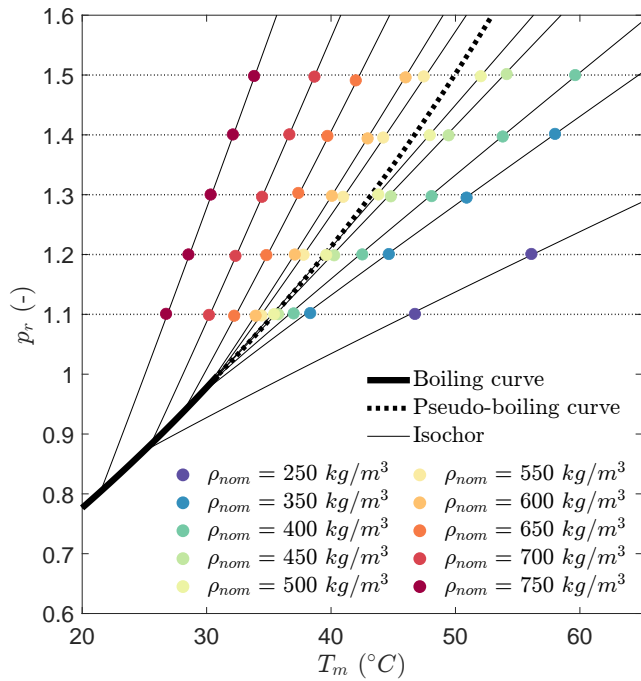


Figure 3: Lines of constant mass at set system volume for carbon dioxide at supercritical pressure. Current experimental data points indicated at measured  $T_m$  and  $P_m$  for all considered nominal densities. Boiling- and pseudo-boiling curves indicated with thick solid and dashed lines, respectively

In order to fill the loop, the system is first brought to moderate pressures. Consequently, a blow-off valve at the top of the loop is used to purge the system of non-condensable gases. Additionally, a valve at the bottom of the loop is opened to drain the loop of unwanted liquids. After evacuating the system with a vacuum pump, liquid carbon dioxide of a high purity is fed to the system from a cylinder with a dip tube. As the bottle is weighed, the filling mass of the loop is known. Once an equilibrium in pressure is reached between the bottle and the experimental facility, the loop is cooled. As a result, the loop pressure decreases to below the vapor pressure of the bottle, resulting in a flow of carbon dioxide towards the facility. By moderately heating the loop during this cooling step, a natural flow is generated that allows for greater cooling rates, and therewith accelerates the filling process.

In this work, the thermodynamic space is explored by traversing a set of isochors. As shown in figure 3, a desired supercritical pressure can be attained for different filling masses at different loop temperatures. During operation, the coolant temperature is adjusted at a constant volume to attain the appropriate pressure. As such, a constant mean state can be maintained for varying heating rates. The mean state is both continuously and a posteriori evaluated by assuming a linear distribution of  $T$  in the heat transfer equipment. The range of states that was therewith reached in this work is listed in table 2, and depicted in figure 3. The distinct thermodynamic states were attained for heating rates of both 400 W and 800 W, and are used in discussions of the dependency on thermodynamic state of the mass flow rate and the assessment of the performance of the generalized equation.

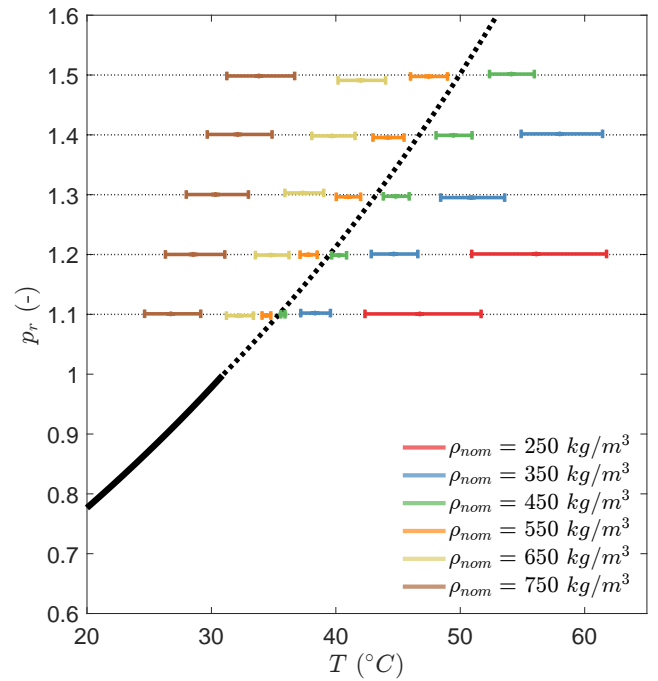


Figure 4: System temperature ranges for selected loop filling masses, at  $\dot{Q} = 800$  W,  $\Delta z = 2.5$  m. Range is bound by greatest and lowest measured temperature in the loop. Boiling- and pseudo-boiling curves indicated with solid and dashed lines, respectively.

Parameter & Description		Value/Range	Unit
$\dot{Q}$	Heating rate	$\leq 2$	kW
$\rho_m$	Mass density	$250 \leq \rho_m \leq 750$	$\text{kg m}^{-3}$
$P_m$	Operating pressure	$81 \leq P_m \leq 111$	bar
$T_m$	Operating temperature	$20 \leq T_m \leq 60$	$^{\circ}\text{C}$

Table 2: Operating range

## RESULTS & DISCUSSION

During the steady operation of the natural circulation loop, the loop temperature distribution varies with thermodynamic state. The loop temperature distribution for an assortment of states within the considered range is depicted in figure 4. The natural flow is driven by moderate temperature gradients, especially in the vicinity of the pseudo-critical line. With increasing pressure beyond the critical point, the pseudo-critical curve gradually transforms from a point of near-discrete phase transition to a gradually increasing region of mild property gradients. Additionally, as the fluid's specific heat near this curve decreases with pressure, less variation of driving temperature is found along isobars of greater magnitudes. Of course, a quantitative assessment of the loop temperature distribution follows from the steady state mass flow rate. If the loop mass flow rate is known, the loop temperature maxima and minima can be obtained using  $T_{\max,\min} = T_m \pm \dot{Q}/(2\dot{m}c_{p,m})$ . Using the experimental mass flow rate  $\dot{m}_{\text{exp}}$ , close agreement with experimental data is found for the considered range of thermodynamic states.

In this work, equation (9) is proposed for the prediction of steady mass flow rate  $\dot{m}$ . A comparison of equation (9) with experimental data is given in figure 5. Here, no minor pressure



losses are considered in determining the viscous loss term of equation (9), consistent with previous approaches in existing literature. As the value of  $Re_D$  for all current empirical data exceeds  $10^4$ , Blasius viscous loss constants for hydrodynamically smooth turbulent pipe flow  $p = 0.25$  and  $b = 0.0791$  are used. The experimental data for this figure is obtained in the absence of the regulating valve depicted in figure 2. The current prediction is expected to yield values of comparable magnitude as the generalized formulae of Swapnalee and Liu [11], [15], as similar approaches are undertaken. As shown in figure 5, significantly lower empirical Reynolds numbers were however obtained in the current experiments. Disagreement of the dimensionless quantities of a similar extent was also found in the work of Sadhu et al., [9]. In search of generality, an attempt is made to find the source of disparity between the prediction and the found experimental data. Hence, the contributions of the individual terms in dimensional equation (6) are further investigated.

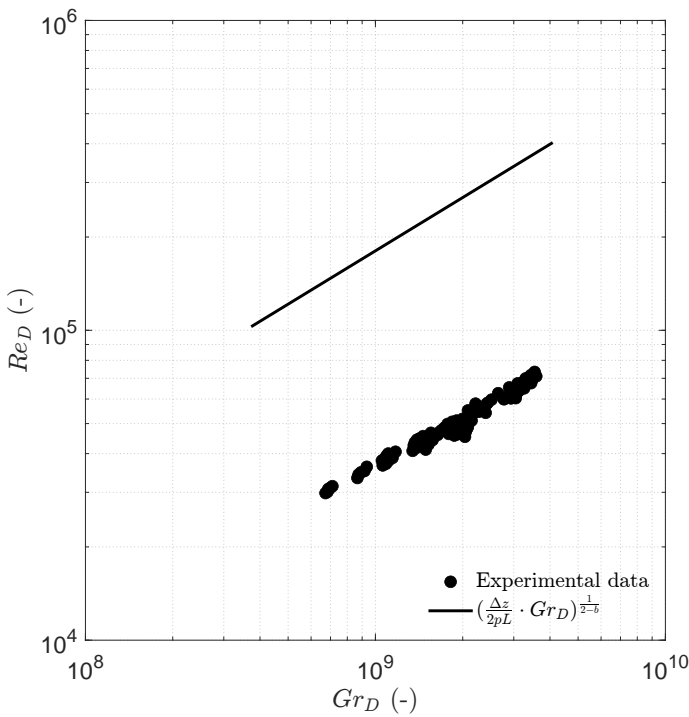


Figure 5:  $Re_D$  as function of  $Gr_D$  for experimental data in the range of operating values indicated in table 2. Prediction of equation (8) indicated in figure with solid curve.

In order to consider the independent contribution of  $\dot{Q}$  in equation (6), all other terms have to attain constant values when  $\dot{Q}$  is varied. Through variation of the coolant temperature, a constant thermodynamic mean state can be maintained with varying heating rates. As the measured value of  $\Sigma(f_i L_i)$  is however non-constant due to variation in  $U$ ,  $\dot{m}_{\text{exp}}$  has to be compensated for using

$$\dot{m}_{\text{cor,fl}} = \dot{m}_{\text{exp}} \cdot \left( \frac{C_{\text{fl}}}{\Sigma(f_i L_i)_{\text{exp}}} \right)^{1/3}. \quad (10)$$

Here,  $\dot{m}$  is assumed to scale with  $\Sigma(f_i L_i)^{-1/3}$ , following equation (6). The value of  $C_{\text{fl}}$  should be chosen such that it matches one of the values of  $\Sigma(f_i L_i)$  within the considered experimental

data set. As will be shown later in this work, the experimental uncertainty is the least for  $\rho \geq 700 \text{ kg m}^{-3}$  and  $p_r \geq 1.3$  within the considered range of thermodynamic states. As such, this range of thermodynamic conditions is chosen for the assessment of the individual contributions of  $\dot{Q}$ ,  $\Delta z$ , and  $\Sigma(f_i L_i)$ . In figure 6, the expected contribution of  $\dot{Q}$  is compared to corrected empirical data. Here, the measured increase in heating rate  $\dot{Q} = \dot{m}_{\text{cor,fl}} \Delta h$  is used rather than the imposed electrical heating rate  $\dot{Q}_{\text{imp}}$ , in order to account for heating losses in the system. Close agreement is found between the predicted trend in mass flow rate and the experimental data for the considered range, hence  $\dot{m}$  is assumed to scale with  $\dot{Q}^{1/3}$  from this point onwards. As such, heating losses can be compensated for in investigations of data sets in which  $\dot{Q}$  is to be kept constant using

$$\dot{m}_{\text{cor},\dot{Q}} = \dot{m}_{\text{exp}} \cdot \left( \frac{\dot{Q}_{\text{imp}}}{\dot{m} \Delta h} \right)^{1/3}. \quad (11)$$

One such corrected set of empirical data is shown in figure 7. The depicted experimental data has been corrected for both variation in viscous losses, and variation in heating losses. Here, the expected change in  $\dot{m}$  with variation in  $\Delta z$  is compared to data from experiments in which  $\Delta z$  is independently varied. Again, close agreement is found between theory and practice, and the source of the discrepancy in figure 5 has not yet been identified.

An investigation of the influence of thermodynamic state follows in figure 8. For the current analysis, the measured value of  $\Sigma(f_i L_i)$  has been found to vary with pressure, whereas its value remains predominantly constant along each isobar. Hence, the theoretical fluid property contribution of equation (6) is multiplied with  $C_{f(p_r)}$ . The value of this constant is chosen as such that the theoretical curve intersects with the lowest mean temperature data point for each reduced pressure. Heating losses are compensated for using equation (11), and the corrected mass flow rate values  $\dot{m}_{\text{cor},\dot{Q}}$  are shown in the figure. The proposed theoretical contribution of thermodynamic state is found to closely and continuously describe the corrected data for any degree of sub-cooling in the considered range of parameters. Note that the size of the confidence intervals of  $\dot{m}_{\text{cor},\dot{Q}}$  varies greatly with thermodynamic state. The uncertainty in measurements of temperature and pressure is however mostly constant within the current range of experiments. As the sensitivity of enthalpy to temperature however varies with pressure, the uncertainty in enthalpy follows accordingly. This makes that the uncertainty in the determination of the fluid enthalpy used for the correction of heating losses is greatest near maxima of specific heat, hence at the pseudo-critical line at pressures in the vicinity of the critical pressure. Therefore, investigations of individual contributions of equation (6) should be performed away from the pseudo-critical curve, to reduce the uncertainty of the findings. As such, the more liquid-like, high pressure thermodynamic states are considered for these analyses, as previously elaborated on in this work.

Finally, the effect of pressure losses caused by equipment is investigated. For this, the joint pressure drop  $\Delta p_e$  over the flow meter and the regulating valve section is monitored. Pressure drop  $\Delta p_e$  is the summed value of the readings over



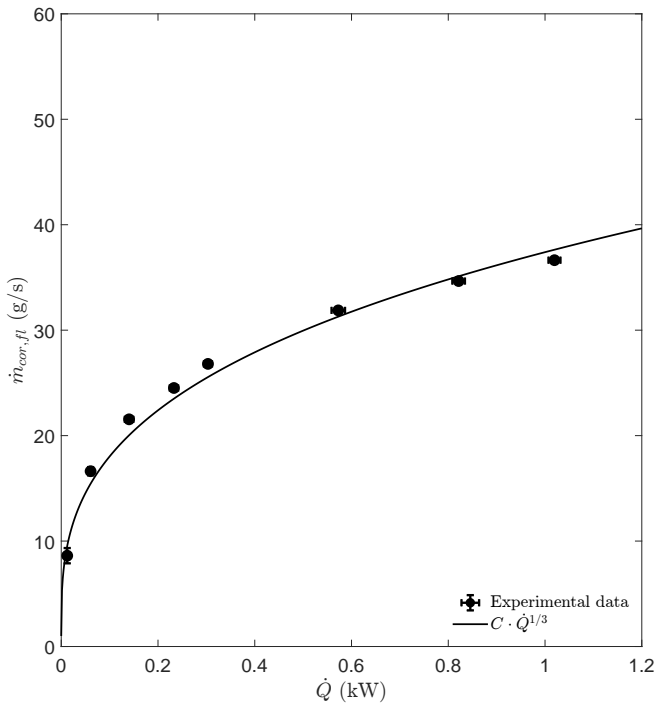


Figure 6: Variation of  $\dot{m}_{\text{cor,fl}}$  with  $\dot{Q} = \dot{m}_{\text{cor,fl}}\Delta h$ , at  $\rho_{\text{nom}} = 700 \text{ kg m}^{-3}$ ,  $p_r = 1.5$ ,  $\Delta z = 2.5 \text{ m}$ , with 95% confidence intervals. Constant  $C$  is chosen as such that the leftmost data point coincides with the theoretical curve.

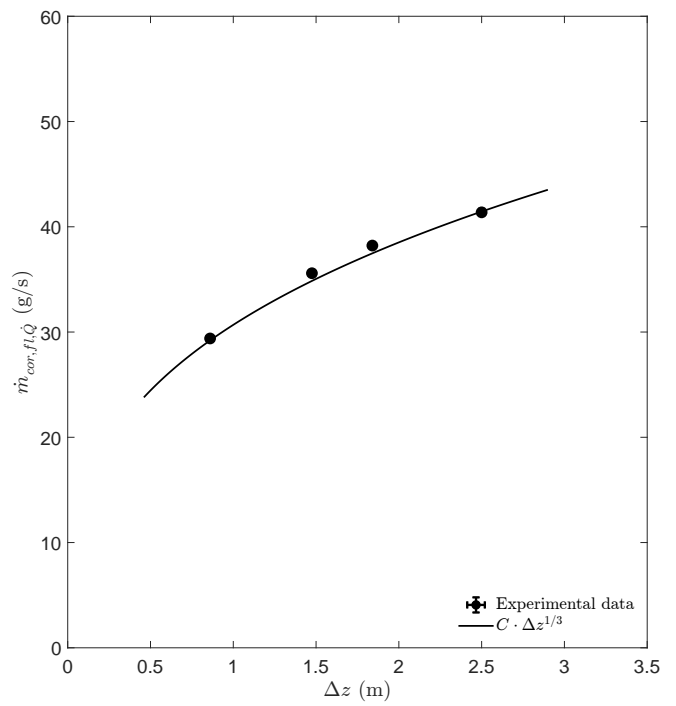


Figure 7: Variation of  $\dot{m}_{\text{cor,fl}}\dot{Q}$  with  $\Delta z$ , at  $\rho_{\text{nom}} = 700 \text{ kg m}^{-3}$ ,  $p_r = 1.3$ ,  $\dot{Q} = 800 \text{ W}$ , with 95% confidence intervals. Constant  $C$  is chosen as such that the rightmost data point coincides with the theoretical curve.

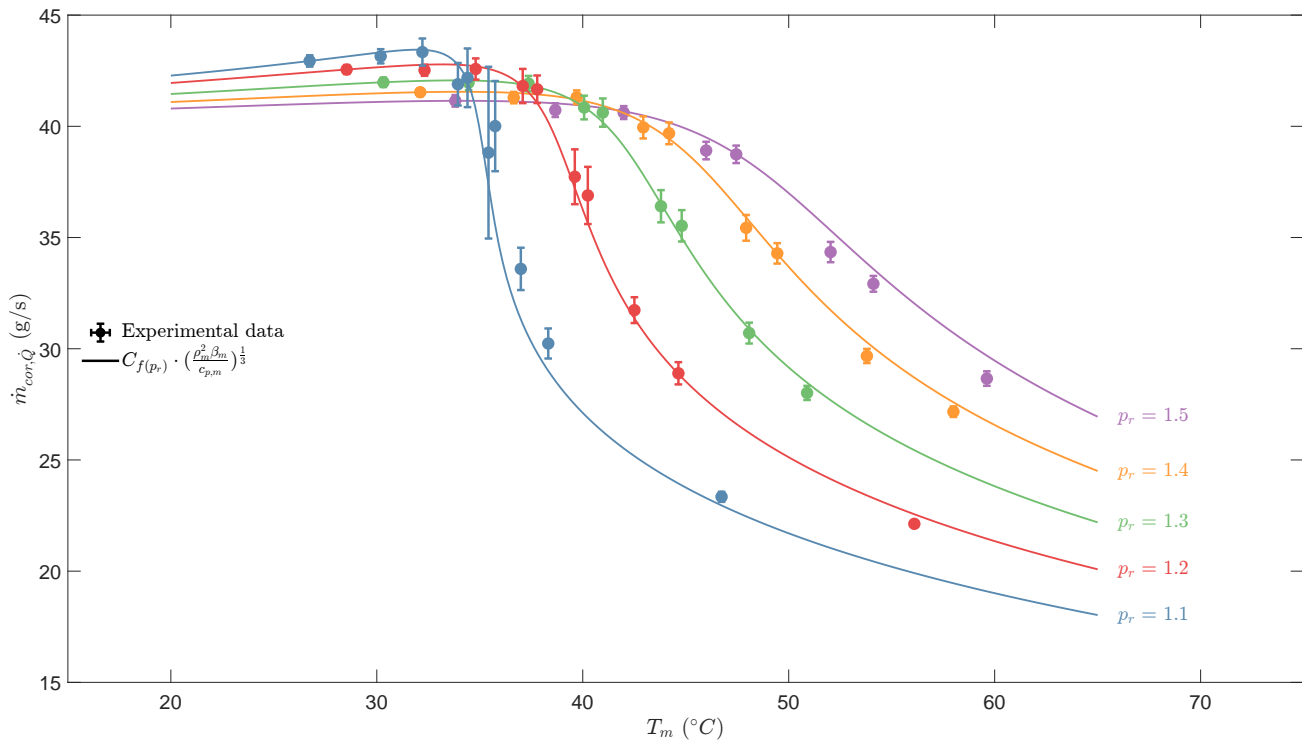


Figure 8: Variation of  $\dot{m}_{\text{cor,Q}}$  with  $T_m$  and  $P_m$ , at  $\Delta z = 2.5 \text{ m}$ ,  $\dot{Q} = 800 \text{ W}$ , with 95% confidence intervals.  $C_{f(p_r)}$  is chosen as such that the leftmost data point for each  $p_r$  coincides with the theoretical curve.

both differential pressure transmitters indicated with  $\text{dPT}$  in figure 2. Despite having different means to generate a driving force with, both natural and forced convective flows are driven by steady pressure gradients. As such, the flow in a NCL should

only deviate from a developed pipe flow near heat transfer equipment where radial temperature gradients are present, and at flow obstructions. Hence, measurements of pressure losses only in obstructive equipment combined with pressure loss

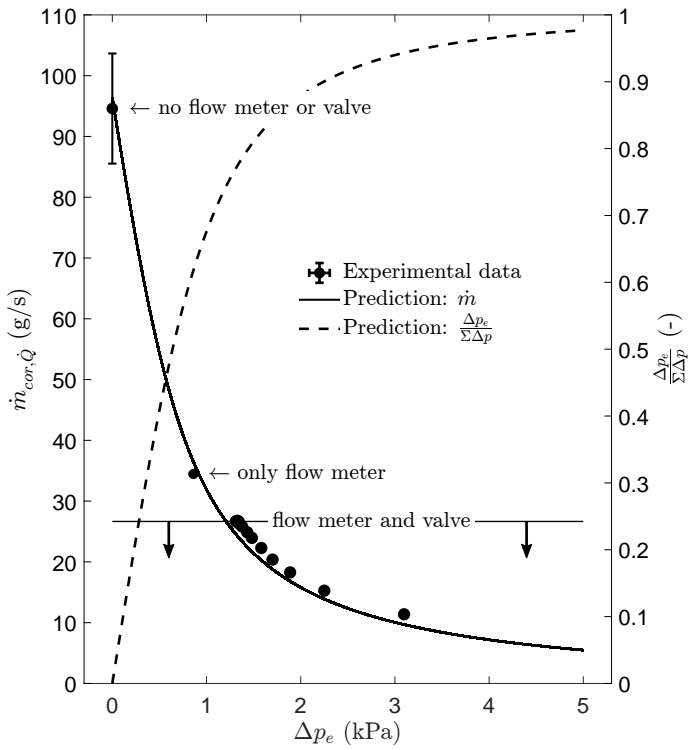


Figure 9: Left axis, full line and markers: variation of  $\dot{m}_{cor, \dot{Q}}$  with  $\Delta p_e$ , at  $\rho_{nom} = 730 \text{ kg m}^{-3}$ ,  $p_r = 1.1$ ,  $\Delta z = 2.5 \text{ m}$ ,  $\dot{Q} = 400 \text{ W}$ , with 95% confidence intervals. Predictive curve found by varying the equipment loss term  $(fL)_e$  in equation (6), and iteratively solving for  $\dot{m}$ . The leftmost data point has not been corrected to take heating losses into account. Right axis, dotted line:  $\Delta p_e$  as a fraction of the estimated total loop pressure loss  $\Sigma \Delta p$ .

correlations based on ideal and developed pipe flows should suffice in reconstructing the NCL's sensitivity to pressure losses.

Figure 9 shows the loop mass flow rate as a function of the experimental values of  $\Delta p_e$ , and the relative magnitude of  $\Delta p_e$  with respect to the total viscous pressure losses in the system. The regulating valve is present in all but two data points of the current analysis, for which it is removed from the supercritical NCL. In the leftmost data point in the figure, both the valve and the mass flow meter are removed from the experimental facility. Here, the mass flow rate is estimated from the imposed heating rate and the measured enthalpy increase over the heater, i.e.  $\dot{m}_{exp} = \dot{Q}_{imp} / (h_{h,exp} - h_{c,exp})$ . As heating losses cannot be reliably estimated for this data point, they are not compensated for. The predictive curve is obtained by adding an equipment loss term  $(fL)_e = (\Delta p_e D) / (2\rho_c U_c^2)$  in the viscous loss term in equation (6). For each value of  $\Delta p_e$ , the distribution of the viscous losses in the system has to be iteratively solved for. As such, the presented theoretical curve in figure 9 is state- and configuration dependent and therewith only applicable to the current analysis.

The theoretical curve is found to closely resemble the experimental data. The value of the predictive curve at a zero value of  $\Delta p_e$  corresponds to the expected mass flow rate in

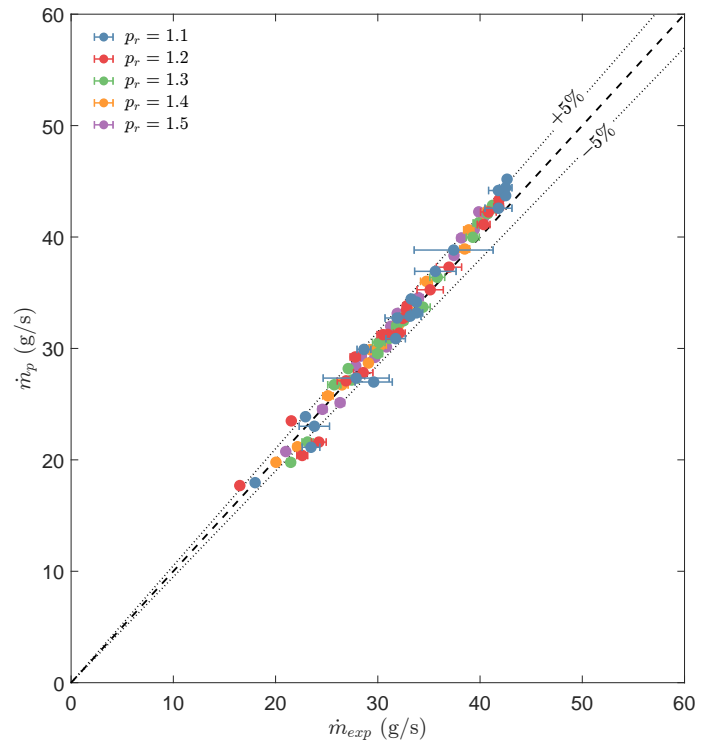


Figure 10: Steady state prediction error with inclusion of measured  $\Delta p_e$  into equation (6), at  $\Delta z = 2.5 \text{ m}$ ,  $\dot{Q} = 400 \text{ W} \vee \dot{Q} = 800 \text{ W}$ , with 95% confidence intervals.

case no equipment losses are assumed. For this point, the total loop pressure loss is solely predicted using the turbulent Blasius viscous loss constants specified previously in this section. Whilst this modeling assumption is likely to be accurate for the majority of the loop, the relatively large uncertainty in the unobstructed and leftmost data point makes that no definitive claims regarding the validity of the modeling choice can be made. Furthermore, a comparison of the two leftmost points in the figure shows that a threefold decrease in mass flow rate is the direct consequence of the inclusion of a flow meter in the experimental loop. The difference in mass flow rate is of similar magnitude as the shift in figure 5, in which equipment pressure losses were not taken into account. As can be seen from figure 9, the losses in the flow meter alone are estimated to exceed the regular viscous losses in the loop.

Figure 10 shows the error in the prediction of the experimental steady state mass flow rate  $\dot{m}_{exp}$ , if the measured  $\Delta p_e$  is included in the viscous loss term of equation (6). As shown in the figure, close agreement is found with the predicted mass flow rate  $\dot{m}_p$  for the majority of the data.

Albeit moderately, the value of  $\dot{m}_{exp}$  is systematically over-predicted for the more liquid-like data points of the considered range, shown mostly in the top half of figure 10. A possible cause for the above is an under-prediction of the viscous losses in the flow in the vicinity of the heat transfer equipment of the setup. As qualitatively described in the work of Wahl et al. [17], the alignment of the direction of both forced- and natural convection can result in near-wall velocities that are greater than in an adiabatic setting. For flows of supercritical

media, this is the case for downward cooled and upward heated pipe flows. As such alignment is present in both heat transfer configurations of the investigated loop for the preferential flow direction, enhanced buoyancy-aided shear is expected in- and directly downstream of the cooler and heater. From the correlations presented in the review of Fang et al. [18], it follows that the greatest degrees of shear enhancement can be found for more liquid-like states beyond the critical point. As these additional viscous losses are not measured and hence not taken into account for the determination of  $\dot{m}_p$  in figure 10, the true steady state is likely over-predicted.

For all the considered experimental data points of this work, the total loop viscous losses are dominated by the equipment losses of a single Coriolis transmitter. The associated loss of flow rate is expected to be even more prevalent in facilities with less simple geometries, in which the flow is forced through a greater amount of instruments, or past series of turbine blades. Hence, the a priori characterization of the equipment minor losses is essential for an accurate prediction of the steady mass flow rate of supercritical NCLs, which are generally inflexible to changes in maximum heat throughput. Without the proper portrayal of such losses, an empirical fit based on equation (8) yields little insights for the development of future circulation loops. Additionally, equation (6) will only serve as a qualitative measure of the evolution of  $\dot{m}$  with thermodynamic state,  $\Delta z$  and  $\dot{Q}$  from some configuration specific steady state value.

## CONCLUSIONS

The steady state behavior of a natural circulation loop that employs thermodynamically supercritical carbon dioxide was experimentally investigated in this work. The experiments were conducted using a novel facility at the Process & Energy laboratory of the Delft University of Technology. Distinct empirical data points were obtained by varying the system's filling mass, its heating rate, and the temperature of the coolant. The

experimental data was compared to a newly proposed generalized equation for the prediction of the steady state mass flow rate of supercritical NCLs. Whereas the effects of changes in heating rate, differential heating height, and state were shown to be accurately captured in isolated experiments, the experimental mass flow rate was significantly over-predicted. The over-prediction was attributed to the viscous losses in the instrumentation, which can significantly limit the flow rates in these systems in which the driving forces are generally of moderate magnitudes. Therefore, an in-advance assessment of equipment losses is required for the accurate prediction of yet to be developed supercritical NCL systems.

## ACKNOWLEDGEMENTS

This work was funded by the European Research Council grant no. ERC-2019-CoG-864660, Critical.

## REFERENCES

- [1] S. Sadhu, M. Ramgopal, and S. Bhattacharyya, "Steady-state analysis of a high-temperature natural circulation loop based on water-cooled supercritical co<sub>2</sub>," *Journal of Heat Transfer*, vol. 140, no. 6, 2018.
- [2] P. K. Jain and R. Uddin, "Numerical analysis of supercritical flow instabilities in a natural circulation loop," *Nuclear Engineering and Design*, vol. 238, no. 8, pp. 1947–1957, 2008.
- [3] M. Sharma, D. Pilkhwal, P. Vijayan, D. Saha, and R. Sinha, "Steady state and linear stability analysis of a supercritical water natural circulation loop," *Nuclear Engineering and Design*, vol. 240, no. 3, pp. 588–597, 2010.
- [4] A. S. Pegallapati, P. Banoth, and R. Maddali, "Dynamic model of supercritical co<sub>2</sub> based natural circulation loops with fixed charge," *Applied Thermal Engineering*, vol. 169, p. 114 906, 2020.

## NOMENCLATURE

Symbol	Property	Unit	Symbol	Property	Unit
<i>Symbols</i>			<i>Greek symbols</i>		
$A_{cs}$	Cross sectional area ( $\pi D^2/4$ )	m <sup>2</sup>	$\beta$	Volumetric expansivity	K <sup>-1</sup>
$A_p$	Pipe wall area ( $\pi DL$ )	m <sup>2</sup>	$\gamma$	Directional coefficient in eq (2)	-
$b$	Constant in eq (9)	-	$\mu$	Dynamic viscosity	Pa s
$c_p$	Specific heat	J kg <sup>-1</sup> K <sup>-1</sup>	$\rho$	Density	kg m <sup>-3</sup>
$C_{fl}$	Constant in eq. (10)	-	<i>Subscripts</i>		
$D$	Internal pipe diameter	m	c	Value taken at temperature and pressure of cold leg	
$f$	Fanning friction factor	-	cor, $\dot{Q}$	Corrected for variation in $\dot{Q}$	
$F$	Force	N	cor,fl	Corrected for variation in $\sum(f_i L_i)$	
$g$	Gravitational acceleration	m s <sup>-2</sup>	crit	Value at critical point	
$Gr_D$	Grashof number, eq (7)	-	D	Pipe inner diameter as characteristic lengthscale	
$h$	Specific enthalpy	J kg <sup>-1</sup>	e	Value at specified equipment	
$H$	Total loop height	m	exp	Experimental value	
$L, L_i$	Loop length, section length	m	h	Value taken at temperature and pressure of hot leg	
$\dot{m}$	Mass flow rate	kg s <sup>-1</sup>	imp	Imposed value	
$p$	Constant in eq (9)	-	m	Value taken at loop mean temperature and pressure	
$P$	Pressure (absolute)	Pa	nom	Nominal/intended value	
$\dot{Q}$	Heating rate	W	p	Predicted value	
$s$	Streamwise coordinate	m	r	Reduced value, with respect to value at critical point	
$T$	Temperature	K			
$U$	Streamwise velocity component	m s <sup>-1</sup>			
$\Delta z$	Vertical point-source heater-cooler distance	m			

- [5] M. K. Sarkar and D. N. Basu, "Influence of geometric parameters on thermalhydraulic characteristics of supercritical co<sub>2</sub> in natural circulation loop," *Nuclear Engineering and Design*, vol. 324, pp. 402–415, 2017.
- [6] H. Tokanai, Y. Ohtomo, H. Horiguchi, E. Harada, and M. Kuriyama, "Heat transfer of supercritical co<sub>2</sub> flow in natural convection circulation system," *Heat transfer engineering*, vol. 31, no. 9, pp. 750–756, 2010.
- [7] G. Liu, Y. Huang, J. Wang, F. Lv, and L. K. Leung, "Experiments on the basic behavior of supercritical co<sub>2</sub> natural circulation," *Nuclear Engineering and Design*, vol. 300, pp. 376–383, 2016.
- [8] L. Chen, B.-L. Deng, and X.-R. Zhang, "Experimental investigation of co<sub>2</sub> thermosiphon flow and heat transfer in the supercritical region," *International Journal of Heat and Mass Transfer*, vol. 64, pp. 202–211, 2013.
- [9] S. Sadhu, M. Ramgopal, and S. Bhattacharyya, "Experimental studies on an air-cooled natural circulation loop based on supercritical carbon dioxide—part a: Steady state operation," *Applied Thermal Engineering*, vol. 133, pp. 809–818, 2018.
- [10] S. Yoshikawa, R. L. Smith Jr, H. Inomata, Y. Matsumura, and K. Arai, "Performance of a natural convection circulation system for supercritical fluids," *The Journal of supercritical fluids*, vol. 36, no. 1, pp. 70–80, 2005.
- [11] B. Swapnalee, P. Vijayan, M. Sharma, and D. Pilkhwal, "Steady state flow and static instability of supercritical natural circulation loops," *Nuclear Engineering and Design*, vol. 245, pp. 99–112, 2012.
- [12] P. Vijayan and H. Austregesilo, "Scaling laws for single-phase natural circulation loops," *Nuclear Engineering and Design*, vol. 152, no. 1-3, pp. 331–347, 1994.
- [13] P. Vijayan, "Experimental observations on the general trends of the steady state and stability behaviour of single-phase natural circulation loops," *Nuclear engineering and design*, vol. 215, no. 1-2, pp. 139–152, 2002.
- [14] W. Ambrosini and M. Sharabi, "Dimensionless parameters in stability analysis of heated channels with fluids at supercritical pressures," *Nuclear Engineering and Design*, vol. 238, no. 8, pp. 1917–1929, 2008.
- [15] G. Liu, Y. Huang, and J. Wang, "A new theoretical model of steady-state characteristics of supercritical carbon dioxide natural circulation," *Energy*, vol. 189, p. 116323, 2019.
- [16] L. Ansaloni, B. Alcock, and T. A. Peters, "Effects of co<sub>2</sub> on polymeric materials in the co<sub>2</sub> transport chain: A review," *International Journal of Greenhouse Gas Control*, vol. 94, p. 102930, 2020.
- [17] A. Wahl, R. Mertz, E. Laurien, and J. Starflinger, "Heat transfer deterioration in vertical sco<sub>2</sub> cooling in 3 mm tube," *Energy*, p. 124240, 2022.
- [18] X. Fang, L. Xu, Y. Chen, and W. Chen, "Correlations for friction factor of turbulent pipe flow under supercritical pressure: Review and a new correlation," *Progress in Nuclear Energy*, vol. 118, p. 103085, 2020.

## THERMODYNAMIC ANALYSIS OF A REACTIVE PARTICLE-TO-sCO<sub>2</sub> HEAT EXCHANGER FOR RECOVERING STORED THERMOCHEMICAL ENERGY

**Bryan J. Siefering\***

The Pennsylvania State University  
University Park, PA, USA  
bjs6878@psu.edu

**Ellen B. Stechel**

Arizona State University  
Tempe, AZ, USA

**Muhammad Umer**

The Pennsylvania State University  
University Park, PA, USA

**Brian M. Fronk**

The Pennsylvania State University  
University Park, PA, USA

### ABSTRACT

The objective of this paper is to investigate the effect of off-design supercritical carbon dioxide (sCO<sub>2</sub>) Brayton cycle operation on the thermodynamic performance of a heat exchanger/chemical reactor for transferring stored energy from hot, reduced, metal oxide particles into the power cycle. The device, termed an Energy Recovery Reactor (ERR), feeds gravity-driven particles through a bank of zigzag, finned, serpentine tubes containing sCO<sub>2</sub> flowing in counterflow to the particles. Preheated air introduced at the bottom of the reactor flows through the zig-zag channels also in counterflow with the particles and parallel flow with the sCO<sub>2</sub>. The air supplies oxygen (O<sub>2</sub>) as the reactant to drive exothermic re-oxidation of particles. The air also functions as a heat transfer medium between the energized particles and sCO<sub>2</sub>.

In this study we develop a steady-state 1-D thermodynamic model of the ERR system. By defining controllable inputs such as inlet temperatures and flow rates of particles, air, and sCO<sub>2</sub>, the remaining state points are calculated based on mass and energy balances. With set flow rates of particles, adjusting the sCO<sub>2</sub> cycle operating conditions (e.g., inlet temperature, flow rate, etc.) demonstrate how the performance of the ERR will change during off-design operation. Increasing the inlet temperature of the sCO<sub>2</sub> while maintaining the required outlet temperature results in a smaller temperature lift and decreases the heat duty of the system as a whole. When the system runs with a constant particle flow rate, the total amount of chemical heat available is constrained based on the redox reaction. Therefore, adjusting the heat transfer to the sCO<sub>2</sub> based on changes to the operating conditions results in changes to the recovery effectiveness and the ratio of sensible to chemical heat released by the particles. This model outputs the steady state operating conditions of the three domains within the reactor at

various off-design conditions that are input to an existing segmented heat transfer model to calculate the temperature profiles and local heat transfer performance, which will be verified experimentally in future work.

### INTRODUCTION AND BACKGROUND

The next generation of high temperature, central receiver concentrated solar power (CSP) systems are well suited for providing thermal energy to high efficiency power cycles using supercritical carbon dioxide (sCO<sub>2</sub>) as the working fluid, [1]. The U.S. Department of Energy (DOE) has identified the recompression sCO<sub>2</sub> Brayton cycle as the most promising power cycle for coupling to next-generation, high temperature (>700°C) central receiver CSP systems due to the potential of higher cycle thermal efficiency than steam Rankine cycles. The sCO<sub>2</sub> power cycle also operates with a smaller physical size and higher power density, resulting in a less complex power block that can be implemented at lower capital costs, [2]. These power cycles operate at high pressure (~25 MPa) and require a turbine inlet temperature of >700°C to operate in the target efficiency window. Coupling an sCO<sub>2</sub> Brayton cycle to a CSP plant requires a high temperature heat transfer fluid to capture the thermal energy from the concentrated solar flux which is either sent to a thermal energy storage (TES) system or directly to the power cycle via a high temperature heat exchanger. In the U.S., three main types of high temperature heat transfer fluids are being investigated for third generation CSP systems: gas-phase, molten salt, and particles, [1].

The main benefit that concentrated solar thermal technologies have over other forms of intermittent renewable energy is the relative simplicity of large-scale thermal energy storage. While the thermal energy captured via one of the aforementioned heat transfer fluids in a solar receiver could be

\* corresponding author(s)

used immediately to generate electricity via the power cycle, most systems incorporate thermal energy storage to enable continual energy output during periods of low solar resource. Most existing central receiver CSP systems using molten nitrate salt as both the heat transfer fluid in the receiver and the thermal storage medium. However, these salts tend to break down temperatures around 565°C, [1]. Thus, thermal storage technology for next-generation plants must be capable of storing and releasing energy at higher temperatures. For short term or daily storage, a common and inexpensive means of thermal energy storage is to use the sensible energy of the receiver heat transfer fluid itself, [3,4]. For high temperature CSP plants, this thermal storage includes the use of hot particles, [5], or higher temperature chloride molten salt, [6], stored for durations up to 18 hours, depending on the capacity of the TES system, [7].

Due to the high amount of recuperation in recompression sCO<sub>2</sub> Brayton cycles, the temperature lift through the primary heat exchanger is relatively small, ~200 K, [8]. Thus, when coupling this cycle to sensible thermal storage, large volumes are required. To reduce the size and cost of the storage tank while maintaining the stored energy content, the energy density of the storage media must be increased. This increase can be achieved by using a material with a higher specific heat capacity, though this approach comes at the cost of using a less developed and more expensive material. Another way to increase the energy density of the storage system while also releasing heat over a narrower range of temperatures is to store latent heat via a phase change material. However, these materials are often limited to lower temperatures and have low thermal conductivities, which leads to long charge/discharge rates, [4].

To address these challenges, the focus of this study is on coupling sCO<sub>2</sub> Brayton cycles to a system that stores energy through a combination of sensible heating and a reversible chemical reaction. An example of the system is shown in Figure

1. This practice is known as thermochemical energy storage (TCES). In this study, we consider the use of redox active metal oxide (MO<sub>x</sub>) particles with diameters on the order of 300 μm. During system charging, the particles are sensibly heated and endothermically reduced in a low O<sub>2</sub> environment. When energy is required, sensible heat and the energy from an exothermic re-oxidation reaction can be transferred to heat sCO<sub>2</sub> from a temperature of approximately 550°C to 720°C. This process significantly increases the energy density of the stored material. For example, the enthalpy of reaction is 370 kJ kg<sup>-1</sup> material at maximum extent of reduction for CAM28, the material considered in this study, [9]. TCES also potentially allows matching of the temperature at which exothermic energy is released with the temperature lift required for the sCO<sub>2</sub> cycle.

The use of MO<sub>x</sub> particles for energy storage in an air-Brayton cycle was explored by Gorman *et al.*, [10]. In their work, the particles and the Brayton cycle working fluid (air) were directly mixed, exchanging both sensible and chemical energy. The heated, O<sub>2</sub> depleted air is the working fluid used directly in the Brayton cycle. They showed that in certain cases the air outlet (turbine inlet) temperature from their reactor could exceed the stored particle temperature due to the exothermic re-oxidation reaction. Other researchers have begun to explore different TCES materials and the coupling to power cycles, [10–15]. At present, there are no studies exploring the performance of the coupling reactor between the TCES system and the sCO<sub>2</sub> power cycle. Direct contact between stored particles and the working fluid is not possible for sCO<sub>2</sub> systems. Thus, this paper explores the performance of the Energy Recovery Reactor (ERR) when the coupled sCO<sub>2</sub> power cycle runs at off design conditions. Performance is evaluated using a steady state thermodynamic model where the operating conditions of the sCO<sub>2</sub> (inlet temperature, flow rate) are varied from their design values. The metric of performance is the effectiveness of recovery, a value

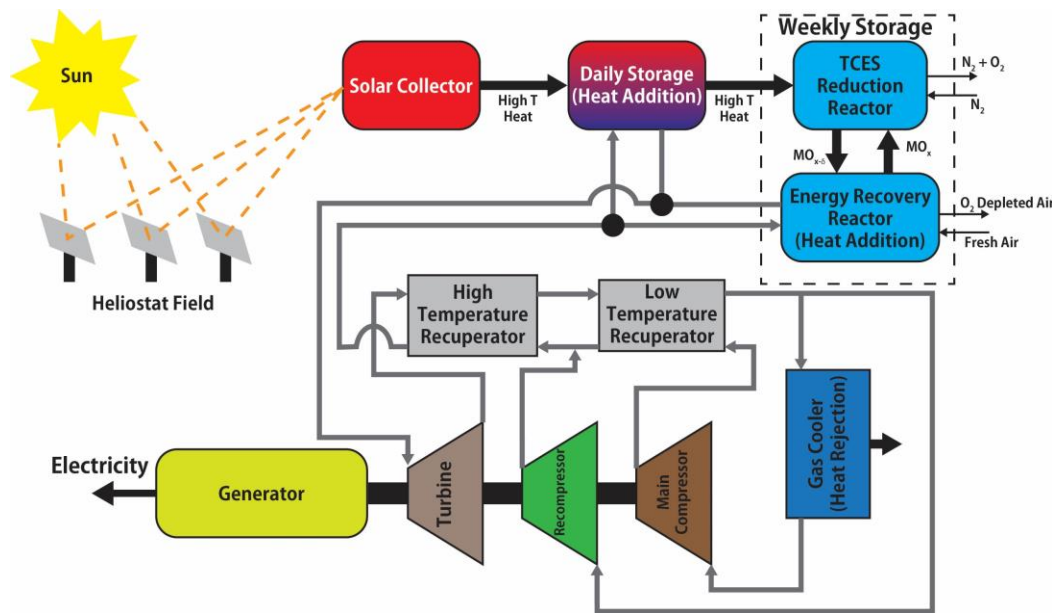


Figure 1: sCO<sub>2</sub> Brayton cycle with recompression coupled to CSP system with daily and weekly storage.

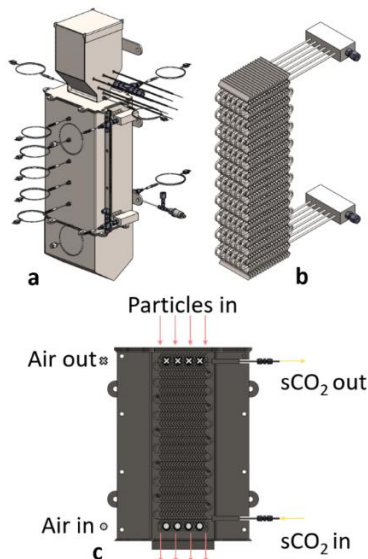


comparing how much energy transfers into the sCO<sub>2</sub> versus how much stored energy is supplied by the particles' sensible and chemical energy.

This model also compares the amount of energy recovered from the particles with how much is theoretically possible at the different off-design conditions. A complementing heat transfer model uses the conditions calculated in the thermodynamic model as inputs to calculate temperature profiles of the air, particles and sCO<sub>2</sub> through the reactor. It also calculates the local sensible and chemical energy release rates of the particles through the reactor height, which can be compared to the sensible energy change of the sCO<sub>2</sub> to again evaluate the effectiveness of recovery. These models are used to evaluate how off-design conditions of the sCO<sub>2</sub> Brayton cycle effect the performance of reactor coupling the power cycle and the TCES system.

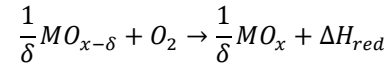
### ENERGY RECOVERY REACTOR SYSTEM DESIGN

Figure 1 shows a schematic of a concentrated solar power plant with TCES and an sCO<sub>2</sub> Brayton cycle. Our group has developed a novel device called the Energy Recovery Reactor (ERR) to couple the TCES system to a sCO<sub>2</sub> power cycle. Figure 2 shows conceptual rendering of the prototype scale ERR. This device serves as the primary heat exchanger in a recompression Brayton cycle. Within the device, both sensible and chemical energy are recovered by oxidizing the reduced TCES particles using near-ambient pressure air in counter flow. The air then transfers its energy via convection to the sCO<sub>2</sub> flowing through a bank of finned serpentine tubes through the body of the reactor. The wavy fins aid in heat transfer by increasing the heat transfer area of the sCO<sub>2</sub> circuit and increase the residence time to allow for complete oxidation of particles.



**Figure 2:** (a) Rendering of ERR prototype, (b) ERR heat exchanger core with wavy fins, (c) ERR fluid flow paths.

The reactor has three domains: MO<sub>x</sub> particles, air, and sCO<sub>2</sub>. The chemical equation used in the redox reaction is as follows:



Where  $\delta$  is the reduction extent of the metal oxide particles. The particles transfer sensible and chemical energy primarily to the air via convection, though at the high temperature, radiation effects become important.

As shown in Figure 3, the inputs to the ERR system are fresh air, hot reduced MO<sub>x</sub> particles, and sCO<sub>2</sub> returning from the power block. The ERR has been developed to recover the stored sensible and chemical energy of the particles at a high recovery efficiency, however because the reactor behaves as a counterflow heat exchanger between the particle and air, the air leaving the system carries away a large amount of sensible energy. To reduce this potential parasitic, within the system recuperation and recirculation are used to recover the exiting energy and preheat the incoming ambient fresh air. The air domain of the ERR must operate as an open cycle because the O<sub>2</sub> within the air is consumed by the particles during re-oxidation, thus limiting the ability to continually recirculate.

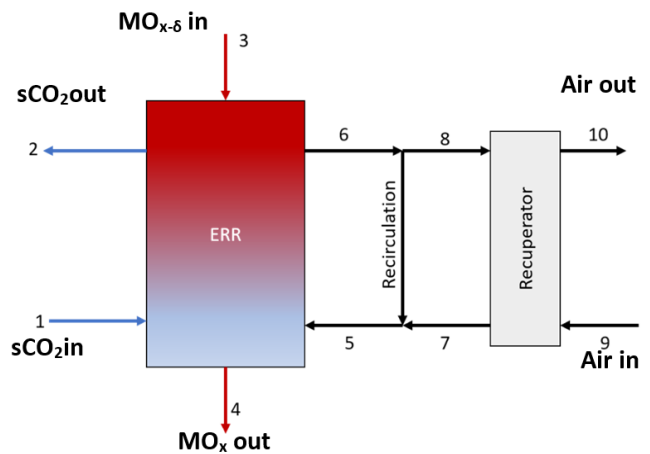


**Figure 3:** Flow schematic of ERR with recirculation and recuperation.

### THERMODYNAMIC MODEL DEVELOPMENT

A black-box thermodynamic state point model has been developed in *Engineering Equation Solver* (EES), [16] to study the steady state operating conditions of the ERR. The model calculates the required flow rate of air to completely oxidize all particles and the conditions at each state points in Figure 3 using energy and mass balances. The required model inputs are inlet temperatures of the particles (State 3), air (State 9), and sCO<sub>2</sub> (State 1) and flow rates of particles and sCO<sub>2</sub>. These results can be used to evaluate the recovery effectiveness (Eq. 1).

A mass balance is used to determine the amount of O<sub>2</sub> required to fully re-oxidize the MO<sub>x-δ</sub> particles while in the ERR. The amount of O<sub>2</sub> needed relates directly to the off-stoichiometric  $\delta$  of the stored, incoming particles. From the assumed inlet  $\delta$  and the molar flow rate of particles, the flow rate of O<sub>2</sub> that is consumed by the particles during the re-oxidation reaction is calculated using Equation 1.

$$\dot{n}_{O_2,consumed} = \frac{\delta}{2} \dot{n}_{MOx} \quad (1)$$

At steady state stoichiometric conditions, the air stream leaving the reactor is completely depleted of O<sub>2</sub>, thus the air cannot be fully recirculated through the system without the introduction of fresh air, requiring the air domain of the ERR to operate as an open loop. In this study, a theoretical air percentage of 101% is used, which ensures that there is always excess oxygen to drive the reaction. To calculate the air flow rate that enters the ERR, the molar flow rate of O<sub>2</sub> consumed is converted into mass flow rate through the molecular weight of O<sub>2</sub>. The flow rate of O<sub>2</sub> entering the reactor at state point 5 is the product of the consumed O<sub>2</sub> mass flow rate and the theoretical air percentage value, assumed constant at 101% in this study. With this value defined, an energy balance and mass around the recirculation system is used to solve the required flow rate of fresh air that must be brought into the system depending on the amount recirculated to keep the air oxygenated to fully re-oxidize the particles.

With all the flow rates defined and either the outlet temperature of sCO<sub>2</sub> or heat transfer rate into the sCO<sub>2</sub> specified, an energy balance is used to solve the individual state point temperatures and flow rates by solving a system of equations (Eq. 1 – Eq. 4). Equation 2 is the energy balance used in the model to couple all three domains of the ERR.

$$\Delta\dot{H}_{sCO_2} = \Delta\dot{H}_{MOx,chem} + \Delta\dot{H}_{MOx,sens} + \Delta\dot{H}_{N_2} + \Delta\dot{H}_{O_2} \quad (2)$$

The enthalpy change of the sCO<sub>2</sub> on the left-hand side of the equation is specified by either directly setting the desired thermal output of the ERR or setting the required outlet temperature and mass flow rate for the sCO<sub>2</sub> cycle. In this study, we consider the baseline design of a 1 kW<sub>th</sub> ERR prototype that heats sCO<sub>2</sub> from 550°C to 720°C. For these conditions, the sCO<sub>2</sub> flow rate is then calculated.

The energy addition from the chemical reaction is the product of the consumed O<sub>2</sub> and the enthalpy of reaction, represented in Equation 3.

$$\Delta\dot{H}_{MOx,chem} = \dot{n}_{O_2,consumed} H_{rxn} \quad (3)$$

The TCES material used in this model is a doped calcium manganite perovskite denoted as CAM28. Babiniec *et al.*, reported in [9], that CAM28 has a reduction enthalpy of 320 kJ mol O<sub>2</sub><sup>-1</sup> when reduced to a  $\delta$  of ~0.3. Miller *et al.* developed a thermodynamic model to further relate the equilibrium  $\delta$  as a function of the temperature and partial pressure of O<sub>2</sub> in [17]. With this material, the reaction enthalpy extraction is possible at temperatures up to 1250°C, enabling larger energy storage densities through sensible recovery by storing the particles at higher temperatures, [9]. The sensible energy recovery of the particles is shown in Equation 4.

$$\Delta\dot{H}_{MOx,sens} = \dot{m}_p \bar{c}_{p,p} (T_{p,in} - T_{p,out}) \quad (4)$$

The last two enthalpy terms in Equation 2 are the sensible parasitic losses from O<sub>2</sub> and N<sub>2</sub> in the system. The contribution of O<sub>2</sub> to the parasitic is very minimal as the only O<sub>2</sub> that removes energy from the system is from the excess air provided through the theoretical air percentage. The N<sub>2</sub> in the air does not react and absorbs heat from the particles during the process of flowing through the ERR. Heat transfers to the sCO<sub>2</sub> during this process, however even after recirculation and recuperation the outlet air, containing mostly N<sub>2</sub>, leaves at an elevated temperature compared to the inlet and therefore contributes to parasitic loss. There are no parasitic losses accounted for in the model from heat loss from of the ERR. It is assumed to be a perfectly insulated system.

The performance of the Energy Recovery Reactor system is evaluated using an energy recovery effectiveness defined above in Equation 5. The recovery effectiveness is the amount of energy put into the sCO<sub>2</sub> compared to how much stored energy is recovered from the particles sensibly and chemically. As shown by the energy balance in Equation 2, the only parasitic of this system come from energy leaving the system via a flow.

$$\eta_{recovery} = \frac{\Delta H_{sCO_2}}{\Delta H_{MOx,sens} + \Delta H_{MOx,chem}} \quad (5)$$

Because the sCO<sub>2</sub> enters the ERR nominally at 550°C, the counterflow air temperature should enter the system at or above that temperature to ensure that all the energy from the particles is going towards heating the sCO<sub>2</sub>, and that the air isn't removing initially cooling the sCO<sub>2</sub> when it first enters the reactor chamber. Therefore, the air temperature entering the reactor chamber is constrained in the model at 550°C. In practice, this temperature would be achieved via a combination of recirculation and recuperation, as shown in Figure 3. This value also defines the minimum temperature the particles can leave exit the system and ties it to the inlet temperature of the sCO<sub>2</sub>. To evaluate the amount of energy removed from the particles versus the total amount of energy available for removal. Equation 6 defines an additional performance quantifier.

$$\eta_{recovery,potential} = \frac{\Delta H_{MOx,sens} + \Delta H_{MOx,chem}}{\Delta H_{MOx,sens,max} + \Delta H_{MOx,chem}} \quad (6)$$

The maximum particle sensible energy in this equation is calculated from Equation 5, where the particle outlet temperature is set to the inlet temperature of the sCO<sub>2</sub>.

These criteria are used in the thermodynamic model to evaluate the off-design performance of the ERR when coupled to an sCO<sub>2</sub> Brayton cycle. By modifying particle and sCO<sub>2</sub> flow rates, and sCO<sub>2</sub> inlet temperature and heat duty, the changes in recovery effectiveness and sensible heat recovery potential describe the performance of the ERR at steady state.

## HEAT TRANSFER MODEL DEVELOPMENT

To complement the thermodynamic model, a 1-D segmented heat transfer model has been developed to evaluate the local temperature distributions and heat transfer rates within the reactor for a given physical geometry. This model enables the identification of pinch points and locations where exothermic reactions were not possible due to insufficient O<sub>2</sub> or temperature. In this model, it is assumed the particles only transfer energy into the air via convection, which then subsequently transfers the heat into the sCO<sub>2</sub> loop. Radiation and conduction from the dilute particle flow directly to the wall are not considered. These effects will be considered in a future study. The full reactor domain is set based on the geometry of the ERR. The domain is segmented in the flow direction of air/particles. Each segment has an equal non-dimensional height of  $dx$ , determined by the total number of nodes  $N$  and the reactor physical height. In this work, the total height of the reactor is 16 inches and 300 nodes are used to discretize the domain. Grid independence was tested by running the model with various numbers of nodes and found that the model operated independently of the number of nodes used. This is because the model is heavily based on a resistance network that is not sensitive to mesh size. The heat transfer area of the sCO<sub>2</sub> domain is determined from the total length of tubing used in the heat exchanger core and the tube inside and outside diameter in addition to the surface area enhancement provided by the wavy fins. The tube diameter used in this study is 1/8 inch outside diameter with a 0.028 inch wall thickness. The fin surface area is calculated by taking the product of the total unbent length of a fin and the width of the fin, in this case 3 inches. Figure 4 displays the discretized domain, overlaid on a cross section of the ERR showing the flow directions of the particles, air, and sCO<sub>2</sub>.

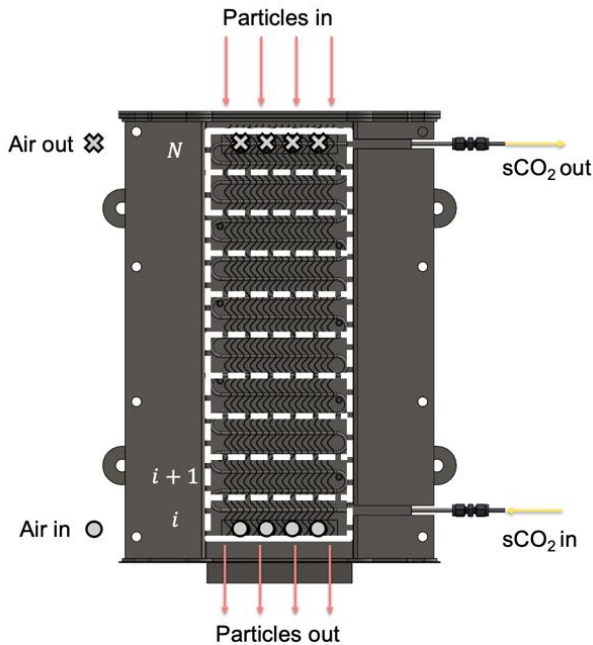


**Figure 4:** Discretized domain of ERR and flow directions.

The general transport equation is used to create an energy balance for the three flow domains within each segment, each treated as a control volume. Figure 5 shows the heat transfer taking place within each of the control volumes. This control volume segment provides a visual representation of the modes of energy exchange within each segment. The reduced general transport equation energy balances are shown in Equations 7-9.

$$\dot{m}_{CO_2} c_{pCO_2} (T_{CO_2i+1} - T_{CO_2i}) = \frac{UA}{N} [T_{Air_i} - T_{CO_2i}] \quad (7)$$

$$\dot{m}_{Air} c_{pAir_i} (T_{Air_i} - T_{Air_{i+1}}) = -\frac{UA}{N} [T_{Air_i} - T_{CO_2i}] + \frac{h_{a,p,i} A_p}{N} [T_{p_i} - T_{Air_i}] \quad (8)$$

$$\dot{m}_p c_{pp} (T_{p_i} - T_{p_{i+1}}) = \frac{h_{a,p,i} A_p}{N} [T_{p_i} - T_{Air_i}] - \Delta H_{rxn} \dot{n}_{O_2 \text{ consumed}} \quad (9)$$

The overall conductance ( $UA$ ) of the heat exchanger is calculated within the model based on the geometry of the ERR heat exchanger and the input flow rates. It is comprised of the resistances from convection between the air and tube, conduction through the tube and convection of sCO<sub>2</sub> in the tube. The correlation used for air to heat exchanger core convection is the Zukauskas correlation for flow over a bank of in-line tubes [18]. Additionally, the internal flow convection of the sCO<sub>2</sub> is estimated using the Dittus-Boelter correlation for fully developed internal turbulent flow in a tube [19]. The value of each of the thermophysical property used in the evaluation of the conductance or energy balance equations is calculated locally using the CoolProp Python package, based on the temperature and pressure within the specific node [20].

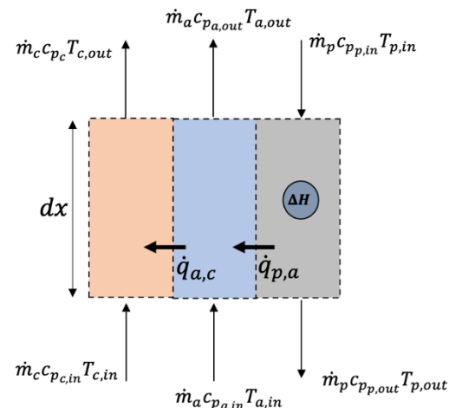


**Figure 5:** Control volume of heat transfer within ERR.

Convection heat transfer between the particles and air is calculated from a Nusselt number correlation for flow past a

single sphere, from Whitaker [21]. The total particle heat transfer area is a function of the residence time and particle flow rate. These two values are used to calculate the total number of particles within the reactor. An assumption is made that the particles are evenly distributed within the reactor, and thus the total surface area of particles, calculated from the product of the number of particles and a single particle surface area, a function of the particle diameter, is evenly distributed among the segmented control volumes.

The heat transfer model accounts for the chemical energy release by evaluating  $\delta$  at thermodynamic equilibrium. A molar balance subfunction within the model takes the particle temperature, the local  $O_2$  and  $N_2$  mole fraction in the air stream, the molar flow rate of  $O_2$  and the  $\delta$  of the particle coming into the control volume. It then evaluates what the equilibrium  $\delta$  of the particle should be based on the temperature and partial pressure of  $O_2$ , using the thermodynamic modeling fit from Miller *et al.* in [17]. A change in the  $\delta$  then can be related to the amount of  $O_2$  consumed in the node, and then further related to the heat release through the exothermic enthalpy of reaction. The sub function outputs new values for  $\delta$ , and the mole fractions and molar flow rate of  $O_2$  to be used as inputs for the next segment. The heat released through the exotherm contributes to the particle temperature as shown in Equation 9.

Because the ERR behaves as a counterflow heat exchanger, a minimization approach is needed to solve the outlet temperature of the particles. The Euler method is used to calculate the temperature of each domain in each control volume, starting with the inlet of  $sCO_2$  and air and outlet of particles. Because the inlet temperature of particles is a controllable variable, it is set and a guess value for the outlet temperature is made. A minimization function within the SciPy [22] package of Python is used to iterate the particle outlet temperatures until the results of the Euler method calculation produces a result within the convergence criteria, set at  $1^\circ C$ .

In addition to the local temperature profiles, the model calculates the local heat transfer rate through the reactor within each control volume. The sensible heat release rate by the particles in an individual segment is calculated from the product of the particle mass flow rate, specific heat capacity and the temperature difference through the node. Likewise, the local chemical heat transfer rate is calculated using the product of the  $O_2$  consumed within a segment, found from the molar balance subfunction, and the enthalpy of reaction. Summing the local chemical and sensible heat release rates at all nodes results in a total heat release rate by the particles which can be used in a recovery effectiveness equation, like Equation 5. A cumulative sum of the heat transfer rate into the  $sCO_2$  is also done using the flow rate and change in specific enthalpy across an individual node. Similar to the thermodynamic model, the heat transfer model does not include heat losses to the environment.

## THERMODYNAMIC MODEL RESULTS

To perform parametric analyses on the steady state thermodynamic model, the model must be fully defined. This constraint results in some fixed parameters during the study. All

of the controllable inputs to the model are set as fixed values except those studied in the parametric analysis. Table 1 shows a list of the constrained values within the model. These values were chosen based on the storage condition of the particles and expected performance of the  $sCO_2$  Brayton cycle. The inlet air temperature is defined at  $550^\circ C$  in the system to ensure that the air is not removing energy from the  $sCO_2$  cycle during operation. This is one of the ways the off-design operation the  $sCO_2$  cycle impacts the performance of the ERR system. The recirculation percentage of 75% was chosen to increase the air velocity within the ERR without adding additional  $O_2$ . The effectiveness of the recuperator was chosen based on an estimate for a small commercially available recuperator.

**Table 1: Fixed parameters in steady state thermodynamic model.**

Variable	Value [Units]
$\delta$	0.2 [-]
$\Delta H_{rxn}$	320 [kJ mol $O_2^{-1}$ ]
Theoretical Air Percentage	101 [%]
$T_{p,in,3}$	1000 [ $^\circ C$ ]
$T_{a,in,5}$	550 [ $^\circ C$ ]
$T_{a,in,9}$	25 [ $^\circ C$ ]
$P_{sCO_2}$	25 [MPa]
$\varepsilon$	0.5 [-]
Recirculation Percentage	75 [%]

The thermodynamic model is used to evaluate the effect of different inlet  $sCO_2$  operating conditions on the ERR performance via a parametric analysis. The range of conditions are representative of  $sCO_2$  Brayton cycle off-design operation. Figure 6 shows the variation of  $sCO_2$  inlet temperature  $\pm 100$  K from the design temperature of  $550^\circ C$  at two different particle mass flow rates. The air mass flow rates for these studies calculated from the model were  $0.57$  g  $s^{-1}$  and  $0.97$  g  $s^{-1}$  for the respective particle flow rates of  $1.75$  g  $s^{-1}$  and  $3$  g  $s^{-1}$ . As shown,

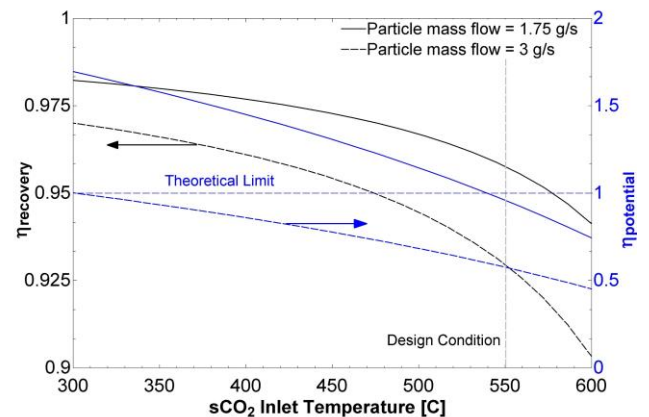


**Figure 6:** Thermodynamic model results for various  $sCO_2$  inlet temperatures *versus* recovery effectiveness and potential.

the recovery effectiveness of the system increases as the temperature drops below the design condition for both particle flow rates. Because the flow rate of sCO<sub>2</sub> is fixed in this study (4.644 g/s for 1 kW at design temperatures), decreasing the inlet temperature while maintaining the outlet temperature at the design value of 720°C increases the required heat duty of the ERR.

Because the flow rate of particles is fixed, the amount of chemical energy potentially released by the particles is also fixed (assuming complete re-oxidation), and therefore if more heat is required to transfer into the sCO<sub>2</sub> the particles must release more sensible heat in the process. For given flow rates of particles and sCO<sub>2</sub>, 1.0 is the maximum theoretical value for the potential energy recovery, defined previously in Equation 6. This limit is where the particle outlet temperature is equal to the sCO<sub>2</sub> inlet temperature, and the particles have been completely oxidized. The right axis of Figure 6 shows how this value changes with inlet temperature of sCO<sub>2</sub>. In the case of the sCO<sub>2</sub> flow rate used in this study, the theoretical maximum limit for the recovery potential occurs at sCO<sub>2</sub> inlet temperature of 539°C and 302°C for the 1.75 and 3 g s<sup>-1</sup> particle flow rates respectively.

Figure 7 shows that as the sCO<sub>2</sub> inlet temperature rises, and thus the required heat duty decreases, the sensible ratio, defined in Equation 10, decreases as the heat needed for heating sCO<sub>2</sub> provided by the particles comes primarily from re-oxidation, especially at higher flow rates of particles.

$$\text{Sensible Ratio} = \frac{\Delta H_{MO_x,sens}}{\Delta H_{MO_x,sens} + \Delta H_{MO_x,chem}} \quad (10)$$

A key takeaway from these results is that the mass flow rate of particles must be controlled as the required heat duty of the system changes to maximize recovery effectiveness. If the inlet sCO<sub>2</sub> temperature increases above the design value, the particle mass flow rate must be decreased to utilize more of the sensible energy available.

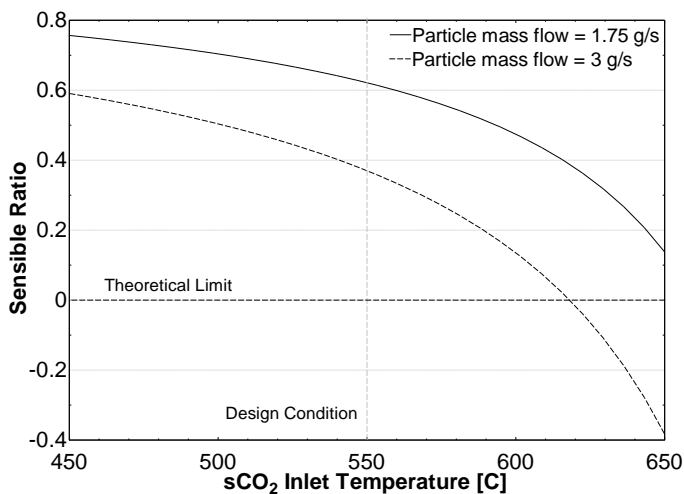


**Figure 7:** sCO<sub>2</sub> inlet temperature versus sensible heat ratio for fixed sCO<sub>2</sub> mass flow and outlet temperature.

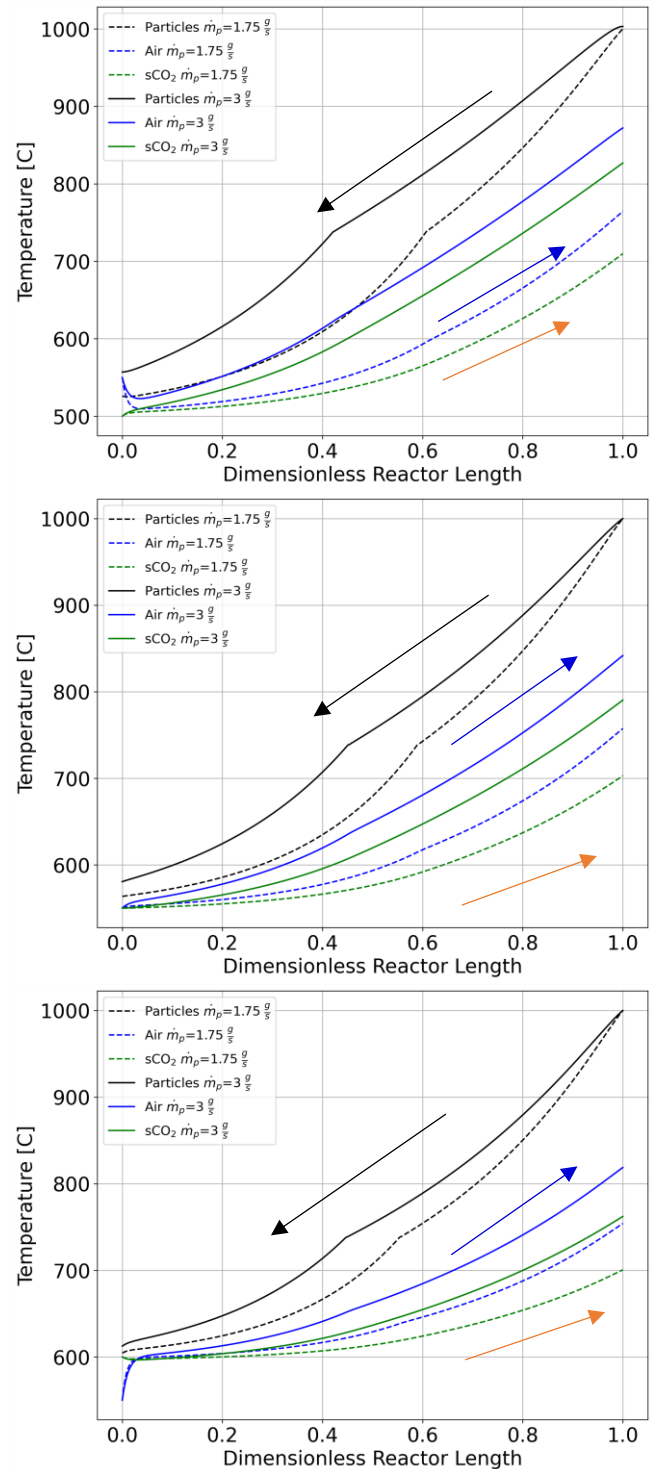


**Figure 8:** Heat transfer model results for ERR temperature profiles with sCO<sub>2</sub> inlet temperature of (top) 500°C (middle) 550°C (bottom) 600°C.

With fixed temperatures of the sCO<sub>2</sub> at their design values, and changing flow rates of sCO<sub>2</sub>, similar trends to the results shown in Figure 6 and Figure 7 can be observed. As the flow rate



decreases, the heat duty of the system decreases and at a fixed particle flow rate the amount of heat available from the particles is used at various effectiveness depending on the change in operating condition. This model can be used to gain insight on how the flows of the other domains within the ERR must be adjusted if the sCO<sub>2</sub> Brayton cycle coupled to the ERR is operating off design conditions.

### HEAT TRANSFER MODEL RESULTS

The 1-D segmented heat transfer model calculates the temperature profiles and local heat transfer rates through the reactor. Steady state operation is again assumed in this model, however the only constraints in this model are on the inlet conditions and reactor physical geometry (e.g., height, heat transfer area, etc.).

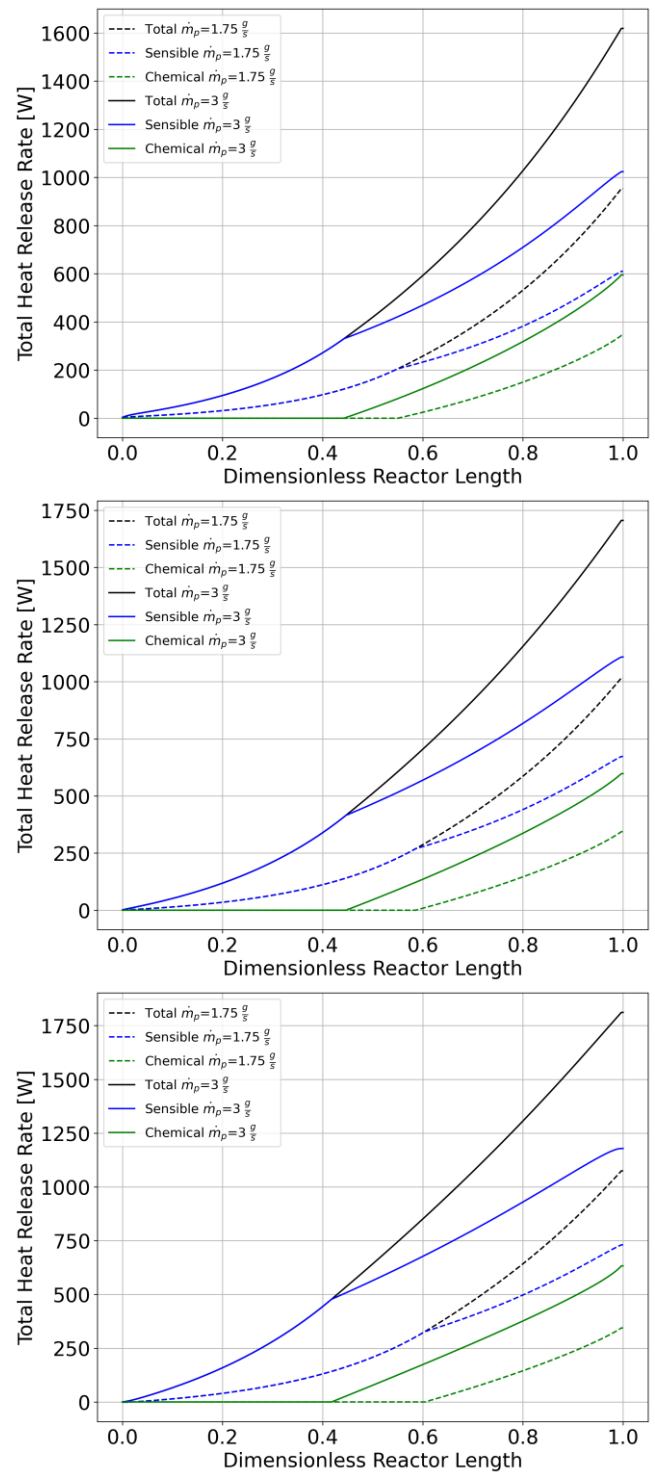
Unlike the thermodynamic model, the sCO<sub>2</sub> outlet temperature and heat duty are calculated, and therefore change based on inlet conditions. Using the same particle flow rates investigated in the thermodynamic model parametric study, the off-design inlet conditions of sCO<sub>2</sub> are investigated for conditions both above and below the design conditions.

Figure 8 shows the temperature profiles of the ERR operating at two particle flow rates (1.75 g/s, 3 g/s) and three sCO<sub>2</sub> inlet temperatures, (500°C, 550°C, 600°C). The arrows indicate the flow direction of each domain. As expected, for each of the sCO<sub>2</sub> inlet temperatures, the temperature lift of sCO<sub>2</sub> is less at the lower particle flow rate. This trend is due to less available total energy within the system, both chemical and sensible. As the sCO<sub>2</sub> inlet temperature increases, at a particle flow rate of 3 g/s, the outlet temperature of sCO<sub>2</sub> decreases because the inlet temperature of air is again constrained to 550°C, and therefore heat does not immediately transfer into the sCO<sub>2</sub> from the air, rather the sCO<sub>2</sub> is initially cooled by the air. The inlet sCO<sub>2</sub> temperature has a major impact on the convective heat transfer between the air and the sCO<sub>2</sub> because of varying temperature differences between the two domains. The particles reacting in the air flow allow the air to behave like a fluid with an infinite heat capacity, hence why the temperature can climb even while energy is transferring to the sCO<sub>2</sub>.

The total heat release rate from the particles within the ERR for the design condition case is 1016 W and 1705 W for 1.75 and 3 g s<sup>-1</sup> particle flow rates respectively. Increasing the sCO<sub>2</sub> inlet temperature to 600°C results in a 5.8% increase for the 1.75 g s<sup>-1</sup> case and 4.0% increase for 3 g s<sup>-1</sup>. Decreasing sCO<sub>2</sub> inlet temperature to 550°C decreases the total heat release rate by 6.1% and 5.1% for the particle flow rates respectively. However, similar to the thermodynamic model, increasing the particle flow rate does have a significant impact on the total heat released by the particles. The total amount of chemical heat is a function of the particle flow rate, and thus it is uniform in each varying temperature run, around 343 W for the 1.75 g s<sup>-1</sup> case and 597 W for the 3 g s<sup>-1</sup>. Figure 9 shows the cumulative heat release rate through the length of the reactor. The particles do not begin reacting until they reach a temperature and partial pressure of O<sub>2</sub> where the exothermic reaction can move forward based on the

local reduction extent. When they are introduced into the reactor at the top, they require O<sub>2</sub> to undergo reaction.

Depending on inlet conditions, there may be zero O<sub>2</sub> at the exit of the air stream, which is the same location as the inlet of



**Figure 9:** Heat transfer model results for ERR heat release rate profiles with sCO<sub>2</sub> inlet temperature of (top) 500°C (middle) 550°C (bottom) 600°C.



the particle stream. The particles will then remain reduced until they encounter sufficient  $O_2$  to begin the exothermic reaction. The reaction proceeds while the local particle temperature and environment partial pressure of  $O_2$  are satisfactory to carry the reaction forward. Uniform chemical heat release is desired as then the particles are providing the condition where the air acts as a quasi-infinite capacitance fluid and can maintain a larger temperature difference between the air and  $sCO_2$ . The increased  $sCO_2$  inlet temperature allows for the particles to remain in the equilibrium conditions for longer, and therefore reduces the need for sensible energy in this region, indicated by the change in slope when the chemical reaction begins. This trend is shown in the plots as the  $sCO_2$  inlet temperature is increased, the cumulative sensible heat release rate is lower, and the chemical heat release begins at a lower dimensionless reactor length.

## CONCLUSIONS

This paper investigated the effects of operating an  $sCO_2$  Brayton cycle at off-design conditions on the performance of the coupling device between a TCES system and the power cycle. A steady state thermodynamic model has been developed to determine the recovery effectiveness and potential, as well as the sensible-to-chemical energy ratio over a variety of  $sCO_2$  inlet temperature conditions. A complementing 1-D segmented heat transfer model calculated the temperature profiles and cumulative heat release rates through the reactor at various particle flow rates and  $sCO_2$  inlet temperatures. The following observations can be made about the Energy Recovery Reactor system when operating at off-design conditions:

- Because the ERR utilizes both chemical and sensible energy to heat the  $sCO_2$ , increasing the particle flow rate does not linearly increase the energy into the  $sCO_2$  due to ratio of sensible and chemical heat release changing with particle flow rate
- As the  $sCO_2$  inlet temperature increases, recovery effectiveness decreases from increased parasitic losses flowing out of the reactor and recovery potential decreases from not utilizing all the sensible energy available in the particles and relying more on chemical energy
- If other operating conditions (particle flow rate, air inlet temperature) are not changed with variances in the  $sCO_2$  flow conditions, the system effectiveness decreases and target conditions will not be met

Understanding the implications of running an  $sCO_2$  Brayton cycle at off design conditions on a device used to add heat to the system is important as any changes can lead to inefficiencies or failures. The thermodynamic and heat transfer models developed in this study mimic steady state operating conditions, so transient effects are not represented in this work. Future work will investigate the transient effects of changing these flow conditions. These two models also assume a fixed air inlet temperature set to match the design condition for  $sCO_2$ . This assumption is appropriate because the experimental setup

associated with this work uses inline air heaters to preheat the air to the desired temperature, so off design effects in the  $sCO_2$  loop will not affect the inlet temperature of air as they are controlled by separate systems. Future work will use this experimental setup to validate the model-based results. Finally, the results of these models can serve as the basis for model-based control of particle flow rates as power cycle conditions change.

## NOMENCLATURE

$c_p$	Specific heat capacity [ $J\ kg^{-1}\ K^{-1}$ ]
$dx$	Non-dimensional control volume height [-]
$H_{rxn}$	Reaction enthalpy [ $J\ kmol^{-1}$ ]
$h$	Convective heat transfer coefficient [ $W\ m^{-2}\ K^{-1}$ ]
$\dot{m}$	Mass flow rate [ $kg\ s^{-1}$ ]
$N$	Total number of nodes [-]
$T$	Temperature [K]
$UA$	Heat exchanger conductance [ $W\ K^{-1}$ ]

### *Greek*

$\delta$	Reduction extent
$\varepsilon$	Recuperator effectiveness
$\eta$	Effectiveness

### *Subscripts*

$a$	Air
$c$	$sCO_2$
$i$	Current node
$MO_x$	Metal oxide particles
$p$	Particle

## ACKNOWLEDGEMENTS

This material is based upon work supported by the U.S. Department of Energy's Office of Energy Efficiency and Renewable Energy (EERE) under the Solar Energy Technologies Office Award Number DE-EE0008991. The views expressed herein do not necessarily represent the views of the U.S. Department of Energy or the United States Government. We also gratefully acknowledge Drs. Ivan Ermanoski, Ryan Milcarek, and Arindam Dasgupta and the rest of the project team for helpful conversations.

**Full Legal Disclaimer:** This report was prepared as an account of work sponsored by an agency of the United States Government. Neither the United States Government nor any agency thereof, nor any of their employees, makes any warranty, express or implied, or assumes any legal liability or responsibility for the accuracy, completeness, or usefulness of any information, apparatus, product, or process disclosed, or represents that its use would not infringe privately owned rights. Reference herein to any specific commercial product, process, or service by trade name, trademark, manufacturer, or otherwise does not necessarily constitute or imply its endorsement, recommendation, or favoring by the United States Government or any agency thereof.

## REFERENCES

- [1] Mehos, M., Turchi, C., Vidal, J., Wagner, M., Ma, Z., Ho, C., Kolb, W., Andraka, C., and Kruizenga, A., 2017, *Concentrating Solar Power Gen3 Demonstration Roadmap*.
- [2] Turchi, C. S., Ma, Z., Neises, T. W., and Wagner, M. J., 2013, "Thermodynamic Study of Advanced Supercritical Carbon Dioxide Power Cycles for Concentrating Solar Power Systems," *Journal of Solar Energy Engineering, Transactions of the ASME*, **135**(4), pp. 1–7.
- [3] Gil, A., Medrano, M., Martorell, I., Lázaro, A., Dolado, P., Zalba, B., and Cabeza, L. F., 2010, "State of the Art on High Temperature Thermal Energy Storage for Power Generation. Part 1-Concepts, Materials and Modellization," *Renewable and Sustainable Energy Reviews*, **14**(1), pp. 31–55.
- [4] Evans, A., Strezov, V., and Evans, T. J., 2012, "Assessment of Utility Energy Storage Options for Increased Renewable Energy Penetration," *Renewable and Sustainable Energy Reviews*, **16**(6), pp. 4141–4147.
- [5] Ho, C. K., 2016, "A Review of High-Temperature Particle Receivers for Concentrating Solar Power," *Appl Therm Eng*, **109**, pp. 958–969.
- [6] Ding, W., and Bauer, T., 2021, "Progress in Research and Development of Molten Chloride Salt Technology for Next Generation Concentrated Solar Power Plants," *Engineering*, **7**(3), pp. 334–347.
- [7] Thonig, R., and Lilliestam Richard, 2022, *CSP Projects Around the World*.
- [8] Brun, K., Friedman, P., and Dennis, R., eds., 2017, *Fundamentals and Applications of Supercritical Carbon Dioxide (SCO<sub>2</sub>) Based Power Cycles*, Woodhead Publishing.
- [9] Babiniec, S. M., Coker, E. N., Miller, J. E., and Ambrosini, A., 2016, "Doped Calcium Manganites for Advanced High-Temperature Thermochemical Energy Storage," *Int J Energy Res*, **40**(4), pp. 280–284.
- [10] Gorman, B. T., Miller, J. E., and Stechel, E. B., 2015, "Thermodynamic Investigation of Concentrating Solar Power with Thermochemical Storage," *ASME*, San Diego, CA, pp. 1–10.
- [11] Jackson, G. S., Imponenti, L., Albrecht, K. J., Miller, D. C., and Braun, R. J., 2019, "Inert and Reactive Oxide Particles for High-Temperature Thermal Energy Capture and Storage for Concentrating Solar Power," *Journal of Solar Energy Engineering, Transactions of the ASME*, **141**(2), pp. 1–14.
- [12] Babiniec, S. M., Miller, J. E., Ho, C. K., Coker, E. N., and Loutzenhiser, P. G., 2016, "Considerations for the Design of a High-Temperature Particle Reoxidation Reactor for Extraction of Heat in Thermochemical Energy Storage Systems," *ASME 2016 10th International Conference on Energy Sustainability*, pp. 1–6.
- [13] Albrecht, K. J., Jackson, G. S., and Braun, R. J., 2018, "Evaluating Thermodynamic Performance Limits of Thermochemical Energy Storage Subsystems Using Reactive Perovskite Oxide Particles for Concentrating Solar Power," *Solar Energy*, **167**(April), pp. 179–193.
- [14] Albrecht, K. J., Jackson, G. S., and Braun, R. J., 2016, "Thermodynamically Consistent Modeling of Redox-Stable Perovskite Oxides for Thermochemical Energy Conversion and Storage," *Appl Energy*, **165**, pp. 285–296.
- [15] Schrader, A. J., Muroyama, A. P., and Loutzenhiser, P. G., 2015, "Solar Electricity via an Air Brayton Cycle with an Integrated Two-Step Thermochemical Cycle for Heat Storage Based on Co<sub>3</sub>O<sub>4</sub>/CoO Redox Reactions: Thermodynamic Analysis," *Solar Energy*, **118**, pp. 485–495.
- [16] Klein, S. A., 2020, "F-Chart Software: EES."
- [17] Miller, J. E., Babiniec, S. M., Coker, E. N., Loutzenhiser, P. G., Stechel, E. B., and Ambrosini, A., 2022, "Modified Calcium Manganites for Thermochemical Energy Storage Applications," *Front Energy Res*, **10**.
- [18] Žukauskas, A., 1972, "Heat Transfer from Tubes in Crossflow," *Advances in Heat Transfer*, J.P. Hartnett, and T.F. Irvine, eds., pp. 93–160.
- [19] Dittus, F. W., and Boelter, L. M. K., 1985, "Heat Transfer in Automobile Radiators of the Tubular Type," *Int. Comm. Heat and Mass Transfer*, **12**, pp. 3–22.
- [20] Bell, I. H., Wronski, J., Quoilin, S., and Lemort, V., 2014, "Pure and Pseudo-Pure Fluid Thermophysical Property Evaluation and the Open-Source Thermophysical Property Library CoolProp," *Ind Eng Chem Res*, **53**(6), pp. 2498–2508.
- [21] Whitaker, S., 1972, "Forced Convection Heat Transfer Correlations for Flow In Pipes, Past Flat Plates, Single Spheres, and for Flow in Packed Beds and Tube Bundles," *AIChE Journal*, **18**(2), pp. 361–371.
- [22] Virtanen, P., Gommers, R., et al. 2020, "SciPy 1.0: Fundamental Algorithms for Scientific Computing in Python," *Nat Methods*, **17**(3), pp. 261–272.

**EXPERIMENTAL AND NUMERICAL STUDY ON THERMAL HYDRAULIC  
PERFORMANCE OF TRAPEZOIDAL PRINTED CIRCUIT HEAT EXCHANGER FOR  
SUPERCRITICAL CO<sub>2</sub> BRAYTON CYCLE**

**Yuxuan Ji**

State Key Laboratory of Clean Energy Utilization,  
Zhejiang University, Hangzhou, China

**Zheng Wang**

State Key Laboratory of Clean Energy Utilization,  
Zhejiang University, Hangzhou, China

**Mingxuan Wang**

State Key Laboratory of Clean  
Energy Utilization, Zhejiang  
University, Hangzhou, China

**Yafei Liu**

State Key Laboratory of Clean  
Energy Utilization, Zhejiang  
University, Hangzhou, China

**Haoran Xu**

State Key Laboratory of Clean  
Energy Utilization, Zhejiang  
University, Hangzhou, China

**Peiwang Zhu**

State Key Laboratory of Clean Energy Utilization,  
Zhejiang University, Hangzhou, China

**Gang Xiao \***

State Key Laboratory of Clean Energy Utilization,  
Zhejiang University, Hangzhou, China  
Email: xiaogangtianmen@zju.edu.cn

**ABSTRACT**

The supercritical carbon dioxide (sCO<sub>2</sub>) Brayton cycle is the preferred power cycle for future nuclear energy, fossil energy, solar energy, and other energy systems. As the preferred regenerator in the cycle, the printed circuit heat exchanger (PCHE) exhibits a high heat transfer efficiency, compactness, and robustness. The structure design of its internal flow channel is one of the most important factors to enhance the heat transfer and reduce pressure loss. In the present work, trapezoidal channel structure is developed and its thermal-hydraulic performances are compared with the straight, the S-shape, and the zigzag structures. Further, a trapezoidal PCHE prototype is manufactured and experimentally studied as a regenerator in the sCO<sub>2</sub> test loop. The overall heat transfer coefficient exceeds 1.10 kW/(m<sup>2</sup>·K) and reaches a maximum of 2.53 kW/(m<sup>2</sup>·K) with the changes in the inlet temperature, the working pressure, and the mass flow rate. Correlations of the Nusselt numbers are proposed on both sides, with the Reynolds numbers ranging from 10,000 to 30,000 and 4800 to 14,000, and the Prandtl numbers ranging from 0.91 to 1.61 and 0.77 to 0.98 on the cold side and hot side, respectively. The pressure drop of the channels calculated by the peeling method using a single-plate straight prototype is less than 7 kPa and 15 kPa on the hot and the cold side, respectively. The heat recovery efficiency is analyzed to evaluate the performance of the PCHE used as a regenerator. Finally, simulation works are carried out to verify the experimental results and expand the Reynolds numbers ranging from 3796 to 30,000 and 1821 to

14,000, on the cold side and hot side, respectively. This work provides the test methods and experimental correlations for the development of an efficient PCHE in the sCO<sub>2</sub> Brayton cycle.

**INTRODUCTION**

Printed circuit heat exchanger (PCHE) is a preferred heat-exchange device in supercritical carbon dioxide (sCO<sub>2</sub>) Brayton cycle because of its high heat transfer efficiency, compactness, and robustness. The flow microchannels, formed by chemical etching on the metal plates, have a decisive influence on the thermal-hydraulic performance of PCHE. Many kinds of channel structures have been studied such as straight, zigzag, S-shaped fin, and airfoil fin. The straight channel is the basic structure with a simple etching process. Mylavarapu et al. [1] fabricated two straight-channel PCHEs and connected them in series to a high-temperature helium test facility (HTHF). The heat transfer and friction characteristics were analyzed based on the experimental data under the conditions corresponding to the laminar to turbulent transition region. Chen et al. [2] developed a numerical dynamic model and successfully predicted the steady-state and transient behaviors of a straight PCHE by comparing with the experimental results. Chu et al. [3] studied the PCHE thermo-hydraulic performance on the sCO<sub>2</sub>-water experiment platform at the transcritical and supercritical states, indicating that the comprehensive performance reduced by about 17.6% at the transcritical state. The zigzag structure can significantly improve the heat transfer area and coefficient, accompanied by the

\* corresponding author(s)

DOI: 10.17185/duerpublico/77317

disadvantage of increased pressure loss. Nikitin et al. [4] investigated the heat transfer performance and pressure drop of a zigzag PCHE through experiments and numerical simulations. The overall heat transfer coefficient ranged from 300 to 650 W/(m<sup>2</sup>·K) with a compactness of approximately 1050 m<sup>2</sup>/m<sup>3</sup> and a maximum power density of 4.4 MW/m<sup>3</sup>. Kim et al. [5–7] carried out a detailed study on the zigzag-structure PCHE using He, CO<sub>2</sub>, and water as working fluids. The correlations of Nusselt numbers and Fanning friction factors were fitted, and the effects of the channel geometric parameters were analyzed. Zhou et al. [8] designed and manufactured a 100 kW class zigzag PCHE prototype as a recuperator and tested using sCO<sub>2</sub> on both sides. The effectiveness was over 95% and the pressure drop was less than 50 kPa on both sides. S-shaped structure was proposed by Tsuzuki et al. [9], which can reach the same thermal performance as the zigzag flow channel, but its pressure loss reduction can be reduced to one - fifth. Ngo et al. [10,11] developed a new S-shaped-fin PCHE and compared its thermal-hydraulic performance with that of zigzag fins. The empirical correlations of Nusselt numbers and pressure-drop factors were proposed, which proved that the pressure drop factor of the S-shaped microchannels was 4–5 times less than the zigzag one through a 24–34% reduction in the Nusselt numbers. Kim et al. [12] proposed an airfoil fin structure which may have a smaller pressure drop than S-shaped. Chen et al. [13] compared the performance of four types of NACA00XX airfoil structures with zigzag and found that the airfoil structure can significantly reduce the flow pressure drop loss while maintaining heat transfer performance. Pidaparti et al. [14] investigated two kinds of discontinuous PCHEs with an offset rectangular and NACA0020 airfoil fin. Empirical correlations for the friction factor and the Nusselt number were proposed, which could match the experimental results.

From the above studies, it can be found that balancing heat transfer and pressure drop and developing flow channel structures with higher comprehensive performance have always been the focus of PCHE research. Especially in regenerators with the largest heat load, the comprehensive performance of PCHE will significantly affect the efficiency of sCO<sub>2</sub> cycle system. However, most existing experiments focused on precoolers, which studied the heat transfer characteristics between sCO<sub>2</sub> and water, and the conditions for testing were usually near the CO<sub>2</sub> critical point. It also needs to study the performance of PCHE regenerators by using sCO<sub>2</sub> as the heat transfer medium on both sides. In this work, a trapezoidal channel structure model is developed and compared with the straight, the S-shape, and the zigzag structures. Then a trapezoidal PCHE prototype is manufactured and experimentally studied as a regenerator in the sCO<sub>2</sub> test loop. The heat transfer coefficient and heat recovery efficiency are calculated and analyzed under different thermal parameters. Correlations for Nusselt numbers on both trapezoidal channels are proposed with respect to Reynolds numbers and Prandtl numbers, and the pressure drop in the flow channels is evaluated and peeled off by designing a single-plate straight channel prototype. In addition, the numerical simulation results verify and expand the experimental conclusions. This

work provides new trapezoidal channel experimental results and heat transfer correlations for an advanced PCHE regenerator design in the sCO<sub>2</sub> Brayton cycle.

### TRAPEZOIDAL CHANNEL STRUCTURE

A counterflow trapezoidal channel PCHE heat transfer unit model is established for numerical simulation study as shown in Figure 1, the channels had semicircular cross - sections with 2 mm diameters and a 0.50 mm space in between. The period and amplitude of the trapezoid are 10 mm and 1 mm, respectively. Further, to compare the performance with other structures, straight, zigzag and S-shaped channels are established. The four models only have differences in geometric shapes. The unstructured tetrahedral mesh is divided and the SST k-omega turbulence model is chosen due to the Reynolds number range and flow bending [15-17]. Periodic boundary conditions are applied on the top, the bottom, the left, and the right sides, and adiabatic boundary conditions are applied on the front and the back surfaces. The inlet temperature and pressure boundary conditions on the hot and cold channels are 726.85 K, 7.6 MPa and 388.75 K, 20.2 MPa, respectively. The inlet mass flow rate range on both sides is from  $4.82 \times 10^{-4}$  to  $14.45 \times 10^{-3}$  kg/s. All conditions are selected based on the regenerator parameters of the 200-kW class sCO<sub>2</sub> simple recuperation cycle demonstration system.

Table 1 summarizes the heat transfer coefficient and pressure drop results by simulations. The trapezoidal structure has the highest heat transfer coefficient over 5000 W/(m<sup>2</sup>·K). The hot side and cold side are 47.84% and 52.31% higher than that of the straight channel, 13.49% and 17.10% higher than that of the S-shaped, and 7.69% and 10.84% higher than that of the zigzag channel, respectively. However, the pressure drop of the trapezoid is also the highest in the four structures, especially on the hot side, which pulls down the comprehensive thermal-hydraulic performance.

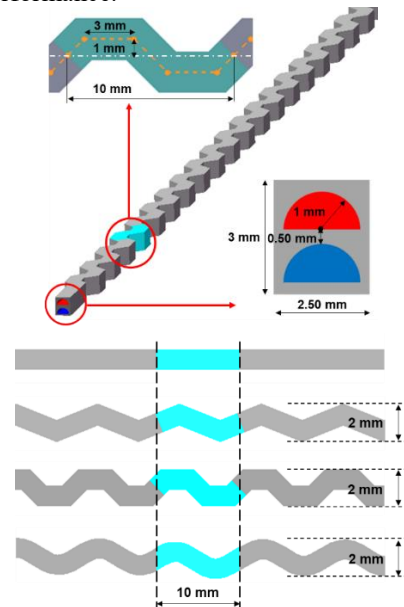


**Figure 1:** Channel structure models for numerical simulation

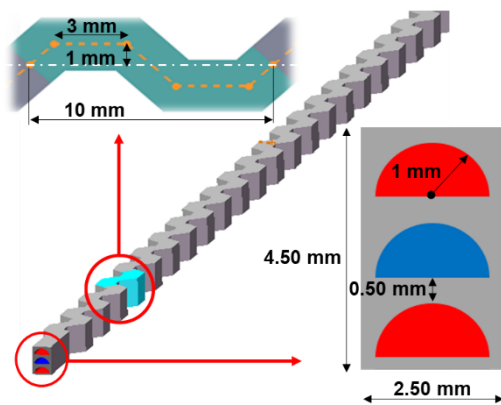
To reduce the pressure loss problem, a sandwiched trapezoidal flow channel structure is designed as shown in Figure 2 (a), where the cross-section of the flow unit model is increased to 2.50 mm × 4.50 mm with one cold flow channel sandwiched between two hot flow channels. Table 2 shows that the significant reductions in pressure drop loss in the hot channel are obtained, where the values are 75.4% (from 154.81 kPa to 38.37 kPa) and 74.7% (from 39.65 kPa to 10.05 kPa) at 42 kPa and 11 kPa pressure loss cases in the cold side, respectively. Figure 2(b) also indicates the heat recovery efficiency is increased by about 5% in the sandwich structure.

**Table 1:** Simulation results of four channel structures

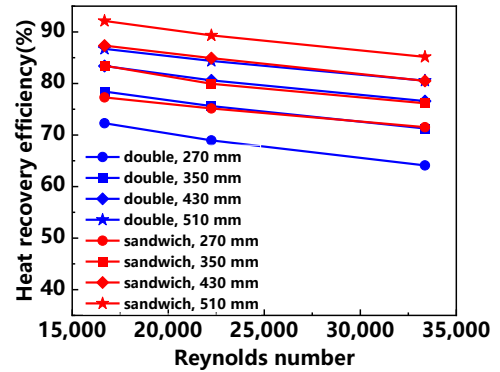
Channel structure	Heat transfer coefficient [W/(m <sup>2</sup> ·K)]		Pressure drop (kPa)		Heat recovery efficiency (%)
	Hot side	Cold side	Hot side	Cold side	
	Straight	3402.20	3302.66	26.32	
Zigzag	4670.64	4538.54	104.57	30.11	60.93
S-shaped	4431.90	4295.62	56.78	17.10	59.67
Trapezoid	5029.80	5030.37	159.30	45.80	64.09

**Table 2:** Pressure loss comparisons between sandwich and double-channel structure

Reynolds Number of the Cold Side	Pressure Loss (kPa).			
	Double-Channel Structure		Sandwich Structure	
	Cold Side	Hot Side	Cold Side	Hot Side
33,366	42.62	154.81	41.94	38.37
22,244	19.73	71.11	18.60	17.77
16,683	11.07	39.65	11.04	10.05



(a) sandwich trapezoidal channel model



(b) heat recovery efficiency comparison

**Figure 2:** Sandwich trapezoidal channel structure and comparison of heat recovery efficiency

### EXPERIMENTAL SYSTEM AND PROTOTYPE

A supercritical carbon dioxide heat transfer and circulation test loop was constructed to investigate the heat transfer and pressure drop characteristics, as shown in Figure 3. The loop can be roughly divided into four parts, namely the CO<sub>2</sub> gas source and pump, the cooling system, the PCHE test part, and the heat transfer test section. It also includes a pulsation damper, a mass flowmeter, a filter, various valves, thermocouples, pressure/differential pressure sensors, etc. The maximum temperature of the loop can reach 500 °C, the working pressure can be adjusted within 7 ~ 15 MPa, and the maximum mass flow rate is 60 kg/h.

The test trapezoidal PCHE prototype is shown in Figure 5, which is the main research object in this work. There are 20 channels on one plate, each of which has a length of 120 mm, including ten periods and two 10 mm long straight channel zones at both ends, and a 4 mm interval is left between two adjacent channels. The prototype has two hot plates and one cold plate, resulting in the mass flow of the hot channel being half of the cold side in each heat transfer unit to balance the flow velocity and heat capacity. Using diffusion bonding, the plates are combined into a 168 mm × 90 mm × 10.50 mm device with a 120 mm × 80 mm × 4.50 mm heat transfer core. The total heat transfer area is about 0.36 m<sup>2</sup> with a 0.30 m<sup>2</sup> area in the heat transfer core. Four 90 mm long pipes are welded on the top of the prototype and connected to the test loop by tube fittings.

The experimental test conditions are shown in Table 3, and the direct measuring instruments and accuracy are shown in Table 4. In order to evaluate the pressure drop of trapezoidal channel, as shown in Figure 4, a straight channel PCHE prototype with only one layer of plates was designed and manufactured for pressure drop peeling, which has the same structure and size as trapezoidal channel. In the pressure drop peeling experiment, the temperature and pressure of the straight channel PCHE prototype were controlled in accordance with the conditions of the trapezoidal one. Since the pressure drop of the straight channel PCHE was found to be very small, the pressure

loss of the trapezoidal channel core could be considered equivalent to the difference between the measurement results of trapezoidal channel PCHE and the straight channel PCHE.

**Table 3:** The experimental test conditions

Parameters	Hot side	Cold side
Inlet temperature, °C	200 – 400	40 – 100
Inlet pressure, MPa	7.50 - 12	8.25 – 12.75
Mass flow rate, kg/h	20 - 60	20 - 60
Reynolds number range	4,800 – 14,000	10,000 – 30,000

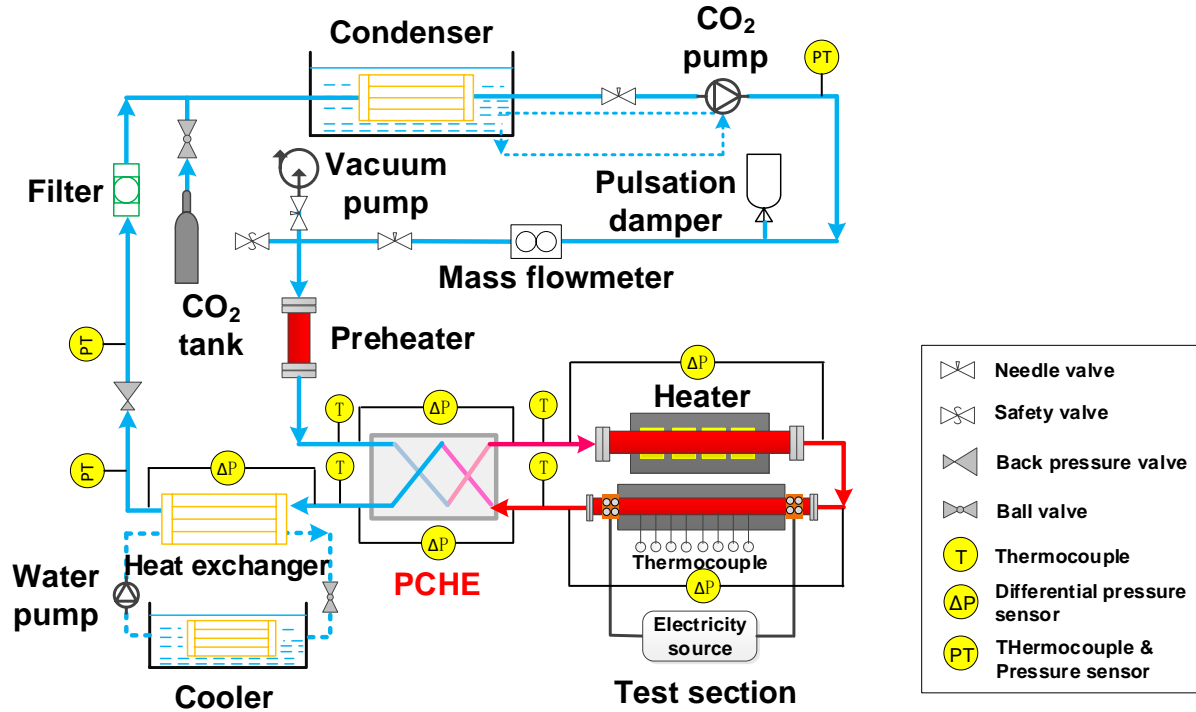


**Figure 3:** Schematic of the sCO<sub>2</sub> heat transfer and circulation test loop

**Table 4:** The direct measuring instruments and accuracy

Parameters	Position	Instruments	Range	Accuracy
Mass flow rate	Pump outlet	Coriolis flowmeter	0 ~ 300 kg/h	0.20%
Temperature	Preheat outlet	PT100	-50 ~ 200 °C	A level
Temperature	PCHE cold inlet	K-type thermocouple	0 ~ 1100 °C	0.75%
Temperature	PCHE cold outlet	K-type thermocouple	0 ~ 1100 °C	0.75%
Temperature	PCHE hot inlet	K-type thermocouple	0 ~ 1100 °C	0.75%
Temperature	PCHE hot outlet	K-type thermocouple	0 ~ 1100 °C	0.75%
Pressure loss	PCHE cold side	Differential pressure sensor	0 ~ 500 kPa	0.10%
Pressure loss	PCHE hot side	Differential pressure sensor	0 ~ 500 kPa	0.10%

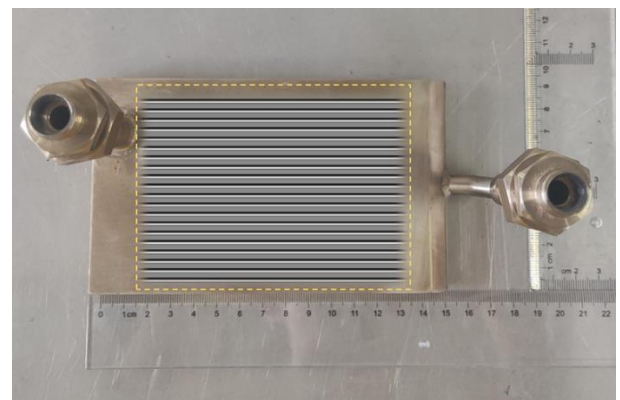


**Figure 4:** The straight channel PCHE prototype for pressure drop peeling



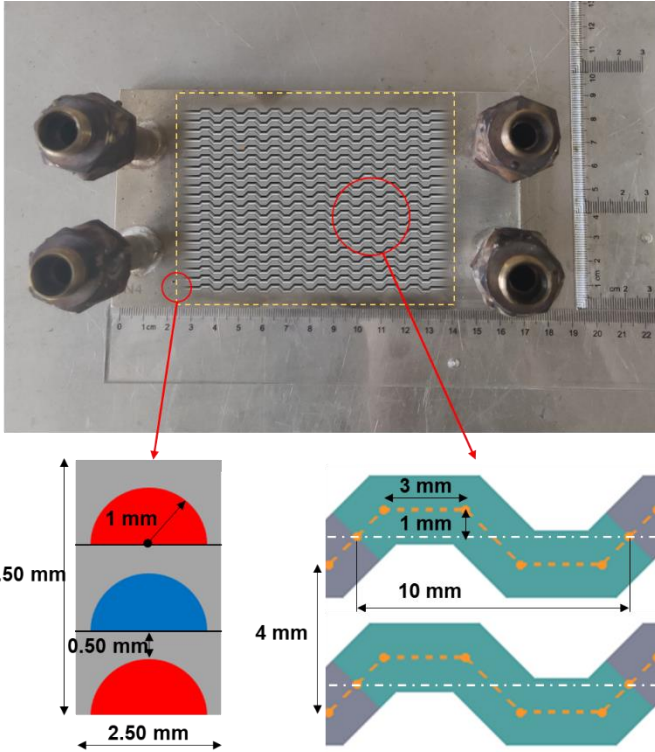


**Figure 5:** The test trapezoidal PCHE prototype and its channel geometric parameters

## RESULTS AND DISCUSSION

Firstly, the overall heat transfer coefficient is introduced to evaluate the performance of the PCHE prototype. The effects of the inlet temperature on both sides, the working pressure, and the mass flow rate on the cold overall heat transfer coefficient are shown in Figure 6. It can be seen that the  $U_c$  exceeds 1.10 kW/(m<sup>2</sup>·K) and reaches a maximum of 2.53 kW/(m<sup>2</sup>·K) with the changes of various conditions.

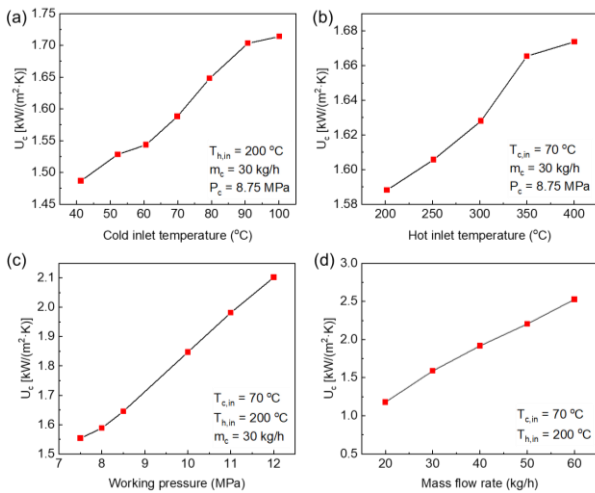


**Figure 6:** The effects of (a) cold inlet temperature, (b) hot inlet temperature, (c) working pressure, and (d) mass flow rate on the cold overall heat transfer coefficient

Then the average convective heat transfer coefficient is used to analyze the heat transfer characteristics of sCO<sub>2</sub> on each side. And dimensionless Nusselt numbers are calculated and fitted the correlations as Equations (1) and (2) with the average Reynolds numbers and Prandtl numbers on the cold and the hot sides, respectively.

On the cold side:

$$Nu_c = 0.8937Re_c^{0.5176}Pr_c^{0.1106} \quad (1)$$

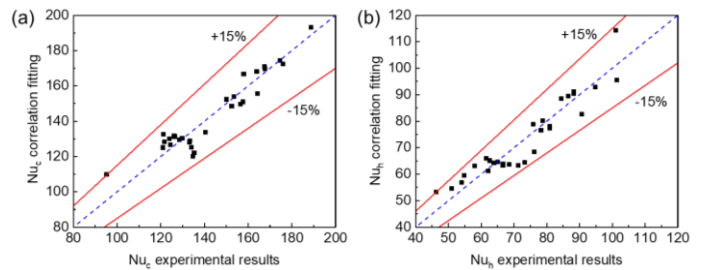
$$\begin{cases} 10,000 \leq Re_c \leq 30,000 \\ 0.91 \leq Pr_c \leq 1.61 \end{cases}$$

On the hot side:

$$Nu_h = 0.1817Re_h^{0.6741}Pr_h^{0.6980} \quad (2)$$

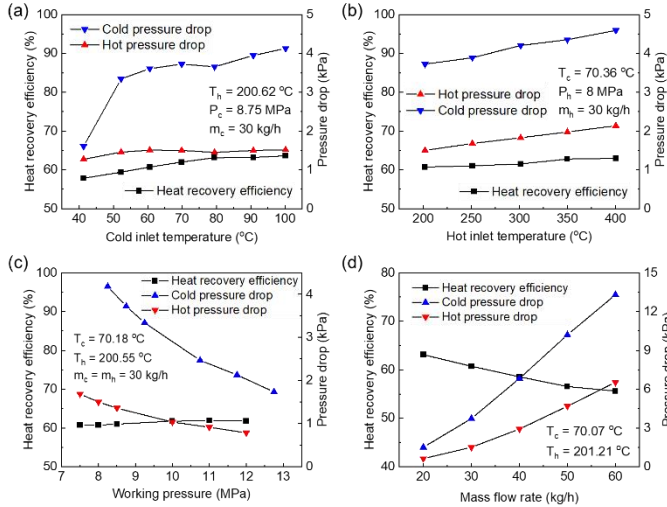
$$\begin{cases} 4,800 \leq Re_h \leq 14,000 \\ 0.77 \leq Pr_h \leq 0.98 \end{cases}$$

Figure 7 reflects the difference between the correlations and the experimental results. All the correlations values are within 15% deviation with the experimental results, and 92% and 86% values are within 10% deviation on the cold and the hot sides, respectively.



**Figure 7:** The difference between the correlations and the experimental results on (a) the cold side and (b) the hot side

Finally, the heat recovery efficiency and pressure drop are discussed in Figure 8 under different conditions in Table 3. The heat recovery efficiency is generally low at about 60% level, the maximum value is only 63.10%, mainly because the size of the prototype is small and the heat transfer area is limited. The pressure drop on the cold side is generally higher than that on the hot side. It is greatly affected by the working pressure and mass flow rate, but little changes with the inlet temperature of hot and cold sides. The cold pressure drop increases significantly when the cold inlet temperature rises from 40 °C to 50 °C due to drastic changes in physical properties of sCO<sub>2</sub>. Besides, it can be concluded increasing the working pressure is helpful to reduce the pressure loss and improve the cycle performance.



**Figure 8:** The effects of (a) the cold inlet temperature, (b) the hot inlet temperature, (c) the working pressure and (d) the mass flow rate on the efficiency and pressure drop

### SIMULATION VERIFICATION

A three-dimensional CFD model is established as shown in Figure 9 for numerical simulation verification, which is the same as the internal heat transfer unit of the test trapezoidal prototype. The model unit size is 2.50 mm × 4.50 mm × 120 mm with 2,240,000 unstructured tetrahedral meshes after grid independence verification.

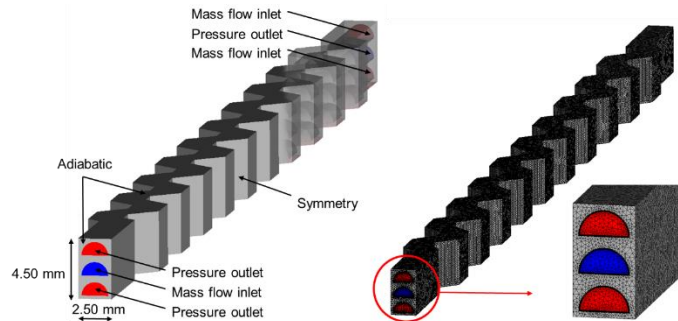


**Figure 9:** The mesh model unit and boundary conditions

The same setup is applied as the trapezoidal PCHE unit model in Figure 1, and the simulation results are compared with the test values under the experimental conditions, as shown in Figure 10. The outlet temperature between simulation and experimental results are in good agreement with each other except at the point of 40 °C due to the drastic changes in physical properties in Figure 10(a) and (c). The maximum deviation between them is 2.80% and 7.92% on the cold and the hot side, respectively. As for the pressure drop, the variation trend of simulation and experiment results is consistent in Fig. 10(b) and (d), with a maximum deviation of 9.22% and 24.54% on the cold and the hot side. The larger deviation on the hot side may be due

to the roughness of the hot plate channels exceeding the design requirements. In general, it can be considered that the simulation model can accurately reflect the experimental situations.

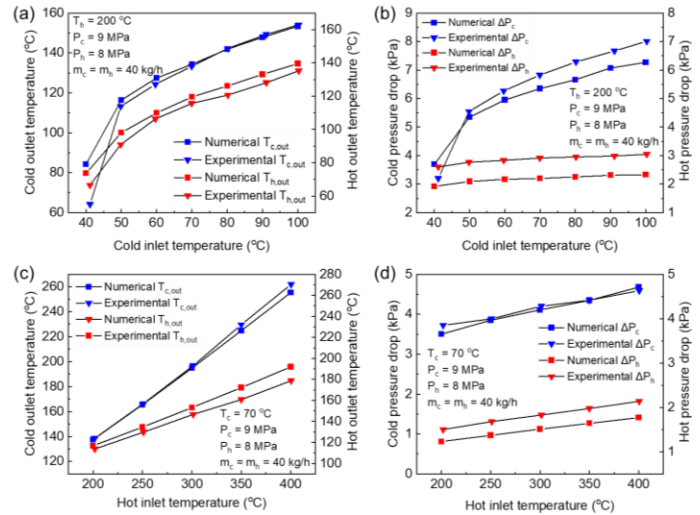


**Figure 10:** Comparison of simulation and experimental results of (a) & (c) outlet temperature and (b) & (d) pressure drop on both sides

Due to the fluctuations caused by pump operation, it is difficult to accurately measure the heat transfer parameters when the inlet mass flow rate is less than 15 kg/h in the circulation loop. The above verified numerical simulation model can effectively solve this problem, thereby extending the Nusselt number correlations to a lower Reynolds number range as Equations (3) and (4). The deviation of new correlations with all experimental and extended numerical simulation results are within 16%, and 85% of the data on both cold and hot side deviate within 10% as shown in Figure 11.

On the cold side:

$$Nu_c = 0.1232 Re_c^{0.7193} Pr_c^{0.1007} \quad (3)$$

$$\left[ \begin{array}{l} 3,796 \leq Re_c \leq 30,000 \\ 0.91 \leq Pr_c \leq 1.61 \end{array} \right]$$

On the hot side:

$$Nu_h = 0.0501 Re_h^{0.8131} Pr_h^{0.5540} \quad (4)$$

$$\left[ \begin{array}{l} 1,821 \leq Re_h \leq 14,000 \\ 0.77 \leq Pr_h \leq 0.98 \end{array} \right]$$

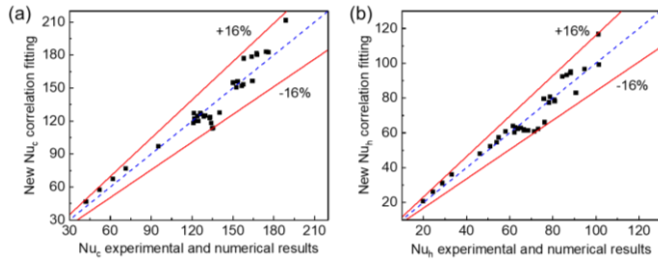


**Figure 11:** The difference between the new correlations and the experimental and numerical results on (a) the cold side and (b) the hot side

## CONCLUSIONS

In this work, a trapezoidal channel structure model is developed and compared with the straight, the S-shape, and the zigzag structures. It indicates that trapezoidal structure owns the highest heat transfer coefficient but also the largest pressure loss. A sandwich model is to optimize the problem, improving the heat recovery efficiency by 5% while reducing the pressure loss by about 75% on the hot side.

The experimental tests of trapezoidal PCHE prototype are carried out in the sCO<sub>2</sub> test loop. The correlations of the Nusselt numbers related to the average Reynolds numbers and Prandtl numbers are proposed on both sides, within 15% deviation with the experimental results, and 92% and 86% values are within 10% deviation on the cold and the hot sides, respectively. The pressure drop on the hot and the cold side is less than 7 kPa and 15 kPa under test conditions, respectively. The heat recovery efficiency is defined to evaluate the performance of PCHE as a regenerator. It decreases with the increase of mass flow rate, and basically remains unchanged with the increase of inlet temperature and working pressure.

A simulation model is established for verification and expansion. It has been proved to reflect the experimental results well with a maximum temperature deviation of 2.80% and 7.92% on the cold and hot side, respectively. Extended simulations are studied based on the model, which expand the Reynolds numbers ranging from 3796 to 30,000 and 1821 to 14,000 on the cold side and hot side, respectively. And new Nusselt numbers correlations are obtained within 16% deviation.

## ACKNOWLEDGEMENTS

The authors gratefully acknowledge the support from the Zhejiang Provincial Key R&D Program (grant number NO. 2022C01043) and the Zhejiang Provincial Natural Science Foundation (grant number NO. LR20E060001).

## STATEMENTS

The relevant results of this paper have been published in *MIRCOMACHINES* and *ENERGIES* journals.

[1] Ji Y, X. K. Numerical study on flow and heat transfer characteristics of trapezoidal printed circuit heat exchanger. China, Hangzhou.

[2] Ji Y, W. Z. Experimental and numerical study on thermal hydraulic performance of trapezoidal printed circuit heat exchanger for supercritical CO<sub>2</sub> Brayton cycle. China, Hangzhou.

## REFERENCES

- [1] Mylavarapu SK, S. X. (2014). Thermal hydraulic performance testing of printed circuit heat exchangers in a high-temperature helium test facility. USA, Columbus.
- [2] Chen M, S. X. (2016). Experimental and numerical study of a printed circuit heat exchanger. USA, Columbus.
- [3] Chu W, Li. X. (2017). Experimental investigation on SCO<sub>2</sub> - water heat transfer characteristics in a printed circuit heat exchanger with straight channels. China, Shaanxi.
- [4] Nikitin K, K. Y. (2006). Printed circuit heat exchanger thermal-hydraulic performance in supercritical CO<sub>2</sub> experimental loop. Japan, Tokyo.
- [5] Kim IH, N. H. (2009). Thermal hydraulic performance analysis of the printed circuit heat exchanger using a helium test facility and CFD simulations. Republic of Korea, Daejeon.
- [6] Kim IH, N. H. (2011). Thermal hydraulic performance analysis of a printed circuit heat exchanger using a helium-water test loop and numerical simulations. Republic of Korea, Daejeon.
- [7] Kim IH, N. H. (2013). Thermal-hydraulic physical models for a Printed Circuit Heat Exchanger covering He, He-CO<sub>2</sub> mixture, and water fluids using experimental data and CFD. Republic of Korea, Daejeon.
- [8] Zhou J, C. K. (2020). Test platform and experimental test on 100 kW class printed circuit heat exchanger for supercritical CO<sub>2</sub> Brayton cycle. China, Beijing.
- [9] Tsuzuki N, K. Y. (2007). High performance printed circuit heat exchanger. Japan, Tokyo.
- [10] Ngo TL, K. Y. (2006). New printed circuit heat exchanger with S-shaped fins for hot water supplier. Japan, Tokyo.
- [11] Ngo TL, K. Y. (2007). Heat transfer and pressure drop correlations of microchannel heat exchangers with S-shaped and zigzag fins for carbon dioxide cycles. Japan, Tokyo.
- [12] Kim DE, K. M. (2008). Numerical investigation on thermal-hydraulic performance of new printed circuit heat exchanger model. Republic of Korea, Daejeon.
- [13] Chen F, Z. L. (2017). Comprehensive performance comparison of airfoil fin PCHEs with NACA 00XX series airfoil. China, Beijing.
- [14] Pidaparti SR, A. M. (2019). Experimental investigation of thermal-hydraulic performance of discontinuous fin printed circuit heat exchangers for supercritical CO<sub>2</sub> power cycles. USA, Atlanta.

- [15] Xu X, M. T. (2014). Optimization of fin arrangement and channel configuration in an airfoil fin PCHE for supercritical CO<sub>2</sub> cycle. China, Shaanxi.
- [16] Lee S, K. K. (2014). A parametric study of the thermal-hydraulic performance of a zigzag printed circuit heat exchanger. Republic of Korea, Incheon.
- [17] Wang K, X. X. (2015). Numerical investigation on heat transfer of supercritical CO<sub>2</sub> in heated helically coiled tubes. China, Chongqing.

## DESIGN AND TESTING OF A SUPERCRITICAL CO<sub>2</sub> COMPANDER FOR 2 MW OUTPUT POWER

**Markus Sauerborn\***

Atlas Copco Gas and Process  
Cologne, Germany  
Email: markus.sauerborn@atlascopco.com

**Ulrich Schmitz**

Atlas Copco Gas and Process  
Cologne, Germany  
Email: ulrich.schmitz@atlascopco.com

**Dr. Jürgen Bohn**

Atlas Copco Gas and Process  
Cologne, Germany  
Email:  
juergen.bohn@atlascopco.com

**Dr. Martin Enneking**

Atlas Copco Gas and Process  
Cologne, Germany  
Email:  
martin.enneking@atlascopco.com

**Jens Brenner**

Atlas Copco Gas and Process  
Cologne, Germany  
Email:  
jens.brenner@atlascopco.com

### ABSTRACT

Around the globe, there has been a growing interest in using sCO<sub>2</sub> power cycles to recover waste heat from various heat sources. This paper will focus on the case of a supercritical CO<sub>2</sub> compander designed, built, tested, and supplied by the authors' company.

The compander is applied in a Brayton cycle to recover waste heat from a gas engine providing the output power to a generator connected to a gear box via a coupling. To design the heat-recovery cycle with the highest possible efficiency, a low-operation temperature at the compressor inlet was required. At the given pressure, this leads to a subcooled fluid.

With support from the client and additional internal studies, it was confirmed that this suction condition at the compressor inlet will lead to the lowest power consumption on the compression side. This, in turn, results in the highest cycle efficiency, in addition to a small machinery footprint. Therefore, the solution fits into marine applications or other projects which face space constraints.

During the compression process, a phase change of the CO<sub>2</sub> from the subcooled to the supercritical state occurs with a low temperature and density change. CFD simulations of the compression process were performed in advance, considering the real fluid behavior near the critical point.

This paper presents the test results and a comparison with the CFD analysis.

\* corresponding author(s)

### INTRODUCTION

Starting back in 1984, Atlas Copco Gas and Process began its involvement in many projects and activities that have aimed at carbon-footprint reduction with its supply of centrifugal compressors and expanders. Since then, the company has delivered compressors for CO<sub>2</sub> compression that rises from 1 bar in eight stages of compression to 202 bar.

Building on these technological advancements, another step was to develop a machine design that could be applied in an sCO<sub>2</sub> Brayton cycle for waste heat recovery applications. Since these demands are driven by the market, the process and the associated design conditions for the compressor and the turbine are typically defined by our client.

For the case presented in this paper, among the various investigated sCO<sub>2</sub> cycle configurations for power generation applications [1], due to the moderate turbine inlet temperature of below 300 °C, a simple recuperated Brayton cycle was selected for the demo plant [2, 3]. Besides simplicity, this configuration allows for the implementation of a single-stage compressor – and a single-stage turbine stage combined on the same gearbox (compander) as intended for highest compactness.

DOI: 10.17185/duerpublico/77319



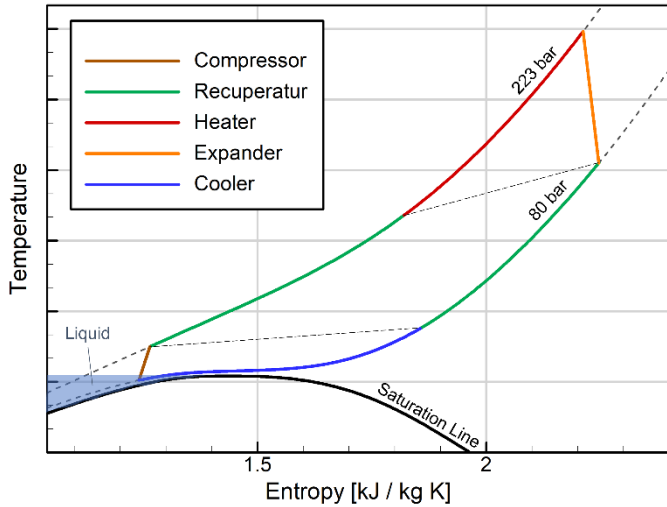


**Figure 1:** Ts-diagram of sCO<sub>2</sub> power cycle

As shown in Figure 1, the compression inlet conditions are specified with 80 bar and 28 °C, i.e. in the liquid phase of the CO<sub>2</sub>, which is a novelty in compression technology. Supported by our client and with further internal studies, it was confirmed that this point will lead to the lowest power consumption on the compression side, resulting in the highest cycle efficiency combined with a small footprint of machinery, which fits nicely into marine applications or projects having space constraints (see Table 1).

length (up to bullgear shaft end)	mm	1442
width	mm	2160
height	mm	1410

**Table 1:** overall dimensions of compander

Following the R&D study and subsequent hardware orders, Atlas Copco Gas and Process supplied the project's sCO<sub>2</sub> compander for the sCO<sub>2</sub> power cycle, which recovered waste heat from the gas-engine driver.

## WASTE-HEAT RECOVERY CYCLE AND MACHINE DESIGN

Figure 2 shows the machine layout principle of the compander and its implementation in the sCO<sub>2</sub> cycle. This is an integrally geared design in which the single-stage centrifugal-type compressor and the single-stage turbine stage are running back-to-back on the same pinion, and connected to the generator via bull gear and coupling on a single gearbox.

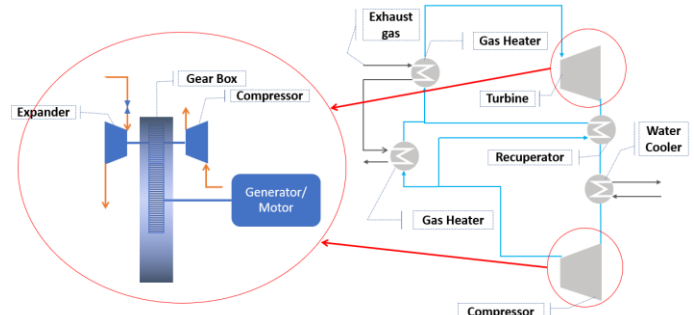


**Figure 2:** Compander layout principle & process flow diagram

The client intended to install the compander on its test site, which had a gas engine available as the heat source. The sCO<sub>2</sub> Brayton cycle was designed to recover 2 MW of the exhaust heat of the engine as net output power.

The thermal efficiency of the Brayton cycle is defined as the ratio of net output power (= turbine power minus compressor power) divided by the input heat flow:

$$\eta_{th} = \frac{|P_T| - |P_C|}{|\dot{Q}_{heat}|} \quad (1)$$

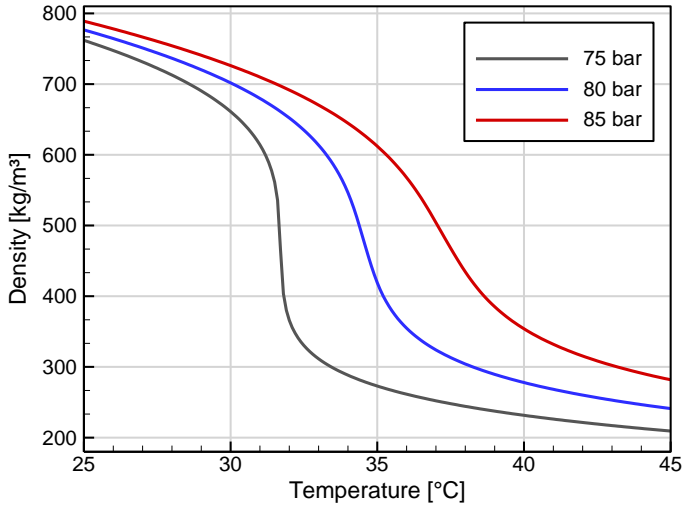
The Gibbs equation follows from the 1st and the 2nd laws of thermodynamics of a reversible process:

$$dh = Tds + \frac{dp}{\rho} \quad (2)$$

It can be concluded, therefore, that for achieving the same pressure increase  $dp$  at the same losses  $Tds$ , the lowest compressor work input  $dh$  is required, when the average density is high [4].

Near the critical pressure, CO<sub>2</sub> shows a strong dependency on the density when the temperature is varied only slightly around the critical temperature. For example, at 80 bar the density jumps from 613.7 kg/m<sup>3</sup> to 736.5 kg/m<sup>3</sup> when the temperature is decreased from 33 °C to 28 °C (see Figure 3).





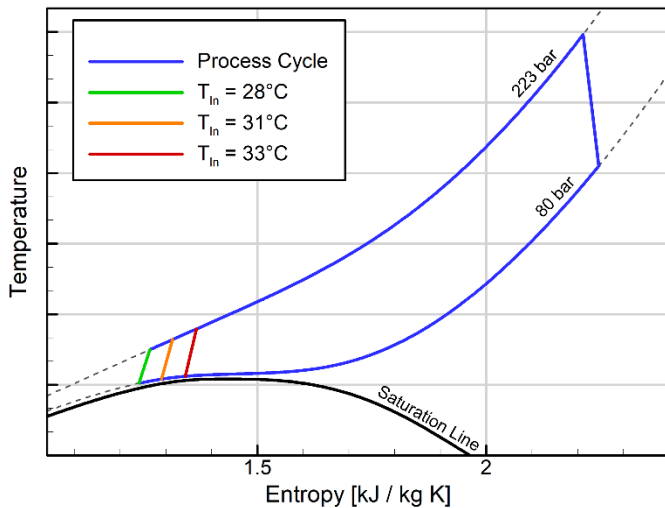
**Figure 3:** Density of CO<sub>2</sub> near the critical point (NIST REFPROP)

Table 2 shows the relative increase of compressor power required for the compression from 80 to 223 bar (at constant efficiency), when the inlet temperature is varied between 28 and 33°C.

$T_{C,inlet}$ [°C]	relative power $P_C/P_C@28^\circ C$
28	1.000
31	1.060
33	1.136

**Table 2:** Relative power vs compressor inlet temperature

Equation 1 (see above, page 2) means that for highest-thermal cycle efficiency, the compressor inlet conditions are found in the liquid phase of CO<sub>2</sub>, just left to the critical point.



**Figure 4:** Ts-diagram simple Brayton Cycle for variation of the compressor inlet temperature

Figure 4 shows the shift of the Brayton cycle in the Ts-diagram for the variation of the compressor inlet temperature.

To avoid falling into the two-phase region, some margin to the saturation line must be kept, as shown in the zoomed area of the Ts-diagram in Figure 5.

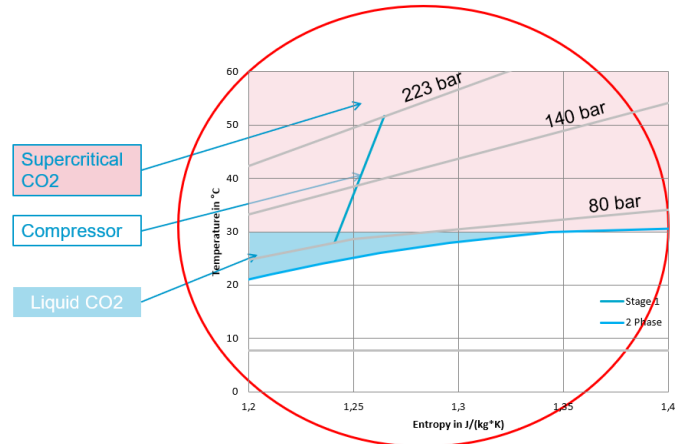


**Figure 5:** Ts-diagram: zoomed area compressor operating conditions

Finally, the compressor inlet pressure was set to 80 bar and the inlet temperature to 28 °C. At these inlet conditions and with an outlet pressure of 223 bar, the compression process takes place from the liquid to supercritical state, which is an innovation because such compressors are not yet available on the commercial market.

The associated challenges for the aero and mechanical design of the machine were accepted, and it was agreed with the client to carry out theoretical and experimental investigations on the compression process in parallel to delivering the compander unit.

## CFD SIMULATION

A CFD (computational fluid dynamics) analysis of the compressor stage was performed using ANSYS CFX software [5]. The CFD model comprises a single-blade channel of the shrouded impeller, including the inducer part, and the impeller labyrinth seal, followed by the full 360° vaneless diffuser and the volute casing (see Figure 6). Frozen rotor interfaces connect the inducer with the impeller and labyrinth seal. The outlet of the impeller is connected via a mixing plane interface to the full 360° diffuser domain. A General Grid Interface (GGI) is used to connect the diffuser and volute.

Inlet boundary conditions are total pressure and total temperature derived from test conditions, and the wall functions approach with  $y^+ \approx 50$  is applied to model the wall boundary layers.  $k\omega$ -SST was selected as turbulence model.

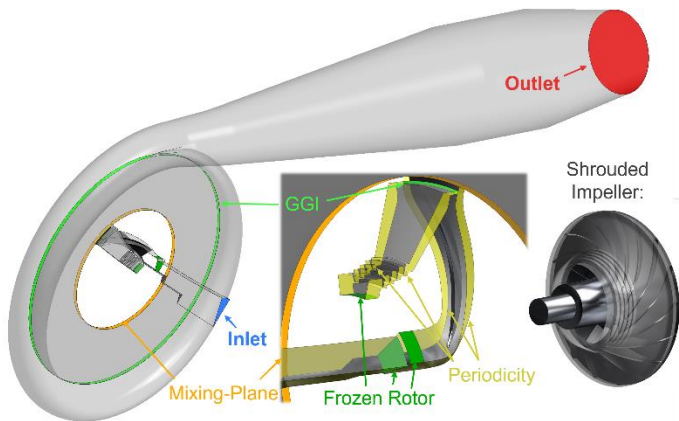


**Figure 6:** Domain for CFD analysis

The total grid size is 12.7 mio nodes, as shown in Table 3, and the main aerodynamic design parameters of the compressor stage are shown in Table 4.

Inducer (1 passage)	0.5 mio
Impeller (1 passage)	4.3 mio
Labyrinth sealing area (1 passage)	1.1 mio
Diffuser (360 °)	5.0 mio
Volute	1.8 mio
<b>Total</b>	<b>12.7 mio</b>

**Table 3:** Grid size of the CFD model

Impeller type		centrifugal, shrouded
Shaft sealing		dry face seal
Impeller outer diameter	mm	104
Speed	rpm	38000
Mass flow	kg/h	174600
Inlet pressure	bar	80
Inlet temperature	°C	28
Outlet pressure	bar	223

**Table 4:** Aerodynamic design parameters of the compressor

Because the compressor inlet operates at a subcooled condition near the saturation line and at outlet at a supercritical condition, a real gas property approach is mandatory for the CFD setup. Therefore, the NIST REFPROP real gas property database was incorporated into the CFD model, and the fluid is modelled as a homogeneous mixture of (subcooled) liquid and vapor.

In the following, the mass fraction of vapor and the density inside the impeller channel, and the labyrinth seal are shown at design point operation (see Table 4).

As expected, a sudden phase change of the CO<sub>2</sub> from the liquid to the supercritical phase in the first third of the blade chord is observed, while the density increases smoothly from impeller inlet to outlet (see Figure 7, right-hand side).

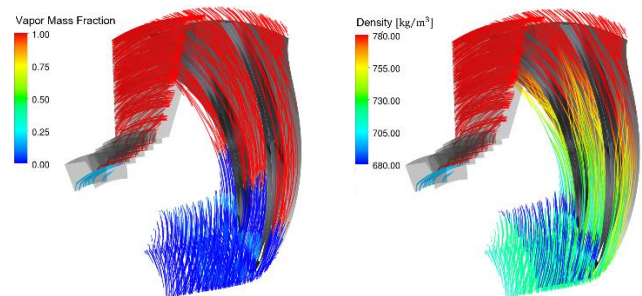


**Figure 7:** Vapor mass fraction and density of impeller and labyrinth seal flow

The smooth density increase results in a smooth blade loading distribution along the suction and pressure side (see Figure 8).

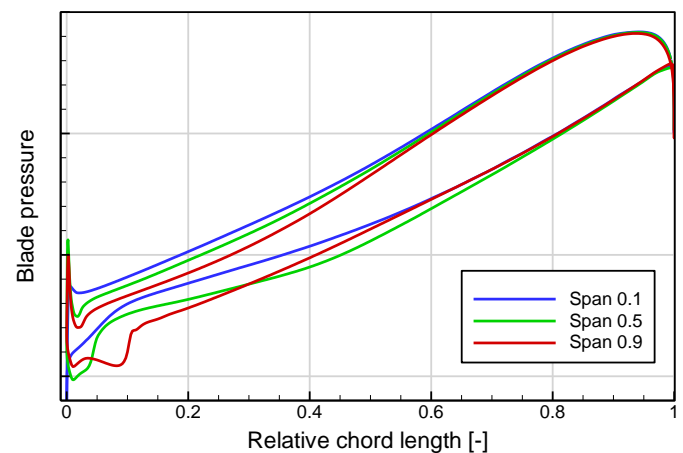


**Figure 8:** Blade loading at span 0.1, 0.5 and 0.9

## TEST SET-UP AND SAFETY ISSUES

To demonstrate the compression process and machine integrity as well as to validate the CFD results, a second identical test unit was built in addition to the client machine for in-house performance testing with CO<sub>2</sub> at original operating conditions.

Since the investigations were focused on the compressor only, the expander was not tested. This means the actual CO<sub>2</sub> test cycle consisted of the compressor stage, a recycle valve, and a cooler only (see Figure 9).

1. Compressor stage
2. Inlet pipe
3. Discharge pipe
4. Temperature & pressure tapping for performance measurement



**Figure 9:** sCO<sub>2</sub> test unit

On the other side of the common pinion shaft a dummy disk was mounted instead of the expander impeller to serve as an axial thrust compensation cylinder for the compressor impeller. The expander housing was pressurized with helium at an appropriate pressure to balance the axial force. Although no blading existed on the dummy expander disk and the viscosity of helium was low, a significant amount of heat was generated in the expander housing due to disk friction. Therefore, an additional cooling system for the expander housing using liquid nitrogen had to be installed (see Figure 10).

1. Core Unit
2. Expander
3. Compressor loop (filled with CO<sub>2</sub>)
4. Orifice (for flow measurement)
5. Throttle valve
6. Oil supply system
7. Cooling system for expander casing
8. Seal gas panel

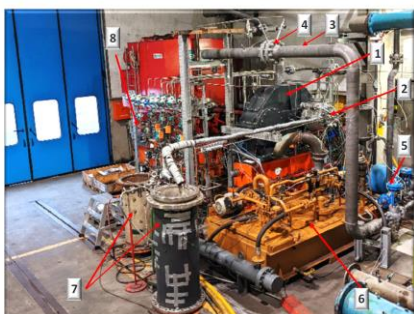


**Figure 10:** sCO<sub>2</sub> test loop with periphery

As well as the installation of a safety relief valve, in order to ensure safe operation an emergency shut-down scenario was performed using the dynamic process simulation software UniSim Design [6] for determination and evaluation of the settle-out pressure and the expected state of the CO<sub>2</sub> after standstill or machine trip (see Figure 11).

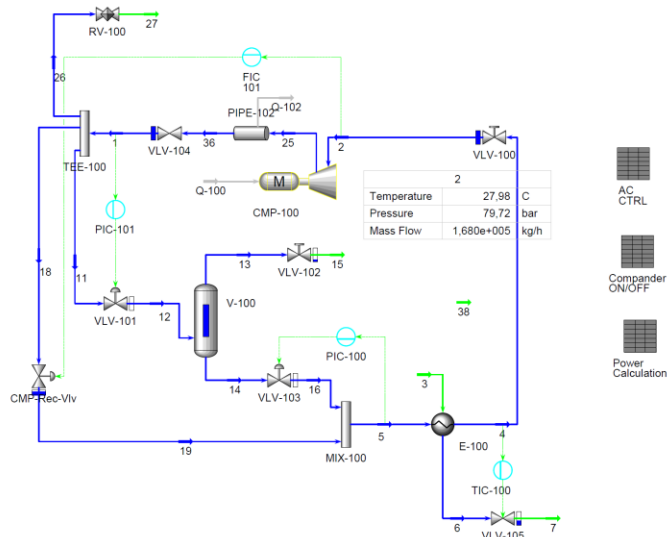


**Figure 11:** Dynamic simulation model of the test set-up.

The solver calculates the heat and mass balance using pressure flow relations of the components as further input. NIST REFPROP was selected as gas property package. For calculating the machine trip scenario, the volumes of all components in the loop, such as piping, heat exchangers, and so on must be specified. Further input variables are the compressor performance curves, the Cv values, and the rotational inertia of the complete drive train.

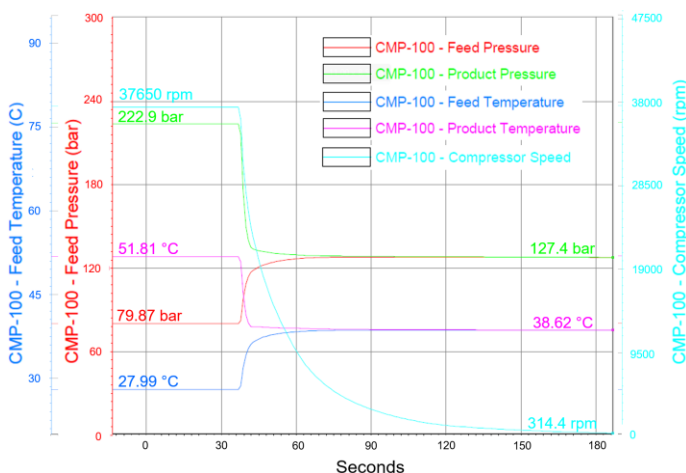


**Figure 12:** Pressure and temperature trends at compressor inlet and outlet after a machine trip.

Figure 12 shows the pressure and temperature trends at compressor inlet and outlet after a machine trip. As settle out conditions, a pressure of 127 bar and a temperature of 39 °C are calculated. This means, after a machine trip, the CO<sub>2</sub> remains in the supercritical phase and the possible maximum pressure in the loop is safely below the mechanical-design pressure of the components.

Due to the excessive pressure of the CO<sub>2</sub> in the loop of up to 242 bar, a HAZOP (hazard and operability) analysis was also carried out with test-service provider TÜV Rheinland. As a residual risk, the failure of the dry face shaft-sealing system was identified. At nominal operating conditions, a small amount of leakage gas passed through the contact-free shaft sealing, which is a system of labyrinths, carbon rings, and a dry face seal as the main sealing element (see Figure 13).

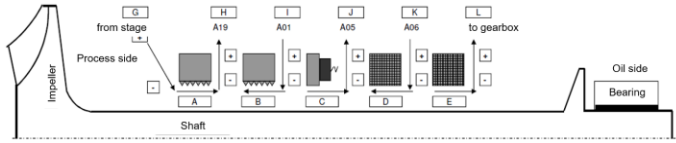


**Figure 13:** Shaft sealing system of the sCO<sub>2</sub> compressor stage

Figure 14 shows the associated seal-gas panel connected to the compressor stage.

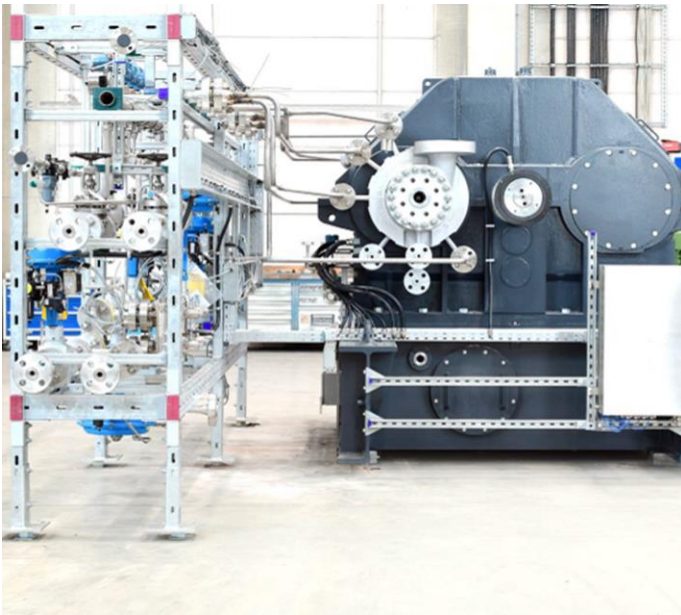


**Figure 14:** sCO<sub>2</sub> compressor & seal-gas panel

In case of a failure of the dry gas seal, the labyrinths and carbon rings would also be damaged due to increased shaft vibration, while an excessive amount of process gas would flow via the gearbox into the oil tank.

The oil tank is a non-pressurized reservoir with a venting line outside to the atmosphere. Due to the limited capacity of venting gas to the atmosphere, there might be a potential risk of blowing up the oil tank. Therefore, another simulation was carried out in which the damaged seal parts were simulated as throttling elements. Figure 15 shows the Ts-diagram of the expansion process, starting from the impeller outlet pressure of 169 bar in a supercritical state to atmospheric pressure in the two-phase region.

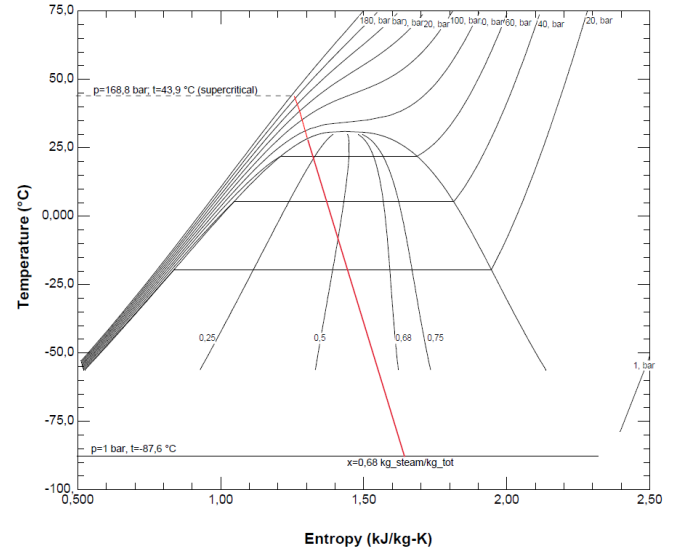


**Figure 15:** Throttling process after shaft-seal-failure scenario

As a result of the simulation, the short-term pressure increase in the oil tank due to a failure of the shaft-sealing system was calculated to be in the range of 100 mbar and therefore considered to be non-critical. After all these extensive tests, the loop was accepted for operation by TÜV Rheinland [7].

The start-up of the loop was a further challenge. Initial starting conditions were determined at 30 bar supplied by the CO<sub>2</sub> reservoir. A minimum starting temperature of 5 °C is required to avoid compressor operation in the two-phase region. This requirement also applies to the complete start-up sequence. After starting the machine, the compressor suction pressure was increased stepwise by filling the loop via an external high-pressure piston compressor while the temperature was controlled by cooling water. The duration needed for the pressurization was about four hours. The specific steps are shown in the Ts-diagram in Figure 16.

Thus, the nominal operating conditions on the compressor suction side (80 bar, 28 °C) are reached by following the path in the Ts-diagram around the dome, starting from gaseous to supercritical and finally to liquid state by avoiding the two-phase region. Figure 16 also shows the test-loop operating cycle (compression, valve expansion, and re-cooling).



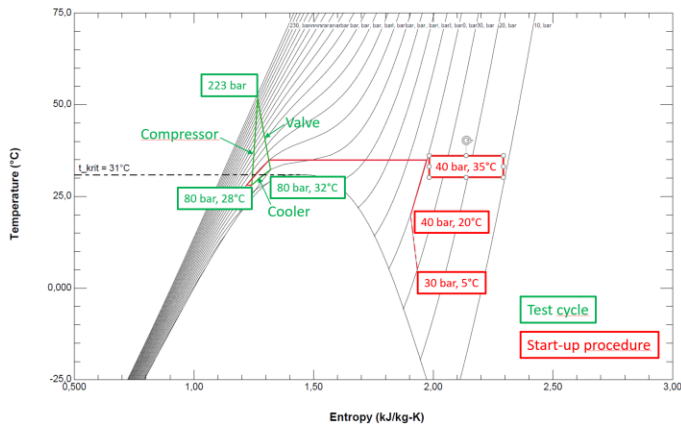


**Figure 16:** Ts-diagram of test-loop and start-up procedure

During the last step of the start-up sequence, it was found that accurate adjustment of the nominal operating point at the compressor inlet (80 bar, 28 °C) was a challenge due to the strong dependance of the pressure ratio and the density on the inlet temperature (see Figure 3).

However, after stable inlet operating conditions were reached, the subsequent performance test was carried out over a period of three hours without any incidents. Neither increased vibration levels were observed nor axial thrust issues during the test, which were previously considered as crucial items.

After the test, the machine was completely dismantled, and no indication of excessive wear was found on any of the main components, such as the impeller or the shaft seal system.

## RESULTS

Besides demonstrating the fundamental compression process, the test objective was to compare theoretical design figures and the results from the CFD analysis with measurement data. Therefore, the measurement campaign included compressor operation at nominal inlet conditions from choke to near surge by setting the recycle valve.

Figure 17 shows the compressor performance curves comparing test data with CFD results. Additionally, the theoretical design point (DP) is added to the maps.

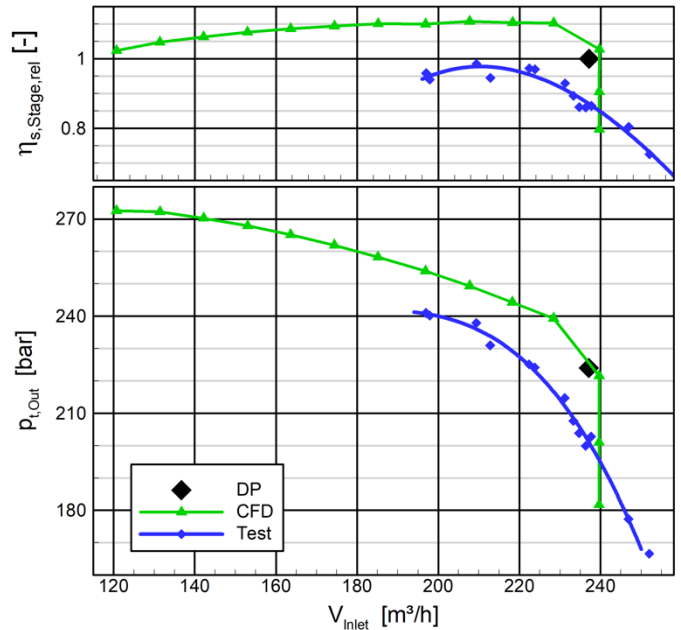


**Figure 17:** Total outlet pressure and relative isentropic efficiency vs inlet volume flow

A comparison of the measured and calculated pressure curves in Figure 17 shows a shift towards slightly lower pressure values for the test data, whereas the curve shape including rise to surge shows good agreement. This also applies to the prediction of the choke limit, just with a steeper decrease of the CFD curve.

Due to the maximum allowable working pressure in the loop of 242 bar, which was controlled by the safety relief valve, the measured curves are cut towards low volume flow. Therefore, the surge line was not reached experimentally, whereas the CFD calculation continues up to surge.

The points of maximum efficiency of both the measured and the calculated curves can be found at nearly the same flow. When compared to the theoretical design point, a shift towards lower flow values is observed. This indicates above all the influence of the impeller sealing gap, which was set to relatively high values during the test and in the CFD simulation, and led to increased recirculation mass flow rates, shifting the curves to lower flow rates.

One explanation for the deviation between the measured and predicted efficiency is the high measuring tolerances in the range of 1.8 %. The reason the measuring tolerances are high is because the impeller size is small and the temperature probes are protected by sleeves. Due to testing the machine at real operating conditions, there was no need to convert the test data except for the calculation of the isentropic head using the NIST REFPROP database.

In contrast, notable uncertainties of the CFD model have to be considered [8], which are basically higher than for standard

applications, such as high-pressure gradients within the impeller and diffuser (high pressure on small spatial dimensions).

Uncertainties arise from geometry model simplifications, such as not taking into account the back cavity and leakage through shaft seal (approx. 1%), possible deviations in all roughness assumptions (1-2%), as well as idealized blade geometry neglecting fillet radii, grooves and milling joints, which have a higher influence here due to the very low stage size (see Table 4).

Additional uncertainties are based on the mesh: discretization errors and the wall function approach (0.5 % each). Further impact comes from the possible model errors on both thermodynamics (interpolation table of real gas properties) and turbulence (underestimation of the turbulence on coarser grid accounts for 0.5-1 %).

Summing up the influencing factors on both experimental and CFD side, however, it can be concluded that the CFD model is able to predict the real machine behavior sufficiently.

## SUMMARY AND CONCLUSION

In this paper, the design and the test-setup of a supercritical CO<sub>2</sub> compander were presented followed by the comparison of the compressor performance test results with a CFD analysis. While the machine delivered to the client is applied in a Brayton cycle to recover waste heat from a gas engine, a second identical unit was built for testing the compressor operating at the inlet slightly above the critical pressure but in the liquid phase of the CO<sub>2</sub>. During the compression process, a sudden phase change of the CO<sub>2</sub> from the liquid to the supercritical state occurs, which is an innovation in the market. At these operating conditions, the compressor input work for compression is minimized, leading to the highest thermal efficiency of the cycle.

Therefore, the test was carried out with CO<sub>2</sub> at original operating conditions, which was a challenge for several reasons. For operating the compressor at the nominal suction conditions (80 bar, 28 °C), the start-up sequence included a stepwise pressurization of the loop following the path in the Ts-diagram around the dome by avoiding the two-phase region. Due to the excessive pressure and the hazardous working fluid, extensive safety measures were taken in advance, including a HAZOP meeting with TÜV Rheinland to determine the residual risks. As a result, the test-setup was accepted for operation.

During the test, a smooth operation at nominal operating conditions of the compressor could be demonstrated. The test data showed a slight shift of the pressure and efficiency curves towards lower flow and pressure, and lower efficiency values when compared to the CFD results but with good agreement concerning the curve shape, rise to surge, and choke limit.

Finally, both, the test data and the CFD results provide a valuable database for future sCO<sub>2</sub> machine designs.

## NOMENCLATURE

$\eta_{th}$	Thermal cycle efficiency	(%)
$P$	Power	(kW)
$\dot{Q}$	Heat Flow	(kW)
$h$	Enthalpy	(kJ/kg)
$p$	Pressure	(Pa)
$T$	Temperature	(K)
$s$	Entropy	(kJ/kgK)
TÜV	Technischer Überwachungsverein	
GGI	General Grid Interface	
DP	Design Point	
Cv	Valve flow coefficient	(USPGM or m <sup>3</sup> /h)

## REFERENCES

- [1] Crespi, F., Gavagnin, G., Sánchez, D. and Martínez, G.S., 2017. "Supercritical carbon dioxide cycles for power generation: A review". Applied Energy, 195, pp.152-183
- [2] Lariviere B., Macadam S., McDowell S., Lesemann M., Marion J., 2021, "sCO<sub>2</sub> Power Cycle Development and STEP Demo Pilot Project", The 4th European sCO<sub>2</sub> Conference for Energy Systems, Prague
- [3] Vesely L., Prabu T., Gopinathan S., Otakar F., Subbaraman G. Kapat J., 2021, "Greening a Cement Plant using sCO<sub>2</sub> Power Cycle", The 4th European sCO<sub>2</sub> Conference for Energy Systems, Prague
- [4] Schuster S., Hacks A., Brillert D., 2022, "Lessons from Testing the sCO<sub>2</sub>-HeRo turbo-compressor-system", 7th International Supercritical CO<sub>2</sub> Power Cycles Symposium, San Antonio, Texas
- [5] ANSYS CFX User Guide
- [6] Honeywell UniSim Design User Guide
- [7] TÜV Rheinland, Risikoorientierte Gefahrenanalyse ROGA Test Unit scCO<sub>2</sub>, 2020
- [8] Toni L., Bellobuono E.F., Valente R., Romei A., et al, 2022, "Computational and Experimental Assessment of a MW-Scale Supercritical CO<sub>2</sub> Compressor Operating in Multiple Near-Critical Conditions", *Journal of Engineering for Gas Turbines and Power* Vol 144 (Issue 10), pp. 144-153



## INFLUENCE OF VARIATIONS OF FLUE GAS AND AMBIENT TEMPERATURE ON THE DYNAMICS AND PERFORMANCE OF A MW SCALE SUPERCRITICAL CO<sub>2</sub> WASTE HEAT TO POWER UNIT

**Olumide Olumayegun**  
Brunel University London  
Uxbridge, United Kingdom

**Matteo Marchionni**  
Brunel University London  
Uxbridge, United Kingdom  
Email: [matteo.marchionni2@brunel.ac.uk](mailto:matteo.marchionni2@brunel.ac.uk)

**Muhammad Usman**  
Brunel University London  
Uxbridge, United Kingdom

**Savvas A Tassou\***  
Brunel University London  
Uxbridge, United Kingdom

### ABSTRACT

Waste heat availability from many industrial plant can vary not only during start up and shut down of the process but also as a response to many other factors such as process control and varying demand of heat by diverse and distinct unit operations in the plant.

Implementing heat recovery from exhaust waste heat for power generation purposes, therefore, requires knowledge of the variation in the mass flow rate and temperature of the waste heat as well as variations in other conditions that affect the performance of the power generation system such as the temperature and flow rate of the heat sink medium.

This paper presents a numerical model and simulation results of the dynamic behaviour of a 2.0 MWe sCO<sub>2</sub> power system, designed to recover heat from the exhaust gases of a cement manufacturing plant. The design employs an indirect heat recovery loop utilising thermal oil as the heat transfer medium and direct heat rejection from the CO<sub>2</sub> gas cooler to the ambient.

The results show that fluctuations in the exhaust gas conditions within the operating range of the sCO<sub>2</sub> power system are damped by the large quantity of heat transfer fluid in the indirect heat transfer loop and do not present a significant challenge to the control of the conditions entering the turbine. On the other hand, the limited thermal mass of the gas cooler does not have the capacity to absorb significant quantities of thermal energy and as a result the response of the sCO<sub>2</sub> system to variations in ambient temperature is much faster than the response to changes in exhaust gas temperature and flow rate. This will require a more sophisticated control strategy to ensure the sCO<sub>2</sub> temperature at inlet to the compressor and other components remains within the design operating range.

### INTRODUCTION

The recovery of waste heat from existing industrial facilities is considered among the most promising ways to improve their energy efficiency, create new business opportunities and mitigate their carbon footprint [1]. However, despite intensive research effort and interest in recent years, there are still challenges in the exploitation of industrial waste heat sources. The availability of waste heat, temperature and composition of the heat carrier, the intensity or modality of supply, and the ease or economic feasibility of its re-utilization are critical factors for the selection and design of the waste heat recovery (WHR) technology [2].

For the recovery of high temperature waste heat, over 300°C, bottoming thermodynamic cycles, such as the emerging supercritical carbon dioxide (sCO<sub>2</sub>) power systems, offer the potential of high energy conversion efficiency [3]. Carbon dioxide has very good thermo-physical properties. It is a non-toxic, non-flammable and thermally stable compound and in its supercritical state, has properties, including high density, that can lead to high cycle efficiencies and a substantial reduction in the size of components compared to alternative heat to power conversion technologies [3].

Smaller components present lower metal mass and less thermal inertia, making the technology attractive for its higher operational flexibility and fast response to variations in waste heat availability. These advantages have driven academic and industrial research in recent years to investigate sCO<sub>2</sub> power cycles for WHR applications. Many works are available in the literature on thermodynamic design and optimization [4,5], techno-economic analysis [6], system and standalone component modelling [7–11], and system off-design analysis [12,13]. However, less attention has been devoted to the transient dynamics of this cycle and its control, mainly due to the unavailability, as yet, of large pilot plants and experimental facilities for the investigation of fully integrated power cycles.

\* corresponding author(s)

Understanding of the dynamic behaviour of sCO<sub>2</sub> waste heat to power systems is very important for WHR applications since waste heat availability from the topping manufacturing process, can vary on hourly, daily and weekly basis due to variations in the manufacturing processes in the plant, including start-up and shut-downs, and ambient temperature. The latter has an indirect influence on thermal energy inputs and heat losses from the manufacturing processes.

Variations in the temperature and flowrate of the exhaust gases will be reflected in variations in the sCO<sub>2</sub> cycle's thermodynamic conditions, i.e. the temperature of CO<sub>2</sub> at the outlet of the primary heat exchanger (where the waste heat recovery occurs) and, therefore, at the turbine inlet. Such variations if are not mitigated by the control of the sCO<sub>2</sub> power system, may impact on the functional integrity of the components and system itself, with detrimental impacts on the long-term performance of the unit and its operational lifetime.

To understand how these effects can be mitigated, the dynamic behaviour of the system during transient operating conditions must be investigated to provide useful insights from a controls perspective.

To fill this gap this research focuses on the transient analysis of a 2.0 MWe sCO<sub>2</sub> power system for the recovery of waste heat from a cement plant. Such system is being developed in the framework of the CO2OLHEAT project, funded by the EU [14].

The sCO<sub>2</sub> system employs an indirect heat recovery loop utilising thermal oil as the heat transfer medium and direct heat rejection from the CO<sub>2</sub> gas cooler to the ambient. Equation based models have been used for the turbomachines and the heat exchangers (waste heat recovery unit, primary heater, recuperator and gas cooler). In particular, heat exchangers are modelled using a one-dimensional approach whilst turbomachines are considered as lumped objects given their faster dynamics.

For the analysis, real data for the flue gas have been used from a CEMEX cement plant at Prachovice in Czechia. After presenting the modelling methodology, the paper presents results of the transient response of the sCO<sub>2</sub> system to step variations of flue gas temperature and flowrate and variations in ambient temperature during a typical day's operation of the cement plant. The modelling results are very useful for the development of control strategies to ensure stable and efficient operation whilst maintaining the integrity of the major components in the system.

## CEMENT PLANT

A schematic diagram of the cement facility at Pracovice is shown in Figure 1. After the rotary kiln (point 1), the exhaust gases pass through the pre-heater (point 2) before entering the conditioning towers (points 5 and 6), to be finally rejected to the environment from the stack (point 7). A position for the possible installation of the heat recovery unit was selected to be before the conditioning tower, between points 3 and 4 in Figure 1, to maximise heat recovery potential.

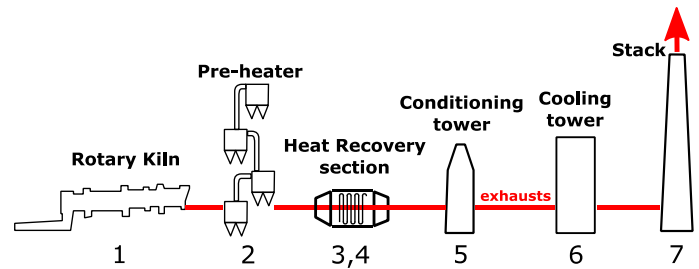


**Figure 1:** Schematic of the cement plant showing position of measurement of the exhaust flowrate and temperature.

The waste heat recovery units (two units in parallel), use an intermediate heat transfer carrier, thermal oil, to recover heat from the exhaust gases. The oil transfers this heat to the sCO<sub>2</sub> power block through the primary heater, Figure 2. At the outlet of the heater, point 5 in Figure 2, the sCO<sub>2</sub> is at high pressure and temperature, and is expanded in the first turbine unit (T), which drives the compressor unit (C). A helper motor provides additional power when the power from the turbine is not sufficient to drive the compressor, for example at start-up. Both the compressor and the turbine units are two-stage machines.

After the first expansion, the sCO<sub>2</sub> flows into an axial power turbine (PT), which is designed to generate 2.2 MW of power (Figure 2). An air cooler is designed to use ambient air to reject heat from the sCO<sub>2</sub> flow and restore the initial cycle conditions.

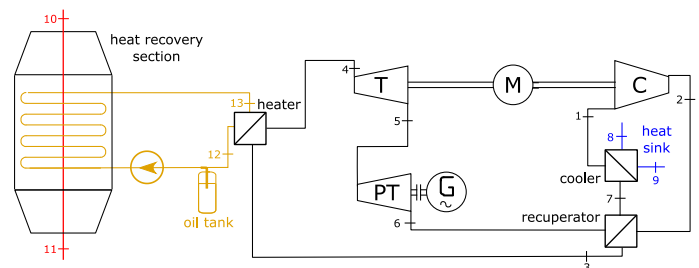


**Figure 2:** CO2OLHEAT sCO<sub>2</sub> simplified cycle representation.

## MODELLING METHODOLOGY

The dynamic model of the sCO<sub>2</sub> WHR plant has been implemented in the MatLab Simulink® programming and simulation environment using sFunctions [15]. Such model can be divided into three main parts: i) the intermediate heat transfer oil loop; ii) the sCO<sub>2</sub> power block and iii) the interface between the power block and the exhaust gases in the WHRU and the power block and the air in the gas cooler. These domains include individual component sub-models such as heat exchangers, pipes, pumps, expansion tank, and turbomachinery.

The models have been developed using mass, energy and momentum conservation equations as well as other constitutive equations. The thermodynamic and physical properties of CO<sub>2</sub> and flue gas have been determined using NIST Refprop (version 10.0) [16] while the properties of the heat transfer oil (FRAGOLTHERM® X-76-A) have been obtained from the oil manufacturer.

The different components have been represented as independent blocks having input and output ports for interconnection between components in accordance with the plant layout. For example, the port carrying information about the fluid flow, contains details on the mass flow rate, pressure and temperature of the fluid stream. This results in a model which provides a more realistic visual representation of the plant. The models of the different system components are presented in the following sections.

### Pipe model

The implementation of the mass, energy and momentum conservation equations for fluid flow in pipes as well as in heat exchanger ducts follows the rigorous modelling approach of Franke et al. [17].

The conservation of mass equation for the pipe is given as:

$$A \frac{\partial \rho}{\partial t} + \frac{\partial \dot{m}}{\partial x} = 0 \quad (1)$$

which, for a pipe section of cross-sectional area,  $A$ , can be written as a derivative of pressure and specific enthalpy:

$$A(\Delta L) \left[ \frac{\partial \rho}{\partial p} \frac{\partial p}{\partial t} + \frac{\partial \rho}{\partial h} \frac{\partial h}{\partial t} \right] + \Delta \dot{m} = 0 \quad (2)$$

The governing equation for the conservation of energy can be written as:

$$A \frac{\partial (\rho u)}{\partial t} + \frac{\partial (\dot{m} h)}{\partial x} - \omega \phi = 0 \quad (3)$$

$$A(\Delta L) \left[ \left( h \frac{\partial \rho}{\partial p} - 1 \right) \frac{\partial p}{\partial t} + \left( \rho + h \frac{\partial \rho}{\partial h} \right) \frac{\partial h}{\partial t} \right] + \Delta (\dot{m} h) - Q = 0 \quad (4)$$

For the pipe model, the heat loss,  $Q$ , is assumed to be negligible. The momentum conservation equation, ignoring the gravitational force term, can be expressed as:

$$\frac{\partial \dot{m}}{\partial t} + A \frac{\partial p}{\partial x} + A \frac{\partial (\rho v^2)}{\partial x} + f \frac{\dot{m}^2}{2\rho D_h A} = 0 \quad (5)$$

$$\Delta L \frac{\partial \dot{m}}{\partial t} + A(\Delta p) + \frac{\Delta (\dot{m}^2 / \rho)}{A} + f \frac{\Delta L}{2D_h A} \frac{\dot{m}^2}{\rho} = 0 \quad (6)$$

### Heat exchanger model

The WHRU, PHE and recuperator were modelled as counter-flow heat exchangers. The ACHE was discretised into nodes and modelled as a cross-flow heat exchanger. Figure shows the implementation of the discretised model of the ACHE in Matlab®/Simulink®.

The heat exchanger models consider the hot stream, cold stream and the separating metal wall. The hot and cold stream mass, energy and momentum conservation equations are similar to those used for the pipe model above. The dynamics of the

separating metal wall temperature were modelled using the approach outlined in Olumayegun and Wang [22]:

$$M_w c_w \frac{dT_w}{dt} = Q_h - Q_c \quad (7)$$

Where,  $Q_h$  and  $Q_c$  represent the heat transferred from the hot stream to the metal and from the metal wall to the cold stream respectively.

$$Q_h = U_h A_s (T_h - T_w) \quad (8)$$

$$Q_c = U_c A_s (T_w - T_c) \quad (9)$$

$U_h$  and  $U_c$  represent the convective heat transfer coefficients and  $A_s$  is the surface area for heat transfer.

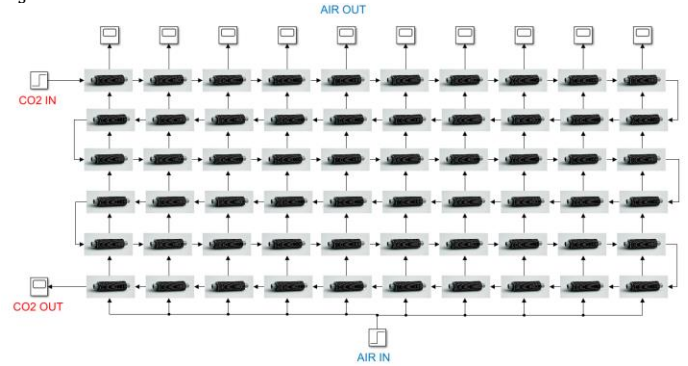


**Figure 3:** Discretised dynamic modelling of air-cooled heat exchanger (ACHE) in Matlab®/Simulink®.

### Compressor and turbine models

The modelling of CO<sub>2</sub> compressors is challenging due to the non-ideal gas properties of CO<sub>2</sub> close to the critical point. One modelling approach presented in the literature considers the use of corrected performance maps taking into account the compressibility of the gas close to the critical conditions [18]. Despite good prediction accuracy away from the critical point, this method has been found to decrease in accuracy at operation close to the CO<sub>2</sub> critical conditions [9, 19]. A more reliable method suggested for compressor modelling by Gong et. al. [20], is the one developed for incompressible turbomachinery (pumps). According to the authors, when the sCO<sub>2</sub> compressor is treated like a pump, its estimated work is within 2% of that computed using real gas CO<sub>2</sub> properties. Thus, instead of correcting the mass flow rate using the method for ideal gas turbomachinery, the flow coefficient of the compressor can be determined from [18- 21]:

$$\phi = \frac{\dot{m}}{U\rho} \quad (10)$$

Where  $U$  is the impeller tip speed and  $\rho$  is the fluid density. For the turbine, the CO<sub>2</sub> working fluid can be considered as ideal gas and the flow coefficient can be taken as per Equation (11) [20].

$$\phi = \frac{\dot{m}\sqrt{T_{in}}}{p_{in}} \quad (11)$$

The turbomachinery performance map, which gives the pressure ratio and efficiency as function of the flow coefficient is used to determine the pressure ratio and efficiency of the compressor and turbine. The turbomachinery outlet conditions and power are then calculated from the pressure ratio and efficiency. Further details about the turbomachinery modelling approach can be found in Olumayegun and Wang [22].

### Integrally geared shaft models

The compressors are driven by an expander supported by an electric motor. The compressors, expander and motor are positioned on separate shafts rotating at different speeds. The compressors and expander shafts are connected to the motor shaft through an integral gear system. The transient of the motor shaft speed,  $N_m$ , can be determined from the shaft dynamic equation [22]:

$$\begin{aligned} (I_m + I_{exp} + I_{LPC} + I_{HPC})N_m \frac{dN_m}{dt} \\ = (P_m + P_{exp} - P_{LPC} - P_{HPC} \\ - P_{loss}) \end{aligned} \quad (12)$$

Where  $I$  represents the inertia and  $P$  the power.

The motor-expander and motor-compressor gear ratio are given by Equation (13) and (14).

$$R_{m-exp} = \frac{N_m}{N_{exp}} \quad (13)$$

$$R_{m-cc} = \frac{N_m}{N_{cc}} \quad (14)$$

### Oil tank model

The expansion tank is assumed to have a cross-sectional area,  $A$ , with a fluid level of height,  $H$ . The mass and energy conservation equations for the fluid in the tank can be expressed as:

$$\frac{dM}{dt} = \dot{m}_{in} - \dot{m}_{out} \quad (15)$$

$$\frac{d(Mh)}{dt} = \dot{m}_{in}h_{in} - \dot{m}_{out}h_{out} \quad (16)$$

Where  $h$  is the specific enthalpy of heat transfer fluid and  $M$  is the mass of fluid in the tank.

$$M = \rho AH \quad (17)$$

The pressure of the oil at the tank outlet is given as:

$$p_{out} = p_{atm} + \rho gH \quad (18)$$

Where  $\rho$  is the density of oil and  $g$  is acceleration due to gravity.

## RESULTS AND DISCUSSIONS

### Steady state simulation results at design operating point

In this study, the design operating point values for the sCO<sub>2</sub> plant were based on the operating data of the exhaust gas from the cement plant and ambient air conditions. The main parameters for the model related to the system components have been taken from the preliminary design stage of the CO2OLHEAT demonstrator and are reported in Table 1. The compressor designed by Baker Hughes, which is a partner in the CO2OLHEAT project, considers two compressor stages with isentropic efficiency at nominal conditions of 86% for stage 1 and 80% for stage 2. Design data for the heat exchangers are given in Table 2.

**Table 1:** Operating conditions and performance of sCO<sub>2</sub> plant at the design point.

Parameters	Value
<b>Compressor</b>	
Isentropic efficiency	86%/80 %
Nominal power	887 kW
<b>Expander</b>	
Isentropic efficiency	81%
Power	783 kW
<b>Power-turbine</b>	
Isentropic efficiency	83%
Power	2355 kW
<b>Heat exchangers thermal duty</b>	
PHE	9128 kW
PCHE	10479 kW
ACHE	6876 kW
WHRU	9114 kW
<b>Intermediate thermal oil loop</b>	
Oil tank volume	36 m <sup>3</sup>
Total oil volume	72 m <sup>3</sup>

**Table 2:** Performance and design parameters of sCO<sub>2</sub> plant at the design point.

Heat Exchanger design parameters	WHRU	PHE	PCHE	ACHE
Fluid (hot/cold)	FG/Oil	Oil/CO2	CO2/CO2	CO2/Air
Surface area [m <sup>2</sup> ]	1328	114	194	16600
Pressure loss (hot/cold side) [kPa]	10/50	50/350	100/100	127/10
Overall heat transfer coefficient [w/m <sup>2</sup> K]	351	1020	1912	40
Volume [m <sup>3</sup> ]	25	2.3	0.3	276
Dry mass [kg]	9800	841	4940	15600

Tables 3 and 4 show the results of the steady-state simulations which are in agreement with the thermodynamic design carried out for the CO<sub>2</sub>OLHEAT demonstrator. In particular, Table 3 shows the thermodynamic state points of the plant (numbers refer to Figure 2) for the different circuits (sCO<sub>2</sub> power block, cooling air and intermediate thermal oil loop). Table 4, reports the main results from the steady state simulation. It can be seen that the sCO<sub>2</sub> heat recovery plant should be able to recover approximately 9 MWth of waste heat from the exhaust gases and convert it to 2 MWe of electrical power with an efficiency of approximately 22%.

**Table 3:** Results of steady state simulation

State	$\dot{m}$ (kg/s)	P (bar)	T (°C)	h (kJ/kg)
<b>SCO<sub>2</sub> loop</b>				
1	41	85	33	294
2	41	215	58	316
3	41	214	187	575
4	41	210	360	800
5	41	171	339	781
6	41	88	275	723
7	41	87	68	464
<b>Cooling air</b>				
8	298	1	20	419
9	298	1	43	442
10	131	1	400	1048
11	131	1	342	978
<b>Intermediate thermal oil loop</b>				
12	61	14	317	739
13	61	14	386	887

**Table 4:** Performance parameters of sCO<sub>2</sub> plant at the design point.

Parameters	Value
Compressor Rotational speed	19500 RPM
Expander Rotational speed	12500 RPM
Generator power	2205 kW
Generator power	2205 kW
Turboexpander motor power	211 kW
Net power output	1994 kW
Cycle thermal efficiency	22 %

### Open loop dynamic response to step change in exhaust gas and ambient air conditions

The main sources of external disturbance for the sCO<sub>2</sub> WHP plant are the fluctuation in the cement plant exhaust gas and ambient conditions. In particular, the exhaust gas temperature and mass flow rate can vary as a result of variations in process operations and their control, while variations in the flow of the air across the gas cooler can result from control actions or failure of heat exchanger fans.

For these reasons, open loop simulation of the sCO<sub>2</sub> plant (i.e. without control actions) have been carried out considering step changes in these variables to provide insights into the inherent transient behaviour of the cycle due to such changes [22]. Open loop transient response results can also inform the choice of potential control variables and strategies. Tables 4, 5 and 6 summarise the main results and assumptions of the three open loop simulations.

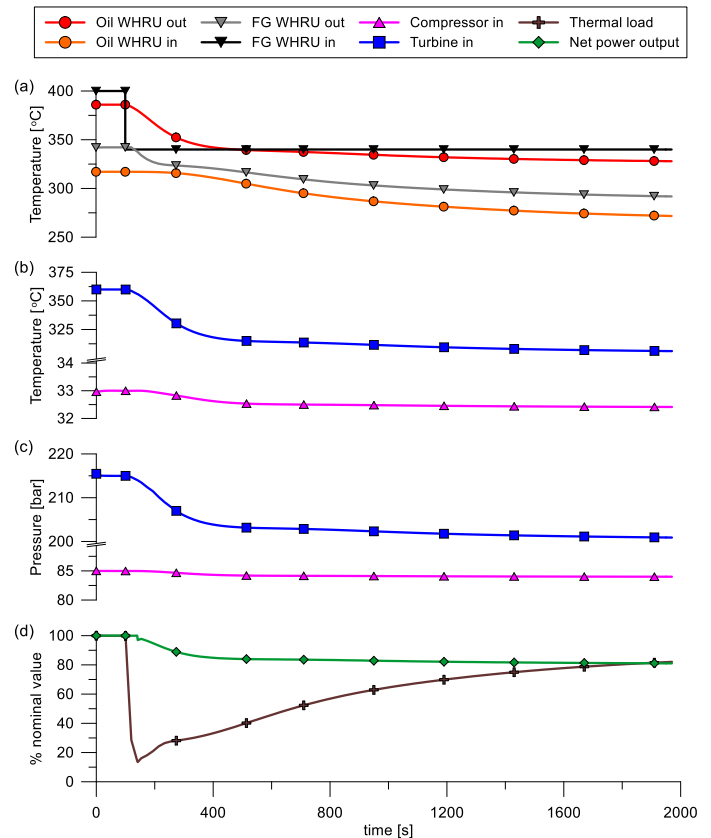


**Figure 4:** Open loop transient response to step change in exhaust gas temperature: (a) flue gas (FG) and oil temperatures at the inlet and outlet of the WHRU; (b) compressor and turbine inlet temperatures; (c) pressures, and (d) percentage variation of the cycle net power output and thermal load (waste heat recovered) in respect to the nominal value.

Figure shows the transient response of various parameters of the sCO<sub>2</sub> cycle to a step change in exhaust gas temperature from 400°C to 340°C (15% reduction), 100 seconds into operation at steady state conditions. This results in a drop of the temperature of the heat transfer oil at PHE inlet (WHRU outlet), from 385°C down to 325°C (Figure 4.a). Consequently, the oil temperature at the outlet of the PHE (WHRU inlet) also decreases from 317°C to 267°C. The decrease in temperature leads to an increase in the oil density and a 10% increase in the oil mass flow rate. The drop in the thermal oil temperature across the PHE leads to a 15% decrease in the CO<sub>2</sub> temperature at the turbine inlet (Figure 4.b) which in turn leads to variation in all other main cycle parameters such as the compressor inlet

temperature and pressure (Figure 4.b and 4.c respectively), the turbine inlet pressure (Figure 4.c) as well as the fluid thermodynamic conditions at the power turbine. In particular, while at the compressor inlet the temperature and pressure changes are 0.6°C and 1 bar respectively, the turbine inlet pressure shows a slightly higher change of 15 bar (Figure 4.c).

The new thermodynamic conditions reached by the cycle at steady state conditions after the step decrease of the flue gas temperature at the WHRU inlet lead to a 19% decrease in the net power output generated, Figure 4.d. This drop is caused mainly by a decrease in the power generated by the turbines, since the compressor power consumption stays approximately constant. In fact, higher variation of fluid thermodynamic conditions occurs at the inlet of the expander and power turbine, leading to a lower performance of these components. The thermal load available at the WHRU also decreases by 12% (Figure 4.d), meaning that the thermal efficiency of the cycle drops as well.

From a dynamic perspective, the turbine inlet temperature and pressure show a time constant of 313s (Figure 4.b and 4.c respectively). The other cycle parameters show similar transient behaviour. The large thermal inertia introduced by the metal mass of the heat exchangers and pipes as well as the thermal oil, is not sufficient to damp the temperature fluctuations of the flue

gas. A 60°C temperature drop of the exhaust gas results in a temperature decrease rate of 10.8°C/min, which may exceed the thermal stress limits of the components. In such a case, controls should be implemented to reduce the rate of temperature reduction to protect the components from premature failure.

A similar trend can be noticed in the case of a step change in the exhaust gas mass flow rate (Figure 5). Similar to the case of step decrease in exhaust gas temperature, a 15% step reduction in exhaust gas mass flowrate was introduced 100s into operation at steady state conditions. However, in this case the magnitude of the variations is lower compared to the step change in exhaust gas temperature. Figure 5.a shows that the 15% step decrease in the mass flow rate of the exhaust gases leads to a reduced drop in the temperature of the thermal oil, and a reduction in the temperature of the sCO<sub>2</sub> at the turbine inlet, Figure 5.b.

Figure 5.c, shows that the step change in exhaust gas flowrate leads to a reduction in the pressure ratio across the sCO<sub>2</sub> cycle and approximately a 3% reduction in power generated compared to the 15% reduction in the case of the step change in exhaust gas temperature, Figure 4.d. These results demonstrate that the effect of reduction in the exhaust mass flowrate is partially compensated by increased temperature difference across the WHRU.

**Table 5:** Results of open loop transient response to a 15% step decrease in flue gas (FG) temperature while keeping the flue gas mass flow rate and the cooling conditions (air temperature and flow rate) constant. Cooling air temperature equal to 20°C and 297 kg/s respectively.

Parameters	Initial value	Final value	Time constant [s]
Flue gas mass flow rate	130 kg/s	130 kg/s	N/A
Flue gas inlet temperature	400°C	340°C	N/A
Thermal oil outlet temperature (from WHRU)	386°C	326°C	207
Thermal oil inlet temperature (to WHRU)	317°C	288°C	910
Thermal load	100% (9.10 MW)	88% (8.05 MW)	910
Turbine inlet temperature	360°C	304°C	213
Turbine inlet pressure	215.4 bar	200.8 bar	203
Compressor inlet temperature	33.0°C	32.4°C	313
Compressor inlet pressure	85.0 bar	84.0 bar	293
Net power output	100% (2.20 MW)	80% (1.77 MW)	203

**Table 6:** Results of open loop transient response to a 15% step decrease in flue gas (FG) mass flow rate while keeping the flue gas temperature and the cooling conditions (temperature and flow rate) constant. Cooling air temperature and mass flow rate equal to 20°C and 297 kg/s respectively.

Parameters	Initial value	Final value	Time constant [s]
Flue gas mass flow rate	130 kg/s	111 kg/s	N/A
Flue gas temperature	400°C	400°C	N/A
Thermal oil inlet temperature	386°C	379°C	490
Thermal oil outlet temperature	317°C	311°C	1140
Thermal load	100% (9.10 MW)	95% (8.62 MW)	1140
Turbine inlet temperature	360°C	354°C	350
Turbine inlet pressure	215.4 bar	211.2 bar	330
Compressor inlet temperature	33.1°C	33.0°C	545
Compressor inlet pressure	85.0 bar	84.9 bar	415
Net power output	100% (2.20 MW)	97% (2.14 MW)	330



**Table 7:** Results of open loop transient response to a 20% step decrease in cooling air mass flow rate while keeping the cooling air inlet temperature and the heating conditions constant. (Flue gas temperature and mass flow rate at 400°C and 130 kg/s respectively).

Parameters	Initial value	Final value	Time constant [s]
Air mass flow rate	297 kg/s	238 kg/s	N/A
Air inlet temperature	20°C	20°C	N/A
Air outlet temperature	42.9	46.9°C	89
Cooling load	100% (6.9 MW)	94% (6.4 MW)	89
Turbine inlet temperature	360°C	338°C	140
Turbine inlet pressure	215.4 bar	209.2 bar	94
Compressor inlet temperature	33.0°C	32.7°C	104
Compressor inlet pressure	85.0 bar	84.6 bar	90
Net power output	100% (2.20 MW)	93% (2.05 MW)	94

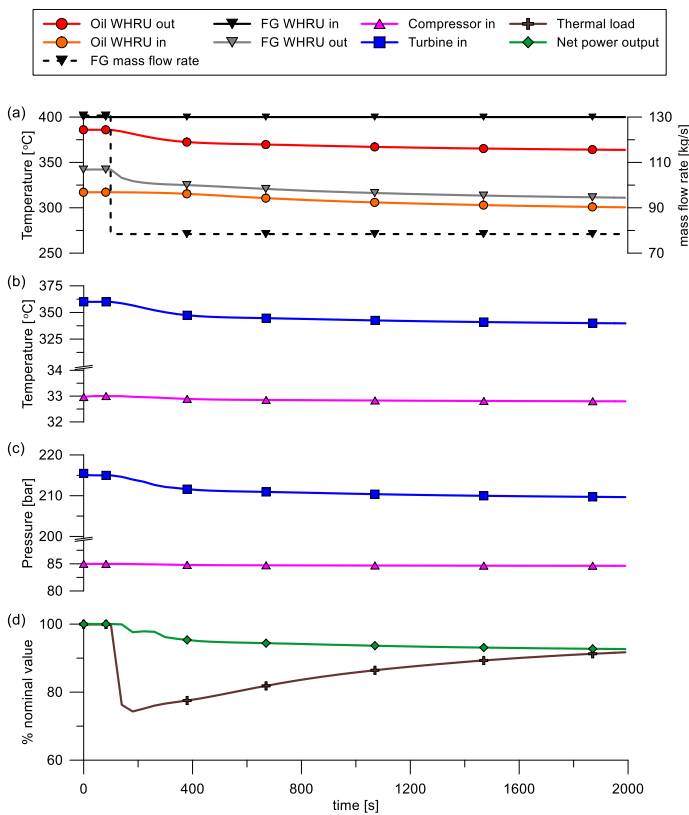


**Figure 5:** Open loop transient response to step change in exhaust gas mass flow rate: (a) flue gas (FG) and oil temperatures at the inlet and outlet of the WHRU; (b) compressor and turbine inlet temperatures and (c) and pressures; (d) percentage variation of the cycle net power output and the waste thermal load recovered in respect to the nominal value.

Compared to the flue gas temperature step reduction case, the transient response of the cycle parameters is slower when a drop in the flue gas mass flow rate occurs. Figure 5 shows for instance that the time constant of the temperature and pressure at the turbine inlet is 350s and 330s respectively. For mass flow rate variations of the flue gas, the risk of component damage due to thermal stress is low as the rate of temperature decrease is only 2.8°C/min (Figure 5.b).

Since the changes in thermodynamic conditions of the cycle from the step change in exhaust mass flow rate investigated are quite small, the thermal load available when the new steady state is reached is only 5% lower than the initial steady state value (Figure 5.d).

Figure 6 shows the results for a step decrease in the air flow rate provided by the cooler. Such variation could be caused by a failure of one of the heat exchanger fans.

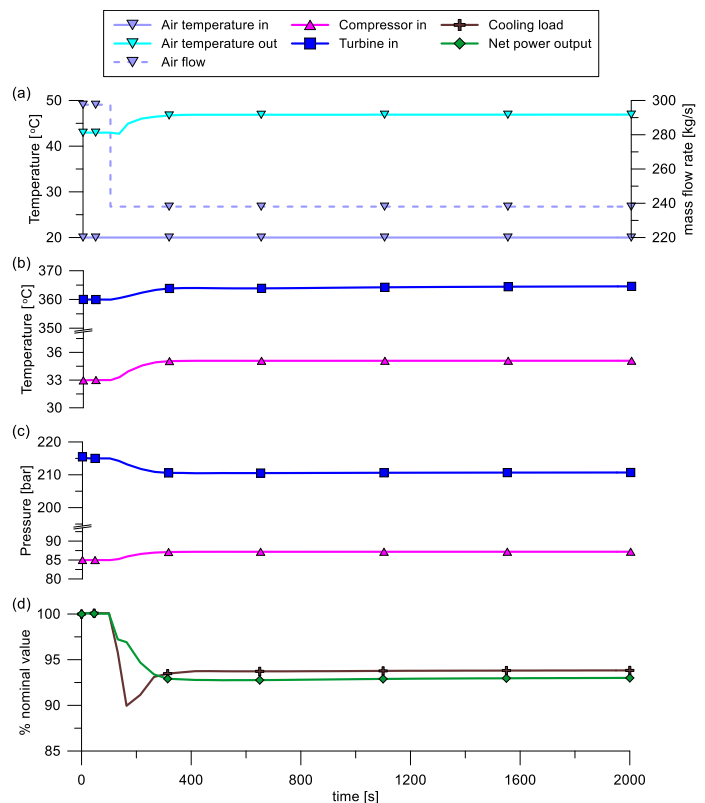


**Figure 6:** Open loop transient response to step change in air flow rate provided by the ACHE: (a) air mass flow rate and temperature at the inlet and outlet of the ACHE; (b), compressor and turbine inlet temperatures and (c) and pressures; (d) percentage variation of the cycle net power output and of cooling available at the ACHE with respect to the nominal value.

Figure 6.a shows the increase in the air temperature at the outlet of the ACHE following a 20% step decrease in the air mass flow rate provided by the fans. It can be seen that the cooling capacity available decreases by 8% (figure 6.d), and leads to a 2 °C increase in the compressor inlet temperature, which rises from 33°C to 35°C (Figure 6.b). As a consequence, the turbine inlet temperature increases as well, from 360°C to 365°C. At these conditions, the compressor operates at off-design, which leads to a reduction in the pressure ratio across the two turbines. This lower pressure ratio together with the reduced efficiency of the compressor itself cause a drop of 17% in the net power output generated by the system (Figure 6.d). These results show that the performance of the unit is very sensitive to variation of the cooling capacity of the heat rejection heat exchanger and this, if not controlled effectively, can have a negative impact on the operation of the component and other major components in the system.

Figure 6 also shows that the sCO<sub>2</sub> cycle transient response to the 20% step change in air mass flow rate has a time constant in the order of 100s which is much shorter compared to those of step changes in exhaust gas conditions. The lower time constant shows that an eventual control action on the cooler fans results in a prompt response of the temperature at the outlet of the cooler. For prompt control, cooler by-pass must be considered.

#### Dynamic response to actual variations in exhaust gas conditions and ambient air flowrate

One of the key contributions of this work is the study of the dynamic performance of sCO<sub>2</sub> WHP plant using actual real-time variations in exhaust gas and ambient air conditions. Simulations were performed to understand the dynamic behaviour of the sCO<sub>2</sub> cycle to actual fluctuations in the cement plant exhaust gas flow rate and temperature as well as changes in ambient air temperature over a 24-hour period. A sample data consisting of the exhaust gas and ambient air conditions on 17 July 2021 was used for the simulation (Figure 7). The variations in the exhaust gas flow rate is shown in **Error! Reference source not found..a**. The maximum and minimum flow rate values were approximately 168 kg/s and 66 kg/s respectively. However, for most of the time, the exhaust gas flow rate remained relatively constant at 144 kg/s, except for some periods of large drop in flow rate. For instance, about 54% drop in flow rate, which lasted for about 20 minutes, occurred at 2:24 pm. The design operating point for the WHP plant was set close to the average value of the flow rate to cater for periods of dip in value. This would also ensure the availability of sufficient thermal energy in the exhaust gases for the heat transfer oil during periods of reduced exhaust gas temperature and high exhaust gas flow rate.

Variations in exhaust gas temperature are shown in **Error! Reference source not found..b** and indicate a maximum value of 403°C and minimum value of 378°C. The exhaust gas temperature is seen to vary widely between the minimum and maximum value during the 24-hour period. The design operating point value was chosen as 400°C to be near the maximum exhaust gas temperature and enable the WHP plant to be operated as efficiently as possible. The ambient

air temperature variation for the 24-hour at the cement plant is shown in **Error! Reference source not found.7.c**. As expected, the ambient temperature started to increase at dawn and reached maximum value of 32°C at 3:25 pm before starting to decrease into the night time. This is in no way a depiction of typical variation in ambient air condition at the cement plant as the ambient condition could vary considerably depending on the time of the year. A look at data across the whole year indicates ambient temperatures as low as -13°C in the winter and reaching as high as 41°C in the summer.

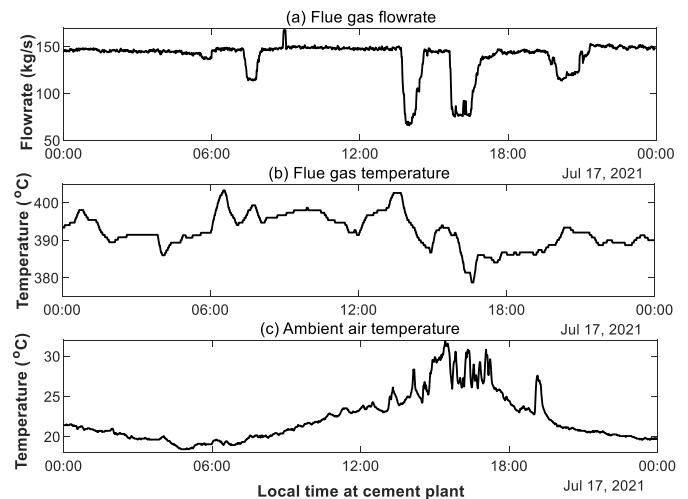


**Figure 7:** Actual real-time variations in exhaust gas conditions and ambient air temperature at the cement plant on 17<sup>th</sup> July, 2021

The dynamic response to combined variations in exhaust gas and ambient air conditions was simulated to show a realistic dynamic behaviour of the plant. Figure 8 shows the results of these simulations. In particular, Figures 8.a and 8.b show the variations of the turbine and compressor inlet temperatures respectively. Figure 8.c shows the variations in the duty of the main heat exchangers in the plant while Figures 8.d and 8.e show the performance of the sCO<sub>2</sub> unit in terms of net power output and efficiency.

The results show that from the parameters investigated, variations in ambient air temperature have the most significant impact on plant performance. The transients of the sCO<sub>2</sub> cycle variables look similar to the transients, of the ambient air temperature. This could be due to the fact that changes in ambient air temperature directly affect the compressor inlet temperature through the CO<sub>2</sub> gas cooler unlike the exhaust gas conditions which are damped by the intermediate oil loop.

The results also highlight the sensitivity of the sCO<sub>2</sub> cycle to changes in CO<sub>2</sub> properties close to the critical point at compressor inlet. Therefore, any control strategy for the sCO<sub>2</sub> cycle needs to consider the control of the gas cooler outlet (or compressor inlet) temperature or density [23] within the design operating value. This could be achieved through air recirculation and manipulation of air flow rate through the gas cooler. Control of the sCO<sub>2</sub> cycle for variations in exhaust gas conditions (within

allowable operation limit) might not be as imperative as gas cooler control. For instance, when exhaust gas flow rate or temperature drops, it may be appropriate not to take any control action as long as the cycle stays within the design operating envelope. Any attempt to control the sCO<sub>2</sub> cycle either through CO<sub>2</sub> bypass or reduction in CO<sub>2</sub> mass flow rate will lead to

reduction in waste heat recovery capacity and may force the turbomachinery to operate further away from the design point. Exhaust gas data from the cement plant indicate that values are not expected to increase significantly above the design envelope and if this occurs it can be addressed effectively through oil by-pass control at the PHE.

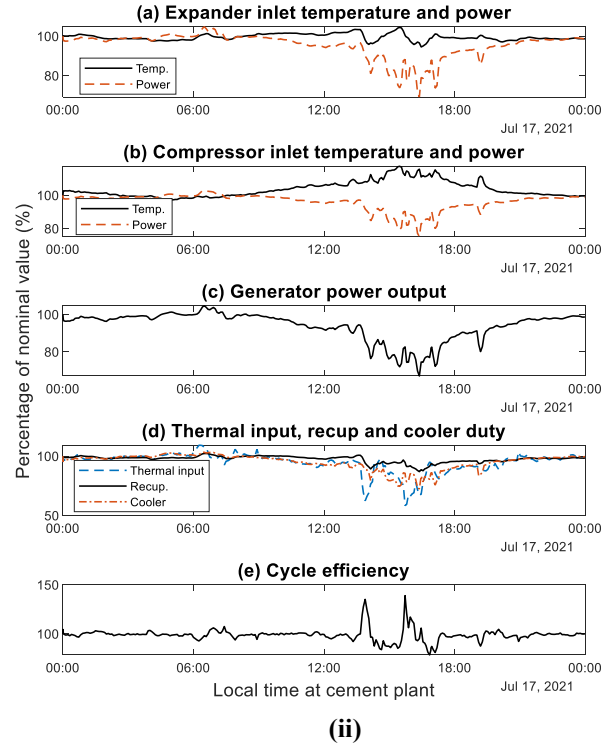
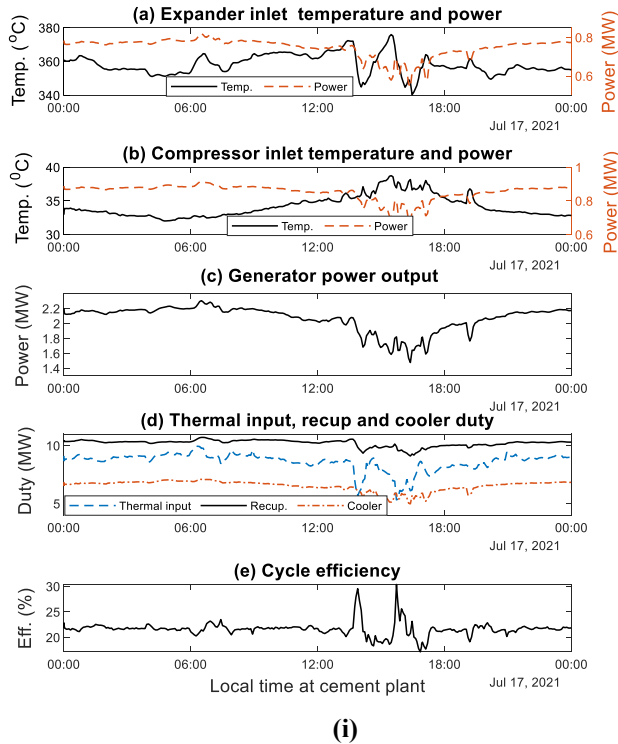


**Figure 8:** Dynamic response to combined actual real-time variations in exhaust gas conditions and ambient air temperature at the cement plant on 17<sup>th</sup> July, 2021: in absolute values (i) and in percentage variation from nominal conditions (ii)

### Discussion on possible control strategies

One of the main advantages of adopting power units based on sCO<sub>2</sub> technology is the potential flexibility of such systems in adapting quickly to large variations in operating conditions and being more efficient compared to conventional systems both at full and part load as well as during startups and shutdowns [24]. This is a desired feature for base load power systems, especially in a scenario characterized by a higher penetration of renewables and decentralized energy systems, but also for waste heat recovery applications.

Sudden and unforeseen variations in the waste heat source temperature or flow rate, may in fact require frequent shutdowns and startups of the power block, increasing plant idle times. This may lead to a decreased utilisation rate of the unit and prevent the maximization of economic benefits. Moreover, a reduced operating part-load range will increase further the need of shutting the system down in case of large variations in the waste heat source from nominal conditions.

Despite the potential of sCO<sub>2</sub> power technology, limitations may arise during transients and at part-load conditions such as: compressor instabilities; turbine choking; CO<sub>2</sub> pressures and temperatures above design values; excessive

shaft rotational speeds; and heat rejection requirements exceeding the capacity of the cooler [25]. In addition, the control systems should also be able to meet thermal load variations and ramp rates, keeping cycle efficiency at an optimal level and damping process disturbances such as small variations in heat input or heat rejection capacity particularly when direct heat rejection to air is employed [26].

To achieve these objectives among the main cycle variables to control are the compressor and turbine inlet conditions. The compressor inlet conditions are particularly important since, as showed in the previous sections, have a strong effect on system performance. With reference to the system analysed in this research, the control variables suitable to regulate the compressor inlet conditions are the regulation of the cooling load (air mass flow rate and cooler by-pass), mass flow rate recirculation (compressor by-pass), as well as shaft speed and inventory control.

If inventory control is not implemented due to its complexity, meaning that the fluid mass in the circuit is fixed, the isobaric regulation of the compressor temperature requires the simultaneous regulation of the turbine inlet temperature as well [27]. This can be done through by-passing the waste heat

recovery unit or controlling the mass flow rate of the intermediate heat transfer fluid (i.e. thermal oil). However, this control action can be actuated only in one direction (to decrease the turbine inlet temperature) since it is not usually possible to increase the thermal grade of the waste heat available.

The response to such changes, depend on the thermal inertia of the different components in the system as well as the ratio between the hot and cold volumes in the power block [28]. Reduced hot-and-cold volume ratios lead to reduced time constants and inertia while larger ones lead to slower dynamic response.

Other approaches are turbine flow bypass and throttling as well as the regulation of the shaft speed [29]. Even though such strategies typically lead to faster dynamic response, they also cause variations in CO<sub>2</sub> pressures in the circuit. Turbine by-pass and throttling flow control are usually employed in emergency scenarios and to adjust the power generated by the system to the load [29]. However, they could also be used to regulate the main compressor when it is driven by an expander.

The regulation of the shaft speed may also be used to control the compressor and turbine inlet conditions, but requires particular attention in the design of the compressor operating maps to avoid the occurrence of instabilities.

When inventory control is implemented, it is possible to regulate the density in the different parts of the system and therefore the conditions at the inlet of the turbomachines. Despite its slower response, it was found to be an efficient strategy to maximise the cycle efficiency at part-load conditions [25] but stability considerations due to the withdrawals/additions of CO<sub>2</sub> have been identified as a major issue to be addressed. Other key limiting factors in inventory control lie in the finite capacity of the storage tanks as well as the need of having ancillary control equipment which can substantially increase the cost of the power block. [30,31].

Figure 9 shows a possible arrangement of the different equipment required in the CO<sub>2</sub>OLHEAT demonstrator to realise the control strategies discussed in this section.

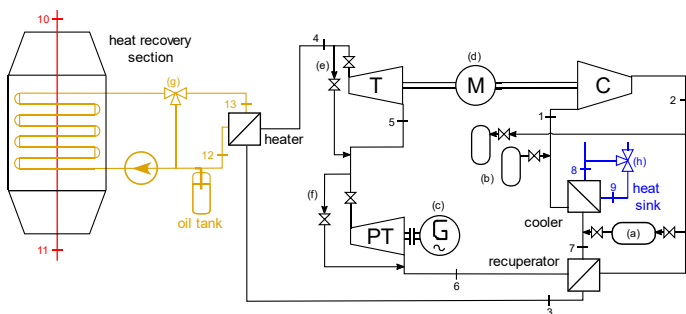


**Figure 9:** CO<sub>2</sub>OLHEAT sCO<sub>2</sub> available control variables: (a) compressor flow recirculation; (b), inventory control; (c) power turbine (PT) shaft speed; (d) TurboExpander (TE) shaft speed, (e) Expander (T) by-pass and throttling flow control (f) Power Turbine (PT) by-pass and throttling flow control (g) Waste Heat Recovery Unit (WHRU) by-pass; (h) Power Turbine (PT) by-pass and throttling flow control.

## CONCLUSIONS

In this work a numerical model for a 2.0 MW sCO<sub>2</sub> power unit is presented. The model is suitable for dynamic simulation and control studies given the reduced computational effort required for each simulation.

The model has been used to investigate the system's transient response to variations in exhaust heat parameters and ambient temperature during a typical day at the a cement plant.

The main findings from the analysis show that variation of heat rejection to ambient air conditions have the strongest impact on system performance since they impact on the sCO<sub>2</sub> temperature at the compressor inlet. An increase of 8°C in the ambient temperature leads to a CO<sub>2</sub> temperature rise of 6°C at the compressor inlet. This suggests that control strategies must be designed to deal with such disturbances during operation, given that the system performance are sensitive to the compressor inlet temperature. When the compressor inlet temperature increases by 18%, the net power output of the system shows approximately a 20% decrease.

Small variations in exhaust gas parameters are cushioned by the thermal mass of components, particularly by the thermal oil in the indirect heat transfer loop.

In general, the results show that fast and accurate control of the CO<sub>2</sub> conditions at compressor inlet is key to ensuring reliable and efficient system performance. The system thermal inertia can filter small fluctuations in exhaust gas conditions reducing the impact on the turbine inlet temperature and control complexity.

## NOMENCLATURE

### Abbreviations

ACHE	Air-cooled heat exchanger
NIST	National Institute of Standards and Technology
PHE	Primary heat exchanger
sCO <sub>2</sub>	supercritical carbon dioxide
WHP	Waste heat to power
WHR	Waste heat recovery
WHRU	Waste heat recovery unit

### Symbols

$A$	Area (m <sup>2</sup> )
$D$	Diameter (m)
$f$	Friction factor (-)
$g$	Acceleration due to gravity (m/s <sup>2</sup> )
$H$	Liquid height or level (m)
$h$	Specific enthalpy (J/kg)
$I$	Inertia (kg.m <sup>2</sup> )
$L$	Length (m)
$M$	Mass (kg)
$\dot{m}$	Mass flow rate (kg/s)
$N$	Rotational speed (rev/s)
$P$	Power (watt or J/s)
$p$	Pressure (Pa)
$R$	Gear ratio
$T$	Temperature (K)

$t$	Time (seconds)
$U$	Impeller tip speed (rad/sec)
$u$	Specific internal energy (J/kg)
$v$	Velocity (m/s)
$Q$	Heat transfer rate or duty (watt or J/s)
$\Delta$	Increment or change
$\rho$	Density (kg/m <sup>3</sup> )
$\varphi$	Heat flux (W/m <sup>2</sup> )
$\phi$	Flow coefficient
$\omega$	Perimeter (m)

### Subscripts

$atm$	Atmospheric
$c$	Cold stream
$cc$	Compressor
$exp$	Expander
$HPC$	High Pressure Compressor
$h$	Hydraulic or hot stream
$in$	Inlet
$LPC$	Low Pressure Compressor
$m$	Motor
$out$	Outlet
$s$	Surface
$w$	Metal wall

### ACKNOWLEDGEMENTS

The CO2OLHEAT project has received funding from the European Union's Horizon 2020 research and innovation programme under grant agreement N° 101022831. The authors would like to acknowledge this funding as well as funding received from the Engineering and Physical Sciences Research Council (EPSRC) UK, for the SCOTWAHR project, grant reference EP/V001795/1. Exhaust gas data have been provided by CEMEX, a partner in CO2OLHEAT, whose contribution is gratefully acknowledged. Data related to the paper and other information relating to the paper can be obtained by contacting the corresponding author.

### REFERENCES

[1] Cullen JM, Allwood JM. Theoretical efficiency limits for energy conversion devices. *Energy* 2010; 35:2059–69. <https://doi.org/10.1016/J.ENERGY.2010.01.024>.

[2] Forman C, Muritala IK, Pardemann R, Meyer B. Estimating the global waste heat potential. *Renewable and Sustainable Energy Reviews* 2016;57:1568–79. <https://doi.org/10.1016/J.RSER.2015.12.192>.

[3] Marchionni M, Bianchi G, Tassou SA. Review of supercritical carbon dioxide (sCO<sub>2</sub>) technologies for high-grade waste heat to power conversion. *SN Appl Sci* 2020;2:1–13. <https://doi.org/10.1007/s42452-020-2116-6>.

[4] Crespi F, Gavagnin G, Sánchez D, Martínez G. Supercritical carbon dioxide cycles for power generation: A review. *Appl Energy* 2017.

[5] Kulhánek M, Dostál V. Supercritical Carbon Dioxide Cycles Thermodynamic Analysis and Comparison. *Proceedings of SCCO<sub>2</sub> Power Cycle Symposium 2011*:1–12.

[6] Marchionni M, Bianchi G, Tassou SA. Techno-economic assessment of Joule-Brayton cycle architectures for heat to power conversion from high-grade heat sources using CO<sub>2</sub> in the supercritical state. *Energy* 2018;148:1140–52. <https://doi.org/10.1016/J.ENERGY.2018.02.005>.

[7] Chai L, Tassou SA. Numerical study of the thermohydraulic performance of printed circuit heat exchangers for supercritical CO<sub>2</sub> Brayton cycle applications. *Energy Procedia* 2019; 161:480–8. <https://doi.org/10.1016/j.egypro.2019.02.066>.

[8] Marchionni M, Chai L, Bianchi G, Tassou SA. Numerical modelling and transient analysis of a printed circuit heat exchanger used as recuperator for supercritical CO<sub>2</sub> heat to power conversion systems. *Appl Therm Eng* 2019;161:114190. <https://doi.org/10.1016/j.applthermaleng.2019.114190>.

[9] Baltadjiev ND, Lettieri C, Spakovszky ZS. An investigation of real gas effects in supercritical CO<sub>2</sub> centrifugal compressors. *Journal of Turbomachinery*. 2015 Sep 1;137(9):091003. <https://doi.org/10.1115/1.4029616>

[10] Fuller, Robert L, Eisemann K. Centrifugal Compressor Off-design performance for supercritical CO<sub>2</sub>. *Supercritical CO<sub>2</sub> Power Cycle Symposium*, Boulder, Colorado: 2011, p. 12.

[11] Thatte A, Loghin A, Shin Y, Ananthasayanam B. Performance and Life Characteristics of Hybrid Gas Bearing in a 10 MW Supercritical CO<sub>2</sub> Turbine. Volume 9: Oil and Gas Applications; *Supercritical CO<sub>2</sub> Power Cycles; Wind Energy*, ASME; 2016, p. V009T36A018. <https://doi.org/10.1115/GT2016-57695>.

[12] Alfani D, Astolfi M, Binotti M, Silva P. Part load strategy definition and annual simulation for small size sCO<sub>2</sub> based pulverized coal power plant. *Proceedings of the ASME Turbo Expo*, vol. 11, American Society of Mechanical Engineers (ASME); 2020. <https://doi.org/10.1115/GT2020-15541>.

[13] Marchionni M, Saravi SS, Bianchi G, Tassou SA. Modelling and performance analysis of a supercritical CO<sub>2</sub> system for high temperature industrial heat to power conversion at off-design conditions. 3rd European sCO<sub>2</sub> conference, 2019. <https://doi.org/10.17185/dupublico/48908>.

[14] Supercritical CO<sub>2</sub> power cycles demonstration in Operational environment Locally valorising industrial Waste Heat. CO2OLHEAT Project H2020. European Commission. <https://cordis.europa.eu/project/id/101022831> (accessed October 26, 2022).

[15] Ozana S and Macháček Z. Implementation of the mathematical model of a generating block in matlab and simulink using s-functions. *The Second International Conference on Computer and Electrical Engineering ICCEE*. Session 8. p. 431–435. 2009.

[16] Lemmon EW, Bell IH, Huber ML, McLinden MO. NIST Standard Reference Database 23: Reference Fluid Thermodynamic and Transport Properties (REFPROP), Version 10.0; National Institute of Standards and Technology, Standard Reference Data Program: Gaithersburg, MA, USA, 2018.

[17] Franke R, Casella F, Sielemann M, Proelss K, Otter M. Standardization of thermo-fluid modelling in Modelica. Fluid. In Proceedings of the 7th International Modelica Conference 2009 (pp. 122-131). Linköping University Electronic Press.

[18] Pham HS, Alpy N, Ferrasse, JH, Boutin O, Tothill M, Quenaut J, Gastaldi O, Cadiou T, Saez M. An approach for establishing the performance maps of the sc-CO<sub>2</sub> compressor: Development and qualification by means of CFD simulations. *International Journal of Heat and Fluid Flow* 2016, 61, pp.379-394. <https://doi.org/10.1016/j.ijheatfluidflow.2016.05.017>

[19] Lambruschini F, Liese E, Zitney SE, Traverso A. Dynamic model of a 10 MW supercritical CO<sub>2</sub> recompression Brayton cycle. In *Turbo Expo: Power for Land, Sea, and Air 2016 Jun 13* (Vol. 49873, p. V009T36A004). American Society of Mechanical Engineers. <https://doi.org/10.1115/GT2016-56459>

[20] Gong Y, Carstens NA, Driscoll MJ, Matthews I. Analysis of radial compressor options for supercritical CO<sub>2</sub> power conversion cycles. Massachusetts (USA): Center for Advanced Nuclear Energy Systems 2006.

[21] Zhang Y, Li H, Li K, Yang Y, Zhou Y, Zhang X, Xu R, Zhuge W, Lei X, Dan G. Dynamic characteristics and control strategies of the supercritical CO<sub>2</sub> Brayton cycle tailored for the new generation concentrating solar power. *Applied Energy* 2022; 328, p.120190. <https://doi.org/10.1016/j.apenergy.2022.120190>

[22] Olumayegun O, Wang M. Dynamic modelling and control of supercritical CO<sub>2</sub> power cycle using waste heat from industrial processes. *Fuel* 2019; 249:89–102. <https://doi.org/10.1016/J.FUEL.2019.03.078>.

[23] Casella F, Mangola G, Alfani D. Density-Based Control of Air Coolers in Supercritical CO<sub>2</sub> Power Cycles. *IFAC-Papers OnLine*, 53 (2), 2020:12554-12559. <https://doi.org/10.1016/j.ifacol.2020.12.1810>

[24] Cagnac A, Mecheri M, Bedogni S. Configuration of a flexible and efficient sCO<sub>2</sub> cycle for fossil power plant. 3rd

European Supercritical CO<sub>2</sub> Conference, 19-20 September, Paris, France, 2019, <https://dx.doi.org/10.17185/dupublico/48907>.

[25] Trinh TQ. Dynamic Response of the Supercritical CO<sub>2</sub> Brayton Recompression Cycle to Various System Transients (Ph.D. thesis), Massachusetts Institute of Technology, 2009.

[26] P. Mahapatra, S.E. Zitney, J. Albright, E.A. Liese, Advanced regulatory control of a 10 MWe supercritical CO<sub>2</sub> recompression Brayton cycle towards improving power ramp rates, in: *The 6th International Symposium on Supercritical CO<sub>2</sub> Power Cycles*, 27-29 March, Pittsburgh Pennsylvania, 2018.

[27] N. Carstens, Dynamic Response and Safety Implications for Supercritical CO<sub>2</sub> Brayton Cycles Coupled to Gen-IV Reactors (Ph.D. thesis), Massachusetts Institute of Technology, 2007.

[28] Hacks AJ, Schuster S, Brillert D. Impact of volumetric system design on compressor inlet conditions in supercritical CO<sub>2</sub> cycles. *Journal of the Global Power and Propulsion Society*. 2021;5:104-110. <https://dx.doi:10.33737/jgpps/140118>.

[29] J. Kwon, J.I. Lee, Development of accelerated PCHE off-design performance model for optimizing power system control strategies in s-CO<sub>2</sub> system, in: *The 6th International Symposium on Supercritical CO<sub>2</sub> Power Cycles*, 27-29 March, Pittsburgh Pennsylvania, 2018.

[30] Marchionni M, Usman M, Chai L, Tassou SA. Inventory control assessment for small scale sCO<sub>2</sub> heat to power conversion systems. *Energy*. 2022 Dec 26:126537. <https://doi.org/10.1016/j.energy.2022.126537>

[31] B.S. Oh, J.I. Lee, Study of autonomous control system for s-CO<sub>2</sub> power cycle, in: *3rd European Supercritical CO<sub>2</sub> Conference*, 19-20 September, Paris, France, 2019, pp. 345–352, <http://dx.doi.org/10.17185/dupublico/48913>, 145.



## DESIGN AND EVALUATION OF LOW SPECIFIC SPEED EXPANDER FOR GEOTHERMAL ENERGY APPLICATION

**Abhay Patil\***

Southwest Research Institute, USA  
Email: [abhay.patil@swri.org](mailto:abhay.patil@swri.org)

**Jordan Nielson**

Southwest Research Institute, USA

**Natalie Smith**

Southwest Research Institute, USA

**Nathan Weiss**

Sage Geosystems, USA

### ABSTRACT

The increased interest in harnessing geothermal energy requires more attention to exploring and optimizing the design space for expanders with a specific focus on efficiency and reliability under off-design conditions. This study focuses on the design of a low-specific speed radial expander with a targeted shaft power of 0.5 MW at 22,000 rpm for the geothermal application utilizing CO<sub>2</sub> as a working fluid at 150°C. The design analysis includes exploration of the effects of loading and flow coefficients on low-specific speed expanders and iterative design optimization using coupled 3D design and CFD simulations. The 3D optimization shows that designing a turbine with higher loading enables optimal efficiency point (92% isentropic) with the desired off-design performance, however, with increased reaction thrust as the consequence of increased loading. Further CFD simulations of the entire expander control volume including front and back seals show that thrust force in the direction from outlet to inlet (upthrust) increases as the flow rates and rotational speeds reduce. The study concludes with a discussion about the control scheme for turbine start-up and the performance of low-specific speed turbines for geothermal applications.

### INTRODUCTION

Significant research has been focused on investigating the use of CO<sub>2</sub> in power cycles for existing and future applications. Supercritical Co<sub>2</sub> (sCO<sub>2</sub>) is dense like a liquid yet behaves like gas with compression or expansion processes occurring without phase change. Compared to steam, sCo<sub>2</sub> is nearly twice as dense, easier to compress, and an inert and stable fluid even at very high temperatures (600°C and above). Density change due to shifts in pressure and temperature enables a large amount of energy extraction subsequently reducing equipment size with high thermodynamic efficiencies. The use of CO<sub>2</sub> is also beneficial to harnessing different heat sources including geothermal energy.

Current methods to use geothermal energy include dry steam, flash steam, and the binary Organic Rankine Cycle (ORC) plants [1]. Dry steam and flash steam plants use steam directly to harness geothermal energy while ORC uses moderately heated geothermal fluid (~200 °C) to heat the secondary fluid. Binary power plants using ORC inherently uses a low source temperature that represents a large portion of available geothermal energy for electricity generation.

Many researchers [2][3] recently focused on evaluating the performance of ORC using different fluids and mixtures for geothermal and waste heat recovery applications. In comparison, the desirable thermophysical properties of sCO<sub>2</sub> for power cycles offer improved efficiencies and net power compared to the current state of the art [4]. CO<sub>2</sub> has desirable density, particularly near the supercritical region, at different cycle conditions as well as single phase conditions during the heat exchange process that enables the design of small-size turbomachinery and heat exchangers with a possible roadmap for optimal architecture based on source temperature [5]. Co<sub>2</sub> Plume Geothermal (CPG) technology presents an outstanding Co<sub>2</sub> storage option utilizing geothermal formations that exhibit desired energy potential for extraction. Part of stored Co<sub>2</sub> is used for energy generation, and equivalent heat extraction using CPG requires less auxiliary pumping power due to an improved thermosiphon effect compared to water-based geothermal energy extraction [6], [7]. However, the reservoir permeability and temperature play a critical role in yielding competitive LCOE values compared to other established renewable energy conversion methods. The majority of geothermal sites targets mid-enthalpy (150-250°C, ~5.5 km depth) dry and sedimentary rock, accessible throughout the United States and the world. One of the envisioned thermal well architectures includes a closed-loop vertical geothermal well design with cooled fluid pumped from the surface via the outer ring for heat extraction and the inner ring for the return path for hot fluid. This ensures no hydrogen sulfide or steam leakage

\* corresponding author(s)

during the operation and improved natural convection due to the downward fractures [8].

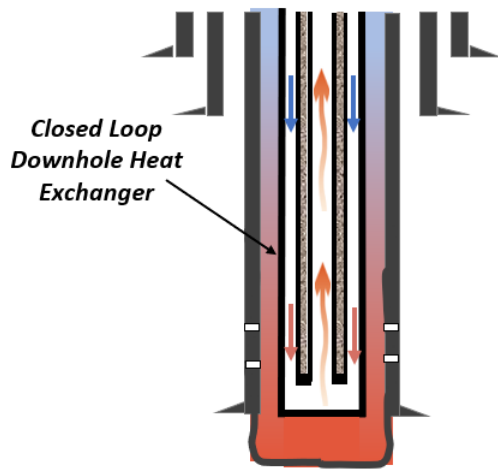


**Figure 1: Closed loop geothermal well [8]**

For the geothermal energy plants, the power output and turbine inlet conditions vary widely for different well conditions [9]. Additionally, fluctuations in ambient conditions and degradation in well output conditions through its life cycle will affect the turbine power output. Anticipating those factors in the design of the power generation unit and developing a modular approach that allows the operator to replace the aerodynamic portion of the turbine (without replacing the gearbox, generator, and support system) to accommodate the changing well conditions will enable optimal recovery as well as reduced time to maintenance over the well life [10]. However, using a synchronized generator requires a fixed rotational speed to meet the operational requirements. Further work focused on utilizing 1D Balje analysis to investigate the optimal rotational speed for a single-stage radial expander for different power flow conditions representing different sites. From the bounds of optimal speeds for each case, 22000 rpm was selected because it could meet the desired power output levels to achieve the required design, manufacturing, and operational flexibility (). The focus of the current study is to develop a turbine option for the lowest flow condition that will enable validation of the proposed plan under a laboratory-scale test environment. The proposed operational conditions include 15.75 MPa inlet pressure, 7.5 MPa outlet pressure, 15 kg/s mass flow rate, and 150°C inlet temperature with a fixed rotational speed of 22,000 rpm. The analysis will focus on aerodynamic design to develop an expander, nozzle, and volute for the proposed condition, 3D CFD simulations to quantify the performance, and the development of a full numerical model including balance piston seals to quantify the shift in performance as well as prediction of thrust for the proposed operating conditions.

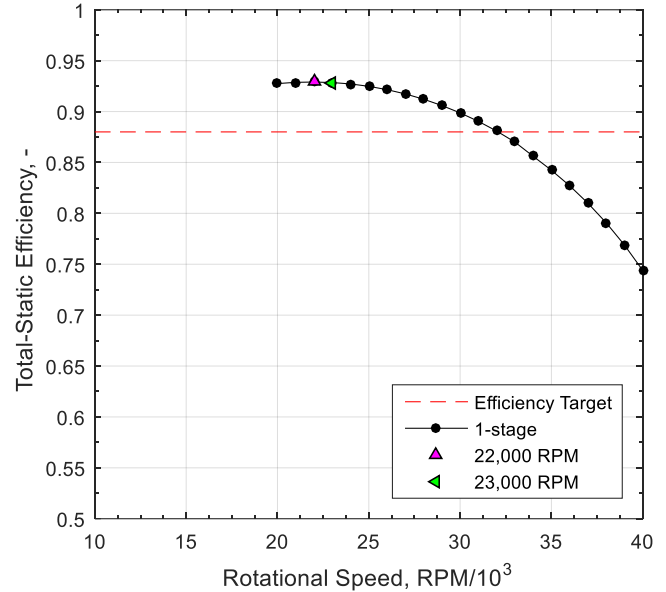


**Figure 2: 1D Balje analysis of the rotational speed at lower flow case [10]**

## DESIGN METHODOLOGY AND THE DESIGN RESULTS

Operating conditions and constraints from cycle modeling with well conditions are used to define preliminary turbine design parameters. The 1D turbine design process initiates by using these parameters as input conditions, and the 1D modeling outcomes are fed to the 3D design optimization process from which the final detailed design is obtained after iterations. The approach is shown in Figure 3.

An in-house pseudo-1D aerodynamic design tool based on the experience chart is used to develop initial estimates for the rotor geometry. The tool uses head and flow coefficients with assumed values of total-to-total efficiencies to calculate velocity triangles at the inlet and outlet based on desired outlet pressure. The tool doesn't account for any loss mechanisms, but rather uses a combination of loading and flow coefficients to output the geometry parameters within the given bound of geometrical and velocity constraints at the inlet and outlet for an initial estimate of the optimal design.

The design procedure is outlined in Baines, 2005 [11]. Figure 4 shows the total-to-static efficiency correlation with these coefficients and how this design compares with experience. The experience chart is a good starting point in the sense that the outcomes from testing different turbine rotors enable drawing constant efficiency lines and hence setting up a baseline for the initial design point. As for the current operational conditions, design point falls on the low specific speed side ( $N_s$ : 0.25) which requires the design selection with a larger inlet tip-to-exit tip ratio. However, the low flow conditions make it easier to achieve the optimal trade-off between friction and separation losses due to low flow instability and flow alignment from inlet to outlet. This trade-off is balanced with the iterative selection of loading and flow coefficients.

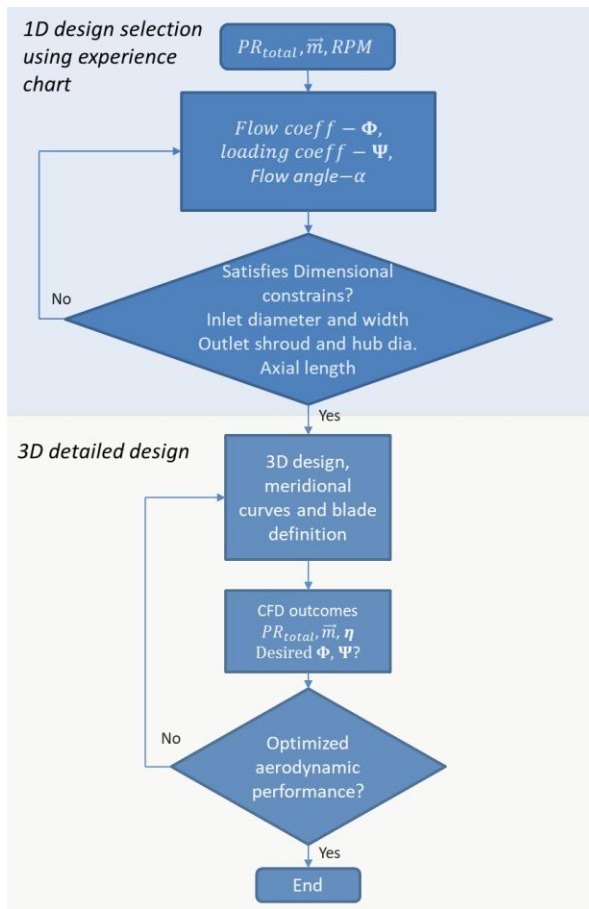


Figure 3: Expander design approach

The next step involves creating a 3D detailed design of the rotor including blade definition, nozzle, and volute. This requires an iterative approach of generating rotor geometry including blade designs and flow passages and then evaluating the different candidates using 3D steady CFD. Turbine 3D aerodynamic design definition includes hub, shroud, and blade angle profiles from inlet to outlet. CFTurbo was utilized to develop and iterate 3D aerodynamic design. The next step included developing a periodic numerical model using Turbogrid and simulation in CFX2020 R1. A mesh sensitivity study revealed a 0.5% difference between the coarse and fine mesh. Design iterations employed coarse mesh for the design optimization. The efficiency from the previous iteration is fed back to the 1D design tool to iterate the next design. Figure 6 shows the final shrouded rotor geometry and the geometric parameters. The same iterative process is employed to design the volute and nozzle to ensure the desired interaction at the stator rotor interface defined using the flow angle and slip. After the design of the rotor and volute is complete, a final transient CFD simulation is performed using

Fluent 2020R1 to ensure the expected performance in terms of shaft power and efficiency at design and off-design conditions.

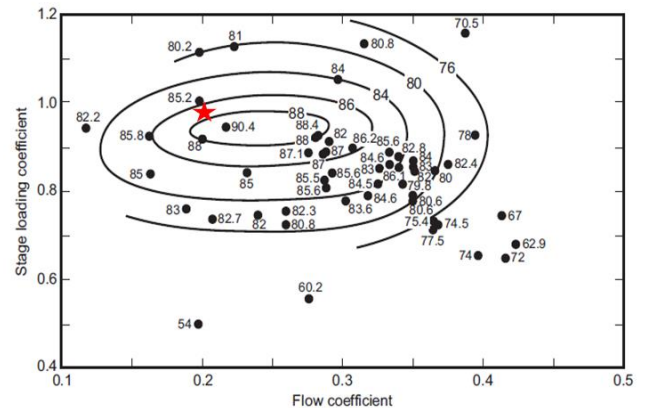


Figure 4: Correlations of blade loading and flow coefficients for radial inflow turbines (Total-to-static efficiency) [11]

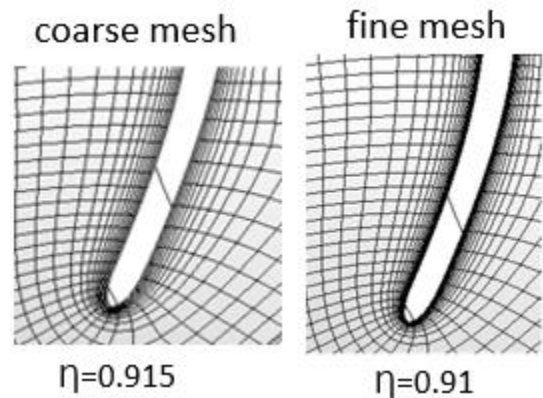
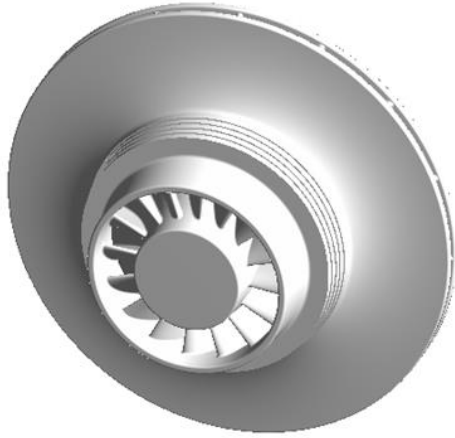


Figure 5: Mesh sensitivity

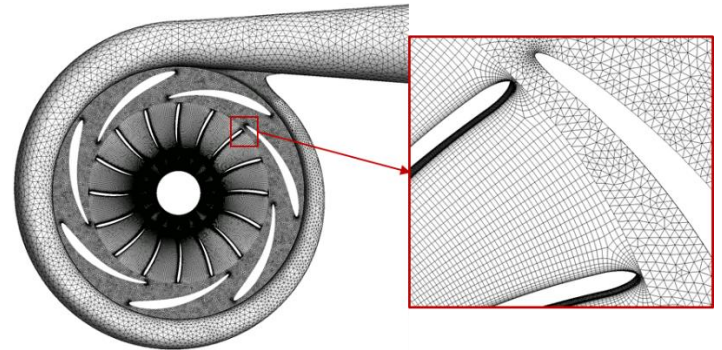


Geometric parameters	Values
Inlet diameter (m)	0.172
Outlet shroud Diameter (m)	0.072
Outlet hub diameter (m)	0.042
Number of blades	16
Average blade thickness (m)	0.00325
Axial Length (m)	0.051
Inlet Width (m)	0.0035

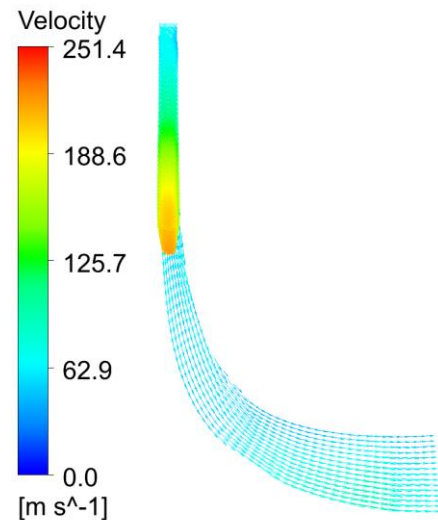
**Figure 6: Rotor geometric information**

Figure 7 shows the mesh model of the aerodynamic flow path including the volute, nozzle, and rotor. The numerical scheme employs a hybrid approach utilizing a combination of hexahedral and tetrahedral elements. Boundary conditions include total pressure at the inlet and pressure outlet. The model employs the steady-state moving reference frame to simulate the rotor rotation. The rotor zone is rotational with an assigned speed of 22,000 rpm. All other zones are stationary. K- $\omega$  SST turbulence model is employed. The pressure-velocity coupling is achieved using the SIMPLE scheme, a segregated solution method provided by Fluent. Convergence of the mass flow rate and outlet pressure are monitored to ensure the resulting residue is less than  $10^{-5}$ . Figure 8 shows the meridional velocity profile at design conditions, and Figure 9 shows blade-to-blade pressure and velocity profiles at 0.5 span. Figure 10 shows the entropy generation as a result of the fluid-structure interaction. Increased entropy represents the losses and contributes to the rotor performance degradation. Increased flow velocity on the suction side surface triggers the entropy generation that extends to the rotor zone. The increased surface area due to the curved design may have been the contributing factor that may need attention in further optimization of the nozzle. In the rotor passage, slight flow separation on the suction side of the blade further triggers and extends the entropy generation into the flow field. The blade loading profile on the suction side in Figure 11 shows this effect with a slight flattening of the suction side curve on the back half

of the blade. Figure 10 shows the off-design performance with the 22,000 rpm Speedline including efficiencies and shaft power at design. The design point seats on the right side of the performance curve to enable the desired efficiency outcomes over the wide range of flow conditions.



**Figure 7: Mesh model**



**Figure 8: Meridional velocity profile**

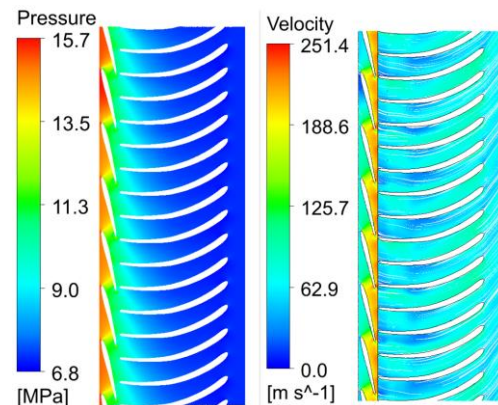


**Figure 9: Blade to blade pressure and velocity profiles at 0.5 span**



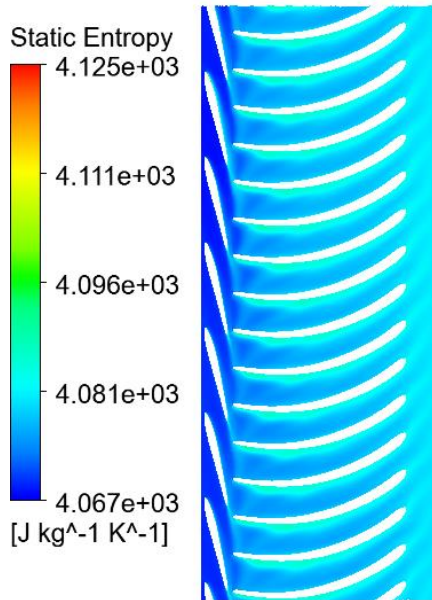


Figure 10: Entropy generation at 0.5 span

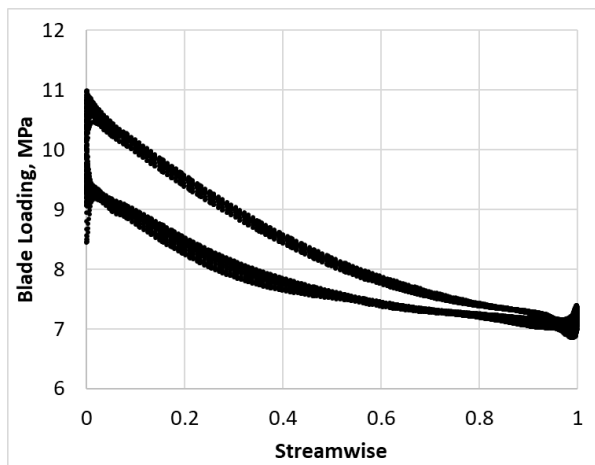


Figure 11: Blade loading at 0.5 span

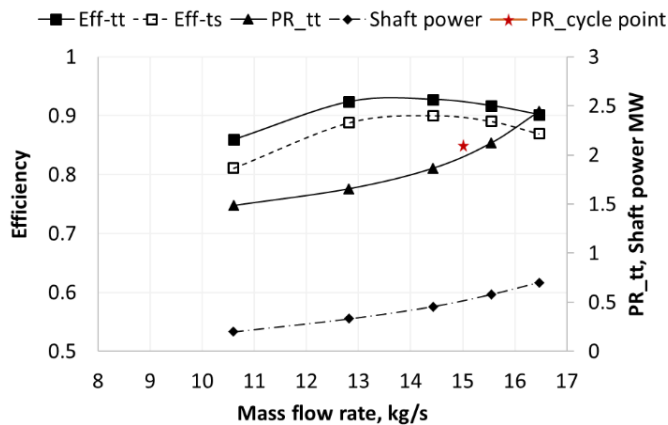


Figure 12: Performance map of the final design

## THRUST PREDICTION

Usually, single-rotor expanders are an overhung design with bearing support provided to handle radial and axial loads (Figure 13). For this design, The rotor support includes oil film bearings to keep dynamic operation below the first critical speed and fluid film thrust bearings to large thrust loads during off-design conditions. As discussed previously, the focus is to develop a modular design that allows for the interchangeability of aerodynamic parts (volute, nozzle, and turbine stage) without modifying the generator, gearbox, and rotor support. The expander-generator rig is sized for 3 MW. However, performance validation under a laboratory environment required scaling down the aerodynamic section from 3 MW to 0.5 MW with an entirely different specific speed design. The scaling was done based on the flow loop's ability to handle the maximum flow rate. The temperature, inlet pressure, and pressure ratio were kept the same to size the turbine for lab-scale testing. While the simulated design meets the performance criterion, the unknowns surrounding the start-up conditions and thrust information necessitated quantifying the full numerical performance.

Thrust estimation relies upon analytical calculations by summing pressure and impulse forces over rotor surface areas. Those methods don't necessarily include factors such as blade loading and effects of seal geometries, and the deviation can be significant leading to either oversized or undersized bearings. CFD modeling is a more reliable method to quantify the thrust predictions and optimize the thrust balance. The majority of research [12][13][14] on thrust prediction methods focused on pumping devices, specifically multistage pumps due to high accumulated axial thrust and spatial restrictions to provide support in downhole applications. As for the radial expanders, the only reported work by Huo et al [15] focuses on numerical modeling to predict the effect of balance holes on thrust reduction. This section will focus on developing a numerical model to predict thrust information for the design and off-design conditions and different rotational speeds. One of the objectives of this study is to help make an informed choice regarding the start-up control scheme for the turbine loop using thrust information for different rotational speeds. The numerical model is shown in Figure 14. The model includes volute geometry with actual inlet size, nozzle vanes, shrouded rotor, front and back seals, and the diffuser. Low-specific speed turbine experience efficiency degradation due to leakage flow through front and back seals. Figure 15 shows the cross section of the mesh model with enlarged front and back seals. The front seal is designed to minimize the leakage flow, specifically, the low specific speed expanders struggle with efficiency degradation due to induced leakage flow as a function of the high-pressure ratio. The numerical methods and boundary conditions follow the previous section's model. Boundary conditions also include constant back pressure from the back seal side. Figure 16 shows the resulting velocity vectors across the front seal. The direct impingement of flow from the seal cavity generates circulation regions that oppose and creates a blockage effect. This is anticipated to

minimize the leakage flow. The front seal also includes swirl brakes to minimize the tangential velocity component for improved rotordynamic performance.

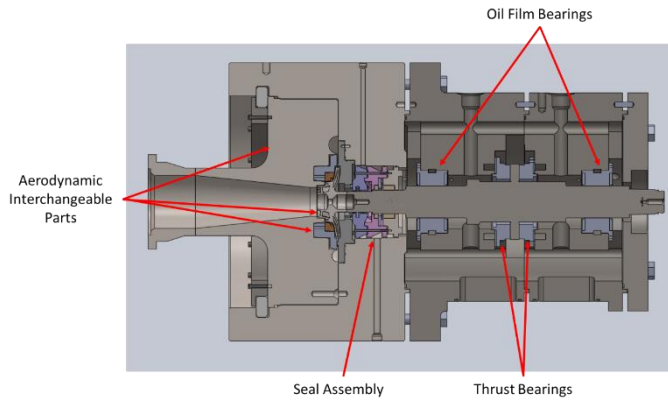


Figure 13: Designed expander section [10]

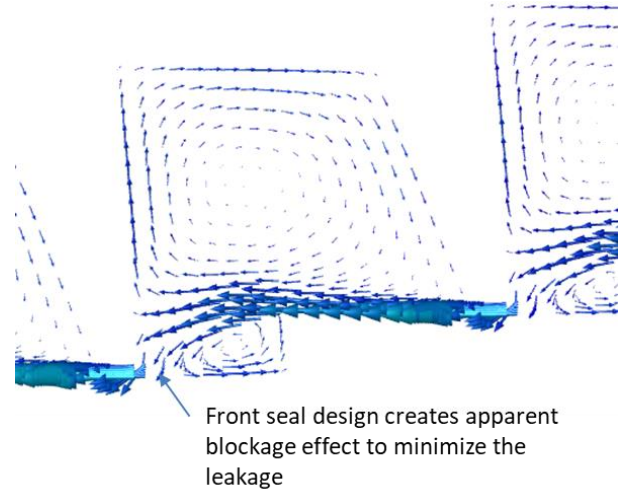


Figure 16: Velocity vectors in the front seal

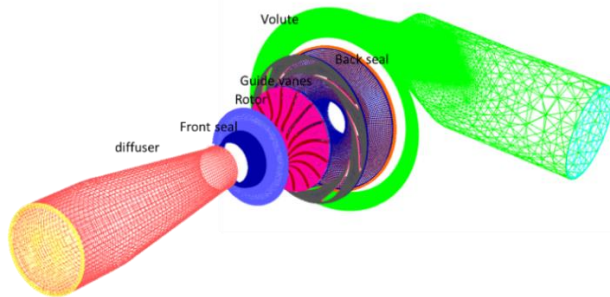


Figure 14: Numerical mesh model

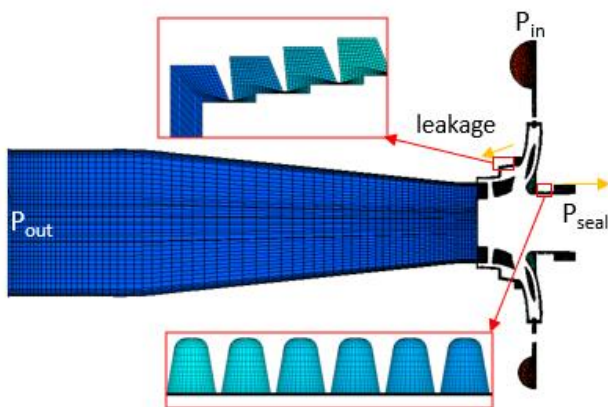


Figure 15: front back seal meshing

The front seal design creates an apparent blockage effect to minimize the leakage.

Figure 17 shows the pressure distribution across rotor surfaces. Thrust is estimated by summing all the forces in the axial direction. Figure 18 shows the performance change due to the leakage flow through the front and back seals. The efficiency of the turbine degrades due to leakage flow through the seal by about ~9% compared to the model without the leakage flow included. Also, the additional flow passing through the leakage would shift the efficiency plot. One of the challenges the current rotor will face is difficulty in manufacturing the narrow aerodynamic path and achieving the required level of surface roughness. Increased surface roughness would induce additional friction losses resulting in efficiency degradation. Additional simulation by including surface roughness predicts performance reduction by ~13% compared to the base model.

Figure 19 shows axial thrust values as a function of different rotational speeds. Increased surface area at outlet side enable thrust direction from outlet to inlet for all the speeds. Increased rotational speed and mass flow rate (pressure ratio) results in reduced thrust force.



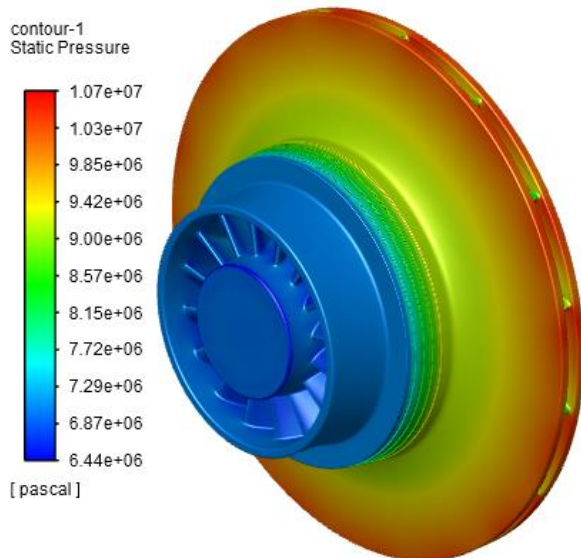


Figure 17: Pressure distribution

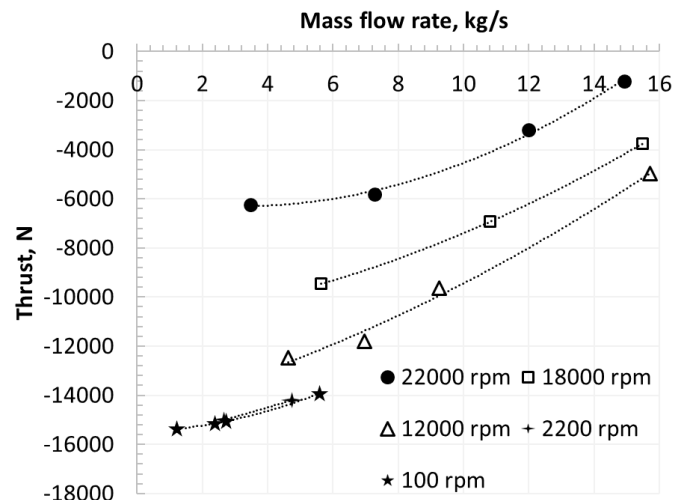


Figure 19: Thrust prediction at different rotational speeds

Initiating the turbine start-up can be challenging based on rotor configuration, weight, drag friction losses, and thrust load. The overall reactive load and torque outcomes from the performance data can be utilized to initiate the start-up and control mechanism.

### CONCLUSION

The study presented a low-specific speed expander design approach using pseudo 1D and 3D modeling methods and numerical demonstration of the performance at design and off-design conditions. The outcomes from numerical investigations revealed the aerodynamic performance of nozzle guide vanes and the rotor highlighting areas for design improvement. Overall, the performance map of the proposed expander design meets the desired efficiency metric for the extended flow range. The full numerical modeling helped develop an improved understanding of the performance change due to the flow leakage through the front and back seals and thrust change for the wide range of operating speeds and flow rate conditions. The analysis outcomes reveal the flow losses could be significant due to the disc friction, incidence, and leakage flow path for low specific speed designs (9-13 % reduction in efficiency compared to the numerical model without seals included). Due to increased rotor surface at the outlet side, upthrust force increases with a reduction in rotational speeds and flow rate conditions. The analysis outcomes are incorporated in start-up and control schemes for the experimental investigation of the expander-generator unit in a laboratory environment.

### ACKNOWLEDGEMENTS

This material is based upon work supported by Sage geosystems.

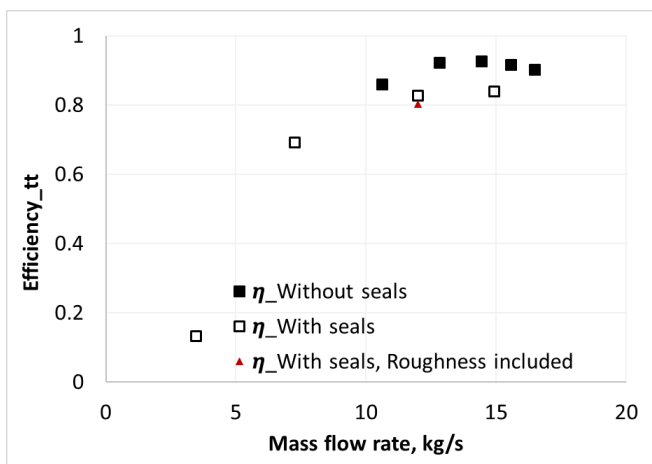


Figure 18: Total-to-total efficiency comparison

## REFERENCES

- [1] Bao J, Zhao L. A review of working fluid and expander selections for organic Rankine cycle. *Renew Sustain Energy Rev.* 2013;24:325–42.
- [2] Garg P, Kumar P, Srinivasan K, Dutta K. Evaluation of isopentane, R-245fa and their mixtures as working fluids for organic Rankine cycles. *Appl Therm Eng.* 2013;51:292–300.
- [3] Gong YL, Luo C, MA WB, WU ZJ. Thermodynamic analysis of geothermal power generation combined flash system with binary cycle, *Proceedings World Geothermal Congress, 2010, Bali, Indonesia; 25–29 April; 2010.*
- [4] Flegkas, S., Klemencic, G., Haider, M., Werner, A., & Leibinger, H. (2016). “Comparison of Conventional and CO<sub>2</sub> Power Generation Cycles for Waste Heat Recovery”, 1st European Seminar on Supercritical CO<sub>2</sub> (sCO<sub>2</sub>) Power Systems, Wien, Austria.
- [5] Wolf V., et al, 2022, “Investigation of sCO<sub>2</sub> Cycle Layouts for the Recovery of Low Temperature Heat Source” The 7th International Supercritical CO<sub>2</sub> Power Cycles Symposium, San Antonio.
- [6] Hansper, J., et. al., 2019, “Assessment of Performance and Costs of Co<sub>2</sub> based Geothermal Power Systems, 3rd European Conference on Supercritical CO<sub>2</sub> (sCO<sub>2</sub>) Power Systems
- [7] Katcher, K., et. al., 2021, “Estimated cost and Performance of a Novel sCO<sub>2</sub> Natural Convection Cycle for Low-grade Waste Heat Recovery”, The 4th European sCO<sub>2</sub> Conference for Energy Systems
- [8] <https://www.sagegeosystems.com/sage-meta-unlocking-the-potential-of-geothermal-for-clean-compact-renewable-baseload-power/>
- [9] Nielson, Jordan, Kelsi Katcher, and Douglas Simkins. 2022. “Techno-Economic Analysis of a Geothermal SCO<sub>2</sub> Thermosiphon Power Plant.” The 7th International Supercritical CO<sub>2</sub> Power Cycles Symposium.
- [10] Nielson J., and Weiss N., 2022, Sage Geosystems Proprietary sCO<sub>2</sub> Turbine Flow Loop Testing, GRC Transactions, Vol. 46, 2022
- [11] Baines, N. C., 2005, “Radial Turbines: An Integrated Design Approach,” *Proceedings of the 6th European Turbomachinery Conference - Fluid Dynamics and Thermodynamics*, Lille, France.
- [12] Salvadori, S., Marini, A., and Martelli, F., 2012, “Methodology for the Residual Axial Thrust Evaluation in Multistage Centrifugal Pumps,” *Eng. Appl. Comput. Fluid Mech.*, 6(2), pp. 271–284.
- [13] Zhou, L., Shi, W., Li, W., and Agarwal, R., 2013, “Numerical and Experimental Study of Axial Force and Hydraulic Performance in a Deep-Well Centrifugal Pump With Different Impeller Rear Shroud Radius,” *ASME J. Fluids Eng.*, 135(10), p. 10450
- [14] Patil, Abhay & Kasprzyk, Marie & Adolfo, Delgado & Morrison, Gerald. (2019). Effect of Pump Leakage Flow PATH Wear On Axial Thrust in Downhole ESP Unit. *Journal of Fluids Engineering.* 142. 10.1115/1.4045571.
- [15] Huo, C., Sun, J., Song, P., and Sun, S. (September 20, 2021). "Investigating the Influence of Impeller Axial Thrust Balance Holes on the Flow and Overall Performance of a Cryogenic Liquid Turbine Expander." *ASME. J. Eng. Gas Turbines Power.* October 2021; 143(10): 101014. <https://doi.org/10.1115/1.4051501>

## DESIGN OF COMPACT RADIAL TURBOEXPANDERS FOR sCO<sub>2</sub> POWER SYSTEMS

**Alessandro Romei**  
**Giacomo Persico\***  
Politecnico di Milano  
Milan, Italy

**Davide Biliotti**  
**Alberto Milani**  
Baker-Hughes Nuovo Pignone  
Florence, Italy

**Fabrizio Lottini**  
**Michele Marconcini**  
Università degli studi di Firenze  
Florence, Italy

### ABSTRACT

The development of novel conversion technologies for recovering waste heat is one of the technical goals of the European Commission, considering the large amount of thermal energy discharged by industrial processes in Europe. The recently launched EU-H2020 project CO2OLHEAT aims at contributing to industrial waste heat recovery by developing a novel sCO<sub>2</sub> power system of 2 MW power capacity. Considering the wide range of conditions featuring waste heat recovery applications (in terms of both flue gas temperature and flow rate), as well as the flexibility of operation required by such installations, a simple recuperative cycle was selected for the CO2OLHEAT plant. The system, however, features a relatively non-conventional multi-shaft configuration, composed of a radial-inflow turboexpander, which drives the near-critical compressor, and by an axial-flow turbine to generate the 2 MW output power.

The present study focuses on the design of the radial turbines of the CO2OLHEAT turbo-expander. Due to the low volumetric flow rate, the turbine features small size and, therefore, significant aerodynamic challenges have to be considered in the design process. A preliminary design of the machine was performed by applying a mean-line approach, then a conceptual design of the bladings and of the meridional channels was performed by resorting to industrial in-house database and criteria. Once the turbine design was finalized, the aerodynamics and performance of the machine were evaluated by applying two different computational fluid dynamic simulation tools, which exhibit remarkable agreement.

One CFD tool was then used to investigate and quantify the impact of wheel tip clearance and surface roughness, as well as to quantify the deviation with respect to mean-line predictions. Relevant quantitative data are extracted as well as aerodynamic indications are inferred, with the aim of establishing a reference for the future design of compact sCO<sub>2</sub> radial turbines.

### INTRODUCTION

The industrial sector in Europe releases in the environment a large amount of waste heat, as a result of the thermal processes involved in the production of cement, glass, steel, etc. The flue gases discharged by such processes are released in a wide temperature range and could be efficiently and effectively converted into useful mechanical or electrical energy. On the quantitative ground, considering recent statistics on waste heat not exploited [1], and assuming an average conversion efficiency of 25% with an operating factor of 0.8, the conversion of 5% of the European waste heat would lead to more than 500 GWh of primary energy savings per year and, assuming 0.46 tCO<sub>2</sub>/MWh, it would avoid more than 100.000 tons of CO<sub>2</sub> per year. It would also provide important economical relapses, further enhanced by the recent severe increase of fossil-fuel prices.

Mature technologies are presently available for waste heat recovery and conversion, in particular Organic Rankine Cycles and conventional Steam Rankine Cycles; however, the former guarantee effective performance especially for flue gas temperature below 300°C, while the latter are best optimized for flue gas temperature above 500°C. As a result, in the temperature range 300-500°C, which represents a large share of the overall available waste heat, alternative technologies might provide better effectiveness, both technically and economically. Among them, closed Joule-Brayton thermodynamic cycles working with carbon dioxide in supercritical conditions (sCO<sub>2</sub>) are particularly attractive due to the expected cycle efficiency and the overall system compactness, which might foster fast response to transients and reduced footprint, crucial features for effective waste-heat recovery systems [2].

Even though advanced calculations were performed at both system ([3], [4]) and component ([5], [6], [7], [8]) level, and the first experimental verification of components have given promising outcomes (especially for the compressor, see [9], [10]), a proper demonstration of the overall system operation in the real environment is still needed. To this end, the EU-H2020 project CO2OLHEAT (Supercritical CO<sub>2</sub> power cycles demonstration in Operational environment Locally valorising

\* corresponding author: giacomo.persico@polimi.it

industrial Waste Heat) was launched in 2021, with the aim of developing a novel sCO<sub>2</sub> power system demonstration plant of 2-MW capacity, to be installed and operated in a real industrial environment, recovering waste heat from flue gases released at about 400 °C. By considering the flue gas conditions, as well as the required flexibility of operation, a simple recuperative sCO<sub>2</sub> cycle has been selected for the CO2OLHEAT system, with the sCO<sub>2</sub> compressor powered by a radial turboexpander and a subsequent axial turbine for electrical power generation.

The present study focuses on the design of the sCO<sub>2</sub> radial turbines used to drive the CO2OLHEAT compressors, which combined constitute the turbo-expander unit of the system. The design of sCO<sub>2</sub> turbines has to face different challenges with respect to sCO<sub>2</sub> compressors. The fluid, even though highly pressurized, is usually in a thermodynamic state sufficiently far from the critical point, so that the ideal-gas model becomes accurate to represent the fluid behavior and no phase change process can occur. The limited overall pressure ratio (of the order of 3–4 for sCO<sub>2</sub> systems, and 2.55 in the present case) combined with the multi-stage configuration greatly limit the Mach number, avoiding transonic effects. This, however, does not make the design of these machines straightforward: the high density of the fluid has relevant implications on aerodynamics (low aspect ratio bladings, high leakage flow rates in the seals), structural integrity (high aerodynamic forcing), and rotordynamics (high vibration and stress in the bearings) [11]; the combination of high temperature and high density makes critical the selection of the material for blades and casing [12].

The relative weight of these features changes depending on the turbine architecture, so the preliminary selection of the machine configuration is crucial to construct a turbine design tailored to sCO<sub>2</sub> applications. As discussed in the next section, the characteristics of the thermal source, preliminary considerations on the primary heat exchanger, and the thermodynamic optimization of the cycle led to select the turbine intake state at 216.9 bar and 360°C. Given the small power capacity, the low volumetric flow rate, and the limitations in angular speed, statistical and similarity considerations recommend selecting a radial-inflow architecture for these turbines. The two resulting turbines were, therefore, designed by leveraging the Baker Hughes experience on expanders, with a special focus on structural and rotordynamic aspects; however, the compactness of the machine suggested investigating the impacts of the tip clearance and wall roughness.

The paper reviews the turbine design process and it is structured as follows: at first the CO2OLHEAT system is presented and the turbine configuration is described; then, the turbine aerodynamics and performance are analysed by discussing the results of three computational models, namely one mean-line and two CFD simulation tools, to provide a multi-fidelity perspective of the turbine operation. Then, size effects related to tip clearance and wall roughness are analysed and quantitatively discussed.

## CO2OLHEAT POWER UNIT

The CO2OLHEAT power unit was conceived to recover waste heat from an existing cement plant, whose flue gases in nominal conditions are available at temperature of 400°C and with a flow rate of 230,000 Nm<sup>3</sup>/h. The core of the system is a simple recuperated cycle without either recompression or recuperator bypass, due to the relatively low maximum temperature of the heat source and the high minimum stack temperature to avoid acid condensates (150°C). As reported in Figure 1, in the overall system the power unit is complemented by a waste-heat recovery unit and by a water-based heat-rejection unit.

The thermodynamic optimization of the sCO<sub>2</sub> cycle led to setting the compressor-intake thermodynamic conditions at 32°C and 85 bar respectively, to properly exploit the high density of CO<sub>2</sub> in the proximity of the critical point. The compressor-outlet pressure is set to 216.9 bar, resulting from a trade-off between cycle performance, material selection, and cost. The resulting cycle pressure ratio is equal to 2.55, which is obtained by two centrifugal compressors in series; they are mechanically driven by two centripetal turbines in series, thus creating a compact turbo-expander unit. The maximum temperature of the cycle is set at 360°C, namely 40°C lower than the flue gas nominal temperature in order to limit the surface area of the primary heat exchanger. The expansion is completed in an axial turbine, which is responsible for the power output of the system.

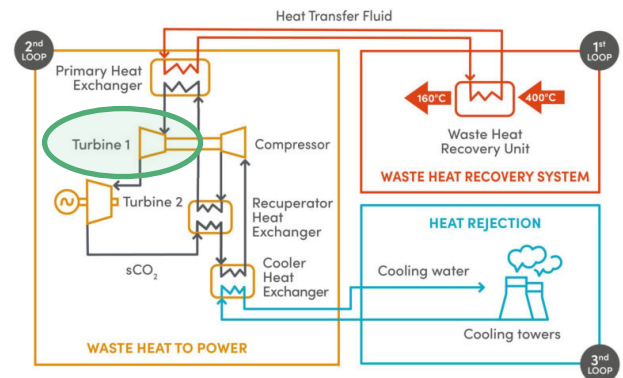


**Figure 1:** CO2OLHEAT concept – the focus is on turbine 1 (turboexpander).

The resulting net power output exceeds 2 MW, with a cycle efficiency of 23.2% referred to the inlet thermal power. Full details on the CO2OLEAT power system design and off-design operation can be found in [13].

## MACHINE ARCHITECTURE

The optimization of selected thermodynamic cycle requires the compressor to operate between 85 and 216.9 bar with inlet conditions very close to CO<sub>2</sub> critical point (32°C, 670 kg/m<sup>3</sup>). The inlet conditions of the expander that will drive the compressor are consequently at 210.0 bar, 360°C. Actual process conditions and demo site available power lead to compact machine size with compressor impeller diameter lower than 150

mm and a rotating speed close to 20,000 RPM, and an expander impeller diameter in the range of 160-170 mm and a rotating speed close to 12,500 RPM. To minimize the impact of internal leakages and to manage residual axial thrust, an integrally geared configuration has been selected, which includes two shaft, one dedicated to compression section and one to expansion phase.

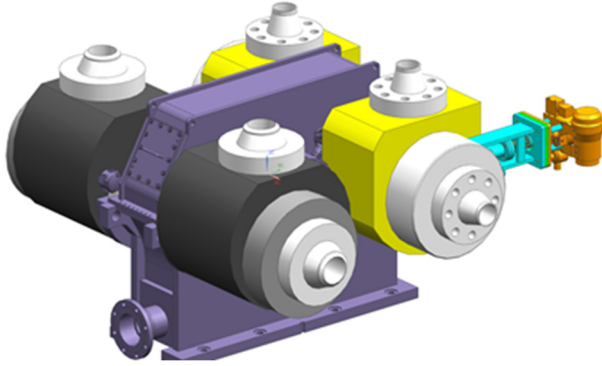


**Figure 2:** Machine schematic  
© 2022 Baker Hughes Company - All rights reserved

The overall pressure ratio, for both compressor and expander, has been split into two stages in back-to-back arrangement. First compression phase is equipped with movable axial inlet guide vane (IGV) to guarantee a fine tuning of the suction operating condition, and to improve compressor flexibility in off-design conditions. No movable nozzles are provided at the inlet of the two expander stages. The integrally geared arrangement has a starter motor connected to the low-speed shaft. To maintain the operating speed of the machine constant during operation, the electric motor will take care of around 20% of the compressor absorbed power, acting as a helper motor. The remaining power, to sustain the compressor, will be provided by the expander wheel.

**TURBOEXPANDER DESIGN**

The design of the turbo-expander is realized by Baker Hughes. The first step is turbine selection. From the boundary conditions of the machine, the size and rotational speed of the turbo-expander are calculated. This phase relies on correlations and graphs proprietary of Baker Hughes. In particular, the expected efficiency  $\eta_{TS}$  of the machine is a function of the specific speed  $N_s$ , defined as:

$$N_s = \frac{N\sqrt{Q_{t5}}}{\Delta h^{3/4}} \tag{1}$$

The relationship between the efficiency  $\eta_{TS}$  and the specific speed  $N_s$  is shown in Figure 3. There is an optimum value of the specific speed, which guarantees the best performance. In particular, the specific speed value is selected where the stage performance curve is flat. Once a suitable value of  $N_s$  is chosen, the rotational speed  $N$  is known.

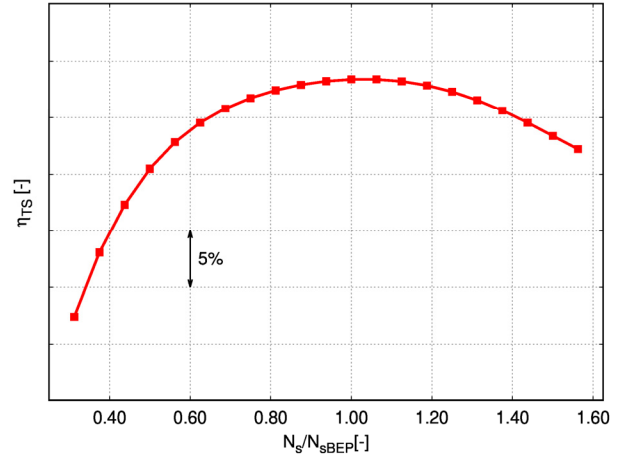


**Figure 3:** Efficiency  $\eta_{TS}$  as a function of the specific  $N_s$   
© 2022 Baker Hughes Company - All rights reserved

The specific speed is experimentally connected to the ratio  $u/c$ , where  $c$  is the spouting velocity, defined as:

$$c = \sqrt{2 \cdot (h_{t0} - h_{5,is})} \tag{2}$$

This quantity corresponds to the flow velocity if the entire enthalpy drop was realized by the nozzle vanes.

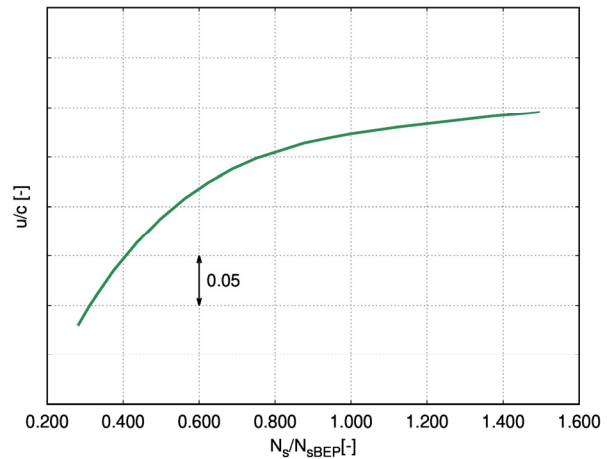


**Figure 4:**  $u/c$  ratio as a function of the specific speed  $N_s$   
© 2022 Baker Hughes Company - All rights reserved

With the specific speed value it is possible to enter the graph in Figure 4 to obtain a value of the ratio  $u/c$ . Since the isentropic enthalpy drop of the stage and the rotational speed are known, a value for the wheel outer diameter  $D_3$  can be calculated. The boundary conditions together with the information derived from the selection phase ( $N, D_3, \eta_{TS}$ ) constitute the input required by the Baker Hughes preliminary design tool. This tool



uses a 1D analysis of the turbo-expander stage to generate the geometry for the nozzle vanes and the wheel. The stage geometry is designed to ensure a negative incidence angle on wheel blades, an almost axial flow at the rotor outlet, and an optimal value for the ratio between the wheel outlet hub diameter and the rotor outer diameter  $D_{5h}/D_3$ . Further details on the preliminary design tool are reported in [14]. A simple convergent profile is designed for the nozzles because of low expansion ratios. Figure 5 shows a view of the geometry generated for the present activity.



**Figure 5:** Three-dimensional view of the stage geometry  
© 2022 Baker Hughes Company - All rights reserved

## NUMERICAL METHODS

In this section, the numerical methods that are used to carry out the design and performance analysis of the radial turboexpander are discussed.

### Mean-Line Model

A mean-line model is used to estimate the performance of the turbine at a preliminary stage. The tool is written in *python* language, making use of its library and modules for root-finding algorithms and minimization. The thermodynamic and flow conditions at each section along the machine are computed at the mean-line in the stage meridional plane and are representative of mass-weighted averaged conditions over the whole section.

The tool focuses on the modelling of nozzles, the nozzle-rotor interspace, and the rotor. Figure 6 shows a scheme of the radial turbine flow path illustrating the main sections, the terminology, and the symbols used in the following.

The thermodynamic and flow conditions at the main sections in the stage are calculated by solving simultaneously the mass continuity, the energy balance, and the loss equations. The fluid properties are computed using the real gas modeling of the REFPROP library [15]. The following working input variables are required by the mean-line model: inlet total pressure  $p_{t0}$ , inlet total temperature  $T_{t0}$ , outlet static pressure  $p_{s5}$ , rotational speed  $N$ , tip clearance if present, number of nozzles  $Z_N$  and wheel blades  $Z_W$ . Moreover, the code takes input also from the geometry of the stage, described with the nozzles profiles, the wheel blade profiles at the hub and tip sections, and the stage flow path. For each section along the stage, a system of equations is resolved. The first set of equations is applied to the nozzle throat section, and consists of the following equations:

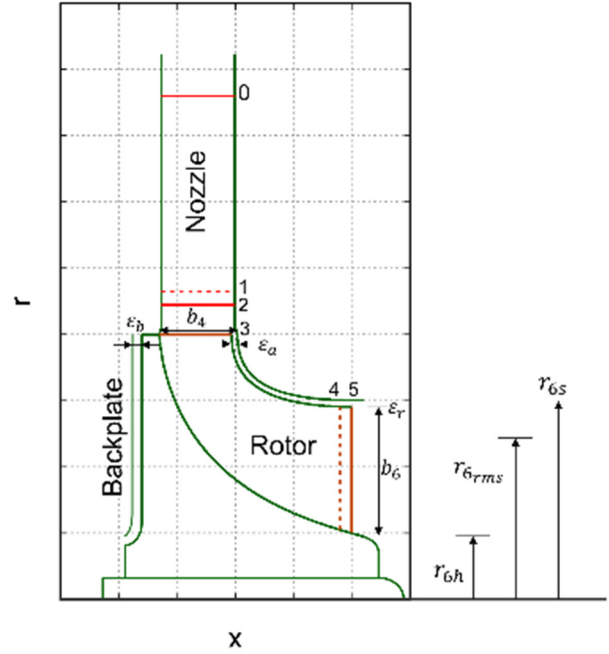


**Figure 6:** Schematic flow path of a radial in-flow  
© 2022 Baker Hughes Company - All rights reserved

$$c_1 = \frac{\dot{m}}{\rho_1 \cdot A_1 \cdot (1 - BF_1)} \quad (3)$$

$$h_1(\rho_1, T_1) = h_{t0} - \frac{1}{2} c_1^2 \quad (4)$$

$$\sum_1^{n_L} \Delta h_{loss,n} + h_{1,ts}(p_1, s_0) - h_1(\rho_1, T_1) = 0 \quad (5)$$

The term  $\Delta h_{loss,n}$  represents the specific loss contribution in the blade row, which is calculated through an empirical correlation. All the loss correlations used in the model are reported in Table 1. The flow angle in section 1 for the nozzle is predicted using the cosine rule:

$$\alpha_1 = \cos^{-1}(o_1/s_1) \quad (6)$$

where  $o_1$  is the nozzle throat opening and  $s_1$  is the vane circumferential spacing.

The nozzle vanes resolution is based on the continuity (3), the equation of energy (4), and the loss equation (5). This system of equations can be graphically described by Figure 7.

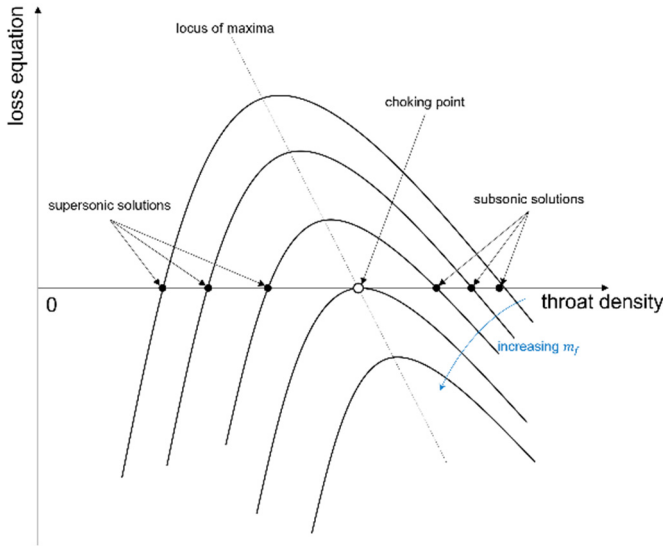


**Figure 7:** Solutions for a blade row section in the mean-line model.

Each curve in the graph of Figure 7 refers to a given mass flow rate. As the mass flow rate increases, the curve shifts downward. For a very high mass flow rate, the curve lays entirely below the x-axis, meaning that no solutions can be found. The choke condition corresponds to the curve being tangent to the 0 of the loss equation. For higher values of the mass flow rate, two solutions can be found. The solutions that are on the left with respect to the curve maximum refer to the supersonic solutions, which are not physical since the model only considers convergent profiles. The solutions on the right side of the curve maximum are the subsonic solutions, so they represent the actual solutions of the system.

If the nozzle vanes are choked, a post-expansion takes place after the nozzle throat. In this case, the energy and mass balances and the post-expansion loss equation are solved, respectively as follows:

$$c_2 = \sqrt{2 \cdot (h_{t0} - h_2(p_2, \rho_2))} \quad (7)$$

$$\alpha_2 = \cos^{-1} \left( \frac{m}{\rho_2 \cdot c_2 \cdot A_1 \cdot (1 - BF_1)} \right) \quad (8)$$

$$\Delta h_{pe_N} + h_{2is}(p_2, s_1) - h_2(\rho_2, p_2) = 0 \quad (9)$$

After the nozzle, the flow continues its expansion in the vaneless space before entering the wheel. The expansion in this interspace can be modelled using the following set of equations:

$$c_3 = \frac{\dot{m}}{\rho_3 \cdot \cos \alpha_3 \cdot A_3 \cdot (1 - BF_3)} \quad (10)$$

$$\frac{c_2 \cdot \sin \alpha_2}{c_3 \cdot \sin \alpha_3} = \frac{r_3}{r_2} + \frac{2\pi C_f \cdot \rho_3 c_3 \sin \alpha_3 (r_2^2 - r_2 r_3)}{\dot{m}} \quad (11)$$

$$h_3(\rho_3, T_3) = h_{t0} - \frac{1}{2} c_3^2 \quad (12)$$

$$\Delta h_{loss_{VS}} + h_{3is}(p_3, s_2) - h_3(\rho_3, T_3) = 0 \quad (13)$$

Equation (11) represents the Stanitz correlation [16] for the correction of the flow angle in the conservation of the momentum.

The set of equations for the rotor resolution is the same as the nozzle vanes, but referred to the relative frame:

$$w_4 = \frac{\dot{m}}{\rho_4 \cdot A_4 \cdot (1 - BF_4)} \quad (14)$$

$$h_4(\rho_4, T_4) = I_3 - \frac{1}{2} w_4^2 + \frac{1}{2} u_4^2 \quad (15)$$

$$\sum_1^{n_L} \Delta h_{loss_W} + h_{4is}(p_4, s_3) - h_4(\rho_4, T_4) = 0 \quad (16)$$

where  $I = h + \frac{1}{2} w^2 - \frac{1}{2} u^2$  is the rothalpy. The term  $\Delta h_{loss,r}$  represents the specific loss contribution in the rotor, which is calculated using empirical correlations for each loss source described in Table 1. The exit relative flow angle in section 4 is evaluated using the cosine rule:

$$\beta_4 = \cos^{-1}(o_4/s_4) \quad (17)$$

where  $o_4$  is the wheel throat spacing and  $s_4$  is the rotor pitch at the throat section. In case of the rotor choking point is reached, the mass flow rate is kept constant, and the nozzle operation is fixed since any further expansion downstream of the wheel cannot affect the conditions upstream of the rotor throat.

In this case of a choked rotor, any further expansion is allowed by means of a post-expansion process after the wheel throat, which is resolved using the following set of equations:

$$w_5 = \sqrt{2 \cdot (I_4 - h_5(p_5, \rho_5)) + u_5^2} \quad (18)$$

$$\beta_5 = \cos^{-1} \left( \frac{m}{\rho_5 \cdot w_5 \cdot A_4 \cdot (1 - BF_4)} \right) \quad (19)$$

$$\Delta h_{pe_W} + h_{5is}(p_5, s_4) - h_5(\rho_5, p_5) = 0 \quad (20)$$

Loss source	Loss model	Reference
Nozzle passage	$\Delta h_{pl, noz} = K_{p1} \frac{0.05}{Re_1^{0.2}} \left[ \frac{3 \tan \alpha_1}{\sigma_1/c_n} + \frac{\sigma_1 \cos \alpha_1}{b_1} \right] \frac{1}{2} c_1^2$	Rodgers [17]
Nozzle trailing edge	$\Delta h_{te,N} = \left( \frac{Z_n t_2}{2\pi r_2 \cos \alpha_2} \right)^2 \frac{1}{2} c_2^2 \cdot Y_2$	Glassman [18]
Nozzle post-expansion	$\Delta h_{pe,N} = \left( \frac{M_2 - M_1}{M_2} \right)^2 \frac{1}{2} c_2^2 \cdot \frac{1}{Y_2}$	Aungier [19]
Interspace	$\Delta h_{vs} = K_{vs} C_f \left( \frac{L_{vs}}{D_{vs}} \right) \frac{1}{2} (c_2 + c_3)^2$	Kastner and Bhinder [20]
Rotor incidence	$\Delta h_{inc,W} = K_{inc} (\sin  \beta_3 - \beta_{3,opt} )^2 \frac{1}{2} w_3^2$	Baines [21]
Rotor passage	$\Delta h_{pl,W} = K_p \left\{ K_{p2} \left( \frac{L_H}{D_H} \right) + 0.68 K_{p3} \left[ 1 - \left( \frac{r_{4rms}}{r_3} \right)^2 \right] \left( \frac{\cos \beta_4}{b_4/ch_W} \right) \right\} \frac{1}{2} (w_3^2 + w_4^2)$	Baines [21]
Rotor clearance	$\Delta h_{cl} = \frac{u_3 Z_W}{8\pi} (K_a \varepsilon_a C_a + K_r \varepsilon_r C_r + K_{ar} \sqrt{\varepsilon_a \varepsilon_r C_a C_r})$	Baines [21]
Rotor trailing edge	$\Delta h_{te,W} = \left( \frac{Z_W t_5}{\pi (r_{5s} + r_{5h}) \cos \beta_5} \right)^2 \frac{1}{2} w_5^2 \cdot Y_5$	Glassman [18]
Rotor disk friction	$\Delta h_{df} = 0.25 K_f \frac{\bar{\rho} u_3^3 r_3^2}{\dot{m}}$ where $\bar{\rho} = \frac{\rho_3 + \rho_5}{2} Re_4 = \frac{\rho_3 u r_3}{\mu_3}$	Aungier [19]
Rotor post-expansion	$\Delta h_{pe,W} = \left( \frac{M_{5rel} - M_{4rel}}{M_{5rel}} \right)^2 \frac{1}{2} w_5^2 \cdot \frac{1}{Y_5}$	Daily and Nece [22]

**Table 1:** Loss models for a radial in-flow turbine.

The loss models are summarized in Table 1. Details on the values of loss coefficients  $K_i$  reported in Table 1 can be found in [23] and [24]. The validation of the mean-line model based on several experimental test cases available in literature is described in [23].

### TRAF Code

The TRAF code is a RANS/URANS viscous multi-block flow solver for the 3D Reynolds-averaged Navier-Stokes equations developed at the University of Florence [25]. Real gas behavior can be modelled by providing gas property tables generated offline [26]. Steady-state analyses with a perfect gas model are carried out in the present activity. Uniform total pressure and total temperature distributions of a radial inflow are applied at the domain inlet section. A static pressure value is applied at the hub radius of the domain outlet section and the radial equilibrium is used to obtain the spanwise pressure distribution. The rows coupling is handled by means of a mixing plane. The code has been previously used to calculate subsonic and supersonic turbo-expander stage flows [27] [28] [14].

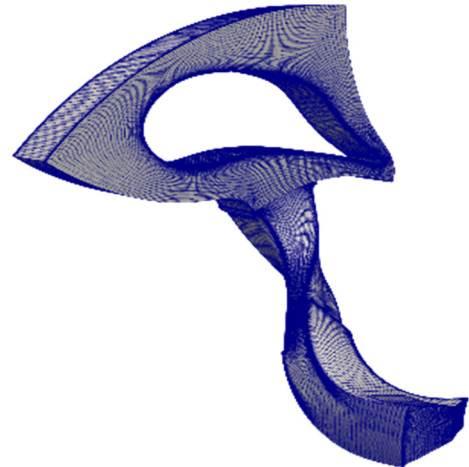


**Figure 8:** CFD grid for TRAF calculations.  
© 2022 Baker Hughes Company - All rights reserved

The convective fluxes are resolved using a 2nd order TVD-MUSCL strategy built on top of the Roe's upwind scheme [29].

The high-Reynolds formulation of the Wilcox  $k - \omega$  model [30] is used for the turbulence closure.

The CFD grid is composed of about 4.5 M cells. An O-type structured grid of  $\sim 3$  M is adopted for the nozzle vane, while a  $\sim 1.4$  M H-type structured grid is used for the rotor passage. The first cell distance from the wall is imposed to ensure a  $y^+ < 1$  on solid walls. The fillets on the wheel blades are included in the model. Figure 8 shows the computational grid investigated by the CFD simulations.

### CFD – POLIMI

The computational flow model is based on the ANSYS-CFX finite-volume flow solver, using high-order numerical schemes for both inviscid and viscous fluxes. Turbulence effects are introduced by resorting to the  $k - \omega$  SST model assuming fully turbulent flows. Whenever walls are modelled as smooth, the turbulence equations are resolved at the wall having wall-adjacent cells in the viscous sublayer, i.e.  $y^+ \sim 1$ . Otherwise, wall functions are employed to account for roughness effects.

In the thermodynamic conditions of interest, CO<sub>2</sub> behaves as a polytropic ideal gas (compressibility factor  $\sim 1.0$ ). Therefore, the perfect gas model with  $\gamma = c_p/c_v = 1.181$  is employed for the thermodynamic properties. Due to the small temperature drop across the expansion, constant values for the transport properties are assigned. A comparative assessment was carried out using look-up tables built on the basis of real-gas property estimates by REFPROP. Deviations below 0.1% confirmed the suitability of the perfect gas model as a thermodynamic model for subsequent analyses.

Radial inward flow is prescribed at the nozzle inlet together with total pressure and temperature. No-slip and adiabatic boundary conditions were imposed on the solid walls. A static pressure is specified at the midspan outlet radius, imposing a pressure distribution along the span that complies with the radial equilibrium. A mixing-plane interface is placed halfway between the nozzle and the wheel. Across this interface, the velocity from the nozzle outlet is circumferentially averaged and passed as an inlet boundary condition to the wheel inlet together with the averaged static pressure. The circumferential average enables the simulation of a single nozzle and wheel passage by imposing periodic boundary conditions likewise to the computational domain reported in Figure 8.

Both nozzle and wheel mesh are generated with Ansys Turbogrid and are made of hexahedral elements. The computational grid of the wheel includes fillets. Whenever an open wheel is simulated, the clearance gap is discretized with 35 grid points with proper cell clustering near walls to account for the viscous sublayer. A dedicated grid study has shown that a nozzle mesh composed of 2.5 million cells plus a wheel mesh composed of 3.1 million cells provide a grid convergence index for the total-to-total efficiency equal to 0.10%.

### TURBINE PERFORMANCE

In this section, the performance of the high-pressure turbine that will be part of the CO2OLHEAT demo plant is discussed. In the early stages of the design phase, an open wheel was taken

into consideration because of the medium temperature level combined with the small size. A shrouded design was ultimately selected after a careful assessment of stresses and corresponding deformations. The high-pressure and low-pressure stages feature similar design aspects and performance, therefore only the high-pressure turbine will be discussed.

Figure 9 reports the trend of total-to-static efficiency and the ratio  $u/c$  across the flow range. CFD results are obtained by extracting mass-weighted averages of relevant quantities from corresponding sections as illustrated in Figure 6. The only exception is the static pressure, for which the area-weighted average is considered. The two independent CFD studies agree remarkably well in predicting both  $\eta_{TS}$  and  $u/c$ . Differences are below 0.2%, fostering our confidence in the numerical results.

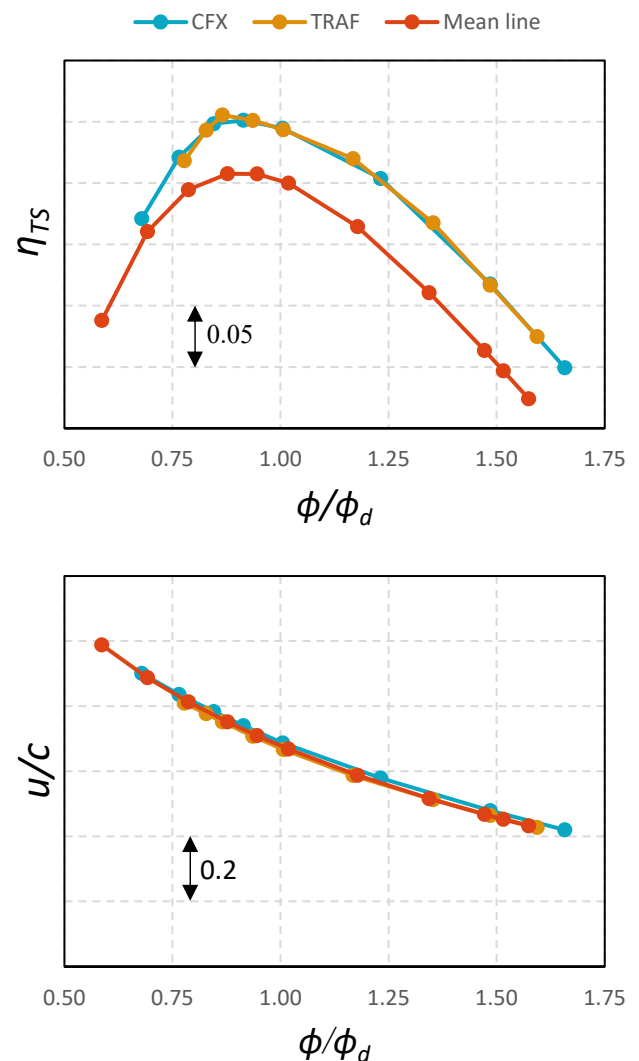


**Figure 9:** Total-to-static efficiency and  $u/c$  ratio across the normalized flow range as predicted by two independent CFD studies (different codes and meshes) and by the mean line.

© 2022 Baker Hughes Company - All rights reserved

Looking at CFD trends, it can be noted that, even when the flow rate increases by 75% with respect to the nominal one, the turbine is not choked. This is due to the relatively small expansion ratio across the turbine, which in turn elaborates a subsonic flow ( $M < 0.3$ ), as highlighted by the Mach number field in Figure 10. Therefore, the efficiency keeps reducing almost linearly after  $\phi/\phi_a > 1.25$ , with an efficiency drop of 10% for each 25% flow increase. The peak efficiency is at  $\phi/\phi_a \sim 0.9$ . This choice allows a higher efficiency at part load conditions, for which the efficiency drop is more pronounced than the one at higher flow rates.

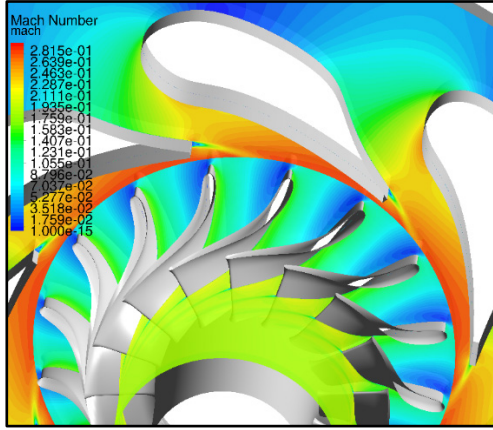


**Figure 10:** Flow fields in terms of relative Mach number at midspan in nominal conditions.

© 2022 Baker Hughes Company - All rights reserved

Finally, the mean line predicts trends across the flow range that are consistent with the CFD predictions, but it returns comparably smaller efficiencies, which are reduced by 5% percent. Opposed to such efficiency discrepancy, the trend  $u/c$  is well reproduced by the mean line model. It is worth noting that  $u/c$  is directly correlated with the internal aerodynamics that is simulated via CFD calculations, while the mean-line efficiency includes additional loss sources which occur outside the CFD domain, namely disk and casing friction. Therefore, the good matching between CFD and mean-line in predicting  $u/c$  serves as verification of the mean-line tool, which can be then used to have a more realistic representation of the stage efficiency by including external loss mechanisms.

### SIZE EFFECTS (CLEARANCE AND ROUGHNESS)

Owing to the small size of sCO<sub>2</sub> turbines, the effect of non-scalable geometrical parameters, such as roughness and, possibly, clearances, are expected to significantly affect the turbine efficiency. In this section, such classes of efficiency penalties are quantified, by considering four cases:

- Open wheel with  $\varepsilon_r/D_{wheel} = 0.03$ , smooth walls
- Shrouded wheel, smooth walls
- Open wheel with  $\varepsilon_r/D_{wheel} = 0.03$ , rough walls with  $k_s = 5 \mu\text{m}$

- Shrouded wheel, rough walls with  $k_s = 5 \mu\text{m}$

This study is undertaken by using the CFD tool based on ANSYS-CFX. Each case corresponds to a different wheel mesh: open wheels require the introduction of the tip clearance and the corresponding geometrical discretization, while wall functions accounting for roughness ask for a first-cell distance from the wall compatible with the roughness level. The cell distribution in the free stream is retained among different cases.

Figure 11 reports the total-to-total efficiency for the four examined cases. Both roughness and tip clearance appreciably affect the efficiency. The shrouded design, which was eventually selected for the CO2OLHEAT project after a considerable effort to ensure structural reliability, has an efficiency that is 3.6% higher than the unshrouded counterpart. Regarding the roughness, the indicated value is just a representative value for the roughness level and not indicative of the manufacturer's capabilities. Nonetheless, the viscous sublayer is estimated to be of the order of  $10^{-3} - 10^{-2} \mu\text{m}$ , thus one might expect that, in this kind of machine, the surface roughness will alter the development of the boundary layer and the associated entropy generation. For this specific study, it was found that a sand-grain roughness of  $5 \mu\text{m}$  produces a 2.3% of efficiency drop. This result confirms that roughness effects can be significant and suggests care in the selection of the manufacturing process.

The analysis is extended by decomposing each component contribution to overall loss. The following loss coefficients are introduced for the nozzle and wheel, respectively:

$$\Delta\eta_N = \frac{h(P_{t2}, S_2) - h(P_{t2}, S_0)}{h_{t0} - h_{t6, is}} \quad (21)$$

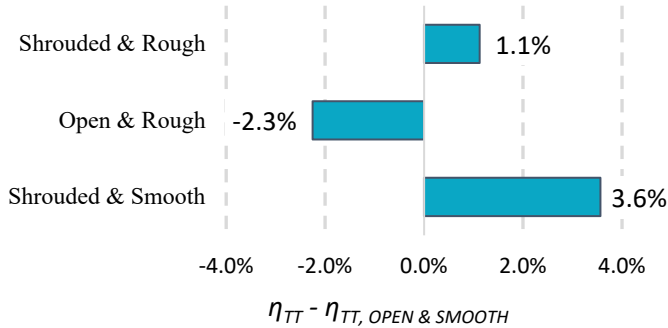
$$\Delta\eta_W = \frac{h(P_{t6}, S_6) - h(P_{t6}, S_2)}{h_{t0} - h_{t6, is}} \quad (22)$$

Figure 12 reports the loss coefficients for the four examined cases. Leaving aside the cases with open wheels, for which the tip clearance loss dominates in the overall loss generation, the largest share of entropy is however generated in the wheel, which is responsible for an efficiency reduction of 0.9-1.5 percentage points more than the nozzle depending on smooth/rough wall modelling, respectively. Besides friction loss, which prevails in the wheel because of the larger wetted surface, the analysis of the flow field reveals a flow separation along the wheel suction side at 75% of the span. Further, the negative incidence generates a small flow separation after the leading edge on the pressure side. Nonetheless, the generated entropy is relatively small compared to the suction-side separation, and the flow reattaches almost immediately.

Finally, comparing the flow fields between roughness- and smooth-wall simulations, secondary flow structures do not change, and the increase of entropy by adding roughness is



provided by an increase in the profile loss due to boundary-layer thickening. Consistently, the roughness raises wheel losses more than nozzle losses because of the larger wetted surface of the former than the latter.



**Figure 11:** Variations in total-to-total efficiency by introducing the roughness and tip clearance.

© 2022 Baker Hughes Company - All rights reserved

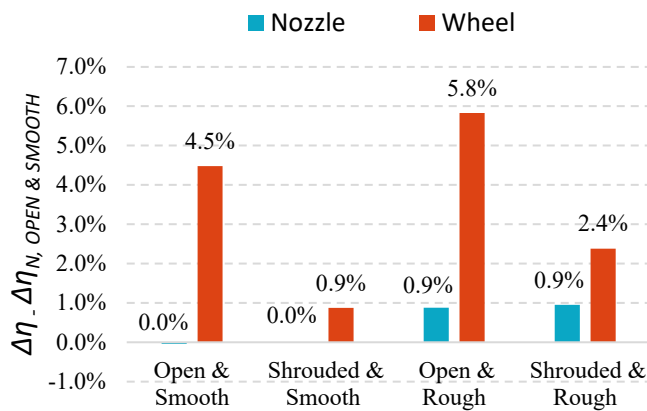


**Figure 12:** Loss decomposition in nozzle and wheel for the examined cases.

© 2022 Baker Hughes Company - All rights reserved

## CONCLUSION

This paper has examined the workflow that has led to the definition of the turbine in the turboexpander unit of the CO2OLHEAT project. The high power density of the sCO<sub>2</sub> power system coupled with high operating pressures dictates low volumetric flows, therefore a radial-inflow turbine was selected as the most promising architecture. The overall expansion ratio was split into two consecutive radial-inflow stages, which were arranged in a back-to-back configuration to balance axial thrusts. The aerodynamic stage design stemmed from the selection of a few characteristic design parameters, namely specific speed and spouting-to-peripheral velocity ratio. After this first step, a preliminary turbine design was accomplished by using a validated mean-line tool.

The turbine performance was assessed by means of two independent CFD studies, which agree remarkably well with minor quantitative differences (< 0.2%). A comparison between the mean line and the CFD estimates confirmed *a posteriori* the good predicting capability of the former, which had laid the foundation for the whole turbine design.

Finally, the effects of clearance and roughness were investigated. These non-scalable geometrical parameters were deemed to be relevant for turbine performance owing to the small scale of the machine. It was found that a clearance-to-diameter ratio of 0.03 yields an efficiency drop of 3.6%. In the same vein, a sand-grain roughness of 5 μm reduces the efficiency by 2.3%. The impact of the clearance has convinced the manufacturer to select a shrouded wheel after a considerable effort to ensure structural reliability. Advanced manufacturing processes will be possibly considered to minimize surface roughness. As a future follow-up activity, unsteady simulations at design and off-design conditions will be performed to assess the impact of non-stationary interactions on the performance, and the aeromechanical forcing on the system.

## NOMENCLATURE

- b Spanwise height
  - BF Blockage factor
  - c Absolute velocity
  - ch Chord
  - D Diameter
  - h Specific enthalpy
  - I Rothalpy
  - $k_s$  Sand-grain roughness
  - L Length
  - m Mass flow
  - M Mach number
  - N Rotational speed
  - $N_s$  Specific speed
  - p Pressure
  - Q Volume flow rate
  - r Radius
  - Re Reynolds number
  - s Specific entropy
  - t Thickness
  - T Temperature
  - u Peripheral speed
  - w Relative velocity
  - Y Mach expression factor at section  $i$ ,  $Y_i = \left[1 + \frac{\gamma_i - 1}{2} M_i^2\right]^{\frac{\gamma_i}{1 - \gamma_i}}$
  - $y^+$  Dimensionless distance from solid wall
  - Z Blade count
- Greek:**
- $\alpha$  Absolute flow angle

$\beta$	Relative flow angle
$\gamma$	Specific heats ratio
$\Delta$	Variation
$\varepsilon$	Clearance
$\eta$	Efficiency
$\varphi$	Flow coefficient
$\mu$	Dynamic viscosity
$\rho$	Density

#### Subscript

a	Axial direction
cl	Clearance
df	Disk Friction
H	Hydraulic
inc	Incidence
is	Isentropic state
N	Nozzle
pe	Post-expansion
pl	Passage loss
r	Radial direction
rel	Referred to the relative frame
rms	Root Mean Square Value
s	Static quantity
t	Total quantity
te	Trailing edge
$\theta$	Tangential direction
vs	Vaneless Space
W	Wheel

#### ACKNOWLEDGEMENTS

The CO2OLHEAT project has received funding from the European Union's Horizon 2020 research and innovation programme under grant agreement N° 101022831.

#### REFERENCES

- [1] O. Reimann, "CEWEP Energy Report III (Status 2007-2010)," Confederation of European Water-to-Energy Plants, www.cewep.eu, 2012.
- [2] M. Marchionni, G. Bianchi and S. Tassou, "Review of supercritical carbon dioxide (sCO<sub>2</sub>) technologies for high-grade waste heat to power conversion," *SN Applied Sciences*, vol. 2, no. 4, pp. 1-13, 2020.
- [3] A. Romei, P. Gaetani, A. Giotri and G. Persico, "The role of turbomachinery performance in the optimization of supercritical carbon dioxide power systems," *Journal of Turbomachinery*, vol. 142, no. 7, p. 071001, 2020.
- [4] D. Alfani, M. Binotti, E. Macchi, P. Silva and M. Astolfi, "sCO<sub>2</sub> Power Plants for Waste Heat Recovery: Design Optimization and Part-Load Operation Strategies," *Applied Thermal Engineering*, vol. 195, 2021.
- [5] R. Pecnik, E. Rinaldi and P. Colonna, "Computational fluid dynamics of a radial compressor operating with supercritical CO<sub>2</sub>," *Journal of Engineering for Gas Turbines and Power*, vol. 134, no. 12, 2012.
- [6] S. Saxena, R. Mallina, F. Moraga and D. Hofer, "Numerical Approach for Real Gas Simulations: Part II – Flow Simulation for Supercritical CO<sub>2</sub> Cen-trifugal Compressor," in *ASME Turbo Expo 2017*, 2017.
- [7] A. Hosangadi, Z. Liu, T. Weathers, V. Ahuja and J. Busby, "Modeling multiphase effects in CO<sub>2</sub> compressors at subcritical inlet conditions," *Journal of Engineering for Gas Turbines and Power*, vol. 141, no. 8, 2019.
- [8] G. Persico, P. Gaetani, A. Romei, L. Toni, E. Bellobuono and R. Valente, "Implications of phase change on the aerodynamics of centrifugal compressors for supercritical carbon dioxide applications," *Journal of Engineering for Gas Turbines and Power*, vol. 143, no. 4, 2021.
- [9] J. Mortzheim, D. Hofer, S. Piebe, A. McClung, J. J. Moore and S. Cich, "Challenges With Measuring Supercritical CO<sub>2</sub> Compressor Performance When Approaching the Liquid-Vapor Dome," in *ASME Turbo Expo 2021*, 2021.
- [10] L. Toni, E. Bellobuono, R. Valente, A. Romei, P. Gaetani and G. Persico, "Computational and Experimental Assessment of a MW-Scale Supercritical CO<sub>2</sub> Compressor Operating in Multiple Near-Critical Conditions," *Journal of Engineering for Gas Turbines and Power*, vol. 144, no. 10, 2022.
- [11] S. D. Cich, J. Jeffrey Moore, M. Marshall, K. Hoopes, J. Mortzheim and D. Hofer, "Radial Inlet and Exit Design for a 10 MWe sCO<sub>2</sub> Axial Turbine," in *ASME Turbo Expo 2019*, 2019.
- [12] T. El Samad, J. Amaral Teixeira and J. Oakey, "Investigation of a Radial Turbine Design for a Utility-Scale Supercritical CO<sub>2</sub> Power Cycle," *Applied Sciences*, vol. 10, no. 12, 2020.
- [13] D. Alfani, M. Asolfi, M. Binotti, P. Silva and G. Persico, "Part load analysis of a constant inventory supercritical co<sub>2</sub> power plant for waste heat recovery in cement industry," in *The 5th European sCO<sub>2</sub> Conference for Energy Systems*, 2023.
- [14] F. Lottini, M. Marconcini, A. Arnone, D. Biliotti and L. Toni, "Numerical investigation on radial turbines aerodynamics aimed at the definition of design rules for industrial applications," *Proceedings of ASME Turbo Expo 2022*, 2022.
- [15] E. Lemmon, I. Bell, M. Huber and M. McLinden, *NIST Standard Reference Database 23: Reference Fluid Thermodynamic and Transport Properties-REFPROP, Version 10.0*, National Institute of Standards and Technology, 2018.
- [16] H. Rohlik, Kofskey and Milton, "Recent radial turbine research at the NASA Lewis Research Center," *American Society of Mechanical Engineers*, vol. 79818, 1972.
- [17] C. Rodgers, "Mainline performance prediction for radial inflow turbines," *Von Karman Inst. for Fluid Dynamics*, 1987.

- [18] A. Glassman, "Enhanced analysis and users manual for radial-inflow turbine conceptual design code RTD," NASA, 1995.
- [19] R. H. Aungier, Turbine aerodynamics, New York: American Society of Mechanical Engineers Press, 2006.
- [20] L. J. Kastner and F. S. Bhinder, "A method for predicting the performance of a centripetal gas turbine fitted with a nozzle-less volute casing," in *American Society of Mechanical Engineers*, 1975.
- [21] N. C. Baines, "A meanline prediction method for radial turbine efficiency," 1998.
- [22] J. W. Daily and R. E. Nece, "Chamber Dimension Effects on Induced Flow and Frictional Resistance of Enclosed Rotating Disks," *Journal of Fluids Engineering*, vol. 82, no. 1, p. 217–230, 1 March 1960.
- [23] A. Meroni, M. Robertson, R. Martinez-Botas and F. Haglind, "A methodology for the preliminary design and performance prediction of high-pressure ratio radial-inflow turbines," *Energy*, vol. 164, pp. 1062--1078, 2018.
- [24] D. Fiaschi, G. Manfrida and F. Maraschiello, "Design and performance prediction of radial ORC turboexpanders," *Applied Energy*, vol. 138, pp. 517--532, 2015.
- [25] A. Arnone, "Viscous analysis of three-dimensional rotor flow using a multigrid method," 1994.
- [26] P. Boncinelli, F. Rubecchini, A. Arnone, M. Cecconi and C. Cortese, "Real Gas Effects in Turbomachinery Flows: a CFD Model for Fast Computations," *ASME J. Turbomach.*, vol. 162, no. 2, pp. 268-276, 2004.
- [27] M. Marconcini, F. Rubecchini, A. Arnone, A. Scotti Del Greco and R. Biagi, "Aerodynamic investigation of a high pressure ratio turbo-expander for organic Rankine cycle applications," *Turbo Expo: Power for Land, Sea, and Air*, vol. 44748, pp. 847--856, 2012.
- [28] F. Rubecchini, M. Marconcini, A. Arnone, A. Scotti Del Greco and R. Biagi, "Special challenges in the computational fluid dynamics modeling of transonic turbo-expanders," *Journal of engineering for gas turbines and power*, vol. 135, 2013.
- [29] R. Pacciani, M. Marconcini and A. Arnone, "Comparison of the AUSM+-up and other advection schemes for turbomachinery applications," *Shock Waves*, vol. 29, pp. 705--716, 2019.
- [30] D. C. Wilcox, Turbulence modeling for CFD, vol. 2, DCW industries La Canada, CA, 1998.

## A METHODOLOGY TO DESIGN AIR-COOLED CONDENSERS FOR SUPERCRITICAL POWER CYCLES USING CARBON DIOXIDE AND CARBON DIOXIDE MIXTURES

**Pablo Rodríguez-de Arriba**  
Department of Energy Engineering,  
University of Seville  
Seville, Spain  
Email: prdearriba@us.es

**Francesco Crespi\***  
Department of Energy Engineering,  
University of Seville  
Seville, Spain  
Email: crespi@us.es

**David Sánchez**  
Department of Energy Engineering,  
University of Seville  
Seville, Spain  
Email: ds@us.es

**Antonio Muñoz**  
Department of Energy Engineering,  
University of Seville  
Seville, Spain  
Email: ambl@us.es

### ABSTRACT

The SCARABEUS project investigates the use of CO<sub>2</sub>-based mixtures as working fluid in power cycles for next-generation Concentrated Solar Power plants. These fluids exhibit a critical temperature higher than pure CO<sub>2</sub>, enabling dry condensation of the working fluid even at the high ambient temperatures typical of sites with a high solar radiation. As a consequence, the SCARABEUS power cycle achieves higher thermal efficiency than standard sCO<sub>2</sub> cycles, whose performance deteriorates significantly with ambient temperature. In any case, the actual feasibility of this concept is still to be confirmed by a complete techno-economic assessment. To that purpose, it is critical to accurately estimate the power consumption of the Heat Rejection Unit (HRU), which is one of the most important parasitic loads of the system.

Bearing all this in mind, this manuscript presents the design of a horizontal, direct air-cooled condenser (ACC). The bundle geometry proposed is comprised of seven tubes in three passes, with a staggered arrangement. The complete thermal model, developed in MatLab, has been already disclosed by the SCARABEUS consortium in a previous paper, and validated both experimentally in a dedicated test rig and against results obtained by the commercial software Xace®. The novelty in the present manuscript lies in the integration of this thermal model of the tubes with a complete design and integration tool of the whole heat rejection sub-system, including the design of a rotor-only axial fan and supporting frame. The impact of several design parameters (i.e., air temperature rise, acceptable hot pressure drops, tube length) is studied, taking into account auxiliary power consumption, footprint and cycle efficiency as main figures of merit. Two candidate mixtures are taken into

account, identified in previous works by the same authors (85%CO<sub>2</sub>-15%C<sub>6</sub>F<sub>6</sub> and 80%CO<sub>2</sub>-20%SO<sub>2</sub>), and a pure sCO<sub>2</sub> case is also considered for the sake of comparison. The results show that, for a given gross cycle output, using pure sCO<sub>2</sub> yields the smallest ACC with the lowest fan power consumption. Moreover, tube length and air face velocity are found to be the key-parameters driving the design process of an ACC, for which increasing tube length is always beneficial as far as the ACC design is concerned. Finally, various considerations regarding the role played by the optimum design of the ACC within the global optimisation of the power plant are made. It is found that the rationale employed for the design of the ACC may be in conflict with that used from an overall plant optimisation standpoint. It is hence concluded that the definition of the optimal design space of an Air-cooled Heat Exchanger (ACHE) must be included in the global optimisation of the power plant.

### INTRODUCTION

Concentrated Solar Power (CSP) plants are expected to play a key role in the decarbonisation of the power generation sector. Nevertheless, as of today and despite dispatchability of CSP being a major advantage over photovoltaics and wind, the former is still far from being cost-effective due to the high LCoE [1]. This poses a need for further investigation in order to increase the solar-to-electric efficiency of this technology (hence smaller solar fields) and to reduce the overall capital cost of CSP plants, thus making it more feasible from an economic standpoint [2]. One possible solution to accomplish this objective, which is being widely investigated in literature, is to raise turbine inlet temperature up to 700-800°C, a value significantly higher than the state-of-the-art power plants, currently operating at ~550°C

\* corresponding author(s)

[2]. Nevertheless, this implies overcoming several technological challenges, from the development of improved designs of both solar receivers and Thermal Energy Storage (TES) systems [3,4], to the identification of thermally stable heat transfer fluid able to operate at such high temperatures [5]; in addition to these, the development of power cycles able to take full advantage of these very high temperatures is also of primary interest. In this latter regard, supercritical CO<sub>2</sub> power cycles are being extensively studied, due to their noteworthy features such as higher thermal efficiency, smaller footprint and lower cycle complexity than steam-based Rankine cycles, among others. Nevertheless, at high ambient temperatures (>35°C), usual in semi-arid locations with high solar irradiance, sCO<sub>2</sub> cycles experience an important efficiency drop due to the compression process being performed far from the critical point (31°C, 73.8 bar).

To find a solution to this problem, the SCARABEUS project is currently investigating the addition of specific dopants/additives to produce a mixture with CO<sub>2</sub> which can be used as the working fluid in a power cycle [6]. These innovative working fluids exhibit higher critical temperatures than CO<sub>2</sub>, which enables fluid condensation at higher. This SCARABEUS concept has already been demonstrated thermodynamically, confirming that thermal efficiencies of around 50% with minimum cycle temperatures as high as 50°C can be achieved [7-9].

In addition to enabling higher efficiencies in sites with high ambient temperatures, the SCARABEUS concept also paves the way for the utilisation of dry cooling, which yields additional advantages in terms of reduced water consumption at reasonable auxiliary power demand. Indeed, dry cooling systems usually lead to high auxiliary power consumption (fan motors) which can potentially offset the theoretical thermodynamic advantage of advanced cycles like sCO<sub>2</sub> or others. Therefore, it is of utmost importance to demonstrate the technical and economic feasibility of SCARABEUS concept from a net (global) standpoint. To this end, the development of specific tools for the design and simulation of major and balance of plant (BoP) components is crucial, in particular the accurate estimate of the required heat exchange area and its auxiliary power consumption.

Modular air-cooled condensers incorporating multiple unitary cells with the same design are currently employed in CSP plants based on steam turbines (e.g., Ivanpah Solar Power Plant [10]). Each cell is typically composed of inclined finned tubes in an A-frame structure, with cooling air being forced upwards by motor-driven axial fans. For sCO<sub>2</sub> power cycles though, the identification of the most suitable technology for dry air cooling is not trivial, as credited by the different options considered in literature so far. Compact diffusion-bonded counter-current heat exchangers were initially studied by Moiseyev & Sienicki [11], concluding that dry air cooling was cost-prohibitive in comparison with water cooling. Later, Moiseyev *et al.* [12] provided a comparative analysis of two existing technologies: a modular finned tube air cooler and a compact diffusion-bonded cross-flow heat exchanger. The former was found to be the most interesting solution for dry cooling in sCO<sub>2</sub> cycles, yielding six times lower investment costs than if Printed Circuit Heat

Exchangers (PCHE) were used, for the same power consumption.

Later studies have investigated other dry air cooling technologies. Ehsan *et al.* [13,14] investigated dry natural draft cooling towers in both direct and indirect configuration, employing an intermediate water-to-sCO<sub>2</sub> shell-and-tube pre-cooler in the second case. This concept reduces the operating cost significantly but, as the investment costs of a dry natural draft cooling tower are also higher than those of a mechanical draft air cooler, a techno-economic study to assess the actual feasibility of this design is still needed. Finally, Pidaparti *et al.* [15] studied four different cooling technologies: force-draft wet indirect cooling towers, indirect dry air cooling in finned tube heat exchanger, V-shape direct air coolers and direct adiabatic cooling. For drier and hotter locations, the adiabatic cooling is seen to perform better in terms of plant efficiency and LCoE than direct dry cooling [16], though this is at the expense of a significantly higher water consumption.

The aforementioned past works refer to cycles using pure Carbon Dioxide and there are virtually no references in literature on the design of air-cooled condensers for sCO<sub>2</sub> mixtures. A first investigation was carried out by Illyés *et al.* [17] in the framework of SCARABEUS project. That work presents a finite-volume thermal model for the design of the pipe bundling of a finned tube ACC, validated against data provided by Kelvin Thermal Solutions, a commercial partner of the consortium.

With this in mind, the present manuscript takes this research path a step further with the aim to extend the model carried out by Illyés *et al.* to the detailed design of a modular air-cooled condenser for a 100MW (gross) CSP plant. To this end, the same tube bundling proposed in [17] is considered and, then, modules for the design and assembly of the cooling fans are developed. Two mixtures are taken into account, based on past works by the authors: Hexafluorobenzene (C<sub>6</sub>F<sub>6</sub>) [7] and Sulphur Dioxide (SO<sub>2</sub>) [8]. Moreover, a pure-sCO<sub>2</sub> air cooler is also designed, for the sake of comparison, employing the same overall configuration of the heat rejection unit.

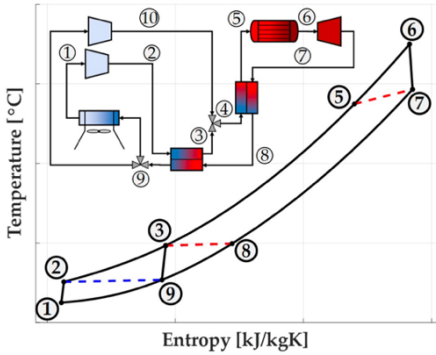
In the first part of the manuscript, the impact of several design variables is studied in order to find the design yielding the best balance between fan power, overall footprint, bay length and cycle efficiency. A series of Pareto fronts are produced for a set value of total-to-static fan efficiency, identifying the best ACHE design parameters for each working fluid considered. In the second part, various fan designs are produced, in order to assess the impact of incorporating case specific fan efficiencies into the previous analysis (impact on Pareto fronts). As a conclusion, and based on the results obtained, a series of considerations and suggestions are provided in order to define the best engineering practice to design ACCs for CO<sub>2</sub>-based power cycles.

## COMPUTATIONAL ENVIRONMENT WORKING FLUID AND THERMODYNAMIC CYCLE MODELS

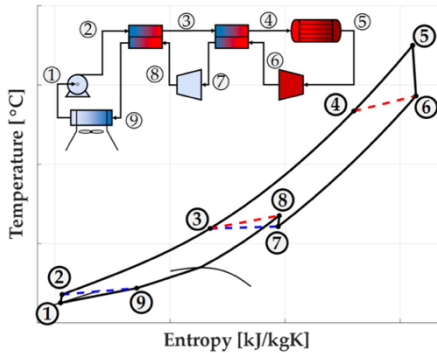
In order to define the boundary conditions for the design of the Air-Cooled Condenser, three different combinations of cycle layout and working fluid composition are considered: Precompression cycle with 85%CO<sub>2</sub>-15%C<sub>6</sub>F<sub>6</sub> (molar fractions),



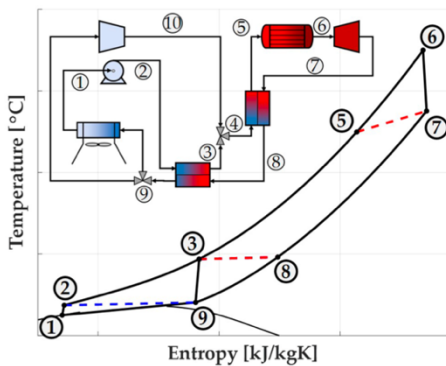
Recompression cycle with 80%CO<sub>2</sub>-20%SO<sub>2</sub> and Recompression cycle with pure sCO<sub>2</sub>. The layouts temperature-entropy diagrams of these cycles are provided in Figure 1.



(a) Recompression with pure sCO<sub>2</sub> (supercritical)



(b) Precompression with 85%CO<sub>2</sub>-15%C<sub>6</sub>F<sub>6</sub> (transcritical)



(c) Recompression cycle with 80%CO<sub>2</sub>-20%SO<sub>2</sub> (transcritical)

**Figure 1:** Cycle layouts considered for pure (a) and blended (b,c) CO<sub>2</sub> systems (adapted from [9])

The first two configurations are representative of the SCARABEUS concept and have already been studied by the authors in previous publications [7,8], while the Recompression cycle is possibly the most studied configuration for sCO<sub>2</sub>

technology, in particular for CSP applications [18]. The power cycles have been modelled using Thermoflex v.30, a commercial software by Thermoflow Inc [19], with the necessary user-defined-modules to enable simulation of SCARABEUS-specific components and features. Since these power cycles are employed to define the boundary conditions of the ACC only, a detailed description of the models falls out of the scope of this work; interested readers are therefore directed to references [7,8] where all the information of interest can be found. Table 1 presents a summary of the main features of these three cycle layouts, together with the boundary conditions to be employed in the ACC design model. It is to note that although a 1% pressure drop has initially been considered for the reference heat rejection unit during the simulations of the power cycles, the impact of this parameter on cycle performance and air-cooled condenser design is also assessed later in this work.

**Table 1.** Main features of different power cycle technologies and HRU boundary conditions.

	CO <sub>2</sub> -C <sub>6</sub> F <sub>6</sub>	CO <sub>2</sub> -SO <sub>2</sub>	Pure CO <sub>2</sub>
<b>Layout</b>	Precompr.	Recompr.	Recompr.
<b>Common param.</b>	<i>TIT</i> =700°C, <i>Wel</i> = 100 MW (gross)		
<b><math>\eta_{th}</math> [%]</b>	50.4	51.3	49.7
<b><math>Q_{cond}</math> [MW]</b>	101	95.7	102.1
<b><math>\dot{m}_{wf}</math> [kg/s]</b>	880	516	752
<b><math>T_{wf,in}</math> [°C]</b>	87.1	81.1	107
<b><math>T_{wf,out}</math> [°C]</b>	50	50	50
<b><math>P_{wf,out}</math> [bar]</b>	77.8	79.1	102
<b><math>P_{wf,in}</math> [bar]</b>	Calculated from pressure drops		

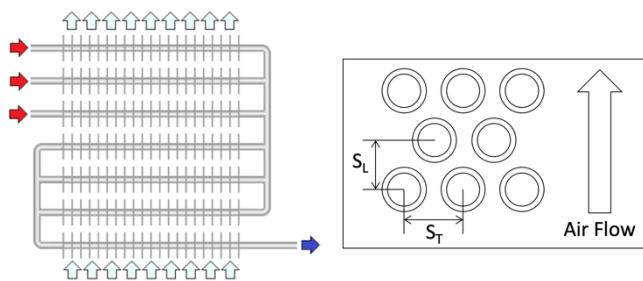
The thermo-physical properties of the mixtures have been calculated with the commercial software Aspen Plus v12 [20] and embedded in Thermoflex by means of look-up tables. A thorough description of the two dopants hereby considered, C<sub>6</sub>F<sub>6</sub> and SO<sub>2</sub>, can be found in previous works by the authors, together with a discussion of their safety hazards according to NFPA704 standard. The main specifications needed to obtain the thermo-physical properties, including the specific equation of state used and the corresponding binary interaction parameters, are summarised in Table 2. Attention must be paid to transport properties (i.e. thermal conductivity and dynamic viscosity), for which limited information is found in literature. Refprop10 includes a calculation model for pure CO<sub>2</sub> and for CO<sub>2</sub>-SO<sub>2</sub> mixtures, which is employed in the present [21]. On the other hand, only very limited information is available for CO<sub>2</sub>-C<sub>6</sub>F<sub>6</sub> mixtures; in fact, the SCARABEUS consortium is currently undertaking experimental activity in order to calibrate a suitable model to estimate transport properties of this fluid, based on the SUPERTRAPP methodology. The results of this investigation will be disclosed in the coming months by other partners of the SCARABEUS consortium. Thus, due to the lack of available data, the TRAPP predictive model as calculated by Aspen Plus v12 has been used in this work.

**Table 2.** Specifications of working fluids

	85%CO <sub>2</sub> 15%C <sub>6</sub> F <sub>6</sub> (v)	80%CO <sub>2</sub> 20%SO <sub>2</sub> (v)	Pure sCO <sub>2</sub>
$T_{cr}$ [°C]	102.1	64.2	31
$P_{cr}$ [bar]	121.3	91.85	73.8
EoS	Peng-Robinson	PC-SAFT	Span & Wagner
Kij	0.16297 – 0.0003951·T	0.0121	-
Transport prop.s method	TRAPP	REFPROP 10	REFPROP 10

**FINNED TUBE HEAT EXCHANGER MODEL**

The Heat Rejection Unit design model presented in this work is an ACC based on a finned-tube heat exchanger. Similarly to the original configuration proposed by Moisseytsev in [12], the working fluid flows inside horizontal tubes, whose thermal performance is enhanced by the addition of circular fins. Nevertheless, rather than considering a fully horizontal layout as in [12], the tubes are here arranged in three vertical passes, with a staggered distribution. Thus, the air flows upwards, driven by axial fans, and across seven rows of tubes, distributed in three different passes. The hot fluid flow on the inside enters from the upper part of the ACC and is split in three tubes, constituting the first pass of the bundle. The second pass is also composed of three tubes, whilst the flow is mixed in a single tube in the final pass. This tube bundling, presented in [17] originally, is selected in order to reduce pressure drops on the hot fluid side. The tubes at the end of each pass discharge into a header, where the fluid is mixed so that its conditions are homogeneous at the inlet to the next pass. A graphical representation of the aforesaid heat exchanger is provided in Figure 2, whilst Table 3 provides the main characteristics of the tubes and fins.

**Figure 2:** Tube geometry and bundling staggered arrangement (adapted from [17])

The finned tube heat exchanger has been modelled in MATLAB. Following the work by Shah & Sekulic [22], each row is discretized in several sub-heat exchangers (sub-HX), in order to reduce the impact of the high variation of thermo-physical properties of the working fluid (constant fluid properties in each sub-HX can hence be used). The number of sub-HX is set to 50 after a specific sensitivity analysis, a number found to be a good compromise between numerical consistency and computational burden.

**Table 3.** Specifications of reference tube bank and fins (ACC)

Parameter	Value
Tube internal / external diameter	20.76 mm / 26.8 mm
Transversal / Longitudinal pitch	66.7 mm / 57.7 mm
Tube material	Carbon Steel
Fin type	Circular fins
Fin material	Aluminium 1100-annealed
Fin height / thickness / spacing	15.9 mm / 120µm / 2.52 mm
# tubes per row	7
# passes / # tubes per pass	3 / 3-3-1
Tube bundle arrangement	Staggered
Fan draft type	Induced

Definitions for the geometry of tube-fin heat exchangers can be found in [22] whilst fin efficiency of circular fins is computed according to the information in [23]. The condensation heat transfer coefficient of the SCARABEUS mixtures is computed by means of Cavallini's model [24], as suggested in [17], which is also valid for zeotropic mixtures as it is the case for the working fluids in SCARABEUS. For the cooling of sCO<sub>2</sub>, the correlation by Krasnoshchekov and Protopopov [25] is recommended in literature to estimate heat transfer near the critical point [26]. The air-side convective coefficient is calculated using Briggs & Young's correlation as suggested in [22] for finned tubes. Finally, the fouling factors are set to 0.00176 m<sup>2</sup>·K/W on both sides [27]. Each sub-HX can be treated as a cross-flow heat exchanger, where both fluids remain unmixed. The effectiveness-NTU functions for such configuration are reported in [23].

Estimating pressure drop on both sides accurately is crucial in the design of an ACHE. The pressure drop on the inner side (working fluid) has a negative influence on the thermal efficiency of the power block whereas the pressure drop on the air side brings about a higher auxiliary power consumption and, accordingly, lower net plant efficiency. The model by Del Col *et al.* [28] is recommended in [17] for the calculation of pressure drops during condensation of the SCARABEUS mixtures. For sCO<sub>2</sub>, Colebrook's correlation modified by the property ratio method, as explained in [29](Chap.8), is implemented to account for property variations between the fluids near the wall and the bulk fluid. For the air-side pressure drop, Robinson and Briggs' correlation is employed for circular finned tubes [22,30], and an additional 20% of the bundle pressure drop is added to account for other sources of friction loss as explained in [22].

The heat transfer model of the finned tube heat exchanger is solved by starting from the hot end. A priori, only the air temperature distribution at the inlet (lower row) is known, as this is assumed uniform and equal to ambient temperature. On the other hand, the mean value of air temperature at outlet can be defined by means of an energy balance, but not its distribution along the length of the pass. Therefore, the heat exchange must be solved through an iterative procedure, guessing an initial outlet air temperature distribution and converging the inlet distribution which can be computed by solving the aforesaid model.

The design of the ACHE requires the user to specify the thermodynamic state at the inlet and the outlet of both the hot fluid and air, as well as a target hot side pressure drop. From these specifications, the number of tubes and the length of the pass are determined. A flowchart of the ACHE design tool is depicted in Figure 3.

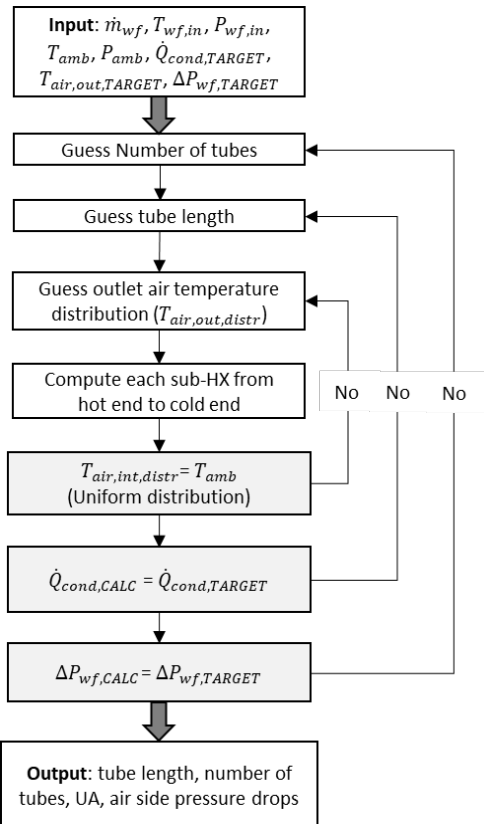


Figure 3: Flow chart of ACHE design code

### AXIAL FAN MODEL

A numerical tool capable of producing a preliminary design of a (single-rotor, no stator) axial fan and of estimating its total-to-static efficiency has been implemented, based on the work by Wilkinson [31]. In order to produce the fan design, a number of specifications such as fan diameter ( $D_{fan}$ ), air flow rate, total-to-static pressure, blade tip speed, inlet temperature and inlet pressure are needed. Blade tip speed is set to 58 m/s, according to Wilkinson’s work, whilst the other parameters are optimised for each case, depending on the working fluid and on the performance required from the fan. The hub-to-tip ratio is estimated using the model developed by Bruneau [32]. The exit axial and swirl velocities are computed by means of an optimisation procedure with the aim to minimise the kinetic energy flux as described in Von Backström [33]. Finally, the

<sup>1</sup> The enhanced configuration corresponds to corrugated surfaces both inside the tubes and in the fins on the air side, as thoroughly explained in [17]. The specifications of this enhanced configuration are confidential, proprietary of Kelvion Thermal Solutions, and cannot be disclosed here. For the sake of accessibility of this study, authors decided to

chord length distribution is computed as explained in Bruneau [32], assuming a reference airfoil (NASA-LS-0413, in the present work). With this information, the total-to-total and total-to-static efficiencies are computed.

### AIR-COOLED HEAT EXCHANGER MODEL

The entire set of tubes is divided into independent units (bays), constituting the ACHE module represented in Figure 4. Due to the large length of the tubes, each bay is typically equipped with more than one axial fans, which can be of either the forced or induced draft type. The bay face area and the plenum height are linked to the fan casing area in order to ensure a good air distribution across the tube bundle [34]. The plenum height is set to  $0.3 \cdot D_{fan}$ , following best engineering practice [34], and a minimum threshold of the ratio between fan area and bay face area is set to 40% [30]. Additionally, in this work, the projected face area covered by each fan is set to  $1.5 \cdot D_{fan}$  in the longitudinal direction of the bay and  $1.2 \cdot D_{fan}$  in the transversal direction. This yields a fan-area-to-tube-bundle-face-area ratio of 43.6%, which is aligned with the aforementioned common engineering practice. It is worth noting that these reference values and constraints have been set in this work according to common engineering practice, but they will be subject to techno-economic optimisation in future, according to the scope of activities in SCARABEUS.

Under these assumptions, the total number of fans, the number of bays and the number of tubes per bay are calculated and then rounded up to the nearest integer in all cases.

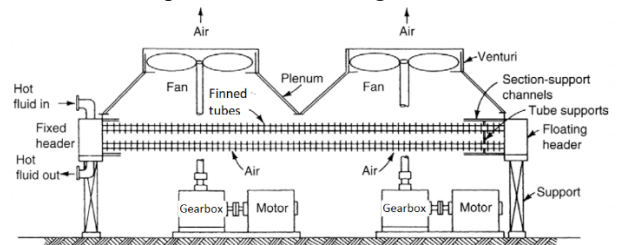


Figure 4: General scheme of an induced draft ACHE [Adapted from 30]

### MODELS VALIDATION

The finned-tube heat exchanger model has been validated against three different designs presented in [17]: a 92%CO<sub>2</sub>-8%C<sub>6</sub>F<sub>6</sub> blend, with both simple and enhanced tubes, and pure CO<sub>2</sub> with enhanced tubes<sup>1</sup>. The heat exchanger has been designed imposing the same heat duty, the same target inner pressure drop and the same air temperature rise. The results are compared in terms of external HX area ( $A_{HX}$ ), pass length, number of tubes and Overall Heat Transfer Coefficient (U). The results of this validation are provided in Table 4.

employ the simple configuration in the design of the ACC. The enhanced configuration has been considered in the validation of the tool only.

**Table 4.** Specifications of reference tube bank and fins (ACC)

Working Fluid (WF)	CO <sub>2</sub> -C <sub>6</sub> F <sub>6</sub>			CO <sub>2</sub> -C <sub>6</sub> F <sub>6</sub>			Pure CO <sub>2</sub>		
Enhanced	No			Yes			Yes		
$Q_{cond}$ [MW]				236					
$\dot{m}_{wf}$ [kg/s]	1200			1200			1749		
$P_{wf,in}$ [bar]	92			92			100		
WF temperatures				114°C to 51°C					
$\Delta P_{wf}$ [bar]				0.46					
Air temperatures	36°C to 59.5 °C			36°C to 63.1 °C			36°C to 65.4 °C		
	This work	Illyés <i>et al.</i> [17]	$\Delta$ [%]	This work	Illyés <i>et al.</i> [17]	$\Delta$ [%]	This work	Illyés <i>et al.</i> [17]	$\Delta$ [%]
$A_{HX}$ [m <sup>2</sup> ]	481135	487800	-1.37	412990	417300	-1.03	390412	381700	2.28
$L_{tube}$ [m]	20.85	19.30	8.04	15.92	14.90	6.81	10.15	10	1.49
# tubes	1858	2030	-8.47	2091	2250	-7.07	3100	3055	1.47
$U$ [W/m <sup>2</sup> K]	21.93	23.00	-4.67	27.35	28.80	-5.05	28.75	28.6	0.52

The total (external) heat exchange area shows very good agreement in all three cases, with relative deviations in the order of 1% for CO<sub>2</sub>-C<sub>6</sub>F<sub>6</sub> blends and slightly above 2% for the pure sCO<sub>2</sub> case; this latter difference could be explained by the different correlation used to estimate the sCO<sub>2</sub> heat transfer coefficient. As previously commented, Krasnoshchekov and Protopopov's correlation is used in this work instead of Gnielinski's (employed in [17]), given that the former is more adequate to predict the behaviour of CO<sub>2</sub> near the critical point [26].

Good match is also found for the estimated tube characteristics (length and number), with relative deviations below 1.5% when pure CO<sub>2</sub> is considered. On the contrary, a larger deviation is observed for these parameters when using CO<sub>2</sub>-C<sub>6</sub>F<sub>6</sub>, in the order of 8%. This is caused by the different transport properties considered (Illyés *et al.* employed preliminary results obtained with SUPERTRAPP) and, to a lesser extent, by fin efficiency. In this regard, this parameter is set to the constant value of 77.5% in [17], whilst it is calculated for each case in the present work, yielding values around 65.5% for the boundary conditions presented in Table 4. It is worth noting that, for a given heat duty, length and number of tubes present inversely proportional trends (i.e., reducing the length poses the need for a higher number of tubes, and vice versa). Thus, all the possible combinations of these two parameters yield very similar total  $A_{HX}$ . This highlights the need to reduce the uncertainty introduced by transport properties of the working fluid, a task which is currently being undertaken within the SCARABEUS consortium.

On the other hand, the axial fan design tool has been validated against the case study from [31]. The fan design tool has been validated for the reference case defined in Table 3.2 from [31]. Relative deviations of both total-to-static efficiency and hub-to-tip ratio are lower than 1%.

## DISCUSSION OF RESULTS

### PRELIMINARY CONSIDERATIONS REGARDING ACHE DESIGN

Once the capacity of the condenser to actually reject the amount of thermal energy that is needed to produce saturated liquid at the outlet is verified, it is the time to assess other techno-economic features of this component: size (total volume occupied by the bundles,  $V_{HX}$ ), fan power ( $W_{fan}$ ) and pressure drop on the inner side of the tubes ( $\Delta P_{wf}$ ). The first two parameters are linked to the design of the ACHE only and do not have any impact on the thermal performance of the power cycle. On the contrary, cycle efficiency is sensitive to  $\Delta P_{wf}$ , which has an impact on the global optimisation of the SCARABEUS system. This global optimisation is out of the scope of this paper though, which introduces a methodology to design the HRU only, and hence only trade-offs between component size and power consumption are studied here. Some high-level considerations about the impact on cycle performance will nevertheless be given in the concluding section of the paper. The total volume occupied by the tube bundles (see Equation 1) is proportional to the product of tube length ( $L_{tube}$ ) and number of tubes in parallel ( $N_{tubes}$ ), given that the number of rows is set to seven and the longitudinal and transversal pitches are those indicated in Table 3.

$$V_{HX} = L_{tube} \cdot N_{tubes} \cdot S_L \cdot N_{rows} \cdot S_T \quad (1)$$

Fan power consumption is calculated as the product of volumetric air flow rate ( $\dot{V}_{air}$ ) and the pressure drops across the bundle ( $\Delta P_{air}$ ) divided by fan total-to-static efficiency ( $\eta_{TS}$ ), as shown in Equation 2. It is to note that, in this section,  $\eta_{TS}$  is set to 68%, an assumption that will be revised in a later section.

$$\dot{W}_{fan} = \dot{V}_{air} \cdot \Delta P_{air} / \eta_{TS} \quad (2)$$



With the geometrical specifications of the tubes (including  $D_{fan}$ ) and fins set to the values indicated in Table 3, the design code for the finned-tube heat exchanger presents two degrees of freedom: the temperature rise experienced by the air stream ( $\Delta T_{air}$ ) and target  $\Delta P_{wf}$ . The first parameter is inversely proportional to the volumetric air flow rate circulating across the heat exchanger. The second parameter directly affects the number of tubes in parallel constituting the bundling, for a given tube diameter: lower pressure drops imply a higher number of tubes (reduction of flow velocity).

It is worth noting that either if the inner pressure drop is reduced or if the air temperature rise is increased, the overall transfer coefficient ( $U$ ) decreases as a consequence of the lower flow velocity of both fluids (low Nusselt number); this brings

about a need for larger heat transfer areas to meet the required heat duty. Interestingly, a larger air temperature rise also brings a larger logarithmic mean temperature difference in the condenser (LMTD), which would partly offset this need (heat transfer area decreases when LMTD increases).

Regarding  $V_{HX}$ , this increases with the number of tubes in parallel and with their length (and so does the total heat transfer area), and it also increases for decreasing values of  $U$ . On the other hand, the auxiliary power consumption is strongly sensitive to the air face velocity ( $v_{face}$ ), as it represents the product of  $\dot{V}_{air}$  (proportional to  $v_{face}$ ) and  $\Delta P_{air}$  (proportional to  $v_{face}^2$ ). The air face velocity is defined as the volumetric flow rate divided by the frontal area of the heat exchanger, in Equation 3, which is in turn proportional to the number of tubes and their length (thus, to  $V_{HX}$ ). As a consequence,  $V_{HX}$  and  $\dot{W}_{fan}$  present an opposite trend with respect to  $\Delta T_{air}$  and  $\Delta P_{wf}$ , since  $\dot{W}_{fan}$  decreases for higher  $\Delta T_{air}$  and lower  $\Delta P_{wf}$ .

$$v_{face} = \dot{V}_{air}/A_{FR} = \dot{V}_{air}/(L_{tube} \cdot N_{tubes} \cdot S_T) \quad (3)$$

Bearing all this in mind, the existence of Pareto fronts defining the design space of the ACHE is proven. In other words, the optimal design space for the ACHE (i.e., Pareto front) is formed by the designs for which a certain fan power can be achieved with the minimum heat exchanger volume or, conversely, the designs for which, given a certain heat exchanger volume, fan power is minimised.

To generate these Pareto fronts, an extensive sensitivity analysis to  $\Delta T_{air}$  and  $\Delta P_{wf}$  is performed for the three systems under study: Recompression cycle with  $\text{CO}_2\text{-SO}_2$ , Precompression cycle with  $\text{CO}_2\text{-C}_6\text{F}_6$  and Recompression cycle with  $\text{sCO}_2$ . The results of this preliminary analysis are presented in Figure 5, where the overall design spaces for these systems, (i.e., the trend of  $\dot{W}_{fan}$  as a function of  $V_{HX}$  for different combinations of  $\Delta T_{air}$  and  $\Delta P_{wf}$ ) are provided. It can be observed that the best compromise between  $\dot{W}_{fan}$  and  $V_{HX}$  corresponds to the pure  $\text{sCO}_2$  case. This means, in other words, that the ACHEs designed for the two SCARABEUS mixtures always present higher  $\dot{W}_{fan}$  than the pure  $\text{CO}_2$  case for a given  $V_{HX}$ , or higher  $V_{HX}$  for given  $\dot{W}_{fan}$ . This is probably due to the higher working fluid temperature at the inlet to the HRU in the

pure  $\text{sCO}_2$  case (see  $T_{wf,in}$  in Table 1), and presents a twofold explanation: i) LMTD is increased, reducing the total heat transfer area needed (and  $V_{HX}$ ); ii) higher  $T_{wf,in}$  also leads to higher  $\Delta T_{air}$ , which in turn reduces  $\dot{V}_{air}$  and, consequently,  $\dot{W}_{fan}$ . Finally, it is noted that this could also be caused by the characteristics of the condensation of zeotropic mixtures. This is nevertheless, beyond the scope of the present manuscript and will be addressed in future works.

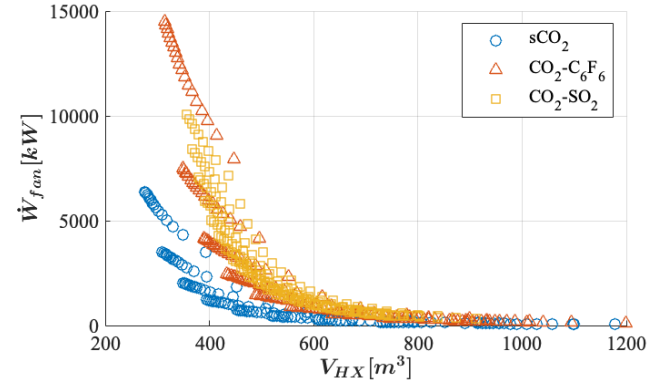


**Figure 5:** Overall design spaces based on  $\dot{W}_{fan}$  and  $V_{HX}$ , considering the three different systems under analysis.

#### IDENTIFICATION OF KEY PARAMETERS FOR ACHE DESIGN

Apart from these considerations, another key parameter in the design of the ACHE is the maximum allowable tube length, which influences both mechanical integrity and economic feasibility of this component. Two conditions can lead to higher  $L_{tube}$ : higher  $\Delta P_{wf}$  (a reduction in the number of tubes needs to be balanced by longer lengths to yield similar heat transfer area) and higher  $\Delta T_{air}$  (due to the reduced overall heat transfer coefficient). As a consequence, it is clear that the Pareto front is obtained where either  $\Delta T_{air}$  or  $\Delta P_{wf}$  take highest values, compliant with the constraint on maximum tube length.

The impact of considering different maximum  $L_{tube}$  is now studied. For the sake of simplicity, this discussion is limited to the  $\text{CO}_2\text{-SO}_2$  case, but the results are representative of the other two systems. Figure 6 highlights the points of the previous sensitivity analysis where tube length is set to 12, 15, 18 and 22 m respectively. It is worth noting that additional simulations have been done for this analysis, hence some of the new points fall outside of the original overall design space of Figure 5 (represented by light grey square markers in Figure 6). First and foremost, it is observed that the highlighted points constitute different Pareto fronts. This is not a trivial conclusion, and it means that the optimal design spaces are actually driven by  $L_{tube}$ , and that longer tubes are always preferred in terms of either  $V_{HX}$  and  $\dot{W}_{fan}$ . Nevertheless, it is also observed that the Pareto fronts tend to converge if  $L_{tube}$  is increased, with the yellow square markers (18m tubes) being very close to the red triangle (22m). This means that, even if from a purely theoretical standpoint, a higher  $L_{tube}$  is always beneficial, exceeding 18m does not provide any practical improvement from an engineering standpoint. Bearing this in mind,  $L_{tube}$  is proven to be a key-parameter for ACHE design.



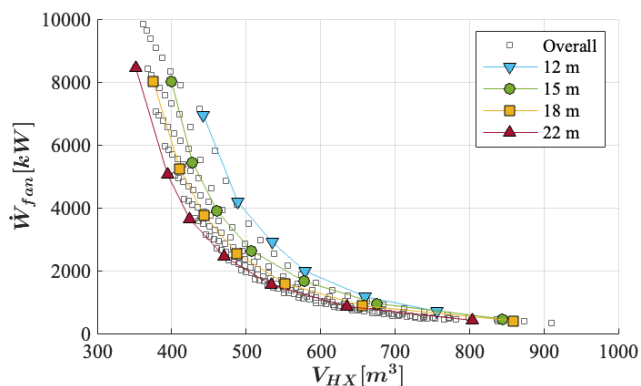


**Figure 6:** Overall design space for CO<sub>2</sub>-SO<sub>2</sub> system. Pareto fronts obtained setting  $L_{tube}$  of 12, 15, 18 and 22 m are highlighted.

A further step would be to identify a variable capable of unequivocally defining a given point of the Pareto front, which can also maintain this feature independently from the working fluid taken into account, hence affecting the three systems considered similarly. Such parameter seems to be the  $v_{face}$  which, indeed, is proportional to the cube root of fan power to heat exchanger volume ratio, multiplied by a constant that depends on air properties and fan efficiency. As  $\eta_{TS}$  is considered constant in this section and air properties hardly change for the temperature variations in the design space, the correlation between  $v_{face}$  and  $(\dot{W}_{fan}/V_{HX})^{1/3}$  is perfectly linear (see Figure 7). With all this in mind, it can be concluded that the optimal design space of an ACHE should be defined in terms of tube length and air  $v_{face}$ , rather than  $\Delta T_{air}$  and  $\Delta P_{wf}$ .

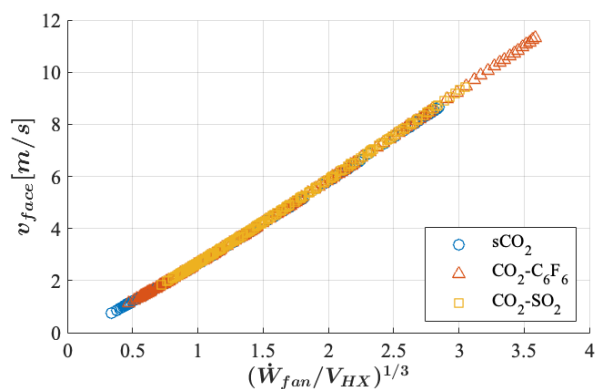


**Figure 7:**  $v_{face}$  as a function on  $\dot{W}_{fan}$  to  $V_{HX}$  ratio.

### IMPACT OF FAN DESIGN

The previous analysis was developed under the assumption of constant fan total-to-static efficiency for the sake of simplicity. Nevertheless, this does not necessarily hold true for all points explored during the sensitivity analysis, since they correspond to different fan design conditions (different flow rate and different required pressure rise). To test the validity of the hypothesis, several points of the Pareto front corresponding to a tube length of 18m are collected and an axial fan is designed

for each one of them. These points are defined by a  $v_{face}$ , as explained before. Fan diameter is set to 5.18 m (17 ft), and an induced draft configuration is chosen in order to reduce hot air recirculation [30]. Results are provided in Table 5.

**Table 5.** Fan  $\eta_{TS}$  as a function of  $v_{face}$ . Results obtained with in-house fan design model.

$v_{face}$ [m/s]	sCO <sub>2</sub>	CO <sub>2</sub> -C <sub>6</sub> F <sub>6</sub>	CO <sub>2</sub> -SO <sub>2</sub>
2	65.0%	64.9%	65.8%
3	68.1%	68.7%	68.6%
4	67.2%	68.7%	66.9%
5	64.0%	62.4%	62.9%
6	62.8%	59.4%	59.9%

Observing the results provided in Table 5, it is found that a fan efficiency of 68% is a good assumption for  $v_{face}$  in the 3-4 m/s range. At lower values, the tip speed needs to be reduced below that of the maximum allowable (58m/s) in order to find a suitable solution, penalising efficiency. At higher  $v_{face}$ , fan performance deteriorates importantly and  $\eta_{TS}$  falls below 64%.

### BEST ENGINEERING PRACTICE AND FINAL CONSIDERATIONS

This section introduces some basic design guidelines gathered from ACHE handbooks. Maximum tube length is usually limited by either manufacturing, transportation or plant layout constraints. The horizontal ACHE studied in Moisseytsev [12], taken from a vendor quote, has a tube length of 18.6 m (61 ft), what is consistent with catalogues from other manufacturers. According to Kakaç, tube length is ultimately limited to 30 m by transportation [27]. Regarding bundle width, Serth claims it to be limited to a maximum of 4.3 m (14 ft) due to transportation constraints [30], but several bundles can be placed together within the same ACHE bay. This same author recommends  $v_{face}$  between 2 and 4 m/s to achieve a good trade-off between air side pressure drop and external heat transfer coefficient [30]. This set of common practises is in line with the results presented in this paper; therefore, a reference ACHE design for the three systems is proposed by setting tube length to 18 m and  $v_{face}$  to 3 m/s. The results are presented in Table 6.

**Table 6.** Reference bay design

	sCO <sub>2</sub>	CO <sub>2</sub> -C <sub>6</sub> F <sub>6</sub>	CO <sub>2</sub> -SO <sub>2</sub>
$L_{tube}$ [m]	18	18	18
$v_{face}$ [m/s]	3	3	3
$\Delta P_{wf}$ [bar]	0.81	0.51	0.16
$\Delta T_{air}$ [°C]	24.9	19.8	17.1
$D_{fan}$ [m]	5.18	5.18	5.18
$\eta_{TS}$ [%]	68.1	68.7	68.6
Fan arrangement	Induced	Induced	Induced
$U$ [W/m <sup>2</sup> K]	23.58	21.5	21.4
$A_{HX}$ [m <sup>2</sup> ]	222480	278160	304880
Pinch point [°C]	9.48	9.88	9.2
# bays	11	14	15
# fans per bay	3	3	3
$N_{tubes}$	90	89	91
$V_{HX}$ [m <sup>3</sup> ]	481	601	660
$\dot{W}_{fan}$ [kW]	678	812	872

Figure 8 plots the Pareto fronts for the three systems balancing heat exchanger volume and fan power for a tube length of 18 m. The aforementioned recommendation in terms of  $v_{face}$  ranging from 2 to 4 m/s is added and highlighted with filled markers. The black markers for each Pareto front indicate the reference bay from Table 6.

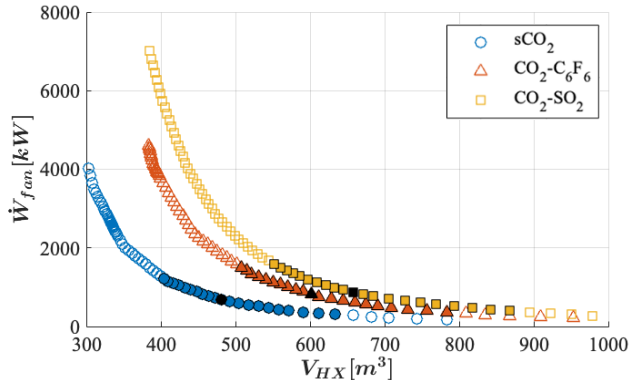


**Figure 8:** Pareto fronts corresponding to a tube length of 18 m. Reference bay designs are highlighted with black markers. Filled-in coloured markers correspond to  $v_{face}$  ranging 2 to 4 m/s.

According to the results in Figure 8, the optimum ACHE design stems from the best compromise between  $\dot{W}_{fan}$  and  $V_{HX}$ , which is found in the left-bottom corner of the Pareto front and corresponds to high values of  $L_{tube}$ . This means that, as far as the ACHE is concerned, it is always beneficial to increase the length of the tubes. Nevertheless, even if longer tubes allow the rejection of the same heat duty with lower  $\dot{W}_{fan}$  and  $V_{HX}$ , this comes at the expense of larger  $\Delta P_{wf}$  (for given  $\Delta T_{air}$ ), which can be detrimental for cycle performance. In order to assess how much thermal efficiency is affected by changes in  $\Delta P_{wf}$ , simulations are carried out with Thermoflex for the three systems in analysis. Pressure drops in the range from 0 (ideal case) to 2 bar are considered (0.46 bar being the reference value employed in [17], see Table 4), and the results are provided in Figure 9. Similar thermal efficiency drops ( $\Delta\eta_{th}$ ) are observed for both Recompression with pure sCO<sub>2</sub> and transcritical Recompression with CO<sub>2</sub>-SO<sub>2</sub>, rounding 0.4 percentage points (pp) at 2 bar. This confirms the very similar performances obtained by these two systems, already highlighted in [8,9]. On the other hand, Precompression with CO<sub>2</sub>-C<sub>6</sub>F<sub>6</sub> shows smaller  $\Delta\eta_{th}$ , in the order of 0.15 pp. This is due to the further degree of optimisation that characterises this system, enabled by the addition of the precompressor (stations 7-8 in Figure 1(b)), which is capable of overcoming the limitation imposed by condensing pressure on turbine exhaust pressure (more information in [9]).

Although at first glance these performance drops look small, it is also true that they have a negative impact on the upstream component of the power plant. For instance, lower cycle efficiency implies larger aperture area (hence cost) of the solar field and also larger inventory of HTF to be pumped (hence higher cost and auxiliary power consumption).

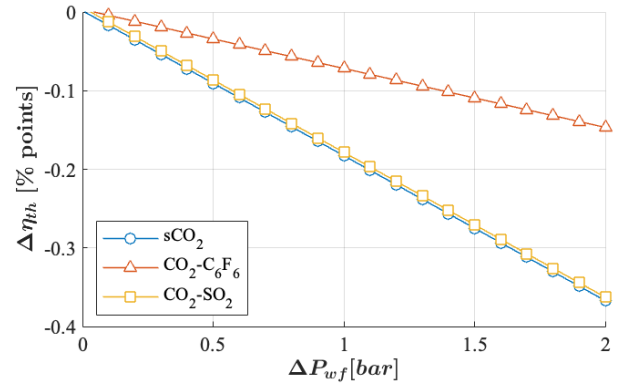


**Figure 9:** Thermal efficiency change as a function of internal pressure drops across the ACC, considering the three different systems under analysis.

In addition, it is to note that, for a given  $L_{tube}$ ,  $\Delta P_{wf}$  and  $\Delta T_{air}$  exhibit opposite trends that create a counteracting effect on cycle thermal efficiency. In fact,  $\Delta T_{air}$  must increase in order to reduce  $\Delta P_{wf}$ . Nevertheless, if a reduction in  $\Delta P_{wf}$  is beneficial for cycle efficiency, a higher  $\Delta T_{air}$  leads to increasing air temperatures at ACC outlet. This latter effect could lead to higher minimum cycle temperatures with a subsequent reduction of thermal efficiency, offsetting the potentially beneficial effect of a lower  $\Delta P_{wf}$ . Similarly, reducing  $\Delta T_{air}$  could be beneficial for cycle efficiency (lower minimum cycle temperatures could be achieved), and this becomes even more interesting considering the possibility to tailor the composition of the mixtures to maximise cycle efficiency according to minimum cycle temperature, as discussed in [7]. In this regard, thermal efficiency gains in the order of 1 pp can be obtained when reducing cycle minimum temperature from 50°C to 40°C [8]. Nevertheless, for a given  $L_{tube}$ , lower  $\Delta T_{air}$  would lead to higher  $\Delta P_{wf}$  (lower thermal efficiency) and, following the Pareto front, to higher fan power consumption (lower net efficiency). With all of this in mind, the identification of the optimum value of  $L_{tube}$  and, generally speaking, the optimum design of the ACHE, must stem from global system global optimization rather than addressed independently in an optimization of condenser design.

Last but not least, some considerations regarding fans optimisation and their integration in the ACC are worthwhile, even if this task falls out of the scope of the present work. Generally speaking, larger fans are desirable as they enable a lower number of fans and, following the bay design guidelines presented above, also the number of bays (reduced capital cost), since multiplicity of components is usually detrimental for plant economics. However, by reducing the number of independent bays, the capacity of the system to control part-load performance effectively (i.e., off-design cooling capacity) at partial load is also compromised. Again, it is not trivial to provide a solution for this problem, which will be addressed from a techno-economic standpoint in future works by the authors also considering ACC integration and part-load operation strategies.

## CONCLUSIONS

In this paper, a methodology to design a finned tube air-cooled condenser for pure sCO<sub>2</sub> and CO<sub>2</sub>-based mixtures is presented and discussed. An in-house code for the design of axial fans is included. Three different systems are considered, identified in previous works by the authors: a transcritical precompression cycle running on 85%CO<sub>2</sub>-15%C<sub>6</sub>F<sub>6</sub>, a transcritical recompression cycle with 80%CO<sub>2</sub>-20%SO<sub>2</sub> and a supercritical sCO<sub>2</sub> recompression cycle. A sensitivity analysis to air temperature rise and hot pressure drop is carried out in order to obtain Pareto fronts defining the optimal design space for the ACC of the three systems under analysis.

The main outcomes of this study are as follows:

- The model presented is a specific tool developed for the design of ACCs, and it is here employed to study the effect of various design parameters.
- The optimal design of the ACC depends strongly on the working fluid considered.
- The common practice of limiting the length of the tubes to ~18.3m and air face velocity to ~4 m/s is confirmed by the results of the analysis.
- Tube length and air face velocity are found to be the two key-parameters in the design of the ACHE.
- Increasing the length of the tubes is always beneficial for ACHE design since it reduces both fan power and HX size of. Nevertheless, this also leads to higher n pressure drops on the hot side, with a detrimental effect on thermal efficiency.
- As a consequence, it cannot be concluded that the optimum ACC design, corresponding to the highest internal pressure drop, also corresponds to the optimum conditions of the overall plant. In fact, it is very likely not the case.
- In this regard, it is shown that the rationale employed for the design of the ACHE is actually the opposite to the one that should be used from a global plant optimisation standpoint, which is evidently not a trivial task.
- As a conclusion, it becomes clear that the definition of the optimal design space of an ACHE must be included in the global optimisation of the power plant.

## NOMENCLATURE

$A_{FR}$	Tube bundling frontal area	(m <sup>2</sup> )
$A_{HX}$	External Heat Exchanger area	(m <sup>2</sup> )
ACC	Air-cooled condenser	(-)
ACHE	Air-cooled heat exchanger	(-)
CSP	Concentrated Solar Power	(-)
$D_{fan}$	Fan diameter	(m)
HRU	Heat Rejection Unit	(-)
HX	Heat Exchanger	(-)
LCoE	Levelised Cost of Energy	(\$/MWh)
LMTD	Logarithmic mean temperature difference	(K)
$L_{tube}$	Length of tubes	(m)
$N_{rows}$	Number of rows	(-)
$N_{tubes}$	Number of tubes	(-)

PCHE	Printed Circuit Heat Exchanger	(-)
pp	percentage points	(%)
SoA	State of the Art	(-)
$S_L$	Longitudinal pitch	(m)
$S_T$	Transversal pitch	(m)
TES	Thermal Energy Storage	(-)
TIT	Turbine Inlet Temperature	(°C)
U	Heat transfer coefficient	(W/m <sup>2</sup> K)
UA	Thermal conductance	(W/K)
$\dot{V}_{air}$	Air volumetric flow rate	(m <sup>3</sup> /s)
$v_{face}$	Air face velocity	(m/s)
$V_{HX}$	Total volume of tube bundling	(m <sup>3</sup> )
WF	Working fluid	(-)
$W_{fan}$	Fan power consumption	(kW)
$\Delta P_{air}$	Air pressure drop	(Pa)
$\Delta P_{wf}$	Workng fluid pressure drop	(Pa)
$\Delta T_{air}$	Air temperature rise	(°C)
$\eta_{th}$	Cycle thermal efficiency	(%)
$\eta_{TS}$	Fan total-to-static efficiency	(%)

## ACKNOWLEDGEMENTS

The SCARABEUS project has received funding from the European Union's Horizon 2020 research and innovation programme under grant agreement N ° 814985. The SCARABEUS team at Kelvion Thermal Solutions is gratefully acknowledged for their valuable contribution in the definition of the operational limits and best engineering practice of the ACC.

## REFERENCES

- [1] IRENA (2021), Renewable Power Generation Costs in 2020, *International Renewable Energy Agency, Abu Dhabi*.
- [2] He, Y. L., Qiu, Y., Wang, K., Yuan, F., Wang, W. Q., Li, M. J., & Guo, J. Q. (2020). Perspective of concentrating solar power. *Energy*, 198, 117373.
- [3] Merchán, R. P., Santos, M. J., Medina, A., & Hernández, A. C. (2021). High temperature central tower plants for concentrated solar power: 2021 overview. *Renewable and Sustainable Energy Reviews*, 111828.
- [4] Ho, C. K. (2017). Advances in central receivers for concentrating solar applications. *Solar energy*, 152, 38-56.
- [5] Polimeni, S., Binotti, M., Moretti, L., & Manzolini, G. (2018). Comparison of sodium and KCl-MgCl<sub>2</sub> as heat transfer fluids in CSP solar tower with sCO<sub>2</sub> power cycles. *Solar Energy*, 162, 510-524.
- [6] Supercritical CARbon dioxide Alternative fluids Blends for Efficiency Upgrade of Solar power plants. <https://www.scarabeusproject.eu/>. Retrieved October 24<sup>th</sup> 2022.
- [7] Crespi, F., de Arriba, P. R., Sánchez, D., Ayub, A., Di Marcoberardino, G., Invernizzi, C. M., ... & Manzolini, G. (2022). Thermal efficiency gains enabled by using CO<sub>2</sub> mixtures in supercritical power cycles. *Energy*, 238, 121899.
- [8] Crespi, F., de Arriba, P. R., Sánchez, D., & Muñoz, A. (2022). Preliminary investigation on the adoption of CO<sub>2</sub>-SO<sub>2</sub>

working mixtures in a transcritical Recompression cycle. *Applied Thermal Engineering*, 211, 118384.

[9] Rodríguez-deArriba, P., Crespi, F., Sánchez, D., Muñoz, A. & Sánchez, T. (2022). The potential of transcritical cycles based on CO<sub>2</sub> mixtures: An exergy-based analysis. *Renewable Energy*, vol. 199, p. 1606-1628.

[10] Ivanpah Solar Electric Generating System CSP Project. <https://solarpaces.nrel.gov/project/ivanpah-solar-electric-generating-system>. Retrieved October 24<sup>th</sup> 2022.

[11] Moiseyev, A., & Sienicki, J. J. (2014). Investigation of a dry air cooling option for an S-CO<sub>2</sub> cycle. *Proceedings of Supercritical CO<sub>2</sub> Power Symposium, Pittsburgh (PA)*

[12] Moiseyev, A., Lv, Q., & Sienicki, J. J. (2017). Heat Exchanger Options for Dry Air Cooling for the sCO<sub>2</sub> Brayton Cycle. *Proceedings of ASME Turbo Expo 2017*

[13] Ehsan, M. M., Guan, Z., Klimenko, A. Y., & Wang, X. (2018). Design and comparison of direct and indirect cooling system for 25 MW solar power plant operated with supercritical CO<sub>2</sub> cycle. *Energy conversion and management*, 168, 611-628.

[14] Ehsan, M. M., Wang, X., Guan, Z., & Klimenko, A. Y. (2018). Design and performance study of dry cooling system for 25 MW solar power plant operated with supercritical CO<sub>2</sub> cycle. *International Journal of Thermal Sciences*, 132, 398-410.

[15] Pidaparti, S. R., White, C. W., & Weiland, N. T. (2022). Cooling System Cost and Performance Models to Minimize Cost of Electricity of Direct sCO<sub>2</sub> Power Plants. In *Proceedings of the 7th International Supercritical CO<sub>2</sub> Power Cycles Symposium*.

[16] Pidaparti, S.R. White, C. W., Weiland, N.T. (2021). Impact of Plant Siting on Performance and Economics of Indirect Supercritical CO<sub>2</sub> Coal Fired Power Plants. En *Turbo Expo: Power for Land, Sea, and Air*. American Society of Mechanical Engineers. p. V010T30A009.

[17] Illýes, V., Morosini, E., Doninelli, M., David, P.L., Guerif, X., Werner, A., Di Marcoberardino, G. & Manzolini, G. (2022) Design of an air-cooled condenser for CO<sub>2</sub>-based mixtures: model development, validation and heat exchange gain with internal microfin. *Proceedings of ASME Turbo Expo 2022*.

[18] Neises, T., & Turchi, C. (2019). Supercritical carbon dioxide power cycle design and configuration optimization to minimize levelized cost of energy of molten salt power towers operating at 650 C. *Solar Energy*, 181, 27-36.

[19] Thermoflow Inc, Thermoflow suite - Thermoflex software, [https://www.thermoflow.com/products/\\$generalpurpose.html](https://www.thermoflow.com/products/$generalpurpose.html). Retrieved October 24<sup>th</sup> 2022.

[20] Aspen plus - leading process simulator software. <https://www.aspentech.com/en/products/engineering/aspen-properties>. Retrieved October 24<sup>th</sup> 2022.

[21] Lemmon, E., Bell, I. H., Huber, M. & McLinden, M., NIST Standard Reference Database 23: Reference Fluid Thermodynamic and Transport Properties-REFPROP, Version

10.0, *National Institute of Standards and Technology, Standard Reference Data Program, Gaithersburg.*

[22] Shah, R. K., & Sekulic, D. P. (2003). Fundamentals of heat exchanger design. *John Wiley & Sons*.

[23] Incropera, F. P., DeWitt, D. P., Bergman, T. L., & Lavine, A. S. (1996). Fundamentals of heat and mass transfer. *New York: Wiley*.

[24] A. Cavallini, D. Del Col, L. Doretti, M. Matkovic, L. Rossetto, C. Zilio and G. Censi, "Condensation in Horizontal Smooth Tubes: A New Heat Transfer Model for Heat Exchanger Design," *Heat Transfer Engineering*, pp. 31-38, 2006.

[25] Krasnoshchekov, E. A. (1966). Experimental study of heat exchange in carbon dioxide in the supercritical range at high temperature drops. *High Temperature*, 4, 375-382.

[26] White, M. T., Bianchi, G., Chai, L., Tassou, S. A., & Sayma, A. I. (2021). Review of supercritical CO<sub>2</sub> technologies and systems for power generation. *Applied Thermal Engineering*, 185, 116447.

[27] Kakac, S., Liu, H., & Pramuanjaroenkij, A. (2002). Heat exchangers: selection, rating, and thermal design. *CRC press*.

[28] Del Col, D., Bisetto, A., Bortolato, M., Torresin, D., & Rossetto, L. (2013). Experiments and updated model for two phase frictional pressure drop inside minichannels. *International journal of heat and mass transfer*, 67, 326-337.

[29] Brun, K., Friedman, P., & Dennis, R. (Eds.). (2017). Fundamentals and applications of supercritical carbon dioxide (sCO<sub>2</sub>) based power cycles. *Woodhead publishing*.

[30] Serth, R. W., & Lestina, T. G. (2014). Air-cooled heat exchangers. *Process Heat Transfer*, 509-553.

[31] Wilkinson, M. (2017) The Design of an Axial Flow Fan for Air-Cooled Heat Exchanger Applications, *MSc thesis, Stellenbosch University*

[32] Bruneau, P. R. P. (1994). The design of a single rotor axial flow fan for a cooling tower application. *PhD Thesis, University of Stellenbosch*.

[33] Von Backström, T.W., Buys, J.D. & Stinned, (1996). Minimization of the exit loss of a rotor-only axial fan. *Engineering Optimization+ A35*, vol. 26, no 1, p. 25-33.

[34] Meyer, C.J., Kröger, D.G. (1998). Plenum chamber flow losses in forced draught air-cooled heat exchangers. *Applied Thermal Engineering*, vol. 18, no 9-10, p. 875-893.



## CO<sub>2</sub> PURIFICATION AND PURITY CONTROL FOR THE sCO<sub>2</sub> EXPERIMENTAL LOOP AT REŽ – A SUMMARY OF THE TEST RESULTS

**Jan Berka\***

Centrum výzkumu Řež s.r.o.  
University of Chemistry and Technology, Prague  
Řež, Prague, Czech Republic  
Email: jan.berka@cvrez.cz

**Tomáš Hlinčík**

University of Chemistry and Technology Prague  
Prague, Czech Republic

**Eliška Purkarová**

University of Chemistry and  
Technology Prague  
Prague, Czech Republic

**Alice Vagenknechtová**

University of Chemistry and  
Technology Prague  
Prague, Czech Republic

**Jakub – Vojtěch Ballek**

University of Chemistry and  
Technology Prague  
Prague, Czech Republic

### ABSTRACT

In project No. TK02030023, titled ‘Purification and purity control of CO<sub>2</sub> gas in power cycles’ (funded by the Technology Agency of the Czech Republic [TA CR]), methods for gas purification in an sCO<sub>2</sub> loop were proposed and tested. First, moisture separation was investigated using adsorption techniques, and the initial results of the experiment are presented in this paper.

### INTRODUCTION

Power cycles with supercritical carbon dioxide (sCO<sub>2</sub>) can be adopted in numerous applications in both nuclear (including advanced Generation IV reactors) and non-nuclear power production. These power cycles are characterised by higher efficiency compared to steam power cycles. Another advantage is the more compact size of their components, particularly the turbine [1, 2]. The operational temperature range of the sCO<sub>2</sub> cycle is wide, typically ca. 350–700 °C.

Various arrangements and configurations of sCO<sub>2</sub> power cycles have been proposed. According to the heat source, the cycles can be designed as ‘indirectly fired’ or ‘directly fired’ (see [2] for details). More commonly, indirectly fired cycles use a closed sCO<sub>2</sub> circuit heated by an external heat source over a heat exchanger. Directly fired sCO<sub>2</sub> power cycles use flue gas from combustion as a heat source, as well as CO<sub>2</sub>. These cycles can be combined with carbon capture and storage technology [2].

There are various research activities and projects on sCO<sub>2</sub> power cycles, which include investigations into sCO<sub>2</sub> medium chemistry, purification and purity control. Other activities are centred on the compatibility of structural materials with sCO<sub>2</sub> as a medium.

One of these research projects is titled ‘Purification and purity control of CO<sub>2</sub> gas in power cycles’ (No. TK02030023) and is supported by the Technology Agency of the Czech Republic (TA ČR) [3]. The project has been made possible in

cooperation with two organisations, i.e. Centrum výzkumu Řež s.r.o. (CV Řež) and the University of Chemistry and Technology, Prague (UCT). Finalisation of the project is planned for 2025, and its principal objectives are as follows:

- Gain, summarise and utilise information concerning purity, purification processes and analytical purity control techniques for sCO<sub>2</sub> power systems;
- Carry out analytical method verification;
- Implement impurity separation methods, based on adsorption testing;
- Propose and manufacture a purification unit for an sCO<sub>2</sub> experimental loop at CV Řež;
- Propose and manufacture an sCO<sub>2</sub> autoclave for material testing;
- Propose a CO<sub>2</sub> purification system for an sCO<sub>2</sub> power station.

The selected information and specific results obtained during the process of drawing up the project solution are presented in this paper.

### ANTICIPATED IMPURITIES IN sCO<sub>2</sub> POWER CYCLES

The first phase of identifying a solution for project No. TK02030023 involved listing the impurities expected in CO<sub>2</sub> and sCO<sub>2</sub> power systems.

Impurities may affect the lifetime, effectivity and reliability of a power station, and sources of impurities can include leakages from the surroundings, desorption from internal surfaces, admixtures in source gas and chemical reactions during operation.

One cause of impurities is the source gas, which is used for filling the system. The purity levels of individual types of CO<sub>2</sub> gases available on the market are different (see the examples in Table 1) [4]. In particular, cheap gases with low purity contain reasonably significant quantities of admixtures.

\* corresponding author(s)



**Table 1:** The CO<sub>2</sub> purity levels of gases available on the market [3] in vppm (1 vppm = 0.0001 % by volume).

CO <sub>2</sub> type	Purity	Impurities (vppm)					
	% vol.	H <sub>2</sub> O	O <sub>2</sub>	CO	C <sub>n</sub> H <sub>m</sub>	N <sub>2</sub>	Oil
SFC/SFE	99.9993	1	2	0,5	1	3	-
CO <sub>2</sub> for food industry (E290)	99.5	52	-	10	-	-	5
4.8	99.998	5	2	1	2	10	-
4.5	99.995	5	15	1	2	30	-
R-744	99.9	10	15	1	2	30	-
3.0	99.9	120	500	-	50	500	-
5.3	99.9993	1	2	0,5	1	3	-

Other impurities seep into the circuit during operation.

In indirectly fired sCO<sub>2</sub> power cycles, during stable operation, only minor impurities are anticipated (in concentrations well below 1 % by volume). The following compounds are likely present in sCO<sub>2</sub>: H<sub>2</sub>O, O<sub>2</sub>, CO, N<sub>2</sub>, organic compounds and oil. Some of these compounds may influence the lifetime and reliability of a power station due to corrosion (particularly H<sub>2</sub>O). Organic compounds and oil may worsen heat exchange, albeit only in high concentrations.

In the case of directly fired cycles, the concentration of impurities is expected to be higher (in units of % by volume) due to the use of flue gas as a source of CO<sub>2</sub>. In this scenario, more compounds, i.e. sulphur oxides, are expected to be present in the sCO<sub>2</sub> power cycle. Other than corroding the power device, these higher impurity levels may also lower the efficiency of the power cycles [3]. Project No. TK02030023 is primarily aimed at the more commonly used indirectly fired sCO<sub>2</sub> power cycles.

In identifying the project solution, the presence of organic impurities in sCO<sub>2</sub> during the experimental loop operation was monitored [3, 4] using gas chromatography and the gas chromatography–mass spectrometry (GC-MS) technique. In the operation of larger (semi-industrial) scale experimental devices, there are fairly common problems with organics in a gas medium for various reasons [5]. Before the operation, the loop was filled with CO<sub>2</sub> with a purity of 4.0; then, the loop was operated at 550 °C and 25 MPa. During operation, several CO<sub>2</sub> extractions were taken through sampling tubes filled with active carbon. Subsequently, the adsorbed organics were determined using GC-MS. The concentration of organic

compounds detected was relatively low, with the highest being ca. 1700 ng/l (25 °C, 1 bar) and the concentration decreased during operation (see Figure 1). Of the detected organic compounds, benzene predominated. The source of these organic impurities may have been residual oils and degreasers in the internal apparatus of the sCO<sub>2</sub> experimental loop or oil from the circulator, and sCO<sub>2</sub> is known to be a very effective solvent of organics. Other compounds can also be formed by reactions at a high temperature. The details of the experiment are described in [6].

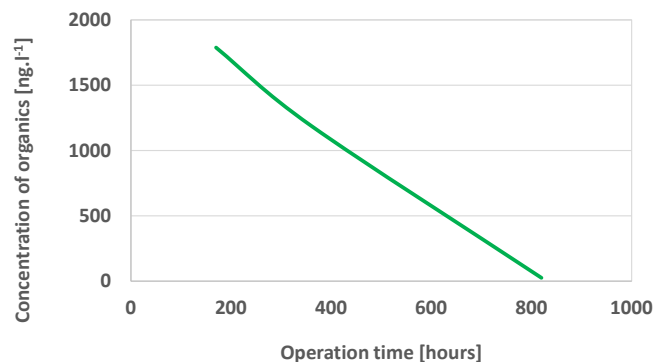


**Figure 1:** The organic compounds present in sCO<sub>2</sub> during operation of the experimental loop at Řež.

#### CO<sub>2</sub> ANALYTICAL PURITY CONTROL

To determine the above-mentioned compound concentrations, different methods can be adopted. The applicability of a particular method depends on the required sensitivity, its usability in a specific environment, the demands on operators and purchase costs. General-purpose methods suitable for identifying a wide range of compounds are based on gas chromatography. Therefore, some of the activities carried out in project No. TK02030023 was aimed at researching this technique. The sensitivity and other properties of these methods depend on their configuration and settings (see Table 2 for details).

**Table 2:** The configurations and basic characteristics of gas chromatography systems.

Configuration	Detector	Utilisation	Sensitivity/detection limit	Note
GC-TCD	Thermal conductivity	Universal	Approx. 10 vppm	Not suitable for mixtures containing H <sub>2</sub> and He as a carrier gas
GC-FID	Flame ionisation	Flammable compounds, sensitive, typically C <sub>x</sub> H <sub>y</sub>	Not sensitive to permanent compounds	
GC-HID	Helium ionisation	Universal, high sensitivity	Bellow 1 vppm, bellow 0,1 vppm for selected compounds	Requires He as a carrier gas
GC-MS	Mass spectrometry	Universal, depends on the configuration	Suitable, especially for the identification and determination of organic compounds	Demanding in terms of staff qualification, operation conditions, compliance and maintenance. Higher purchase cost.

In addition to the analytical technique, the sampling method is also important. Samples can, for example, be taken in a special vessel (e.g. a sampling canister) or adsorption tube (as in the identification of organics described above) for ex-situ analysis in a laboratory. The sampling site can also be directly connected to the analytical device to reduce the probability of sample contamination by the surrounding air. In the gas sampling of an sCO<sub>2</sub> system (e.g. the experimental loop), the gas pressure must be reduced. The pressure drop is accompanied by a temperature decrease (the Joule–Thomson effect) and freezing of the sampling valve. This phenomenon may affect the results of the analysis due to cold trapping the selected components in the frozen valve (Figure 2). This problem can be resolved using a multistage sampling line and by gradually reducing the pressure with heated reduction valves. For CO<sub>2</sub> sampling in the sCO<sub>2</sub> experimental loop, a three-stage sampling line with a pressure reduction of 12.5→7→2 MPa via heated valves was manufactured (Figure 3).



**Figure 2:** Freezing the single-valve sampling line during gas sampling.



**Figure 3:** The three-stage sampling line employing gradual pressure reduction of the sCO<sub>2</sub> in the experimental loop.

To control the analytical purity of the CO<sub>2</sub>, the application of gas chromatography with a helium ionisation detector (GC-HID) seemed a suitable configuration because of good sensitivity to most trace-concentration compounds. Thus, this GC-HID chromatographic method was developed, and the standard gas mixture, the composition of which is listed in Table 3, was used to verify the method. The test results are

depicted in the form of a chromatogram as shown in Figure 4. The resolution of most of the trace compounds was relatively good; only acetylene is not visible in the chromatogram, establishing the method as suitable for simple gas impurity determination. Nevertheless, for the identification of higher levels of hydrocarbons, either the method would need to be improved or another analytical technique would have to be employed.

**Table 3:** The model's gas mixture composition.

Compound	Concentration (vppm)
H <sub>2</sub>	100
O <sub>2</sub>	100
N <sub>2</sub>	100
CH <sub>4</sub>	500
Acetylene	500
CO	500
CO <sub>2</sub>	Bal.

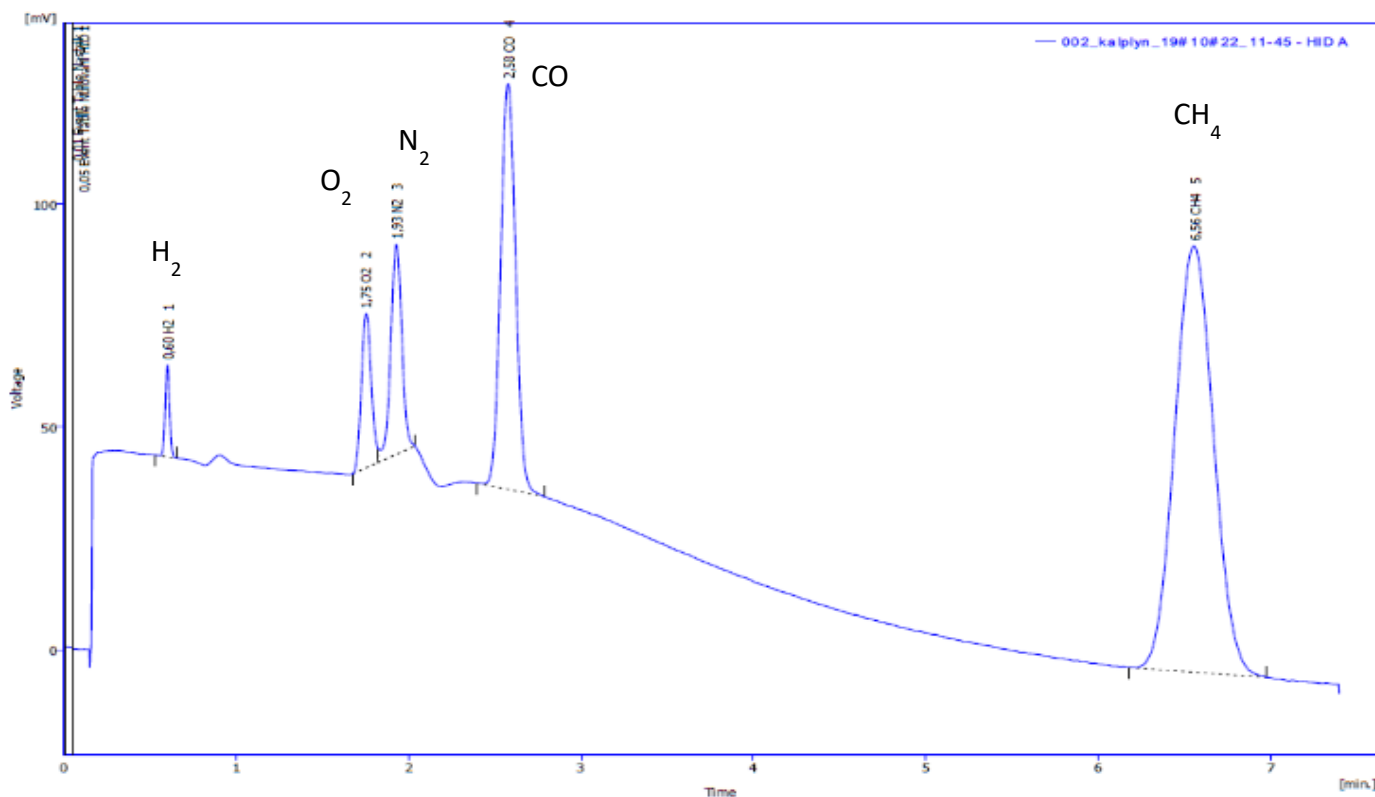


**Figure 4:** A GC-HID chromatogram of the model gas mixture detailed in Table 3.

Gas chromatography methods are not particularly convenient for detecting and determining moisture (H<sub>2</sub>O) content. This is important because moisture typically accelerates corrosion. Special moisture analysers (hygrometers) that operate on different principles are available on the market, and the parameters of some of these are listed in Table 4. Several of these devices enable the probe to be placed directly in the medium, where moisture is monitored. In particular, probes of capacitive and optical hygrometers are designed for higher pressures, which are characteristic of sCO<sub>2</sub> systems.

For the verification of moisture monitoring in the sCO<sub>2</sub> infrastructure at Řež, an infra-red optical analyser was procured. Hygrometers are also used in the natural gas industry; according to the German manufacturer, standard

probes are designed for 10 MPa and special probes (recommended for sCO<sub>2</sub> systems) are designed for a pressure of 20 MPa and tested at 25 MPa. The system can further be calibrated for use in a CO<sub>2</sub> environment. However, the manufacturer states that the measurement accuracy cannot be guaranteed under supercritical conditions and that, to achieve an accurate measurement, the recommended conditions for the probe site are a pressure range of 0.1–5 MPa, a temperature range of 10–40 °C and the maintenance of stable values. To create these conditions, both the pressure and temperature of the probe site must be reduced. The system will be tested during the next experimental phase of this project.

**Table 4:** Selected methods for moisture determination

Method	Max. pressure (MPa)	Measurement range (dew point °C)	Uncertainty (°C)	Note
Cooled mirror	1,1 (2)	- 35 až + 25 (- 65 až + 25) <sup>a</sup>	± 0.2	<sup>a</sup> Depends on the connected probe
Cooled mirror (mobile)	10	- 35 až + 25 (-50 až + 25) <sup>b</sup>	± 1	<sup>b</sup> Depends on the ambient temperature
Optical	25	- 80 až + 20	± 1	
Capacity	34.5	- 80 až +10	± 2 (± 3)	Frequent calibration is needed to maintain measurement accuracy
Quartz crystal microbalance – QCM	0.4	- 80 až - 13	± 3 až ± 1	
Tunable diode laser absorption spectroscopy – TDLAS	0.17	- 71 až - 2,6*	± 4 až ± 0,1	

## PROPOSAL FOR AND VERIFICATION OF A CO<sub>2</sub> PURIFICATION SYSTEM

The proposed purification unit for the sCO<sub>2</sub> experimental loop in Řež should predominantly extract H<sub>2</sub>O and, if possible, other impurities in the form of residual organic compounds, such as CO, H<sub>2</sub> and O<sub>2</sub> from the CO<sub>2</sub> in the loop. The unit is based on the principles of oxidation and adsorption. The proposed purification unit will be set up and implemented in the next phase of the project.

In this phase, the moisture separation was tested with a laboratory device at UCT in Prague (see Figure 5). The gas

was saturated to the requisite moisture level using a moisture generator (1) and subsequently passed through the adsorber (2), where the adsorbents were tested. The moisture level of the outlet gas was measured by way of three hygrometers operating on different principles: cooled mirror, capacity and infra-red.

The moisture separation was tested on three selected adsorbents, i.e. silica gel, a 13 X molecular sieve and active carbon SC 40 (Figure 6). The tests were performed with CO<sub>2</sub> and nitrogen to simulate the effects of a gas matrix.

The results are shown in the graphs in Figure 7 and can be summarised as follows:

- For higher levels of moisture adsorption, both the silica gel and 13 X molecular sieve were effective.
- When the moisture concentration in the inlet gas was low, the 13 X molecular sieve was more effective.
- Active carbon AC 40 was not found to be suitable at all for moisture adsorption.
- The adsorption capacities of the nitrogen matrix gas were approximately 20 % higher than those of the CO<sub>2</sub> matrix gas, with CO taking up part of the adsorbent capacity.

In accordance with the results, the 13 X molecular sieve is recommended as a filler in the purification unit for the experimental loop.

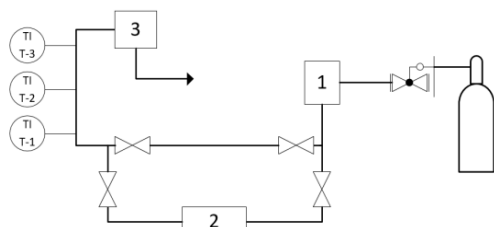


**Figure 5:** The laboratory device for moisture separation testing. 1 – moisture generator; 2 – adsorber; 3 – gas meter; T-1 – Moisture Monitor Series 35; T-2 – hygrometer HYGROPHIL Model F 5672; T-3 – cooled mirror hygrometer HYGRO M4.

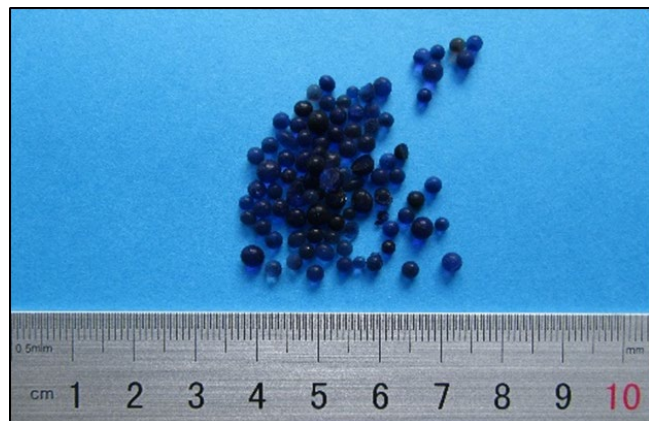


b)



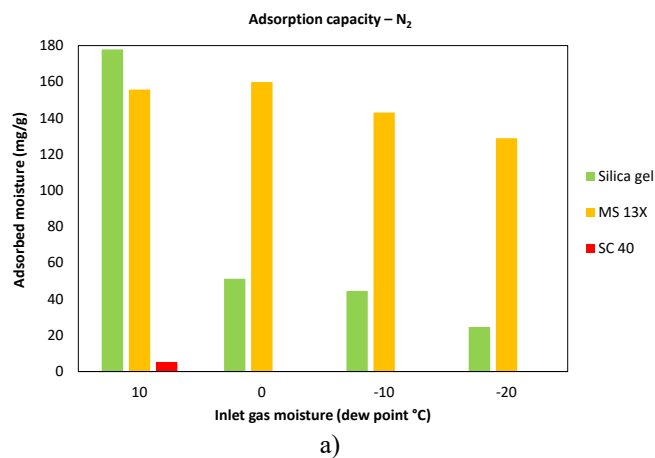
c)

**Figure 6:** The tested adsorbents for moisture removal: a) silica gel; b) 13 X molecular sieve; c) active carbon SC 40.



a)

The experimental programme is still being conducted, and the removal of other selected impurities is planned for the next phase. Verification of the adsorbents' resistivity in a CO<sub>2</sub> environment in a special sCO<sub>2</sub> autoclave is also planned. The autoclave is currently under construction.



a)



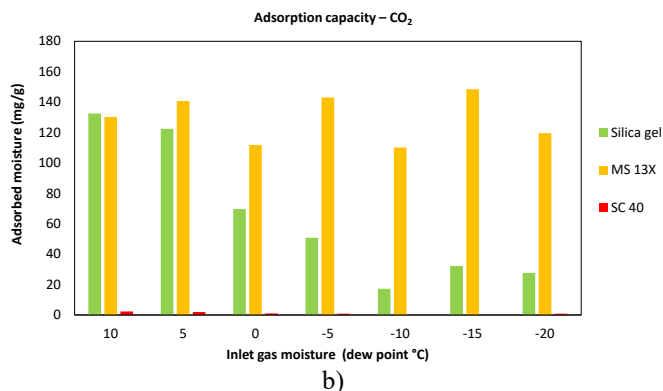


**Figure 7:** Results of the moisture adsorption tests: a) with a nitrogen gas matrix; b) with a CO<sub>2</sub> gas matrix.

## CONCLUSION

CV Řež. and the Department of Gaseous and Solid Fuels and Air Protection, UCT participated in the research activities described herein concerning the purification and purity control of CO<sub>2</sub> in sCO<sub>2</sub> power cycles. In these activities, methods for CO<sub>2</sub> purification and purity control were proposed and verified. Gas chromatography with a helium ionisation detector and an optical infrared hygrometer appeared to be the most effective combination for removing the majority of impurities that were expected to be present in sCO<sub>2</sub> monitoring. These methods were sufficiently sensitive for concentrations of compounds from 0.1–1 vppm. The application of gradual pressure reduction via heated valves in a sampling line prevented it from freezing. The tests of impurity extraction from the CO<sub>2</sub> gas are currently in progress; in the first instance, the adsorption of moisture by different types of materials is currently being investigated. According to the experimental results obtained, the 13 X molecular sieve seemed to be effective for H<sub>2</sub>O adsorption from gas with both higher and lower moisture concentrations. The research activities will continue for at least several more years, and another set of results is expected.

## ACKNOWLEDGEMENTS

The presented work was funded by TA CR, project No. TK02030023.

## REFERENCES

- [1] SCO<sub>2</sub> Power Cycles for Fossil Fuels. Department of Energy. [online]. [vid. 2020-04-03]. Available at: <https://www.energy.gov/sco2-power-cycles/sco2-power-cycles-fossil-fuels>.
- [2] Brun, K., Friedman, K., Dennis, R. (2017). Fundamentals and Applications of Supercritical Carbon Dioxide (sCO<sub>2</sub>) Based Power Cycles. Duxford, United Kingdom: Elsevier. 465 s. ISBN: 978-0-08-100804-1
- [3] Available at: <https://backup.isvavai.cz/cep?s=jednoduche-vyhledavani&ss=detail&n=0&h=TK02030023>
- [4] Berka, J., Hlinčík, T., Purkarová, E., Vagenknechtová, A., Rozumová, L. Investigation of material degradation and coolant chemistry for sCO<sub>2</sub> power cycles. The 4th European sCO<sub>2</sub> Conference for Energy Systems March 22–26, 2021, Prague, Czech Republic, paper No. 139
- [5] Berka, J., Víden, I., Kozmík, V. (2012): Organic Compounds Detectable in the He Loop of Experimental Research Device for Simulation of Nuclear Reactor Cooling at Opening Operation, Chem. Listy 106, 980-987
- [6] Berka, J., Ballek, J. V., Velebil, L. et al. (2021): CO<sub>2</sub> power chemistry in the CV Řež experimental loop, Acta Polytechnica, vol. 61, no. 4, p. 1-7, doi: 10.14311/AP.2021.61.0504

## DESIGN AND COMPUTATIONAL ASSESSMENT OF A SUPERCRITICAL CO<sub>2</sub> COMPRESSOR FOR WASTE HEAT RECOVERY APPLICATIONS

**Alessandro Romei**  
**Giacomo Persico\***  
**Paolo Gaetani**  
Energy Department  
Politecnico di Milano  
Milan, Italy

**Ernani Fulvio Bellobuono**  
**Lorenzo Toni**  
**Roberto Valente**  
Centrifugal compressors and expanders NPD  
Baker-Hughes Nuovo Pignone  
Florence, Italy

### ABSTRACT

The development of novel technical solutions for the effective recovery of waste heat is crucial for making accessible the enormous amount of thermal energy released by industrial processes, thus supporting the EU energy strategy. To this end, the EU-H2020 project CO2OLHEAT aims at developing, and demonstrating in a real industrial environment, a novel sCO<sub>2</sub> power unit of 2-MW capacity recovering energy from flue gases at 400 °C. The thermo-economic optimization of the system and the complexity of its implementation led to select a simple recuperative cycle for the CO2OLHEAT unit, which features a relatively unconventional multi-shaft configuration where the sCO<sub>2</sub> compressor is driven by a dedicated radial expander, while the electrical power is generated via a separated axial turbine.

The present study focused on the design and computational assessment of the compressor for the CO2OLHEAT system. The thermodynamic optimization of the cycle led to an overall pressure ratio slightly above 2.5, delivered with a two-stage centrifugal compressor. As typically found in sCO<sub>2</sub> power systems, the thermodynamic state of the fluid at the machine intake (P = 85 bar; T = 32°C) is close to the critical point and to the saturation curve; therefore, the first stage of the machine demands a dedicated aero-thermodynamic design, which can account for the effects of non-ideal thermodynamics and of the potential onset of two-phase flows. The paper discusses the conceptual aero-mechanical design of the compressor and then focuses on its performance assessment over the full operating range via Computational Fluid Dynamics. Two alternative flow models are considered, the first one based on the experimentally-validated barotropic fluid representation, while the second one featuring a complete thermodynamic model which assumes homogeneous equilibrium between the phases. The approaches provide similar outcomes, showing that the compressor fulfills the system requirement and guarantees large rangeability.

\* corresponding author: giacomo.persico@polimi.it

### INTRODUCTION

Energy-intensive industries across Europe release in the environment a large amount of hot flue gases, resulting in an enormous waste of heat which could, instead, be efficiently converted into useful mechanical or electrical energy. On the quantitative ground, considering recent statistics on waste heat not exploited [1], an average conversion efficiency of 25%, and an operating factor of 0.8, the conversion of 5% of the European waste heat would lead to more than 500 GWh of primary energy savings per year and, assuming 0.46 tCO<sub>2</sub>/MWh, it would avoid more than 100.000 tons of CO<sub>2</sub> per year, with important economical relapses, further enhanced by the recent severe increase of fossil-fuel prices.

While for flue gas temperature below 300 °C and above 500 °C mature energy conversion technologies are available (Organic and Steam Rankine Cycles, respectively), such technologies exhibit techno-economical limitations for flue gas temperature within this range. For such conditions, which represent a large share of the overall available waste heat in Europe, alternative technologies are presently under study. Among them, closed Joule-Brayton thermodynamic cycles working with carbon dioxide in supercritical conditions (sCO<sub>2</sub>) are particularly attractive due to the high efficiency of the system and the compactness of their components, which might foster fast response to transients and reduced footprint, which are crucial features for effective waste-heat recovery systems [2].

Even though advanced calculations were performed at both component ([3], [4], [5], [6], [7], [8], [9]) and system ([10], [11], [12], [13]) level, and the first experimental verification of components have given promising outcomes ([14], [15]), a proper demonstration of the overall system operation in the real environment is still needed. To this end, the EU-H2020 project CO2OLHEAT was launched in 2021, with the aim of developing a novel sCO<sub>2</sub> power system demonstration plant of 2-MW

DOI: 10.17185/duerpublico/77332

capacity, to be installed and operated in a real industrial environment, recovering waste heat from flue gases released at about 400 °C. By considering the flue gas conditions, as well as the required flexibility of operation, a simple recuperative sCO<sub>2</sub> cycle has been selected for the CO2OLHEAT system, with the sCO<sub>2</sub> compressor powered by a radial turboexpander and a subsequent axial turbine for electrical power generation.

The present study focuses on the design and the computational assessment of the sCO<sub>2</sub> compressor for the CO2OLHEAT power system. The thermodynamic optimization of the cycle led to an overall pressure ratio of 2.55, delivered by a two-stage centrifugal compressor. As typically found in such systems, at the machine intake the thermodynamic state of the fluid is close to the critical point and to the saturation curve (P = 85 bar; T = 32 °C); therefore, the first stage of the machine demands a proper aero-thermodynamic design, which must be capable to account for both the non-ideal thermodynamics of the fluid and the potential onset of phase change.

The design of the compressor was approached by leveraging the computational and modeling techniques developed in previous studies [9] and on the experimental survey recently carried out on a 5.4 MW sCO<sub>2</sub> prototype compressor [15], [16]. At first, a conceptual design of the meridional channel and of the blade was carried out, then the compressor aerodynamics was verified by applying Computational Fluid Dynamics (CFD) over the entire flow range of the machine. Two thermodynamic models of the fluid were considered: at first, the experimentally validated barotropic model was considered [17], which allows representing in a simplified way the non-ideal thermodynamics of the fluid and the onset of two-phase flows assuming homogeneous equilibrium between the phases; then, to enhance the reliability of the prediction, the compressor was also analyzed by applying a ‘complete’ homogeneous equilibrium model, which does not require the barotropic fluid assumption [18] and retains the actual thermodynamic complexity of the near-critical fluid.

The paper is structured as follows: at first the CO2OLHEAT system is presented and the compressor design process is described; then the compressor aerodynamics and performance are analyzed with the two computational models, to derive conclusions on the machine operation and on its modeling.

## THE CO2OLHEAT POWER UNIT

The CO2OLHEAT power unit was conceived to recover waste heat from an existing cement plant, whose flue gases in nominal conditions are available at temperature of 400 °C and with a flow rate of 230000 Nm<sup>3</sup>/h. The core of the system is a simple recuperated cycle without either recompression or recuperator bypass, due to the relatively low maximum temperature of the heat source and the high minimum stack temperature in order to avoid acid condensates (150 °C). As reported in Figure 1, in the overall system the power unit is complemented by a waste-heat recovery unit and by a water-based heat-rejection unit.

The thermodynamic optimization of the sCO<sub>2</sub> cycle led to set the compressor-intake thermodynamic conditions are set to

32 °C and 85 bar respectively, to properly exploit the high density of CO<sub>2</sub> in the proximity of the critical point. The compressor-outlet pressure is set to 216.9 bar, resulting from a trade-off between cycle performance, material selection, and cost. The resulting cycle pressure ratio is equal to 2.55, which is obtained by two centrifugal compressors in series; they are mechanically driven by two centripetal turbines in series, thus creating a compact turbo-expander unit. The maximum temperature of the cycle is set at 360 °C, namely 40 °C lower than the flue gas nominal temperature in order to limit the surface area of the primary heat exchanger. The expansion is completed by an axial turbine, which is responsible for the power output of the system.

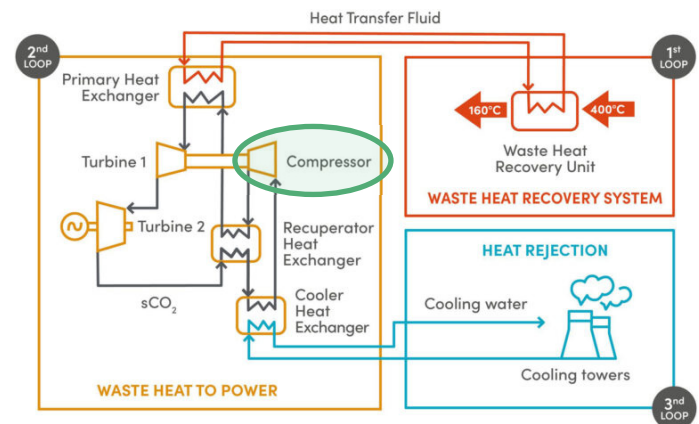


**Figure 1:** CO2OLHEAT system concept, with a focus on the compressor object of the study

The resulting net power output exceeds 2 MW, with a cycle efficiency of 23.17% referred to the inlet thermal power. Full details on the CO2OLEAT power system design and off-design operation can be found in [19].

## COMPRESSOR DESIGN

The optimization of selected thermodynamic cycle requires the compressor to operate between 85 and 216.9 bar with inlet conditions very close to CO<sub>2</sub> critical point (32 °C, 670 kg/m<sup>3</sup>). Actual process conditions and the demo site available power lead to a compact machine size with an impeller diameter lower than 150 mm and a rotating speed close to 20000 RPM. In order to minimize the impact of internal leakages and to manage the residual axial thrust, an integrally geared configuration has been selected, which includes two shafts, one dedicated to the compression section and one to the expansion phase, as shown in Figure 2.

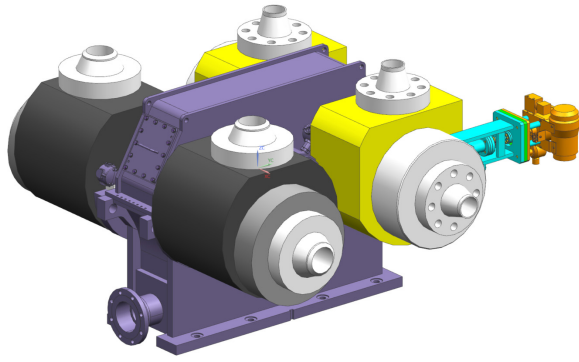


**Figure 2:** Turbo-expander compact system  
 © 2022 Baker Hughes Company - All rights reserved

The overall pressure ratio has been split into 2 centrifugal compressor stages in a back-to-back arrangement, as reported in Figure 3. The first compression phase is equipped with a movable axial inlet guide vane (IGV) to guarantee a fine-tuning of the suction operating condition, and to improve compressor flexibility in off-design conditions.

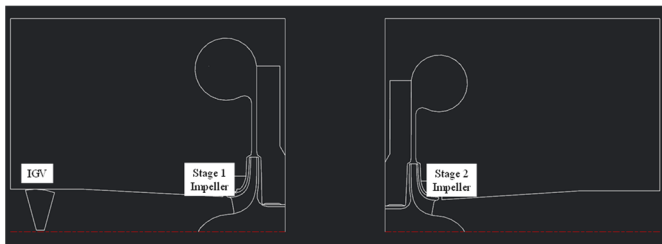


**Figure 3:** Back-to-back compressors configuration  
 © 2022 Baker Hughes Company - All rights reserved

The first impeller has a flow coefficient  $\phi=0.0320$ , defined as  $4Q_0/(\pi D_2^2 u_2)$ , and it features a dedicated design to cope with the CO<sub>2</sub> supercritical characteristics. CO<sub>2</sub> thermodynamic conditions at the inlet flange, in fact, are slightly above the critical ones, with small margins with respect to the saturation lines. Moreover, the unavoidable pressure drop which occurs from the inlet flange to the first impeller suction section further decreases this margin.

For these reasons, phase change could occur in suction regions inside the machine, around the IGV blades and inside the first impeller. Specifically, the suction side of the blade, in the proximity of the leading edge, typically shows the lowest static pressure level and, potentially, a two-phase flow could onset in the rotor channel. Where static pressure decreases below the saturation one, an abrupt change occurs in many thermodynamic quantities, the most important of which are density and speed of sound. As described in the following paragraph, the design of this machine requires an approach leveraged on proper numerical modeling, able to deal with both strong non-ideal gas behavior and the effect of potential phase change.

Impeller design, therefore, has been focused on avoiding phase change or limiting it to very small regions with also actual

CO<sub>2</sub> real gas characteristics considered. To this end, in the stage conceptual design, the following features have been selected: at first, an impeller equipped with splitter blades to decrease the blockage at the inlet and mitigate the risk of anticipated choking; secondly, an appropriate definition of the impeller cross-section evolution to take into account the low compressibility of sCO<sub>2</sub>.

## NUMERICAL METHODS

The computational flow model is based on the pressure-based Ansys Fluent finite-volume flow solver. In this work, we compare two computational frameworks to deal with non-ideal compressible two-phase flows of CO<sub>2</sub>, named *homogeneous equilibrium model* (HEM) and *barotropic mode*, respectively. Both models describe the two-phase flow in terms of mixture properties, hence single-phase governing equations are recovered and expressed in terms of proper averaged properties. The turbulence effects are included with the  $k - \omega$  SST model [20], adding a rotation-curvature correction to the production terms of  $k$  and  $\omega$  [21]. Whenever walls are modeled as smooth, the turbulence equations are resolved at the wall having wall-adjacent cells in the viscous sublayer, i.e.  $y^+ < 3$ . Otherwise, wall functions are employed to account for roughness effects.

The HEM features an enthalpy-based energy equation in place of the standard energy equation based on the total enthalpy. In this way, thermodynamic equilibrium properties for the two-phase flow can be easily invoked by using pressure and static enthalpy as independent state variables. To speed up the calculation, a look-up-table (LUT) approach is implemented to call thermodynamic properties within flow solver iterations. The LUT boundaries are set to avoid extrapolated values in the solution, and they are  $P \in [20, 300] \text{ bar}$  and  $h \in [151, 588] \text{ kJ/kg}$ , with  $h_{ref} = 200 \text{ kJ/kg}$  at  $T = 273.15 \text{ K}$  and saturated liquid condition.  $1201 \times 1201$  grid points are identified by uniform steps in pressure (0.233 bar) and specific enthalpy (0.364 kJ/kg). The detailed formulation of the flow model, its validation against experimental data, and the appropriateness of the LUT discretization are discussed in [18].

On top of the HEM assumptions, the barotropic model introduces a simplification in the thermodynamic treatment. Thermodynamic and transport properties are computed as a function of the local pressure and the upstream entropy, hence neglecting the thermal and volumetric contributions due to loss generation. Thanks to the barotropic assumption the mass and momentum equations are decoupled from the energy one, which does not need to be explicitly resolved. A similar LUT approach is implemented for the barotropic model: thermophysical properties are tabulated as a function of pressure at the upstream entropy, using for pressure the same boundaries and discretization step reported for the HEM. Such a model, though thermodynamically simplified, is deemed to be particularly relevant for turbocompressor applications, since heat transfer is usually negligible in such components and computational efficiency is crucial for their aerodynamic design and optimization. The barotropic model was first proposed for application to sCO<sub>2</sub> compressors by the same authors in [9], and

it was subsequently validated against experimental data of a MW-scale sCO<sub>2</sub> centrifugal compressor prototype in [15].

The system of equations (continuity, momentum, energy, and turbulence) is solved in the following way: continuity and momentum are solved in a coupled fashion, then the two turbulence equations and, if needed, the enthalpy-based energy equation. After this step, thermo-physical properties are updated, and the procedure is iterated until achieving numerical and physical convergence. Advective terms of continuity, momentum, and enthalpy-based energy equation are discretized with the QUICK scheme. A cell-to-cell flux limiter is applied to reduce spurious oscillations near discontinuities. Advective terms of turbulence equations are discretized with a linear upwind scheme. All diffusive terms are discretized with a second-order central differencing scheme. The gradients are computed with the least squares cell-based method. A second-order accurate method is selected to interpolate the pressure from cell centers to cell faces.

The computational grid is composed of hexahedral elements and was generated with AutoGrid™. The computational domain includes the main and splitter blade, with fillet radii, and the vaneless diffuser. A single-blade passage is modelled, by exploiting periodic boundary conditions. As the aim is to investigate the internal flow aerodynamics, the inlet guide vanes, as well as the leaks in the seals and the related secondary flows, were not the object of the CFD simulation. After a preliminary grid-dependence analysis, a mesh composed of about 3 million cells was adopted.

Calculations were performed by assigning the total state at the inlet section. The flow rate was imposed at the outflow, except close to choked-flow conditions, for which an average static pressure was assigned at the outlet. No-slip boundary conditions were imposed on the solid walls. As the flow domain is rotating with the impeller, a counter-rotating velocity was assigned at the endwalls of the vaneless diffuser.

### COMPRESSOR PERFORMANCE

The computational flow models described in the previous section were applied to investigate the aerodynamic performance of the first stage of the CO<sub>2</sub>OLHEAT compressor, namely the one most affected by the near-critical fluid state and which demanded a tailored design. Since the predictions obtained by applying the barotropic model were experimentally validated in previous studies [15], this model was considered for a first assessment of the compressor performance. In this first analysis, conventional smooth walls are considered. Figure 4 reports two operational curves of the machine, related to the pressure ratio (top) and total-total efficiency (bottom) for the nominal angular speed and meridional flow at the intake (corresponding to IGV stagger position equal to 0°). The curves are scaled with respect to the values obtained for the nominal condition, for confidentiality reasons.

Curves cover a wide range of flow conditions, from 75% to 145% of the design flow rate. On the curves, the choking limit (labelled as “C”) and the left one (labelled as “L”) are reported.

The left limit was, in fact, set *a priori*, since no expected plant operating condition should require flow coefficients below that value (also in consideration of the availability of IGVs). However, it is important to remark that the simulations for the lowest flow rate condition did not exhibit any trace of computational instabilities which normally arise approaching aerodynamic stall, thus suggesting that the actual left limit of the machine may be extended below the 75%.

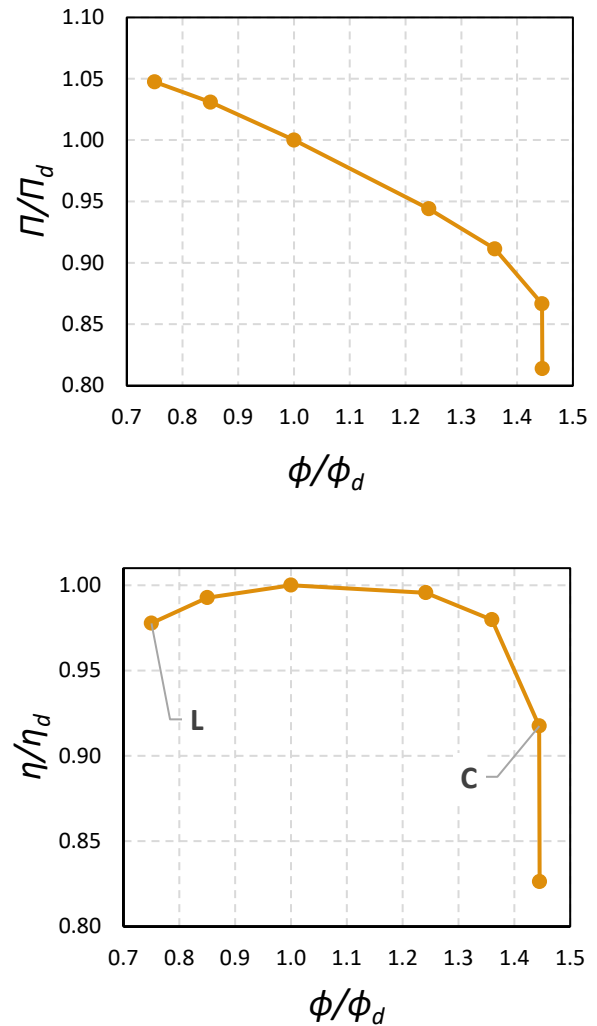


**Figure 4:** Operational curves of the first stage of the compressor simulated with the barotropic model and smooth walls. Top: pressure ratio; bottom: total-total efficiency  
© 2022 Baker Hughes Company - All rights reserved

As further proof of that, the left frame of Figure 5 shows the distribution of relative Mach number in the midspan section for the lowest flow rate considered. The figure indicates a low level of compressibility, as the relative Mach number remains below 0.3 in almost the whole blade midspan section; local accelerations appear on the suction side of the blades, as a



consequence of the positive incidence, but no traces of local separation appear, thus excluding any risk of blade stall. Similar considerations apply to the flow in the endwall regions, in particular close to the blade tip, where the highest relative Mach number and incidence are found. In the context of sCO<sub>2</sub> compressors, due to the near-critical intake state, the aforementioned local accelerations may lead to the onset of phase change, which occurs as cavitation for the present case [3], [22], [9]. Due to the abrupt drop of speed of sound in the two-phase region [23], the cavitation is normally accompanied by an abrupt rise in Mach number. Since such a feature clearly does not appear in the present case, one can conclude that the combination of the selected thermodynamic state and of the compressor intake design prevents from the onset cavitation, at least for low flow rate conditions.

An analysis of the flow, density, and pressure fields in the nominal condition, not reported for sake of brevity, confirms that the risk of phase change at the compressor intake is almost completely avoided thanks to the tailored rotor design.

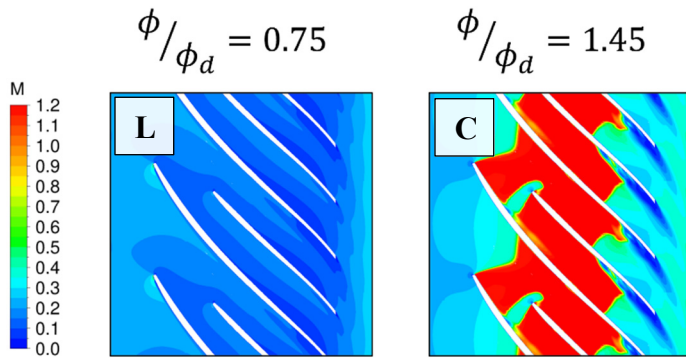


**Figure 5:** Mach number distributions at midspan for 75% (left) and 145% (right) of the nominal flow rate.

© 2022 Baker Hughes Company - All rights reserved

The situation is completely different for the conditions close to right limit. The curves clearly show the onset of choking for a flow rate equal to 145% of the design, verified by running multiple CFD simulations for different pressure ratios. Even though occurring at high flow rate, the choking is anticipated with respect to the value expected by neglecting the onset two-phase flows; this phenomenon was clearly shown in a previous study, where a CO<sub>2</sub> compressor was operated in conditions near and far from the critical point [24]. The right frame of Figure 5, showing the Mach number distribution at midspan for the right limit condition, shows that upstream of the blades the Mach number remains below 0.5; however, as the flow enters within the bladed channel, the combination of blade thickness, blade aerodynamics, and negative incidence promotes a static pressure drop sufficiently large to trigger phase change; this, in turn, implies an abrupt rise of relative Mach number, causing the onset of choking. The value of the choking flow rate, which in principle might depend on the degree of chemical and thermal equilibrium established between the phases of mixture, was

found to be properly captured by models based on the homogeneous equilibrium assumption, such as the present barotropic one, by virtue of an experimental validation study made on a MW-scale sCO<sub>2</sub> compressor [15].

In light of the present analysis, the first CO<sub>2</sub>OLHEAT compressor is capable to provide the expected performance in a very large range of operation, greatly limiting the most severe effects of two-phase flows to very high flow rate conditions, not even expected in the off-design operation of the system.

## MODEL COMPARISON

The CFD model based on the barotropic fluid assumption was experimentally validated and features a computationally-effective mathematical formulation. However, in an effort of improving the generality of sCO<sub>2</sub> compressor simulation tools, its verification against more complex models is relevant, at least to evaluate its range of validity and limitations. To this end, the aerodynamics of the first CO<sub>2</sub>OLHEAT compressor was simulated with a complete CFD-HEM, namely a computational model capable of simulating the dynamics of two-phase mixtures without resorting to the barotropic assumption. In this way, the thermal and volumetric effects of entropy generation across the compressor are taken into account and, hence, a correction on the meridional flow component might occur, with potential implications on the work exchange, pressure rise, and compressor efficiency. When constructing this ‘reference’ simulation tool, we still focused on a model that treats the two-phase flow assuming homogeneous equilibrium between the phases. This is motivated by the experimental validations available in literature for flashing flows in sCO<sub>2</sub> nozzles [17], ejectors [25] and sCO<sub>2</sub> compressors [15], which all agree in recognizing a good capability of the HEM in reproducing the phase change processes evolving from near-critical states. For this reason, the generalization of the barotropic model was focused on the single-phase thermodynamics rather than on the multi-phase model.

Figure 6 reports the operational curves, in terms of pressure ratio and efficiency as simulated by both the barotropic model and the HEM. The curves exhibit a noteworthy agreement, both qualitative and quantitative, suggesting that the thermal effects play a negligible role in the compressor performance. In an effort of explaining the obtained results, Figure 7 reports the streamwise evolution of density and meridional velocity component along the compressor in the nominal operation for both the computational models. The density distribution exhibits a slight reduction upstream of the main-blade leading edge (placed at a streamwise coordinate equal to 0.23), followed by a regular increasing trend, which terminates with a density increase of about 10% of the intake value (which indicates the low compressibility of the fluid in the present condition). As already stated, the physical effect not captured by the barotropic model is the volumetric implication of dissipation, which increases the thermal energy of the fluid as entropy generates along the irreversible compression process.

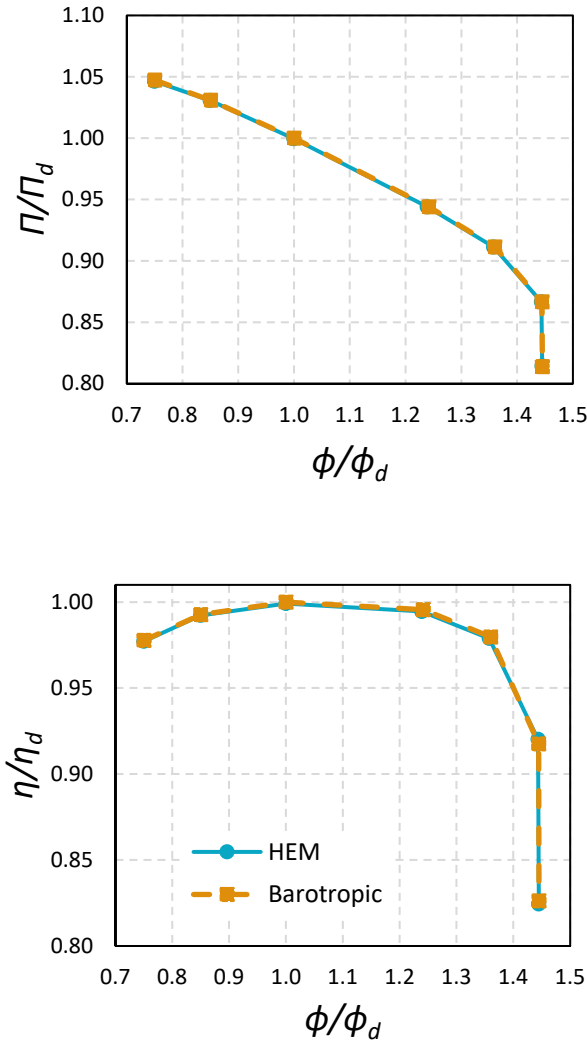


**Figure 6:** Comparison between operational curves of the first stage of the compressor simulated with the barotropic model and the HEM, for smooth walls.

© 2022 Baker Hughes Company - All rights reserved

Figure 7 actually shows a deviation between barotropic and HEM predictions as the compression proceeds along the machine with, as expected, a lower density computed by the HEM. Such differences are completely negligible along the impeller (the trailing edge of the blades is placed at a streamwise coordinate of 0.62) while they become visible in the vaneless diffuser section (due to the entropy generated downstream of the impeller). The maximum difference, however, is of the order of 0.2% of the actual density value, or 2% of the (already low) overall change in density across the machine.

The change in density, though small, might have an impact on the flow configuration and in the velocity triangles, as it alters the meridional flow component. For this reason, Figure 7 also reports the streamwise distribution of the meridional flow velocity for barotropic and HEM predictions. The distribution shows an increase in meridional velocity within the impeller,

with local disturbances in correspondence of the leading and trailing edge of the blades. The diagram indicates that the impact of the barotropic assumption is everywhere negligible, so the cinematics of the machine is properly estimated by both the models.

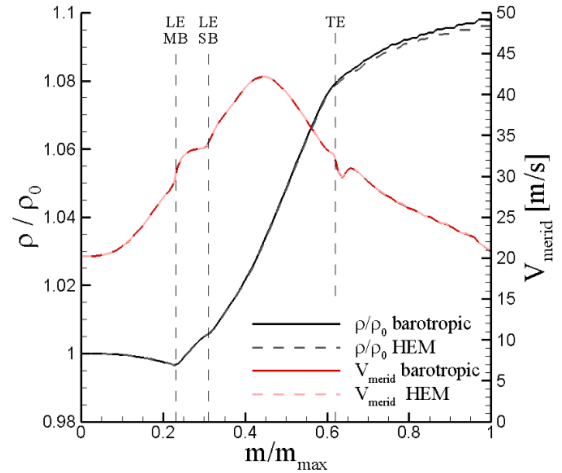


**Figure 7:** Streamwise evolution of density and meridional flow velocity along the meridional coordinate in nominal condition (LE-MB : leading edge main blades, LE\_SB : leading edge splitter blades; TE: blades trailing edge).

© 2022 Baker Hughes Company - All rights reserved

Figure 8 reports the same quantities as Figure 7 for the two limit conditions of operation of the compressor, identified in Figure 4. The same considerations made for the nominal condition apply to the low flow rate one, while a different flow configuration emerges at high flow rate, which is characterized by cavitation-induced choking. In this latter case, the density of the fluid undergoes a severe drop in the proximity of the main-blade leading edge and further reduces in correspondence to the leading edge of the splitter blade; the density finally reaches its minimum value in the central region of the channel, where the meridional velocity exhibits its peak value, and the two-phase mixture occupies the whole channel. Then, the density progressively rises and the fluid reverts to single phase in the rear part of the impeller (from  $\sim 0.52$  streamwise coordinate onwards). In the central part of the channel, where the largest oscillations take place, the models exhibit slight local differences in density, which however disappear in the rear part of the impeller; as already observed in the other conditions, a residual marginal difference in density remains at the stage exit, of about 0.6% of the local density value, or 1.6% of the density variation along the impeller. In terms of meridional flow velocity, minor variations appear also in this case, even in the two-phase region in the center of the channel.

This analysis explains why the barotropic flow model is able to reproduce the complexity of the sCO<sub>2</sub> compressor aerothermodynamics, at least for the thermodynamic condition of interest for this study. However, operating sCO<sub>2</sub> in the present thermodynamic region is advantageous for sCO<sub>2</sub> power systems,

so the validity of the present modeling is deemed relevant for the sCO<sub>2</sub> technology and not only for this specific case.

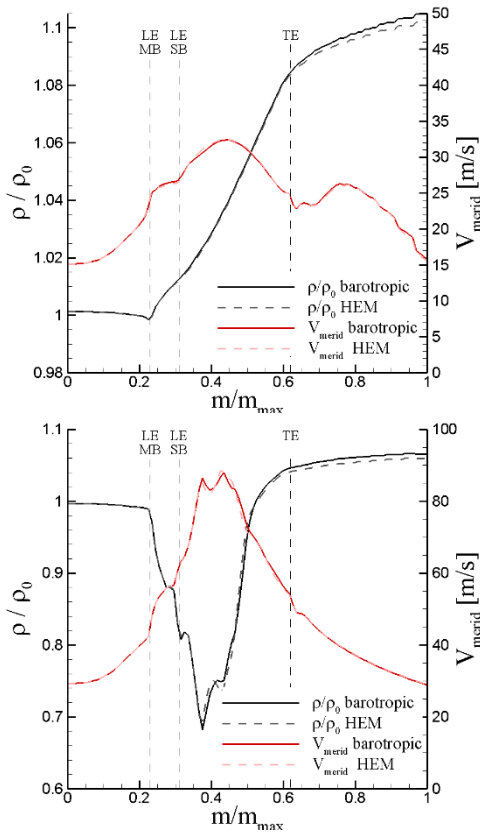


**Figure 8:** Streamwise evolution of density and meridional flow velocity along the meridional coordinate for 75% (top) and 145% (bottom) of the nominal flow rate.  
© 2022 Baker Hughes Company - All rights reserved

### IMPACT OF WALL ROUGHNESS

The power capacity of waste heat recovery systems is relatively low with respect to conventional power systems, especially in the present demonstration plant. This feature, combined with the inherent compactness of sCO<sub>2</sub> machines, makes size-effects particularly relevant for the CO<sub>2</sub>OLHEAT compressors. In an effort of investigating the aerodynamic impact of small size, a computational evaluation of the wall roughness was performed, using the complete HEM model and simulating the entire range of machine operation. An equivalent sand grain roughness  $k_s$  equal to 5  $\mu\text{m}$  was selected, representative of a standard manufacturing technology, though not indicative of the manufacturer's capabilities. Nonetheless, for this fluid in the thermodynamic conditions of interest the thickness of the viscous sublayer is estimated to be of the order of  $10^{-2} \mu\text{m}$ , thus one might expect that such a value of surface roughness will alter the development of the boundary layer and the associated loss generation.

Figure 9 compares the curves of total-total pressure ratio and efficiency of the first stage of the CO<sub>2</sub>OLHEAT compressor

showing important quantitative effects. In the nominal flow rate conditions, the roughness reduces by 1% the pressure ratio and 3% the efficiency. These differences are maintained fairly constant along the whole operating range (the lower difference appearing at the choking is, in fact, an artificial effect of the nearly vertical shape of the curve in this region, which greatly complicates the comparison between different conditions). Moreover, the roughness does not influence the left limit, where, again, no traces of stall onset appeared in the simulations, and especially at choking, which is reached for the same flow rate as the smooth-wall calculation.

These results confirm the significant quantitative role of wall roughness in terms of compressor performance, suggesting care in the selection of the manufacturing process, but they also indicate a limited impact of roughness on compressor rangeability.

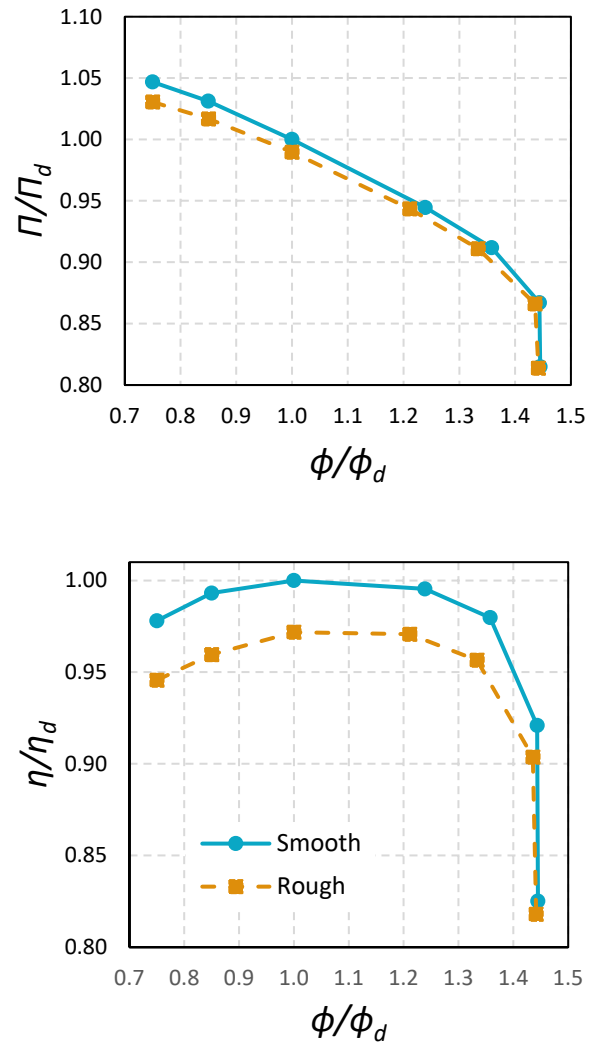


**Figure 9:** Effect of the wall roughness on the operational curves of the first stage of the compressor simulated with the HEM.  
© 2022 Baker Hughes Company - All rights reserved

## CONCLUSION

This paper has presented the design and the computational analysis of the near-critical sCO<sub>2</sub> compressor of the CO2OLHEAT waste heat recovery system. The machine, composed by two back-to-back compressor stages, features an integrated architecture and a non-conventional design approach for the first impeller, due to the thermodynamic complexity associated to the working fluid, which is operated close to the thermodynamic critical point.

The aerodynamics of the first stage of the compressor was analyzed with Computational Fluid Dynamics, applying both an experimentally-validated solver based on the barotropic fluid model and an alternative solver based on a more complete thermodynamic model. Both the solvers are capable of simulating non-ideal two-phase flows of sCO<sub>2</sub>, under the assumption of homogeneous equilibrium between the phases. The two models have been shown to provide very similar results, with minor quantitative differences in local regions of the flow, negligible in terms of fluid kinematics.

The first stage of the compressor was analyzed in multiple operating conditions, so to characterize the entire range of machine operation, and it was shown to guarantee rangeability in the range 75% - 145% of the nominal flow rate. The left limit is, in fact, set a priori and does not exhibit any stall onset; the right limit is caused by the onset of choking, due to the phase-change process. A detailed investigation of the compressor aerodynamics reveals that, thanks to the dedicated machine design of the intake region, two-phase flows are negligible for the left side of the curve, and become significant only above nominal flow rate.

Finally, the size-effect associated with the wall roughness was investigated, showing a relatively significant influence on the compressor performance (up to 3% of efficiency, for a sand grain roughness of 5 microns, fairly constant along the compressor curve), but a negligible impact on the compressor rangeability.

## NOMENCLATURE

$\Pi$	total-total pressure ratio
$\eta$	total-total efficiency
$\phi$	flow coefficient
M	Mach number
$\rho$	density [kg/m <sup>3</sup> ]
V	velocity [m/s]
m	streamwise coordinate

### Subscripts

0	intake thermodynamic state
d	nominal condition
max	maximum value
merid	meridional component

## ACKNOWLEDGEMENTS

The CO2OLHEAT project has received funding from the European Union's Horizon 2020 research and innovation programme under grant agreement N° 101022831.

## REFERENCES

- [1] O. Reimann, "CEWEP Energy Report III (Status 2007-2010)," Confederation of European Water-to-Energy Plants, www.cewep.eu, 2012.
- [2] M. Marchionni, G. Bianchi and S. Tassou, "Review of supercritical carbon dioxide (sCO<sub>2</sub>) technologies for high-grade waste heat to power conversion," *SN Applied Sciences*, vol. 2, no. 611, 2020.
- [3] R. Pecnik, E. Rinaldi and P. Colonna, "Computational fluid dynamics of a radial compressor operating with supercritical CO<sub>2</sub>," *Journal of Engineering for Gas Turbines and Power*, vol. 134, no. 12, 2012.
- [4] N. D. Baltadjiev, C. Lettieri and Z. S. Spakovszky, "An investigation of real gas effects in supercritical CO<sub>2</sub> centrifugal compressors," *Journal of Turbomachinery*, vol. 137, 2015.
- [5] R. Pelton, T. Allison, S. Jung and N. Smith, "Design of a Wide-Range Centrifugal Compressor Stage for Supercritical CO<sub>2</sub> Power Cycles," in *ASME Turbo Expo 2017*, Charlotte, NC, USA, 2017.
- [6] A. Hacks, S. Schuster, H. J. Dohmen, F. K. Benra and D. Brillert, "Turbomachine Design for Supercritical Carbon Dioxide Within the sCO<sub>2</sub>-HeRo.eu Project," *Journal of Engineering for Gas Turbines and Power*, vol. 140, 2018.
- [7] M. Marchionni, L. Chai, G. Bianchi and S. Tassou, "Numerical modelling and transient analysis of a printed circuit heat exchanger used as recuperator for supercritical CO<sub>2</sub> heat to power conversion systems," *Applied Thermal Engineering*, vol. 161, no. 114190, 2019.
- [8] A. Hosangadi, Z. Liu, T. Weathers, V. Ahuja and J. Busby, "Modeling multiphase effects in CO<sub>2</sub> compressors at subcritical inlet conditions," *Journal of Engineering for Gas Turbines and Power*, vol. 141, no. 8, 2019.
- [9] G. Persico, P. Gaetani, A. Romei, L. Toni, E. Bellobuono and R. Valente, "Implications of phase change on the aerodynamics of centrifugal compressors for supercritical carbon dioxide applications," *Journal of Engineering for Gas Turbines and Power*, vol. 143, no. 4, 2021.
- [10] V. Dostal, A Supercritical Carbon Dioxide Cycle for Next Generation, Ph.D. thesis, Massachusetts Institute of Technology, 2004.
- [11] S. A. Wright, R. F. Radel, M. E. Vernon, G. E. Rochau and P. S. Pickard, *Operation and Analysis of a Supercritical CO<sub>2</sub> Brayton Cycle*, Sandia Report SAND2010-0171, 2010.
- [12] A. Romei, P. Gaetani, A. Giostri and G. Persico, "The role of turbomachinery performance in the optimization of supercritical carbon dioxide power systems," *Journal of Turbomachinery*, vol. 142, no. 7, p. 071001, 2020.
- [13] D. Alfani, M. Binotti, E. Macchi, P. Silva and M. Astolfi, "sCO<sub>2</sub> Power Plants for Waste Heat Recovery: Design

- Optimization and Part-Load Operation Strategies," *Applied Thermal Engineering*, vol. 195, 2021.
- [14] J. Mortzheim, D. Hofer, S. Piebe, A. McClung, J. J. Moore and S. Cich, "Challenges With Measuring Supercritical CO<sub>2</sub> Compressor Performance When Approaching the Liquid-Vapor Dome," in *ASME Turbo Expo 2021*, 2021.
- [15] L. Toni, E. Bellobuono, R. Valente, A. Romei, P. Gaetani and G. Persico, "Computational and Experimental Assessment of a MW-Scale Supercritical CO<sub>2</sub> Compressor Operating in Multiple Near-Critical Conditions," *Journal of Engineering for Gas Turbines and Power*, vol. 144, no. 10, 2022.
- [16] M. Bigi, V. Bisio, S. Evangelisti, M. Giancotti, A. Milani and T. Pellegrini, "Design and Operability Challenges for Supercritical CO<sub>2</sub> Plants: The sCO<sub>2</sub>-Flex Centrifugal Compressor Test Experience," in *ASME Turbo Expo 2022*, 2022.
- [17] A. Romei and G. Persico, "Computational fluid-dynamic modelling of two-phase compressible flows of carbon dioxide in supercritical conditions," *Applied Thermal Engineering*, 2021.
- [18] A. Romei, P. Gaetani and G. Persico, "Computational fluid-dynamic investigation of a centrifugal compressor with inlet guide vanes for supercritical carbon dioxide power systems," *Energy*, 2022.
- [19] D. Alfani, M. Asolfi, M. Binotti, P. Silva and G. Persico, "Part load analysis of a constant inventory supercritical CO<sub>2</sub> power plant for waste heat recovery in cement industry," in *The 5th European sCO<sub>2</sub> Conference for Energy Systems*, 2023.
- [20] F. R. Menter, "Two-Equation Eddy-Viscosity Turbulence Models for Engineering Applications," *AIAA Journal*, vol. 32, no. 8, pp. 1598-1605, 1994.
- [21] P. E. Smirnov and F. R. Menter, "Sensitization of the SST Turbulence Model to Rotation and Curvature by Applying the Spalart-Shur Correction Term," *Journal of Turbomachinery*, vol. 131, no. 4, p. 041010, 2009.
- [22] S. Saxena, R. Mallina, F. Moraga and D. Hofer, "Numerical Approach for Real Gas Simulations: Part II – Flow Simulation for Supercritical CO<sub>2</sub> Centrifugal Compressor," in *ASME Turbo Expo 2017*, 2017.
- [23] C. E. Brennen, *Fundamentals of Multiphase Flows*, Cambridge University Press, 2005.
- [24] L. Toni, E. F. Bellobuono, R. Valente and A. R. P. G. G. Persico, "Experimental and Numerical Performance Survey of a MW-Scale Supercritical CO<sub>2</sub> Compressor Operating in Near-Critical Conditions," in *The 7th international supercritical CO<sub>2</sub> power cycle symposium*, San Antonio, Texas, 2022.
- [25] K. Ringstad, Y. Allouche, P. Gullo, Å. Ervik, K. Banasiak and A. Hafner, "A detailed review on CO<sub>2</sub> two-phase ejector flow modeling," *Thermal Science and Engineering Progress*, 2020.
- [26] S. D. Cich, J. Jeffrey Moore, M. Marshall, K. Hoopes, J. Mortzheim and D. Hofer, "Radial Inlet and Exit Design for a 10 MWe sCO<sub>2</sub> Axial Turbine," in *ASME Turbo Expo 2019*, 2019.
- [27] A. Hosangadi, Z. Liu, T. Weathers, V. Ahuja and J. Busby, "Modeling Multiphase Effects in CO<sub>2</sub> Compressors at Subcritical Inlet Conditions," *Journal of Engineering for Gas Turbines and Power*, vol. 141, 2019.



# DuEPublico

Duisburg-Essen Publications online

UNIVERSITÄT  
DUISBURG  
ESSEN

*Offen im Denken*

ub | universitäts  
bibliothek

This text is made available via DuEPublico, the institutional repository of the University of Duisburg-Essen. This version may eventually differ from another version distributed by a commercial publisher.

**DOI:** 10.17185/duepublico/77259

**URN:** urn:nbn:de:hbz:465-20230427-152859-2



This work may be used under a Creative Commons Attribution 4.0 License (CC BY 4.0).